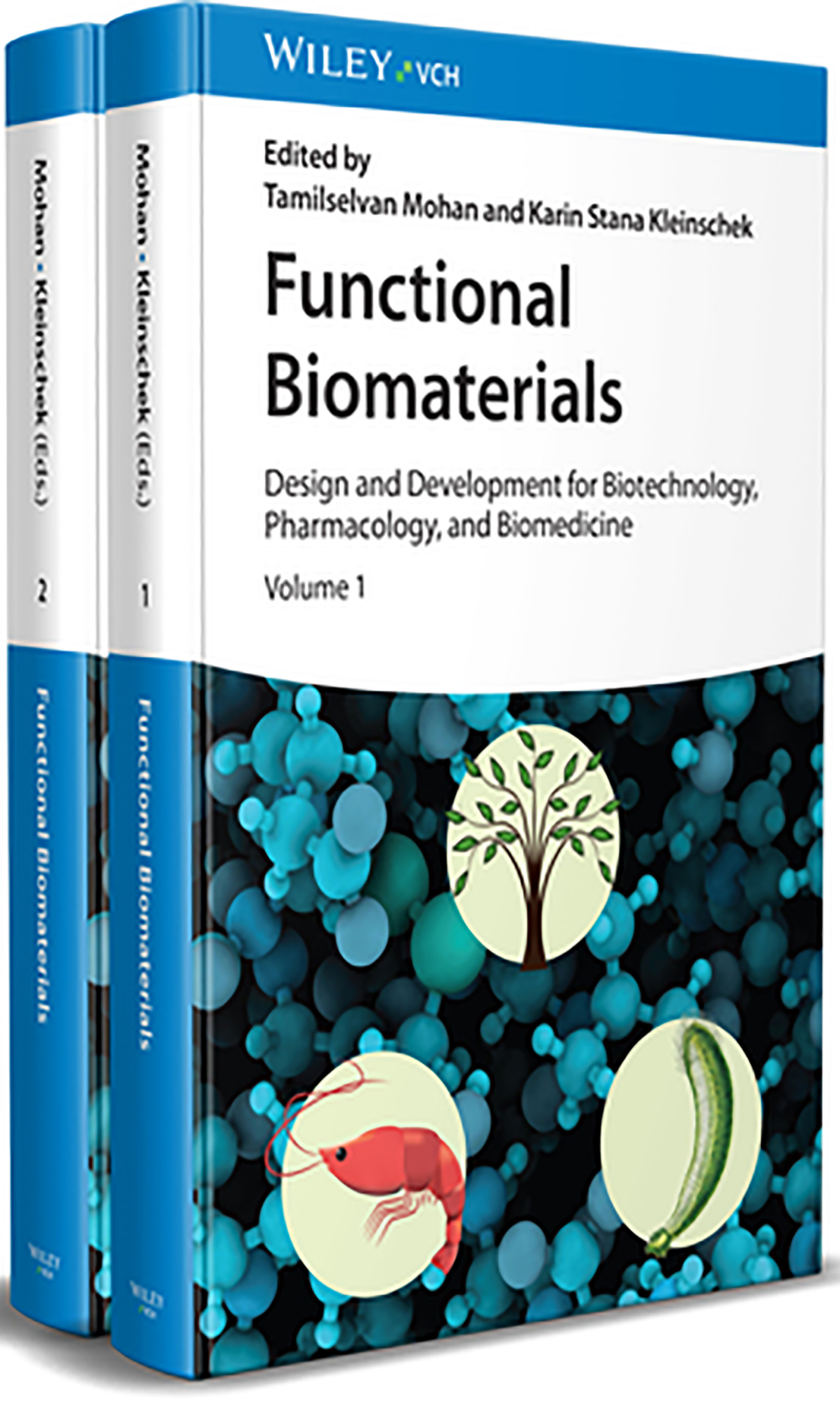
WILEY VCH
Edited by
Tamilselvan Mohan and Karin Stana Kleinschek
Functional Biomaterials
Design and Development for Biotechnology, Pharmacology, and Biomedicine
Volume 1
Mohan • Kleinschek (Eds.)
1
Functional Biomaterials
Mohan • Kleinschek (Eds.)
2
Functional Biomaterials

Functional Biomaterials

Functional Biomaterials

Design and Development for Biotechnology, Pharmacology, and Biomedicine

Volume 1

Edited by Tamilselvan Mohan and Karin Stana Kleinschek

WILEY VCH

Functional Biomaterials

Design and Development for Biotechnology, Pharmacology, and Biomedicine

Volume 2

Edited by Tamilselvan Mohan and Karin Stana Kleinschek

WILEY VCH

The Editors

Prof. Tamilselvan Mohan
Graz University of Technology
Institute for Chemistry and Technology
of Bio-Based Systems (IBioSys)
Stremayrgasse 9
8010 Graz
Austria

and

University of Maribor
Faculty of Mechanical Engineering
Laboratory for Characterization and
Processing of Polymers
Smetanova Ulica 17
2000 Maribor
Slovenia

Prof. Karin Stana Kleinschek
Graz University of Technology
Institute for Chemistry and Technology
of Bio-Based Systems (IBioSys)
Stremayrgasse 9
8010 Graz
Austria

Cover Image: © Pixabay

Library of Congress Card No.: applied for

British Library Cataloguing-in-Publication Data
A catalogue record for this book is available from the British Library.

Bibliographic information published by the Deutsche Nationalbibliothek
The Deutsche Nationalbibliothek lists this publication in the Deutsche Nationalbibliografie; detailed bibliographic data are available on the Internet at <http://dnb.d-nb.de>.

Print ISBN: 978-3-527-35157-2
ePDF ISBN: 978-3-527-82764-0
ePub ISBN: 978-3-527-82766-4
oBook ISBN: 978-3-527-82765-7

Typesetting Straive, Chennai, India

The Editors

Prof. Tamilselvan Mohan
Graz University of Technology
Institute for Chemistry and Technology
of Bio-Based Systems (IBioSys)
Stremayrgasse 9
8010 Graz
Austria

and

University of Maribor
Faculty of Mechanical Engineering
Laboratory for Characterization and
Processing of Polymers
Smetanova Ulica 17
2000 Maribor
Slovenia

Prof. Karin Stana Kleinschek
Graz University of Technology
Institute for Chemistry and Technology
of Bio-Based Systems (IBioSys)
Stremayrgasse 9
8010 Graz
Austria

Cover Image: © Pixabay

Library of Congress Card No.: applied for

British Library Cataloguing-in-Publication Data
A catalogue record for this book is available from the British Library.

Bibliographic information published by the Deutsche Nationalbibliothek
The Deutsche Nationalbibliothek lists this publication in the Deutsche Nationalbibliografie; detailed bibliographic data are available on the Internet at <http://dnb.d-nb.de>.

Print ISBN: 978-3-527-35158-9
ePDF ISBN: 978-3-527-82764-0
ePub ISBN: 978-3-527-82766-4
oBook ISBN: 978-3-527-82765-7

Typesetting Straive, Chennai, India

Contents

Contents

Preface

Broadening the spectrum of biopolymers, their classification, chemical nature, isolation, and characterization is very important for better understanding the usability of biopolymers in new applications. It is also important for the development of completely new materials based on the special properties of polysaccharides (cellulose-based and others) compared to the biomaterials currently used in various high-tech applications (e.g. inorganic materials and non-degradable synthetic polymers). In this context, this book focuses largely on the fundamental knowledge of biopolymers (natural: cellulose and its derivatives; other polysaccharides such as chitosan, glycosaminoglycans (GAG's), etc.; and synthetic ones such as polyethylene terephthalate and others), their origin, classifications, chemical nature, and isolation methods. This book also covers various classical and modern approaches to the transformation of these biopolymers into different forms, from thin films (model surfaces), nanoparticles, nanofibers, to 3D scaffolds. The application of these biopolymer-based multifunctional materials (e.g. 2D thin films to 3D scaffolds) in applications such as biosensors (e.g. for detection of DNA, antibodies, affibodies, and moisture sensors), antifouling surfaces, drug delivery systems, microfluidic devices, microarrays, two-photon absorption lithography, enzymatic digestion systems, wound models, to name a few important areas are also discussed in detail. A library of analytical methods used for the analysis of morphology, structure, shape, thermal, electrical, and surface properties, as well as for the study of solid–liquid interaction of biomaterials, is also covered in detail in this book.

It also provides a comprehensive overview of the latest developments in the applicability of biopolymers, especially polysaccharides, for the production of sustainable biomaterials used in medicine, focusing on potential applications and future developments. Therefore, it is unique and of interest not only to students and scientists but also to industry as well as stakeholders and policy makers. This coincides with recent trends to replace fossil materials with indigenous materials. In addition, readers will get an overview of the specific and very special properties of biopolymers that can be used for the production of sustainable but high-quality functional biomaterials. Overall, this book will contribute to a better understanding of the physicochemical properties of biopolymers and their use in the preparation of completely new materials for various advanced biomedical applications. In summary, there are no books

to date that deal exclusively with the classification, isolation, preparation, and characterization of biopolymers and the design of new functional biomaterials, with a particular emphasis on the application of biomaterials in various advanced technological applications.

The content of the book is formulated to serve as a reference for the fundamental understanding of biopolymers/biomaterials and can be used by academicians, industrialists, researchers, graduate, and undergraduate students.

Graz/Austria, April 2022

Tamilselvan Mohan
Karin Stana Kleinschek

1

Definitions and Types of Microbial Biopolyesters and Derived Biomaterials

Martin Koller[1,2]

[1] *University of Graz, Institute of Chemistry, NAWI Graz, Heinrichstrasse 28/VI, 8010 Graz, Austria*
[2] *ARENA – Association for Resource Efficient and Sustainable Technologies, Inffeldgasse 21b, 8010 Graz, Austria*

1.1 Introduction

The increasing quantities of petrol-based plastics used for numerous applications in our daily life are among the most prevailing ecological threats of our days. In this regard, we are steadily confronted with phrases currently circulating in the media such as "plastic contamination of marine ecosystems," "microplastic," "growing garbage dumps," and "bans on everyday plastic materials" such as traditional "plastic shopping bags" or, more recently, cotton swabs with plastic rods or plastic drinking straws. Indeed, the currently produced plastics amount to more than 400 megatons (Mt) annually; their production exploits limited fossil resources, and, after their life span, these plastics need to be disposed of due to their lacking biodegradability [1–3]. In the beginning of 2020, approximately 150 Mt of plastics have already accumulated in the world's oceans alone, estimated to cause perishing of 100 000 marine mammals and about ten times as many birds year by year [4]. Just the other day, the dramatic death of a sperm whale carrying an unbelievable number of around eighty plastic bags in its, making it impossible for the animal to take organic food, and shocked the general public [5]. Only recently, Zheng et al. reported an estimate that, by 2050, the global production of plastics will quadruple, which will be connected with a doubling of plastic waste [6].

In fact, significantly less than one third of plastic waste is recycled in Europe, the rest ends up in landfills or in the environment, or is simply burned [7]. In this context, the increased release of microplastics from recycled food containers, especially from plastic bottles ("Re-PET"), into food, been described [8]. Moreover, it should be noted that recycling of plastic delays, rather than prevents, its final disposal in landfills [9]. Landfilled plastic waste, in turn, returns to the sea via detours, such as wind or river systems, and finally enters the food chain as microplastic and eventually into the human metabolism. This cycle applies to about 500 000 t

Functional Biomaterials: Design and Development for Biotechnology, Pharmacology, and Biomedicine, First Edition. Edited by Tamilselvan Mohan and Karin Stana Kleinschek.

of plastic waste per year in the EU alone. It is self-explanatory that this represents enormous risks for the biosphere and the health of the entire world population. But from the resource-technological perspective as well, our today's dependence on plastic is inadequate, unsustainable, and short sighted not only because current plastics production depends on exploiting limited fossil resources, but also because most plastic products are *per definitionem* designed as disposable products for single use only. This circumstance is a major environmental "fire accelerator"; as typical "end-of-the-pipe" product, plastics donate high short-term benefits through their favorable nature and, at the same time, are available at the discount price.

In particular, microplastics directly endanger food security and human health; starting from their consumption by plankton, such microplastics, which *per definitionem* have particle sizes ranging from 0.1 to 5.000 µm, easily climb up the entire trophic chain, until they finally get accumulated in its top, namely the human metabolism. Only during the last few years, concrete understanding of the detritus mechanisms of microplastic on the ecosystem and the metabolism of animals and humans is developing. In addition to microplastic uptake via the trophic chain, diverse techniques during food production using equipment with plastic parts, in addition to food storage in plastic containers like bottles, are also direct source of microplastic contamination of food, mainly by abrasion and by the currently fashionable use of recycled poly(ethylene terephthalate) (PET) bottles [8]. The documentation and quantification of possible diverse effects of microplastics on human health is currently only in its infancy. In 2018, microparticles in the size of 50–500 µm of a total of nine different petrochemical plastics, predominately poly(propylene) (PP) and PET, were for the first time clearly identified by an Austrian research team in the human intestine [10]. Considering the fact that the deterioration of intestine cells (villi) by microplastics was already demonstrated for fish and nematodes [11], it has to be expected that such microplastic particles also cause negative reactions in the human intestine, such as inflammation or even cancer. Moreover, by intestinal uptake, microplastics could potentially be transported to the blood and lymph system and to various organs.

To change this situation, a reasonable and fair pricing of plastics is required, reflecting not only its benefits but also the damage caused by the high environmental footprint of this end-of-pipe technology. In this way, plastics would no longer be disposed of in bulk; even more important, a fair pricing would, wherever possible, foster the production and implementation of alternative materials like bioinspired alternatives in order to finally find the way out of the "plastic predicament" [4].

1.2 Biopolymers as Bioinspired Alternatives

1.2.1 Defining "Bioplastics" Is No Trivial Task!

Looking back to the very beginnings of the "plastic age," we remember that the first plastic-like polymer indeed was biobased, namely natural *cis*-1,4-poly(isoprene) rubber obtained from the rubber tree *Hevea brasiliensis* (reviewed by Wycherley [12]).

However, especially the decades between 1940 and the turn of the millennium were dominated by synthetic, not biodegradable, polymers of petrochemical origin. As a real alternative to many of the currently used plastics, one can switch to bio-inspired alternatives [13]. In this context, we have to be careful when talking about "bioplastics," which is a scientifically ambiguous expression. It is of major importance to differentiate different groups of "bioplastics":

(a) Plastics that are biobased (originating from renewable resources) and, at the same time, biosynthesized (monomers converted to polymers by the action of living organisms), and biodegradable/compostable. Prime examples: microbial polyhydroxyalkanoates (PHA life cycle). As additional characteristic, PHAs are also biocompatible; hence, they do not exert any negative effect on the biosphere surrounding them (e.g. living organisms, cell lines, ecosystems) according to the standardized ISO 10993 norm. Other natural polymers, which can be processed to generate materials with plastic-like properties (e.g. processing starch to thermoplastic starch [14] – TPS life cycle; see Figure 1.1), or others, e.g. proteins gelatin [15], whey proteins [16], etc., chitin [17], or cellulose [18], which are compatible with PHA and other polymers, also belong to the group of biopolymers *sensu stricto*.
(b) Plastics that are biobased and biodegradable/compostable, but not biosynthesized (monomers converted to polymers by classical chemical methods, often demanding toxic catalysts). Prime example: poly(lactic acid) (PLA), which currently is considered a competitor of PET or poly(styrene) (PS); for the life cycle of PLA, please refer to Figure 1.2. Here, one has to consider high recalcitrance of highly crystalline PLA toward biodegradation and restrictions regarding its *in vivo* biocompatibility [19].
(c) Plastics that are biobased, but neither biosynthesized nor biodegradable/compostable. Prime example: biobased poly(ethylene) (bio-PE), which resorts to chemical conversion of saccharose to ethylene via ethanol and chemical polymerization of ethylene to PE (life cycle; see Figure 1.3). Such "bio-PE" is currently strongly emerging regarding its market volume, which is expected to amount to estimated 300 000 t per year in 2022. In 2018, even the company LEGO™ switched to bio-PE to manufacture their globally famous toy bricks; however, bio-PE is not biodegradable, and its production exploits food resources [20]. Partly, this group also encompasses the "green bottle" commercialized by The Coca Cola™ company, which consists of so-called "biobased PET"; however, this material has a biobased carbon content stemming from renewable resources (the ethylene part) of only 30%, and is not biodegradable/compostable [21].
(d) Other plastics are not biobased and not biosynthesized, but still biodegradable/compostable; they have a petrochemical origin. Prime examples are poly(ε-caprolactone) (PCL [22] life cycle: see Figure 1.4), or the random copolyester poly(butylene adipate terephthalate) (PBAT), which is used for materials commercialized by, e.g. the company BASF SE under the trade name Ecoflex® and follow-up products ([23] life cycle: see Figure 1.5). These materials enter the natural cycle of carbon after being biodegraded; hence, they do not

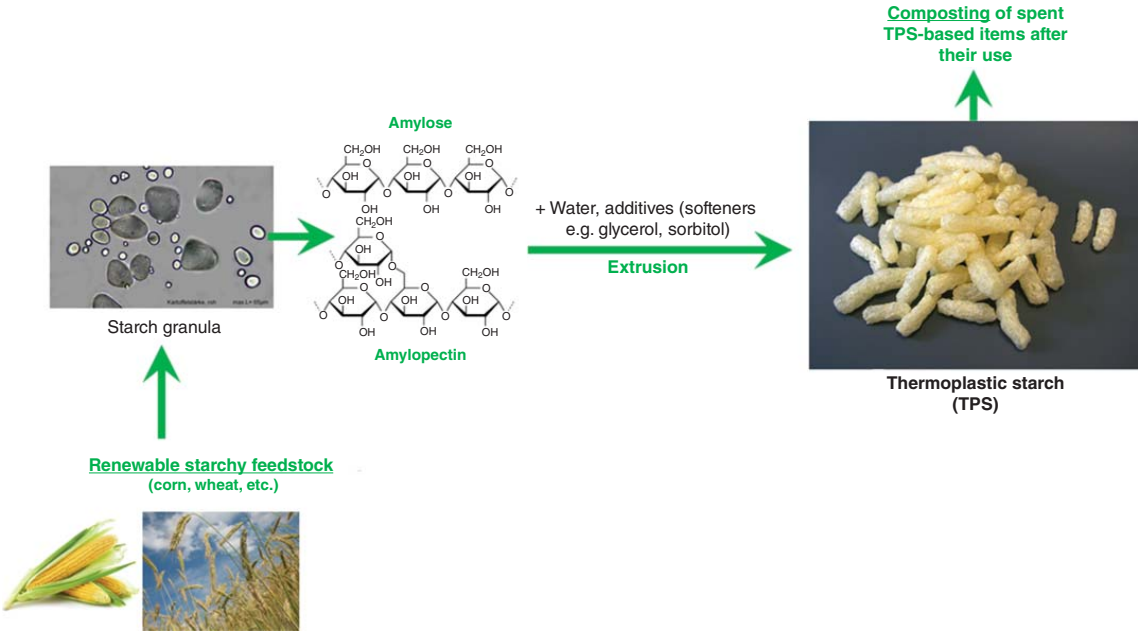

Figure 1.1 Production and life cycle of TPS. Source: Christian Gahle/Wikimedia Commons/CC BY-SA 3.0; atoss/Adobe Stock; Robin/Pixabay.

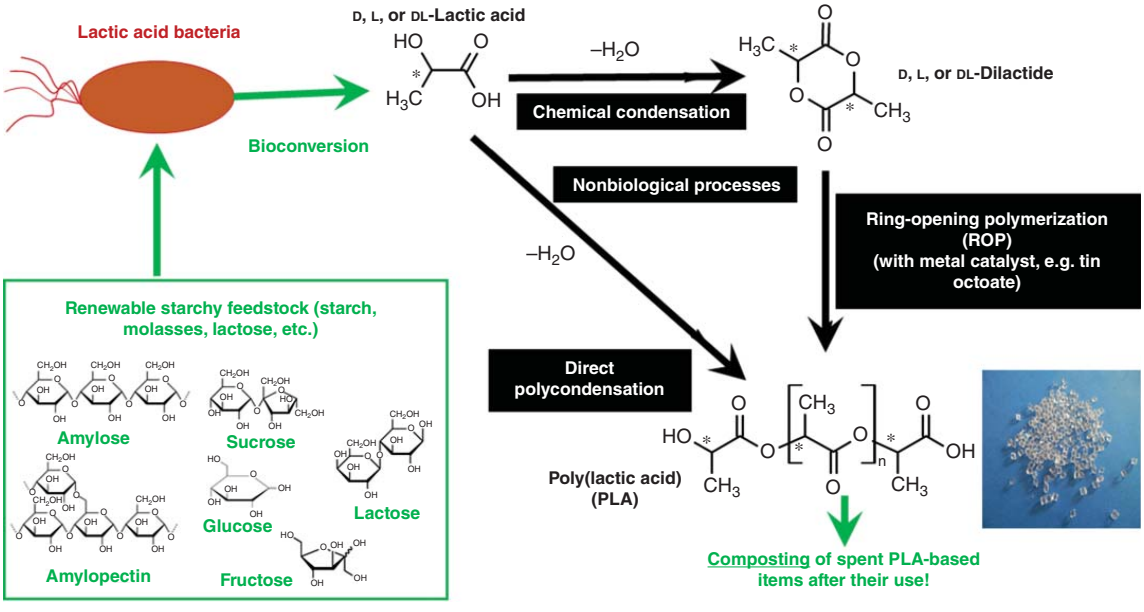

Figure 1.2 Production and life cycle of PLA. The * in the graphic indicates chiral centers. Source: epitavi/Adobe Stock.

Figure 1.3 Production and life cycle of "bio-PE." Source: lzf/Adobe Stock.

Figure 1.4 Production and life cycle of PCL. Source: epitavi/Adobe Stock.

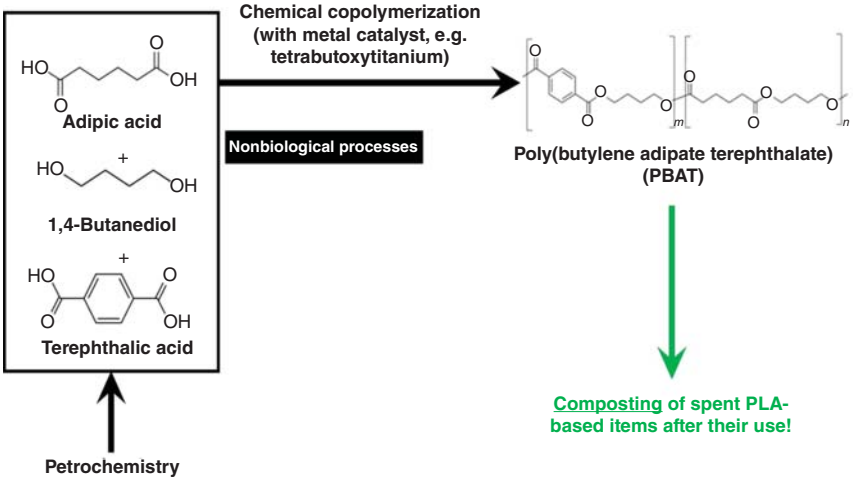

Figure 1.5 Production and life cycle of PBAT (Ecoflex®).

need to be incinerated or landfilled, but their production still exploits fossil resources (cyclohexanone made of cyclohexane in the case of PCL, or adipic acid, 1,4-butanediol, and terephthalic acid in the case of PBAT, respectively) [22].

(e) Classical synthetic thermoplastic and elastomeric resins, among them PE (life cycle: see Figure 1.6), PP (these two account for more than half of all plastics currently produced!), PS, poly(vinyl chloride) (PVC), poly(urethane) (PU), poly(vinyl alcohol) (PVA), PET, or silicone rubbers are extensively used, and omnipresent in our today's world. Yes, they brought progress to numerous goods and services, but they are not accessible toward biodegradation/composting within a manageable time frame. Here, some data for moderate

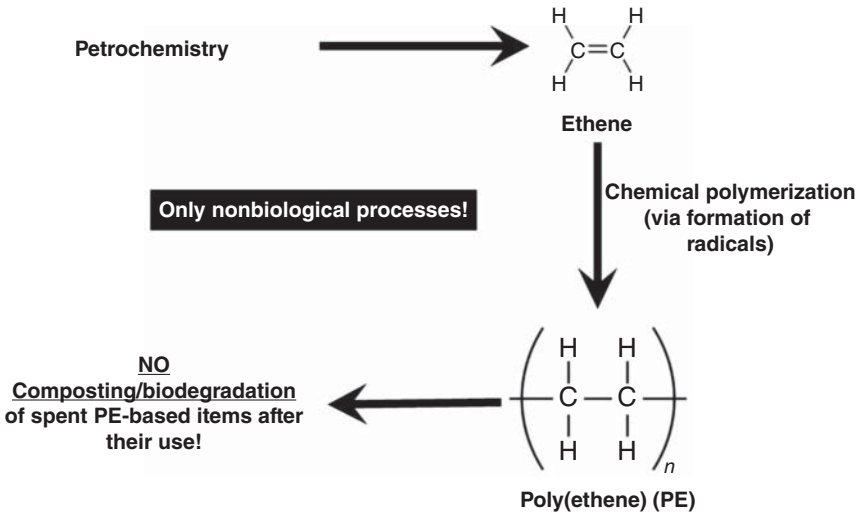

Figure 1.6 Production and life cycle of PE.

biological degradation of hydrolyzable petrochemical plastics like PET or PU are available for laboratory-scale enzymatic experiments, while full-carbon backbone polymers, making up more than 80% of all plastics, can only undergo degradation after prior oxidation, which makes them highly recalcitrant [24]. In any case, they all entirely resort to fossil resources.

1.2.2 Biodegradability of PHA and Other Biopolymers

In the context of integration of PHA into nature's closed carbon cycle, it should be reminded that "*biodegradability*" is not equal to "*compostability*." Both characteristics are defined via norms and assessed by certificates. Here, the norm EN-13432 addressing biodegradation and composting of polymeric packaging materials claims that a material is "biodegradable," if 90% of its carbon is metabolized within 180 days. In contrast, the same norm postulates that a material is "compostable" when leftovers in a sieve of 2 mm pore size after 180 days of composting do not exceed 10% of the material (reviewed by Koller et al. [25]). Generally, aerobic degradation of PHA by microorganisms like fungi or bacteria generates CO_2 and water, while anaerobic PHA consumption by living organisms, e.g. in biogas plants, results in the formation of methane in addition to water and CO_2 [26]. Factors influencing biodegradability of PHA, such as shape and thickness of polymer specimens, crystallinity, composition, environmental factors (pH value, temperature, humidity, UV exposure), and surrounding microflora, were comprehensively summarized before [27].

Most importantly, plastic-like biopolymers like PLA, TPS, or, as the subject of the chapter at hand, microbial PHAs, are based on renewable resources; hence, they do not deplete limited fossil resources. Beyond that, these biomaterials are integrated into the closed carbon cycle on our planet; this means that their biodegradation does

not further increase the concentration of CO_2 in the atmosphere. This can simply be understood by considering that raw materials typically implemented for the production of PHA and other "bioplastics" are renewable resources (prime examples: carbohydrates, alcohols, or lipids), hence, products of the natural metabolism of plants and microorganisms, which were not entrapped inside our planet since millions of years. This is a pivotal difference to crude oil, the raw material for the production of established plastics [4]. After their life span as bioplastic items, aerobic biodegradation of PHA and other biopolymers generates biomass and CO_2, which again becomes part of the natural carbon cycle, by getting fixed by green plants or phototrophic microbes; the generation of renewable feedstocks for biopolymer synthesis can start *de novo*. This is a fundamental difference to the degradation of petrochemistry-derived plastics by incineration; here, carbon that had been deprived of its natural cycle by fossil fuel fixation for millions of years is suddenly released into the atmosphere as additional CO_2 [3].

In this context, extracellular enzymes like PHA depolymerases and biocatalysts of lower specificity are excreted by various microbes and degrade PHA into microbially convertible substrates, namely small oligomers and monomers [28]. PHAs are typically degraded *in vivo* by microbial depolymerases and other hydrolytic effects during a 52-week period [29]. Moreover, several studies have compared biodegradability of PHA with (semi)synthetic polymers. In this context, Gil-Castell et al. compared the durability of poly(lactic-*co*-glycolic acid) (PLGA), polydioxanone (PDO), poly(ε-caprolactone) (PCL), and the PHA homopolyester poly(3-hydroxybutyrate) (PHB) when used as scaffolds. It was shown that PCL and PHB were more appropriate materials when used for long-term applications compared to PLGA and PDO, which should rather be used for short-term applications [30]. Concerning PHB biodegradability under not biocatalytic conditions in water or phosphate buffer saline at 37 °C, a progressive decrease of molecular mass was described; after 650 days of immersion, molecular mass was reduced by almost 50%. Importantly, biodegradability of PHA depends on various factors such as the composition of the biopolyesters on the monomeric level (homopolyesters typically degraded faster than copolyesters), the stereoregularity, crystallinity (higher degradability at lower crystallinity), molecular mass (biopolymers of lower molecular mass are typically biodegraded faster than their counterparts of higher molecular mass), and environmental conditions (temperature, pH value, humidity, and availability of nutrients) [27]. Figure 1.7 illustrates the categorization of PHA biopolyesters, among other heavily used plastic-like polymers, based on the categories "biobased," "biodegradable/compostable," and "biosynthesized."

1.2.3 PHA as Versatile Microbial Biopolyesters – Fields of Actual and Potential Applications

PHAs, as a versatile class of microbial-produced biopolyesters, are currently in the scientific focus of material scientists, process engineers, microbiologists, and, more and more, of systems- and synthetic biologists. This interest originates from PHA's versatile material characteristics, making it attractive to be used in numerous areas

Figure 1.7 Classification of diverse polymers. Polymers marked in green meet the criteria "biobased," "biosynthesized," or "biodegradable/compostable." PHA: polyhydroxyalkanoates; PLA: poly(lactic acid); Bio-PE: biobased poly(ethylene); Bio-PP: biobased poly(propylene); PCL: poly(ε-caprolactone); PU: poly(urethane); PVC: poly(vinyl chloride); PVA: poly(vinyl alcohol); PS: poly(styrene); CA: cellulose acetate; PTFE: poly(tetrafluoroethylene) (Teflon®); PDO: poly(dioxanone); PTT: poly(trimethylene terephthalate); PBAT: poly(butylene adipate terephthalate) (Ecoflex®); PET: poly(ethylene terephthalate); PBS: poly(butylene succinate); PGLA: poly(glycolic-*co*-lactic acid). *Nota bene*: PHA is the only group marked in green in all categories which displays plastic-like properties without the need for special processing techniques and/or additives.

of the plastics market, which is currently dominated by diverse technomers and plastomers of petrochemical origin [31, 32].

PHA was for the first time detected by light microscopy more than 90 years ago, when Maurice Lemoigne described light-refractive inclusions in cells of the Gram-positive bacterium *Bacillus megaterium* (reviewed by Jendrossek et al. [33]). Most importantly, PHAs display all features characterizing "green plastics"; they are biobased, biosynthesized, biodegradable, compostable, and biocompatible. Hence, they can be considered the only group of real "green plastics" *sensu stricto*, as described earlier. Regarding the major material properties, PHAs are water insoluble, heat resistant (at least the highly crystalline representatives) and have attractive surface structure. Importantly, PHA pellets can be processed on standard machines used for processing of petrochemistry-derived plastics. PHA melt behaves like liquid crystalline polymers, which allows molding thin-walled or complex structures, which is of significance to produce scaffolds for biomedical use, even on small machines [34].

1.2.3.1 PHA as Packaging Materials

Among the most prominent fields of application, PHA-based biodegradable packaging materials come in first. This is of high significance especially in the field of food packaging, where it is often desired to have compostable, transparent

packaging with high barrier for oxygen, CO_2, and moisture [35]. These barrier properties can be further fine-tuned by developing PHA-based nanocomposite materials, which contain nanosized organic (e.g. cellulose nanowhiskers) or inorganic particles (e.g. nanoclay, nanoglass, etc.); for details of PHA-based nanocomposites, see 1.2.3.6. Considering the expedient compostability of PHA, it appears definitely reasonable to pack perishable food in such materials; after unpacking, the PHA-based packaging material, which is contaminated with food remains, can be easily disposed of as organic waste. Particularly, the high oxygen permeation barrier of PHA's attracts huge interest for the development of packaging materials, preventing oxidative spoilage of wrapped goods. In direct comparison to the long-established petrochemical packaging plastic high-density PE (HDPE), it was demonstrated that preservation of quality of food packed in PHA-based packaging materials is at least as good. In 1996, the PHA copolyester poly(3-hydroxybutyrate-*co*-3-hydroxyvalerate) (PHBHV), which can be processed to plastic films and containers for food packaging, was EU approved for food contact application [36]. While food packaging based on PHA might have a bright future, the switch to PHA-based shopping bags for single use still appears doubtful due to cost reasons; despite the fact that PHA can be processed, especially after addition of plasticizers, to biodegradable films, this is for sure not the method of choice for economic reasons; here, TPS seems to be the better, already broadly implemented solution to globally downsize the mountain of noncompostable shopping bags.

Paper coating with biopolymers like PHA presents a stimulating route to develop the packaging materials of the future. In this context, a study by Sängerlaub et al. demonstrates the coating of a paper substrate with PHBHV by an extrusion technique. The effect of adding up to 15% of the plasticizers triethyl citrate (TEC) or polyethylene glycol (PEG) on the processability (film thickness, melting point) and resulting characteristics (elongation at break, crystallinity) of the biopolyesters were studied. Processing, structural properties (melting and crystallization temperature and surface structure), mechanical properties (adhesion, elasticity modulus, elongation at break, tensile strength), and barrier properties of the blends and their coating performance (film thickness on paper) were assessed for different extrusion temperatures. The melting temperature (T_m) and elasticity modulus of PHBHV were reduced by both plasticizers, while the elongation at break slightly increased. Owing to PHBHV's low melt strength, the lowest obtained polymer film thickness on paper amounted to 30 μm. Moreover, the grease barrier was low due to cracks and voids in the biopolymer layers and, similar to mechanical properties and bond strength, correlated with the extrusion temperature. Extrusion coating of paper with PHBHV was successfully demonstrated, but, according to the authors, the minimum possible poly(3-hydroxybutyrate-*co*-3-hydroxyvalerate) (PHBV) film thickness has to be further reduced to become cost effective. Further, higher flexibility is needed in order to avoid the formation of cracks, which reduce the barrier properties of films [37].

1.2.3.2 PHA as Implant Materials

The convenient biocompatibility of PHB and PHBHV, the precondition to use these materials as implants, was confirmed in diverse animal-model experiments. In this context, rodents were implanted with PHA sutures, and investigated the

physiological and metabolic reactions in long-term test series. Monitoring the animals during one year showed good health and normal activity; hence, implanted PHA sutures did not negatively affect the homeostasis of tested animals [38, 39].

Mechanical properties such as elasticity modulus, tensile strain, and tensile strength of PHA like PHB and its composite materials are in a similar range to that reported for bones; thus, these biomaterials hold promise for application as implant materials, e.g. for femoral fractures. In comparison to surgically used polymers such as PLA, poly(glycolate) (PGA), or PLGA, implants based on PHA have the added advantage of not reducing the local pH value during *in vivo* degradation; this lack of acidogenesis makes PHA well accepted by cells and the immune system. As drawbacks, the low *in vivo* degradation rate of PHA-based implants and the high crystallinity, especially of PHB, complicate the enzymatic degradation of the implants, as shown by the remarkable recalcitrance of tiny bar-shaped PHB-based femoral implants against *in vivo* degradation in living rats [40].

In the context of biomaterials used for implants, modern implantation surgery often faces the problem of biomaterial-associated microbial infections, which calls for the improvement of implant surfaces to prevent bacterial adhesion at the start of biofilm formation. To overcome this issue, a recent study developed drug-delivery systems consisting of antibiotic-embedding PHB and PHBHV for coating titanium implants. A simple multilayer dip-coating technique was used for optimal coating of the implants. Drug delivery, antibacterial effect, toxicity, and cell adhesion were studied for individual coated implants. Both antibiotic-loaded PHA coatings resulted in protection against microbial adhesion, and PHBHV coatings displayed a better drug-release profile by faster degradation compared to coatings with the homopolyester PHB. When coatings with different antibiotic concentration per layer were used, a better controlled and more homogenous release was noticed. Because the PHA coatings degrade with time under physiological conditions, these new drug-delivery systems performed expediently not only by preventing the initial bacterial adhesion, but also by inhibiting the subsequent bacterial reproduction and biofilm formation, which serves for a prolonged drug release [41, 42].

1.2.3.3 PHA for Tissue Engineering

"Tissue engineering" deals with the generation of vital tissues (either hard-tissue-like bone and cartilage or soft-tissue-like skin and vascular grafts) to repair damaged or dead tissues and organs; this can be accomplished by combining biomaterials, cells, and bioactive compounds [43]. To perform as suitable tissue repairer, a biomaterial needs two central characteristics: appropriate mechanical properties to support organs during generation of new tissue and a surface topography allowing adhesion and growth of cells. Here, "engineered scaffolds" support cell growth and differentiation by mimicking the topography, spatial distribution, and chemical environment of the natural extracellular matrix of the target tissue [44]. Because of the high versatility of their mechanical properties, combined with excellent biocompatibility and *in vivo* degradability, PHA biopolyesters are among the most auspicious biomaterials for tissue engineering, and have been used to replace and

heal different types of hard or soft tissue [34]; PHA-based tissue engineering is described for restoring cartilage, skin, cardiovascular tissues, bone marrow, and nerve conduits (for recent reviews, see references [34, 45–48]).

Laser-perforated biodegradable scaffold films of solvent-casted PHBHV were prepared by Ellis et al. and studied for tissue repair performance. Generated pore sizes were in the μm range, which allowed human keratinocyte cells to attach and proliferate on the film surface; moreover, cells were able to penetrate pores and reach the injured tissue. This advanced cell adhesion and expedient cell growth and migration, as anticipated in regenerative medicine, were mechanistically explained by the authors by a considerably reduced crystallinity at the perforation edges [49].

In bone tissue regeneration, bioactive glass nanoparticles were embedded in PHA microspheres by Francis et al.; it was shown that the surface topography of the microspheres was beneficial for cell attachment and growth, and enhanced hydroxyapatite growth rate if compared with not-PHA-coated bioactive glass nanoparticles, which favors bone tissue repair. Moreover, these microspheres were loaded with the antibiotic gentamycin, which was slowly released during tissue growth [50]. These authors also demonstrated the positive effect of nanosized bioactive glass particles embedded in PHA microspheres pressed to films; these composites were used for wound healing. This is based on the hemostatic effect of bioactive glass by releasing Ca^{2+} ions, which supports blood clotting. The authors reported that these novel PHA composite microsphere films containing nanosized bioactive glass particles hold great promise for wound healing including protective, blood clotting, and tissue regeneration properties; importantly, surface nanotopography of the composite microsphere films has to be optimized [51].

Computer-aided wet spinning is a hybrid additive-manufacturing technique to process polymers dissolved in organic solvents; it enables preparing scaffolds of predefined geometry and custom-made internal architecture. This technique was used by Puppi et al. to develop biodegradable stents consisting of poly(3-hydroxybutyrate-*co*-3-hydroxyhexanoate) (PHBHHx)/PCL blends, which could be used to heal small blood vessels. Morphological characteristics like pore size, stent wall thickness, and others were adjusted during stent manufacturing by fine-tuning the process parameters. While pure PHBHHx stents displayed excellent radial elasticity, PCL stents revealed higher axial and radial mechanical strength. Continued proliferation of human umbilical vein endothelial cells was demonstrated by *in vitro* cultivations; moreover, when in contact with human blood, exceptional resistance of the stents against blood clotting was shown [52].

Engineering of cartilage tissue by the aid of biopolymers like PHA was already extensively investigated [53]. In this context, Deng et al. seeded rabbit articular cartilage chondrocytes on scaffolds consisting of PHB, PHBHHx, or blends thereof. After four weeks of incubation, chondrocytes preserved their phenotype and proliferated well on all tested biopolymer scaffolds, with superior results for the blends [54]. As shown by Zhao et al., particularly a PHBHHx content of 60 wt% in such blends enhances mechanical properties compared to the pure biopolyesters; again, this study confirmed enhanced growth and physiological function of chondrocytes when using polymer blends [55].

Lizarraga-Valderrama et al. prepared blends of PHB/poly(3-hydroxyoctanoate) (PHO) blends to investigate their appropriateness as base materials for nerve tissue engineering. Chemical, mechanical, and biological properties of PHB/PHO blends were compared with neat PHB and PHO homopolyesters. As shown by using NG108-15 neuronal cells, all tested blends were biocompatible; the blend containing 25% PHO turned out as the best support material for cell growth and differentiation, and revealed mechanical properties appropriate for its use as base material for manufacture of nerve guidance conduits [56].

1.2.3.4 PHA as Drug Carrier Materials

The biodegradability of PHA under diverse environmental conditions makes this biopolymer family expedient candidates for drug carriers. In this context, extracellular enzymes like PHA depolymerases and not-that-specific biocatalysts are excreted by various microbes, and degrade PHA into microbially convertible substrates, namely small oligomers and monomers [28, 57, 58]. The drug-retarding properties of PHA-based systems can be controlled primarily by their composition on the monomeric level and their molecular mass. Additionally, PHAs have already proved to have a substantial impact on the bioavailability of bioactive compounds, enhanced drug encapsulation, and reduced toxicity in comparison to other biodegradable polymers, as recently reviewed [34].

By an emulsification and solvent evaporation approach, Masood et al. prepared randomly distributed PHBHV nanoparticles containing different 3HV fractions of 200–300 nm size and coated them with PVA. Here, Gram-positive *Bacillus cereus* was used as production strain because this organism generates endotoxin-free PHBHV biopolyesters. Importantly, these nanoparticles contained the antineoplastic drug Ellipticine, which is used in cancer therapy. The high biocompatibility of PHBHV nanoparticles not loaded with Ellipticine was demonstrated by *in vitro* cytotoxicity tests; here, the "placebo" nanoparticles did not affect survival of cancer cells, while Ellipticine-loaded PHBHV nanoparticles considerably inhibited their growth. Remarkably, growth inhibition was even more pronounced than when using the free (not encapsulated) drug; the authors proposed that supplying Ellipticine embedded in nanoparticles increases its bioavailability, which in turn enhances the drug's cytotoxic effect [59].

As another example for use of PHA in drug delivery, Rhodamine-B-loaded nanoparticles of random distributed PHBHHx copolyesters of a mean size of about 150 nm were prepared by Wu et al. These nanoparticles were coated with subcytotoxic concentrations of poly(ethylene imine) to assist attachment to and uptake by different cell types. Cell response to this nanoparticle system was studied *in vitro* and *ex vivo*. It was shown that the nanoparticles were transported along endolysosomal cell compartments, the endoplasmic reticulum, and the Golgi complex, without negatively affecting cell morphology or respiration [60].

The company Bio-On currently develops PHA nanoparticles to diagnose and treat cancer. These nanoparticles simultaneously contain two different contrast media, namely magnetic nanoparticles and gold nanocylinders, which can rapidly mark

tumor mass by nuclear magnetic resonance (NMR). Moreover, these nanoparticles can additionally contain chemotherapeutics to combat tumors [61].

1.2.3.5 PHA Biosynthesis Coupled to Bioremediation

Microbial PHA production is often coupled to parallel degradation of environmental pollutants. This was demonstrated by Berezina et al. who studied the degradation of benzoic acid as a key aromatic pollutant in bioremediation processes by *Cupriavidus necator*; metabolic pathways of the biodegradation were precisely analyzed. The 2,3-dioxygenase pathway was shown to be responsible for benzoic acid degradation by this strain; in batch setups, an initial concentration of benzoic acid should not exceed 2.5 g/l, also in case of adapted cells. In repeated fed-batch experiments, the transformation of a total of 43.7 g/l benzoic acid was achieved in 12 weeks; this transformation was coupled to PHA biosynthesis [62].

Styrene is another toxic pollutant, which is typically found in plastic-processing industry waste water. The bioconversion of this severe eco-pollutant styrene into PHA by different microorganisms was demonstrated by Tan et al. Twelve new isolates from the *Pseudomonas* genus turned out to degrade styrene and utilized it to accumulate medium-chain-length-PHA (*mcl*-PHA) contents between 0.05 and 23.10 wt% in their biomass. *Pseudomonas putida* NBUS12 was the best performing strain among these isolates; it achieved a final biomass of 1.28 g/l and an intracellular PHA content in biomass of 32.5 wt%. The *mcl*-PHA mainly consisted of the monomers 3-hydroxyhexanoate (3HHx), 3-hydroxyoctanoate (3HO), 3-hydroxydecanoate (3HD), 3-hydroxydodecanoate (3HDD), and 3-hydroxytetradecanoate (3-HTD) [63]. In 2019, Goudarztalejerdi et al. isolated 15 different PHA-accumulating strains, all belonging to the family of pseudomonads, from the crude-oil-contaminated area to investigate their bioremediation potential of these strains. Later, culture conditions were optimized for maximum biomass growth and PHA production from crude oil. Under optimized cultivation conditions, the best intracellular PHA fraction amounted to about 22 wt%. Based on their study, the authors stressed that unfavorable environments such as areas contaminated with crude oil can be rich sources of natural PHA producers. Such strains could be used for bioremediation of crude-oil-contaminated sites, while in parallel they accumulate PHA biopolyesters as side products of the process [64]. Similar studies were carried out by Revelo Romo et al., who isolated 18 crude oil-degrading bacteria with Class I, II, or IV PHA synthase genes, from oil-contaminated seawater from the Bay of Tumaco at the Colombian coast. These isolates belonged to the genera *Pseudomonas*, *Bacillus*, *Halomonas*, *Alcanivorax*, *Stenotrophomonas*, and *Haererehalobacter*, a genus for the first time described to produce PHA in this study, which presents new "hydrocarbonoclastic" marine organisms combining PHA biosynthesis and bioremediation of marine oil spills [65].

In 2017, the company Bio-On announced that tests were successfully carried out for bioremediation of oil slicks on ocean's surface. Here, PHA powder is applied to the oil film and acts as feedstocks for various microbes; *inter alia*, it nourishes those organisms which are capable of hydrocarbon degradation [66].

1.2.3.6 Special Applications of PHA

More recently, PHA biopolyesters started entering the field of smart high-performance materials. In this context, Janakiraman et al. studied the dielectric and optical properties of pristine PHB films and of PHB films reinforced with 15–30% ZnO nanoparticles. The nanocomposite films showed improved relative permittivity with adequate loss tangent which is greater than that of pure PHB films. In addition, the nanocomposites showed high absorption in the UV region. The prepared nanocomposites were suggested by the authors for use as dielectric substrates for microwave applications, as coating material for LED encapsulation to block UV radiation, or to develop UV-resistant materials in textile industry [67]. In the cosmetic and body care sector, PHAs find use in the form of microbeads for peeling in emulsions like body and face scrubs, cleansers, toothpastes. Here, PHAs replace microplastics made of, e.g. PE. As micro-sized powder particles, only 5–20 μm in size, they give texture to additional creamy cosmetic products. In this context, the lipophilic and hydrophobic nature of such micro-powder PHA particles makes them especially interesting for skin care; beneficially, they do not remove water from skin, but provide greasy skin a natural matt appearance [68].

Smart adhesives are another field of future application for PHA. Here, nonwoven films consisting of poly(3HB-*co*-4HB) were successfully tested in reducing inflammation, improving the angiogenic properties of skin and enhancing the wound-healing process in rat-model experiments. Presence of fibroblast cells on the biopolymer films accelerated wound healing, vascularization, and regeneration; it was shown that cells excreted proteins which formed a layer on the membrane surface and supported the movement of epidermal cells from wound-surrounding tissue [69]. Later, the adhesive properties of a *mcl*-PHA consisting of at least five different monomers, produced by the strain *Pseudomonas chlororaphis* from crude glycerol phase from the biodiesel production, were recently demonstrated by Pereira et al.; this semi-crystalline material revealed very low melting temperature T_m (44 °C) and glass transition temperature T_g (−48 °C). Films made of this *mcl*-PHA were translucid, highly elastic, water repellent, relatively permeable to O_2 and CO_2, and demonstrated excellent adhesion properties toward skin, which makes them potential candidates for a new class of natural adhesives for wound dressings or closure [70].

Currently, PHA has also started penetrating the toy sector. In 2018, the company Bio-On started commercializing their so-called Minerv Supertoys, which are LEGO™-like toy bricks made of stained PHA [71].

1.2.3.7 Application of PHA's Follow-Up Products

Hydrolysis of PHA generates a cocktail of stereochemically pure *R*(−)-bifunctional hydroxyalkanoates (note: in natural PHA, no *S*(+)-configurated monomers are found!); these can act as synthons for synthesis of industrially relevant fine chemicals like fragrances, pheromones, aromatics, antibiotics, or vitamins; some hydrolysis products even serve as pharmaceuticals [72]. As an example, 3HB and its oligomers are important for therapeutics by promoting cell proliferation

and avoiding necrotic death of cells. 3HB, a natural ketone body of nutritional importance [73], seems to play a pivotal role in maintaining the intraocular pressure [74], and was also used as carbon and energy source to prevent protein loss for obese patients exposed to therapeutic starvation [75], or as intravenous glucose substitute to restore the nitrogen balance after cholecystectomy surgeries [76]. Currently, methyl esters of PHA monomers are applied as drug in Alzheimer's disease therapy; here, 3HB-methyl ester is converted by cells as an alternative to glucose, which overcomes hypoglycemia and mitochondrial damages in cerebral cells [77]. Typically, PHA follow-up compounds are by far more expensive than the polyesters themselves because their production via chemical alcoholysis is not economical. Therefore, methods for *in vivo* depolymerization of intracellular PHA by altering the activities of intracellular enzymes were developed [78]; PHA accumulated in cells gets rapidly hydrolyzed at drastically increased PHA depolymerase activity, which can be provoked by rigorously decreased pH-value, which stops *R*(−)-3HB dehydrogenase activity; pure *R*(−)-3HB is excreted by the cells into the medium [79].

In 2019, Bio-On has patented a cigarette filter containing a liquid follow-up product of PHA to replace triacetin. The patent claims that this new filter system can retain up to 60% of dangerous reactive oxidative species from tobacco smoke [80]. Completely different PHA follow-up products were presented by Zhang et al., who, via acid methanolysis, converted PHB and *mcl*-PHA to methyl esters of the corresponding building blocks. These products were tested as potential novel "biofuels" by comparing their combustion heats with established fuels and fuel additives like gasoline, ethanol, or 1-butanol. It was shown that combustion heats of 3-hydroxyalkanoate methyl esters amounted to 20–30 kJ/g, which is in the same range like reported for ethanol (27 kJ/g) [81]. Soon, these researchers showed that addition of 3HB-methyl ester to gasoline outperforms the addition of ethanol in terms of oxygen content, flash point, boiling point, and dynamic viscosity, and blending of gasoline with about 10% 3HB-methyl ester resulted in only insignificant reduction of the octane number [82]. It is of importance that PHA used for this purpose does not need high polymer quality or purity; on large scale, it should therefore be produced in simple, inexpensive, nonsterile setups by mixed microbial cultures using sewage water as substrate [81].

Mcl-PHA consisting of C6–C12 (3-hydroxyhexanoate to 3-hydroxydodecanoate) monomers was accumulated by *P. chlororaphis* when supplied with rapeseed oil; the biopolyester was extracted by Cerrone et al. using acetone as solvent, and subjected toward acidic methanolysis, generating a mixture of fatty acid methyl esters, which were subsequently reduced by $NaBH_4$ to corresponding 1,3-diols. Both alcohol groups of these diols were sulfated by chlorosulfonic acid; this generated alkyl-1,3-disulfates, which turned out to act as expedient anionic biosurfactants, with considerably better performance in surface tension tests, wettability, very low specific critical micelle concentration, and formed foam of higher stability and volume when compared with the established not-biological-surfactants sodium dodecyl sulfate (SDS), sodium alkyl disulfate mixture (SADM), and sodium dodecyldisulfate. According to the authors, use of this PHA-based biosurfactant

instead of established products contributes to reduce the current use of palm oil for detergents production [83].

Typically, high PHA synthesis rates are observed for cultures exposed to limitation of an essential nutrient medium component, typically nitrogen or phosphate, while at the same time, an exogenous carbon source needs to be present in excess. As their primary biological function, PHAs serve the microbial production strains as carbon-rich reserve compounds to better survive periods of starvation, and as "pseudo-fermentative" electron sinks serving for the regeneration of reducing equivalent in situations when central metabolic pathways (e.g. the tricarboxylic acid cycle, TCC, or nucleic acid biosynthesis) are blocked [84].

In addition, a range of further functions of PHA were more recently revealed, such as their protective role against stress factors [85] like elevated temperature [86], UV irradiation [87], challenging freezing and thawing cycles [88], heavy metals [89], or oxidative stress [86, 90]. A recently reported integrated electromicrobial experiment evidenced that PHA is produced by microbes to an increasing extent as a protective reaction to the sudden generation of reactive oxygen species (ROS) [91]. In the context of halophilicity, hence, the adaptation of organisms to high salinity, presence of PHA in living cells was shown to support them to overcome the detrimental effects of osmotic up-shock [92] or sudden osmotic imbalances in general [93], which explains their frequent occurrence in haloarchaea typically thriving in extremely saline habitats [94].

1.2.4 PHA Granules Are More than Simple Bioplastic Spheres

Inside the microbial cell, PHA is organized in the form of complex granular inclusion bodies, which are currently understood as complex *de facto* organelles ("carbonosomes"). Center of these PHA granules is a hydrophobic core region consisting of the PHA biopolyesters chains; this hydrophobic core is coated by different granule-associated enzymes and other proteins [33, 95]. The most significant ones among these proteins are PHA synthase (PhaC), PHA depolymerase (PhaZ), the repressor protein (PhaR), and different PHA phasins (PhaP) (formerly simply termed as "PHA-granule-associated proteins"), which are a versatile group of structural proteins. In the meanwhile, it was elucidated that phasins determine the intracellular number, size, and location of PHA granules; it was shown that higher activity of phasins in a cell results in a higher number of granules, albeit of smaller size [96, 97]. While the role of phasins in PHA biosynthesis in free-living bacteria is already well understood, their contribution in the symbiosis between PHA-accumulating bacteria and associated plants was only recently elucidated by Sun et al. For *Shinorhizobium* sp., a bacterial microsymbiont of the legume plant *Vigna unguiculata*, especially phasin PhaP2, turned out to dominate the regulation of PHA granule size both in free-living cells and cells cultivated under symbiotic conditions. Importantly, when testing a total of four different phasins (termed PhaP1-4), the authors showed that these proteins are involved in a number of additional intracellular processes different from PHA formation [98]. Figure 1.8 illustrates the organization of intracellular, native PHA granules.

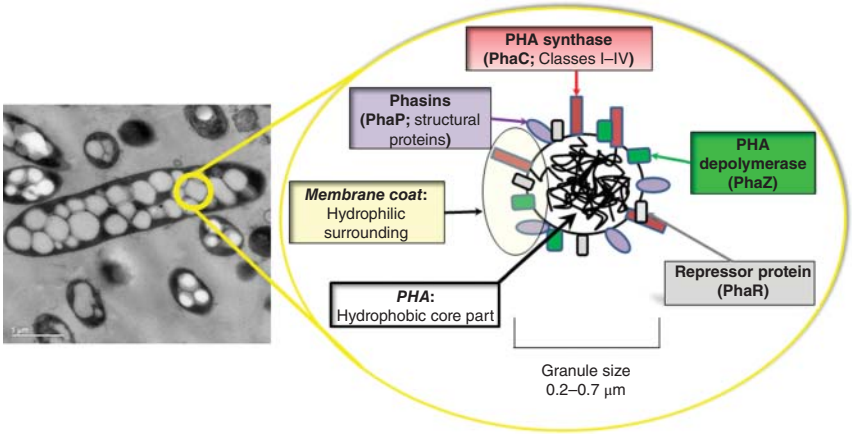

Figure 1.8 Organization of native PHA granules in living cells of *C. necator*.

More recently, it was demonstrated by microscopic observations and footprint area analysis of PHA-containing cells that the number of PHA granules per cell and the granule size in cells of a microbial culture are highly dependent on the metabolic state of the culture and the environmental conditions, as shown for cells cultured in a multistage continuous process with different nutritional conditions in each individual stage, ranging from balanced growth conditions via conditions prevailing during the transition between growth and PHA accumulation phase, until a stage where cells are exposed to carbon source excess and long-term nitrogen deprivation. During balanced biomass growth, cells containing rather small granules were predominately formed, whereas under ongoing PHA accumulation conditions, both the maximum and the average sizes of PHA granules increased, until a maximum size limit, predetermined by the intracellular steric conditions in the cells, was reached. Additionally, the number of granules per cell decreases with increasing residence time and long-term exposure of cells to nitrogen limitation in the multistage bioreactor cascade [99].

Regarding the distribution of PHA granules during binary cell division between two daughter cells, it was for a long time believed that this distribution occurs in parallel with the nucleic acids; hence, both daughter cells were supposed to contain similar quantities of PHA granules. For example, Galán et al. suggested that the nucleoid-associated phasin PhaF, which has a DNA-binding and a PHA-binding domain, was responsible for the intracellular localization and homogenous segregation of PHA granules together with the two new chromosomes upon cell division in *P. putida* KT2442 [100]. This assumption was fundamentally revised in 2017, when Karmann et al. discovered by flow cytometry that dividing cells of *P. putida* KT2440, when exposed to carbon-limited conditions, separate in an asymmetric way into two "sub-populations," one containing high amounts of PHA granules, and one being almost PHA-free. This is in contrast to the expected behavior of cells under carbon-rich conditions, when PHA granules were homogenously distributed in all cells of a culture. Hence, cells of this organism display a "bi-stable" behavior under

conditions favoring PHA depolymerization, which might be caused by PHA-free cells growing faster by consuming PHA monomers released from PHA-degrading cells [101].

1.2.5 A Short Overview of the Metabolism of PHA Biosynthesis and Degradation

1.2.5.1 The Key Enzymes for PHA Biosynthesis

The principles of the enzymatic apparatus responsible for microbial PHA biosynthesis and intracellular degradation are already well described [84]. After uptake by the cells, carbon sources, e.g., sugars, glycerol, and fatty acids, undergo degradation via pathways like glycolysis, the 2-keto-3-desoxy-6-phosphogluconate (KDPG) pathway, and pyruvate decarboxylation. Resulting end products, in many cases the central metabolite acetyl-CoA, are converted to ketoacyl-CoA (=oxoacyl-CoA) thioesters ("fatty acid-CoA"), the most common among them being acetoacetyl-CoA, which is generated by condensation of two acetyl-CoA molecules, a reaction catalyzed by the key enzyme 3-ketothiolase, a transferase dependent on the cofactor potassium (EC 2.3.1.9, a.k.a. acetyl-CoA–acetyltransferase (ACAT) or Thiolase II; formerly also known as β-ketothiolase) [84].

In a next step, the ketoacyl-CoA thioesters get reduced by NADPH-dependent oxoacyl-CoA reductases (mainly the oxidoreductase acetoacetyl-CoA reductase; EC 1.1.1.36); by this reaction, the corresponding (*R*)-hydroxyacyl-CoA thioesters are formed. In analogy to ethanol formation by reduction of the intermediate acetaldehyde in yeasts, this reaction regenerates the oxidized form of reduction equivalents ($NADP^+$); therefore, this reductive step in PHA biosynthesis is understood as a "pseudo-fermentation." Lastly, PHA synthases (PHA polymerases; EC 2.3.1.x) get on the scene; these enzymes, belonging to the group of acyltransferases, catalyze the polymerization of (*R*)-hydroxyacyl-CoA thioesters to polyesters; free CoA is regenerated. Notably, the genes encoding 3-ketothiolase (phaA), acetoacetyl-CoA reductase (phaB), and PHA synthase (PhaC) are organized together on one single operon called *PhaCAB* (reviewed by Braunegg et al. [84]).

1.2.5.2 Factors Impacting PHA Synthases Activity

Generally, high intracellular adenosine triphosphate (ATP), NAD(P)H, and acetyl-CoA concentrations and low free CoA pools are beneficial for the activity of earlier discussed enzymes involved in PHA biosynthesis. These conditions exist, e.g., when the TCC or other central metabolic routes (e.g., those generating nucleotides needed for biosynthesis of DNA, RNA, and adenosine phosphates) cannot work because of the absence of a growth-essential growth factor (e.g., nitrogen source, phosphate, oxygen, and sulfur) [84]. Nowadays, the classification of PHA synthases into four classes (I–IV) is generally recognized by the scientific community [102].

PHA synthases belonging to Class I and Class II are enzymes composed of only one subunit type (PhaC); molecular masses of these enzymes range between 61 000 and 73 000. According to their substrate specificity *in vivo* and *in vitro*, Class I PHA synthases, e.g., the Class I PHA synthase found in the best described PHA

production strain *C. necator*, accepts different (*R*)-hydroxyacyl-CoA thioesters, which contain an acyl group with 3–5 carbon atoms; 3-hydroxybutyryl-CoA, 3-hydroxyvaleryl-CoA, and 4-hydroxybutyryl-CoA are the most important representatives. This is different to Class II PHA synthases found in prototype organisms like *P. putida* or *Pseudomonas aeruginosa*; Class II PHA synthases favorably use such (*R*)-hydroxyacyl-CoA thioesters as substrates, which contain an acyl group consisting of 6–14 carbon atoms; *mcl*-PHA is formed by these enzymes. Such longer (*R*)-hydroxyacyl-CoA thioesters are typically formed by β-oxidation of fatty acids. This β-oxidation first produces (*S*)-3-hydroxyacyl-CoA; since the PhaC subunit is highly stereospecific and requires (*R*)-isomers as substrates, these (*S*)-enantiomers cannot be directly polymerized to *mcl*-PHA. Therefore, specific isomerases convert the (*S*)- into the (*R*)-isomers, which act as substrates for Class II synthases [102].

Class III PHA synthases, such as those found in *Allochromatium vinosum* as the prototype strain, are enzymes consisting of a PhaC subunit with an amino acid sequence with about 21–28% similarity to the sequence in Class I and II PHA synthases, and of a PhaE subunit with an amino acid sequence considerably different to those found in Class I or II PHA synthases. Similar to Class I, such Class III PHA synthases preferentially polymerize (*R*)-hydroxyacyl-CoA thioesters with acyl groups containing 3–5 carbon atoms [102]. As a more recently introduced group, Class IV PHA synthases catalyze PHA biosynthesis especially in Bacilli; by consisting of two subunits, they are of similar structure to Class III PHA synthases, but the PhaE subunit is replaced by the PhaR subunit, which has a lower molecular mass (reviewed by Tsuge et al. [103]).

1.2.5.3 Intra- and Extracellular PHA Depolymerization

Intracellularly, PHA can be depolymerized by the catalytic action of intracellular depolymerases of the hosting strain; cells resort to the carbon and energy content of their storage compound PHA by mobilizing it when no convertible exogenous carbonaceous nutrients are available. Intracellular PHA degradation is initiated by the reaction catalyzed by PHA depolymerases, which generates monomeric (*R*)-3-hydroxyalkanoates and their oligomers; (*R*)-3-hydroxybutyrate dehydrogenase (EC 1.1.1.30), an oxidoreductase, reversibly oxidizes them to acetoacetate, which next gets converted to acetoacetyl-CoA by the catalysis of the transferase acetoacetyl-CoA synthetase (EC 2.3.1.194). Finally, acetoacetyl-CoA is hydrolyzed to the central metabolic compound acetyl-CoA by the reversible enzyme 3-ketothiolase, which was already introduced earlier as the enzyme catalyzing the condensation of two acetyl-CoA molecules during PHA biosynthesis [27].

Besides intracellular PHA depolymerases needed to keep the intracellular cycle of PHA biosynthesis and degradation running, also extracellular PHA depolymerases, required for PHA biodegradation by other organisms, are reported; they catalyze biodegradation and composting of PHA (reviewed by Yutaka and coworker [28]). In a nutshell, intracellular depolymerases display higher substrate specificity, while their extracellular counterparts constitute rather unspecific hydrolytic enzymes (esterases), which also occur in many fungi. Notably, intracellular PHA depolymerases do not hydrolyze isolated, extracellular PHA, while extracellular

depolymerases, when expressed *in vivo*, are not able to hydrolyze intracellular granules, since there exist considerable differences in the physical structures of intact, native intracellular granules and denatured extracellular PHA, especially regarding the different crystallinities [28]. In addition, depolymerization of intracellular PHA to a certain extent takes place simultaneously to PHA biosynthesis, even under conditions which are beneficial for PHA formation (excess carbon source in parallel to nutrient deprivation). This results in a steady assemblage and disassembly of PHA in living cells; hence, a permanent modification of the polyester chains, the frequently cited "cyclic nature of the PHA metabolism," occurs [104]. Yet, under conditions advancing PHA biosynthesis, intracellular PHA depolymerases reveal drastically lower activity than the activity measured at the same time for PHA synthases. If intracellular PHA depolymerases are not active at all, which happens in the case of recombinant *Escherichia coli* containing PHA synthesis genes (*PhaCAB*), but no PHA depolymerases-encoding genes, ultra-high-molecular-mass PHA can be produced by the cells [105]. This effect was also demonstrated when inactivating (knocking out) PHA depolymerase in the *Azotobacter vinelandii* genome, which resulted in the generation of PHA of highly uniform molecular mass [106].

In 2004, Choi et al. demonstrated the high impact of PHA crystallinity on extracellular degradability. These authors produced PHBHV with different 3HV fractions by cultivation of the strain *Alcaligenes* sp. MT-16 on glucose plus the 3HV precursor levulinic acid. It was shown that increasing 3HV fractions in PHBHV samples drastically decreased the polyesters' crystallinity, which resulted in faster extracellular degradation when incubating the polyesters in solutions of extracellular PHA depolymerase from *Emericellopsis minima* W2. Enzyme-free degradation experiments carried out for 20 weeks with the same polyesters in alkaline medium did not show any degradation at all [107].

In addition, it was shown that all discovered PHA depolymerases are specifically hydrolyzing the oxoester bonds of PHA, while thioester bonds in polythioesters (PTEs), a group of sulfur-containing PHA analogues, are not cleaved by these enzymes [108]. PTE copolyesters of 3-hydroxyalkanotes and 3-mercaptoalkanoates, such as poly(3HB-*co*-3MP) or poly(3HB-*co*-3MB), are biosynthesized when supplying PHA producers like *C. necator* precursor substrates accessible only chemically, such as 3-mercaptobutyrate (3MB) or 3-mercaptovalerate (3MV), in addition to gluconate as main carbon source [109]. These copolyesters were shown to be degraded by only a limited number of bacteria like *Schlegelella thermodepolymerans* [110], while for poly(3-mercaptopropionate) (P3MP) and other PTE homopolyesters, which are accessible by cultivating recombinant *E. coli* on appropriate precursor substrates, no degradation was observed at all, even when exposing the polyester to soil, compost, or activated sludge for half a year [111]. Figure 1.9 provides a schematic illustration of the simplified PHA biosynthesis and biodegradation pathway starting from diverse renewable resources.

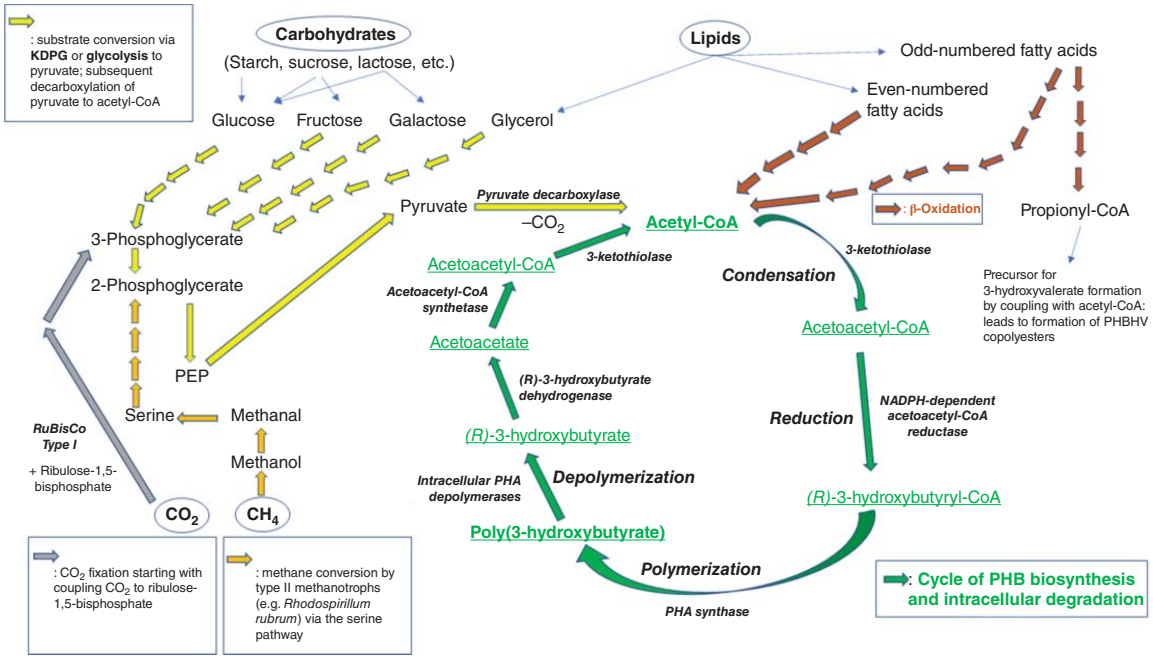

Figure 1.9 Simplified illustration of the PHA metabolism starting from diverse important renewable feedstocks (carbohydrates – yellow arrows, lipids – brown arrows, CO_2 – gray arrows, CH_4 – orange arrows). Key enzymes of PHA biosynthesis and intracellular degradation (green cycle) are indicated in the central PHA cycle.

1.3 Types of PHA Biopolyesters

1.3.1 The "PHAome" Describes the High Complexity and Versatility of Natural PHA

The designation "PHAome," analogous to an organism's "genome," "proteome," "lipidome," "transcriptome," or "metabolome," was introduced in the scientific literature by Chen and Hajnal; the "PHAome" describes the complexity of PHA, which can occur at the same time in a studied microbial sample [112]. This complexity of PHA encompasses its monomeric composition (PHA homopolyesters vs. PHA heteropolyesters, see Section 1.2.2; *scl*-, *mcl*-, or *lcl*-PHA, see Section 1.3.2), microstructure (here, we distinguish between random distribution or blocky structure of heteropolyesters, and the occurrence of intracellular polyester blends; see Section 1.2.4), and molecular mass distribution of the individual PHA molecules (low-molecular-mass PHA, high-molecular-mass PHA, ultra-high-molecular-mass PHA) in a biological sample [113].

1.3.2 PHA Homo- and Heteropolyesters

For the manifold possible usages on the plastic market, such as packaging, biomedical applications, or use in smart technologies, PHA biopolyesters not only need to be manufactured in a cost-efficient way; beyond that, these biopolymers also have to meet the quality standards and material performance known for plastics from petrochemistry in order to seriously compete with them. A multitude of differently assembled PHA homo and heteropolyesters are described, accumulated either by wildtype microbes, genetically modified organisms, or even *in vitro* by isolated PHA-synthesis enzymes.

Depending on the number of distinct building blocks, hence, monomers present in a PHA polyester, it is possible to distinguish PHA homopolyesters from PHA heteropolyesters. Homopolyesters contain only one single monomer type, with PHB, an isotactic, linear, thermoplastic polyester, being the most prominent and by far the best studied example. Heteropolyesters in turn are divided into copolyesters consisting of two different types of monomers (PHBHV being the best studied example) and terpolyesters (generally: three different building blocks; *sensu stricto*: three different building blocks with differences both in the length of the side chain and the backbone of the individual monomers) [113]. More recently, also quarter-polyesters with four different monomers (typically 3HB, 3HV, 4HB, and 3HHx) were introduced in the scientific literature as a new PHA group; these materials reveal excellent material properties in terms of processability and flexibility [114].

1.3.3 *Scl*-, *Mcl*-, and *Lcl*-PHA and Their Characteristics

A limited range of PHA monomers belong to the group of short-chain-length-PHA (*scl*-PHA) building blocks; this group encompasses all PHA monomers with three to five carbon atoms, with the chiral monomers (*R*)-3-hydroxybutyrate (3HB) and

(*R*)-3-hydroxyvalerate (3HV), and the achiral monomers 4-hydroxybutyrate (4HB) and, to a minor extent, 3-hydroxypropionate (3HP) being the most important representatives [113]. In contrast, medium-chain-length and long-chain-length-PHA (*mcl*-PHA and *scl*-PHA, respectively) building blocks describe those monomers having six to 14 (*mcl*-PHA) or more than 14 (*lcl*-PHA) carbon atoms. Representatives of *scl*-PHA are typically crystalline, often brittle thermoplastic materials with narrow melting temperature ranges, and low flexibility expressed as elongation at break; the homopolyester of 4HB and 4HB-rich copolyesters of 3HB and 4HB are exceptions in this group by having high flexibility and decreased crystallinity. *Mcl*- and *lcl*-PHA, in contrast, are latex-like resins; hence, they have the characteristics of typical elastomers with a low glass transition temperature, low crystallinity, typically broad melting temperature ranges, and often considerably lower molecular masses than those observed for *scl*-PHA [115]. Figure 1.10 illustrates the composition of *scl*-, *mcl*-, and *lcl*-PHA based on the general structure of PHA biopolyesters.

1.3.3.1 *Scl*-PHA

In the case of *scl*-PHA, high T_g (typically at least 0 °C), sharp melting points of even more than 180 °C for highly crystalline PHB, and high-molecular mass are characteristic material features of *scl*-PHA [116]. Generally, lower polydispersity ($Đ$), describing molecular mass distribution in a PHA sample, is found in the case of *mcl*-PHA than for *scl*-PHA, which means that *scl*-PHA have a narrower distribution of PHA chain length in an investigated sample [117].

PHB, the homopolyester of 3HB, is by far the best studied member *scl*-PHA and the entire PHA family. PHB was discovered about 90 years ago [118], and, until 1974, it was believed to be the only natural PHA accumulated by microorganisms. Since PHB is highly brittle, has a high melting point (up to 180 °C), and high crystallinity (X_c; typically 60–70%), its application, especially for flexible packaging, is not feasible. In 1974, Wallen and Rohwedder isolated microorganisms from samples of sewage water and noticed that the characteristics of the PHA accumulated by

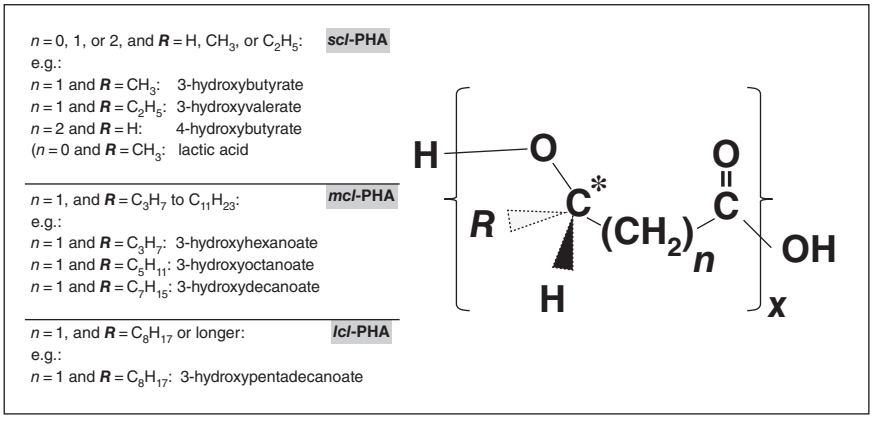

Figure 1.10 Composition of *scl*-, *mcl*-, and *lcl*-PHA based on the general structure of PHA biopolyesters. The * in the graphic indicates chiral centers.

these species were substantially different than known for the homopolyester PHB; especially the low Tm of less than 100 °C was unexpected. It was revealed that the PHA contained not only 3HB, but also 3HV monomers [119]. For production of PHBHV copolyesters instead of PHB homopolyester, most described *scl*-PHA production strains, e.g. *C. necator*, need to be supplied with precursor cosubstrates structurally related to 3HV. This was first demonstrated by simultaneously supplying *Alcaligenes eutrophus* (today: *C. necator*) with butyric acid (3HB precursor) plus valeric acid as 3HV precursor. Feeding valeric acid as the only carbon source resulted PHA consisted of up to 90% of 3HV [120].

4HB is the only thoroughly studied achiral building block in microbial PHA. 4HB-containing PHA was first detected when supplying *C. necator* butyric acid and the 4HB-precursor compounds 4-hydroxybutyric acid or 4-chlorobutyric acid, while supplying butyric acid as sole carbon source resulted in PHB homopolyester biosynthesis. Especially a drastically decreased crystallinity was observed when increasing the 4HB fraction in poly(3HB-*co*-4HB) [121]. The effect of varied 4HB fractions in poly(3HB-*co*-4HB) on T_m, T_g, and storage modulus was also studied, revealing that all these parameters decreased when increasing the 4HB share. While yield stress and breaking stress only slightly decrease with increasing 4HB fraction, the elongation at break strongly increases, making these materials highly flexible and elastic. Material features of the homopolyester poly(4HB) are entirely different to those of other *scl*-PHA like PHB or poly(3HB-*co*-3HV); poly(4HB) has an enormous elongation at break (up to 1000%), is highly flexible and stretchable, and of interest for surgical applications [122]. In this context, the company Tepha, Inc., USA, produces and commercializes various PHA-based biomedical products such as sutures or bioresorbable surgical threads; TephaFLEX® sutures consisting of poly(4HB) are approved by the US Food and Drug Administration (FDA) [123].

1.3.3.2 *Mcl*-PHA

Mcl-PHA contain monomers with 6–14 carbon atoms and are less crystalline than *scl*-PHA. Some *mcl*-PHA even contain monomers with functional (e.g., olefinic) groups; this paves the way for postsynthetic modification as a tool to adapt PHA's properties. *Mcl*-PHA samples often look like rubbers or biological latexes; since their T_g values are remarkably low, they are highly amorphous materials with structures which do not easily crystallize and do not become brittle even far below the freezing point. *P. putida* (formerly *Pseudomonas oleovorans*) is the most frequently used *mcl*-PHA production strain; it incorporates also functionalized (epoxy-group harboring, halogenated, unsaturated, etc.) building blocks into *mcl*-PHA when supplied with appropriate functionalized precursor compounds [115, 124].

Mcl-PHA synthesis occurs via fatty acid β-oxidation of substrates, generating a mixture of different (*S*)-acyl-CoAs, which are isomerized to the (*R*)-isomers; these are polymerized toward *mcl*-PHA copolyesters [125]. Alternatively, *mcl*-PHA production also occurs via fatty acid *de novo* synthesis from structurally unrelated substrates like sugars or glycerol [126]. Different to β-oxidation, fatty acid *de novo* synthesis directly provides the (*R*)-isomers of acyl-CoAs. In this context, it was

only recently reported by Sathiyanarayanan et al. that the psychrophilic species *Pseudomonas* sp. PAMC 28620, isolated from Arctic glacier fore-field soil, accumulates the *mcl*-PHA poly(3HTD-*co*-3HDD-*co*-3HD-*co*-3HO) with high *mcl*-PHA contents in biomass of more than 50 wt% when using glycerol as sole carbon source [127].

1.3.3.3 *Lcl*-PHA

Reports on *lcl*-PHA, polyesters containing building blocks with more than 14 carbon atoms, are still scarcely described. Barbuzzi et al. reported the first study on a 3-hydroxypentadecanoate (3HPD)-containing PHA by detecting low 3HPD fractions of 2% in PHA produced by *P. aeruginosa* ATCC 27853 grown on pentadecanoic acid as sole carbon source [128]. The up-to-date longest PHA building block found in microbial PHA, 3-hydroxyoctadecanoate (3HOD), was detected by Ray and Kalia, who produced PHA copolyesters containing 3HD, 3HHD, and 3HOD by cofeeding *Bacillus thuringiensis* EGU45 with glucose, CGP, and propionate [129]. A more recent report describes *lcl*-PHA production when cultivating *C. necator* IPT027 on the inexpensive carbon source crude palm oil rich in unsaturated lipids. This *lcl*-PHA contained mainly 3HD besides several other saturated and unsaturated monomers with 18 carbon atoms; it was highly amorphous with high thermal stability and low polydispersity [130].

1.3.4 Microstructure of PHA Heteropolyester

Besides the type of monomers present in PHA, one can also differentiate diverse types of PHA regarding their microstructure. In this context, intracellular polymer blends display mixtures of different homo- or heteropolyesters present in microbial cells; such blends can often be fractionated by enhanced solation techniques and typically show multiple melting endotherms in DSC thermograms. The blends can consist of fractions of heteropolyesters with different fractions of given monomers and/or of fractions of PHA with strongly different molecular mass (reviewed by Tripathi et al. [131]).

In addition, heteropolyesters can either display random distribution of the building blocks or consist of different homo- or heteropolyester blocks ("blocky structured PHA" – "*b*-PHA") (Figure 1.11). Chains of *b*-PHA comprise a minimum of two distinctive polymer sections (blocks), which are covalently linked. Properties of each block contribute to the properties of the entire polyester, which paves the way toward novel polymer properties, which are not reachable by simply blending polymers with the composition of the individual bocks. Diblocks like $[3HB]_x$–$[3HV]_y$, triblocks like $[3HB]_x$–$[3HV]_y$–$[4HB]_z$, or repeated multiblocks like [3HB–3HV] can be differentiated [131]. Recently, *b*-PHA production has increasingly fascinated polymer scientists, firstly, because of the outstanding controllability of polymer properties during their biosynthesis, and, secondly, since the processes and properties are better reproducible if compared to PHA of random distribution. In addition, *b*-PHA are not so prone to polymer aging by progressing crystallization, as shown for the diblock copolymer poly(3HB-*b*-3HHx) [132]. Moreover, novel diblock copolymers

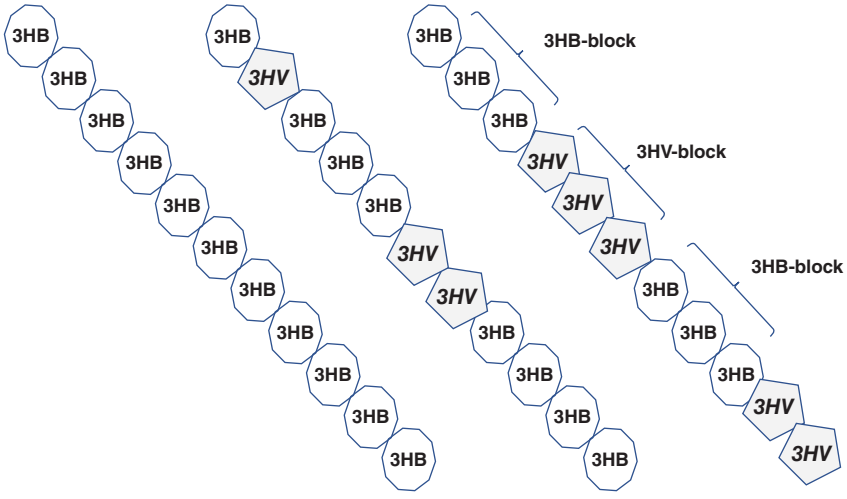

Figure 1.11 Schematic of PHA homopolyester (left polymer chain; the polyester represents PHB), poly(3HB-*co*-3HV) with random distribution (middle polymer chain), and blocky structured poly(3HB-*b*-3HV). Spheres represent 3HB building blocks, pentagons 3HV.

of PHB, PHBV, or PHO and atactic PHB (chemically produced) were developed and appeared promising for use as blend compatibilizers for cardiovascular engineering [133].

Practically, *b*-PHA are produced by living cells when supplying them subsequently with one type of carbon substrate after depletion of another, both acting as precursor compounds for the monomers building the individual PHA blocks [134]. Especially dual nutrient-limited conditions mentioned earlier, where both carbon and nitrogen sources are supplied at low concentrations, which enables their immediate uptake by the cells, are convenient to generate *b*-PHA [134]. Such processes can be efficiently performed in continuous bioreactors; in case it is desired to generate a *b*-PHA composed of a series of different blocks, a continuously operated multistage cascade of bioreactor should be the most appropriate engineering setup to generate such tailor-made PHA by strict sequence regulation (idea originally proposed in [135]).

The most recent development in the field of *b*-PHA deals with production of the diblock copolyester poly(2-hydroxybutyrate-*b*-3-hydroxybutyrate) [P(2HB-*b*-3HB)] in genetically engineered *E. coli* from exogenous 2HB and 3HB. 2HB is a definitely unusual PHA-building block which, like other 2-hydroxy compounds like lactate and glycolate, was never found in products of any natural PHA synthase. However, 2HB was incorporated in the recombinant *E. coli* PHA by transforming the strain with genes encoding a "chimeric" Class I PHA synthase, consisting of the N-terminal part of *Aeromonas caviae* PHA synthase, and the C-terminal part of *C. necator* PHA synthase, 3-ketothiolase, acetoacetyl-CoA reductase, and the 2HB-CoA supplying lactate dehydrogenase and CoA transferase. As substrates, hydrophobic amino acids were supplied; among them, utilization of valine and cofeeding of valine and threonine resulted in P(2HB-*b*-3HB) biosynthesis [136].

1.3.5 Factors Determining the Molecular Mass of PHA

1.3.5.1 General Aspects of PHA Molecular Mass

Generally, the mechanical properties, such as tensile strength, and the processability of PHA biopolyesters are better in case of high-molecular mass. During PHA biosynthesis, some factors are decisive for and directly impacting the molecular mass, predominantly the production strain, the selected carbon source, the concentration and activity of PHA synthases, the type of PHA synthase, the degree of intracellular PHA biosynthesis taking place in parallel with PHA biosynthesis, and the occurrence of chain transfer reactions between the PHA synthase enzyme and the growing PHA chains. The influence of these factors on molecular mass of PHA was studied both in living microbial cells and in *in vitro* experiments [137]. Due to the high importance of PHA molecular mass for its postsynthetic processing, the subsequent paragraphs are dedicated to this topic in a rather detailed fashion.

As a general rule, *scl*-PHA display higher molecular mass than *mcl*-PHA; typically, *scl*-PHA produced by the most important eubacterial *scl*-PHA producers like *C. necator*, *Azohydromonas lata*, *Burkholderia sacchari*, or *Haloferax mediterranei* have weight-average molecular mass (M_w) in the range of some 100 000 or even more than 1 000 000, while M_w of *mcl*-PHA produced by Pseudomonades is typically below 100 000. In addition, polydispersity ($Đ$), hence, the uniformity of molecular mass of polymer chains in a given sample, expressed as the ratio of M_w and number-average molecular mass (M_n), is generally higher for *mcl*-PHA than for *scl*-PHA [113].

1.3.5.2 Impact of PHA Synthase Activity on PHA Molecular Mass

Already in 1995, Koizumi et al. noticed an increase in M_n during the course of PHA biosynthesis in nitrogen-limited *C. necator* cultures. After reaching a maximum value of about 100 000, M_n dropped again. The authors developed a mathematical model, which involves a chain transfer agent, which acts as "mediator" between the synthases and the polymer chains [138]. Moreover, it was demonstrated for photosynthetic purple sulfur bacteria that, even for nitrogen-limited cultures, PHA of high-molecular mass is obtained at low mRNA levels of *PhaC* (encoding PHA synthase) and *PhaZ* (encoding PHA depolymerase) genes, which causes low concentration of respective enzymes in the cells; hence, the expression level of PHA-related enzymes strongly impacts PHA molecular mass [139]. Similar findings were recently made for PHA production by *A. vinelandii*; typically, M_w of PHA produced by this organism decreases after longer cultivation, while the lower molecular mass PHA fraction increases. Adaya et al. reported that for a *PhaZ*-negative strain of *A. vinelandii*, hence, a mutant lacking PHA depolymerase activity, M_w did not decrease, and low-molecular mass PHA fractions did not occur, but a higher intracellular PHA content was observed [106]. In this context, the mutant strain *A. vinelandii* OPNA was only recently used in 30 l pilot-scale experiments for PHA biosynthesis via fed-batch feeding of sucrose as carbon source. The produced biopolyester revealed an ultra-high-molecular-mass M_w of about 5.7×10^6 when using a novel recovery method based on ethanol extraction and precipitation, and washing the obtained PHA with acetone; recovering the product

by conventional techniques based on halogenated compound resulted in M_w of not even 10% of this value [140].

Activity of PHA synthase, as typical for an enzyme, is dependent on several environmental factors, such as temperature, pH-value, or salinity. In this context, it was shown only recently that the halophilic eubacterial strains *Halomonas neptunia* and *Halomonas hydrothermalis* produce, when using waste cooking oil as inexpensive carbon source, PHA with a M_w dependent on the salinity of the cultivation medium; for both strains, higher molecular mass was obtained at maximum tested salinity (100 g/l NaCl), while for both organisms, polydispersity $Đ$ did not show any dependence on salinity. Importantly, these high salinity values were exceeding the salinity optimum of the PHA synthase enzymes of the strains, which illustrates the possibility of shifting PHA molecular mass to higher values at the expense of PHA productivity when the culturing conditions move away from the biological optimum of the enzymes. [141]. The impact of cultivation temperature on molecular mass was demonstrated by Agus et al., who demonstrated that for *E. coli* harboring type I PHA synthase genes from *C. necator*, considerably lower PHA productivity was obtained at a temperature of 37 °C (temperature optimum of the host strain *E. coli*), but molecular mass was higher at this temperature than observed at the temperature optimum of the PHA synthase (30 °C) [142]. This effect was even more pronounced when testing *E. coli* harboring *Delftia acidovorans* PHA synthase genes; while at 30 °C (optimum of the PHA synthase), M_n amounted to less than 1 000 000, more than the fivefold molecular mass was obtained at 37 °C (optimum for growth of the host strain). Again, higher molecular mass went in parallel to strongly decreased productivity. In addition, $Đ$ was drastically higher at the enzyme's temperature optimum of 30 °C [143].

1.3.5.3 Impact of the Type of PHA Synthase on PHA Molecular Mass

The effect of different types of PHA synthase on molecular mass and $Đ$ of PHA produced by the same host organism under identical cultivation conditions was demonstrated by Agus et al., who engineered *E. coli* by transferring genes encoding for four different PHA synthases, obtained from five different donor strains: Type I synthase from *C. necator*, *A. caviae*, *D. acidovorans*, type II synthase from *Pseudomonas* sp., type III synthase from *A. vinosum*, and type IV synthase from *Bacillus* sp. While PHA of high M_n and low $Đ$ was produced by the action of type I synthase from *C. necator*, *D. acidovorans*, and the *A. vinosum* type III synthase, the three other synthases, especially the type IV synthase of *Bacillus* sp., produced PHA of rather low M_n with broad distribution of molecular mass (high $Đ$) [142].

1.3.5.4 Impact of Substrate Type and Feeding Conditions on PHA Molecular Mass

The effect of substrate supply on molecular mass of PHA produced by *C. necator* was described by Asenjo et al.; they remarked that in nitrogen-limited continuous cultures, excess of glucose should be avoided for production of high-molecular mass PHA. Moreover, these experiments also showed that magnesium and phosphate concentration should not drop below a critical value to obtain PHA of high-molecular

mass and narrow distribution (low $Đ$) [144]. A similar indirect proportionality between substrate concentration and PHA molecular mass in nitrogen-limited cultures of *C. necator* was described before by Shimizu et al., who noticed decreased M_n values at increasing butyrate concentration. Remarkably, these authors also noticed that, after addition of nitrogen, PHA of low-molecular mass was degraded faster than high-molecular mass PHA, which shifts M_n to higher values [145].

Regarding the impact of substrate/strain combinations on molecular mass of PHA, Taidi et al. found out that M_w of PHA produced by *A. eutrophus* (today: *C. necator*) was independent of the investigated substrates, which encompassed various sugars, glycerol, succinic acid, and acetate. An exception was observed for the case of using glycerol; for this substrate, termination of chain growth was observed, resulting in low-molecular-mass PHA ($5.5 - 8.5 \times 10^5$); for other studied substrates, M_w up to 1.7×10^6 was obtained [146]. This phenomenon was later described as so-called endcapping effect, caused by the coupling of exogenous polyols and other hydroxy compounds on the carboxy terminus of growing PHA chains [147]. A similar effect of glycerol was also noticed in the case of *scl*-PHA by haloarchaea, using whey as carbon source, *Hfx. mediterranei* produced PHA with a M_w of about 700 000, while a M_w of only about 250 000 was obtained when feeding the same organism with crude glycerol from biodiesel production [148]. Another rule of thumb for the dependence of M_w on the substrate use is that feeding sugars typically result in higher M_w if compared to the use of fatty substrates for PHA production by the same production strain. This was shown for *C. necator* when supplied with saturated biodiesel (mixture of fatty acid methyl esters); in this case, M_w did not exceed 306 000, which was even lower than when cultivating this strain on crude glycerol phase in parallel fermentation setups (380 000) [149]. In contrast, cultivating this strain on glucose as main substrate resulted in M_w well above 400 000 in five parallel setups with or without diverse complex growth additives [150]. Beside *C. necator*, Taidi et al. also studied the M_w of PHA produced by the strain *Methylobacterium extorquens*, an organism known to produce PHA of rather low-molecular mass from methanol. Surprisingly, M_w turned out to be dependent on the initial concentration of the studied carbon sources, namely methanol or succinate. Highest M_w (0.6 and 1.7×10^6) was obtained when supplying rather low initial concentrations of substrates; importantly, PHA produced from succinate had always higher M_w than in case of using methanol. The authors emphasized that PHA with a broad range of M_w was accessible by selection of the carbon source and fine-tuning its concentration [146].

1.3.5.5 Production of Ultra-High-Molecular-Mass PHA

A study by Arikawa et al. revealed that a total of nine genes are responsible for intracellular PHA depolymerization in *C. necator* H16, among them are PHA depolymerases and oligomer hydrolases [151]. When PHA biosynthesis enzymes are active in an organism, but depolymerases are lacking, it is possible to produce PHA of ultra-high-molecular mass. Such ultra-high-molecular-mass PHA was produced by Kusaka et al. by using a recombinant *E. coli*. This strain, no natural PHA producer, harbored the PHA biosynthesis genes *PhaCAB* from *C. necator*, but no genes encoding intracellular PHA depolymerase. Using glucose as substrate,

this recombinant *E. coli* XL-1 Blue (pSYL105) produced, in dependence on the pH-value, PHA with M_w between 1.1×10^6 and 1.1×10^7. The authors noticed that PHA samples with M_w exceeding 3.3×10^6 could be easily and reproducibly stretched to a draw ratio of 400–650%, which resulted in further improvement of mechanical properties such as Young's modulus and tensile strength [152]. Later, these authors revealed that the ultra-high M_w PHA produced by this organism was of amorphous character, while, by orientation of the polyester chains, it became highly crystalline after stretching. *In vitro* biodegradation test with an extracellular PHA depolymerase showed that enzymatic erosion of PHA polymer films was not dependent on the molecular mass, but highly on the crystallinity; within three weeks, PHA films with ultra-high-molecular mass were also readily degraded in river water [153].

Hiroe et al. demonstrated that the intracellular concentration of active PHA synthase is negatively correlated to the PHA molecular mass, but positively correlated to the intracellular PHA fraction. Hence, the PHA synthase activity is a bottle neck for the production of ultra-high- molecular mass and is of utmost importance for PHA productivity [143]. Later, the authors substantiated this theory that low amounts of active PHA synthase are beneficial for the production of PHA of higher molecular mass. They studied heterologous expression of PHA synthase either obtained from *Ralstonia eutropha* (today: *C. necator*) or from *D. acidovorans* in *E. coli* harboring *C. necator* genes encoding 3-ketothiolase (phaA) and acetoacetyl-CoA reductase (phaB). Under conditions favoring PHA biosynthesis (nitrogen limitation), levels of translation of PhaA and PhaB were in the same range for both recombinant *E. coli* strains, but the expression of PhaC from *D. acidovorans* was lower than that for the *C. necator*-derived synthase. This lower activity of *D. acidovorans* synthase resulted in PHA of considerably higher molecular mass (M_w of 4 200 000) if compared to PHA produced by *C. necator* PHA synthase (M_w of 270 000) [154]. Ultra-high-molecular-mass PHA was also produced by five different purple bacteria, which were studied by Higuchi-Takeuchi et al. The expression levels of *PhaC* and *PhaZ* genes were studied; they were low under conditions boosting PHA accumulation (nitrogen limitation), which again resulted in the production of PHA with high-molecular weight under limited activity of PHA synthase, that time combined with low activity of PHA depolymerase [139].

Surprising finding for M_w of PHA produced by the methane-utilizing strain *Methylocystis* sp. using methane as sole carbon source and initiated the PHA accumulation phase by limitation of either, iron, sulfur, or potassium. It turned out that potassium limitation resulted in the accumulation of PHA of ultra-high-molecular mass (M_w about 3×10^6), which sheds new light on strategies to improve the quality of PHA produced from gaseous carbon sources [155].

1.4 Conclusions

As demonstrated, the term "bioplastic" should not be used in a careless way. Many currently commercialized materials are labeled as "bioplastics" or "green plastics,"

while being of doubtful sustainability. It is shown that microbial PHA biopolyesters are definitely "bioplastics" in the original meaning, being biobased, biosynthesized, biodegradable, compostable, and biocompatible in accordance to the valid standardizations, regulations, and norms. Importantly, the versatility of PHA's material properties, determined by the polyesters' monomeric composition, molecular mass, and microstructure, allows the fabrication of bioplastic products for innumerable fields of application. Appropriate combinations of microbial production strains, fermentation strategies, feedstocks, and postsynthetic modification and processing with compatible materials open the route to develop novel biopolymeric materials of choice. However, it is of utmost importance to address not only the aspects of biodegradability and the biobased nature of PHA and other biopolymers of technological value, but also the sustainability and economic feasibility of the polymers' entire life cycle. This encompasses the selection of inexpensive feedstocks without value for food purposes, energy supply of the production process from renewable energy sources, and nontoxic techniques for product recovery during the downstream processing.

References

1 Geyer, R., Jambeck, J.R., and Law, K.L. (2017). Production, use, and fate of all plastics ever made. *Sci. Adv.* 3: e1700782.
2 Singh, N., Hui, D., Singh, R. et al. (2017). Recycling of plastic solid waste: a state of art review and future applications. *Compos. Part B: Eng.* 115: 409–422.
3 Koller, M. and Mukherjee, A. (2020). Polyhydroxyalkanoates–linking properties, applications, and end-of-life options. *Chem. Biochem. Eng. Q.* 34: 115–129.
4 Koller, M. (2019). Switching from petro-plastics to microbial polyhydroxyalkanoates (PHA): the biotechnological escape route of choice out of the plastic predicament? *EuroBiotech J.* 3: 32–44.
5 Online resource 1: https://www.kleinezeitung.at/service/newsticker/5439715/Thailand_Wal-verendete-an-ueber-80-Plastiksackerln-im-Magen (accessed 25 June 2018); (in German).
6 Zheng, J. and Suh, S. (2019). Strategies to reduce the global carbon footprint of plastics. *Nat. Clim. Chang.* 9 (5): 374.
7 Huysveld, S., Hubo, S., Ragaert, K., and Dewulf, J. (2019). Advancing circular economy benefit indicators and application on open-loop recycling of mixed and contaminated plastic waste fractions. *J. Clean. Prod.* 211: 1–13.
8 Schymanski, D., Goldbeck, C., Humpf, H.U., and Fürst, P. (2018). Analysis of microplastics in water by micro-Raman spectroscopy: release of plastic particles from different packaging into mineral water. *Water Res.* 129: 154–162.
9 Rochman, C.M., Browne, M.A., Halpern, B.S. et al. (2013). Policy: classify plastic waste as hazardous. *Nature* 494: 169.
10 Schwabl, P., Köppel, S., Königshofer, P. et al. (2019). Detection of various microplastics in human stool: a prospective case series. *Ann. Intern. Med.* 171: 453–457.

11 Lei, L., Wu, S., Lu, S. et al. (2018). Microplastic particles cause intestinal damage and other adverse effects in zebrafish *Danio rerio* and nematode *Caenorhabditis elegans*. *Sci. Total Environ.* 619: 1–8.

12 Wycherley, P.R. (1992). The genus *Hevea*: botanical aspects. In: *Natural Rubber: Biology, Cultivation and Technology* (ed. M.R. Sethuraj and N.T. Mathew), 50–66. Elsevier.

13 Dilkes-Hoffman, L., Ashworth, P., Laycock, B. et al. (2019). Public attitudes towards bioplastics–knowledge, perception and end-of-life management. *Resour. Conserv. Recycl.* 151: 104479.

14 Thunwall, M., Kuthanova, V., Boldizar, A., and Rigdahl, M. (2008). Film blowing of thermoplastic starch. *Carbohydr. Polym.* 71: 583–590.

15 Bradbury, E. and Martin, C. (1951). Mechanical Properties and structure of sol-type and gel-type gelatine films. *Nature* 168: 837–838.

16 Schmid, M., Dallmann, K., Bugnicourt, E. et al. (2012). Properties of whey-protein-coated films and laminates as novel recyclable food packaging materials with excellent barrier properties. *Int. J. Polym. Sci.* 2012: 562381.

17 Qin, Y., Lu, X., Sun, N., and Rogers, R.D. (2010). Dissolution or extraction of crustacean shells using ionic liquids to obtain high molecular weight purified chitin and direct production of chitin films and fibers. *Green Chem.* 12: 968–971.

18 Aulin, C., Gällstedt, M., and Lindström, T. (2010). Oxygen and oil barrier properties of microfibrillated cellulose films and coatings. *Cellulose* 17: 559–574.

19 Drumright, R.E., Gruber, P.R., and Henton, D.E. (2000). Polylactic acid technology. *Adv. Mater.* 12: 1841–1846.

20 Online resource 2: https://www.t-online.de/finanzen/boerse/news/id_83326206/lego-steine-aus-bioplastik-so-umweltfreundlich-sind-sie-wirklich.html (accessed 4 November 2019).

21 Online resource 3: https://www.coca-colacompany.com/plantbottle-technology(accessed 24 October 2019).

22 Labet, M. and Thielemans, W. (2009). Synthesis of polycaprolactone: a review. *Chem. Soc. Rev.* 38: 3484–3504.

23 Online resource 4: https://products.basf.com/de/ecoflex.html (accessed 24 October 2019).

24 Danso, D., Chow, J., and Streit, W.R. (2019). Plastics: environmental and biotechnological perspectives on microbial degradation. *Appl. Environ. Microbiol.* 85: e01095–e01019.

25 Koller, M., Salerno, A., Muhr, A. et al. (2013). Polyhydroxyalkanoates: biodegradable polymers and plastics from renewable resources. *Mater. Technol.* 47: 5–12.

26 Budwill, K., Fedorak, P.M., and Page, W.J. (1992). Methanogenic degradation of poly(3-hydroxyalkanoates). *Appl. Environ. Microbiol.* 58: 1398–1401.

27 Jendrossek, D., Schirmer, A., and Schlegel, H.G. (1996). Biodegradation of polyhydroxyalkanoic acids. *Appl. Microbiol. Biotechnol.* 46: 451–463.

28 Yutaka, T. and Buenaventurada, C. (2004). Degradation of Microbial Polyesters. *Biotechnol. Lett.* 26: 1181–1189.

29 Misra, S.K., Valappil, S.P., Roy, I., and Boccaccini, A.R. (2006). Polyhydroxyalkanoate (PHA)/inorganic phase composites for tissue engineering applications. *Biomacromolecules* 7: 2249–2258.

30 Gil-Castell, O., Badia, J.D., Bou, J., and Ribes-Greus, A. (2019). Performance of polyester-based electrospun scaffolds under *in vitro* hydrolytic conditions: from short-term to long-term applications. *Nanomaterials (Basel)* 9: 786.

31 Kourmentza, C., Plácido, J., Venetsaneas, N. et al. (2017). Recent advances and challenges towards sustainable polyhydroxyalkanoate (PHA) production. *Bioengineering* 4: 55.

32 Lenz, R.W. and Marchessault, R.H. (2005). Bacterial polyesters: biosynthesis, biodegradable plastics and biotechnology. *Biomacromolecules* 6: 1–8.

33 Jendrossek, D. (2009). Polyhydroxyalkanoate granules are complex subcellular organelles (carbonosomes). *J. Bacteriol.* 191: 3195–3202.

34 Rodríguez-Contreras, A. (2019). Recent advances in the use of polyhydroyalkanoates in biomedicine. *Bioengineering* 6: 82.

35 Koller, M. (2014). Poly(hydroxyalkanoates) for food packaging: application and attempts towards implementation. *Appl. Food Biotechnol.* 1: 3–15.

36 Haugaard, V.K., Udsen, A.M., Hoegh, L. et al. (2001). Potential food applications of biobased materials an EU-concerted action project. *Starch* 53: 189–200.

37 Sängerlaub, S., Brüggemann, M., Rodler, N. et al. (2019). Extrusion coating of paper with poly(3-hydroxybutyrate-co-3-hydroxyvalerate) (PHBV)—packaging related functional properties. *Coatings* 9: 457.

38 Shishatskaya, E.I., Volova, T., Puzyr, A.P. et al. (2004). Tissue response to the implantation of biodegradable polyhydroxyalkanoate sutures. *J. Mater. Sci. Mater. Med.* 15: 719–728.

39 Volova, T., Shishatskaya, E.I., Sevastianov, V. et al. (2003). Results of biomedical investigations of PHB and PHB/PHV fibers. *Biochem. Eng. J.* 16: 125–133.

40 Meischel, M., Eichler, J., Martinelli, E. et al. (2016). Adhesive strength of bone-implant interfaces and *in-vivo* degradation of PHB composites for load-bearing applications. *J. Mech. Behav. Biomed.* 53: 104–118.

41 Rodríguez-Contreras, A., García, Y., Manero, J.M., and Rupérez, E. (2017). Antibacterial PHAs coating for titanium implants. *Eur. Polym. J.* 90: 66–78.

42 Rodríguez-Contreras, A., Guillem-Marti, J., Lopez, O. et al. (2019). Antimicrobial PHAs coatings for solid and porous Tantalum implants. *Colloids Surf. B. Biointerfaces* 182: 110317.

43 Findrik Balogová, A., Hudák, R., Tóth, T. et al. (2018). Determination of geometrical and viscoelastic properties of PLA/PHB samples made by additive manufacturing for urethral substitution. *J. Biotechnol.* 284: 123–130.

44 Lizarraga-Valderrama, L.R., Taylor, C.S., Claeyssens, F. et al. (2019). Unidirectional neuronal cell growth and differentiation on aligned polyhydroxyalkanoate blend microfibres with varying diameters. *J. Tissue Eng. Regen. Med.* 13: 1581–1594.

45 Grigore, M.E., Grigorescu, R.M., Iancu, L. et al. (2019). Methods of synthesis, properties and biomedical applications of polyhydroxyalkanoates: a review. *J. Biomater. Sci. Polym. Ed.* 30: 695–712.

46 Butt, F.I., Muhammad, N., Hamid, A. et al. (2018). Recent progress in the utilization of biosynthesized polyhydroxyalkanoates for biomedical applications—Review. *Int. J. Biol. Macromol.* 120: 1294–1305.

47 Singh, A.K., Srivastava, J.K., Chandel, A.K. et al. (2019). Biomedical applications of microbially engineered polyhydroxyalkanoates: an insight into recent advances, bottlenecks, and solutions. *Appl. Microbiol. Biotechnol.* 103: 2007–2032.

48 Koller, M. (2018). Biodegradable and biocompatible polyhydroxy-alkanoates (PHA): auspicious microbial macromolecules for pharmaceutical and therapeutic applications. *Molecules* 23: 362.

49 Ellis, G., Cano, P., Jadraque, M. et al. (2011). Laser microperforated biodegradable microbial polyhydroxyalkanoate substrates for tissue repair strategies: an infrared microspectroscopy study. *Anal. Bioanal. Chem.* 399: 2379–2388.

50 Francis, L., Meng, D., Knowles, J.C. et al. (2010). Multi-functional P(3HB) microsphere/45S5 Bioglass®-based composite scaffolds for bone tissue engineering. *Acta Biomater.* 6: 2773–2786.

51 Francis, L., Meng, D., Locke, I.C. et al. (2016). Novel poly(3-hydroxybutyrate) composite films containing bioactive glass nanoparticles for wound healing applications. *Polym. Int.* 65: 661–674.

52 Puppi, D., Pirosa, A., Lupi, G. et al. (2017). Design and fabrication of novel polymeric biodegradable stents for small caliber blood vessels by computer-aided wet-spinning. *Biomed. Mater.* 12: 035011.

53 Puppi, D., Chiellini, F., Piras, A.M., and Chiellini, E. (2010). Polymeric materials for bone and cartilage repair. *Prog. Polym. Sci.* 35: 403–440.

54 Deng, Y., Zhao, K., Zhang, X. et al. (2002). Study on the three-dimensional proliferation of rabbit articular cartilage-derived chondrocytes on polyhydroxyalkanoate scaffolds. *Biomaterials* 23: 4049–4056.

55 Zhao, K., Deng, Y., Chun Chen, J., and Chen, G.Q. (2003). Polyhydroxyalkanoate (PHA) scaffolds with good mechanical properties and biocompatibility. *Biomaterials* 24: 1041–1045.

56 Lizarraga-Valderrama, L.R., Nigmatullin, R., Taylor, C. et al. (2015). Nerve tissue engineering using blends of poly(3-hydroxyalkanoates) for peripheral nerve regeneration. *Eng. Life Sci.* 15: 612–621.

57 Rodríguez-Contreras, A., Calafell-Monfort, M., and Marqués-Calvo, M.S. (2012). Enzymatic degradation of poly(3-hydroxybutyrate) by a commercial lipase. *Polym. Degrad. Stab.* 97: 2473–2476.

58 Rodríguez-Contreras, A., Calafell-Monfort, M., and Marqués-Calvo, M.S. (2012). Enzymatic degradation of poly(3-hydroxybutyrate-*co*-4-hydroxybutyrate) by commercial lipases. *Polym. Degrad. Stab.* 97: 597–604.

59 Masood, F. (2016). Polymeric nanoparticles for targeted drug delivery system for cancer therapy. *Mater. Sci. Eng. C* 60: 569–578.

60 Wu, L.P., Wang, D., Parhamifar, L. et al. (2014). Poly(3-hydroxybutyrate-*co*-R-3-hydroxyhexanoate) nanoparticles with polyethylenimine coat as simple, safe, and versatile vehicles for cell targeting: population characteristics, cell uptake, and intracellular trafficking. *Adv. Healthc. Mater.* 3: 817–824.

61 Online resource 5: http://www.bio-on.it/biomeds.php (accessed 4 November 2019).

62 Berezina, N., Yada, B., and Lefebvre, R. (2015). From organic pollutants to bioplastics: insights into the bioremediation of aromatic compounds by *Cupriavidus necator*. *New Biotechnol.* 32: 47–53.

63 Tan, G.Y.A., Chen, C.L., Ge, L. et al. (2015). Bioconversion of styrene to poly(hydroxyalkanoate) (PHA) by the new bacterial strain *Pseudomonas putida* NBUS12. *Microbes Environ.* ME14138.

64 Goudarztalejerdi, A., Tabatabaei, M., Eskandari, M.H., and Mowla, D. (2019). Optimization conditions for maximum oil bioremediation and biopolymer production by Pseudomonads. *Iranian J. Sci. Technol. A.* 43: 1439–1446.

65 Revelo Romo, D.M., Obando, M.C., Perdomo, M.I.G., and Izquierdo, P.F. (2014). PHA synthase genes in oil-degrading marine bacteria from the Colombian Pacific coast. *Int. J. Adv. Biotechnol. Res.* 5: 404–414.

66 Online resource 6: http://www.bio-on.it/minerv-biorecovery.php?lin=inglese (accessed 25 October 2019).

67 Janakiraman, V.C., Subramani, S., Devarajan, M., and Abdul Aziz, A. (2017). Impact of ZnO Nanoparticles on dielectric and optical properties of poly(3-hydroxybutyrate) for electronics applications. *Polym. Plast. Technol.* 56: 1495–1504.

68 Online resource 7: http://www.bio-on.it/minerv-cosmetics.php?lin=inglese (accessed 25 October 2019).

69 Shishatskaya, E.I., Nikolaeva, E.D., Vinogradova, O.N., and Volova, T.G. (2016). Experimental wound dressings of degradable PHA for skin defect repair. *J. Mater. Sci-Mater M.* 27: 165.

70 Pereira, J.R., Araújo, D., Marques, A.C. et al. (2019). Demonstration of the adhesive properties of the medium-chain-length polyhydroxyalkanoate produced by *Pseudomonas chlororaphis* subsp. *aurantiaca* from glycerol. *Int. J. Biol. Macromol.* 122: 1144–1151.

71 Online resource 8: http://www.bio-on.it/minerv-supertoys.php (accessed 25 October 2019).

72 Ren, Q., Grubelnik, A., Hoerler, M. et al. (2005). Bacterial poly(hydroxyalkanoates) as a source of chiral hydroxyalkanoic acids. *Biomacromolecules* 6: 2290–2298.

73 Rich, A.J. (1990). Ketone bodies as substrates. *P. Nutr. Soc.* 49: 361–373.

74 Norris, V., Bresson-Dumont, H., Gardea, E. et al. (2009). Hypothesis: poly-(*R*)-3-hydroxybutyrate is a major factor in intraocular pressure. *Med. Hypotheses* 73: 398–401.

75 Pawan, G.L.S. and Semple, S.J.G. (1983). Effect of 3-hydroxybutyrate in obese subjects on very-low-energy diets and during therapeutic starvation. *Lancet* 321: 15–17.

76 Woods, W.G., Pawan, G.L., Semple, S.J., and Ralphs, D.N. (1983). Effect of intravenous 3-hydroxybutyrate on postoperative nitrogen balance. *Hum. Nutr. Clin. Nutr.* 37: 391–394.

77 Zhang, J., Cao, Q., Li, S. et al. (2013). 3-Hydroxybutyrate methyl ester as a potential drug against Alzheimer's disease via mitochondria protection mechanism. *Biomaterials* 34 (30): 7552–7562.

78 Ruth, K., Grubelnik, A., Hartmann, R. et al. (2007). Efficient production of (*R*)-3-hydroxycarboxylic acids by biotechnological conversion of polyhydroxyalkanoates and their purification. *Biomacromolecules* 8: 279–286.

79 Lee, S.Y., Lee, Y., and Wang, F. (1999). Chiral compounds from bacterial polyesters: sugars to plastics to fine chemicals. *Biotechnol. Bioeng.* 65 (3): 363–368.

80 Online resource 9: https://www.bioplasticsmagazine.com/en/news/meldungen/20191106Bio-on-patents-new-cigarette-filter-material-.php (accessed 25 October 2019).

81 Zhang, X., Luo, R., Wang, Z. et al. (2009). Application of (*R*)-3-hydroxyalkanoate methyl esters derived from microbial polyhydroxyalkanoates as novel biofuels. *Biomacromolecules* 10 (4): 707–711.

82 Wang, S.Y., Wang, Z., Liu, M.M. et al. (2010). Properties of a new gasoline oxygenate blend component: 3-hydroxybutyrate methyl ester produced from bacterial poly-3-hydroxybutyrate. *Biomass Bioenergy* 34: 1216–1222.

83 Cerrone, F., Radivojevic, J., Nikodinovic-Runic, J. et al. (2019). Novel sodium alkyl-1, 3-disulfates, anionic biosurfactants produced from microbial polyesters. *Colloid Surf., B* 182: 110333.

84 Braunegg, G., Lefebvre, G., and Genser, K.F. (1998). Polyhydroxyalkanoates, biopolyesters from renewable resources: physiological and engineering aspects. *J. Biotechnol.* 65: 127–161.

85 Obruca, S., Sedlacek, P., Koller, M. et al. (2018). Involvement of polyhydroxyalkanoates in stress resistance of microbial cells: biotechnological consequences and applications. *Biotechnol. Adv.* 36: 856–870.

86 Obruca, S., Sedlacek, P., Mravec, F. et al. (2016). Evaluation of 3-hydroxybutyrate as an enzyme-protective agent against heating and oxidative damage and its potential role in stress response of poly(3-hydroxybutyrate) accumulating cells. *Appl. Microbiol. Biotechnol.* 100: 1365–1376.

87 Slaninova, E., Sedlacek, P., Mravec, F. et al. (2018). Light scattering on PHA granules protects bacterial cells against the harmful effects of UV radiation. *Appl. Microbiol. Biotechnol.* 102: 1923–1931.

88 Obruca, S., Sedlacek, P., Krzyzanek, V. et al. (2016). Accumulation of poly(3-hydroxybutyrate) helps bacterial cells to survive freezing. *PLoS One* 11: e0157778.

89 Chien, C.C., Wang, L.J., and Lin, W.R. (2014). Polyhydroxybutyrate accumulation by a cadmium-resistant strain of *Cupriavidus taiwanensis*. *J. Taiwan Inst. Chem. Eng.* 45: 1164–1169.

90 Obruca, S., Marova, I., Stankova, M. et al. (2010). Effect of ethanol and hydrogen peroxide on poly(3-hydroxybutyrate) biosynthetic pathway in *Cupriavidus necator* H16. *World J. Microbiol. Biotechnol.* 26: 1261–1267.

91 Al Rowaihi, I.S., Paillier, A., Rasul, S. et al. (2018). Poly(3-hydroxybutyrate) production in an integrated electromicrobial setup: investigation under stress-inducing conditions. *PLoS One* 13: e0196079.

92 Obruca, S., Sedlacek, P., Mravec, F. et al. (2017). The presence of PHB granules in cytoplasm protects non-halophilic bacterial cells against the harmful impact of hypertonic environments. *New Biotechnol.* 39: 68–80.

93 Sedlacek, P., Slaninova, E., Koller, M. et al. (2019). PHA granules help bacterial cells to preserve cell integrity when exposed to sudden osmotic imbalances. *New Biotechnol.* 49: 129–136.

94 Koller, M. (2019). Polyhydroxyalkanoate biosynthesis at the edge of water activity-haloarchaea as biopolyester factories. *Bioengineering* 6: 34.

95 Jendrossek, D. and Pfeiffer, D. (2014). New insights in the formation of polyhydroxyalkanoate granules (carbonosomes) and novel functions of poly(3-hydroxybutyrate). *Environ. Microbiol.* 16: 2357–2373.

96 Jurasek, L. and Marchessault, R.H. (2002). The role of phasins in the morphogenesis of poly(3-hydroxybutyrate) granules. *Biomacromolecules* 3: 256–261.

97 Pötter, M., Madkour, M.H., Mayer, F., and Steinbüchel, A. (2002). Regulation of phasin expression and polyhydroxyalkanoate (PHA) granule formation in *Ralstonia eutropha* H16. *Microbiology* 148: 2413–2426.

98 Sun, Y.W., Li, Y., Hu, Y. et al. (2019). Coordinated regulation of the size and number of polyhydroxybutyrate granules by core and accessory phasins in the facultative microsymbiont *Sinorhizobium fredii* NGR234. *Appl. Environ. Microbiol.* 85: e00717–e00719.

99 Vadlja, D., Koller, M., Novak, M. et al. (2016). Footprint area analysis of binary imaged *Cupriavidus necator* cells to study PHB production at balanced, transient, and limited growth conditions in a cascade process. *Appl. Microbiol. Biotechnol.* 100: 10065–10080.

100 Galán, B., Dinjaski, N., Maestro, B. et al. (2011). Nucleoid-associated PhaF phasin drives intracellular location and segregation of polyhydroxyalkanoate granules in *Pseudomonas putida* KT2442. *Mol. Microbiol.* 79: 402–418.

101 Karmann, S., Panke, S., and Zinn, M. (2017). The bistable behaviour of *Pseudomonas putida* KT2440 during PHA depolymerization under carbon limitation. *Bioengineering* 4: 58.

102 Rehm, B.H. (2003). Polyester synthases: natural catalysts for plastics. *Biochem. J.* 376: 15–33.

103 Tsuge, T., Hyakutake, M., and Mizuno, K. (2015). Class IV polyhydroxyalkanoate (PHA) synthases and PHA-producing *Bacillus*. *Appl. Microbiol. Biotechnol.* 99: 6231–6240.

104 Doi, Y., Segawa, A., Kawaguchi, Y., and Kunioka, M. (1990). Cyclic nature of poly(3-hydroxyalkanoate) metabolism in *Alcaligenes eutrophus*. *FEMS Microbiol. Lett.* 67: 165–169.

105 Kusaka, S., Iwata, T., and Doi, Y. (1999). Properties and biodegradability of ultra-high-molecular-weight poly [(R)-3-hydroxybutyrate] produced by a recombinant *Escherichia coli*. *Int. J. Biol. Macromol.* 25: 87–94.

106 Adaya, L., Millán, M., Peña, C. et al. (2018). Inactivation of an intracellular poly-3-hydroxybutyrate depolymerase of *Azotobacter vinelandii* allows to obtain a polymer of uniform high molecular mass. *Appl. Microbiol. Biotechnol.* 102: 2693–2707.

107 Choi, G.G., Kim, H.W., and Rhee, Y.H. (2004). Enzymatic and non-enzymatic degradation of poly (3-hydroxybutyrate-*co*-3-hydroxyvalerate) copolyesters produced by *Alcaligenes* sp. MT-16. *J. Microbiol.* 42: 346–352.

108 Steinbüchel, A. (2005). Non-biodegradable biopolymers from renewable resources: perspectives and impacts. *Curr. Opin. Biotechnol.* 16: 607–613.

109 Lütke-Eversloh, T., Bergander, K., Luftmann, H., and Steinbüchel, A. (2001). Biosynthesis of poly(3-hydroxybutyrate-*co*-3-mercaptobutyrate) as a sulfur analogue to poly(3-hydroxybutyrate) (PHB). *Biomacromolecules* 2: 1061–1065.

110 Elbanna, K., Lütke-Eversloh, T., Van Trappen, S. et al. (2003). *Schlegelella thermodepolymerans* gen. nov., sp. nov., a novel thermophilic bacterium that degrades poly(3-hydroxybutyrate-*co*-3-mercaptopropionate). *Int. J. Syst. Evol. Microbiol.* 53: 1165–1168.

111 Kim, D.Y., Lütke-Eversloh, T., Elbanna, K. et al. (2005). Poly(3-mercapto-propionate): a nonbiodegradable biopolymer? *Biomacromolecules* 6: 897–901.

112 Chen, G.Q. and Hajnal, I. (2015). The 'PHAome'. *Trends Biotechnol.* 33: 559–564.

113 Koller, M. (2018). Chemical and biochemical engineering approaches in manufacturing Polyhydroxyalkanoate (PHA) biopolyesters of tailored structure with focus on the diversity of building blocks. *Chem. Biochem. Eng. Q.* 32: 413–438.

114 Zhila, N. and Shishatskaya, E. (2018). Properties of PHA bi-, ter-, and quarter-polymers containing 4-hydroxybutyrate monomer units. *Int. J. Biol. Macromol.* 111: 1019–1026.

115 Zinn, M. (2010). Biosynthesis of medium-chain-length Poly[(R)-3-hydroxyalkanoates]. In: *Plastics from Bacteria, Natural Functions and Applications* (ed. G.Q. Chen and A. Steinbüchel), 213–236. Münster: Springer.

116 Williams, M. (2002). Applications of PHAs in medicine and pharmacy. In: *Biopolymers 4, Polyesters III – Applications* (ed. Y.A. Doi and A. Steinbüchel), 91–103. Weinheim: Wiley-VCH.

117 Koller, M., Maršálek, L., and M. Miranda de Sousa Dias, G. Braunegg. (2017). Producing microbial polyhydroxyalkanoate (PHA) biopolyesters in a sustainable manner. *New Biotechnol.* 37: 24–38.

118 Lemoigne, M. (1923). Production d'acide β-oxybutyrique par certaines bactéries du groupe du *Bacillus subtilis*. *C. R. Hebd. Seances Acad. Sci.* 176: 1761.

119 Wallen, L.L. and Rohwedder, W.K. (1974). Poly-beta-hydroxyalkanoate from activated sludge. *Environ. Sci. Technol.* 8: 576–579.

120 Doi, Y., Tamaki, A., Kunioka, M., and Soga, K. (1988). Production of copolyesters of 3-hydroxybutyrate and 3-hydroxyvalerate by *Alcaligenes eutrophus* from butyric and pentanoic acids. *Appl. Microbiol. Biotechnol.* 28: 330.

121 Kunioka, M., Kawaguchi, Y., and Doi, Y. (1989). Production of biodegradable copolyesters of 3-hydroxybutyrate and 4-hydroxybutyrate by *Alcaligenes eutrophus*. *Appl. Microbial. Biotechnol.* 30: 569–573.

122 Saito, Y., Nakamura, S., Hiramitsu, M., and Doi, Y. (1996). Microbial synthesis and properties of poly(3-hydroxybutyrate-*co*-4-hydroxybutyrate). *Polym. Int.* 39: 169–174.

123 Brigham, C.J. and Sinskey, A.J. (2012). Applications of polyhydroxyalkanoates in the medical industry. *Int. J. Biotechnol. Wellness Ind.* 1: 52–60.

124 Gopi, S., Kontopoulou, M., Ramsay, B.A., and Ramsay, J.A. (2018). Manipulating the structure of medium-chain-length polyhydroxyalkanoate (MCL-PHA) to enhance thermal properties and crystallization kinetics. *Int. J. Biol. Macromol.* 119: 1248–1255.

125 De Waard, P., Van der Wal, H., Huijberts, G.N., and Eggink, G. (1993). Heteronuclear NMR analysis of unsaturated fatty acids in poly(3-hydroxyalkanoates). Study of beta-oxidation in *Pseudomonas putida*. *J. Biol. Chem.* 268: 315–319.

126 Huijberts, G.N., Eggink, G., De Waard, P. et al. (1992). *Pseudomonas putida* KT2442 cultivated on glucose accumulates poly(3-hydroxyalkanoates) consisting of saturated and unsaturated monomers. *Appl. Environ. Microbiol.* 58: 536–544.

127 Sathiyanarayanan, G., Bhatia, S.K., Song, H.S. et al. (2017). Production and characterization of medium-chain-length polyhydroxyalkanoate copolymer from Arctic psychrotrophic bacterium *Pseudomonas* sp. PAMC 28620. *Int. J. Biol. Macromol.* 97: 710–720.

128 Barbuzzi, T., Giuffrida, M., Impallomeni, G. et al. (2004). Microbial synthesis of poly(3-hydroxyalkanoates) by *Pseudomonas aeruginosa* from fatty acids: identification of higher monomer units and structural characterization. *Biomacromolecules* 5: 2469–2478.

129 Ray, S. and Kalia, V.C. (2017). Co-metabolism of substrates by *Bacillus thuringiensis* regulates polyhydroxyalkanoate co-polymer composition. *Bioresour. Technol.* 224: 743–747.

130 Ribeiro, P.L.L., da Silva, A.C.M.S., Menezes Filho, J.A. et al. (2015). Impact of different by-products from the biodiesel industry and bacterial strains on the production, composition, and properties of novel polyhydroxyalkanoates containing achiral building blocks. *Ind. Crop. Prod.* 69: 212–223.

131 Tripathi, L., Wu, L.P., Chen, J., and Chen, G.Q. (2012). Synthesis of Diblock copolymer poly-3-hydroxybutyrate-block-poly-3-hydroxyhexanoate [PHB-*b*-PHHx] by a β-oxidation weakened *Pseudomonas putida* KT2442. *Microb. Cell Fact.* 11: 44.

132 Pederson, E.N., McChalicher, C.W., and Srienc, F. (2006). Bacterial synthesis of PHA block copolymers. *Biomacromolecules* 7: 1904–1911.

133 Adamus, G., Sikorska, W., Janeczek, H. et al. (2012). Novel block copolymers of atactic PHB with natural PHA for cardiovascular engineering: synthesis and characterization. *Eur. Polym. J.* 48: 621–631.

134 Zinn, B. and Witholt, T.E. (2004). Dual nutrient limited growth: models, experimental observations, and applications. *J. Biotechnol.* 113: 263–279.

135 Atlić, A., Koller, M., Scherzer, D. et al. (2011). Continuous production of poly([*R*]-3-hydroxybutyrate) by *Cupriavidus necator* in a multistage bioreactor cascade. *Appl. Microbiol. Biotechnol.* 91: 295–304.

136 Sudo, M., Hori, C., Ooi, T. et al. (2020). Synergy of valine and threonine supplementation on poly(2-hydroxybutyrate-*block*-3-hydroxybutyrate) synthesis in engineered *Escherichia coli* expressing chimeric polyhydroxyalkanoate synthase. *J. Biosci. Bioeng.* 129: 302–306.

137 Tsuge, T. (2016). Fundamental factors determining the molecular weight of polyhydroxyalkanoate during biosynthesis. *Polym. J.* 48: 1051–1057.

138 Koizumi, F., Abe, H., and Doi, Y. (1995). Molecular weight of poly(3-hydroxy butyrate) during biological polymerization in *Alcaligenes eutrophus*. *J. Macromol. Sci. A* 32: 759–774.

139 Higuchi-Takeuchi, M., Morisaki, K., Toyooka, K., and Numata, K. (2016). Synthesis of high-molecular-weight polyhydroxyalkanoates by marine photosynthetic purple bacteria. *PLoS One* 11: e0160981.

140 García, A., Pérez, D., Castro, M. et al. (2019). Production and recovery of poly-3-hydroxybutyrate [P(3HB)] of ultra-high molecular weight using fed-batch cultures of *Azotobacter vinelandii* OPNA strain. *J. Chem. Technol. Biotechnol.* 94 (6): 1853–1860.

141 Pernicova, I., Kucera, D., Nebesarova, J. et al. (2019). Production of polyhydroxyalkanoates on waste frying oil employing selected *Halomonas* strains. *Bioresour. Technol.* 292: 122028.

142 Agus, J., Kahar, P., Hyakutake, M. et al. (2010). Unusual change in molecular weight of polyhydroxyalkanoate (PHA) during cultivation of PHA-accumulating *Escherichia coli*. *Polym. Degrad. Stab.* 95 (12): 2250–2254.

143 Hiroe, A., Ushimaru, K., and Tsuge, T. (2013). Characterization of polyhydroxyalkanoate (PHA) synthase derived from *Delftia acidovorans* DS-17 and the influence of PHA production in *Escherichia coli*. *J. Biosci. Bioeng.* 115 (6): 633–638.

144 Asenjo, J.A., Schmidt, A.S., Andersen, P.R., and Andrews, B.A. (1995). Effect of single nutrient limitation of poly-β-hydroxybutyrate molecular weight distribution in *Alcaligens europhus*. *Biotechnol. Bioeng.* 46: 497–502.

145 Shimizu, H., Tamura, S., Shioya, S., and Suga, K.I. (1993). Kinetic study of poly-D(−)-3-hydroxybutyric acid (PHB) production and its molecular weight distribution control in a fed-batch culture of *Alcaligenes eutrophus*. *J. Ferment. Bioeng.* 76: 465–469.

146 Taidi, B., Anderson, A.J., Dawes, E.A., and Byrom, D. (1994). Effect of carbon source and concentration on the molecular mass of poly(3-hydroxybutyrate) produced by *Methylobacterium extorquens* and *Alcaligenes eutrophus*. *Appl. Microbiol. Biotechnol.* 40: 786–790.

147 Madden, L.A., Anderson, A.J., Shah, D.T., and Asrar, J. (1999). Chain termination in polyhydroxyalkanoate synthesis: involvement of exogenous hydroxy-compounds as chain transfer agents. *Int. J. Biol. Macromol.* 25: 43–53.

148 Koller, M., Bona, R., Braunegg, G. et al. (2005). Production of polyhydroxyalkanoates from agricultural waste and surplus materials. *Biomacromolecules* 6: 561–565.

149 Koller, M. and Braunegg, G. (2015). Biomediated production of structurally diverse poly(hydroxyalkanoates) from surplus streams of the animal processing industry. *Polimery* 60: 298–308.

150 Koller, M., Bona, R., Hermann, C. et al. (2005). Biotechnological production of poly(3-hydroxybutyrate) with *Wautersia eutropha* by application of green grass juice and silage juice as additional complex substrates. *Biocatal. Biotransformation* 23: 329–337.

151 Arikawa, H., Sato, S., Fujiki, T., and Matsumoto, K. (2016). A study on the relation between poly(3-hydroxybutyrate) depolymerases or oligomer hydrolases and molecular weight of polyhydroxyalkanoates accumulating in *Cupriavidus necator* H16. *J. Biotechnol.* 227: 94–102.

152 Kusaka, S., Iwata, T., and Doi, Y. (1998). Microbial synthesis and physical properties of ultra-high-molecular-weight poly[(*R*)-3-hydroxybutyrate]. *J. Macromol. Sci. A* 35: 319–335.

153 Kusaka, S., Iwata, T., Doi, Y. (1999). Properties and biodegradability of ultra-high-molecular-weight poly[(R)-3-hydroxybutyrate]produced by a recombinant Escherichia coli.. *Int. J. Biol. Macromol*. 25: 87–94.

154 Hiroe, A., Tsuge, K., Nomura, C.T. et al. (2012). Rearrangement of gene order in the phaCAB operon leads to effective production of ultrahigh-molecular-weight poly [(*R*)-3-hydroxybutyrate] in genetically engineered *Escherichia coli*. *Appl. Environ. Microbiol.* 78: 3177–3184.

155 Helm, J., Wendlandt, K.D., Jechorek, M., and Stottmeister, U. (2008). Potassium deficiency results in accumulation of ultra-high molecular weight poly-β-hydroxybutyrate in a methane-utilizing mixed culture. *J. Appl. Microbiol.* 105: 1054–1061.

2

Analysis of Chemical Composition of Biopolymers and Biomaterials: An XPS Study

Alenka Vesel and Miran Mozetic

Jožef Stefan Institute, Department of Surface Engineering and Optoelectronics, Teslova 30, SI-1000 Ljubljana, Slovenia

2.1 Basics of X-Ray Photoelectron Spectroscopy (XPS)

X-ray photoelectron spectroscopy (XPS) is a surface-sensitive technique that can give useful information on the elemental composition of materials as well as on the chemical state of the elements. A sample of the material is exposed to monochromatic X-rays, which cause a photoelectric effect. The use of a monochromator X-ray source is important because it provides better energy resolution (compared to a standard X-ray source) and less degradation damage. Therefore, monochromatic aluminum AlK_α radiation with a photon energy ($h\nu$) of 1486.6 eV is usually used. The absorption of X-ray photons in the material leads to the emission of photoelectrons, as shown schematically in Figure 2.1. The kinetic energy (E_{kin}) of emitted photoelectrons depends on their binding energy (E_B) and is characteristic of the atom of origin. The binding energy is calculated from the equation: $E_B = h\nu - E_{kin} - \phi$, where ϕ is the spectrometer work function, which denotes the energy that a photoelectron needs to escape from the material.

This approach allows the identification of the elements in the investigated material. A typical escape depth of photoelectrons when traveling through the material is only a few nanometers, which makes this technique surface sensitive. In Figure 2.2 is shown an example of the inelastic mean free path (IMFP) (λ) for photoelectrons from polystyrene. IMFP is the average distance traveled by a photoelectron between successive inelastic collisions, and it depends on the photoelectron energy. Most of the photoelectrons will come from 3λ, which is a typical sampling depth of XPS. Data shown in Figure 2.2 were obtained by a simulation based on the National Institute of Standards and Technology (NIST) database [1] provided by Tanuma et al. [2] and IMFPWIN software developed by Jablonski [1]. As shown in Figure 2.2, IMFP of C1s photoelectrons with a binding energy of approximately 285 eV (kinetic energy ~1201.6 eV) is approximately 3.7 nm. Some typical IMFPs for various organic materials can be found in a paper by Cumpson [3]. Values for amino acids and a protein can be found in [4], whereas for polyaniline (PANI) in [5]. Some IMFP values

Functional Biomaterials: Design and Development for Biotechnology, Pharmacology, and Biomedicine, First Edition. Edited by Tamilselvan Mohan and Karin Stana Kleinschek.

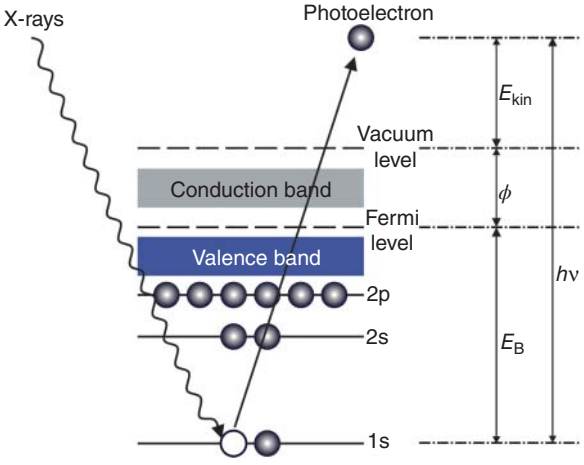

Figure 2.1 The schematic principle of XPS.

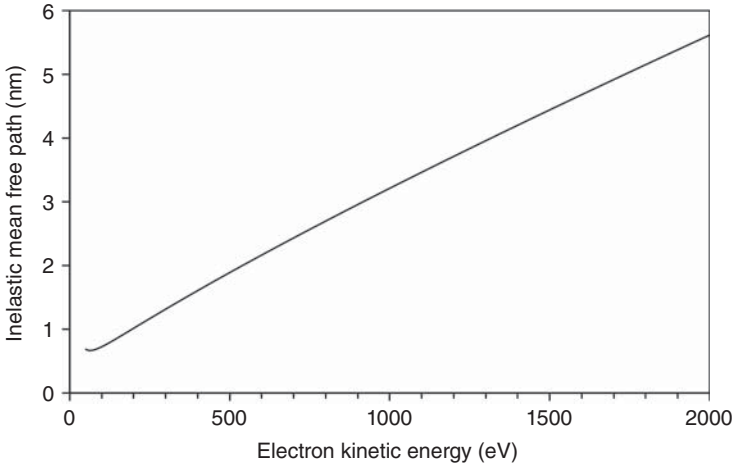

Figure 2.2 An inelastic mean free path (IMFP) of photoelectrons from polystyrene vs. their kinetic energy.

related to biopolymers and for some other important bio-substances are shown in Table 2.1.

When analyzing samples, the energy of emitted photoelectrons in the wide energy range (i.e. up to approximately 1200 eV) is measured first to get the information about the elemental composition of the material. An example of such a survey-scan measurement is shown in Figure 2.3. The lower curve presents the spectrum of a hydrocarbon polymer polyethylene, where only a carbon peak is observed. Hydrogen cannot be detected by XPS because there are no core electrons [6]. We can also observe some oxygen, which is a consequence of surface contamination. The second spectrum presents the same polymer foil, which was coated with a layer of a pomegranate extract. This gives rise to a new nitrogen N1s peak. Furthermore, a significant increase in oxygen peak is observed as well. Both oxygen and nitrogen

Table 2.1 Inelastic mean free paths for photoelectrons with the kinetic energy 1000 eV for some selected biopolymers and biosubstances.

Biopolymer	IMFP (nm)	References
PDMS (polydimethylsiloxane)	4.2	[3]
PVC (polyvinyl chloride)	3.6	[3]
PP (polypropylene)	3.5	[3]
HDPE (high-density polyethylene)	3.3	[3]
PS (polystyrene)	3.2	[3]
PMMA (polymethyl methacrylate)	3.1	[3]
PEI (polyethyleneimine)	3.1	[3]
PU (polyurethane)	3.0	[3]
PEG (polyethylene glycol)	3.0	[3]
PCL (polycaprolactone)	3.0	[3]
PHB (poly-3-hydroxybutyrate)	3.0	[3]
PET (polyethylene terephthalate)	2.9	[3]
PAA (polyacrylic acid)	2.8	[3]
CEL (cellulose)	2.8	[3]
PTFE (polytetrafluoroethylene)	2.4	[3]
Arginine	3.2	[4]
Glycine	2.4	[4]
Methionine	2.9	[4]
Leucine	2.8	[4]
Valine	2.8	[4]
Phenylalanine	2.7	[4]
Lysine	2.5	[4]
Protein	2.8	[4]
DNA	3.1	[2]

are typical constituents of the pomegranate extract. The upper curve presents the polymer foil treated in oxygen plasma to improve the adhesion of the pomegranate extract coating. In this latter case, both oxygen and nitrogen peaks are enhanced, indicating a better adhesion of the coating.

The intensity of the peaks observed in XPS spectra is proportional to the elemental concentration; therefore, XPS can also give quantitative information on the surface composition of materials. Because photoelectrons originating from different elements have different ionization cross-section, thus giving different emission yield, appropriate sensitivity factors must be taken into account, when calculating the elemental composition from the area of the measured peaks. Photoelectrons can be emitted from different electronic levels; however, the most intense peaks correspond to photoelectrons originating from core orbitals. For light elements that are typically

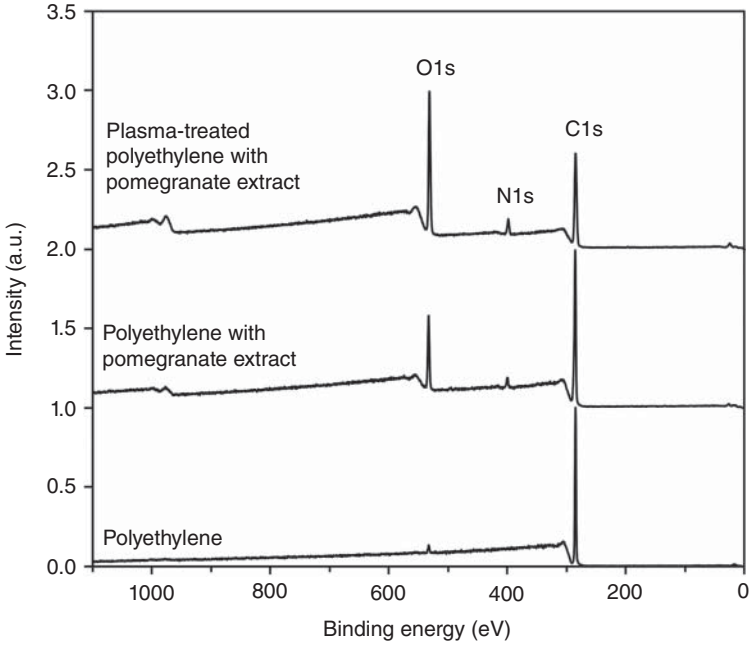

Figure 2.3 An example of the XPS survey spectrum of polyethylene foil (lower curve), polyethylene foil with a coating containing pomegranate extract (middle curve), and oxygen-plasma treated polyethylene foil with a coating containing the pomegranate extract (upper curve).

found in organic materials, there are usually "s" or "p" orbitals, whereas in the case of metals, usually "d" or "f" orbitals give the most intensive peaks. The energy of emitted photoelectrons also depends on the chemical environment of atoms. This is observed as a shift in the position of the peak in the photoelectron spectra. Such chemical shifts (which can be observed when recording spectra with a high resolution in a narrow energy range) are used to determine the chemical state of the elements. Of course, in the case of organic materials, the most important peak of investigation is carbon C1s.

In Figure 2.4 are shown some examples of carbon C1s peaks. Figure 2.4a presents a comparison of carbon peak measured on the polyethylene foil before and after treatment in an oxygen plasma. For the untreated polyethylene, we can observe a dominant peak at approximately 285 eV corresponding to C—C bonds. A small peak at approximately 288 eV is not characteristic for polyethylene and is due to surface contamination. After plasma treatment, we can observe a significant change in the shape of the curve on the high-binding energy side, which is a consequence of plasma functionalization and the appearance of new carbon–oxygen groups. Figure 2.4b shows a comparison of carbon peaks measured on polyethylene foil before and after the deposition of the pomegranate extract. Similarly, as in Figure 2.4a, we can observe a change in the shape of the peak because carbon atoms

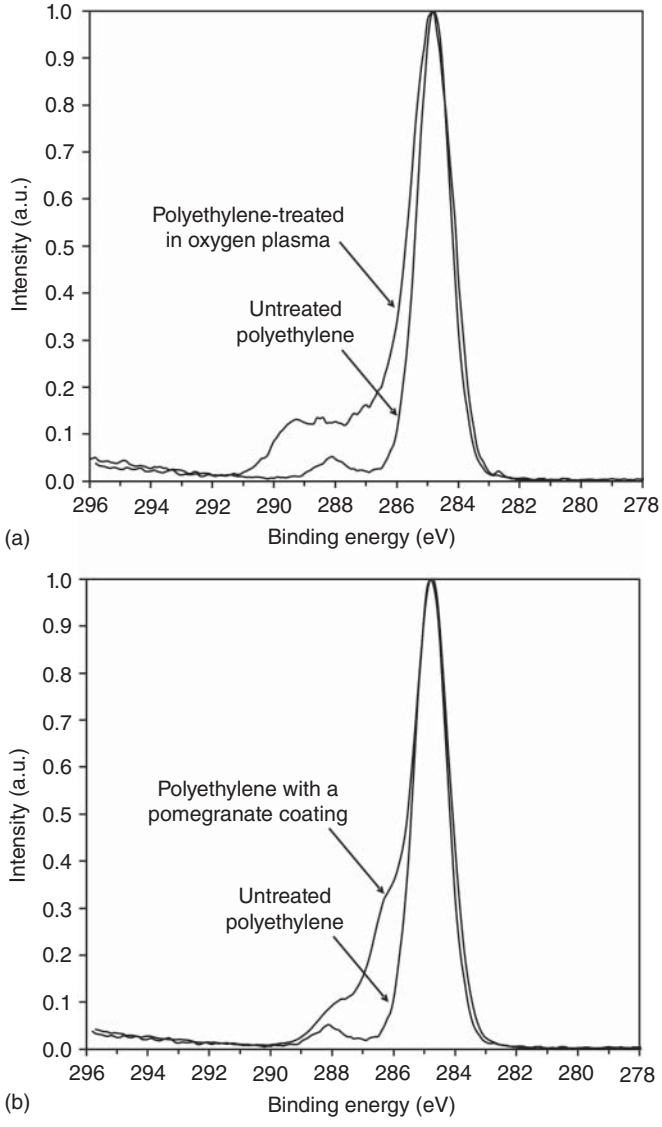

Figure 2.4 An example of the high-resolution carbon C1s peak: (a) comparison of carbon peaks of polyethylene before and after functionalization in oxygen plasma; (b) comparison of carbon peaks of polyethylene before and after deposition of a coating containing the pomegranate extract.

in the pomegranate extract are in different chemical environments. Therefore, several subpeaks corresponding to different carbon–oxygen or carbon–nitrogen groups are present in the tail of the C1s spectrum on the high-binding energy side. When more detailed information is needed, a curve fitting must be performed to reveal individual subpeaks.

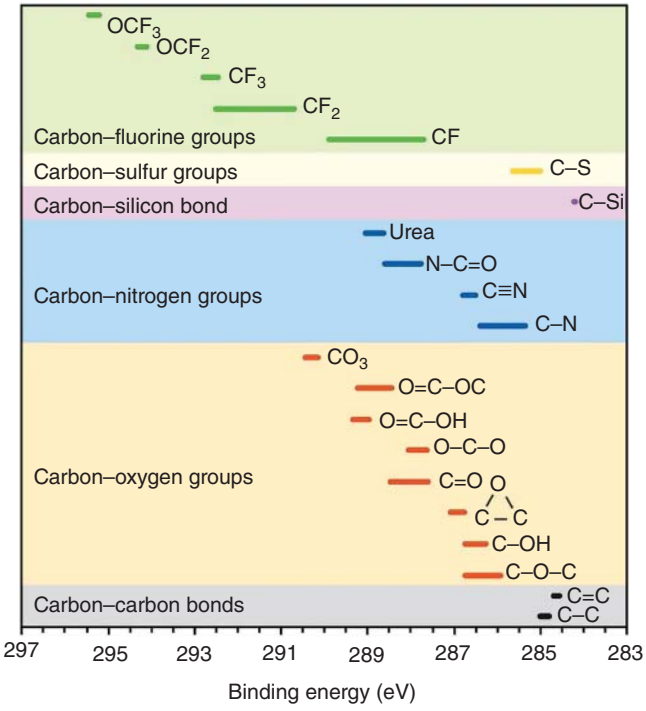

Figure 2.5 Some typical chemical shifts of C 1s in organic samples.

2.1.1 Peak Fitting

For organic samples that contain many different groups and atoms, several chemical shifts may occur, leading to the complex shape of the high-resolution spectra. Some typical chemical shifts of carbon C1s peak that are usually observed for organic materials are summarized in Figure 2.5 [7, 8]. In such a case, when several chemical shifts are present, a curve fitting must be applied to reveal individual subcomponents. However, this mathematical approach does not always lead to a unique result. Therefore, when fitting the measured high-resolution spectra, the knowledge about the chemistry of a sample is needed. The number of subpeaks, their position, peak shape, and width can be manipulated during a fitting procedure. Spectra of polymers are fitted with symmetrical Gaussian–Lorentzian functions, although sometimes a weak asymmetry may be present because of vibrational relaxations [9, 10]. The number of possible subpeaks needed for fitting is estimated from the sample chemistry. The position of a peak (binding energy) and its assignment to a specific functional group is performed by comparing the binding energy of peaks with data from the literature. The help of reference materials is often beneficial. It is worth to fit reference materials first to get the right fitting parameters, which can be then used to fit the measured set of spectra.

The binding energy of photoelectrons originating from the investigated atom mostly depends on the first neighboring atoms that form a chemical bond with the

investigated atom. Second neighboring atoms usually only have a minor influence on the binding energy [11]. Because of this reason, a difference in the binding energy of carbon in the C—O—H and C—O—C group is too small to distinguish [8] (see Figure 2.5). For the same reason, also the peaks corresponding to groups like O—C—O and C=O or O=C—O—H and O=C—O—C appear very close and cannot be resolved [8]. If the sample contains several such groups, it may influence the peak width FWHM (full width at a half maximum), which can be increased. Therefore, some variation of FWHM should be allowed during the curve fitting. It should also be noted that a shift in the binding energy is higher for more electronegative atoms. In the case of the presence of very electronegative elements such as fluorine, it, therefore, causes a significant shift of the binding energy not only of its first neighboring atoms but also of the other neighbors [12]. Therefore, in the case of the presence of fluorine atoms, the interpretation of high-resolution C1s spectra is delicate. An example of chemical shifts caused by the presence of fluorine atoms is shown in Figure 2.6.

In Figure 2.7 is shown an example of the curve fitting of the carbon spectrum of carboxymethyl cellulose (CMC). We can observe that the major peak is from carbon having a single bond with oxygen, which is due to the C—OH and C—OR groups, where R=CH_2COOH. Another two peaks are assigned to O—C—O and O=C—O groups, which are both characteristics of CMC, whereas the C—C component is attributed to the presence of some hydrocarbons. Another example is shown in Figure 2.8, which presents an example of the high-resolution carbon C1s peak of heparin grafted to polycaprolactone (PCL) surface via polyethyleneimine (PEI) linker. In this case, we can observe components originating from all three compounds: heparin, PCL, and PEI. The PCL substrate gives rise to O=C—O, C—O, and C—C subpeaks. The PEI linker gives rise to C—N, which is positioned close

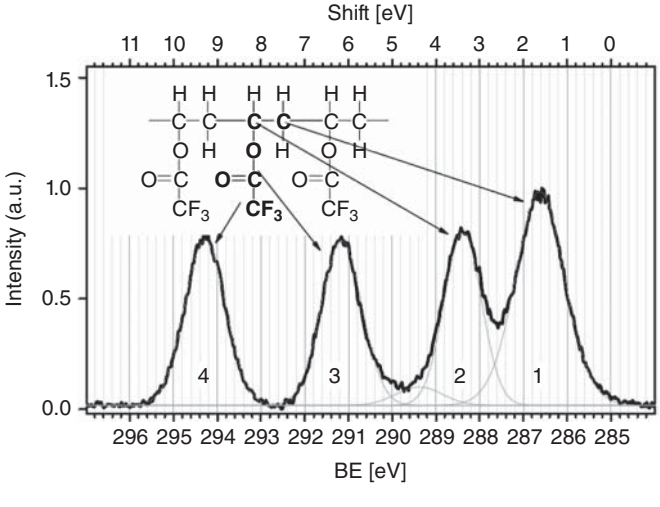

Figure 2.6 The high-resolution spectrum of carbon of polyvinyl trifluoroacetate showing big chemical shifts of C1s as a consequence of the presence of fluorine functional groups. Source: Kröner et al. [12]/with the permission of Elsevier.

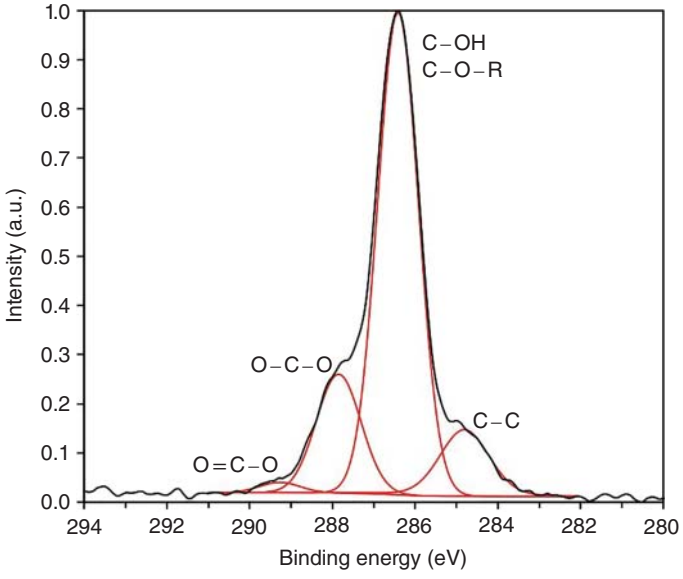

Figure 2.7 An example of the high-resolution carbon C1s peak of carboxymethyl cellulose (CMC) with subcomponents.

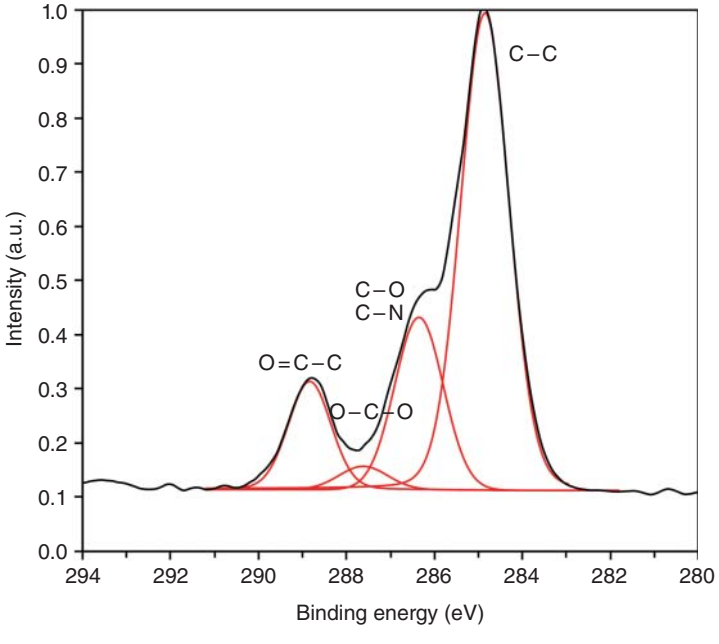

Figure 2.8 An example of the high-resolution carbon C1s peak of heparin grafted to polycaprolactone via polyethyleneimine.

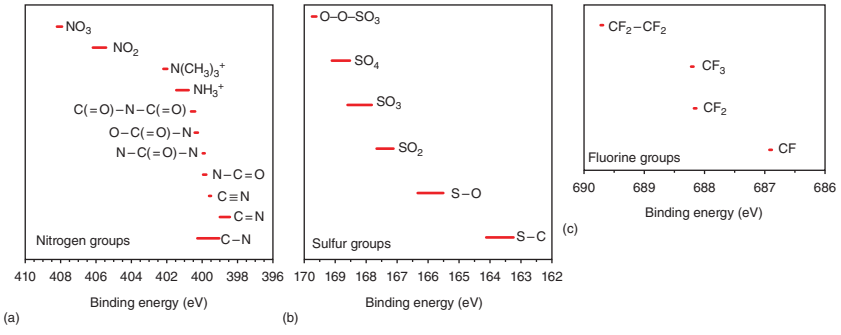

Figure 2.9 (a) Some typical chemical shifts of N1s in organic samples. Source: Adapted from Refs. [8, 13–16]. (b) Some typical chemical shifts of $S2p_{3/2}$ in organic samples. Source: Adapted from Refs. [8, 17–20]. (c) Some typical chemical shifts of F1s in organic samples. Source: Adapted from Beamson and Briggs [8]/with permission of John Wiley & Sons.

to C—O and is therefore not possible to resolve. Therefore, usually only one peak is used to fit C—O and C—N together. Whereas for heparin, characteristic peaks are due to C—O and O—C—O groups as well as O=C—O groups. As is unambiguously evident from Figure 2.5, carbon-oxygen bonds overlap over carbon-nitrogen bonds or with bonds of carbon atoms with other elements if present. Therefore, exact mathematical separation and the development of reliable fitting models is practically impossible. Authors often use different approaches for fitting such multi-component spectra which makes a comparison of results from literature difficult because there are many discrepancies and variations in reported binding energies and appropriate peak assignment. Usually, authors overcome the problem with peak overlapping by applying the fitting procedure by using only one peak for bonds with similar binding energies: e.g. one peak for C—O and C—N functionalities like in Figure 2.8 and one peak for C=O or N—C=O functionalities.

For organic materials, the most important information on the chemical environment is thus obtained from carbon C1s peak. For other peaks such as N1s and O1s, the chemical shifts are much smaller; however, sometimes also these peaks can provide additional information. Especially in the case of the presence of sulfur functional groups, it is easy to distinguish sulfur S2p in different oxidation states. Whereas nitrogen, N1s, from amine or amide groups appears at similar binding energies and is therefore not distinguishable. However, for protonated nitrogen or nitrogen bonded to oxygen, chemical shifts are large enough to observe them. Some typical chemical shifts for nitrogen N1s are summarized in Figure 2.9a [8, 13–16], for sulfur $S2p_{3/2}$ peak in Figure 2.9b [8, 17–20], and for fluorine F1s in Figure 2.9c [8].

2.2 Chemical Derivatization

For organic materials, chemical shifts of carbon appear on the high-binding energy side. If organic materials contain carbon in different chemical environments, it is often impossible to distinguish individual peaks in the C1s spectrum. The situation can be worsened if a material contains different elements bound to carbon. Chemical shifts are often too small, and peaks corresponding to different functional

groups may strongly overlap. As already mentioned above, when organic material contains only carbon and oxygen, it is not possible to distinguish between hydroxyl and ether groups or between carboxyl and ester groups. In such cases, when one wants to determine the concentration of a particular functional group, chemical derivatization can be applied [11, 21–30]. Chemical derivatization is performed by using special chemical agents that specifically react with the functional group of our interest. Chemical agents must contain a marker element (usually fluorine or chlorine) that is not present in the investigated material. After binding of an appropriate chemical agent to the specific functional group, the concentration of a marker element is proportional to the concentration of the investigated functional group [23]. This allows the quantification of specific functional groups. Different derivatization agents can be used to detect specific functional groups. Some of them are shown in Table 2.2.

Table 2.2 Chemical derivatization agents that are the most often used to detect specific functional groups.

Functional group	Derivatization agent	Marker element	References
$-NH_2$	4-Chlorobenzaldehyde	Cl	[11, 31]
	Trifluoroacetic anhydride (TFAA)	F	[11, 31]
	Pentafluorobenzaldehyde (PFB)	F	[11, 25]
	4-Trifluoromethyl benzaldehyde (TFBA)	F	[11, 24]
	5-Bromosalicylaldehyde	Br	[11, 32]
>C=N–	4-Trifluoromethyl benzaldehyde (TFBA)	F	[27, 33]
	2-Mercaptoethanol (ME)	S	[26, 33]
	4-Trifluoromethyl benzylamine (TFMBA)	F	[28, 33]
	4-Trifluoromethyl phenylhydrazine (TFMPH)	F	[28, 33]
	Trifluoroacetic anhydride (TFAA)	F	[27, 29]
>C=C<	Bromine	Br	[32]
–SH	*N*-ethylmaleimide (NEM)	N	[21]
–OH	Trifluoroacetic anhydride (TFAA)	F	[11, 23]
	Trichloroacetic anhydride (TCAA)	Cl	[11, 34]
	Tridecafluoro-1,1,2,2-tetrahydrooctyl-1-trichloro-silane	F	[35]
	Titanium di-isopropoxide-bis(2,4-pentanedionate)	Ti	[36]
	Trifluoroacetic anhydride (TFAA)	F	[37]
	4-(Trifluoromethyl)-benzylamine (TFMBA)	F	[37]
>C=O	Hydrazine	N	[11, 34]
	Pentafluorophenylhydrazine (PFPH)	F	[11, 34, 36]
	2,4,6-trichlorophenylhydrazine (TCPH)	Cl	[34]
–COOH	Trifluoroethanol (TFE)	F	[11, 38, 39]
	Trichloroethanol (TCE)	Cl	[11, 34]
	Tribromoethanol (TBE)	Br	[11, 34]

However, also derivatization can cause some uncertainties. Derivatization agents are often dissolved in liquids, which may cause swelling of the surface [23]. Furthermore, some soluble components may also be removed, or there can be some surface rearrangement [11]. Also, rinsing and drying the surface after derivatization may influence the surface composition. Therefore, derivatization performed in a vapor phase is preferred. Moreover, a problem of derivatization is also the selectivity of the derivatization agents because some of them may react with the other groups [11]. This nonselectivity of the derivatization agents can be also observed in Table 2.2. For example, trifluoroacetic anhydride (TFAA) reacts with OH, NH_2, and NH groups [24]. However, it was also reported that it can react with epoxide groups [40] as well as with imines [29].

Klages et al. have investigated the chemical derivatization of polymers treated in nitrogen-containing plasmas [26–29]. They reported that imines can react with substances that are commonly used for derivatization such as aromatic aldehydes (such as trifluoromethyl benzaldehyde [TFBA]) and acid anhydrides (such as TFAA) [27, 29]. Therefore, these derivatization agents may not be regarded as selective to amines [27, 29]. Consequently, special care must be taken when using chemical derivatization for nitrogen-plasma-treated polymers where a substantial part of nitrogen can be incorporated as imine as well it can be present in the other nitrogen-carbon double bonds and nitrile [28, 29]. In this latter case, it is not possible to accurately quantify amino groups [27]. The very important factor when performing derivatization is also an appropriate selection of the reaction time. Too short reaction time may lead to incomplete reactions, whereas too long reaction time can cause some side reactions. Also, aging effects may become noticeable at long reaction times. A good review of surface derivatization was published by Girard-Lauriault et al. [11].

2.3 Some Further Examples of XPS Analyses of Complex Organic Systems

An interesting approach for analyzing complex organic systems was developed by Rouxhet et al. [41–43]. They used XPS to analyze cakes made from different combinations of oil, sugar, salt, eggs (yolk or white), and flour [41]. Based on model biochemical compounds such as proteins, carbohydrates, phospholipids, and lipids with known composition, it was possible to model the concentration of functional groups rationed toward the total carbon. The same authors used a similar approach for chitosan material also [43]. Data obtained from XPS were related to the known structure of chitosan, which was composed of repeating units containing amine groups with a fraction "*a*" and repeating units containing acetylated amine groups with a fraction "*b*" (Figure 2.10). C1s spectrum was deconvoluted to three components $C_{i\,(i=1,2,3)}$ belonging to C—(C,H) groups, C—(O,N) groups, and O—C—O/N—C=O groups, whereas oxygen was deconvoluted to two peaks

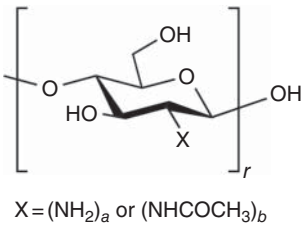

Figure 2.10 Chemical structure of chitosan.

$O_{i\,(i=1,2)}$ corresponding to C—O—(H,C) and O=C—N. The relative amounts of individual chemical contributions were specified as [43]:

$$C_{total} = C_1 + C_2 + C_3, \text{where } C_1 = b \cdot r, C_2 = 5 \cdot r \text{ and } C_3 = (1 + b) \cdot r,$$
$$N_{total} = r,$$
$$O_{total} = O_1 + O_2, \text{where } O_1 = 4 \cdot r \text{ and } O_2 = b \cdot r.$$

This approach allowed determination of fractions "*a*" and "*b*" with a quite good agreement with the expected values.

Cellulose is an important organic and renewable material. However, natural fibers, such as wood fibers, contain also other constituents such as lignin. Johansson et al. have reported a method for the determination of lignin content on cellulose fibers [44, 45]. They have analyzed about 250 different lignocellulose samples and plotted a correlation between C—C content vs. O/C ratio [44]. Pure cellulose does not have C—C carbons, which are typical for lignin. Although the C—C content may be influenced by surface contamination, they have observed a very good linear correlation between C—C/C_{total} and O/C ratio, as shown in Figure 2.11 [44]. Even though different types of lignin could be present, they are still chemically similar enough to allow a good correlation.

Another example of such a correlation is shown in Figure 2.12. Some polymer foils like polystyrene (PS) [46], polypropylene (PP) [47], and polyethylene terephthalate (PET) [48, 49] were exposed to controlled doses of neutral oxygen

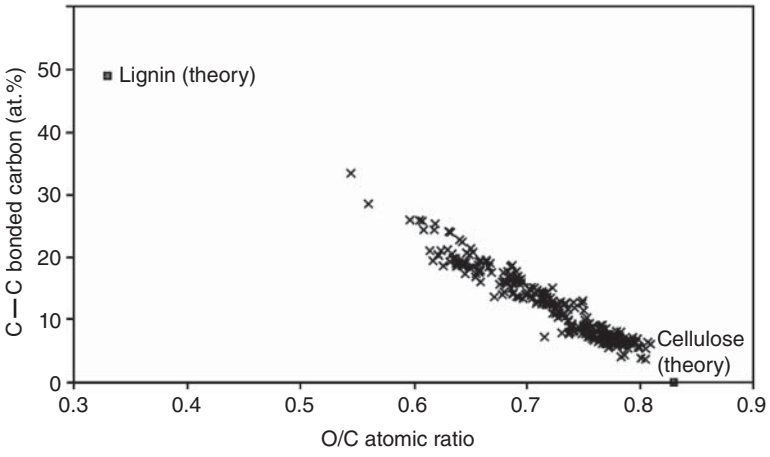

Figure 2.11 A correlation between the C—C content and the O/C ratio for approximately 250 different lignocellulose materials. Source: Johansson et al. [44]/with permission of Elsevier.

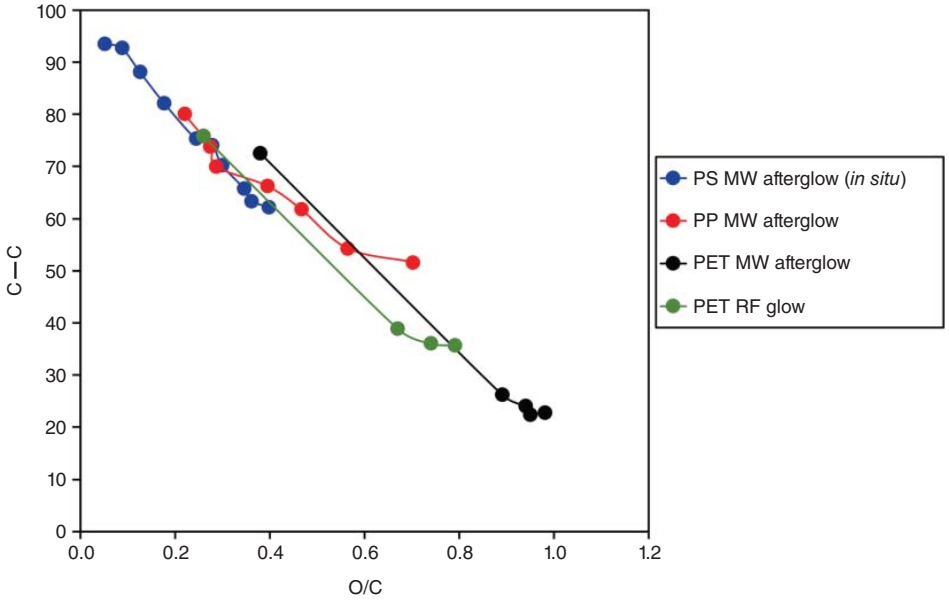

Figure 2.12 A correlation between the C—C content and the O/C ratio for some polymers treated with neutral oxygen atoms from plasma.

atoms to investigate the initial stages of surface functionalization leading to surface saturation with oxygen functional groups. The source of neutral oxygen atoms was oxygen plasma created by microwaves (MW) in a surfatron mode or by a radiofrequency (RF) generator. Similarly, as in Figure 2.11, we can observe a good correlation between the C—C content in the polymer surface and O/C ratio. With increasing oxygen content on the polymer surface as a consequence of surface functionalization with oxygen functional groups, we can observe a decrease of the C—C content. Moreover, the individual curves for various polymer materials follow the same trend line.

2.4 Charging

One problem associated with XPS is the surface charging of samples that are electrically nonconductive [50, 51]. Because photoelectrons are continuously emitted from the surface, the surface becomes positively charged. Accumulation of the positive charge on the surface is causing retarding of emitted photoelectrons. This results in a shift of the peak position to higher binding energies, widening of the peaks, and thus changes in the peak shape. All these effects, of course, lead to a wrong interpretation of the peaks [52]. The problem of surface charging can be overcome by the use of an additional electron gun for compensation of the surface charge. In a case of very rough and inhomogeneous samples, so-called differential charging may occur. Because of inhomogeneous charging, there can be some

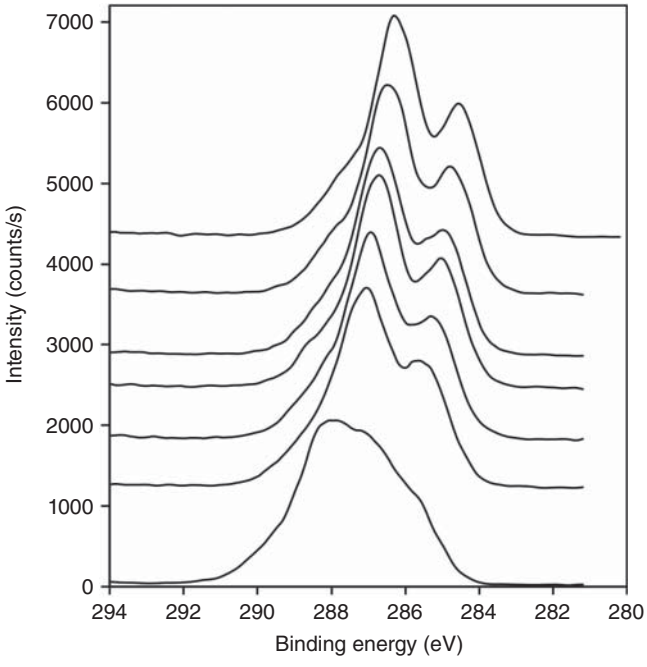

Figure 2.13 Examples of C1s spectra of the filter paper recorded at various parameters (i.e. electron flux) for surface charge compensation.

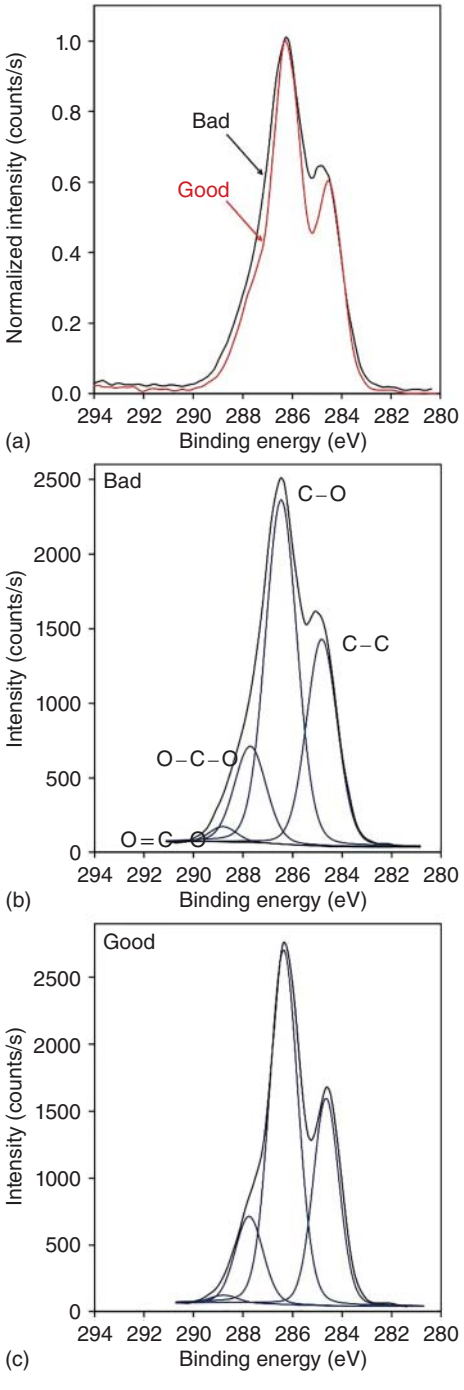

Figure 2.14 (a) A comparison of the two selected C1s spectra from Figure 2.13 as an example of a broadening of the C1s spectra because of charging as a consequence of the good or bad selection of surface neutralization conditions. (b) and (c) Deconvolution of these two selected spectra.

discrete areas that are charging different than the remaining parts of the surface. In such cases, also the use of electron charge neutralizer cannot always sufficiently prevent the accumulation of the charge. Because of inhomogeneous charging, the signal from different areas may be shifted differently, and the resultant spectra may be broadened significantly. Therefore, it is also difficult to obtain reproducible measurements. The spectra may also be shifted during the measurement; thus, the first and the last measured spectra may differ. While this method is regularly used for charge compensation, it was also reported that prolonged and intensive exposure to flood gun for charge compensation may also cause modification of spectra.

In Figure 2.13 is shown an example of the surface charging of the filter paper. A shift of the peaks because of the surface charging is proportional to the accumulated charge on the surface. Spectra of C1s were recorded at different parameters of an electron gun for surface charge compensation. We can observe not only shifts of the measured spectra, but also some modifications of the peak shape and loss of resolution. In Figure 2.14, we can observe that in the case of non-appropriate charge neutralization, C1s peak is wider and has less pronounced individual peaks as well as a higher COOH component; what is, of course, an artifact of charging.

For calibration of the binding energy scale of nonconductive samples, the position of C1s peak must be checked. C1s peak is practically present on all samples because a thin layer of carbon contamination is normally formed on the surface when a sample is exposed to air. This layer of carbonaceous material on the surface is called adventitious carbon, and it is often used for calibration of the binding energy scale by setting the main C—C/H peak of the C1s spectrum to the energy of 284.8 eV. Sometimes, the position of the peak C—C is also set to an energy of 285 eV. Therefore, when comparing data from literature regarding peak positions, the exact position of C1s peak must be checked.

2.5 Background Information

As shown in examples of the survey spectra in Figure 2.3, a typical background is observed in the spectra which is increasing with increasing binding energy. This background is a consequence of the inelastic scattering of photoelectrons that lose some of their kinetic energy at inelastic collisions when traveling through the material. When performing the curve fitting of spectra, this background must be subtracted from the spectra. In general, we can use three different types of background subtraction: (i) the linear background, (ii) the Shirley background, and (iii) the Tougaard background. The most used method for the background subtraction is the Shirley background; however, sometimes special care must be taken regarding the choice of the right background subtraction from the spectra. In Figure 2.15 are shown some examples of different types of background subtraction for C1s peak measured on polystyrene sample. In the C1s spectrum of polystyrene, the main C—C/C—H peak is accompanied by a satellite peak, which is because of the polymer aromaticity and is therefore observed for aromatic polymers. We can see that the linear (Figure 2.15a) and Shirley (Figure 2.15b)-type backgrounds are not satisfactory. Therefore, in the case of polystyrene, the Tougaard background (Tougaard Universal Polymer background) as shown in Figure 2.15c is a much better option [53–55].

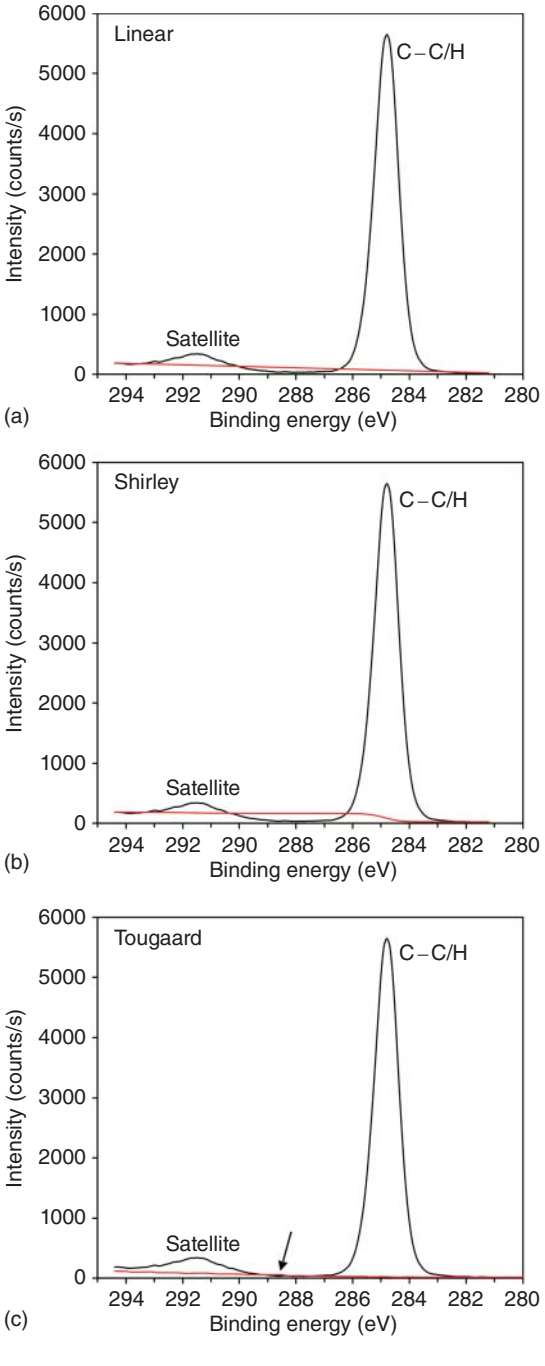

Figure 2.15 Some examples of using different types of background subtraction for C1s peak of polystyrene: (a) linear, (b) Shirley, and (c) Tougaard subtraction. An arrow in Figure 2.15c indicates a small portion of the spectrum, where the background cuts the spectrum. In the case of figures (a) and (b), the part of the cutoff spectrum is much larger.

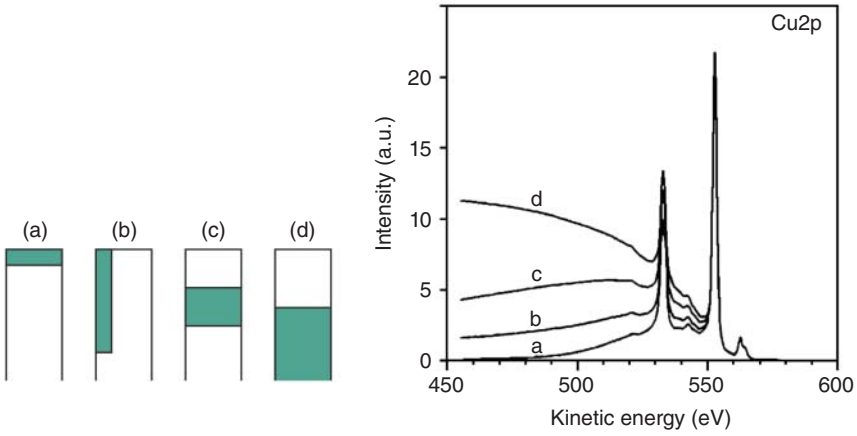

Figure 2.16 Different structure of the surface causes different background on the high-binding energy side of the peak. Source: Tougaard [56]/with permission of John Wiley & Sons.

The background of the XPS spectra can also provide some additional information about the surface morphology of the investigated samples. As shown by Tougaard [56], the photoelectron background of the XPS spectrum may differ depending on the distance the photoelectrons have traveled in the material (Figure 2.16). If the photoelectrons are coming from a thin surface layer, they will not lose much of their energy, and therefore, the background will be low (Figure 2.16a). Opposite, if photoelectrons are coming from a deeper layer like in Figure 2.16b, most of them will lose their energy, and the corresponding background will be high. For the other two examples shown in Figure 2.16c,d, the background will be in between these two extremes.

An example of different peak backgrounds is shown in Figure 2.17, which illustrates the background of fluorine F1s peak of the polymer PET treated in CF_4 plasma before and after coating it with a layer of proteins (upper two curves in Figure 2.17). For comparison, the untreated polymer is shown as well (the lowest curve). The intensity of F1s peak for the polymer treated in CF_4 plasma is very high, whereas the background on the high-binding-energy side of this peak is low and typical for the "surface-type" background. This indicates successful attachment of fluorine to the polymer surface. Furthermore, plasma treatment in CF_4 gas also causes depletion of oxygen in the surface layer of the polymer; therefore, the background for oxygen is more typical for the bulk and thus different from the case of the untreated polymer – i.e. for the untreated polymer, a decline is observed on the high-binding-energy side of the O1s peak. After coating the polymer with a layer of proteins, nitrogen N1s with a typical "surface-type" background appears, originating from the top layer of proteins. The intensity of the fluorine peak decreased, and its background increased. The reason for this occurrence is the origin of the F1s signal, which is now coming from the underlying polymer, and not anymore from the top surface layer. Furthermore, for samples incubated with the proteins (besides nitrogen, proteins also contain carbon and oxygen), we can

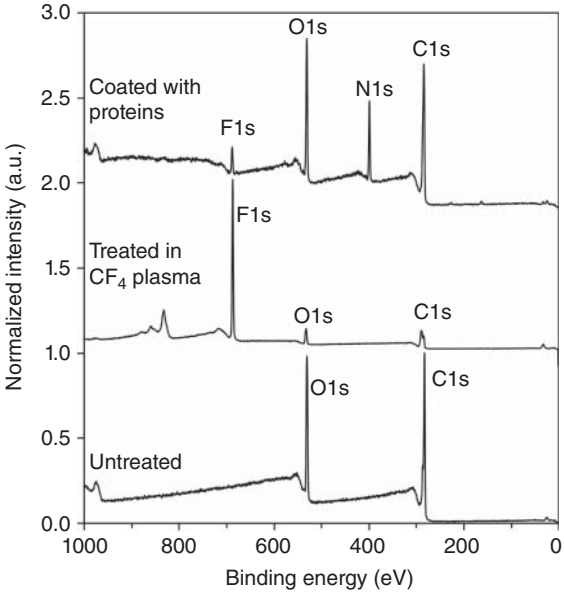

Figure 2.17 Survey spectra showing a background of fluorine F1s peak of fluorinated polymer coated with a layer of proteins.

observe that the background has also changed for carbon and oxygen peaks. Now, a decline is observed on the high-binding energy side of O1s and C1s peaks, which is characteristic for the case, when oxygen and carbon are concentrated at the surface.

2.6 Angle-Resolved XPS (ARXPS)

Although XPS is preferably used for surface investigations due to the surface sensitivity of the method, it can also provide some information on the depth distribution of elements. For that purpose, XPS is combined with etching using an ion gun to remove surface layers and measure the composition underneath. However, such an approach is not appropriate for organic materials because of damage induced by energetic ions in the molecular structure of the material if using conventional Ar ion guns. In recent years, the development of new ion guns based on gas cluster ion sources allows the application of the ion etching technique also for depth profiling of sensitive organic materials. Nevertheless, an alternative approach to obtain some information regarding depth composition is the application of angle-resolved XPS (ARXPS). Surface sensitivity of XPS may be varied by measuring photoelectrons at different angles to the surface plane (Figure 2.18a,b) which allows obtaining information regarding the sample composition as a function of depth. XPS detection depth depends on the IMFP λ and also on the angle θ between the electron energy analyzer and the plane to the sample surface. This angle is often called a take-off angle (TOA). The detection depth (d) is schematically illustrated in Figure 2.18, and the correlation is given with the following equation:

$$d = 3\lambda \sin \theta. \tag{2.1}$$

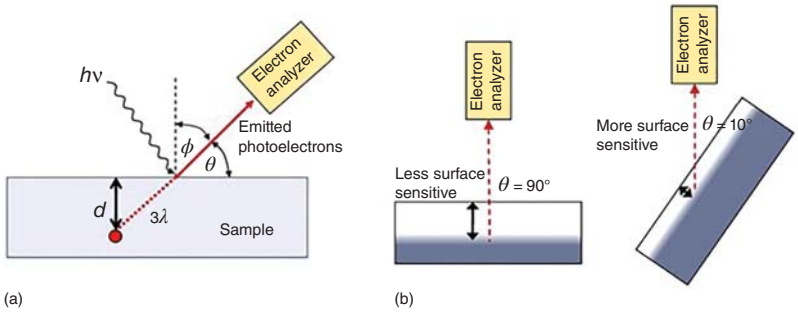

Figure 2.18 (a) A correlation between the sampling depth and the take-off angle θ. (b) Figure 7.21. Schematic presentation of the dependence of the XPS sampling depth on the tilting angle of the sample.

Normally, the electron energy analyzer is positioned at $\theta = 45°$ according to the plane of the sample surface. However, by tilting the sample, and thus modifying θ, the XPS sampling depth can be changed. As shown in Figure 2.18b and Eq. (2.1), at a low θ angle, detection depth is much smaller than at a large θ angle. Therefore, by measuring the spectra at different θ angles, a signal from various depths can be obtained. This procedure can be applied for the investigation of very thin films. Relative concentration profiles of the elements or functional groups as a function of TOA (depth) can be obtained [57]. ARXPS can also be used to determine the film thickness [54, 55, 58–62]. An example of such a film thickness determination can be found in papers by Awsiuk et al. [59, 60, 63, 64]. The authors have developed a model to determine the thickness of the protein layer using ARXPS spectra taken at various take-off angles. Such calculation was shown for the case of aminosilane (aminopropyl)triethoxysilane (APTES)/protein bilayers deposited on SiO_2/Si_3N_4 substrate [59].

One example of high-resolution carbon spectra taken at various TOA is shown in Figure 2.19. This figure shows fluorine functional groups formed of PET polymer surface treated in CF_4 plasma. Spectra recorded at a low TOA (low detection depth) show a higher concentration of fluorine groups than the one recorded at a bigger TOA, where the information is coming from deeper layers. This figure thus demonstrates that the effect of plasma treatment is limited to the surface.

It is known that plasma-treated surfaces are exposed to aging effects. Wang et al. [57] have investigated the aging of the chitosan membrane after treatment in an oxygen plasma. After 15 days of aging, the XPS spectra of the sample were measured at various TOA. They have shown that the concentration of C—OH groups on the surface increased after plasma treatment. After 15 days of aging, the concentration of C—OH groups at the surface decreased, whereas underneath the surface, the C—OH concentration increased as a consequence of the redistribution of polar groups from the surface toward the bulk (Figure 2.20).

Also Mantovani et al. [65] have used ARXPS to investigate depth composition and aging of plasma-deposited fluorocarbon films as a potential stent coating. The fluorocarbon films were deposited on the stainless steel surface and then aged for

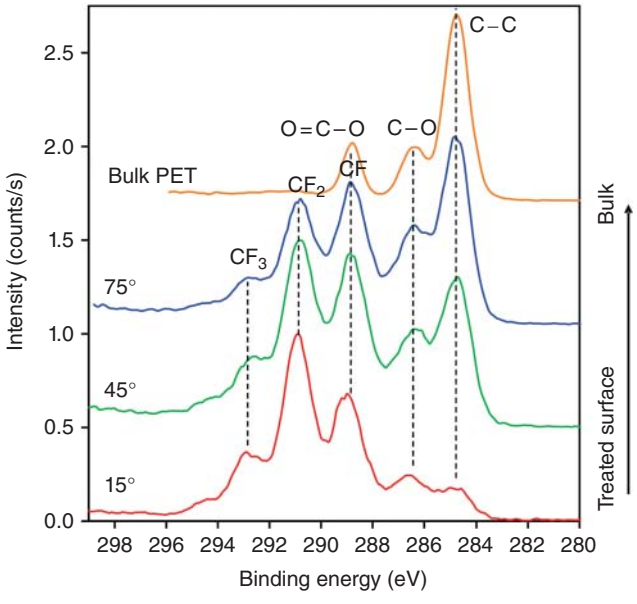

Figure 2.19 Carbon C1s spectra of fluorinated PET polymer recorded at different TOA.

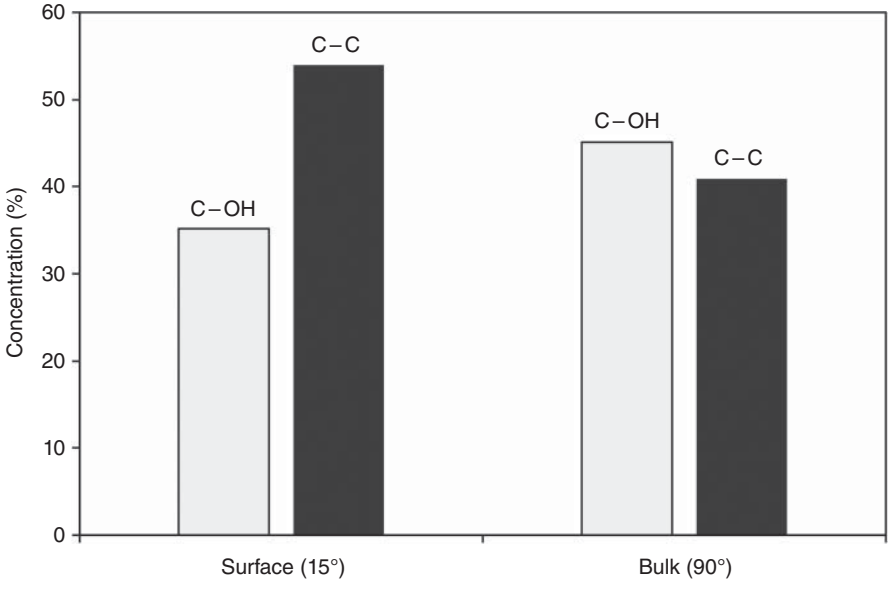

Figure 2.20 A redistribution of functional groups from the surface toward the bulk in plasma-treated chitosan after 15 days of aging as a function of TOA.

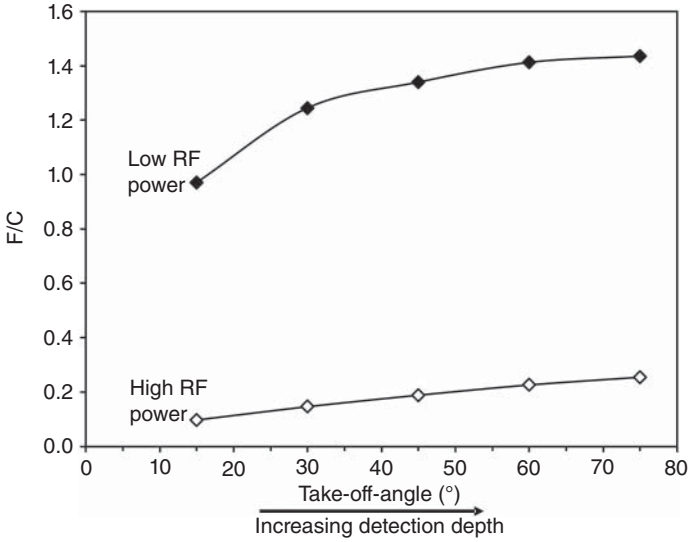

Figure 2.21 The F/C ratio of the defluorinated surface of polymer PTFE after treatment in a hydrogen plasma at two different powers.

four weeks in PBS buffer. Degradation and oxidation of the films with aging time were observed. Another example of a variation of the relative surface composition with a take-off-angle is shown in Figure 2.21. Polymer polytetrafluoroethylene (PTFE) was treated in hydrogen plasma to cause the depletion of fluorine from the surface of PTFE. As shown in Figure 2.21, the F/C ratio is the lowest at the surface as a result of the surface depletion and is increasing with the increasing depth.

As mentioned before, a typical information depth of XPS is 3λ, where λ depends on photoelectron energy. Therefore, in the case of a large difference in the sampling depth of elements (i.e. elements that differ greatly in their binding energy), a problem may appear in the case of samples having a strong compositional depth gradient, which is in the range of the XPS information depth. An example of this is fluorine-containing material because F1s photoelectrons have smaller kinetic energy than C1s, and thus they give information from a smaller sampling depth. However, using the large difference of sampling depth of F1s (which appears at a binding energy (BE) of approximately 689 eV) and F2s (which appears at a binding energy of approximately 35 eV) can give additional information.

Variations of F/C signals of PTFE treated in a hydrogen plasma as calculated either from F1s and F2s photoelectrons are shown in Table 2.3. As already mentioned, hydrogen plasma treatment causes strong depletion of fluorine from the surface of PTFE. We can see that the F/C ratio is larger when calculated from F2s signal than the one calculated from F1s, as F2s photoelectrons come from an almost twice as deep layer as F1s signal. This is a sign of a strong fluorine concentration profile that is in the range of the XPS sampling depth. In a case of a thick and uniform top layer on the sample, F1s and F2s would give similar composition.

Another example of a difference in surface composition when calculated from F1s or F2s photoelectrons is shown in Figure 2.22, which demonstrates a variation of the

Table 2.3 Surface composition of the defluorinated surface of PTFE when calculated from F1s or F2s signals (at.%).

	Concentration (at.%)	
Element	**F1s**	**F2s**
C	80.1	70.7
F	14.8	24.9
O	5.1	4.4

A different composition is a sign of a strong surface gradient of the fluorine concentration. The F2s signal gives higher fluorine concentration because of the bigger detection depth.

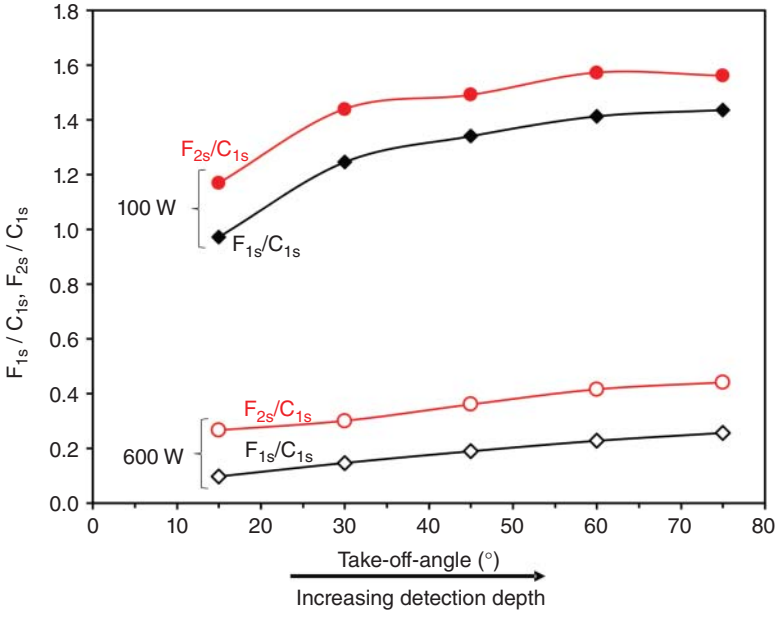

Figure 2.22 The difference in the F/C ratio when computed from F1s or F2s signals.

surface composition of plasma-treated PTFE vs. a TOA. By changing the TOA from 15° to 75°, a detection depth for F1s photoelectrons is changing from approximately 2 to 8 nm and for F2s photoelectrons from approximately 3.5 to 13 nm, whereas for C1s from approximately 3 to 11 nm.

Here it is worth mentioning that besides problems in a detection depth, we can expect other problems in XPS characterization of fluorine-containing polymers, like X-ray-induced degradation, binding energy calibration, and the right peak assignment because of chemical shifts that are also induced in the second neighboring atoms. Some further information regarding problems and solutions of XPS investigation of fluorinated polymers can be found in [66]. Last but not least, it is worth mentioning another possibility for the investigation of a depth

composition of multilayered samples. If the sample is cut, then line analyses of its cross-section can be performed. An example of such an investigation can be found in [67]. The authors have investigated the interface between polyvinilydene difluoride (PVdF)-based topcoat and a polyurethane-based primer and found diffusion of fluorine-containing fragments of the PVdF topcoat into the underlying polyurethane primer.

2.7 Functional Coatings on Polymers

Alginic acid is a natural biodegradable and biocompatible polymer that has an important potential for its use in biomedical or pharmaceutical applications (i.e. for wound treatment). The surface of polyethylene (PE) polymer was activated by plasma treatment, followed by graft polymerization of allylamine (AAM) containing NH_2 groups that act as binding sites for further attachment of alginic acid coating (Figure 2.23).

Figure 2.24 and Table 6.4 show an example of XPS investigation of such surface. Figure 6.27 presents high-resolution carbon peaks of the virgin PE surface (Figure 2.24a), the PE surface after plasma treatment and allylamine grafting (Figure 2.24b), and after further deposition of alginic acid coating (Figure 2.24c). A comparison of Figure 2.24a,b clearly shows the effect of plasma treatment and AAM grafting. While the untreated sample contains only C—C groups, many more groups are observed on the treated sample, where we can observe C—O and C=O groups as a consequence of plasma treatment. Amino groups (C—N) in high-resolution carbon spectra in Figure 2.24b are overlapping with C—O; however, the presence of nitrogen is clearly observed in survey spectra, and its concentration is given in Table 2.4. Figure 2.24c shows the final coating comprising alginic acid, which is a polysaccharide containing – OH and – COOH groups. Because of the high content of oxygen functional groups and a lack of pure C—C bonds in alginic acid, we can observe (in comparison with Figure 2.24b) a shift of the main C1s peak to the higher binding energy. Functional groups that are characteristic of alginic acid are observed.

Another natural biocompatible and biodegradable material of extreme importance is chitosan, which is known as an important antimicrobial agent [68]. In Figure 2.25

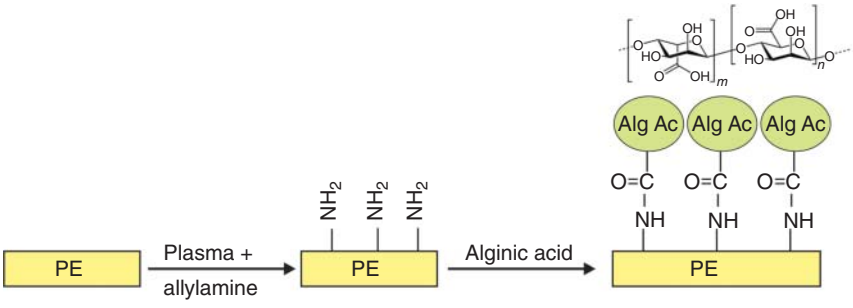

Figure 2.23 Scheme of alginic acid immobilization on the polymer surface.

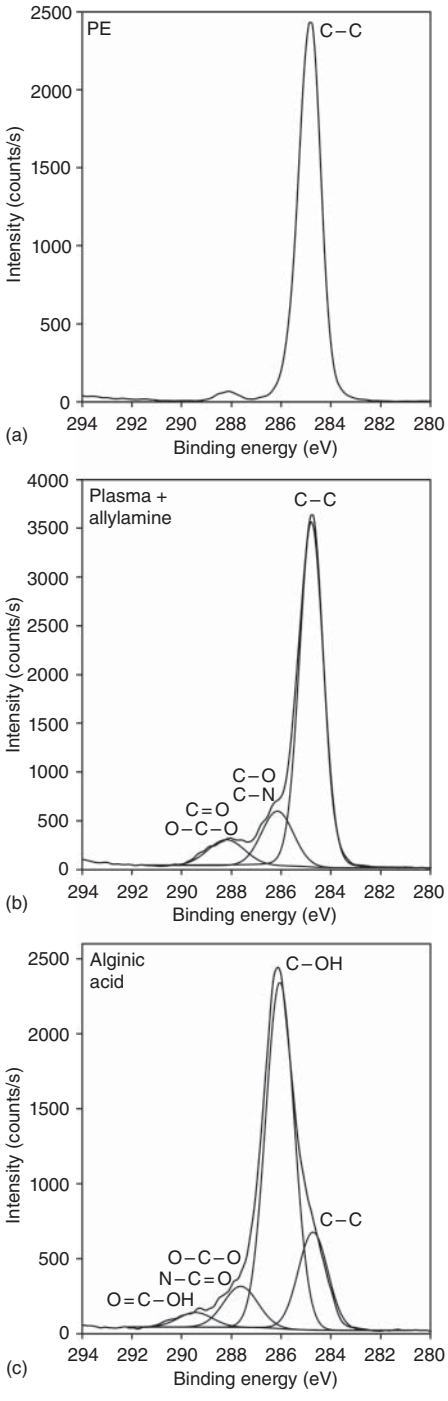

Figure 2.24 XPS high-resolution carbon spectra of (a) PE polymer substrate, (b) plasma-activated PE polymer after grafting with allylamine, and (c) PE polymer with alginic acid coating attached to allylamine linkers.

Table 2.4 Surface composition of the PE sample before and after treatment and deposition of the alginic acid coating (in at.%).

Sample	C	N	O	O/C	N/C
PE control	95.9	2.2	1.9	0.02	0.02
PE plasma + AAM	81.2	3.7	15.1	0.19	0.05
PE plasma + AAM + Alg.Ac.	86.2	1.7	12.0	0.14	0.02

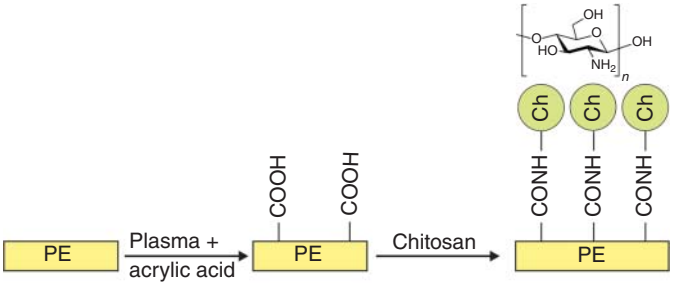

Figure 2.25 The scheme of chitosan immobilization on the polymer surface.

Table 2.5 Surface composition of the PE sample before and after treatment and deposition of the chitosan coating (in at.%).

Sample	C	N	O	O/C	N/C
PE control	100				
PE plasma + AA	84.2		15.8	0.19	
PE plasma + AA + Chitosan	71.8	3.6	24.6	0.34	0.05

is shown the procedure for immobilization of chitosan complex on PE surface via COOH groups that were introduced to the polymer surface by plasma activation and grafting with acrylic acid (AA).

The elemental composition of this surface is shown in Table 2.5, whereas survey spectra are shown in Figure 2.26. Additionally, Figure 2.27 presents high-resolution spectra of the virgin PE sample (Figure 2.27, middle), the surface after plasma treatment and acrylic acid grafting (Figure 6.30b), and after further deposition of the chitosan coating (Figure 2.27, bottom).

As shown in Figure 2.27 (middle), the high content of – COOH groups is observed, which proved successful grafting of acrylic acid groups. This is also proved by a high oxygen content on the surface (Table 2.5). The deposition of chitosan coating takes place via reaction of amino groups from chitosan with – COOH groups from acrylic acid, forming an amide bond. The spectrum in Figure 2.27 (bottom) is significantly different from the one in Figure 2.27 (middle), indicating different surface chemistry. As shown in latter figure, peaks belonging to groups typical for

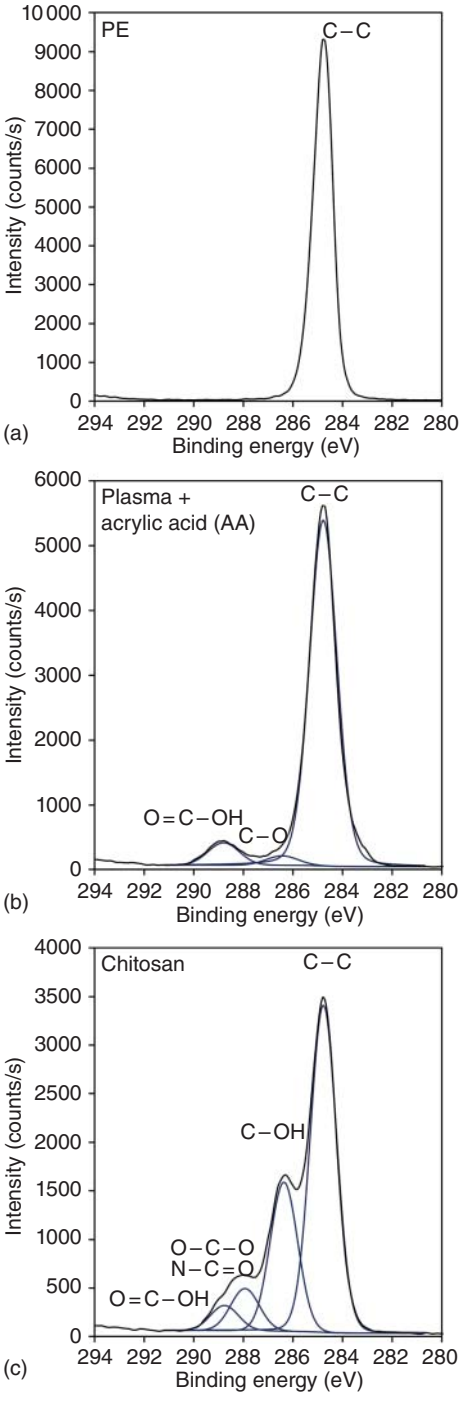

Figure 2.26 XPS survey spectra of PE polymer substrate, plasma-activated PE polymer after grafting with acrylic acid, and PE polymer with chitosan coating attached to COOH groups of acrylic acid.

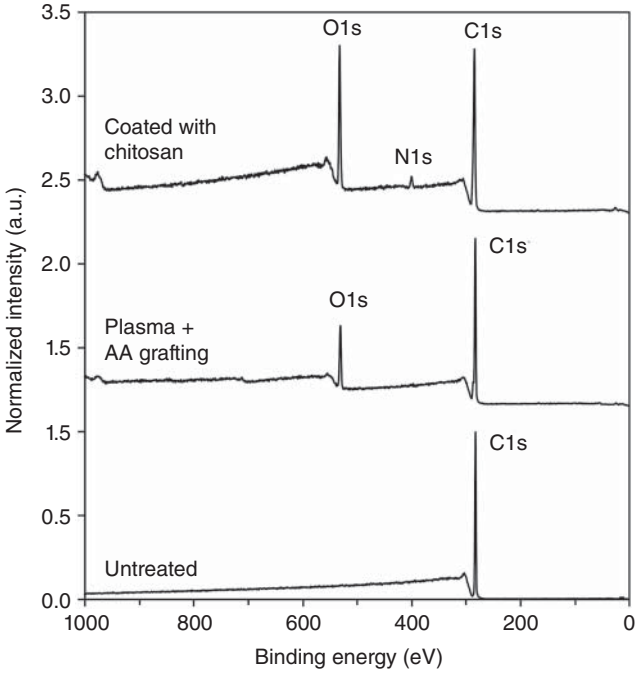

Figure 2.27 XPS survey spectra of PE polymer substrate, plasma-activated PE polymer after grafting with acrylic acid, and PE polymer with chitosan coating attached to COOH groups of acrylic acid.

chitosan are observed. Successful deposition of chitosan coating can be also proved by the appearance of nitrogen in the XPS survey spectra, whose concentration is shown in Table 2.5.

Heparin is an important anticoagulant agent and is used in medical applications to prevent platelet aggregation that leads to thrombus formation. Therefore, it is an important coating for artificial vascular grafts. Kolar et al. [69] investigated the hemocompatibility and chemical properties of PET polymer upon incubation with heparin. PET polymer was first treated in ammonia plasma to introduce amino groups and then coated with heparin. XPS characterization in combination with chemical derivatization with 4-chlorobenzaldehyde was used to determine the content of amino groups. The free-hemoglobin method as well as platelet and cell adhesion were investigated as well.

Buzzacchera et al. [70] prepared chitosan hydrogel coatings with antifouling properties for implantable sensor devices to prevent inflammation of the surrounding body tissue. Chitosan coatings were functionalized with polymer brushes of oligo(ethylene glycol) methyl ether methacrylate and 2-hydroxyethyl methacrylate using radical polymerization. The surfaces were characterized by XPS to confirm the presence of chitosan and different polymer brushes on the chitosan.

Polyaniline is a promising conductive polymer that can be used in biomedical applications for biosensors and drug delivery devices [71]. Junyan Yao et al. synthesized conductive fiber tubes of poly(L-lactic acid)/polyaniline/*p*-toluene sulfonic

acid (PLLA/PANI/TSA). XPS analyses were accomplished to examine the chemical structure of the PLLA/PANI/TSA composite and to investigate the polymerization degree of PANI [72]. Also Qaiser et al. [16] have investigated charge transport in polyaniline-cellulose acetate composite membranes by XPS. By measuring C1s and N1s spectra, they determined oxidation and doping states of PANI. Irgasan (triclosan) is an antibacterial agent that inhibits the growth of bacteria. Asadinezhad et al. [73] developed a multistep physicochemical procedure for the preparation of a novel surface with active antibacterial properties on medical-grade polyvinyl chloride (PVC) that can be used in urinary catheters. This multistep procedure includes the first step of the polymer surface activation with plasma, followed by radical graft copolymerization of acrylic acid and then deposition of irgasan coating. XPS was used to confirm the presence of irgasan coating on the PVC surface.

Also Salmi-Mani et al. [74] developed new antibacterial surfaces by depositing coatings from vanillin-derived biobased monomer on PET surfaces. They developed a method containing two treatment steps. The first step included an aminolysis reaction with *N,N*-diethylethylenediamine that caused the grafting of amino groups onto the PET surface. These amino groups were then used as a photoinitiator to initiate the free radical photopolymerization. In the second step, UV light exposure

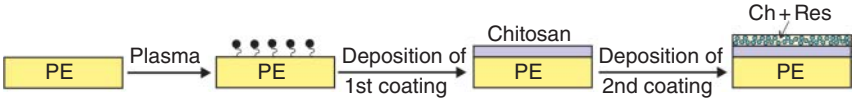

Figure 2.28 The scheme of immobilization of nanoformulation of chitosan with resveratrol on the polymer surface.

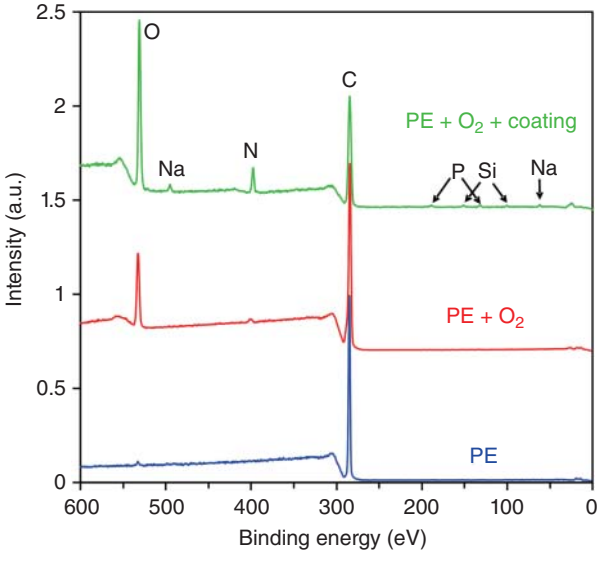

Figure 2.29 XPS survey spectra of the untreated PE foil (lower curve), after oxygen plasma treatment (middle) and with a novel coating (upper).

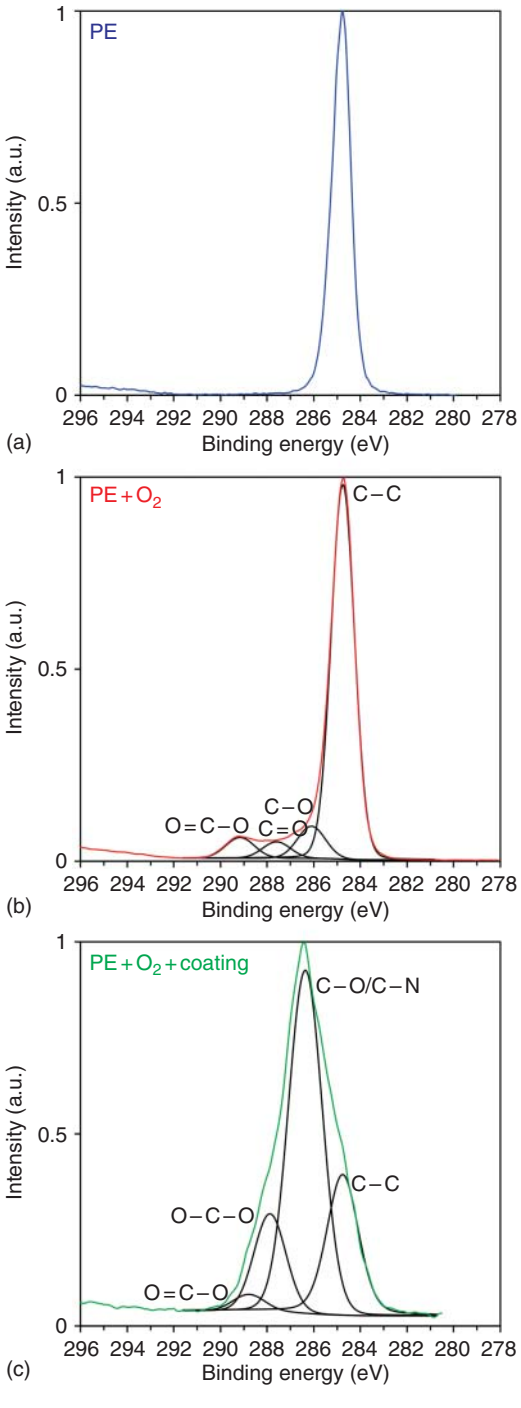

Figure 2.30 High-resolution carbon spectra of: (a) the untreated PE foil, (b) after oxygen plasma treatment, and (c) with a novel coating.

caused the formation of aminoalkyl radicals and photopolymerization of the vanillin-derived biobased monomer. XPS was used to prove the successful binding of *N,N*-diethylethylenediamine after the first step, as well as vanillin after the second treatment step.

Phosphorus-containing organic compounds may have a potential role as hemocompatible moieties and antibacterial coatings. Furthermore, phosphate groups are also present in many biological molecules such as DNA. Siow et al. [75] investigated deposition of plasma-polymer coatings containing phosphorus. XPS analyses of coatings prepared from triisopropyl phosphite (TIP) and diethyl phosphite (DEP) revealed the presence of phosphate PO_4 and polyphosphate groups poly-PO_4, whereas the addition of 1,7-octadiene led to phosphonate PO_3 and phosphate groups PO_4.

Resveratrol belongs to a group of polyphenolic compounds and is an important antioxidant agent. As a natural plant ingredient, it has a promising application in the food packaging industry as well as in the pharmaceutical industry. Because of its potential anticarcinogenic properties, it is also a potential candidate to be used in medicine for cancer treatment [76]. Fras-Zemljič et al. [77] developed a two-step procedure for the deposition of two-layered functional coatings on PP and PE polymer foils for food packaging application. The first coating was a layer of chitosan deposited on the oxygen-plasma-treated foil. This layer acts as the intermediate adhesive layer for further deposition of the macromolecular solution of chitosan nanoparticles with embedded resveratrol extract (Figure 2.28). XPS was used to confirm the presence of this novel functional coating on the polymer foils. An example of such XPS measurement is shown in Figures 2.29 and 2.30. In comparison to the untreated sample, where mostly carbon in the form of C—C

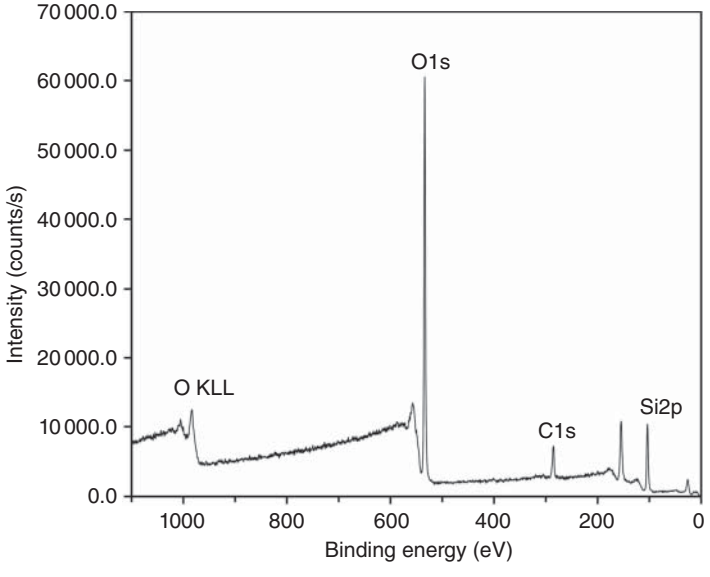

Figure 2.31 The XPS survey spectrum of chestnut honey deposited on the quartz holder.

bonds is observed, the coated surface shows the presence of different functional groups from the organic coating. Using a similar procedure, Fras-Zemljič et al. also prepared other formulations of chitosan nanoparticles with embedded extract of thyme, rosemary, and cinnamon [78].

Natural organic materials often contain microelements in very small concentrations that cannot be detected by conventional methods. In Figure 2.31 is shown an example of the XPS survey spectrum of chestnut honey deposited on the quartz holder. For as-deposited honey, only a few elements are detected, i.e. carbon, oxygen, and silicon, because other microelements from honey are present in too small concentrations to be detectable by XPS. However, if honey is exposed to controlled etching with the flux of neutral oxygen atoms from an oxygen plasma source, the organic part of the honey sample may be etched and removed from the surface, thus revealing the microelements. In this case, as shown in Figure 2.32, the other elements like potassium, fluorine, sulfur, phosphorus, and calcium are observed, and their concentration is shown in Table 2.6.

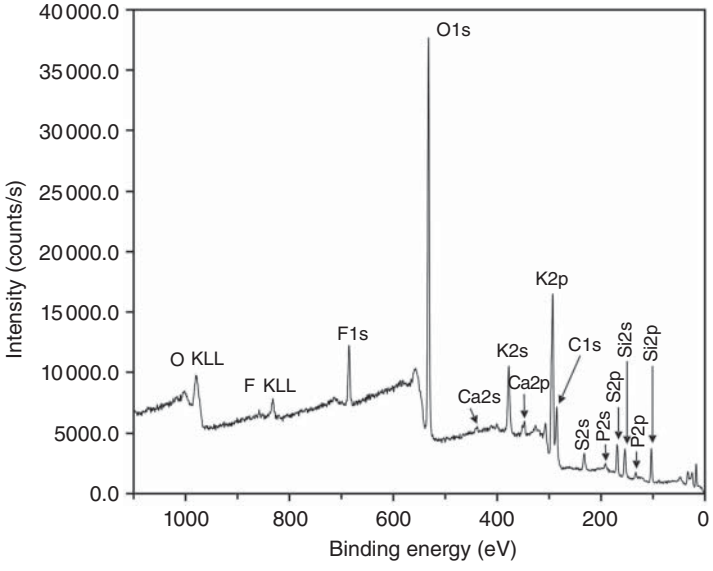

Figure 2.32 The XPS survey spectrum of chestnut honey after cold plasma ashing in oxygen afterglow.

Table 2.6 Surface composition of the as-deposited chestnut honey and after oxygen plasma ashing, which reveals the presence of microelements (in at.%).

Sample	C1s	O1s	F1s	Si2p	P2s	S2p	K2p	Ca2p
As-deposited	17.3	56.4		26.3				
Etched	14.3	49.4	6.7	9.3	2.2	4.5	12.4	1.2

2.8 Practical Considerations

XPS is a surface-sensitive technique so any impurities that might have adsorbed during handling or storage of (bio)materials will result in vague interpretation of results. In order to minimize such effects, the samples are preferably characterized immediately after synthesizing. It this is not feasible; the as-prepared samples should be stored in a dry atmosphere free from organic vapours. Organic vapours, although presented in the atmosphere in minute concentrations, will lead to misinterpretation of the surface composition as well as structure. Any exposure to short-wavelength radiation (including UVA) may cause bond breakage and possible modification of the surface chemistry. Also, exposure of samples to X-rays during characterization may cause modification of the surface composition and structure so one should be aware of this effect, too.

Acknowledgments

The authors acknowledge the financial support from the Slovenian Research Agency – program No. P2-0082 (Thin film structures and plasma surface engineering) and project no. J2-1728.

References

1 NIST (2000). NIST Standard Reference Database 71. In: *NIST Electron Inelastic-Mean-Free-Path Database*, Gaithersburg, USA, https://www.nist.gov/srd/nist-standard-reference-database-71 (accessed 20 January 2020).
2 Tanuma, S., Powell, C.J., and Penn, D.R. (1994). Calculations of electron inelastic mean free paths. V. Data for 14 organic compounds over the 50–2000 eV range. *Surf. Interface Anal.* 21: 165–176.
3 Cumpson, P.J. (2001). Estimation of inelastic mean free paths for polymers and other organic materials: use of quantitative structure–property relationships. *Surf. Interface Anal.* 31: 23–34.
4 Tan, Z., Xia, Y., Zhao, M., and Liu, X. (2006). Electron stopping power and inelastic mean free path in amino acids and protein over the energy range of 20–20,000 eV. *Radiat. Environ. Biophys.* 45: 135–143.
5 Lesiak, B., Jablonski, A., Zemek, J. et al. (2000). Determination of the inelastic mean free path of electrons in different polyaniline samples. *Langmuir* 16: 1415–1423.
6 Stojilovic, N. (2012). Why can't we see hydrogen in X-ray photoelectron spectroscopy? *J. Chem. Educ.* 89: 1331–1332.
7 Vandencasteele, N., Fairbrother, H., and Reniers, F. (2005). Selected effect of the ions and the neutrals in the plasma treatment of PTFE surfaces: an OES-AFM-Contact angle and XPS study. *Plasma Processes Polym.* 2: 493–500.

8 Beamson, G. and Briggs, D. (1992). *High Resolution XPS of Organic Polymers: The Scienta ESCA300 Database*. Chichester: Wiley.

9 Beamson, G., Clark, D.T., Kendrick, J., and Briggs, D. (1991). Observation of vibrational asymmetry in the high resolution monochromatized XPS of hydrocarbon polymers. *J. Electron Spectrosc. Relat. Phenom.* 57: 79–90.

10 Fronzoni, G., Baseggio, O., Stener, M. et al. (2014). Vibrationally resolved high-resolution NEXAFS and XPS spectra of phenanthrene and coronene. *J. Chem. Phys.* 141: 044313.

11 Girard-Lauriault, P.-L., Unger, W.E.S., Dietrich, P.M., and Holländer, A. (2015). Innovative and established strategies for the surface analysis of nitrogen and oxygen-rich plasma polymer films by XPS: An introductory guide. *Plasma Processes Polym.* 12: 953–967.

12 Kröner, D., Ehlert, C., Saalfrank, P., and Holländer, A. (2011). Ab initio calculations for XPS chemical shifts of poly(vinyl-trifluoroacetate) using trimer models. *Surf. Sci.* 605: 1516–1524.

13 Kehrer, M., Duchoslav, J., Hinterreiter, A. et al. (2019). XPS investigation on the reactivity of surface imine groups with TFAA. *Plasma Processes Polym.* 16: 1800160.

14 Lommatzsch, U., Pasedag, D., Baalmann, A. et al. (2007). Atmospheric pressure plasma jet treatment of polyethylene surfaces for adhesion improvement. *Plasma Processes Polym.* 4: S1041–S1045.

15 Situ, Y., Ji, W., Liu, C. et al. (2019). Synergistic effect of homogeneously dispersed PANI-TiN nanocomposites towards long-term anticorrosive performance of epoxy coatings. *Prog. Org. Coat.* 130: 158–167.

16 Qaiser, A.A., Hyland, M.M., and Patterson, D.A. (2011). Surface and charge transport characterization of polyaniline–cellulose acetate composite membranes. *J. Phys. Chem. B* 115: 1652–1661.

17 Siow, K.S., Britcher, L., Kumar, S., and Griesser, H.J. (2009). Sulfonated surfaces by sulfur dioxide plasma surface treatment of plasma polymer films. *Plasma Processes Polym.* 6: 583–592.

18 Siow, K.S., Kumar, S., and Griesser, H.J. (2015). Low-pressure plasma methods for generating non-reactive hydrophilic and hydrogel-like bio-interface coatings – a review. *Plasma Processes Polym.* 12: 8–24.

19 Coen, M.C., Keller, B., Groening, P., and Schlapbach, L. (2002). Functionalization of graphite, glassy carbon, and polymer surfaces with highly oxidized sulfur species by plasma treatments. *J. Appl. Phys.* 92: 5077–5083.

20 Holländer, A. and Kröpke, S. (2010). Polymer surface treatment with SO_2-containing plasmas. *Plasma Processes Polym.* 7: 390–402.

21 Thiry, D., Francq, R., Cossement, D. et al. (2013). Establishment of a derivatization method to quantify thiol function in sulfur-containing plasma polymer films. *Langmuir* 29: 13183–13189.

22 Pippig, F., Sarghini, S., Holländer, A. et al. (2009). TFAA chemical derivatization and XPS. Analysis of OH and NH_x polymers. *Surf. Interface Anal.* 41: 421–429.

23 Holländer, A., Pippig, F., Dubreuil, M., and Vangeneugden, D. (2008). Distinguishing Surface OH and NH_x Using TFAA Derivatization and XPS. *Plasma Processes Polym.* 5: 345–349.

24 Choukourov, A., Kousal, J., Slavínská, D. et al. (2004). Growth of primary and secondary amine films from polyatomic ion deposition. *Vacuum* 75: 195–205.

25 Everhart, D.S. and Reilley, C.N. (1981). Chemical derivatization in electron spectroscopy for chemical analysis of surface functional groups introduced on low-density polyethylene film. *Anal. Chem.* 53: 665–676.

26 Khosravi, Z. and Klages, C.-P. (2014). Nucleophilic derivatization of polyethylene surfaces treated in ambient-pressure N_2–H_2 DBD post discharges. *Plasma Chem. Plasma Process.* 34: 661–669.

27 Klages, C.-P. and Kotula, S. (2016). Critical remarks on chemical derivatization analysis of plasma-treated polymer surfaces and plasma polymers. *Plasma Processes Polym.* 13: 1213–1223.

28 Khosravi, Z., Kotula, S., Lippitz, A. et al. (2018). IR- and NEXAFS-spectroscopic characterization of plasma-nitrogenated polyolefin surfaces. *Plasma Processes Polym.* 15: 1700066.

29 Klages, C.-P., Khosravi, Z., and Hinze, A. (2013). Some remarks on chemical derivatization of polymer surfaces after exposure to nitrogen-containing plasmas. *Plasma Processes Polym.* 10: 307–312.

30 Holländer, A. (2017). Why do we need chemical derivatization? *Plasma Processes Polym.* 14: 1700044.

31 López-Santos, C., Yubero, F., Cotrino, J., and González-Elipe, A.R. (2010). Surface functionalization, oxygen depth profiles, and wetting behavior of PET treated with different nitrogen plasmas. *Appl. Mater. Interfaces* 2: 980–990.

32 Sarra-Bournet, C., Ayotte, G., Turgeon, S. et al. (2009). Effects of chemical composition and the addition of H_2 in a N_2 atmospheric pressure dielectric barrier discharge on polymer surface functionalization. *Langmuir* 25: 9432–9440.

33 Khosravi, Z., Kotula, S., and Klages, C.-P. (2015). Electrophilic character of PE surfaces plasma-treated in N_2 or N_2-H_2 mixtures at atmospheric pressure. In: *22nd International Symposium on Plasma Chemistry* (ed. A. Bogaerts and R. van de Sanden), O-5-5. Antwerp, Belgium: IPCS.

34 Markkula, T.K., Hunt, J.A., Pu, F.R., and Williams, R.L. (2002). Surface chemical derivatization of plasma-treated PET and PTFE. *Surf. Interface Anal.* 34: 583–587.

35 Dang, T.A. and Gnanasekaran, R. (1990). Determination of amino and silanol functional groups on glass via chemical derivatization and ESCA. *Surf. Interface Anal.* 15: 113–118.

36 Malitesta, C., Losito, I., Sabbatini, L., and Zambonin, P.G. (1998). Applicability of chemical derivatization – X-ray photoelectron spectroscopy (CD–XPS) to the characterization of complex matrices: case of electrosynthesized polypyrroles. *J. Electron Spectrosc. Relat. Phenom.* 97: 199–208.

37 Nietzold, C., Dietrich, P.M., Ivanov-Pankov, S. et al. (2014). Functional group quantification on epoxy surfaces by chemical derivatization (CD)-XPS. *Surf. Interface Anal.* 46: 668–672.

38 Alexander, M.R., Wright, P.V., and Ratner, B.D. (1996). Trifluoroethanol derivatization of carboxylic acid-containing polymers for quantitative XPS analysis. *Surf. Interface Anal.* 24: 217–220.

39 Manakhov, A., Kiryukhantsev-Korneev, P., Michlíček, M. et al. (2018). Grafting of carboxyl groups using CO_2/C_2H_4/Ar pulsed plasma: Theoretical modeling and XPS derivatization. *Appl. Surf. Sci.* 435: 1220–1227.

40 Chilkoti, A. and Ratner, B.D. (1991). An X-ray photoelectron spectroscopic investigation of the selectivity of hydroxyl derivatization reactions. *Surf. Interface Anal.* 17: 567–574.

41 Rouxhet, P.G., Misselyn-Bauduin, A.M., Ahimou, F. et al. (2008). XPS analysis of food products: toward chemical functions and molecular compounds. *Surf. Interface Anal.* 40: 718–724.

42 Rouxhet, P.G. and Genet, M.J. (2011). XPS analysis of bio-organic systems. *Surf. Interface Anal.* 43: 1453–1470.

43 Maachou, H., Genet, M.J., Aliouche, D. et al. (2013). XPS analysis of chitosan–hydroxyapatite biomaterials: from elements to compounds. *Surf. Interface Anal.* 45: 1088–1097.

44 Johansson, L.S., Campbell, J.M., Koljonen, K., and Stenius, P. (1999). Evaluation of surface lignin on cellulose fibers with XPS. *Appl. Surf. Sci.* 144–145: 92–95.

45 Johansson, L.S., Campbell, J.M., Fardim, P. et al. (2005). An XPS round robin investigation on analysis of wood pulp fibres and filter paper. *Surf. Sci.* 584: 126–132.

46 Vesel, A., Zaplotnik, R., Kovac, J., and Mozetic, M. (2018). Initial stages in functionalization of polystyrene upon treatment with oxygen plasma late flowing afterglow. *Plasma Sources Sci. Technol.* 27: 094005.

47 Vukusic, T., Vesel, A., Holc, M. et al. (2018). Modification of physico-chemical properties of acryl-coated polypropylene foils for food packaging by reactive particles from oxygen plasma. *Materials* 11: 372.

48 Vesel, A., Junkar, I., Cvelbar, U. et al. (2008). Surface modification of polyester by oxygen- and nitrogen-plasma treatment. *Surf. Interface Anal.* 40: 1444–1453.

49 Vesel, A., Kolar, M., Doliska, A. et al. (2012). Etching of polyethylene terephthalate thin films by neutral oxygen atoms in the late flowing afterglow of oxygen plasma. *Surf. Interface Anal.* 44: 1565–1571.

50 Fernández, A., Espinós, J.P., Leinen, D. et al. (1994). Charging and mixing effects during the XPS analysis of mixtures of oxides. *Surf. Interface Anal.* 22: 111–114.

51 Cros, A. (1992). Charging effects in X-ray photoelectron spectroscopy. *J. Electron Spectrosc. Relat. Phenom.* 59: 1–14.

52 Johansson, L.S. and Campbell, J.M. (2004). Reproducible XPS on biopolymers: cellulose studies. *Surf. Interface Anal.* 36: 1018–1022.

53 Wegewitz, L., Prowald, A., Meuthen, J. et al. (2014). Plasma chemical and chemical functionalization of polystyrene colloidal crystals. *Plasma Chem. Chem. Phys.* 16: 18261–18267.

54 Paynter, R.W. and Ménard, M. (2006). ARXPS study of a plasma-treated polymer surface: an example of Case II diffusion? *J. Electron Spectrosc. Relat. Phenom.* 151: 14–18.

55 Tremblay, M.-C. and Paynter, R.W. (2003). Study of the degradation of plasma-oxidized polystyrene by time- and angle-resolved x-ray photoelectron spectroscopy. *Surf. Interface Anal.* 35: 502–514.

56 Tougaard, S. (1998). Accuracy of the non-destructive surface nanostructure quantification technique based on analysis of the XPS or AES peak shape. *Surf. Interface Anal.* 26: 249–269.

57 Wang, Y., Yin, S., Ren, L., and Zhao, L. (2009). Surface characterization of the chitosan membrane after oxygen plasma treatment and its aging effect. *Biomed. Mater.* 4: 035003.

58 Paynter, R.W. (2002). Angle-resolved XPS study of the effect of x-radiation on the aging of polystyrene exposed to an oxygen/argon plasma. *Surf. Interface Anal.* 33: 14–22.

59 Awsiuk, K., Bernasik, A., Kitsara, M. et al. (2010). Protein coverage on silicon surfaces modified with amino-organic films: a study by AFM and angle-resolved XPS. *Colloids Surf., B* 80: 63–71.

60 Awsiuk, K., Budkowski, A., Psarouli, A. et al. (2013). Protein adsorption and covalent bonding to silicon nitride surfaces modified with organo-silanes: Comparison using AFM, angle-resolved XPS and multivariate ToF-SIMS analysis. *Colloids Surf., B* 110: 217–224.

61 Ton-That, C., Shard, A.G., and Bradley, R.H. (2000). Thickness of spin-cast polymer thin films determined by angle-resolved XPS and AFM tip-scratch methods. *Langmuir* 16: 2281–2284.

62 Strohmeier, B.R. (1990). An ESCA method for determining the oxide thickness on aluminum alloys. *Surf. Interface Anal.* 15: 51–56.

63 Awsiuk, K., Bernasik, A., Kitsara, M. et al. (2012). Spectroscopic and microscopic characterization of biosensor surfaces with protein/amino-organosilane/silicon structure. *Colloids Surf., B* 90: 159–168.

64 Awsiuk, K., Rysz, J., Petrou, P. et al. (2014). Immobilization of oligonucleotide probes on silicon surfaces using biotin–streptavidin system examined with microscopic and spectroscopic techniques. *Appl. Surf. Sci.* 290: 199–206.

65 Holvoet, S., Chevallier, P., Turgeon, S., and Mantovani, D. (2010). Toward high-performance coatings for biomedical devices: study on plasma-deposited fluorocarbon films and ageing in PBS. *Materials* 3: 1515–1532.

66 Ferraria, A.M., Lopes da Silva, J.D., and do Rego, A.M.B. (2003). XPS studies of directly fluorinated HDPE: problems and solutions. *Polymer* 44: 7241–7249.

67 Hinder, S.J., Watts, J.F., and Lowe, C. (2004). Interface analysis and compositional depth profiling by XPS of polymer coatings prepared using ultra-low-angle microtomy. *Surf. Interface Anal.* 36: 1032–1036.

68 Marpu, S.B. and Benton, E.N. (2018). Shining light on chitosan: a review on the usage of chitosan for photonics and nanomaterials research. *Int. J. Mol. Sci.* 19: 1795.

69 Kolar, M., Mozetic, M., Stana-Kleinschek, K. et al. (2015). Covalent binding of heparin to functionalized PET materials for improved haemocompatibility. *Materials* 8: 1526–1544.

70 Buzzacchera, I., Vorobii, M., Kostina, N.Y. et al. (2017). Polymer brush-functionalized chitosan hydrogels as antifouling implant coatings. *Biomacromolecules* 18: 1983–1992.

71 Olad, A. and Azhar, F.F. (2013). Biomedical applications of polyaniline. In: *Trends in Polyaniline Research* (ed. T. Ohsaka, A.-N. Chowdhury, A. Rahman and M. Islam), 361–384. Hauppauge, NY: Nova Science Publishers.

72 Yao, J., Chen, Y., Li, W. et al. (2019). Fabrication and characterization of electrospun PLLA/PANI/TSA fibers. *RSC Adv.* 9: 5610–5619.

73 Asadinezhad, A., Novák, I., Lehocký, M. et al. (2010). A physicochemical approach to render antibacterial surfaces on plasma-treated medical-grade PVC: irgasan coating. *Plasma Processes Polym.* 7: 504–514.

74 Salmi-Mani, H., Terreros, G., Barroca-Aubry, N. et al. (2018). Poly(ethylene terephthalate) films modified by UV-induced surface graft polymerization of vanillin derived monomer for antibacterial activity. *Eur. Polym. J.* 103: 51–58.

75 Siow, K.S., Britcher, L., Kumar, S., and Griesser, H.J. (2014). Deposition and XPS and FTIR analysis of plasma polymer coatings containing phosphorus. *Plasma Processes Polym.* 11: 133–141.

76 Salehi, B., Mishra, A.P., Nigam, M. et al. (2018). Resveratrol: a double-edged sword in health benefits. *Biomedicines* 6: 91.

77 Glaser, T.K., Plohl, O., Vesel, A. et al. (2019). Functionalization of polyethylene (PE) and polypropylene (PP) material using chitosan nanoparticles with incorporated resveratrol as potential active packaging. *Materials* 12: 2118.

78 Zemljič, L.F., Plohl, O., Vesel, A. et al. (2020). Physicochemical characterization of packaging foils coated by chitosan and polyphenols colloidal formulations. *Int. J. Mol. Sci.* 21: 495.

3

Methods for Characterization of Dielectric and Thermal Properties of Biomaterials

Daniela Ioniţă[1], Mihai Asandulesa[2], and Mariana Cristea[1]

[1] *"Petru Poni" Institute of Macromolecular Chemistry, Department of Physics of Polymers and Polymeric Materials, 41A Grigore Ghica Voda Alley, 700487 Iasi, Romania*
[2] *"Petru Poni" Institute of Macromolecular Chemistry, Department of Electroactive Polymers and Plasmochemistry, 41A Grigore Ghica Voda Alley, 700487 Iasi, Romania*

3.1 Introduction to Thermal Analysis Techniques

Thermal analysis is an engineering tool that provides analytical information related to the main thermal and mechanical properties absolutely necessary for a proper characterization, especially when polymers are intended for biomedical applications (tissue engineering, drug delivery). According to International Confederation of Thermal Analysis and Calorimetry (ICTAC), thermal analysis defines a family of techniques in which a property is measured with respect to temperature. The temperature associated with the experiment can be held constant through the experiment (isothermal experiments) or varied in a controlled manner (linear variation of temperature, modulated variation with a certain frequency and amplitude, and variation in temperature from a constant temperature to another constant temperature). Sometimes, a combination of both methods is advisable. Figure 3.1 defines the current techniques which are commonly referred to as being part of thermal analysis and which are the topic of this chapter.

Thermal analysis techniques differ from each other by the principle of the method, sensitivity, and sensibility; therefore, it is necessary each time to choose the most appropriate method for studying a certain temperature range or a certain type of transformation. Most often, the analysis involves more than registration of the changing property; it even surprises the evolution in time of some phenomena. No method of characterization is capable of providing a complete characterization. Therefore, the chemist must provide the most accurate description of the phenomenon by putting together the knowledge gained from each thermal method. This chapter will focus on the thermal and dielectric characterization of cellulose, chitosan, and pullulan using some of the most common thermal analysis methods: thermogravimetric analysis (TGA), differential scanning calorimetry (DSC), dynamic mechanical analysis (DMA), and dielectric analysis (DEA).

Functional Biomaterials: Design and Development for Biotechnology, Pharmacology, and Biomedicine, First Edition. Edited by Tamilselvan Mohan and Karin Stana Kleinschek.

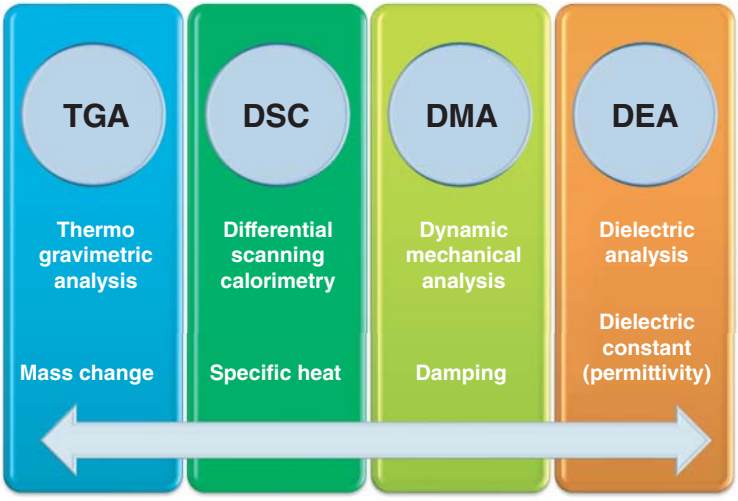

Figure 3.1 Thermal analysis methods.

3.1.1 Thermogravimetric Analysis

TGA is an essential laboratory tool that measures the weight loss as a function of time and temperature in a controlled atmosphere. The weight changes of polymeric materials can be caused by decomposition and oxidation reactions as well as physical processes such as sublimation, vaporization, and desorption. A thermobalance is used to measure the mass change of a sample as a function of temperature or time, under a defined and controlled environment with respect to heating rate, gas atmosphere, flow rate, and crucible type. The process may take place in one or more steps. Figure 3.2 summarizes a TGA curve involving a single mass loss step.

The values m_i and m_f are the mass before heating and the maximum mass loss, respectively. T_i and T_f are the temperatures assigned to the corresponding mass loss.

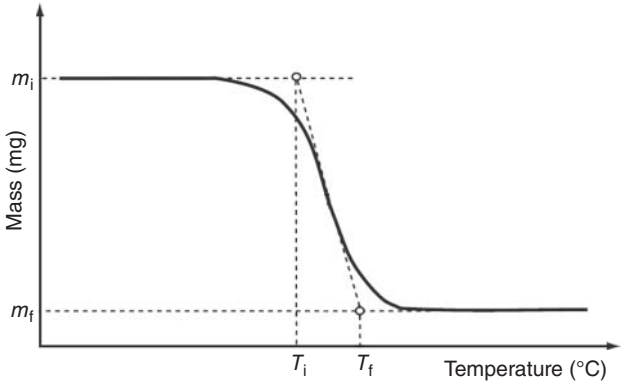

Figure 3.2 Thermogravimetric curve with a single mass loss step.

3.1.1.1 Applications

TGA is the first thermal analysis performed in any approach of thermal investigation of polymers. TGA not only provides better interpretation of weight loss and evolved gas results, but it also supplies complementary and supplementary information to the most commonly used thermal techniques (DSC, DMA, DEA). There are no transitions in DMA and DSC when weight changes occur. TGA has a wide range of properties that can be measured such as thermal stability, study of the kinetics of decomposition, oxidative stability, and determination of material composition based on mass losses due to evaporation and decomposition [1, 2]. On one hand, thermal methods as DMA are not well suited to investigate the thermal degradation as long as the thermal degradation involves chemical reaction processes (scission or crosslinking). On the other hand, thermal degradation, which often involves the release of volatile degradation products complicates the DSC analysis. The baseline quality is affected and the released volatile can contaminate the cell of DSC. Therefore, it is recommended to establish the decomposition temperature first using TGA to avoid these undesirable effects.

TGA provides data on the volatile compounds the sample contains. It is known that the evaporation process is a cause of endothermic peaks in the DSC. In order to avoid confusion concerning the melting process, the existence of an evaporation phenomenon can first be proved by TGA. Secondly, the presence of the solvent (water) may reduce the glass transition temperature and the temperature of the cold crystallization or may influence the crystallization process during cooling.

3.1.2 Differential Scanning Calorimetry

DSC is one of the most widely used methods for polymer analysis. DSC highlights the chemical transitions and evaluates the physico-chemical processes that take place in polymers with increasing temperature [3, 4]. The term calorimetry refers exclusively to the measurement of heat. Heat can be an amount of energy exchanged between two bodies in the form of a *heat flow* within a time frame.

3.1.2.1 Principle

DSC is a technique in which the difference in heat flow between the substance (and/or reaction products) and the reference material is measured according to temperature or time. The substance and reference material are subject to a well-controlled temperature program. According to Eq. (3.1), DSC measurements quantify the heat flow ($\mathrm{d}q/\mathrm{d}t$) supplied by any change in *heat capacity* (C_p) or any other thermal event (phase transformation or chemical reactions) ($f(T,t)$), which occurs within the temperature range of the experiment.

$$\frac{\mathrm{d}q}{\mathrm{d}t} = C_p \frac{\mathrm{d}T}{\mathrm{d}t} + f(T,t) \tag{3.1}$$

The differences in heat flow ($\mathrm{d}q/\mathrm{d}t$) are due to changes in the heat capacity of a sample (C_p) – which increases with the increase in temperature – and structural changes that occur as a result of transitions or physico-chemical processes.

Based on the mechanism of operation, DSC is commercially available as a *power-compensating DSC* or as a *heat-flux DSC*. A single oven is used in the heat-flux DSC which measures the temperature differences occurring between the sample and the reference. In a power-compensated DSC, the sample and the reference have separate ovens. The temperature difference between the sample and the reference material is converted into thermal power necessary to compensate the heat released or gained during the thermal event. The result of a DSC experiment is a curve of heat flow vs. temperature. The measured signal is directly proportional to the heat capacity of the sample. If the sample to be analyzed does not undergo a physico-chemical transformation or a thermal transition, then the signal will appear as a straight line. Any transition or chemical reaction causes a change in the heat flow and is recorded as a step/peak. The shape, size, and orientation of the peaks (endotherms, exotherms) highlight the nature and intensity of the different phenomena; the position along the time axis indicates the stability of the different processes. The area under the endothermic or exothermic peak is proportional to the enthalpy, as shown by the Eq. (3.2):

$$\Delta H = \frac{A}{m} K_{\mathrm{DSC}} \tag{3.2}$$

where A is the area under the peak, K_{DSC} is a temperature constant, and m is the weight of the sample.

3.1.2.2 Applications of DSC

Figure 3.3 shows the DSC thermogram of a semicrystalline polymer. This comprises most of the physical transitions (glass transition, melting, crystallization) and of the chemical processes (crosslinking, oxidation, decomposition) that can be found in polymers.

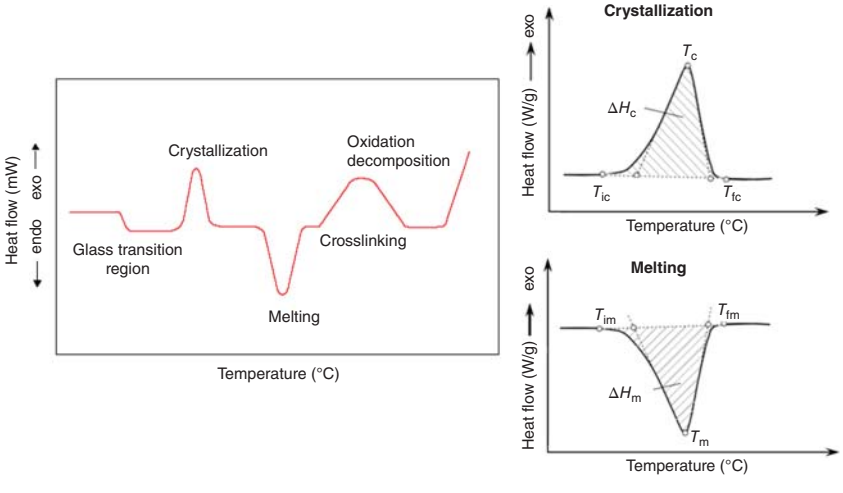

Figure 3.3 The main events that can be detected in polymers by DSC.

3.1.2.2.1 Glass Transition

The DSC is widely used to measure the glass transition temperature, which is an important parameter for polymer characterization. The T_g represents the temperature region at which the amorphous phase of a polymer is transformed from a brittle, glassy material into a tough rubbery phase.

Highlighting the glass transition through DSC is possible due to the fact that the gradual change in molecular mobility (chains acquire more freedom of movement) causes changes in heat capacity and heat flow. This endothermic event is depicted by a shift in the baseline. Five points may be selected and reported as the value of T_g (Figure 3.4): the onset (T_{gi}), the extrapolated onset (T_{geo}), the mid-point temperature (T_{gm}), the extrapolated end temperature (T_{gee}), and the end point of the inflexion appeared in the baseline (T_{gf}). The subscript "m" stands for midpoint, "i" for initial, and "f" for final. The change in the heat capacity at T_g is related to the amorphous content. The percentage of amorphous phase in a semicrystalline material can be determined knowing the glass transition for the material containing 100% amorphous content. Moreover, fully crystalline materials do not show this transition. A single temperature is generally reported for convenience as T_g, but the biopolymer actually changes its properties over a range of temperatures. Glass transition temperature measurements can vary greatly according to technique or experimental conditions (heating rate, mass of the sample).

3.1.2.2.2 Melting

If T_g is a property of the amorphous region, melting is a property of the crystalline region very important for semicrystalline polymers because it outlines the upper temperature limit of the polymer structural integrity. Melting is the process of transforming the crystalline structure into an amorphous structure and shows up as a large endothermic peak in the DSC plot. The heat added to the polymer during the melting process is the latent heat of melting. It is calculated from the area of a melting peak observed in a plot of heat flow against temperature (right side of Figure 3.3). Melting temperature (T_m) is defined as the maximum temperature of the peak.

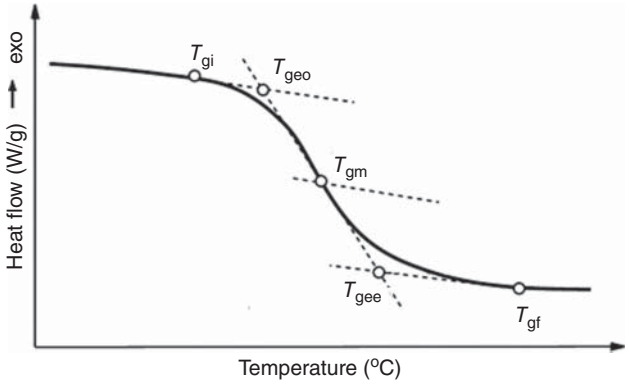

Figure 3.4 Assessment of glass transition by DSC.

3.1.2.2.3 Crystallization

The exothermic peak that is frequently observed in a DSC experiment during heating or cooling is due to a crystallization process. It originates from the rearrangement of amorphous structure into a crystalline one. Cold crystallization is observed on heating a sample that has previously been cooled very quickly and had no time to crystallize during the cooling phase. Crystallization temperature (T_c), defined as the lowest point of the exothermic process, is the temperature at which the crystallization rate is maximum (right side of Figure 3.3). The enthalpy of crystallization is determined from the area of the peak.

3.1.3 Dynamic Mechanical Analysis (DMA)

DMA, also known as rheology of solid, is a powerful analytical instrument that facilitates understanding of the structural and mechanical changes by analyzing the variation of the viscous and elastic properties with temperature and frequency [5, 6].

3.1.3.1 Principle

A specimen of known geometry clamped into a mechanical loading frame (tension, three-point bending, single/dual cantilever, shear, compression) is subjected to an oscillatory stress (σ), usually sinusoidal and causes an oscillatory strain (ε) (Figure 3.5).

Due to the time-dependent properties of viscoelastic materials, the resulting strain lags behind the applied stress by a phase angle (δ).

$$\sigma = \sigma_0 \sin \omega t \tag{3.3}$$

$$\varepsilon = \varepsilon_0 \sin(\omega t + \delta) \tag{3.4}$$

The DMA results are given in term of a complex modulus E^* that distinguishes between the elastic and viscous responses.

$$E^* = E' + iE'' \tag{3.5}$$

$$\tan \delta = \frac{E''}{E'} \tag{3.6}$$

The storage modulus (E') describes the elastic behavior and refers to the ability of a material to store energy; it is related to the stiffness of the material. The loss modulus (E'') describes the viscous behavior and represents the heat dissipated by

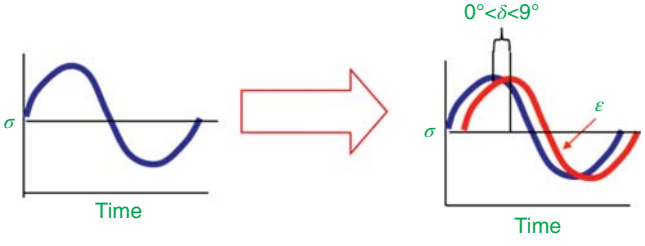

Figure 3.5 Principles of DMA.

the sample as a result of molecular motions. The loss factor (tan δ) is a dimensionless property and quantifies the mechanical damping.

3.1.3.2 Applications of DMA

Most often, DMA is used for assessing *relaxations* (α, β, γ) in polymers by investigating the variation of the storage modulus, loss modulus, and tan δ with temperature using a frequency of 1 Hz. Relaxation temperatures generated by different molecular movements are determined as drops in E' and as peaks on E'' and tan δ curve, the tan δ peak appearing always at a higher temperature than the E'' peak [7]. The most important material characteristic with respect to its applications is *α-relaxation* which is associated with the glass transition temperature (T_g). It corresponds to the onset of long-range coordinated molecular motions. The high sensitivity of DMA in characterizing T_g is related to the great changes in the mechanical properties in terms of loss rigidity and increase of molecular mobility. The storage modulus decreases up to three orders of magnitude in a range of $20 \div 30$ degrees. The loss modulus and tan δ peak reach a maximum. Significant feature of tan δ plot includes the width, magnitude, and temperature of the peak. The magnitude of the tan δ at T_g is a measure of the energy damping characteristic and is related to the impact strength of a material.

Below T_g the polymer is in the *glassy state* and is frequently brittle. This region is characterized by secondary relaxations (β, γ) that cannot be distinguished by other thermal analysis techniques. Identification of this type of relaxations has a significant impact on mechanical properties such as impact resistance and toughness. The chain segments are frozen, and their mobility is limited to motions of short segments of main chain, rotations of terminal groups, or side chains. Thereby, much smaller changes in the mechanical properties can be observed relative to the glass transition region: a storage modulus higher than 10^9 Pa, low loss modulus, and very low tan δ. In the *rubbery state*, the molecular chains gain enough mobility and molecular rearrangements can take place. The rubbery plateau is related to the degree of crystallinity, crosslinking, or molecular weight of the polymer.

Storage modulus, loss modulus, and loss factor values change with temperature and offer information regarding not only the relaxations that occur, but also on changes associated to different processes. From this point of view, DMA overcomes the limitation of DSC and provides high sensitivity in separating a relaxation from a kinetic effect using frequency along with temperature in the study of polymers [8]. Relaxation processes are frequency-dependent (shift to higher temperature with increasing frequency), in contrast to melting processes, crystallization, and chemical reactions, and can therefore be easily identified.

3.1.4 Broadband Dielectric Spectroscopy

The broadband dielectric spectroscopy (BDS) is generally employed for characterization of structural, molecular dynamics, and electrical properties of nonconducting and/or semiconducting-type materials. Since DEA offers a range of frequencies

beyond the typical 100 Hz limit of traditional DMA, it is often used as a complementary material characterization technique.

3.1.4.1 Principle

Dielectric measurements are the analogous measurements of those performed in DMA. The sinusoidal mechanical stress used in DMA is replaced by a cyclic electric field; it is applied across a sample placed between two parallel plate electrodes. The measured response due to charge species present in the sample (dipole or mobile units like free ions, electrons) can be related to conductivity and dielectric permittivity.

The complex dielectric permittivity, ε^*, is an intrinsic property of a system and is generally defined as

$$\varepsilon^* = \varepsilon' - i\varepsilon'' \tag{3.7}$$

where ε' is the dielectric constant and ε'' is the dielectric loss of the material. The dielectric constant quantifies the molecular dipoles of the sample that are rotated by an alternating electric field. The dielectric loss parameter is related to the dissipation of electromagnetic energy for dipoles alignment and movements of charge carriers, as well. In an ideal dielectric system (a material with no conductivity contribution), the dielectric loss is attributed only to dielectric relaxation processes. In real dielectrics, the electric charges are also presented and lead to a variety of charge carriers relaxation-type processes. As a result, the dielectric dispersion is a superposition of dipolar activity (dipole-relaxation) and movement of charges (charge carrier-relaxation). Since dielectric loss comprises both the polarization and conductivity contribution signals, the electrical conductivity σ (S/cm) could be further evaluated with the relation:

$$\sigma = 2\pi\varepsilon_0 f\varepsilon'' \tag{3.8}$$

where ε_0 is the permittivity of the free space and f is the frequency of the alternating electric field [9].

Another tool needed for an appropriate processing of BDS data is the complex modulus (M^*). The modulus expression is generally employed to identify all the relaxation-type processes available in the material that is under investigation, including the dipolar relaxations and the conductivity relaxation processes. In other words, the modulus allows a better identification of relaxation-type processes. The complex quantity, M^*, is estimated from the complex dielectric permittivity with the relation:

$$M^* = \frac{1}{\varepsilon^*} = M' + iM'' = \frac{\varepsilon'}{(\varepsilon')^2 + (\varepsilon'')^2} + i\frac{\varepsilon''}{(\varepsilon')^2 + (\varepsilon'')^2} \tag{3.9}$$

where M' is the real part and M'' is the imaginary part of modulus [10].

3.1.4.2 Applications

3.1.4.2.1 Evolution of Dielectric Parameters with Frequency

Figure 3.6 presents the classical behavior of the most common relaxation-type processes. Generally, for stable systems a dipolar relaxation is revealed as a well-defined

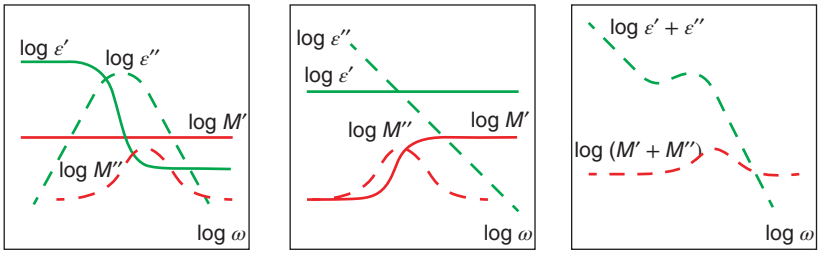

Figure 3.6 The variation of the dielectric constant, dielectric loss, real and imaginary parts of modulus function, revealing the dipolar relaxation (a), the ohmic conductivity (b), and the superposition of dipolar and conductivity signals (c). Source: Symonowicz et al. [11]/with permission of Elsevier.

dielectric peak in the $\varepsilon''(\omega)$ plots associated with a step-like behavior in the $\varepsilon'(\omega)$ dependency.

If the dipolar polarization is not influenced by conductivity, the $M''(\omega)$ spectra also exhibit a dielectric peak that corresponds to the dipolar relaxation (Figure 3.6a). Linear dependencies of $\varepsilon'(\omega)$ and $\varepsilon''(\omega)$ plots indicate the transport of charge carriers. The conductivity relaxation is further revealed as a well-defined peak in $M''(\omega)$ followed by a step-like behavior in $M'(\omega)$ spectra (Figure 3.6b). If the dielectric dispersion is a superposition of the oscillating dipoles and electric charges (Figure 3.6c), the ohmic conductivity is revealed at low frequencies as a linear dependence, while the capacitive-type signal is shown at higher frequencies [11].

3.1.4.2.2 Evolution of Dielectric Parameters with Temperature

BDS is an efficient technique to study the molecular dynamics in polymers. The dielectric data recorded in a broad range of temperature allow investigation of various relaxation-type processes, providing fluctuations of small groups from side-chain macromolecules and even large-scale segment motions [12, 13]. An important parameter that describes the molecular dynamics in materials is the activation energy. In the case of secondary relaxations, the parameter is related to the energy needed to change the conformation of molecular dipoles, while for cooperative α-relaxation it emphasizes the energy used for translation of molecules through the polymer backbone.

The frequency dependence of dielectric properties is processed according to Havriliak–Negami (HN) equation:

$$\varepsilon^* = \varepsilon' - i\varepsilon'' = \varepsilon_u + \frac{\varepsilon_r - \varepsilon_u}{\left[1 + (i\omega\tau_{\mathrm{HN}})^a\right]^b} \tag{3.10}$$

where ε_r and ε_u are the relaxed ($\omega \to 0$) and unrelaxed ($\omega \to \infty$) terms of the dielectric constant, $\omega = 2\pi f$ is the angular frequency, f is the frequency of the applied field, τ_{HN} is the HN relaxation time of the process, a and b represent the broadening and skewing parameters, respectively [14]. For overlapped dielectric signals, an additional

term from conductivity contribution is added. The characteristic relaxation time of the dielectric peak maxima, τ_{max}, is further evaluated with the equation:

$$\tau_{max} = \tau_{HN}\left[\frac{\sin\frac{\pi ab}{2+2b}}{\sin\frac{\pi a}{2+2b}}\right]^{\frac{1}{a}} \tag{3.11}$$

The secondary γ- and β-relaxations activation energy can be described by the Arrhenius-type equation:

$$\tau_{max}(T) = \tau_0 \exp\left(\frac{E_a}{RT}\right) \tag{3.12}$$

where τ_{max} is obtained with Eq. (3.11), τ_0 is a pre-exponential factor, and R is the gas constant.

For adequate description of α-relaxation, the Vogel–Fulcher–Tammann (VFT) equation is used:

$$\tau_{max}(T) = A\ \exp\left(\frac{E_a}{T - T_v}\right) \tag{3.13}$$

A is the pre-exponential factor, T_v is the so-called Vogel temperature and indicates the deviation from linearity.

The relaxation process of electrical conductivity gives information about the type of conduction and transport mechanism of electrical charges through the polymer matrix. Generally, for materials exhibiting the conductivity relaxation before glass transition, the activation energy is evaluated with the Arrhenius equation (Eq. (3.12)). If the conductivity relaxation is detected after the glass transition, the activation energy is determined with VFT equation (Eq. (3.13)), considering also the coupling between the transport of electric charges and the cooperative glassy dynamics [15]. The activation energy of the process is related to the energy required for the transport of charge carriers between the neighbor sites.

3.2 The Significance of Thermal Analysis in Biopolymers

In any biopolymer application, the evaluation of the structure–property relationship is essentially relevant. However, despite their enormous potential, there are several important challenges and issues that should be addressed. One of them is the obtaining of a complete picture of transitions and physico-chemical processes related to biopolymer structural features considering temperature and frequency as variables. A detailed understanding of the molecular mechanisms underlying these relaxation processes is quite difficult, owing to the biopolymers structural complexity and their temperature, moisture, and time dependence. It is a misconception to suggest that the test should be carried out only at the temperature and frequency they will be used in practice. For example, the use of biopolymers as food packaging material involves a wide range of thermal conditions during production, transport, storage, preparation, and consumption, e.g. pasteurization, sterilization, evaporation, cooking, and freezing. Therefore, studying the changes under all these thermal

conditions is necessary in checking that mechanical and barrier integrity is maintained for the safety of the consumer.

Moreover, the environmental moisture (generally unavoidable) should also been taken into account. A tiny amount of adsorbed moisture may dramatically change the mechanical properties of hydrogels. The location of bound water and the interactions of water–biopolymer encountered in hydrogels must be well determined and understood. Water induces structural changes that have a strong effect on the molecular mobility, very important in the case of tissue engineering and other biomedical applications.

3.3 Applications of Thermal Analysis in the Characterization of Biopolymers

This chapter summarizes the suitability of thermal analysis for understanding the changes with temperature and frequency of cellulose, chitosan, and pullulan systems aimed for various cutting-edge technological applications. The described examples include polymeric materials used in different fields and stretch from hydrogels used in biomedical applications to energy storage devices.

Temperature is an important tool in the characterization of hydrogels which should keep their structural integrity until they are released into the body, while frequency is essential in the case of articular cartilage regeneration daily submitted to solicitation during walking.

3.3.1 Characterization of the Thermal Stability of Biopolymers

Thermal stability is an essential parameter to be considered when determining the potential uses of biopolymers in various fields such as packaging and biomedical field. Thermal degradation can be quantitatively measured by TGA and usually involves two main stages. The first step involves water elimination because dried biopolymers almost always contain water (5%). The second degradation step accounts for the largest weight loss because it is associated with the breaking down of polymeric chains. For example, in the case of methyl cellulose, the second step in the TGA, corresponding to the structural degradation of the molecular chains, took place in the temperature range 332–395 °C. It was reported that when methyl cellulose was crosslinked with glutaraldehyde its thermal stability was the same [16]. Contrarily, plasticization with poly(ethylene glycol) (PEG) improved its thermal stability due to the compatibility PEG – methyl cellulose.

According to Lopez et al., degradation of chitosan took place in three steps [17]. Besides the two steps encountered in cellulose, a third step was observed in chitosan in the temperature range 387–471 °C. It corresponds to the residual crosslinking degradation of chitosan.

TGA was also used to monitor changes that occur during different modifications of chitosan. Relative to their potential use in orthopedic applications, Zapata et al. [18] studied the thermal stability of acrylic bone cements nanocomposites

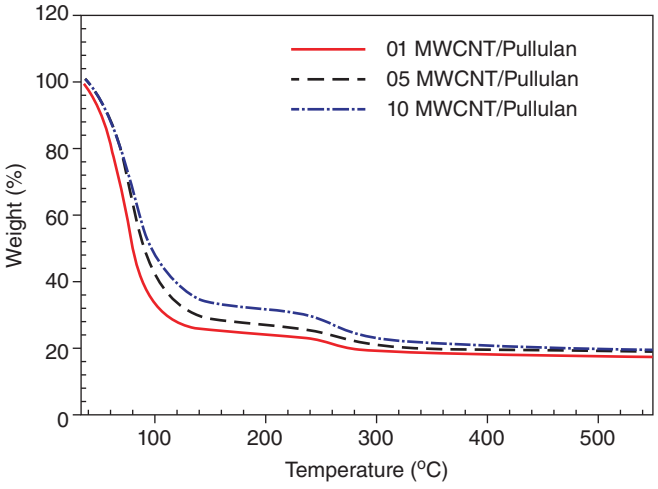

Figure 3.7 Thermogravimetric analysis of pullulan/MWCNT hydrogels. Source: Saeaeha et al. [20]/with permission of Elsevier.

modified with graphene oxide and chitosan. Although the separate introduction of graphene oxide or chitosan causes a decrease in thermal stability, a synergistic effect was observed by the simultaneous addition of both fillers. This can be the result of a homogeneous distribution of the graphene oxide and mechanical reinforcement due to hydrogen-bonding interaction between chitosan and graphene oxide.

Neto et al. [19] reported differences in thermal stability between chitosan crosslinked with glutaraldehyde or blended with poly(ethylene oxide) (PEO). PEO increases chitosan thermal stability, while the crosslinking process decreases it. This decrease in thermal stability can be assigned to a weakened crosslinked structure generated by the interference of intra-crosslinking reaction between chains with the hydrogen bonds. A lower thermal stability was observed in the case of pullulan hydrogels embedded with multiwalled carbon nanotubes (MWCNT) used as electroactive materials (Figure 3.7). The second step in weight loss attributed to pullulan decomposition appears in the range 238–250 °C [20]. A higher crosslinker concentration generates a denser network and reduces the chain mobility inside the hydrogel.

3.3.2 Characterization of the Glass Transition of Biopolymers

Compared with synthetic polymers, biopolymers like cellulose, chitosan, and pullulan are less understood in what concerns the structure–property relationship. The thermomechanical analysis raises some difficulties and leads to multiple interpretations, generated by the presence and superposition of different kind of relaxations, arising from crystallinity and strong intra and/or intermolecular hydrogen bonding. Moreover, due to their strong affinity for water, cellulose, chitosan, and pullulan may be easily hydrated. Hydration may either facilitate (plasticize) or hinder (antiplasticize) the molecular motions, relative to the nature or strength

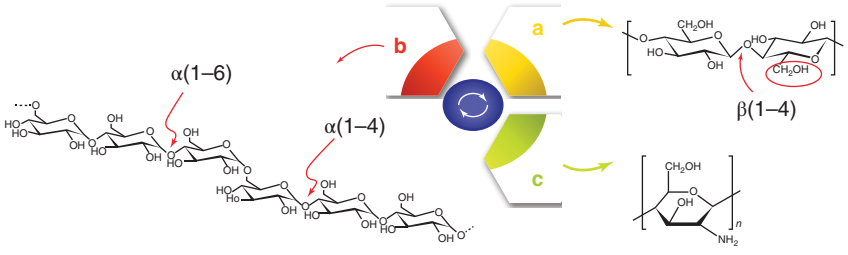

Figure 3.8 Chemical structure of (a) cellulose, (b) pullulan, (c) chitosan.

of water-chain segments interactions. Because of this, the glass transition of biopolymers is not an abrupt event, but rather a succession of processes having as a result pronounced changes in the mechanical, thermal, and dielectric properties.

Cellulose and pullulan have the same repeating anhydroglucose unit. Their chemical structure differs mainly by the position of the glycosidic linkage: cellulose – β(1–4) linkage (Figure 3.8a) and pullulan – α(1–4) and α(1–6) linkage (Figure 3.8b). For each repeating unit they have two hydroxyl side groups and one hydroxymethyl side group. The great number of hydroxyl groups favors the appearance of strong inter- and intramolecular hydrogen bonds; as a consequence, the glass transition temperature of cellulose and pullulan is achieved at high temperatures, usually above the thermal decomposition evidenced by TGA [21, 22].

Changes in the DMA properties as a function of temperature play an important role in evaluating their potential for applications. Simply performing a temperature scan experiment leaves open questions regarding the structural origin of relaxations revealed by DMA. One example in this case is represented by regenerated and stretched cellulose films used as potential packaging materials [23]. Fully swollen cellulose films stretched up to 30% in a DMA sample holder at room temperature were tested using DSC and DMA after being completely dried to prevent shrinkage. Two peaks (α_2 and α_1) evidenced in DMA were attributed to the motions of segments in amorphous regions of cellulose, both of them having the characteristics of a relaxation, but with different densities of inter/intramolecular hydrogen bonds.

DSC step scan method evidenced only one baseline shift due to its ability to distinguish between reversible and nonreversible heat flow. This α_1-relaxation, generated by the strong and dense network of intra/intermolecular hydrogen bonds, was attributed to the glass transition. The broad and weak α_2-relaxation that corresponds to the loose network of hydrogen bonds is not highlighted in the DSC curve. DSC is not a common tool to investigate the glass transition of cellulose taking into account the small variations in heat capacity [24, 25]. However, Szczesniak et al. [26] evaluated the glass transition of cellulose powder with smaller water content, both in heating and cooling runs. DSC cooling runs seemed to be more suitable for glass transition evaluation. The endothermal peak associated with water loss is still present in the second or third DSC heating run, diminished in amplitude and shifted to higher temperature.

The use of pullulan as films and coatings in food applications is constrained by hydrated conditions during handling or storage. Lazaridou et al. studied

the plasticization effect of water/sorbitol on pullulan [27, 28]. The presence of α(1–6) linkage on the pullulan chain is responsible for the flexible conformation and ensures the amorphous character. A DMA experiment performed in single cantilever-bending mode evidenced a large drop in storage modulus E' and a peak in tan δ curve. Increased water content enhanced the molecular mobility, thus decreasing the glass transition temperature. Moreover, the reduction in the storage modulus on the rubbery plateau and the increase in E' drop evidenced a loosening of the hydrogen-bonding network. With increasing water content, polymer–polymer hydrogen bonds are replaced by the polymer–water, conferring higher freedom to polymer chain motion.

Although cellulose and chitosan (Figure 3.8) share the same β(1–4)-anhydroglucosic bond, their properties are different due to the presence of amino functional groups in chitosan besides the hydroxyl ones. Some authors show no evidence of chitosan glass transition by DSC, DMA, DEA, while others report a wide variety of values; this discrepancy between the glass transition temperatures may be related to differences in crystallinity, molecular weight, or degree of deacetylation. It is known that chitosan is highly hydrophilic. The polar functional groups present in the chitosan structure (hydroxyl and amino group) are able to form hydrogen bonds with water molecules. The presence of even small amounts of water results in structural changes of chitosan with strong effects on their molecular mobility, especially in the glass transition region. Water can act as a plasticizer, lowering and broadening the glass transition range or may overlap and distorts the T_g, thus impeding its evaluation.

DMA studies performed by *Lazaridou* and *Biliaderis* in single cantilever-bending mode [29] found T_g of chitosan films ranging from −23 to 67 °C for moisture content between 9% and 20%. The glass transition evidenced by a large drop in storage modulus and a broad peak on tan δ curve was shifted to lower temperature with increase of water content, indicating its plasticizing effect. The correct assigning of this peak to α-relaxation was confirmed by the value of activation energy and its sensitivity to frequency (tan δ peak shifts to higher temperature with increasing frequency) observed in the multifrequency experiment.

Baouche et al. observed for the dried sample of chitosan values of 102 °C measured by DSC and 122 °C according to DMA [30], depending on water content. Similar results of T_g values of about 150 °C were reported by Dong et al. [31] by means of four techniques: dynamic mechanical thermal analysis, DSC, thermally simulated current spectroscopy, and dilatometry. A physical aging treatment (100 °C, 8 hours) of chitosan demonstrates the ability of DSC to differentiate the enthalpic relaxation from the glass transition of chitosan. In the same time, Sakurai et al. [32] attributed another origin to the tan δ peak observed at 153 °C in the DMA first run in pure chitosan (Figure 3.9a). The two cycles of heating performed to eliminate the water content strengthen the idea that this peak is rather due to the molecular motions in a pseudo-stable state than to α-relaxation, since it disappears in the second run (Figure 3.9b).

The T_g appeared in this case in the second heating run around 203 °C as a small baseline step in DSC (Figure 3.10) and as a large shoulder on tan δ peak in DMA.

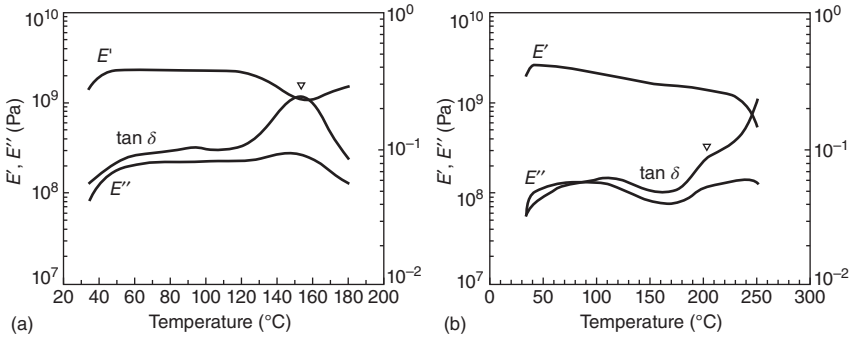

Figure 3.9 DMA of chitosan in the first (a) and second heating run (b). Source: Sakurai et al.[32]/with permission of Elsevier.

Figure 3.10 DSC of chitosan in the second heating run. Source: Sakurai et al. [32]/with permission of Elsevier.

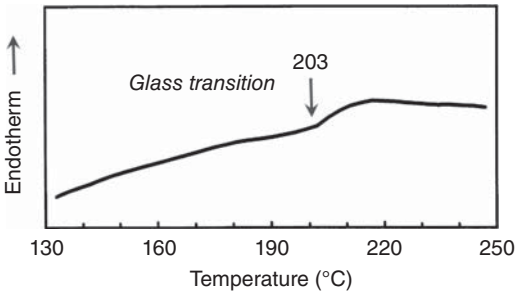

When T_g cannot be directly estimated, chitosan is blended with low molecular weight (plasticizer), which lowers the T_g. Khouri et al. [33] incorporated glycerol into a neutralized chitosan film using this heterogeneous method to observe the glass transition using DMA. Due to its high affinity for water, the dielectric spectra of chitosan are strongly affected by the high conductivity signal, which is ordinarily produced by the proton migration. Therefore, some authors presented only two relaxation-type processes, secondary β-relaxation and conductivity of charge carriers, with no mention about primary α-relaxation [34, 35]. However, Gonzalez-Campos et al. evidenced the presence of α-relaxation in the chitosan with minimum water content [36]. They collected the dielectric spectra of wet (normal ambient conditions) and dry (annealed for 24 hours, at 120 °C) chitosan samples. The α-relaxation was highlighted by subtraction of the dc conductivity signal and exclusion of the electrode polarization and interfacial polarization effects.

The processed dielectric loss was expressed as

$$\varepsilon'' = \varepsilon''_{\text{exp}} - \frac{\sigma_{\text{dc}}}{\omega \varepsilon_0} \tag{3.14}$$

where $\varepsilon''_{\text{exp}}$ is the experimental value of dielectric loss, σ_{dc} is the direct current conductivity, ω is the angular frequency, and ε_0 is the permittivity of free space. Following their assumption, after dc correction, both relaxations (the secondary β-relaxation at high frequencies and the primary α-relaxation at low frequencies) can be identified.

3.3.3 Characterization of the Secondary Relaxations in Biopolymers

The assignment of the low-temperature relaxations in biopolymers is discussed in a broader context, taking into account the role of hydrogen bonds and water. The combination of mechanical and dielectric analyses appears to be the most powerful tools for the study of molecular mobility occurring in glassy polymers having a high density of polar groups.

3.3.3.1 Secondary Relaxations in Cellulose

Amorphous cellulose exhibits in dynamic mechanical and dielectric spectra two relaxations (γ and β) below the glass transition temperature. Their magnitude and temperature vary with the water content or the origin of the cellulose [37, 38]. γ-relaxation is attributed to noncooperative movements of side groups (–CH_2OH and/or –OH) and appears around −120 °C. On the other hand, β-relaxation appears above −75 °C and is associated with the localized and cooperative motions of the cellulose chain segments. According to Montes et al. [39], DMA and DEA are not able to highlight the same relaxation processes in the case of dry cellulose. Two secondary relaxations can be observed in DMA compared to only one broad secondary relaxation in DEA. The absence of the dielectric β-relaxation may be related to its dependence on water content. At temperature close to room temperature Jafarpour et al. [40] observed a β_{wet}-dielectric relaxation and assigned it with rotation of polymer–water complexes developed at the polymer–water interface [41, 42]. This β_{wet}-relaxation signal could be eliminated from the dielectric spectra after an intense drying of the cellulose.

When the water content in cellulose exceeds 6%, only one broad relaxation peak can be observed [37]. This peak can be separated into two independent peaks after a thermal treatment (Figure 3.11). However, Cristea et al. [43] evidenced only one broad tan δ peak between −100 and −50 °C for regenerated cellulose subjected to thermal treatments in the DMA oven (Figure 3.12). In this case, the plasticizer/antiplasticizer role of water was discussed on account of the strong interchain network of hydrogen bonds between macromolecular chains of cellulose and water. After the first heating cycle, an increase in stiffness and a decrease of tan δ peak intensity were observed as the water that acts as a plasticizer was eliminated from the film. The next three heating stages turn out to be useless in terms of removing water. Most probably, water molecules are involved in a strong network of hydrogen bonds and their removal is not possible under the thermal conditions created in the DMA oven.

Zhao et al. investigated the interaction between water and regenerated cellulose backbone, highlighting the evolution of secondary dielectric relaxation behavior during isothermal dehydration of the material [42]. They observed two different drying stages in time during the drying process. The first stage is dominated by the ionic motions among the hydroxyl groups and the interfacial polarization. However, the secondary β_{wet}- and β-relaxations are detectable as shoulders with reduced intensity. This stage emphasizes the loss of free water from the regenerated cellulose backbone. The relaxation behavior in the second drying stage is a result

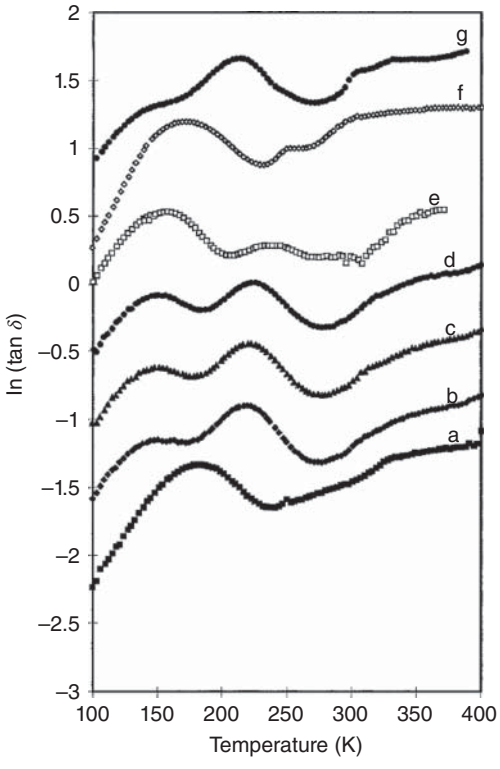

Figure 3.11 DMA data at 0.1 Hz for cellulose (a) before treatment; (b) before (a) +1 hour at 400 K; (c) before (b) +1 hour at 400 K; (d) before; (c) +1 hour at 400 K; (e) before (d) +24 hours at 400 K; (f) after (e) +humid atmosphere; (g) after (f) +1 hour at 400 K. Source: Montes et al. [37]/with permission of American Chemical Society.

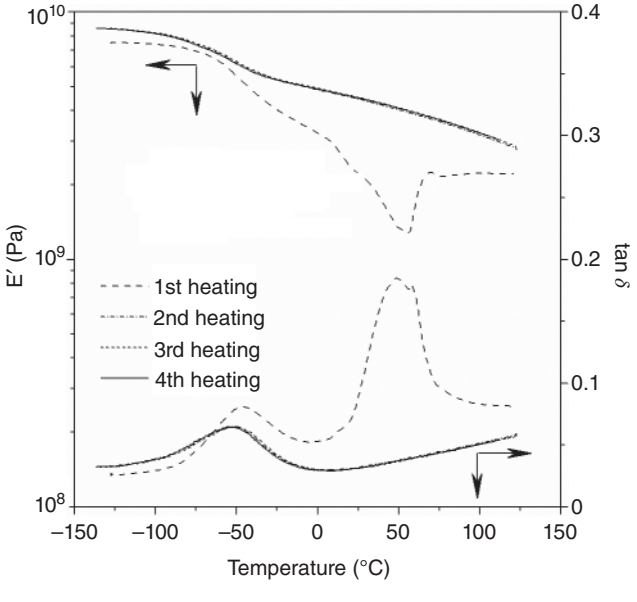

Figure 3.12 DMA data at 1 Hz for cellulose during consecutive heating steps.

of molecular dynamics. The β-relaxation of dried regenerated cellulose is observed in the 10^6–10^7 Hz frequency range and is similar to the typical dipolar relaxation of native cellulose of different origins [42, 44]. More interesting is the appearance of β_{wet}-relaxation as two well-separated relaxations. As temperature increases, the two relaxations approach one another and finally merge into a single integrated one. According to the authors, the unusual behavior of β_{wet}-relaxation suggests the development of a highly ordered phase arrangement of cellulose molecules toward the elimination of freezable loosely bound water from regenerated cellulose [45].

3.3.3.2 Secondary Relaxations in Chitosan

When it comes to the β-relaxation of chitosan, the presence of $-NH_2$ ionizable group should be taken into consideration. In chitosan blended with glycerol, Quijada Garrido et al. attributed the dynamic mechanical β-relaxation to the rotation or local motions of lateral groups of chitosan ($-NH_2$ or as NH_3^+ $^-OOC-CH_3$, $-CH_2OH$, and in some cases $-NH-OC-CH_3$), to hydrogen bonds between amine and alcoholic lateral groups of chitosan and glycerol alcoholic group [46]. Viciosa et al. reported the molecular motions in dry chitosan (annealed for 20 minutes at 150 °C) and wet chitosan (water content being around 13.5%), in order to highlight the influence of water on β-relaxation process [34]. Three relaxations processes were detected using dielectric spectroscopy: a β-relaxation, a β_{wet}-relaxation, and a σ conductivity process. The loss curves of dry chitosan highlight the β-relaxation as a well-defined symmetric dielectric peak. A broader asymmetric peak with a significant lower intensity was observed in the dielectric spectra of the wet chitosan, strongly influenced by conductivity induced by polar water molecules. The differences obtained between β-relaxation of wet and dry chitosan samples, in terms of their broadness and intensity, confirm that the β process is due not only to the glycoside linkage but also to the amine side group, especially its protonated state (NH_3^+/NH_2). The conductivity σ process related to migration of conductive species deviates to higher temperatures with drying.

3.3.3.3 Secondary Relaxations in Pullulan

Scandola et al. evidenced that the amount of water absorbed in pullulan influences dramatically the dielectric properties and the viscoelastic behavior of the polysaccharide [21]. When the pullulan polymer is hydrated, two regimes of hydration are identified: the regime of low water contents includes the molecular interactions of water molecules with pullulan via hydrogen bondings and the regime of high hydration degrees is characterized by water–water associations. The polymer–water relaxation is the only one emphasized in DMA and DEA at temperatures below room temperature.

Kishikawa et al. [47] investigated the molecular dynamics of pullulan in water-rich concentrations by dielectric spectroscopy technique in a broad range of frequencies (between 40 Hz and 50 GHz) and close to room temperature ($T = 25$ °C). The dielectric spectra of pullulan in water reveal the presence of two relaxation processes localized at high frequencies assigned to pullulan and water molecules, and contributions from electrode polarization and DC conductivity localized at low

frequencies. The relaxation specific to the primary process of water (h-process) is detected at frequencies around 10 GHz, while the dielectric relaxation characteristic to the local chain motions of pullulan (m-process) is found at 100 MHz. The purification of pullulan is repeatedly obtained, and the dielectric spectra were collected at each step of purification. It was found that the amount of impurities is considerably reduced by increasing the number of purification steps, enabling in this mode a clear identification of m-process. Furthermore, the dielectric behavior of pullulan (after triple purification) in water at different concentrations was investigated. As the concentration of pullulan increases, the relaxation strength of h-process is reduced, while the relaxation strength of m-process increases linearly. This observation confirms that m- and h-processes are activated by rotation of molecular dipoles of pullulan and water, respectively.

3.3.4 Characterization of Moisture from Hydrogels

Hydrogels are three-dimensional networks of polymer chains that could absorb and retain large amounts of water, but do not dissolve [48]. The ability to absorb water is induced by the hydrophilic functional groups attached to the polymeric backbone. The resistance to dissolution arises from the physical (ionic interactions, hydrogen bonds, and hydrophobic interactions) or chemical crosslinks between network chains. The type of crosslinking induces changes in hydrogel properties. Compared to chemically crosslinked hydrogels, physically crosslinked hydrogels are weaker and fragile. Properties such as biocompatibility and biodegradability recommend the use of hydrogels made from natural polymers (cellulose, chitosan, pullulan) for biomedical devices, drug delivery, and tissue engineering. The successful biomedical application is constrained by a proper characterization of the mechanical strength, being well known that hydrogels are very weak and cannot bear high deformation. The fact that hydrogels may absorb water up to thousands of times their dry weight makes the interpretation of their mechanical properties more difficult.

Three distinct types of water exist in hydrogels: free water, freezing loosely bound water, and non-freezable bound water [49, 50]. Free water does not imply any interaction with polymer chains. It can be removed by heating because it is only physically entrapped within the polymer network. Nonfreezable bound water interacts strongly with polymer chains by hydrogen bonds. It does not exhibit a phase transition within the normal temperature range associated with pure water. Freezing bound water interacts weakly with polymer chains. It freezes and melts at different temperatures with respect to that of free water.

Several thermal methods have been used to examine the dynamics and organization of water, but only few can differentiate them. DMA is by far the less used for water hydrogels characterization mainly from two reasons. The first one is due to the practical difficulty of testing. Although DMA can use various geometries, the parallel-plate compression clamp is the most suited [51, 52]. Due to the higher water content of hydrogels, clamping the cylindrically shaped samples is not always very easy. The thin water layer which appears at the interface geometry/hydrogel acts

as a lubricant. This behavior induces the sliding of the hydrogel between the plates upon application of force. Waterproof sandpaper is usually applied to the plates to overcome these difficulties.

The second reason is related to the DMA inability to differentiate between different types of water. However, in DMA, there is not always a clear evidence of water loss in terms of drop of storage modulus or as peaks in tan δ curve, its presence can be quantified as changes in the molecular mobility [53]. At the molecular level, water plasticization increases the intermolecular distances enhancing the segmental mobility. Meyvis et al. [54] tested hydrogels using two different measuring modes (controlled force and multistrain) and compared the results to those obtained using an oscillatory shear rheometer.

DSC sheds light on the interaction between water and hydrogel. When combining chitosan and cellulose in the same hydrogel, Barros et al. [50] differentiated by DSC two types of water. They assigned the two broad endothermic peaks from 50 to 95 °C and from 170 to 205 °C, to free water and freezing bound water, respectively. Their assumptions were confirmed by the disappearance of these two peaks in the second DSC scan. Moreover, Qiao et al. [55] evidenced using temperature-modulated DSC that the state of water in chitosan films is related to the water content. At low water content (up to 42%), there is no endothermic peak on DSC curve. There is only non-freezable water present in the chitosan which acts as a plasticizer. The enhancement in the chain mobility evidenced by a decrease of the glass transition temperature is due to gradually breaking of hydrogen bonds as water content grows. Above 47% water content, freezable water appears. Hoffman et al. [56] proposed a different method to quantify the quantity of water from a hydrogel. According to them, the bound water content can be calculated as a difference between total water content and the free water. The latter can be evaluated from the endotherm obtained in the heating step of a DSC experiment, considering that only free water may be frozen. It can be also calculated by using the crystallization peak characteristic observed in the cooling process [57].

3.3.5 Characterization of Electrical Conductivity

The development of fuel cells is of a main interest of our civilization since they convert the chemical potential energy into electrical energy. Thus, they have superior efficiency compared to combustion engines. Generally, the perfluoro-sulfonated ionomer membranes, including Nafion as representative example, are known as the most used polymer electrolyte membranes (PEMs), at relatively high humidity. They furnish high thermal stability and good proton conductivity achievements. However, the performances of these materials are limited at high temperatures (under water's boiling point) and low humidity [58].

Biopolymers like cellulose, chitosan, and pullulan are promising candidates among the low-cost PEMs. Particularly, the oxidized cellulose doped with heterocycles-type materials are attractive due to their high thermal stability, the boiling point of heterocycles being higher than that of water. In this way, the proton

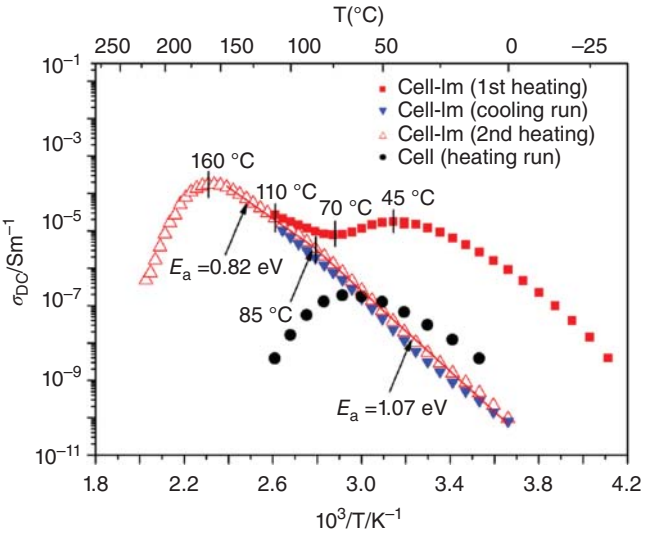

Figure 3.13 Temperature dependences of proton conductivity for pure cell, and cell doped with Im, during two heating cycles. Source: Smolarkiewicz et al.[59]/with permission of Elsevier.

conductivity of the natural membrane might furnish good proton conductivity performances at higher temperatures than Nafion.

Smolarkiewicz et al. have developed a proton-conducting membrane based on pure microcrystalline cellulose (Cell) as the host polymer, doped with imidazole (Im) [59]. The authors evaluated the proton conductivity of Cell-Im membrane during two heating cycles and the corresponding cooling runs. During the first heating cycle (full squares in Figure 3.13), the maximum proton conductivity is observed around 45 °C and is attributed to water molecules which are absorbed in the polymer backbone. After the first heating ends, around 110 °C, the Cell-Im membrane is considered dried since the retained water was eliminated by evaporation from the bulk sample. During the second heating (0–220 °C), the recorded conductivity is related to molecular dynamics of Im and Cell membrane components. The highest conductivity was recorded at 160 °C; after this temperature, the degradation of imidazole was reported. The second run evidenced three important aspects. Firstly, the maximum proton conductivity of Cell-Im membrane (recorded at 160 °C) is four times higher than that of pure Cell (recorded at 70 °C). Secondly, the operation temperature of the Cell-Im membrane (0÷160 °C) is significantly increased, as compared with that of pure Cell (0–70 °C). Finally, considering the region of continuous increase of conductivity toward the temperature, the activation energy was evaluated and the transport mechanism as well. It was suggested that the conductivity of electrical charges is assigned to the movements of protons from protonated to nonprotonated Im molecules, along the hydrogen-bonding network.

Chitosan-based membranes are employed as low-cost electrolyte for production of fuel cell devices. The conductivity of pure chitosan-based membranes and

modified chitosan membranes was previously measured [60–63]. For example, Wan et al. reported in 2006, the ionic conductivity of chitosan membranes filled with potassium hydroxide as ionic functionality around 10^{-6} S/cm [60]. More recently, Mobarak et al. (2013) evaluated the conductivity of carboxymethyl chitosan used as a green polymer electrolyte. They concluded that the conductivity achieved by carboxymethyl chitosan (about 4×10^{-7} S/cm) increased with two orders of magnitude than that of simple chitosan (about 3×10^{-9} S/cm) [61]. On the other hand, the intrinsic protonic conductivity of maleic chitosan and proline chitosan was measured by Deng et al. revealing experimental values around 7×10^{-4} S/cm and 3×10^{-5} S/cm, respectively [62, 63].

The presence of amine groups in the chitosan chemical structure gives the possibility of physical and chemical modifications in order to increase the electrical conductivity [64–66]. In the case of the protonation of amide groups from chitosan by water, the conductivity is supported by migration of hydroxide ions through chitosan backbone via the Grotthus mechanism [67]. Cui et al. proposed an ionic crosslinking of chitosan employing sulfuric acid or tripolyphosphate [68]. They observed that when chitosan is protonated with acidic functional groups, the SO_4^{2-} anions fixed between NH_3^+ groups of the polymer chains could achieve the ionic crosslinking. In this way, the anions interact with the amine groups and furnish ionic bridges between the chitosan chains.

Kim et al. reported a novel material based on cyanoethyl pullulan crosslinked with polyacrylic acid designed for sodium ion batteries [69]. The polysaccharide backbone provides the mechanical toughness, while the cyanoethyl side chains of the pullulan favor the migration of sodium ions through the membrane matrix. The crosslinking of cyanoethyl pullulan with polyacrylic acid prevents the dissolution of the material in the electrolyte. Cyanoethyl pullulan can also be used for the development of composite-film-type capacitors. In this regard, Suematsu et al. investigated the dielectric properties of thin film nanocomposites of barium titanate and cyanoethyl pullulan obtained by sol–gel process [70]. The cyanoethyl pullulan was mixed with $BaTiO_3$ solution in order to obtain a nanocomposited ink. The dielectric constant of the spin-coated thin films was around 40 for 1 KHz frequency and presents a slight variation in a broad temperature range (20÷150 °C). The excellent thermal stability encourages the use of the nanocomposites as capacitors in a large temperature domain.

3.4 Conclusions

Thermo-mechanical and dielectric characterization of biopolymers is challenging due to the specific aspects encountered in this class of compounds. Some major factors should be considered for understanding the experimental results. First of all, the strong inter/intramolecular interactions (mainly by hydrogen bonding) make the compounds more rigid and stable than expected, and some thermal characteristics are hardly emphasized. Then, also as a consequence of the possibility to form hydrogen bonding, the water has a critical role on the behavior. After an intense

browsing of the work done in this direction, it seems that the study of the secondary relaxations prevails, unlike other classes of polymers, where the glass transition region is much more investigated. The interpretation of the peaks and various trends of curves should be done with care, by using the results of complementary techniques.

References

1 Turi, A. (1981). *Thermal Characterization of Polymeric Material*. Academic Press.
2 Wunderlich, B. (1997). *The Basis of Thermal Analysis in Thermal Characterization of Polymeric Materials* (ed. E.A. Turi), 206–472. San Diego: 2, Vol. I, Academic Press.
3 Gallagher, P.K. (1997). *Thermoanalytical instrumentation, techniques and methodology*. In: *Thermal Characterization of Polymeric Materials*, 2e, Vol. I (ed. E.A. Turi), 2–192. San Diego: Academic Press.
4 Gaisford, S. (2015). Evaluation of analytical instrumentation. Part XXV: Differential scanning calorimetry. *Anal. Methods* 7: 1240–1248.
5 Ferry, J.D. (1980). *Viscoelastic Properties of Polymers*. New York: Wiley.
6 Nielsen, L.E. (1974). *Mechanical Properties of Polymers and Composites*. New York: Dekker.
7 Menard, K.P. (2002). *Dynamic mechanical analysis*. In: *Encyclopedia of Polymer Science and Technology* (ed. H.F. Mark), 563–590. Wiley https://doi.org/10.1002/0471440264.pst102.
8 Cristea, M., Ionita, D., and Simionescu, B.C. (2010). A new insight in the dynamo-mechanical behavior of poly(ethylene terephthalate). *Eur. Polym. J.* 46: 2005–2012.
9 Asandulesa, M., Musteata, V.E., Bele, A. et al. (2018). Molecular dynamics of polysiloxane polar-nonpolar co-networks and blends studied by dielectric relaxation spectroscopy. *Polymer* 149: 73–84.
10 Schönhals, A. and Kremer, F. (2003). *Analysis of dielectric spectr*a. In: *Broadband Dielectric Spectroscopy* (ed. F. Kremer and A. Schönhals), 59–98. Berlin-Heidelberg: Springer.
11 Symonowicz, J., Morawski, M., Dusza, M. et al. (2018). Investigation of the light-soaking effect in organic solar cells using dielectric permittivity and electric modulus approaches. *Org. Electron.* 52: 32–41.
12 Chisca, S., Musteata, V.E., Sava, I., and Bruma, M. (2011). Dielectric behavior of some aromatic polyimide films. *Eur. Polym. J.* 47: 1186–1197.
13 Hamciuc, C., Hamciuc, E., Vlad-Bubulac, T. et al. (2016). Silica-containing polyetherimide hybrid films based on methyltriethoxysilane as precursor of inorganic network. *Polym. Test.* 52: 94–103.
14 Havriliak, S. and Negami, S. (1967). A complex plane representation of dielectric and mechanical relaxation processes in some polymers. *Polymer* 8: 161–210.
15 Elloumi, A.K., Miladi, I.A., Serghei, A. et al. (2018). Partially biosourced poly(1,2,3-triazolium)-based diblock copolymers derived from levulinic acid. *Macromolecules* 51: 5820–5830.

16 Park, J.S. and Ruckstein, E. (2001). Viscoelastic properties of plasticized methylcellulose and chemically crosslinked methylcellulose. *Carbohydr. Polym.* 46: 373–381.

17 Lopez, F.A., Merce, L.R., Alguacil, F.J., and Lopez Delgado, A. (2008). A kinetic study on the thermal behavior of chitosan. *J. Therm. Anal. Calorim.* 91: 633–639.

18 Valecia Zapata, M.E., Mina Hernandez, J.H., Grande Tovar, C.D. et al. (2019). Novel bioactive and antibacterial acrylic bone cement nanocomposites modified with graphene oxide and chitosan. *Int. J. Mol. Sci.* 20: 2938 (1–18).

19 Neto, C.G.T., Giacometti, J.A., Job, A.E. et al. (2005). Thermal analysis of chitosan based networks. *Carbohydr. Polym.* 62: 97–103.

20 Saeaeha, K., Thummarungsan, N., Paradee, N. et al. (2019). Soft and highly responsive multi-walled carbon nanotube/pullulan hydrogel composites as electroactive materials. *Eur. Polym. J.* 120: 109231.

21 Scandola, M., Ceccorulli, G., and M, Pizzoli. (1991). Molecular motions of polysaccharides in the solid state: dextran, pullulan and amylose. *Int. J. Biol. Macromol.* 13: 254–260.

22 Hatakeyama, H., Yoshida, T., and Hatakeyama, T. (2000). The efect of side chain association on thermal and viscoelastic properties. Cellulose acetate based polycaprolactones. *J. Therm. Anal. Calorim.* 59: 157–168.

23 Kim, J.W., Park, S., Harper, D.P., and Rials, T.G. (2013). Structure and thermomechanical properties of stretched cellulose films. *J. Appl. Polym. Sci.* 128: 181–187.

24 Duchemin, B.J.C., Staiger, M.P., and Newman, R.H. (2014). High-temperature viscoelastic relaxation in all-cellulose composites. *Macromol. Symp.* 340: 52–58.

25 Vittadini, E., Dickinson, L.C., and Chinachoti, P. (2001). ^{1}H and ^{2}H NMR mobility in cellulose. *Carbohydr. Polym.* 46: 49–57.

26 Szczesniak, L., Rachocki, A., and Tritt-Goc, J. (2008). Glass transition temperature and thermal decomposition of cellulose. *Cellulose* 15: 445–451.

27 Kristo, E. and Biliaderis, C.G. (2006). Water sorption and thermo-mechanical properties of water/sorbitol-plasticized composite biopolymer films: Caseinate–pullulan bilayers and blends. *Food Hydrocoll.* 20: 1057–1071.

28 Lazaridou, A., Biliaderis, C.G., and Kontogiorgos, V. (2003). Molecular weight effects on solution rheology of pullulan and mechanical properties of its films. *Carbohydr. Polym.* 52: 151–166.

29 Lazaridou, A. and Biliaderis, C.G. (2002). Thermophysical properties of chitosan, chitosan-starch, and chitosan-pullulan films near the glass transition. *Carbohydr. Polym.* 48: 179–190.

30 Mati-Baouche, N., De Baynast, H., Vial, C. et al. (2015). Physico-chemical, thermal, and mechanical approaches for the characterization of solubilized and solid state chitosans. *J. Appl. Polym. Sci.* 132: 41257.

31 Dong, Y., Ruan, Y., Wang, H. et al. (2004). Studies on glass transition temperature of chitosan with four techniques. *J. Appl. Polym. Sci.* 93: 1553–1558.

32 Sakurai, K., Maegawa, T., and Takahashi, T. (2000). Glass transition temperature of chitosan and miscibility of chitosan/poly(N-vinyl pyrrolidone) blends. *Polymer* 41: 7051–7056.

33 Khouri, J., Penlidis, A., and Moresoli, C. (2019). Heterogeneous method of chitosan film preparation: effect of multifunctional acid on film properties. *J. Appl. Polym. Sci.* 137: 48648.

34 Viciosa, M.T., Dionisio, M., Silva, R.M. et al. (2004). Molecular motions in chitosan studied by dielectric relaxation spectroscopy. *Biomacromolecules* 5: 2073–2078.

35 Pizzoli, M., Ceccorulli, G., and Scandola, M. (1991). Molecular motions of chitosan in the solid state. *Carbohydr. Res.* 222: 205–213.

36 Gonzalez-Campos, J.B., Prokhorov, E., Luna-Barcenas, G. et al. (2009). Dielectric relaxations of chitosan: the effect of water on the α-relaxation and the glass transition temperature. *J. Polym. Sci.: Part B: Polym. Phys.* 47: 2259–2271.

37 Montes, H., Mazeau, K., and Cavaille, J.Y. (1997). Secondary mechanical relaxations in amorphous cellulose. *Macromolecules* 30: 6977–6984.

38 De La Rosa, A., Heux, L., and Cavaille, J.Y. (2000). Secondary relaxations in poly(allyl-alcohol), PAA, and poly(vinyl alcohol) PVA Part I. Mechanical relaxations compared with mechanical behavior of cellulose and dextran in the presence of polar solvent. *Polymer* 41: 7547–7557.

39 Montes, H. and Cavaille, J.Y. (1999). Secondary dielectric relaxations in dried amorphous cellulose and dextran. *Polymer* 40: 2649–2657.

40 Jafarpour, G., Dantras, E., Boudet, A.M., and Lacabanne, C. (2007). Study of dielectric relaxations in cellulose by combined DDS and TSC. *J. Non-Cryst. Solids* 353: 4108–4115.

41 Einfeldt, J., Meissner, D., and Kwasniewki, A. (2000). Comparison of the molecular dynamics of celluloses and related polysaccharides in wet and dried states by means of dielectric spectroscopy. *Macromol. Chem. Phys.* 201: 1969–1975.

42 Einfeldt, J. and Kwasniewski, A. (2002). Characterization of different types of cellulose by dielectric spectroscopy. *Cellulose* 9: 225–238.

43 Cristea, M., Ionita, D., and Simionescu, B.C. (2008). Dynamic mechanical analysis on regenerated cellulose. *Rev. Chim.* 59: 1088–1091.

44 Zhao, H., Chen, Z., Du, X., and Chen, L. (2019). Contribution of different state of adsorbed water to the sub-T_g dynamics of cellulose. *Carbohydr. Polym.* 210: 322–331.

45 Zhao, H. and Z C.hen, X. Du. (2019). Evolution of dielectric behavior of regenerated cellulose film during isothermal dehydration monitored in real time via dielectric spectroscopy. *Polymers* 11: 1749.

46 Quijada-Garrido, I., Iglesias-Gonzalez, V., Mazon-Arechederra, J.M., and Barrales-Rienda, J.M. (2007). The role played by the interactions of small molecules with chitosan and their transition temperatures. Glass-forming liquids: 1,2,3-propantriol (glycerol). *Carbohydr. Polym.* 68: 173–186.

47 Kishikawa, Y., Seki, Y., Shingai, K. et al. (2013). Dielectric relaxation for studying molecular dynamics of pullulan in water. *J. Phys. Chem. B* 117: 9034–9041.

48 Ghorbani, S., Eyni, H., Razavi Bazaz, S. et al. (2018). Hydrogels based on cellulose and its derivatives: applications, synthesis, and characteristics. *Polym. Sci. Ser. A+* 60: 707–722.

49 Wang, F., Zhang, R., Chen, T., and Sun, P. (2016). H-Solid NMR analysis of the dynamics and organization of water in hydrated chitosan. *Polymers* 8: 149, 1–111.

50 Barros, S.C., Alves da Silva, A., Barbosa Costa, D. et al. (2015). Thermal–mechanical behaviour of chitosan–cellulose derivative thermoreversible hydrogel films. *Cellulose* 22: 1911–1929.

51 Nath, J., Chowdhury, A., and Kumar Dolui, S. (2018). Chitosan/graphene oxide-based multifunctional pH-responsive hydrogel with significant mechanical strength, self-healing property, and shape memory effect. *Adv. Polym. Technol.* 37: 3665–3679.

52 Li, X., Xue, W., Liu, Y. et al. (2016). HLC/pullulan and pullulan hydrogels: their microstructure, engineering process and biocompatibility. *Mater. Sci. Eng. C* 58: 1046–1057.

53 Anseth, K.S., Bowman, C.N., and Brannon-Peppas, L. (1996). Mechanical properties of hydrogels and their experimental determination. Review. *Biomaterials* 17: 1647–1657.

54 Meyvis, T.K.L., Stubbe, B.G., Van Steenbergen, M.J. et al. (2002). A comparison between the use of dynamic mechanical analysis and oscillatory shear rheometry for the characterisation of hydrogels. *Int. J. Pharm.* 244: 163–168.

55 Qiao, C., Ma, X., Zhang, J., and Yao, J. (2019). Effect of hydration on water state, glass transition dynamics and crystalline structure in chitosan films. *Carbohydr. Polym.* 206: 602–608.

56 Hoffman, A.S. (2002). Hydrogels for biomedical applications. *Adv. Drug Deliver. Rev.* 43: 3–12.

57 Yoshida, H., Hatakeyama, T., and Hatakeyama, H. (1992). Characterization of water in polysaccharide hydrogels by DSC. *J. Therm. Anal.* 40: 483–489.

58 Ressam, I., Krins, N., Laberty-Robert, C. et al. (2017). Sulfonic acid functionalized chitosan as a sustainable component for proton conductivity management in PEMs. *ChemistrySelect* 2: 2503–2511.

59 Smolarkiewicz, I., Rachocki, A., Pogorzelec-Glasser, K. et al. (2015). Proton-conducting microcrystalline cellulose doped with imidazole. Thermal and electrical properties. *Electrochim. Acta* 155: 38–44.

60 Wan, Y., Creber, K.A.M., Peppley, B., and Bui, V.T. (2006). Chitosan-based electrolyte composite membranes II. Mechanical properties and ionic conductivity. *J. Membrane Sci.* 284: 331–338.

61 Mobarak, N.N., Ahmad, A., Abdullah, M.P. et al. (2013). Conductivity enhancement via chemical modification of chitosan based green polymer electrolyte. *Electrochim. Acta* 92: 161–167.

62 Deng, Y., Josberger, E., Jin, J. et al. (2013). H^+-type and OH^--type biological protonic semiconductors and complementary devices. *Scientific Reports* 3: 2481.

63 Deng, Y., Helms, B.A., and Rolandi, M. (2015). Synthesis of pyridine chitosan and its protonic conductivity. *J. Polym. Sci., Part A: Polym. Chem.* 53: 211–214.

64 Wan, Y., Creber, K.A.M., Peppley, B., and Bui, V.T. (2003). Ionic conductivity of chitosan membranes. *Polymer* 44: 1057–1065.

65 Fischer, S.A., Dunlap, B.I., and Gunlycke, D. (2017). Proton transport through hydrated chitosan-based polymer membranes under electric fields. *J. Polym. Sci. Part B: Polym. Phys.* 55: 1103–1109.

66 Lupatini, K.N., Schaffer, J.V., Machado, B. et al. (2018). *J. Polym. Environ.* 26: 2964–2972.

67 Wang, J., Bai, H., Zhang, H. et al. (2015). Anhydrous proton exchange membrane of sulfonated poly(ether ether ketone) enabled by polydopamine-modified silica nanoparticles. *Electrochim. Acta* 152: 443–455.

68 Cui, Z., Xiang, Y., Si, J. et al. (2008). Ionic interactions between sulfuric acid and chitosan membranes. *Carbohydr. Polym.* 73: 111–116.

69 Kim, D., Hwang, C., Jeong, J. et al. (2019). A bipolymer-crosslinked binder to improve the reversibility and kinetics of sodiation and desodiation of antimony for sodium ion batteries. *ACS Appl. Mater. Inter.* 11: 43039–43045.

70 Suematsu, K., Arimura, M., Uchiyama, N. et al. (2016). High-performance dielectric thin film nanocomposites of barium titanate and cyanoethyl pullulan: controlling the barium titanate nanoparticle size using a sol–gel method. *RSC Adv.* 6: 20807–20813.

4

Methods for Characterization of Surface Charge and Solid–Liquid Interaction Studies of Biomaterials

Matej Bračič[1], Lidija F. Zemljič[1], Olivija Plohl[1], and Thomas Luxbacher[2]

[1] University of Maribor, Laboratory for Characterization and Processing of Polymers (LCPP), Faculty of Mechanical Engineering, Smetanova ulica 17, 2000 Maribor, Slovenia
[2] Anton Paar GmbH, Particle Characterization & Surface Charge, Anton-Paar-Straße 20, 8010 Graz, Austria

4.1 Introduction

The surface charge of biomaterials is a crucial parameter when interacting with their environment, whether it is interacting with solid surfaces, liquids, or even gases. When we speak of surface charge, we are talking about the functional groups of biomaterials that can either get ionized under certain environmental stimuli or are permanently ionized. These functional groups define the way a biomaterial interacts with its biological environment, whether it is attachment on solid surfaces, initiation of bioreactions and biological cascades, killing of microorganisms, interruption of cell metabolism, etc. It should be clarified firstly that in this chapter biomaterials are defined in consistence with the definition used throughout the book as biological or synthetic substances that can be introduced into body tissue as part of an implanted medical device or used to replace an organ, a bodily function, etc. The term solid–liquid interactions of biomaterials needs explanation as well. In this chapter, the solid–liquid interactions of biomaterials will refer to interactions on the interface between solid materials and liquids in the following instances (Figure 4.1):

1. Interactions of biomaterials in aqueous liquid phase with solid surfaces,
2. Interactions of biomaterials in solid phase with aqueous liquid phases, and
3. Interactions of biomaterials in solid phase with biomolecules in aqueous liquid phase, i.e. biological fluids.

Interactions of biomaterials in aqueous liquid phase with solid surfaces describe nano- and micro-particle dispersions of bioactive materials interacting with various solid surfaces. Here, the focus lies on biomaterials and their surface charge as part of the liquid phase, although some of the solid surfaces also fit the definition of a biomaterial. This is useful to understand attachment of bioactive materials from liquid phases on solid materials as coatings, which can be used for biomodification of implants. Interactions of biomaterials in solid phase with aqueous liquid phases describe solid biomaterials like metals, synthetic polymers, and glass, interacting

Functional Biomaterials: Design and Development for Biotechnology, Pharmacology, and Biomedicine, First Edition. Edited by Tamilselvan Mohan and Karin Stana Kleinschek.

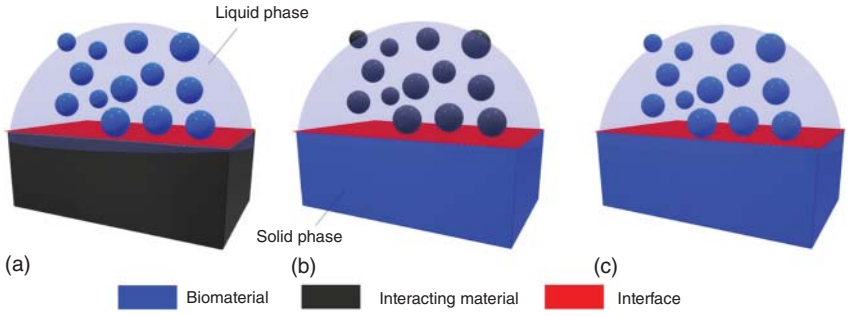

Figure 4.1 A graphical representation of the solid–liquid interactions of biomaterials discussed in this chapter. (a) Biomaterials in liquid phase. (b) Biomaterials in solid phase. (c) Biomaterials in solid and liquid phases

with aqueous liquid phases which are predominantly not defined as biomaterials, like electrolyte and acid–base solutions. Here the focus lies on the biomaterials and their surface charge as part of the solid material. This is useful to understand the interactions of potentially implantable biomaterials with various liquids to predict their behavior in contact with biological fluids. Interactions of biomaterials in solid phase with biomolecules in aqueous liquid phase describe interactions of solid biomaterials with biomolecules in the liquid phase. Here the focus lies on interactions of solid biomaterials with specific biomolecules in liquid phase mimicking the biological processes of the body. This is useful to understand how to design advanced bioactive materials that are able to interact with specific biomolecules and thus provide deep insights in the biological responses upon contact.

The influence of surface charge on these interactions will be revealed through the analytical eyes of electrochemical methods, namely ζ-potential and potentiometric titrations, and methods describing solid–liquid interactions on interfaces, namely quartz crystal microbalance (QCM) and surface plasmon resonance (SPR). The chapter will be concluded by a closer look into the electrokinetic analyzer, an alternative method for description of solid–liquid interactions based on a traditional electrochemical method, the ζ-potential.

4.2 Surface Charge Characterization of Biomaterials

4.2.1 Potentiometric Titration

Most of the biopolymer itself or integrated in different materials ionizes and thus shows a charging behavior that is quite often responsible for its properties that causes a bioactive reaction such as hydrophilicity, antimicrobial activity, antioxidant, and antithrombogenic activities, as well as ionic exchange capacity and adsorption capacity. It is therefore extremely important to determine both the amount of charge and the acidic/base strength as pK_a /pK_b values. Mainly, functional groups that are on biopolymers chains and ionized are carboxyl, amino,

sulfated, and hydroxyl groups [1]. Of these, however, only the carboxyl groups are ionized in neutral or weak acidic conditions, whereas for ionization of hydroxyl groups, the presence of strong alkali is needed [2]. Modifications may also introduce stronger acidic groups (e.g. sulfonated fibers), which are ionized at lower pH than carboxylic groups [3]. Amino groups are protonated in acidic environment [4]. Especially, a big challenge is to determine the amount and strength of ionizable groups for functional materials or functional fibers that are much more complex as biopolymers alone. The charge density is thus defined as the amount of electric charge per mass unit and provides a quantitative measure of the charged groups along the molecular backbone of a biomacromolecule. These groups may be either positively charged (cationic) or negatively charged (anionic groups) [5]. In addition, the charge may be distinguished between the accessible surface and total acidic/base groups (surface and total charge) [6].

There are several methods for the determination of the charge density, among which electrophoretic and light-scattering techniques, colloidal titration, and pH titration are the most widely exploited. Also, adsorption techniques and spectroscopic methods may be used. The electrokinetic (zeta) potential produced by charged surface can be measured indirectly using microelectrophoresis, streaming current, or electro-osmosis techniques [7]. Titration techniques are widely used due to their simplicity, ease of execution, and good repeatability. Titration is an analytical technique, generally used in many applications in research and industrial chemistry. It involves measuring a solution with a known concentration of one chemical (titrant) to determine the concentration of another chemical (analyte) in a second solution. The chemical in the titrant reacts with the analytic material in a known manner. When the reaction of these chemicals/materials is complete, an excess of titrant is recognized as a specific end point that marks the end of the titration. The end point can be determined by various methods: pH indicators, redox indicators, potentiometry, conductometry, isothermal calorimetry, spectrophotometry, and amperometry. Therefore, different areas of titration are indicated as already pointed out earlier [5]. This chapter focuses on potentiometric, conductometric, and polyelectrolyte titrations that are mostly used for monitoring of biomacromolecules/materials charge. Short theoretical background will be followed by further review of our work on this topic.

Potentiometric titration, based on the measurement of pH changes, is a versatile technique with a wide range of applications. It is a well-established analytical method always effective for simple acid–base systems [8, 9]. For over 70 years, it has been applied to study macromolecules, whose early use was limited to the analysis of the behavior of proteins. At that time, the application for studying acid synthetic polymers was applied almost exclusively to poly(acrylic acid) and poly(methacrylic acid) [10]. Nowadays, it is still used to investigate the dissociation behavior of poly(acrylic acid), but has expanded to study poly(itaconic acid), copolymers of maleic acid with various olefins, styrene, and ionization amphiphilic diblock and triblock copolymers [11]. Moreover, the use of potentiometric titration for the characterization of native and modified soluble biopolymers was also highlighted [3, 12–14].

The soluble natural polymers include polynucleotides, polypeptides, and polysaccharides such as starch, cellulose, and chitosan. Due to increased interest in the use of polysaccharides for a wide range of practical applications, potentiometric titration has become a standard method to analyze specific properties of polyelectrolytes in this group. The technique has been widely used to determine the amylose content in the starch [15, 16], the degree of deacetylation of chitosan [17], and the degree of protonation of cellulose derivatives [18], hyaluronic acid (HA), carboxymethylcellulose [19, 20], among other applications. Special focus was also given on characterization of different materials functionalized by these biopolymers. The potentiometric titrations were very well established far away for characterization of proteins charge and its influence by conformation changes [21, 22]. The principle of pH-potentiometric titrations is based on measuring the potential difference between the indicator and the reference electrode of the galvanic cell. The change in potential of the cell during a titration process equals the change in potential of the indicator electrode E, since the potential of the reference electrode is constant for the whole titration process [2]. For example, the characterization of accessible amino groups in materials by means of pH-potentiometric titrations is based on neutralization of dissociated hydrogen ions with hydroxyl ions of a basic titrant [23]. Assuming that the activity coefficients of both above-mentioned ions are constant at certain ionic strength, one can express E for the suspension of a textile material containing amino groups in an electrolyte solution (analyte) with the Nernst equation as follows (Eq. (4.1)):

$$E = E_{\mathrm{H}}^{0} + k_{\mathrm{E}}\mathrm{pH} + E_{\mathrm{j}} = E_{\mathrm{H}}^{0} - k_{\mathrm{E}}\mathrm{pOH} + k_{\mathrm{E}}\mathrm{p}K_{\mathrm{w}} + E_{\mathrm{j}} = E_{\mathrm{OH}}^{0} - k_{\mathrm{E}}\mathrm{pOH} + E_{\mathrm{j}}. \tag{4.1}$$

where E_{H}^{0} is the standard potential, $\mathrm{pH} = -\log[\mathrm{H}^{+}]$, $\mathrm{pOH} = -\log[\mathrm{OH}^{-}]$, and K_{w} is the ionic product of water ($K_{\mathrm{w}} = [\mathrm{H}^{+}][\mathrm{OH}^{-}]$). E_{j} is the diffusion potential, which is mildly and linear dependent on $[\mathrm{H}^{+}]$ in $[\mathrm{OH}^{-}]$. $k_{\mathrm{E}} = RT\ln 10/F$ (=59.16 mV at 25 °C), where R is the gas constant, T is the temperature, and F is the Faraday constant. A typical pH-potentiometric curve for the analyte system (Figure 4.2a) is expressed as

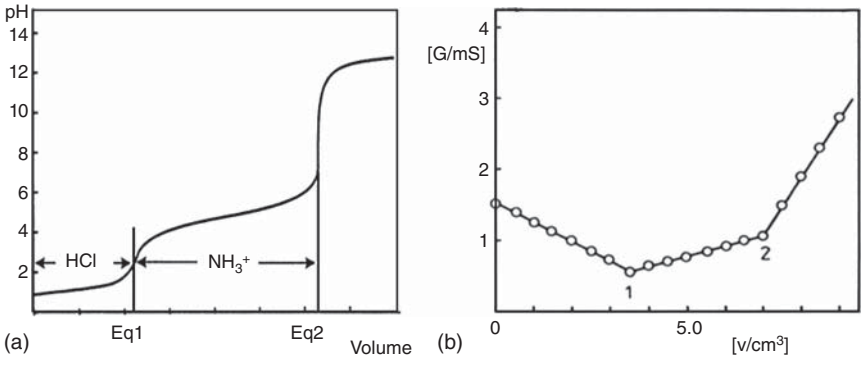

Figure 4.2 (a) pH-potentiometric and (b) conductometric titration curves for a mixed system consisting of a strong and weak acid titrated with a strong base, where Eq1 is the neutralization end point of the strong acid and Eq2 is the neutralization end point of the weak acid.

pH vs. volume of added titrant. Several methods and models may be of further use to create charging isotherms and to determine the pK values [2]. The conductometric titration [2] follows the same basic principles as the pH-potentiometric titration, the only difference being that one measures the conductivity of the analyte instead of pH. The conductivity of solution/dispersion/suspension is the sum of conductivities for all ions present in the analyte. The conductivity depends on several factors, including solute concentration, the degree of solute dissociation, the valence of the ion(s) present in the solution, temperature, and the mobility of the ions in the solution.

With the hydrogen and hydroxyl ions having much higher conductivity than the counter ions in the analyte, the effect of the counter ions can be neglected. Electrolyte solutions also follow the Ohm law as metal conductors do. Considering the length of the measuring cell and its cross-section surface, one can define the specific conductivity as given in Eq. (4.2):

$$\sigma = \frac{l}{\rho} = \frac{1}{RA}. \tag{4.2}$$

where σ is the specific conductivity, ρ is the specific resistance, l is the cell length, R is resistance, and A is the cells cross-section [4, 18]. A typical conductometric curve for the analyte system (Figure 4.2b) is expressed as conductivity (μS/cm) vs. volume of added titrant.

The analyte is usually prepared with an electrolyte solution of a certain ionic strength, which is needed in order to establish equilibrium between the ion concentration on the surface of the biopolymer solution/material dispersion or suspension and the ion concentration in the solution [2]. For example, quantitative determination of accessible amino groups in the analyte system by pH-potentiometric and conductometric titrations follows the same principles as the Broussignac method for the determination of accessible amino groups in chitosan solutions, first introduced in 1968. A known amount of strong acid (for example, hydrochloric acid) is added to the analyte, which is then titrated with a strong base (for example, sodium hydroxide). The amino groups act as proton acceptors in acidic media and therefore get positively charged (protonation process) [18], as shown in Eq. (4.3):

$$NH_2 + H^+Cl^- \rightarrow NH_3^+Cl^- \tag{4.3}$$

The titration process begins in the second phase where strong base is added to the analyte. All the species in the system that can dissociate, and proton will get neutralized by the base titrant successively according to their pK values. In the analyte system, the strong hydrochloric acid is neutralized first (Eq. (4.4)) due to its low pK value, then the protonated amino groups with higher pK values are neutralized (Eq. (4.5)). The volume of strong sodium hydroxide needed to neutralize all the hydrogen ions of a titratable species is referred to as the equivalent volume.

$$H^+Cl^- + Na^+OH^- \rightarrow Na^+Cl^- + H_2O \tag{4.4}$$

$$NH_3^+Cl^- + Na^+OH^- \rightarrow NH_2 + Na^+Cl^- + H_2O \tag{4.5}$$

Typical pH-potentiometric and conductometric curves for a mixed system of a strong acid (hydrochloric acid) and a weak acid (protonated amino groups) titrated

with a strong base (sodium hydroxide) are presented in Figure 4.2. One can observe two equivalent points in both curves corresponding to the neutralization end points of the strong and weak acid successively. The difference between both equivalent points corresponds to the volume of titrant needed for the neutralization of weak acids in the system.

Conductometric titration is a well-established analytical method for simple acid–base systems and has been successfully applied to analyze biological molecules for various purposes. In addition, conductometric measurements are routinely conducted in the pulp and paper industry [24, 25] to assess the mechanical performance of paper by absorption of additives onto the fiber surface, the deposition of colloidal materials, such as small cellulose fragments and filler particles; or when stoichiometric neutralization of anionic trash is required [5]. The potential usefulness of conductometric titration as a routine laboratory technique has been proposed in textbooks over 20 years ago [26]. A broad spectrum of practical applications and an easy-to-use conductometric titration method to quantify the charge density of biomacromolecule polyelectrolytes was pointed out.

Extremely interesting is also polyelectrolyte titration [2]. A long time ago, it was already concluded that polyelectrolyte titration offers an easy access to the determination of the surface charge of proteins and other biopolymers. The data further support the notion of the importance of electrostatic cooperative interactions in biological systems [27, 28], and this method is still very useful to easily determine the charge of biomolecules [29]. What is measured here is the capacity of the polymer solution to adsorb a polyelectrolyte of opposite net charge. However, in the interaction between charged molecules not only electrostatic interactions have effect, but also the nonionic interaction has an impact on the adsorption [30]. Penetration of the polyelectrolytes can occur through the reptation process or through simple diffusion till the saturation of the surfaces of the fiber wall. Polymers can come in interaction through Brownian motion or through turbulent transport [31]. However, in this case, the interaction itself can be observed as an ion exchange reaction; so the basic assumption is that there is 1 : 1 stoichiometric relationship between ionized groups on the surface neutralized by oppositely charged groups [32]. This can be only assumed for the polymers in the flat conformation, which can be applied for the polymers with the high charge density where the electrostatic interaction is not screened by a simple electrolyte in the solution and fully protonation is provided [6], which is quite often dependent on pH [2].

However, for the fibrous and polymer-based solid samples, the situation is a little bit different. Because of its established structure, it is hard to determine the charge of this type of sample. The amount of the adsorbed polyelectrolyte is determined with titrating the excess of the nonadsorbed polyelectrolyte with polyanion. Usually, the adsorption isotherms are created to be precise, i.e. the amount of the adsorbed polyelectrolyte on the fibers is depicted as a function of the equilibrium concentration of polyelectrolyte in solution when the plateau is reached, then with extrapolation of the plateau itself, i.e. to the point A in Figure 4.3 [2] the amount of the adsorbed polyelectrolyte is determined. Usually the surface charge is determined, but if the molecular weight of polymer as titrating

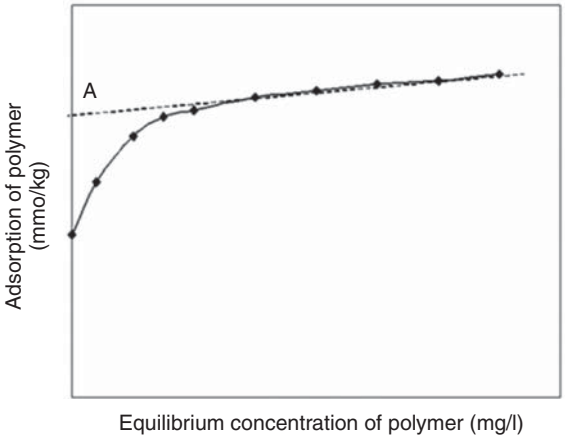

Figure 4.3 Adsorption of polyelectrolyte, as a function of equilibrium concentration of polyelectrolyte in solution. A is the amount of adsorbed polyelectrolyte used for calculation of the charge on the cellulosic fibers. Source: Adapted from Ueno et al. [23].

agent is low enough, as well the accessibility of the groups is great due to porous structure of material, with this method the total charge can be also assessed. Most commonly used titrants for polyelectrolyte titrations are potassium polyvinylsulfate (KPVS), polydiallyldimethylammonium chloride (poly-DADMAC), glycolchitosan, methylglycolchitosan, poly(diallyldimethylammonium) chloride (PDAC), poly-(sodium-polyethylene-sulfonate) (PES-Na), polybrene, and many others. In order to determine the endpoint of the titration, different approaches may be taken into account: visual indicators, turbidic methods, and electrochemical endpoint detection – conductometric titration [23].

It may be concluded that all these methods are very simple, fast, precise, and repeatable. However, for all titration methods the highly purified macromolecules and materials are required.

4.2.2 Zeta Potential

The zeta potential is a fundamental parameter of the solid–water interface and responsible for electrostatic interactions between the solid surface and solutes dissolved or dispersed in the aqueous phase. The zeta potential represents the charge density at the solid–water interface. It is a calculated parameter that requires the measurement of an electrokinetic effect, which arises from the relative movement of solid and aqueous phases [33]. For dispersions of particles with a size below 1 μm, the most common approach is the measurement of the electrophoretic mobility μ_e ($m^2/V/s$) by means of electrophoretic light scattering (ELS). For this purpose, an electric field is applied on a particle dispersion, which drives the charged particles to move toward the respective (oppositely charged) electrode (Figure 4.4a). The velocity of the particles v_p (m/s) is monitored by optical means, e.g. by the detection of light of a laser beam scattered by the nanoparticles. The electrophoretic mobility is then calculated according to Eq. (4.6) by relating the particle velocity to the driving force for particle movement, i.e. the applied electric field E (V/m),

$$\mu_e = \frac{v_p}{E} \tag{4.6}$$

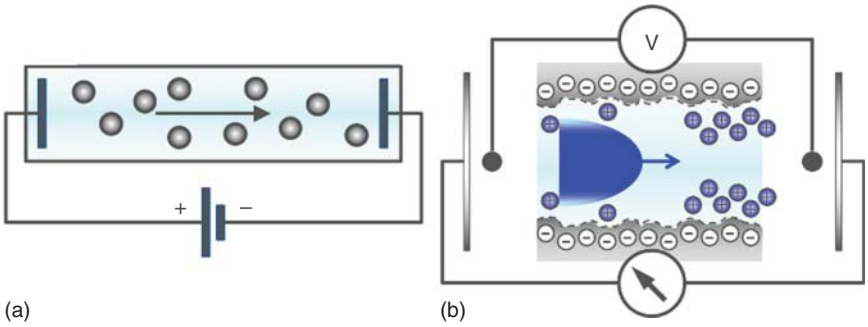

Figure 4.4 Schematic presentations of the principles of (a) electrophoretic mobility and (b) streaming potential measurements.

The zeta potential of dispersed particles ζ_p (V) is then calculated by Eq. (4.7) [34],

$$\zeta_p = \mu_e \frac{\eta}{\varepsilon_{rel}\varepsilon_0} \times f^{-1}(\kappa a_p) \tag{4.7}$$

η (Pas) and ε_{rel} are the dynamic viscosity and dielectric coefficient of the liquid, commonly represented by the corresponding parameters of the solvent, and $\varepsilon_0 = 8.854 \times 10^{-12}$ As/V/m is the vacuum permittivity. The correction term $f(\kappa a_p)$ in Eq. (4.7) is known as the Henry function and considers the ratio between the particle radius a_p (m) and the extension of the electric double layer (EDL) represented by the Debye length κ^{-1} (m; see later the model of the EDL), which is given by Eq. (4.8):

$$\kappa^{-1} = \sqrt{\frac{\varepsilon_{rel}\varepsilon_0 k_B T}{2N_A e^2 I}} \tag{4.8}$$

$k_B = 1.381$ J/K is the Boltzmann constant, T is the absolute temperature (K), $N_A = 6.022 \times 10^{23}$ mol^{-1} is Avogadro's constant, $e = 1.602 \times 10^{-19}$ C is the elementary charge, and I (mol/l) is the ionic strength, which is related to the concentration c_i (mol/l) of electrolyte ions with valency z_i by Eq. (4.9):

$$I = \frac{1}{2}\sum_i z_i^2 c_i \tag{4.9}$$

For spherical particles, the correction term $f(a_p\lambda_D^{-1})$ in Eq. (4.7) can assume values in the range between 2/3 and 1 [35], where $f(\kappa a_p) = 1$ is known as the Smoluchowski limit and applicable to large particles dispersed in a solution with high ionic strength ($a_p \gg \kappa^{-1}$). For $a_p \ll \kappa^{-1}$, $f(\kappa a_p) = 2/3$ and Eq. (4.7) turns into the Hückel approximation for the particle zeta potential calculation.

The measurement of the electrophoretic mobility is popular for the zeta potential analysis of nanoparticle dispersions or proteins but also for liquid–liquid emulsions. Alternatively, the zeta potential of particles in dispersion may be assessed by the application of the electroacoustic effects of the colloid vibration potential (CVP) [36], or colloid vibration current (CVI) [37], and of the electrosonic amplitude (ESA) [38]. CVP (CVI) and ESA require a significant difference in the material densities of the

suspended particle and the solvent. This requirement makes electroacoustic effects less applicable for the zeta potential characterization of particulate biomaterials.

The zeta potential of biomaterial samples that exceed the size range of micrometers cannot be detected by ELS but requires a different method, i.e. the measurement of streaming potential U_{str} (V) and streaming current I_{str} (A). Streaming potential (streaming current) arises from the flow of liquid through a capillary (Figure 4.4b). The driving force for liquid flow is either gravity or an applied pressure gradient between both ends of the capillary. The geometry of the capillary flow channel may be arbitrary but needs to be composed of the material specimen. Furthermore, the capillary flow channel may be of uniform shape, e.g. a rectangular slit channel formed between the surfaces of planar samples [39] or a cylindrical tube [40], or randomly arranged such as the voids between particles of a packed bed of powder [41]. The surface zeta potential is then calculated using the classical Helmholtz–Smoluchowski equations (4.10) and (4.11),

$$\zeta = \frac{\mathrm{d}U_{str}}{\Delta p} \times \frac{\eta}{\varepsilon_{rel} \times \varepsilon_0} \times \kappa_B \tag{4.10}$$

$$\zeta = \frac{\mathrm{d}I_{str}}{\Delta p} \times \frac{\eta}{\varepsilon_{rel} \times \varepsilon_0} \times \frac{L}{A} \tag{4.11}$$

from either streaming potential or streaming current measurements. The streaming potential coupling coefficient $\mathrm{d}U_{str}/\mathrm{d}\Delta p$ (V/Pa) is related to the electric conductivity κ_B (S/m) of the bulk aqueous test solutions, which represents its ionic strength, while the streaming current coupling coefficient $\mathrm{d}I_{str}/\mathrm{d}\Delta p$ (A/Pa) is compensated by the geometry of the flow channel with its length L (m) and cross-section A (m^2). Equation (4.11) makes it obvious that streaming current results can only be converted into the surface zeta potential if the geometry of the flow channel is well described, while the application of Eq. (4.10) is more universal. However, there may also be a restriction in the application of Eq. (4.10) for the calculation of the true zeta potential based on streaming potential measurements. For conductive materials, κ_B no longer represents the electric conductance within the capillary channel, and Eq. (4.10) gives an apparent zeta potential only, which is estimated too small in magnitude.

The beat signal accumulated during ELS, phase plot and distribution of calculated zeta potential, and the linear dependence of streaming potential on pressure difference are shown in Figure 4.5.

Although the measuring principles of the streaming potential (streaming current) and the electrophoretic mobility are completely different, the final zeta potential either at the solid–water interface or of dispersed particles has a common theoretical background. The origin of the zeta potential is founded by the nonequilibrated charge distribution at the solid–water interface, which differs from the distribution of ions (charges) in the bulk aqueous solution. The interfacial charge distribution is triggered by the formation of surface charge. Different mechanisms for surface charge formation are known and dependent on the solid material. Most commonly the interaction of surface functional groups with water described by acid–base reactions is assumed. This mechanism for surface charge formation requires the

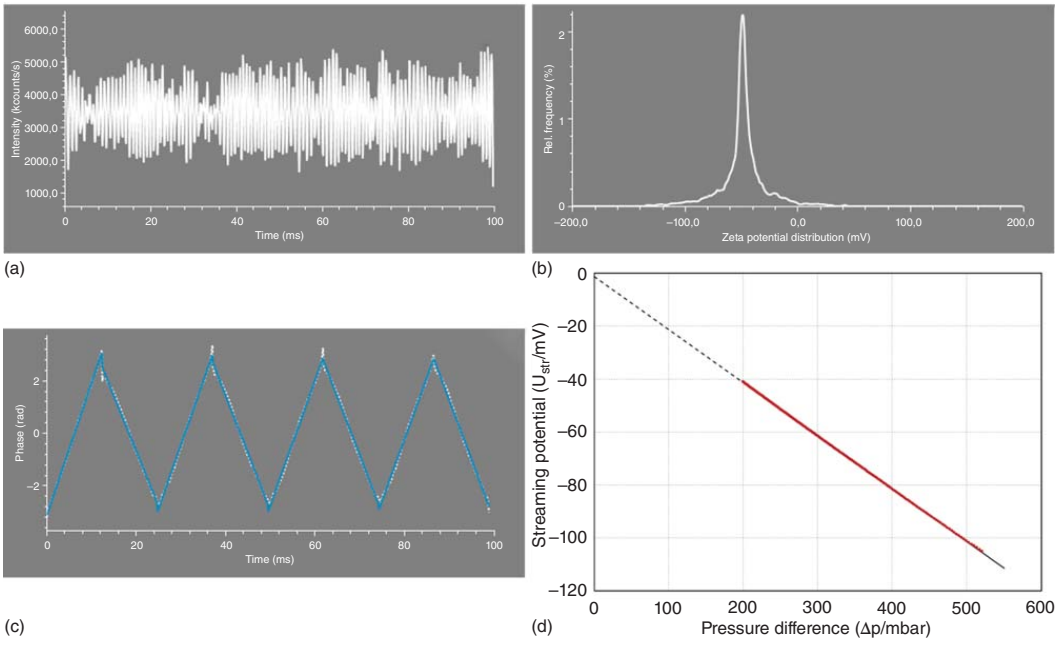

Figure 4.5 Beat signal accumulated during electrophoretic light scattering (a), phase plot (b), and distribution of calculated zeta potential (c). Linear dependence of streaming potential on pressure difference (d).

presence of such surface functional groups, which may behave acidic or basic thereby leading to a negatively or a positively charged surface, respectively. Since the equilibrium of acid–base reactions depends on the pH of the aqueous solution, the conclusion of acidic groups introducing negative surface charge (and basic groups introducing positive surface charge) assumes the condition of neutral pH.

An equally important mechanism for the formation of interfacial charge at otherwise uncharged surfaces such as pristine polymers is the adsorption of water ions (hydroxide, OH^-, and hydronium, H_3O^+). The lack of surface functional groups renders polymer surfaces hydrophobic and thus water repellent. The repulsion of neat water molecules promotes the adsorption of other solutes of the aqueous solution. It was proven that in the absence of complex solutes, interfacial charge at polymer–water interfaces is still present and thus explained by the adsorption of water ions [42]. The concentration of hydronium and hydroxide ions in the bulk aqueous solution determines the adsorption equilibrium of water ions at a pristine polymer–water interface, which makes the pH value again a crucial parameter that affects the sign and magnitude of interfacial charge. Interfacial charge formation has also to be considered as a dominant contribution to the charge at certain metal–water interfaces such as stainless steel or gold.

For minerals composed of inorganic salts with a sufficiently low solubility in water (e.g. calcite, $CaCO_3$), the partial dissolution of cations (Ca^{2+} for $CaCO_3$) and anions (CO_3^{2-} for $CaCO_3$) introduces charged defects in the crystalline lattice and thus surface charge. Unlike the acid–base reaction of surface functional groups or the adsorption of water ions at the polymer–water interface, the surface charge at such mineral–water interfaces is commonly less affected by the pH of the aqueous solution but more by the presence of other so-called potential-determining ions (e.g. Ca^{2+} and CO_3^{2-} in case of calcite).

Either surface or interfacial charges get immediately compensated by an accumulation of hydrated ions that are contained in the bulk aqueous solution. Surface and interfacial charge determine the nature of these counter ions, i.e. negatively charged surfaces attract most positive ions (cations), while positively charged surfaces require negative ions (anions) to establish electroneutral conditions within an extended interfacial region. The details of the charge distribution at the solid–water interface are described by the model of the EDL, which is schematically shown in Figure 4.6 for a negatively charged material surface. The EDL model suggests the occurrence of two distinct layers of water and hydrated ions, which is evidenced by the experimental determination of the zeta potential. At close proximity to the material surface the EDL model predicts a thin layer of tightly bound water. The ions contained in this stagnant or immobile water layer compensate part of the surface charge density (if the formation of surface charge is triggered by the protonation or dissociation of surface functional groups or by the partial dissolution of lattice ions at mineral surfaces) or introduce interfacial charge (for materials that lack of functional groups such as pristine polymers). Adjacent to the stagnant water layer, which is also referred to as the Stern layer, the EDL model suggests a diffuse or mobile layer of ions whose distribution still differs from the electroneutral condition in bulk water. The spatial extension of the diffuse layer toward the bulk

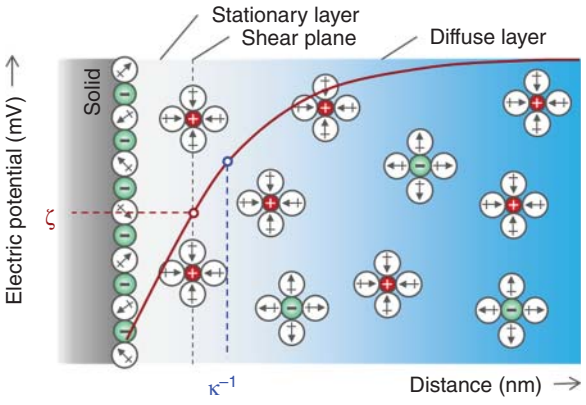

Figure 4.6 Electric double-layer model describing the charge distribution at the solid–water interface. The location of the zeta potential ζ at the plane of shear and the distance corresponding to the Debye length κ^{-1} is indicated.

aqueous solution is determined by the Debye length κ^{-1} according to Eq. (4.8), which indicates the dependence of this extension on the ionic strength (the ion concentration in the aqueous solution). The EDL model further relates the charge density σ_i (C/m^2) at various distances from the solid surface to the electric potential (difference) ψ_i (with reference to the electric potential $\psi_\infty = 0$ V in the bulk aqueous solution). For a monovalent salt (a 1 : 1 electrolyte such as NaCl or KCl), the relation between charge density and electric potential is given by Eq. (4.12) [43],

$$\sigma_i = \sqrt{8\varepsilon_{\mathrm{rel}}\varepsilon_0 cRT}\sin h\left(\frac{zF\psi_i}{2RT}\right) \tag{4.12}$$

$R = 8.314$ J/mol/K is the universal gas constant and $F = 96485$ C/mol is the Faraday constant. The charge density σ_0 located at the solid surface determines the surface potential ψ_0. However, neither the surface charge density nor the surface potential is easily accessible and requires that certain boundary conditions be fulfilled. The potentiometric titration method described in Section 4.2.1 offers access to the surface charge density but is restricted to materials that exhibit a large surface area and are readily dispersed in an aqueous solution, e.g. dispersions of particles or fibers. Scanning probe microscopy and Kelvin probe force microscopy [44], a derivative of atomic force microscopy, or the surface force apparatus [45], are approaches to assess the surface potential on the nanoscale.

At the shear plane between the stagnant and diffuse layers of the EDL at the solid–water interface, we find the electrokinetic or zeta potential ζ, which corresponds to the electrokinetic charge density σ_{ek}. Considering a solid surface with functional groups that introduce surface charge depending on the pH of the aqueous solution, the surface charge density is partially compensated at the location of the shear plane depending on the ionic strength of the aqueous solution, i.e. $|\sigma_{\mathrm{ek}}| < |\sigma_0|$. In case of a pristine polymer–water interface, the surface lacks functional groups and thus of true surface charge. However, the accumulation of water ions in the Stern layer introduces interfacial charge, which experiences again partial compensation within this stagnant layer. Nevertheless, here we find $|\sigma_{\mathrm{ek}}| > |\sigma_0|$. The zeta potential at the location of the shear plane is determined by the measurement of an electrokinetic effect (such as electrophoretic mobility and streaming potential mentioned

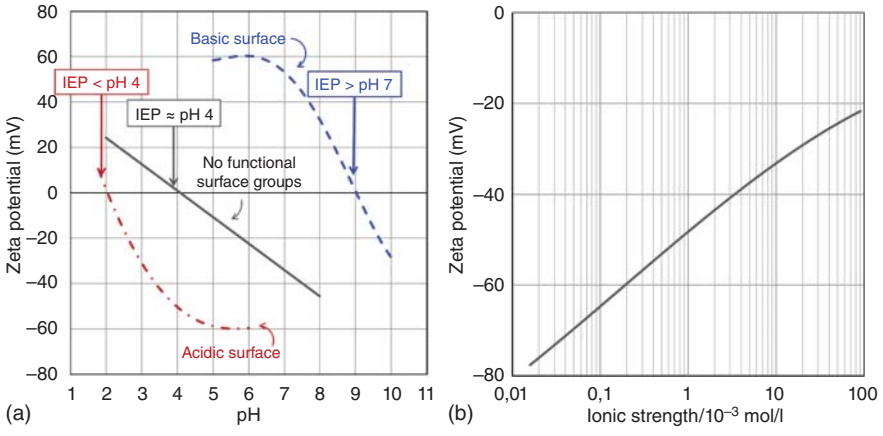

Figure 4.7 (a) Dependence of zeta potential on pH of an aqueous solution for surfaces with acidic and basis functional groups and surface without functional groups. The isoelectric points (IEP) are indicated. (b) Dependence of zeta potential on ionic strength of an aqueous solution at fixed pH.

earlier), which occurs by the relative movement of solid and liquid phases. An electric or mechanical force acts on either the solid or liquid thereby provoking the corresponding phase to move while the opposite phase remains stationary. The electrokinetic effect of the electrophoretic mobility arises when an electric field is applied to a particle dispersion and provokes the charged particles to move. The stagnant layer of the EDL moves together with the corresponding particles. The streaming potential (a DC voltage) is generated by the application of a pressure gradient on the liquid phase activating the liquid to travel through a capillary, which is composed of the solid surface. The electrokinetic response (particle movement or the streaming potential) is then related to the driving force (the electric field or the pressure gradient) to determine the electrokinetic effects of the electrophoretic mobility (Eq. (4.6)) or the streaming potential coupling coefficient $\mathrm{d}U_{\mathrm{str}}/\mathrm{d}\Delta p$ and furthermore the particle or surface zeta potential. The dependence of zeta potential on pH of an aqueous solution for surfaces with acidic and basis functional groups and surface without functional groups and the dependence of zeta potential on ionic strength of an aqueous solution at fixed pH are shown in Figure 4.7.

4.2.3 Application of the Zeta Potential for Biomaterial Characterization

4.2.3.1 Polyelectrolyte Multilayers

A prominent example for the application of the surface zeta potential is the characterization of polyelectrolyte multilayers (PEMs) prepared by the layer-by-layer technique [46]. Various technical and natural polycations and polyanions have been employed to create highly functionalized multilayer coatings on supportive biomaterial surfaces. Polysaccharides (chitosan, hyaluronic acid, and chondroitin sulfate), polypeptides (poly(lysine), poly(glutamic acid)), and proteinaceous coatings (collagen, keratin) represent natural polyelectrolytes, while poly(allylamine

hydrochloride), PAH, poly(ethylene imine), PEI, or poly(styrene sulfonate), PSS, serve as technical polycations and polyanions. The purpose of PEMs in biomaterial and biomedical applications is manifold. PEMs exhibit antiadhesive properties, provide a scaffold for drug-delivery systems, enhance the biocompatibility of the respective biomaterial surface, or supply the functionality for biosensing application.

Picart et al. [47] used a pool of surface-sensitive techniques to determine the evolution of adsorbed mass (QCM with dissipation monitoring), surface charge (streaming potential measurement), and morphology (atomic force microscopy) for a multilayer composed of poly(L-lysine) and hyaluronic acid with the subsequent number of polycation and polyanion layers. After the deposition of 10 bilayers, the surface zeta potential approached steady values of $\zeta = +50$ mV when poly(L-lysine) was the terminating polyelectrolyte, and $\zeta = -50$ mV with hyaluronic acid being the outermost layer. In a similar study, Richert et al. [48] investigated the effect of PEM formation pH on the surface zeta potential of a different combination of polycation and polyanion, i.e. poly(glutamic acid) and poly(L-lysine). In another paper, the same group extended the range of polyelectrolytes to include collagen [49]. Niepel et al. [50] moved from the qualification of growing polyelectrolyte multilayers with alternating polyanion- and polycation-terminal layers by individual zeta potential analyses to a detailed charge characterization of the effect of formation pH on poly(ethylene imine) and heparin multilayer coatings.

Grohmann et al. [51] combined the typical "saw tooth" curve of positive and negative zeta potential values for multilayers with alternating polycations and polyanions as the terminating layer with again a detailed analysis of the effect of different terminal polypeptides (poly(L-lysine), poly(L-glutamic acid)), and polysaccharides (chondroitin sulfate, heparin) of biomimetic PEM coatings (Figure 4.8).

Aggarwal et al. [52] combined the antibacterial cationic polysaccharide chitosan with derivatives of cellulose and heparin, respectively. The same groups of

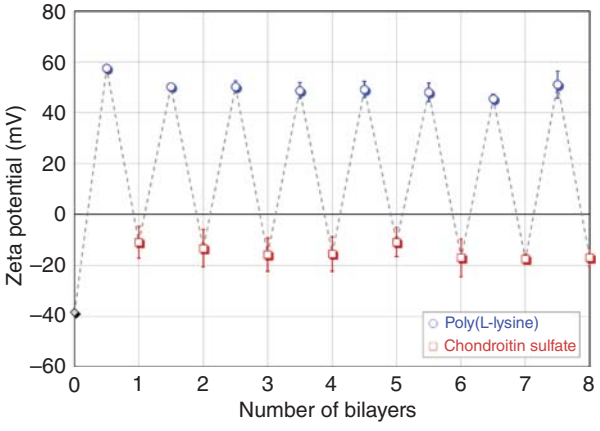

Figure 4.8 Monitoring the formation of a polypeptide–polysaccharide multilayer made of pol(L-lysine), PLL, and chondroitin sulfate, CS, with alternating PLL and CS as the terminal layer by the streaming potential method. Source: Adapted from Grohmann et al. [51].

researchers explored the pH responsiveness of polyelectrolyte multilayer films composed of another combination of cationic and anionic polysaccharides, i.e. chitosan and alginate [53]. Similarly, to macroscopic materials, for nanoparticles in dispersion, the change after coating the core particles with some biomaterial may entail a change in electrophoretic mobility, resulting in a different zeta potential. In this way, the core particles of polylactide latex (PLA) were covered with polypeptide chains. Since the zeta potential of the covered PLA particles was different from the core PLA, this was attributed to the presence of ionizable groups in the polypeptide chains. Indeed, the authors showed that the most effective factor determining the ZP was the number of amino groups at the end of the lysine side chain [54]. In another study, the ZP between two differently charged polymers, confirmed by the determination of their electrophoretic mobility, led to suggestions for model interactions between the polymers, i.e. succinylated calfskin collagen (SCSC) and nhu8-Py. PAA-Py was found to be negatively charged at pH 3, while SCSC exhibited a positive charge at the same pH, strongly suggesting that these two polymers interact at lower pH through electrostatic interactions. These results strongly contribute to the understanding of the interactions between dentin collagen and the polycarboxylate component of glass monomer cements used for dental cements [55]. The potential utility of single-walled carbon nanotubes (SWNTs) assembled layer by layer with the polyelectrolytes poly(L-lysine) and poly(L-glutamic acid) for antimicrobial biomaterials has been demonstrated [56]. Here, the electrophoretic mobility measurements were used for differently modified SWNTs. Polysaccharide multilayer nanocapsules were prepared by a layer-by-layer approach consisting of chitosan (CHI) and sodium alginate (ALG) on polystyrene (PS) nanoparticles as a template, followed by removal of the PS core and loading with a model drug to study the release properties of the formed polyelectrolyte capsule. Here ZP showed the stepwise and alternating adsorption of CHI and ALG layer films resulting in 5 bilayers of CHI/ANG shell wall [57].

4.2.3.2 Polysaccharides

The antimicrobial property of chitosan made this polysaccharide popular for the formation of polyelectrolyte multilayers but also of thin-film coatings on various substrates and as scaffolds and stand-alone films for tissue-engineering applications. Smirnova et al. [58] used chitin nanofibrils to reinforce chitosan films. The zeta potential and the electric conductance derived from a combined streaming potential and streaming current measurement revealed the different degree of film swelling. A similar approach was applied by Sandri et al. [59] for the characterization of blends of chitosan (CH) with anionic polysaccharides such as hyaluronic acid (HAc) and chondroitin sulfate (CS). The CH/HA and CH/CS complexes were embedded in the polysaccharide pullulan (PU), which dominated the isoelectric point. Even for the combination of PU solely with CH, the i.e.p. moved from pH 8–9 expected for chitosan [58] to pH 2.5–3.5.

Freudenberg et al. [60] used the streaming current measurement to assess the true zeta potential of a cellulose film. Cellulose is commonly available in the shape of particles (nanocellulose), natural fibers (cotton, viscose), or fabrics and introduces

challenges for the determination of the zeta potential due to its swelling propensity [61]. The formation of a thin-film coating is beneficial to exclude the effects of interfacial and material conductance, which interfere with the calculation of the zeta potential from streaming potential measurements. In their subsequent paper, Freudenberg et al. [62] extended the analysis of the cellulose–water interfacial to correlate electrokinetics with the swelling of the cellulose film.

The ZP in the case of polysaccharide-based solutions can be used as a useful tool to assess biopolymer interactions with a specific dispersion prior to casting to produce biobased edible films. Lower absolute ZP values (−10 to 10 mV) caused an extremely unstable dispersion/suspension, which consequently affects the physical properties of the derived edible films [63]. Hydrogels based on alginate and the naturally derived cationic biopolymer tanfloc were prepared and showed excellent properties to be used for medicinal purposes. The electrokinetic measurements of ZP as a function of pH of the polyelectrolyte complex based on alginate/tanfloc suspension showed the IEP at pH around 4 [64]. Nanosized Kraft lignin colloidal particles have attracted considerable attention as an advanced bionanomaterial for application in medicine. Mattinen et al. prepared lignin nanoparticles in the size of approximately 200 nm, which were enzymatically and chemically prepared from softwood Kraft lignin [65]. The ZP measurements demonstrated oxidation of the lignin nanoparticles through the formation of surface-oriented carboxylic acid groups, which resulted in a negative ZP. Moreover, enzymatic oxidation caused lower negative ZP values, which further improved the colloidal stability of lignin nanoparticles in aqueous media. Biocompatible scaffolds were prepared from natural polymers, i.e. chitosan (CHI) and gelatin (Gel), to be used for tissue-engineering applications. The ZP of dry and crushed corresponding cryogel in fine powder was measured by electrophoretic mobility in phosphate or acetate buffer. The surface of CHI-DDA prepared at different ratios and CHI-Gel-DDA (1 : 1 : 1) cryogels were slightly positively charged at physiological pH. The latter was explained by the presence of primary amino groups of the positively charged chitosan and unreacted aldehyde groups of DDA that are oxidized to the carboxyl group, leading to the formation of an amphoteric material [66]. Chitin nanocrystals (ChNCs) have been used as reinforcing nanofillers of polymer nanocomposite hydrogels, which offer great potential for various biomedical applications. ChNCs in two different crystal structures were used to reinforce nanomaterials of methylcellulose. The ZP of ChNCs suspensions was measured as a function of pH. Both α-ChNCs and β-ChNCs exhibited positive zeta potential values under acidic conditions, while the isoelectric point (IP) of α-ChNCs suspensions was pH 5.9 and that of β-ChNCs suspensions was pH 8.2 [67].

4.2.3.3 Electrospun Nanofibers

Electrospinning of polymer solutions into nanofibers and fiber meshes has proven to provide a fast and versatile technique for the preparation of biopolymer scaffolds. Subsequent surface modification of these fragile constructs introduces additional functionality, which seeks for a qualitative characterization. The frequently occurring irregular shape of the nonwoven films of electrospun polymer and biopolymer nanofibers and their sensitivity toward humidity exclude common techniques

such as water contact angle measurement to assess the nanofiber–water interfacial properties. Again, the surface zeta potential analysis was demonstrated successfully to characterize surface and interfacial properties of electrospun biopolymer nanofibers. Matsumoto et al. [68] were among the first to report the zeta potential of electrospun nanofibers of a biopolymer. They prepared scaffolds of chitosan nanofibers and compared the zeta potential derived from streaming potential and streaming current measurements to estimate the effects of scaffold porosity and chitosan nanofiber swelling.

Due to the fragile properties of electrospun polymer nanofibers, Asran et al. [69] used the zeta potential of casted films for a series of poly(vinyl alcohol) and poly(hydroxybutyrate) blends to explain the charging behavior of PVA/PHB nanofibers with same composition. Croisier et al. [70] attempted the zeta potential analysis directly on electrospun nanofibers of poly(caprolactone), PCL, and derivatives. They succeeded to distinguish various electrospun nanofiber blends by their average individual zeta potential. However, some of their results show significant error bars, which may arise from the complexity of highly porous, swelling, and fragile electrospun nanofiber nonwovens but also from the application of an indirect analysis of the surface zeta potential by the method of electro-osmotic flow mapping [71]. Metwally et al. [72] succeeded to obtain reliable zeta potential results for electrospun nanofibers of PCL using the streaming potential method and compared these results with the zeta potential of a rigid and nonporous PCL film.

Although electrophoretic mobility to assess the ZP of electrospun nanofibers is rare, there are some reports. A detailed study of the effect of surface charge on the bioactivity of modified collagen fibers was performed by Andrade et al. [73] using the ELS technique. The pH corresponding to the IEP of the collagen was about 10, while the chemically treated samples had an IEP of 6.8, indicating a partial coverage of the collagen surface by silica. The shift in IEP from 10 to 6.8 was sufficient to negatively charge the material surface upon contact with the SBF solution. This explains why treated collagen fibers exhibit bioactive behavior, while untreated fibers do not. In other study, pectin-based nanofibers were electrospun in the presence of the nonionic cross-linker oligochitosan. The fabricated nanofibers were also characterized by ZP measurements. Untreated pectin nanofibers were found to have a negative surface charge due to the polyanionic nature of the pectin polymer. In contrast, a positive charge was obtained when the pectin was cross-linked with oligochitosan due to free amino groups, and the latter was preferred for cell attachment for tissue-engineering applications [74]. Similarly, a more comprehensive study was conducted on electrospinning of gelatin fibers and its effect on ZP. The ZP values in the case of electrospun gelatin were higher than those of gelatin itself at the same concentration in the dispersion. Moreover, the ZP values of dispersions containing electrospun gelatin decreased as the applied voltage increased during electrospinning with larger fiber diameters, while lower applied voltage resulted in higher ZP values for dispersions containing electrospun gelatin nanofibers [75]. Recently, in another study, sacchachitin nanofibers (SCNFs) were prepared with TEMPO–oxidation and mechanical disintegration into a 3D gel structure to have the possibility of being an ideal scaffold [76]. The ZP of the obtained fibers was

calculated from the electrophoretic mobility using Henry's equation and Huckel approximation with $f(\mathrm{ka}) = 2/3$. The largest ZP of TEMPO-oxidized SCNF was measured to be −50 mV without adjusting the ionic strength.

4.2.3.4 Skin and Bone

Besides biomimetic surfaces of polypeptide and polysaccharide multilayers and scaffolds for tissue engineering the zeta potential analyses of biological material such as skin, bone, or cartilage is of interest. As early as 1994, Aguilella et al. [77] published their first attempt to assess the streaming potential coupling coefficient for human skin. A decade later, the same group employed the streaming potential method to investigate the interaction of skin with different drugs [78].

Collagen, one of the main constituents of bone and other tissue, was coated on knitted fabrics of poly(ethylene terephthalate) to enhance the polymer's biocompatibility for its application as a cardiovascular graft [79]. Like their work on grafted cellulose films mentioned in Section 4.2.3.2, Freudenberg et al. [62] employed the streaming current measurement to investigate the charging and swelling behavior of collagen and its specific interaction with divalent Ca^{2+} ions. Iviglia et al. [80] applied a thin-film coating of collagen to improve the acceptance of bone fillers made of hydroxyapatite (HAP) (Figure 4.9).

Courtenay et al. [81] surface modified cellulose scaffolds used for tissue engineering, and the surface zeta potential was measured using EOF approach using polystyrene latex beads as tracer particles. The measured surface zeta potential

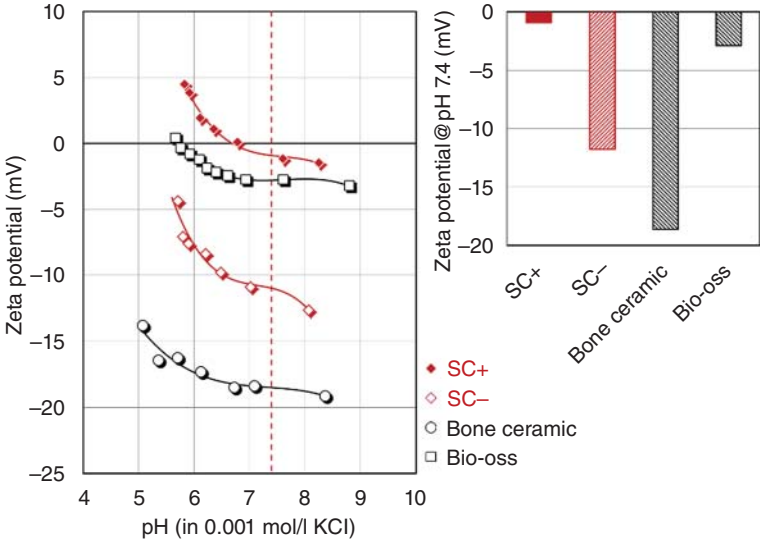

Figure 4.9 Comparison of the pH dependence of the zeta potential for a series of commercial bone fillers BoneCeramic® (Straumann USA LLC), Bio-Oss® (Geistlich Pharma AG), and Synergoss® (Nobil Bio Ricerche srl) with (SC+) and without collagen coating (SC−). The zeta potential at the physiological pH 7.4 indicated by the dashed line is shown in the separate chart. Source: Adapted from Iviglia et al. [80].

for unmodified cellulose films was -20 ± 4 mV; however, when derivatized with GTMAC, the surface zeta potential increased to 25 ± 9 mV due to the introduction of the positively charged trimethylammonium groups from GTMAC. Oxidized cellulose exhibited a negative value, as expected, but was not significantly different from underivatized cellulose.

In 1995, Kowalchuk et al. [82] used particle electrophoresis to investigate in situ potential changes in bovine cortical bone using calcium-deficient HAP, specifically the effects of changes in calcium, phosphate, and fluoride concentrations in Neuman's fluid (NF), which simulates the extracellular fluid of bone *in vivo*. ZP increased with increasing calcium concentration in NF, also an increase in phosphate concentration in NF resulted in increased ZP. The obtained results supported a structural model of the interface between bone matrix and bone fluid, which includes the actual bone surface, the stationary layer, and the extracellular bone fluid. These results indicated that the protein phase probably plays an important role in determining the physiological zeta potential. Biocomposites of natural rubber latex (NRL) coated with HAP were prepared, and their surface charge properties were monitored with electrophoresis by the technique of laser Doppler velocity in a wide pH range [83]. The presence of layers was demonstrated by monitoring the zeta potential, which changes from the negative to the positive direction when HA is on the outside and NRL (approximately -70 mV) is on the inside, and the ZP of NRL-HA nanoparticles at pH 7.4 exhibited the negative values (-40 mV). In another study, the ZP of HA and silver-incorporated Ag, gelatin polymer, and synthesized silver-incorporated HA polymer composite were determined individually at different pH values along with their IEPs. The significant decrease in the IEP of the silver ion-incorporated HA confirmed the presence of silver ions on the surface of HA. Therefore, it was suggested that the measurement of the IEP of metal ion-incorporated HA is a versatile tool to detect the presence of the surface silver ions. In contrast, the IEP of gelatin showed no significant change compared to the composites, indicating the strong binding of gelatin with the silver-incorporated HA [84]. Moreira et al. [85] reported *in situ* formed composite hydrogel based on chitosan and gelatin biopolymer combined with bioactive glass nanoparticles. The measured ZP at 37 °C ranged from $+3.1 \pm 1.4$ mV to $+6.9 \pm 3.2$ mV, demonstrating the cationic nature of these hydrogels, which can interact with negatively charged molecules from the native extracellular matrix and implying that the network formation of the corresponding hydrogels may have occurred through molecular interactions.

The potential application of biodegradable colloidal gels of PLGA-chitosan/PLGA-alginate nanoparticle blends was demonstrated in tissue engineering. PLGA-chitosan nanoparticles exhibited a ZP of $+18.8 \pm 3.2$ mV, and PLGA-alginate nanoparticles had a ZP of -23.4 ± 1.2 mV [86]. The promising properties of cold-adapted methacrylamide gelatin (GelMA) developed from salmon skin were demonstrated in tissue regeneration. The IEP of salmon GelMA solution determined by ZP measurements was ~5.5. Importantly, at physiological pH 7.4, the ZP, which correlates with surface charge, was in the range of -1.3 to -5 mV for modified salmon gelatin, depending on the degree of functionalization [87].

4.2.3.5 Biosensors

Thin-film biopolymer coatings on rigid supports are frequently used as the crucial component of biosensors. The sensitivity of the streaming potential method to the outermost material surface helps to tune the functional groups and surface charge of these coatings. Lin et al. [88] have deposited self-assembled monolayers (SAMs) of thiols with different terminal groups (COOH, NH_2) on gold surfaces (Figure 4.10). They used the isoelectric point to correlate the composition of the SAMs with the mixture of thiols in the bulk solution. Schrems et al. [89] used the capability of the S-layer protein SbpA [90] to self-assemble on a gold surface. They were among the first researchers who determined the zeta potential on QCM-D sensor disks to complement mass adsorption with surface charge information. Katzur et al. [91] investigated surface coatings with similar complexity but used highly functionalized dendrimers for biorecognition. Hao et al. [92, 93] again used homogeneous SAMs of thiols on gold surfaces to investigate the response of mesenchymal stem cells toward these surfaces.

Multifunctional hybrid biomaterials based on SiO_2/lignin have been prepared, which are expected to have a wide range of applications, including as electrochemical sensors. Measurement of ZP values by ELS allowed indirect evaluation of stability for the hybrid systems studied, and the measured ZP indirectly confirmed the effectiveness of the proposed method for synthesis of SiO_2/lignin hybrid materials. The IEP of Kraft lignin was 1, while the ZP assumed negative values over the whole pH range considered, which was attributed to the presence of OH^- groups. In fact, the presence of lignin in silica/lignin hybrids resulted in a decreased value of the ZP and consequently in a decrease of the surface charge compared to that of the silica modified with amino-silane. Moreover, the IEP of the hybrid materials decreases with increasing lignin content [94].

4.2.3.6 Lipids

Lipids and lipid bilayer membranes (LBMs) belong to another category of biomolecules with relevance for coatings of biomaterials, biosensors, and biomedical devices. The limited stability of LBMs makes it challenging to determine the surface

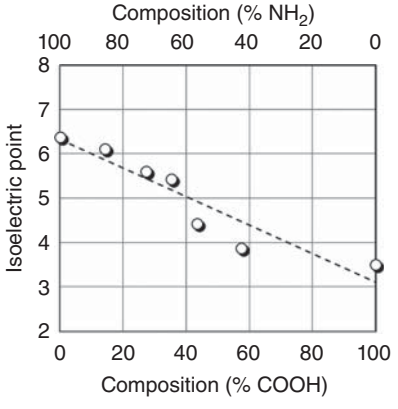

Figure 4.10 Correlation between the isoelectric points and the composition of self-assembled monolayers composed of mixed thiols with carboxylic acid (COOH) and amine (NH_2) terminal groups. Source: Adapted from Lin et al. [88].

zeta potential in an aqueous environment. Lipid monolayers covalently bound to a solid substrate enable the streaming potential measurement as shown by Frant et al. [95] for functionalized tetraether lipid monolayers on silicone catheters. Zimmermann et al. [96] succeeded with the streaming current measurement of supported phospholipid bilayer membranes. The same group investigated the effect of various monovalent and divalent anions and cations on the i.e.p. of these LBMs [97].

Solid lipid nanoparticles (SLNs) are a well-tolerated lipid carrier system due to the use of a physiological and/or biodegradable lipid matrix and physicochemical properties such as ZP are SLNs quality response parameters. To understand the influence of variation in SLN composition (lipid and emulsifier concentration), a Taguchi model of experimental design was applied. The influence of pH and electrolyte, both during and after SLNs preparation, was studied on selected SLN formulations. Slightly polydisperse (PI < 0.3) nanoparticles with a particle size of 450 nm and a ZP range of +5 to −50 mV were developed [98]. Using ELS, Smith et al. [99] conducted a case study to investigate the sensitivity of ZP measurements for cationically, anionically, and neutrally charged liposomes and their dependence on pH and ionic strength and on minor changes in liposome composition. The authors concluded that these findings could be used to formulate similar liposomes with a specific ZP, which could be important for systems sensitive to highly charged species. In another study, the influence of temperature, size distribution, and anions on the ZP of three different lipid vesicles in water and ionic solutions was investigated [100]. The ZP of two types of liposomes, namely 1,2-dipalmitoylsn-glycero-3-phosphatidyl-choline (DPPC) and 1,2-dioleoyl-sn-glycero-3-phos-phatidylcholine (DOPC), were studied in the presence of phospholipase C enzyme action causing hydrolysis [101]. It was found that ZP is not a very sensitive parameter for following the hydrolysis reaction in phosphate buffer, but generally allows the characterization of such reactions by determining the electrokinetic properties of liposomes. ZP has also been used to quantify peptide interactions with lipids and to clarify their mechanism of action. ZP was shown to be a suitable tool for quantifying peptide/lipid interactions of a variety of charged molecules, overcoming some of the limitations of other techniques (e.g. fluorescent labeling) [102]. Experimental design was used to predict the effect of liposomal lipid composition on ZP, resulting in a liposome with a target ZP [103]. Such an approach may accelerate the formulation development of liposomal vaccine adjuvants. Oyarzun-Ampuero et al. [104] reported the development of hyaluronan nanocapsules to be used as vehicles for intracellular drug delivery. These nanocapsules consist of a lipid core and a shell of HAc. The ZP results showed a screening of the initially positive ZP of the nanoemulsion, leading to an inversion to negative values as the concentration of HA increases. This dependence of ZP on the amount of HA is an evidence of surface localization of HA molecules and indicates the need to use a minimal amount of HA to obtain stable nanocapsules. Polysaccharides such as amphiphilic lipochitosan or lipodextran were used for the surface modification of lipid nanocapsules by postinsertion, and the result of surface modification was verified by ZP and confirmed the successful modification of lipid nanocapsules [105].

4.3 Methods for Characterization of Solid–Liquid Interaction of Biomaterials

Once the nature of the surface charge (cationic, anionic, and nonionic) and the amount of functional groups on the surface are defined, one can predict and in some cases control the interactions with other molecules on the solid–liquid interface if the charged functional groups have a major role in the interaction mechanisms [106–108].

There are many methods which allow one to follow solid–liquid interactions like QCM [109], SPR [110], electrochemical methods like potentiometry [111], calorimetry [112], and spectroscopic methods [113]. An alternative method for description of solid–liquid interactions, which is rarely reported and promises larger variability in measurable sample dimensions, shape, and structure while not compromising in accuracy and stability, is electrokinetic analysis (ζ-potential) as a tool to study solid–liquid interaction of biomaterials.

In the first part of this section, two well-established methods for studying solid–liquid interactions will be described. QCM and SPR are complementary to each other and besides the dynamics of the interactions also provide crucial information on some rheological properties of the molecules on the solid–liquid interface, namely the water content of the molecular layer and its viscoelastic properties. Both are important parameters when dealing with interfacial biopolymer layers used in medical purposes, for example. Both methods are widely used in describing solid–liquid interactions, and the existence of many studies describing the use of both allows for a comprehensive review of their benefits as well as their drawbacks.

The second part is dedicated to current breakthroughs in ζ-potential measurements for studies of solid–liquid interactions by following *in situ* adsorption and desorption kinetics.

4.3.1 Quartz Crystal Microbalance and Surface Plasmon Resonance

QCM is a transient mode resonator that measures the frequency of an oscillating quartz crystal [114]. The frequency of the oscillating crystal is fundamentally dependent on its mass and mass changes on its interface. Sauerbrey [115, 116] described the relationship between the frequency and mass in gaseous phase, and in the 1980s and 1990s further development widened its use to liquid phase as well [117–119]. The latter propelled the interest in QCM in the scientific sphere, especially in the field of biomedicine and biomaterials in general as it allowed accurate, stable, and simple measurement of small masses [114]. Some of the applications include interaction studies (i.e. mass and thickness measurement, and kinetics of reaction) during the formation of ultra-thin single- [120] or multilayers [121, 122] of biomaterials in liquid phase on various solid surfaces, solid–liquid interactions of biological molecules such as proteins [123, 124], cells [125], and microorganisms with various functional solids, enzymatic degradation of biomaterials [126],

structural rearrangement of polymers [127], and many others. There are three key elements in understanding and fully utilizing the potential of QCM:

I. piezoelectricity,
II. the quartz crystal, and
III. the mathematical modeling.

(I) **Piezoelectricity** is a material property, an electric charge generating in certain solid materials because of applied mechanical stress [128]. French physicists Jacques and Pierre Curie discovered piezoelectricity in 1880 [129], and it can be described as a result of the linear electromechanical interaction between the mechanical and electrical states in crystalline materials with no inversion symmetry [130]. The piezoelectric effect is a reversible process meaning that mechanical strain can be generated in a piezoelectric material by applying an electrical field. In case of QCM, the crystal is the piezoelectric material that oscillates in the shear mode when AC voltage is applied across its electrodes [131].

(II) **The quartz crystal** is AT-cut at an angle of 35°15′ to its *y*-axis generating a crystalline orientation which generates the shear waves making the crystal oscillate at its fundamental resonance frequency and several overtones [131]. Quartz crystals can be acquired with rigid top layers from various materials ranging from gold, silicon, titanium dioxide, and polymer surfaces like cellulose. A basic setup of a QCM device is shown in Figure 4.11. It contains a measurement unit which consists of a flow cell in which the crystal is mounted, a detection unit, coupled with the flow cell, and a connection to an AC current source. The detection unit measures the shear oscillation of the crystal and displays it as frequency change over time (Figure 4.11b). The flow cell is connected to a peristaltic pump, allowing fluids to pass over the surface of the quartz crystal.
Once the system is established and recordings of frequency and dissipation can be read, one can translate the signal to the corresponding mass of the adsorbed molecules using mathematic modeling.

(III) **Mathematic modeling** tools today are usually a part of the software running the QCM device. The fundamental relation connecting the measured frequency and crystal mass is shown in Eq. (4.13). It is a simplified Sauerbrey relation expressed as

$$\Delta m = -C \cdot \frac{\Delta f}{n} \tag{4.13}$$

The equation was derived from the measured resonant frequency (f) of the quartz crystal (Eq. (4.14)) and its areal mass (m_A; Eq. (4.15)):

$$f = n \cdot \frac{v_q}{2t_q} = n \cdot f_0 \tag{4.14}$$

$$m_A = t_q \cdot \rho_q \tag{4.15}$$

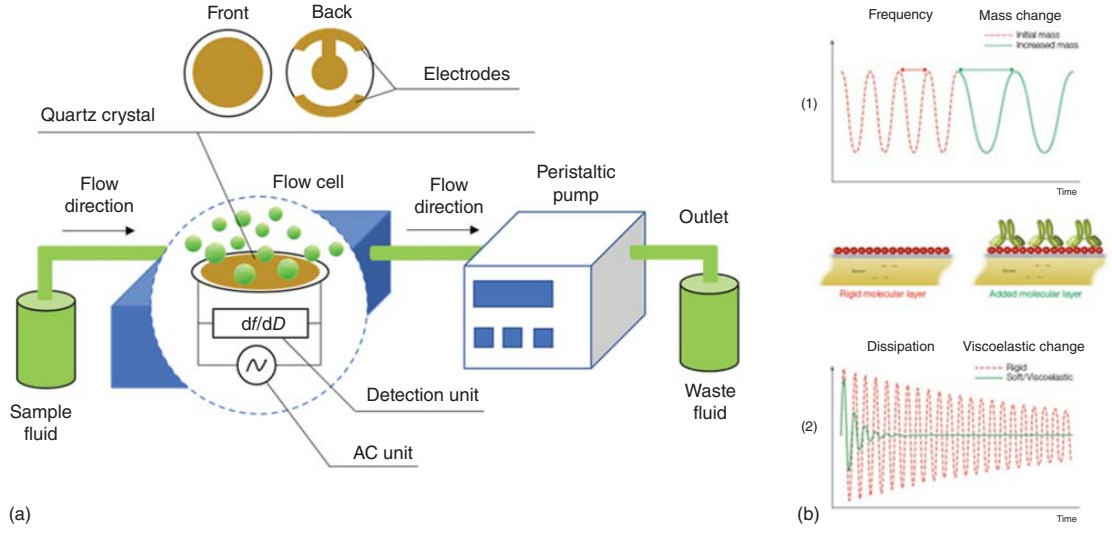

Figure 4.11 (a) A schematic representation of the QCM device and its key elements, (b) examples of frequency and dissipation recordings.

When inserting Eqs. (4.15) into (4.14) and differentiating the expression one gets Eq. (4.16):

$$\mathrm{d}f = -\frac{f}{m_A} \cdot \mathrm{d}m_\mathrm{q} \tag{4.16}$$

One can replace the areal mass and frequency in this equation with the ones from Eqs. (4.14) and (4.15) and express them as shown in Eq. (4.17):

$$\mathrm{d}f = \Delta f = -n \cdot \frac{2f_0^2}{v_\mathrm{q} \cdot \rho_\mathrm{q}} \cdot \Delta m = -n \cdot \frac{1}{C} \Delta m \tag{4.17}$$

where f is the measured resonance frequency, f_0 is the fundamental resonance frequency, n is the harmonic number, m is the mass of the crystal, t_q is the thickness of the crystal, and $C = v_\mathrm{q} \cdot \rho_\mathrm{q} / 2{f_0}^2$ is a proportionality constant composed of intrinsic properties of the quartz itself such as its density (ρ_q), wave velocity (v_q), and fundamental resonance frequency (f_0) [132].

The simplified Sauerbrey relation in Eq. (4.13) can also be used to quantify the mass of adsorbed molecular layers (e.g. biomaterials) on the surface of the quartz crystal, but only under the condition that the layers are rigid and behave elastically similar to the crystal itself, and that their mass is small compared to the mass of the crystal. However, at a certain layer thickness, its viscoelastic nature becomes a significant part of the quartz crystal's response, breaking down the simplified proportionalities in Eq. (4.13). All current QCM devices allow for measurements of dissipative energy (Figure 4.11b) arising from dampening of the crystal's oscillation by the viscoelastic layer, thus providing information on its viscoelastic nature (QCM-D) [133]. The dissipation factor (D) measured by the QCM-D is defined as shown in Eq. (4.18):

$$D = \frac{E_\mathrm{dissipated}}{2\pi E_\mathrm{stored}} \tag{4.18}$$

where $E_\mathrm{dissipated}$ is the energy dissipated during one oscillation period and E_stored is the energy stored during oscillation [114].

First relations between the measured frequency and mass of layers in liquid medium were presented by Kanazawa and Gordon [117] and contain quantities related to the used liquid like its density and viscosity (Eq. (4.19)):

$$\Delta f = -f_0^{\frac{3}{2}} \cdot \left[\frac{(\rho_\mathrm{L} \cdot \eta_\mathrm{L})}{(\pi \cdot \rho_\mathrm{q} \cdot \mu_\mathrm{q}} \right]^{1/2} \tag{4.19}$$

where ρ_q and η_L are the density and the viscosity of the liquid, respectively, and ρ_q and μ_q are the density and the shear modulus of the quartz.

Viscoelastic models have further been developed to deal with more complex viscoelastic layers in liquid systems allowing to extract layers thickness, shear modulus, and viscoelastic phase angle from the measured frequency and dissipation change for various solid–liquid systems [133–137]. This allowed one to estimate the influence of the layer's rheology on the oscillating frequency of the crystal, thus reducing the estimated mass error due to dampening. Most software uses the Voigt–Kelvin [124, 138] viscoelastic model (Eq. (4.20)), which assumes that the

storage modulus (elastic shear) is frequency independent and the loss modulus (shear viscosity) is in linear relationship with the frequency [137]. It predicts the rheology of the viscoelastic layers rather accurately in realm of viscoelastic influence on the crystals oscillation frequency but less so in the realm of the Sauerbrey relation. In this case, it is advised to use Eq. (4.13) for mass determination. The shear modulus (G) in the Voigt–Kelvin model is related to the measured frequency (f) as

$$G = \mu_f + i2\pi f n_f \tag{4.20}$$

where μ_f is the storage modulus (elastic shear) and n_f is the loss modulus (shear viscosity).

Other more realistic models like the power-law [139] model have been studied as well but essentially provide similar accuracy as the Vogt–Kelvin model. A graphical representation of the shear wave propagation during oscillation in a system represented by the Voigt–Kelvin model is shown in Figure 4.12.

Although today many models exist for determination of the mass of viscoelastic layers with high dissipative energy on quartz crystals, the physicochemical parameters of the adsorbed layers, needed for equation solving, such as viscosity and density are often nonexistent or very difficult to determine. Therefore, complementary methods are used to support QCM-D data. SPR is one of them.

The SPR technique is an optical technique utilizing changes in the refractive index at the interface of a conductive material and its surrounding environment (e.g. liquid) upon adsorption of molecules [110]. The SPR method is specific due to its high sensibility (down to 10^{-5}) [136], allowing for detection of nanometric layers [140]. The sensibility is achieved by exploiting the SPR effect. In brief, when infrared or visible light is shined on a conductive material, electromagnetic waves (surface plasmon polaritons) run on the interface of the material and its surrounding in a direction parallel to the interface [141]. These electromagnetic waves are extremely sensitive to changes on the interface (e.g. adsorption of molecules), thus giving rise

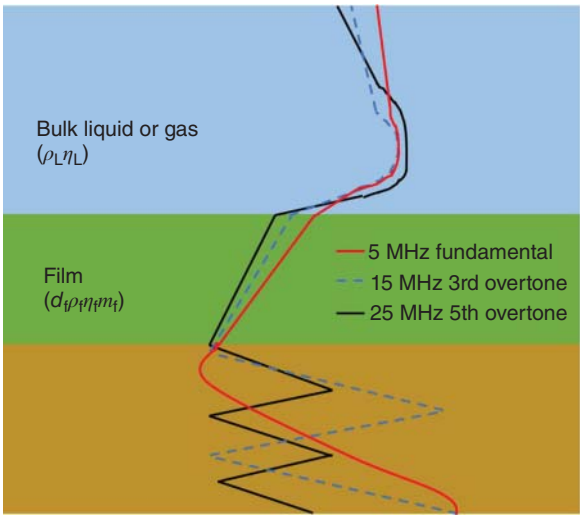

Figure 4.12 Schematic representation of a shear wave propagation through various media (QCM crystal, applied film, bulk liquid, or gas).

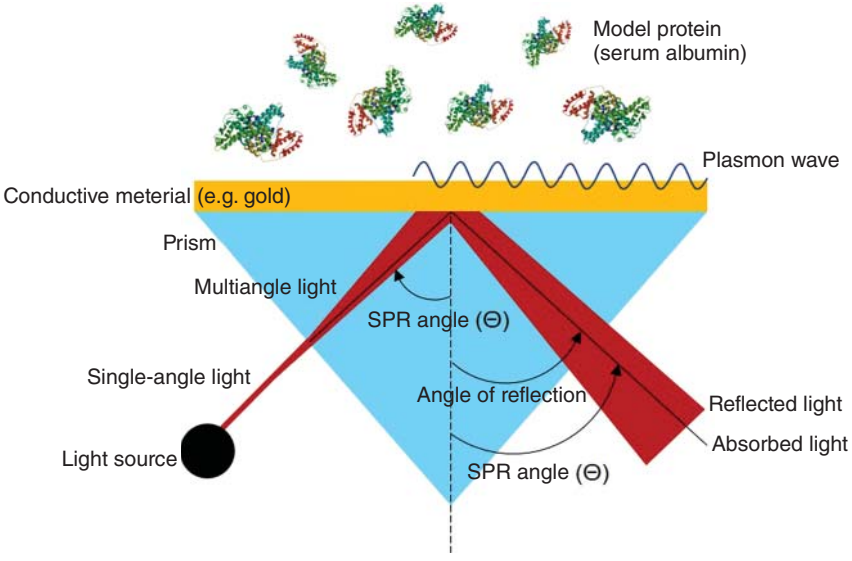

Figure 4.13 Schematic representation of the principles of the SPR technique.

to the sensitivity of the SPR method [141]. The key to utilizing the sensitivity of the surface plasmon polaritons lies in exciting the polaritons in a resonant manner causing SPR [142]. Using visible light, this can be achieved if the incident light matches the momentum of the plasmon. This is usually done by increasing the wavenumber of light by passing it through a block of glass (e.g. a prism). A common SPR setup is shown in Figure 4.13.

At a certain angle of incidence (Θ), when SPR is excited, most light is absorbed and a minimum in the intensity of the reflected light is observed. When the refractive index on the surface of the conductive material changes (e.g. adsorption of molecules), the Θ of SPR excitement changes proportionally; hence, the mass of the adsorbed molecules can be determined [124]. For many cases, mostly uniform films, a simple linear relationship between the Θ of SPR excitement and mass is sufficient and is expressed as

$$m_{\Delta n} = d\frac{\mathrm{d}c}{\mathrm{d}n}\kappa\frac{\Delta\Theta}{1-\mathrm{e}^{-2d/l_{\mathrm{decay}}}} \tag{4.21}$$

where Δn is the refractive index change, d is the thickness of the adsorbed molecules (film), κ is the sensitivity factor of the system relating a change in $\Delta\Theta$ to the change in refractive index within the evanescent field, l_{decay} is the decay length of the evanescent field, and $\mathrm{d}c/\mathrm{d}n$ is the inverse of the refractive index increment with bulk concentration [136, 143].

However, for "films" including both adsorbed molecules and entrapped liquid (e.g. buffer), a two-component formula like the Lorenz–Lorentz formula should be used instead:

$$m_{\Delta n} = \frac{3d\left(n^2-n_{\mathrm{b}}^2\right)}{\left(n^2+2\right)\left(r\left(n_{\mathrm{b}}^2+2\right)-v\left(n_{\mathrm{b}}^2-1\right)\right)} \tag{4.22}$$

where r is the specific refractivity of the adsorbed molecules, v is the partial specific volume, and n is the refractive index of the adsorbed molecular "film" expressed as $n_{\text{film}} = n_{\text{buffer}} + \Delta n$ [144].

Many solid–liquid interaction studies were born through this established knowledge, describing how molecules from liquids interact on the interface with a solid material. In the following text, we will take a closer look at some ground-breaking studies dealing with the interactions of biomaterials in aqueous liquid phase with solid surfaces (e.g. metals, synthetic polymers, and glass), biomaterials in solid phase with aqueous liquid phases (e.g. electrolytes and acid–base solutions), and biomaterials in solid phase with biomaterials in aqueous liquid phase, i.e. biological fluids (plasma proteins, cells, microorganisms, etc.). As mentioned before, in the 1980s and 1990s, the use of QCM-D was extended to liquid phase as well and that opened the door for studies in biomaterial science wide. Studies of biomaterials in solid phase with biomaterials in aqueous liquid phase, i.e. biological fluids (plasma proteins, cells, microorganisms, etc.), started off in the 1990s,and a milestone was reached shortly after with the publication of Rodahl et al., where the authors studied protein adsorption, lipid vesicle adsorption, and cell adhesion studies on gold quartz sensors by means of QCM-D [108]. The study was one of the first of its kind and paved the way for many more to come. Their results have shown that even very thin (few nm) biofilms dissipate a significant amount of energy. Three main contributors for the high dissipation were identified: a viscoelastic porous structure that is strained during oscillation, trapped liquid moving within the pores or in and out of them, and the load from the bulk liquid increasing the strain. These results have shown the importance of measuring crystal frequency and dissipation changes simultaneously (Figure 4.14) in an adsorption experiment as it provides crucial information on how the adsorbed molecules occupy the free space on surfaces, as shown in Figure 4.15. The influence of surface charge on adsorption was not studied particularly; however, adsorption of lipid vesicles was carried out on hydrophobic gold (thiolated by methyl-terminated alkane thiols), and hydrophilic gold (oxidized by UV radiation) revealed a much denser packed nonrigid lipid film formed on the oxidized gold, whereas a multilayer is formed on the hydrophobic gold (Figure 4.14). This provided some evidence of the importance of surface chemistry on the adsorption behavior.

Soon after, publication on this topic started multiplying, and various biomaterials in solid phase were studied by means of QCM-D, ranging from metal and metal oxide surfaces (e.g. gold [145–148], stainless steel [149–152], titanium oxide [109, 146]), polymers (e.g. polyethylene [153–155], polydimethylsiloxane [156–158]), biopolymers like polysaccharides (e.g. cellulose [107, 145, 159–163], chitosan [164, 165]), and others. Especially interesting are polysaccharides, as their structure changes significantly when in contact with fluids, which can be attributed to swelling phenomena. Therefore, it is important to understand how such surfaces behave in liquids alone prior to attempting to understand their interactions with other biomaterials in liquid phase. For example, Ahola et al. studied the effect of cellulose nanofibril charge density, electrolyte concentration, and pH on swelling QCM [159]. Electrolyte concentration experiments showed that nanofibrils with

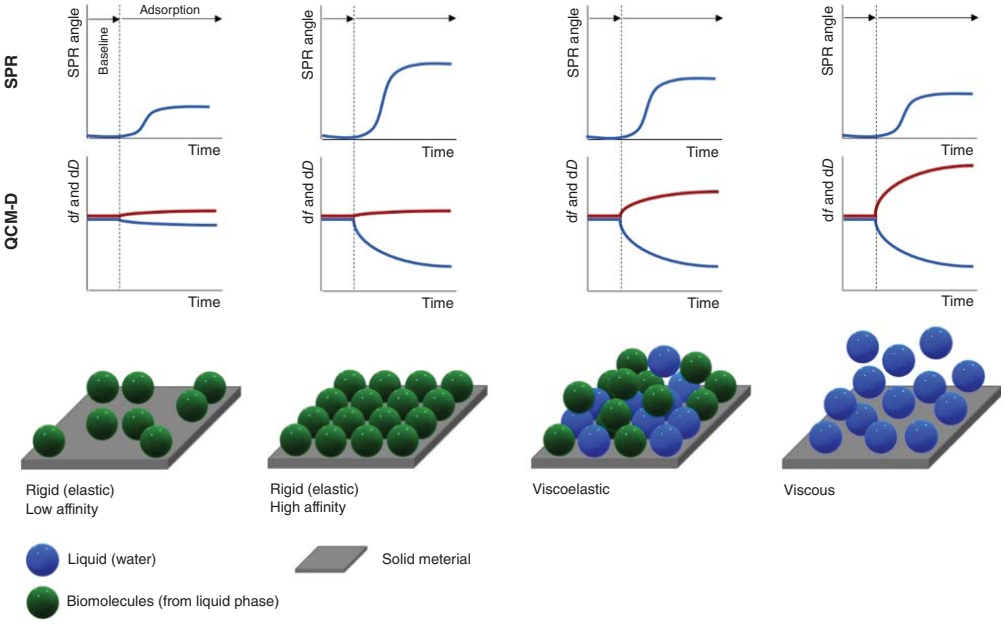

Figure 4.14 (a) Frequency (Δf) and (b) dissipation (ΔD) changes during adsorption of lipid vesicles on hydrophobic and hydrophilic gold substrates [108]. Blue text was added by authors from this chapter for better understanding of experimental results with basic QCM concepts. Source: Rodahl. et al. [108]/with permission of Royal Society of Chemistry.

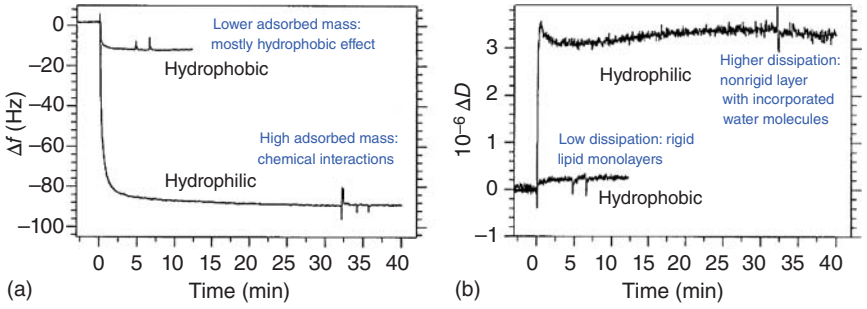

Figure 4.15 A schematic depiction of the mechanics of adsorbed molecules and the responses of QCM-D and SPR signals.

higher charge density (carboxylic groups) absorbed more water than lower charge density nanofibrils. The presence of electrolyte caused the carboxylic groups of the cellulose to deprotonate as it increased the pH inside the nanofibril layers (Donan effect); hence, higher charge density nanofibrils were swelling to a larger extent. Kittle et al. [160] used a different approach to study the amount of water that can be absorbed by cellulose. They soaked the cellulose films in water followed by heavy water (D_2O) and observed the change in frequency and related it to the amount of adsorbed water (Figure 4.16). A similar approach was also used by Mohan et al. [161], which also followed regeneration of trimethylsilyl cellulose to cellulose by acid–vapor hydrolysis using QCM-D.

Simultaneous with studies of interactions of solid-phase biomaterials with liquids, interactions of biomaterials in liquid with solid materials (biomaterials included) were conducted by many authors [107, 109, 154]. Kargl et al. [154] studied interactions of carboxymethyl cellulose (CMC), an anionic derivative of cellulose, with thin films made of various polymers, ranging from cellulose, cellulose acetate, and deacetylated cellulose acetate, to polyethylene terephthalate (PET) and cyclo-olefin

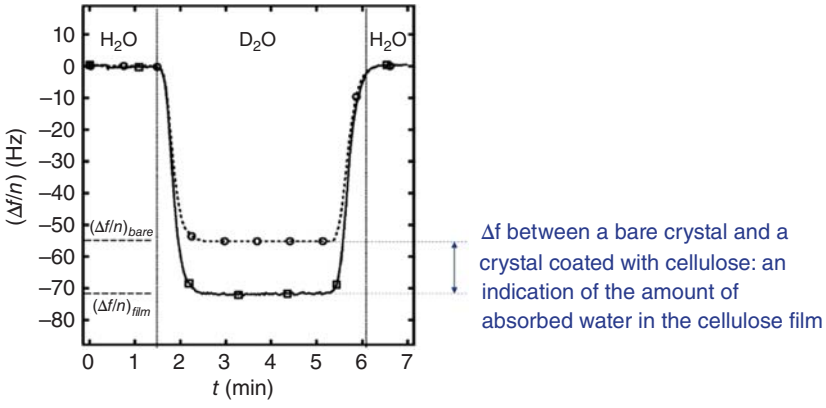

Figure 4.16 Frequency (Δf) changes during absorption water and heavy water (D_2O). Blue text was added by authors from this chapter for better understanding of experimental results with basic QCM concepts. Source: Kittle et al. [160]/with permission of American Chemical Society.

polymer. The interaction of CMC with the thin films was conducted in a range of pH values to observe the influence of ionized and nonionized carboxylic groups of CMC on its deposition on the above-mentioned surfaces. It was shown that at low pH values (pH = 2), where the carboxylic groups are mostly nonionized, the CMC prefers to adsorb to hydrophobic surfaces in shape of small aggregates, a result of low solubility and the hydrophobic effect. Interestingly, on hydrophilic surface the CMC preferably adsorbed on cellulose-based solid substrates rather than on synthetic ones (silicon dioxide or polyvinyl alcohol). This was an important observation showing how QCM-D can be used to follow selective interactions of biomaterials in liquid phase with solid surfaces and how surface charge of biopolymers fundamentally influences their interactions with solid materials (Figure 4.17).

Once a good fundamental understanding of the interactions of biomaterials in liquid phase with solid surfaces and vice versa was established, more complex biological systems were studied by a large number of researchers, e.g. interactions between biomolecules like cells [125, 166–171], proteins [123, 132, 157, 158, 164, 172, 173], DNA [106, 174–176], and microorganisms [177–183] in liquids with biomaterials in solid phase. Höök et al. [109] have studied the adsorption kinetics of three model proteins (human serum albumin, fibrinogen, and hemoglobin) as biomaterials in liquid-phase on solid-phase titanium-dioxide-coated QCM crystals. This publication is an example of the complexity of studying interactions on a molecular level on the interface between biomaterials in liquid phase with biomaterials in solid phase. Proteins (e.g. fibrinogen) were bound to solid surfaces followed by adsorption of antibodies on the formed protein layers. Obtained data allowed the authors to determine the adsorption kinetics of proteins and the antibodies, the conformation of proteins on the titanium dioxide surfaces, and the adsorption selectivity by using selective antibody adsorption experiments. However, the study did not specifically focus on the influence of surface charge on the adsorption behavior. Nevertheless, it paved the way for an exponential growth in research publications in this area allowing for a deeper understanding of the phenomena happening at the interface between biomaterials in solid phase with biological molecules in the liquid phase. The importance

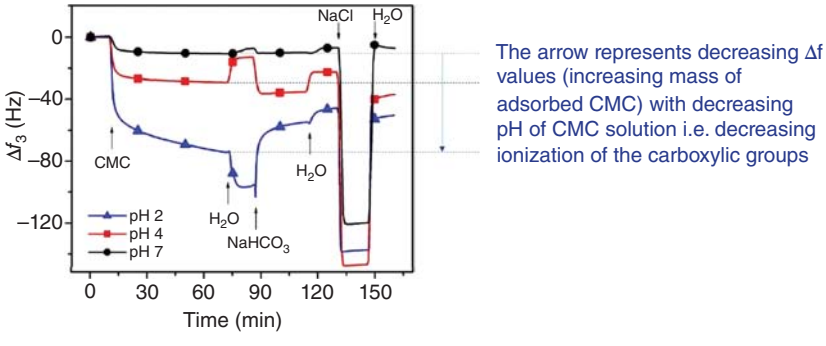

Figure 4.17 Frequency (Δf) changes during adsorption of carboxymethyl cellulose (CMC) at different pH on a thin film of cellulose. Blue text was added by authors from this chapter for better understanding of experimental results with basic QCM concepts. Source: Kargl et al. [154]/with permission of American Chemical Society.

of charge density on adsorption of biomaterials and their interactions with biological molecules was well documented by Gericke et al. [107] where the authors prepared semi-synthetic polysaccharide sulfate solid surfaces as biomaterials to study their anticoagulant properties by looking closely at interactions with blood plasma using QCM-D. Firstly, the authors adsorbed the semi-synthetic polysaccharide sulfates, baring varying sulfate charge densities (DS 0.87 to DS 1.66), on neat and cationically modified PET surfaces. Their results revealed that electrostatic interactions were the main driving force for adsorption as the semi-synthetic polysaccharide sulfates adsorbed less on neat PET and more on the cationically modified. Furthermore, the adsorbed mass on cationically modified PET increased with increasing sulfate charge density of the semi-synthetic polysaccharide sulfates. Additionally, the blood coagulation experiments revealed that the amount of charged sulfate groups on the surface of solid materials also influences the blood coagulation cascade. QCM was shown to be a strong tool to study binding selectivity of biomolecules as shown in publications by Caruso et al. [106] or Kargl et al. [174] while studying hybridization of complementary DNA strains in liquid phase with DNA strains bound to a solid-phase material. Big steps forward were made in cell adhesion studies as well, as several authors took the work of Rodahl et al. [108] to a new level. Watarai et al. [170] studied mouse fibroblast cell adsorption in liquid phase on gold surfaces as biomaterials in solid phase. They generated frequency and dissipation correlation plots and from that defined three regions of interactions: (i) cell adsorption and desorption, (ii) attachment and spreading, and (iii) secretion of microexudates (Figure 4.18). Similarly, great progress was made in the field of studying bacterial attachment on solid surfaces by means of QCM. By the end of the 1990s, Otto and Elwing [181] were one of the first to study the influence of ionic strength on adsorption of *Escherichia coli* strains in liquid phase on solid substrates (e.g. gold QCM sensor). As the attachment of bacterial cells on solid surfaces at low ionic strengths is predominantly driven by van der Waals and electrostatic forces, the increase in ionic strength influences the driving forces and thus also the attachment of bacterial cells, whereas electrostatic repulsion of the negative bacterial wall surface from the negative solid surface is just one of many factors contributing to the complicated mechanism of attachment.

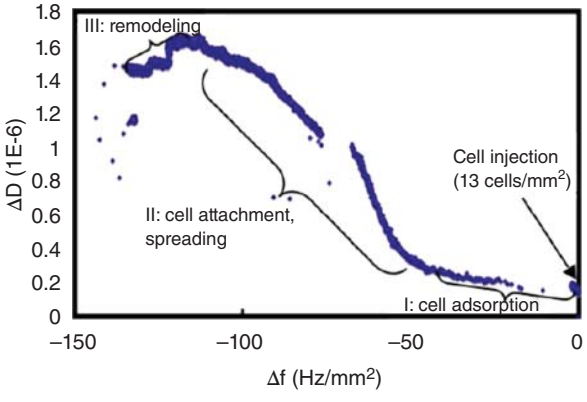

Figure 4.18 Frequency (Δf) vs. dissipation (ΔD) plots for mouse fibroblast cell adsorption in liquid phase on gold surfaces. Blue text was added by authors from this chapter for better understanding of experimental results with basic QCM concepts. Source: Watarai et al. [170]/with permission of Elsevier.

Simultaneous with the growing number of QCM applications and experiments involving increasingly softer materials which behave in contradiction with the Sauerbrey law, skepticism about the applicability of QCM and its models grew as it was difficult to separate the effect on adsorbed mass of the solute and the solvent [114, 133, 135]. Therefore, correlation studies involving simultaneous QCM-D and SPR measurements started to evolve at the same time as well, giving more insights about the rheology of the adsorbed viscoelastic soft films [124, 136, 162, 184–187].

Höök et al. [124] measured the time-resolved adsorption kinetics of the mussel adhesive protein (Mefp-1) on a nonpolar, methyl-terminated (thiolated) gold surface by using QCM-D and SPR. The publication is a milestone in understanding how to utilize both techniques to obtain valuable data on adsorption kinetics, adsorbed mass, and rheological properties of the adsorbed molecular film. Adsorption experiments showed a large difference in the adsorbed mass between QCM and SPR revealing that the Mefp-1 protein adsorbs to the gold surface with inclusion of around 97% of water, forming a gel-like film. Upon cross-linking of the protein, the total mass calculated by QCM reduced drastically as water was ejected and the film got more rigid. The thickness of the film reduced by threefold as shown by SPR. Additionally, an increase in shear viscosity and shear elastic modulus was determined by QCM, due to the decrease in hydration. Reimhult et al. [136] took the experiment further and constructed a system allowing for simultaneous time-resolved SPR and QCM measurements on the same sample (Figure 4.19). The complementary nature of both techniques enabled the authors to separate the kinetics of planar phospholipid bilayer formation on SiO_2 in two parallel processes: vesicle adsorption and supported phospholipid bilayer formation from the adsorbed vesicles. It was shown that the change in SPR angle and the subsequent

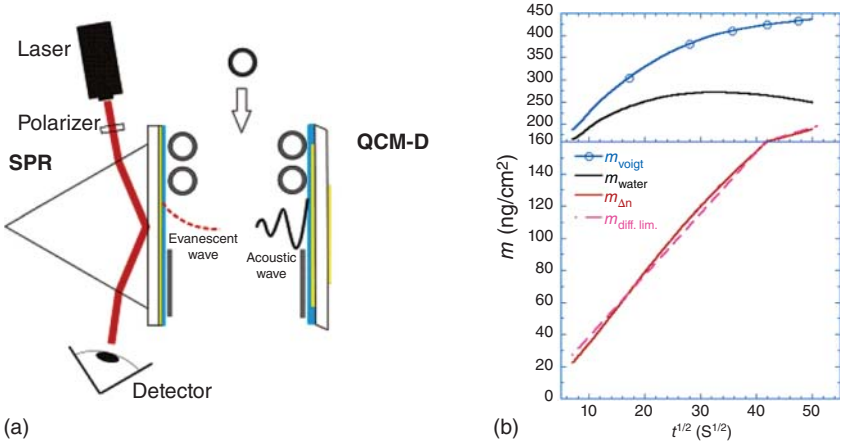

Figure 4.19 (a) Experimental setup allowing simultaneous time-resolved SPR and QCM measurements on the same sample. (b) Experimental data obtained from simultaneous SPR and QCM measurements. Changes in frequency and SPR angle are converted to mass in (b) where m_{Voigt} is the QCM mass, $m_{\Delta n}$ is the SPR mass, and m_{water} is the calculated amount of trapped water. Source: Reimhult et al. [136]/with permission of American Chemical Society.

calculation of adsorbed mass must be used cautiously when the film thickness is in the order of the decay length in SPR. Additionally, the mass increase in QCM was attributed, besides water entrapped within supramolecular assemblies, to dynamically entrapped water between bilayers, which is crucial information when modeling the actual adsorbed mass from QCM data. It was concluded by the authors that omitting either of the techniques from adsorption experiments weakens the analysis and interpretation of the studied kinetics.

Many other authors contributed to spreading the knowledge of the importance of QCM and SPR complementary measurements to study adsorption kinetics. Mohan et al. [162] used cationic cellulose-based surfaces to study interactions with biomolecules in liquid phase using QCM and SPR and compared the data of both. Caruso et al. [185] assembled over 20 polyelectrolyte layers on gold sensors made of oppositely charged polymers, attributing the attachment of the individual layers to electrostatic interactions. The multilayer build-up was studied by means of QCM and SPR. Zhang et al. [188] studied adsorption kinetics and structure of carbohydrate self-assembled monolayers on solid gold substrates. Protein interactions with the carbohydrates were thoroughly characterized by both techniques offering a viable alternative to ITC and ELISA tests.

As the strength of scientific data describing solid–liquid interactions (biomaterials in solid phase with liquids, in liquid phase with various solids, and both in liquid phase with solid-phase biomaterials) measured by QCM in complement with SPR grew, new questions composed of problems growing in complexity were arising as well. The solid-phase biomaterials were getting increasingly more application oriented, and composite-like materials were studied more, replacing single-material solid substrates. Multilayered films [47, 122, 189–192], blended composite films [127, 193, 194], brush copolymer films [195], liposomal membranes [196], and self-healing materials [197] are just a few complex solid-phase biomaterials designed nowadays on QCM sensors to study solid–liquid interactions. And the more complex the surfaces get, the more specific their interactions with biomaterials in liquid phase get as well. This allows for design of very specific sensor-like surfaces which can interact with specific binding sites of molecules, e.g. protein-binding sites [125]. This is propelling QCM studies into the future of label-free, fast, and cost-effective biosensoric devices and responsive surfaces [125, 197–200].

The group of Picart published two ground-breaking papers on the formation of multilayers based on oppositely charged polymers. In the first [47], multilayer build-up of biocompatible films based on poly(L-lysine) and HAc (PLL/HA) was studied by QCM, while chitosan (CHI) and hyaluronan (HA) multilayer films were studied in the following publication [192]. In both, the importance of electrostatic charges on the formation of the multilayered films was shown to be utterly important. Other factors like salt concentration were studied in detail as well. QCM proved to be a suitable technique to study the adsorption kinetics during the formation of a multilayer polymer film. The obtained results were compared with zeta potential measurements, which is a technique described in this chapter as well. Both methods showed good compatibility in identifying the exchanging polymer layers in the multilayered film. An antihemoglobin biointerface on

cellulose was prepared by Orelma et al. [172], and QCM was used to monitor a chemical reaction, i.e. cross-linking, of surface-bound CMC with antihemoglobin, *in situ*. Furthermore, the same reaction was repeated and studied by means of SPR. This allowed to directly observe the effect of EDC/NHS cross-linker on the interaction of the antihemoglobin with CMC (Figure 4.20a). Similarly, Elschner et al. [201] prepared reactive hydroxyethyl cellulose furoate films suitable for the covalent immobilization of functional molecules. These were activated by

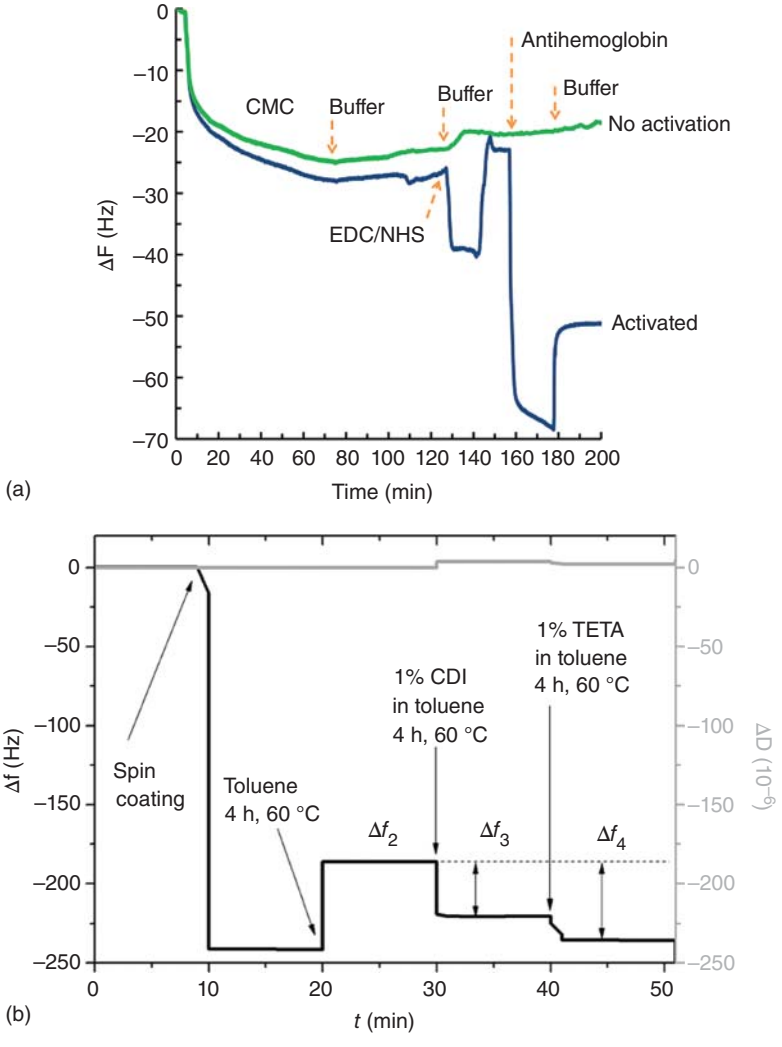

Figure 4.20 (a) QCM frequency (Δf) change during adsorption of CMC, cross-linking reaction, and antihemoglobin binding. Source: Orelma et al. [172]/with permission of American Chemical Society. (b) QCM frequency (Δf) change measured in air of spin-coated cellulose films activated by CDI followed by TETA coupling [201]. Republished with permission of RSC Advances, from Reactive cellulose-based thin films – a concept for multifunctional polysaccharide surfaces. Source: Elschner et al. [201]/with permission of Royal Society of Chemistry.

N,*N*′-carbonyldiimidazole allowing for covalent immobilization of functional molecules bearing primary and secondary amines, namely triethylene tetramine (TETA). The degree of substitution of neat furoate films and amino functionalized ones was determined by measuring changes in oscillation frequency in contact with air by means of QCM-D (Figure 4.20b).

Even though QCM and SPR have evolved over the years, and the information one can obtain from both techniques is rising, some drawbacks which they possess (e.g. limited shape and size of analyzed sample) are eliminated by other techniques, e.g. electrokinetic analyzer. The electrokinetic analyzer measures the ζ-potential on solid surfaces of various sizes and shapes, and changes in ζ-potential are followed during adsorption of molecules from liquids. The technique is described in more detail Section 4.3.2.

4.3.2 Zeta Potential Measurements as a Tool to Study Solid–Liquid Interactions of Biomaterials

The sensitivity of the zeta potential to the outermost surface chemistry of solid materials and the capture of changes in the interfacial charge that occur within the first few layers of water next to the surface make this parameter applicable to monitor water-on-solid surface adsorption and desorption processes. The immediate response of the streaming potential signal to varying pressure gradients but also to a modification of the surface or interfacial layer composition enables the recording of such adsorption and desorption processes also with a reasonable time resolution. A typical set of data for the adsorption of a monoclonal antibody (mAb) on a medical tube is shown in Figure 4.21. The temporal change of the streaming potential signal upon adsorption of the mAb is used to monitor the adsorption kinetics. The effect of adsorption recorded by the streaming potential and the calculated zeta potential depends on the surface and interfacial charges of the

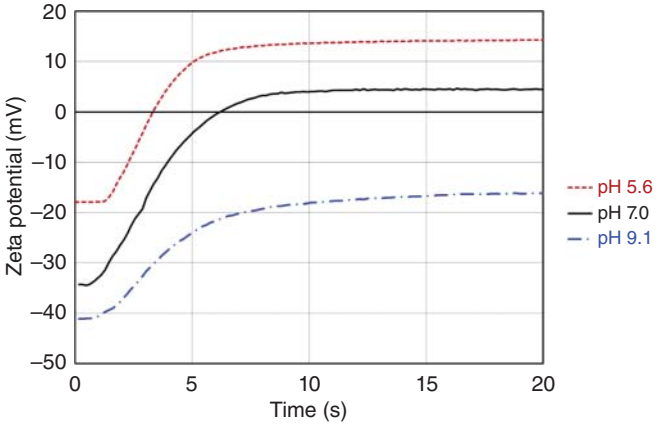

Figure 4.21 Kinetics of adsorption of a monoclonal antibody on a silicone tube at different pH of an aqueous 0.025 mol/l KCl solution monitored by recording the temporal change of the streaming potential.

solid material (the medical tube) and the adsorbate (the mAb) at the respective pH of the aqueous solution, respectively. The mAb used for the adsorption kinetics measurements in Figure 4.21 exhibits an isoelectric point at pH 8.2 and is therefore positively charged at pH 5.6 and pH 7.0 but negatively charged at pH 9.1. The silicone-based medical tube shows an IEP 4.0 and is negatively charged at the pH values studied in this experiment. At pH 5.6 and 7.0 of an aqueous 0.025 mol/l KCl solution, the adsorption of mAb at a bulk concentration of 25 µg/ml leads to a charge reversal of the initially negatively charged tube, while at pH 9.0 the sign of the zeta potential remains negative although its magnitude is significantly decreased. The initial zeta potential at $t = 0$ s represents the charging behavior of the pristine silicone tube at different pH. Besides the effectiveness of mAb adsorption and the time for equilibration, the temporal changes of the streaming potential in Figure 4.21 also indicate a decreasing rate of adsorption with increasing pH.

Norde and Rouwendal [202] were among the first to apply the streaming potential method for the recording of protein adsorption kinetics on material surfaces. The temporal evolution of the streaming potential clearly demonstrates the different rates of adsorption for lysozyme on glass plates depending on the initial protein concentration. At the given measuring conditions (pH 7, ionic strength 0.01 mol/l), the combination of the positively charged lysozyme and the negatively charged glass surface requires an equilibration time of 1 minute only for a protein concentration of 10 mg/l but significantly longer than 10 minutes for a concentration of 0.1 mg/l lysozyme. Zembala and Déjardin [203] applied the streaming potential to study the adsorption kinetics of a different protein, fibrinogen, again on glass but with a different shape. They used a glass capillary to study protein adsorption at the inner capillary surface. Werner et al. [204] compared the adsorption kinetics for human serum albumin and fibrinogen on a perfluorated polymer film. Both proteins show irreversible adsorption with a comparable rate but different effects on the change in the zeta potential. This example represents a limitation in the streaming potential method for recording adsorption processes, i.e. the dependence on the differences in the charges of the adsorbate (e.g. the protein in solution) and the adsorbent (the solid surface).

Ethève and Déjardin [205] evaluated the effect of different flow rates (different shear) on the adsorption kinetics of lysozyme on a silica surface and correlated the changes in the zeta potential with the adsorbed amount of protein. For the estimation of the adsorbed amount in terms of number or mass concentration, a different technique (e.g. radio-labeling, reflectometry, and QCM) is required to complement the streaming potential measurement. Kawasaki et al. [206] extended the investigation of protein adsorption to include lactoglobulin, ovalbumin, and saliva proteins on HAP as a model surface for tooth enamel. Zimmermanna et al. [207] reported a rather slow adsorption for fibrinogen on a polymer film with dicarboxylic acid terminal groups recorded by the streaming current coupling coefficient $dI_{str}/d\Delta p$ accompanied by reflectometric interference spectroscopy measurement.

Protein–polysaccharide interactions have attracted considerable attention in the pharmaceutical industry as they play a key role in the development of novel encapsulation devices. Thus, the interactions of fish gelatin (FG) with HAc have been studied

using ZP measurements determined from electrophoretic mobility in addition to turbidimetric titration, dynamic light scattering, etc. FG forms soluble complexes with HA above a limiting pH ($pH_{\phi 1}$) at which both biopolymers are net negatively charged but forms insoluble complexes as liquid-state complex coacervates below $pH_{\phi 1}$ at which the two biopolymers are oppositely charged. The results suggest that complex formation is driven mainly by electrostatic attractions rather than hydrogen bonding or hydrophobic interactions [208]. In the following study, the ZP value provides relevant information about interactions between colloidal particles, namely amino-modified silica and lignin to form hybrid biomaterials [94]. The ZP results under different conditions, supported by the determination of the electrophoretic mobility of the two biopolymers, led to propose a model of the interactions between collagen and poly(acrylic acid) [55]. In another work, possible electrostatic interactions between the components of hydrogels (i.e. chitosan, gelatin, and bioactive glass nanoparticles) were evaluated using ZP analysis [85]. It was also shown that ZP is a potential technique for quantifying peptide/lipid interactions [102].

References

1 Katchalsky, A., Shavit, N., and Eisenberg, H. (1954). Dissociation of weak polymeric acids and bases. *J. Polym. Sci.* 13 (68): 69–84. https://doi.org/10.1002/pol.1954.120136806.

2 Fras, L., Laine, J., Stenius, P. et al. (2004). Determination of dissociable groups in natural and regenerated cellulose fibers by different titration methods. *J. Appl. Polym. Sci.* 92 (5): 3186–3195. https://doi.org/10.1002/app.20294.

3 Fasl, H., Zemljič, L.F., Goessler, W. et al. (2012). Investigations into amphiphilic chitosan: properties and availability of original and newly introduced functional groups. *Macromol. Chem. Phys.* 213 (15): 1582–1589. https://doi.org/10.1002/macp.201200086.

4 Čakara, D., Fras, L., Bračič, M., and Kleinschek, K.S. (2009). Protonation behavior of cotton fabric with irreversibly adsorbed chitosan: a potentiometric titration study. *Carbohydr. Polym.* 78 (1): 36–40. https://doi.org/10.1016/j.carbpol.2009.04.011.

5 Farris, S., Mora, L., Capretti, G., and Piergiovanni, L. (2012). Charge density quantification of polyelectrolyte polysaccharides by conductometric titration: an analytical chemistry experiment. *J. Chem. Educ.* 89 (1): 121–124. https://doi.org/10.1021/ed200261w.

6 Fras, L., Johansson, L.S., Stenius, P. et al. (2005). Analysis of the oxidation of cellulose fibres by titration and XPS. *Colloids Surf., A* 260 (1): 101–108. https://doi.org/10.1016/j.colsurfa.2005.01.035.

7 Liu, X., Tian, R., Du, W. et al. (2019). A theory to determine the surface potentials of clay particles in electrolyte solutions. *Appl. Clay Sci.* 169: 112–119. https://doi.org/10.1016/j.clay.2018.12.022.

8 Azevedo, M.C.C. and Cavaleiro, A.M.V. (2012). The acid–base titration of a very weak acid: boric acid. *J. Chem. Educ.* 89 (6): 767–770. https://doi.org/10.1021/ed200180j.

9 Hurek, J. and Nackiewicz, J. (2013). A simple method for the consecutive determination of protonation constants through evaluation of formation curves. *J. Chem. Educ.* 90 (5): 604–608. https://doi.org/10.1021/ed300172a.

10 Katchalsky, A. and Spitnik, P. (1947). Potentiometric titrations of polymethacrylic acid. *J. Polym. Sci.* 2 (4): 432–446. https://doi.org/10.1002/pol.1947.120020409.

11 Shaw, J.D., O'Neal, D.J., Siddharthan, K. et al. (2014, 2014). Pilot program to improve self-management of patients with heart failure by redesigning care coordination. In: *Nursing Research and Practice* (ed. K. Finlayson), 836921. Hindawi Publishing Corporation. https://doi.org/10.1155/2014/836921.

12 Genco, T., Zemljič, L.F., Bračič, M. et al. (2012). Physicochemical properties and bioactivity of a novel class of cellulosics: 6-deoxy-6-amino cellulose sulfate. *Macromol. Chem. Phys.* 213 (5): 539–548. https://doi.org/10.1002/macp.201100571.

13 Salomao Pinto Zarth, C., Zemljič, L.F., Čakara, D. et al. (2012). Charging behavior and stability of the novel amino group containing cellulose ester cellulose-4-[N-methylamino]butyrate hydrochloride. *Macromol. Chem. Phys.* 213 (16): 1669–1676. https://doi.org/10.1002/macp.201200057.

14 Soto, D., Urdaneta, J., and Pernia, K. (2014, 2014). Characterization of native and modified starches by potentiometric titration. In: *Journal of Applied Chemistry* (ed. P.H. Parsania), 162480. Hindawi Publishing Corporation. https://doi.org/10.1155/2014/162480.

15 Duan, D.X., Donner, E., Liu, Q. et al. (2012). Potentiometric titration for determination of amylose content of starch – a comparison with colorimetric method. *Food Chem.* 130 (4): 1142–1145. https://doi.org/10.1016/j.foodchem.2011.07.138.

16 Yangcheng, H., Jiang, H., Blanco, M. et al. (2013). Characterization of normal and waxy corn starch for bioethanol production. *J. Agric. Food. Chem.* 61 (2): 379–386. https://doi.org/10.1021/jf305100n.

17 Zhang, Y., Zhang, X., Ding, R. et al. (2011). Determination of the degree of deacetylation of chitosan by potentiometric titration preceded by enzymatic pretreatment. *Carbohydr. Polym.* 83 (2): 813–817. https://doi.org/10.1016/j.carbpol.2010.08.058.

18 Zemljič, L.F., Čakara, D., Michaelis, N. et al. (2011). Protonation behavior of 6-deoxy-6-(2-aminoethyl)amino cellulose: a potentiometric titration study. *Cellulose* 18 (1): 33–43. https://doi.org/10.1007/s10570-010-9467-x.

19 Fras-Zemljič, L., Stenius, P., Laine, J., and Stana-Kleinschek, K. (2006). The effect of adsorbed carboxymethyl cellulose on the cotton fibre adsorption capacity for surfactant. *Cellulose* 13 (6): 655–663. https://doi.org/10.1007/s10570-006-9071-2.

20 Hotzel, K., Fras Zemljič, L., Bračič, M., and Heinze, T. (2019). Protonation behavior of dextran amino acid esters. *TUrk. J. Chem.* 43: 869–880. https://doi.org/10.3906/kim-1901-12.

21 Nitta, K. and Sugai, S. (1972). Potentiometric titration studies on globular proteins. *Biopolymers* 11 (9): 1893–1901.

22 Nozaka, M. and Sugai, S. (1978). Detection and characterization of the intermediate on the folding pathway of human .alpha.-lactalbumin. *Biochemistry* 17 (18): 3753–3758. https://doi.org/10.1021/bi00611a013.

23 Ueno, K. and Kina, K. (1985). Colloid titration - a rapid method for the determination of charged colloid. *J. Chem. Educ.* 62 (7): 627–629. https://doi.org/10.1021/ed062p627.

24 Fardim, P., Holmbom, B., Ivaska, A., and Karhu, J. (2002). Critical comparison and validation of methods for determination of anionic groups in pulp fibres. *Nordic Pulp Paper Res. J.* 17 (3): 346–351. https://doi.org/10.3183/npprj-2002-17-03-p346-351.

25 Laine, J. and Stenius, P. (1997). Effect of charge on the fibre and paper properties of bleached industrial kraft pulps. *Pap. Puu/Pap. Tim.* 79: 257–266.

26 Vogel, A.I. (1989). *Textbook of Quantitative Chemical Analysis*, 5e. Harlow: Longman Scientific & Technical.

27 Horn, D. and Heuck, C.C. (1983). Charge determination of proteins with polyelectrolyte titration. *J. Biol. Chem.* 258 (3): 1665–1670. https://www.sciencedirect.com/science/article/pii/S0021925818330370.

28 Puppo, S., Morpurgo, G., Nardi, S., and Conti, G. (1978). Microbiological titration of proteins and of single amino acid content in biological materials without purification and hydrolysis. *Can. J. Microbiol.* 24 (4): 409–414. https://doi.org/10.1139/m78-067.

29 Tagliabue, A., Izzo, L., and Mella, M. (2019). Impact of charge correlation, chain rigidity, and chemical specific interactions on the behavior of weak polyelectrolytes in solution. *J. Phys. Chem. B* 123 (42): 8872–8888. https://doi.org/10.1021/acs.jpcb.9b06017.

30 Kekonen, J. (1996). *Adhesional Properties of Polyamide 6 Fibres Used in Press Felts*. Helsinki University of Tecnology.

31 Wågberg, L. and Hägglund, R. (2001). Kinetics of polyelectrolyte adsorption on cellulosic fibers. *Langmuir* 17 (4): 1096–1103. https://doi.org/10.1021/la000629f.

32 Wågberg, L., Winter, L., Ödberg, L., and Lindström, T. (1987). On the charge stoichiometry upon adsorption of a cationic polyelectrolyte on cellulosic materials. *Colloids Surf.* 27 (1): 163–173. https://doi.org/10.1016/0166-6622(87)80335-9.

33 Delgado, A.V., González-Caballero, F., Hunter, R.J. et al. (2005). Measurement and interpretation of electrokinetic phenomena (IUPAC technical report). *Pure Appl. Chem.* 77 (10): 1753–1805. https://doi.org/10.1351/pac200577101753.

34 Hunter, R.J. (1981). *Zeta Potential in Colloid Science: Principles and Applications*. Academic Press. https://doi.org/10.1016/C2013-0-07389-6.

35 Ohshima, H. (1994). A simple expression for Henry's function for the retardation effect in electrophoresis of spherical colloidal particles. *J. Colloid Interface Sci.* 168 (1): 269–271. https://doi.org/10.1006/jcis.1994.1419.

36 Marlow, B.J., Fairhurst, D., and Pendse, H.P. (1988). Colloid vibration potential and the electrokinetic characterization of concentrated colloids. *Langmuir* 4 (3): 611–626. https://doi.org/10.1021/la00081a021.

37 Dukhin, A.S. and Goetz, P.J. (1998). Characterization of aggregation phenomena by means of acoustic and electroacoustic spectroscopy. *Colloids Surf., A* 144 (1): 49–58. https://doi.org/10.1016/S0927-7757(98)00565-2.

38 O'Brien, R.W., Cannon, D.W., and Rowlands, W.N. (1995). Electroacoustic determination of particle size and zeta potential. *J. Colloid Interface Sci.* 173 (2): 406–418. https://doi.org/10.1006/jcis.1995.1341.

39 Werner, C., Körber, H., Zimmermann, R. et al. (1998). Extended electrokinetic characterization of flat solid surfaces. *J. Colloid Interface Sci.* 208 (1): 329–346. https://doi.org/10.1006/jcis.1998.5787.

40 Werner, C., Jacobasch, H.-J., and Reichelt, G. (1996). Surface characterization of hemodialysis membranes based on streaming potential measurements. *J. Biomater. Sci., Polym. Ed.* 7 (1): 61–76. https://doi.org/10.1163/156856295X00832.

41 Van Den Hoven, T.J.J. and Bijsterbosch, B.H. (1987). Streaming currents, streaming potentials and conductances of concentrated dispersions of negatively-charged, monodisperse polystyrene particles. Effect. *Colloids Surf.* 22 (2): 171–185. https://doi.org/10.1016/0166-6622(87)80219-6.

42 Zimmermann, R., Freudenberg, U., Schweiß, R. et al. (2010). Hydroxide and hydronium ion adsorption — a survey. *Curr. Opin. Colloid Interface Sci.* 15 (3): 196–202. https://doi.org/10.1016/j.cocis.2010.01.002.

43 Lyklema, J. (2011). Surface charges and electrokinetic charges: distinctions and juxtapositionings. *Colloids Surf., A* 376 (1): 2–8. https://doi.org/10.1016/j.colsurfa.2010.09.021.

44 Nonnenmacher, M., O'Boyle, M.P., and Wickramasinghe, H.K. (1991). Kelvin probe force microscopy. *Appl. Phys. Lett.* 58 (25): 2921–2923. https://doi.org/10.1063/1.105227.

45 Israelachvili, J.N. and Tabor, D. (1972). The measurement of van der Waals dispersion forces in the range 1.5 to 130 nm. *Proc. R. Soc. London, Ser. A* 331 (1584): 19–38. https://doi.org/10.1098/rspa.1972.0162.

46 Decher, G., Hong, J.D., and Schmitt, J. (1992). Buildup of ultrathin multilayer films by a self-assembly process: III. Consecutively alternating adsorption of anionic and cationic polyelectrolytes on charged surfaces. *Thin Solid Films* 210–211: 831–835. https://doi.org/10.1016/0040-6090(92)90417-A.

47 Picart, C., Lavalle, P., Hubert, P. et al. (2001). Buildup mechanism for poly(L-lysine)/ hyaluronic acid films onto a solid surface. *Langmuir* 17: 7414–7424. https://doi.org/10.1021/la010848g.

48 Richert, L., Arntz, Y., Schaaf, P. et al. (2004b). pH dependent growth of poly(L-lysine)/poly(L-glutamic) acid multilayer films and their cell adhesion properties. *Surf. Sci.* 570 (1): 13–29. https://doi.org/10.1016/j.susc.2004.06.178.

49 Zhang, J., Senger, B., Vautier, D. et al. (2005). Natural polyelectrolyte films based on layer-by layer deposition of collagen and hyaluronic acid. *Biomaterials* 26 (16): 3353–3361. https://doi.org/10.1016/j.biomaterials.2004.08.019.

50 Niepel, M.S., Peschel, D., Sisquella, X. et al. (2009). pH-dependent modulation of fibroblast adhesion on multilayers composed of poly(ethylene imine) and heparin. *Biomaterials* 30 (28): 4939–4947. https://doi.org/10.1016/j.biomaterials.2009.06.014.

51 Grohmann, S., Rothe, H., Frant, M. et al. (2011). Colloidal force spectroscopy and cell biological investigations on biomimetic polyelectrolyte multilayer coatings composed of chondroitin sulfate and heparin. *Biomacromolecules* 12 (6): 1987–1997. https://doi.org/10.1021/bm200258q.

52 Aggarwal, N., Altgärde, N., Svedhem, S. et al. (2014). Study on multilayer structures prepared from heparin and semi-synthetic cellulose sulfates as polyanions and their influence on cellular response. *Colloids Surf., B* 116: 93–103. https://doi.org/10.1016/j.colsurfb.2013.12.043.

53 Silva, J.M., Caridade, S.G., Costa, R.R. et al. (2015). pH responsiveness of multilayered films and membranes made of polysaccharides. *Langmuir* 31 (41): 11318–11328. https://doi.org/10.1021/acs.langmuir.5b02478.

54 Tanimoto, S., Iwata, T., Yamaoka, H. et al. (2009, 2009). Conformational study of polypeptide chains grafted on the surface of polylactide latex particle. In: *Research Letters in Materials Science* (ed. V. Tsukruk), 196950. Hindawi Publishing Corporation. https://doi.org/10.1155/2009/196950.

55 Nezu, T. and Winnik, F.M. (2000). Interaction of water-soluble collagen with poly(acrylic acid). *Biomaterials* 21 (4): 415–419. https://doi.org/10.1016/S0142-9612(99)00204-5.

56 Aslan, S., Deneufchatel, M., Hashmi, S. et al. (2012). Carbon nanotube-based antimicrobial biomaterials formed via layer-by-layer assembly with polypeptides. *J. Colloid Interface Sci.* 388 (1): 268–273. https://doi.org/10.1016/j.jcis.2012.08.025.

57 Ye, S., Wang, C., Liu, X. et al. (2005). Multilayer nanocapsules of polysaccharide chitosan and alginate through layer-by-layer assembly directly on PS nanoparticles for release. *J. Biomater. Sci., Polym. Ed.* 16 (7): 909–923. https://doi.org/10.1163/1568562054255691.

58 Smirnova, N.V., Kolbe, K.A., Dresvyanina, E.N. et al. (2019). Effect of chitin nanofibrils on biocompatibility and bioactivity of the chitosan-based composite film matrix intended for tissue engineering. *Materials* https://doi.org/10.3390/ma12111874.

59 Sandri, G., Rossi, S., Bonferoni, M.C. et al. (2019). Chitosan/glycosaminoglycan scaffolds for skin reparation. *Carbohydr. Polym.* 220: 219–227. https://doi.org/10.1016/j.carbpol.2019.05.069.

60 Freudenberg, U., Zschoche, S., Simon, F. et al. (2005). Covalent immobilization of cellulose layers onto maleic anhydride copolymer thin films. *Biomacromolecules* 6 (3): 1628–1634. https://doi.org/10.1021/bm0492529.

61 Stana-Kleinschek, K., Kreze, T., Ribitsch, V., and Strnad, S. (2001). Reactivity and electrokinetical properties of different types of regenerated cellulose

fibres. *Colloids Surf., A* 195 (1–3): 275–284. https://doi.org/10.1016/S0927-7757(01)00852-4.

62 Freudenberg, U., Zimmermann, R., Schmidt, K. et al. (2007). Charging and swelling of cellulose films. *J. Colloid Interface Sci.* 309 (2): 360–365. https://doi.org/10.1016/j.jcis.2007.02.047.

63 Sabbah, M., Esposito, M., Di, P.P. et al. (2016). Insight into zeta potential measurements in biopolymer film preparation. *J. Biotechnol. Biomater.* 6 (2): 2–4. https://doi.org/10.4172/2155-952X.1000e126.

64 Facchi, D.P., Lima, A.C., de Oliveira, J.H. et al. (2017). Polyelectrolyte complexes based on alginate/tanfloc: optimization, characterization and medical application. *Int. J. Biol. Macromol.* 103: 129–138. https://doi.org/10.1016/j.ijbiomac.2017.05.033.

65 Mattinen, M.-L., Valle-Delgado, J.J., Leskinen, T. et al. (2018). Enzymatically and chemically oxidized lignin nanoparticles for biomaterial applications. *Enzyme Microb. Technol.* 111: 48–56. https://doi.org/10.1016/j.enzmictec.2018.01.005.

66 Akilbekova, D., Shaimerdenova, M., Adilov, S., and Berillo, D. (2018). Biocompatible scaffolds based on natural polymers for regenerative medicine. *Int. J. Biol. Macromol.* 114: 324–333. https://doi.org/10.1016/j.ijbiomac.2018.03.116.

67 Jung, H.-S., Kim, H.C., and Ho Park, W. (2019). Robust methylcellulose hydrogels reinforced with chitin nanocrystals. *Carbohydr. Polym.* 213: 311–319. https://doi.org/10.1016/j.carbpol.2019.03.009.

68 Matsumoto, H., Yako, H., Minagawa, M., and Tanioka, A. (2007). Characterization of chitosan nanofiber fabric by electrospray deposition: electrokinetic and adsorption behavior. *J. Colloid Interface Sci.* 310 (2): 678–681. https://doi.org/10.1016/j.jcis.2007.02.017.

69 Asran, A.S., Razghandi, K., Aggarwal, N. et al. (2010). Nanofibers from blends of polyvinyl alcohol and polyhydroxy butyrate as potential scaffold material for tissue engineering of skin. *Biomacromolecules* 11 (12): 3413–3421. https://doi.org/10.1021/bm100912v.

70 Croisier, F., Sibret, P., Dupont-Gillain, C. et al. (2015). Chitosan-coated electrospun nanofibers with antibacterial activity. *J. Mater. Chem. B* 3 (17): 3508–1517. https://doi.org/10.1039/C5TB00158G.

71 Plohl, O., Zemljič, L.F., Potrč, S., and Luxbacher, T. (2020). Applicability of electro-osmotic flow for the analysis of the surface zeta potential. *RSC Adv.* 10 (12): 6777–6789. https://doi.org/10.1039/C9RA10414C.

72 Metwally, S., Ferraris, S., Spriano, S. et al. (2020). Surface potential and roughness controlled cell adhesion and collagen formation in electrospun PCL fibers for bone regeneration. *Mater. Des.* 194: 108915. https://doi.org/10.1016/j.matdes.2020.108915.

73 Andrade, Â.L., Ferreira, J.M.F., and Domingues, R.Z. (2004). Zeta potential measurement in bioactive collagen. *Mater. Res.* 7: 631–634.

74 McCune, D., Guo, X., Shi, T. et al. (2018). Electrospinning pectin-based nanofibers: a parametric and cross-linker study. *Appl. Nanosci.* 8 (1): 33–40. https://doi.org/10.1007/s13204-018-0649-4.

75 Okutan, N., Terzi, P., and Altay, F. (2014). Affecting parameters on electrospinning process and characterization of electrospun gelatin nanofibers. *Food Hydrocolloids* 39: 19–26. https://doi.org/10.1016/j.foodhyd.2013.12.022.

76 Chao, F.-C., Wu, M.H., Chen, L.C. et al. (2020). Preparation and characterization of chemically TEMPO-oxidized and mechanically disintegrated sacchachitin nanofibers (SCNF) for enhanced diabetic wound healing. *Carbohydr. Polym.* 229: 115507. https://doi.org/10.1016/j.carbpol.2019.115507.

77 Aguilella, V., Kontturi, K., Murtomäki, L., and Ramírez, P. (1994). Estimation of the pore size and charge density in human cadaver skin. *J. Controlled Release* 32 (3): 249–257. https://doi.org/10.1016/0168-3659(94)90235-6.

78 Raiman, J., Hänninen, K., Kontturi, K. et al. (2003). Drug adsorption in human skin: a streaming potential study. *J. Pharm. Sci.* 92 (12): 2366–2372. https://doi.org/10.1002/jps.10516.

79 Indest, T., Strnad, S., Kleinschek, K.S. et al. (2006). Electrokinetic properties of commercial vascular grafts. *Colloids Surf., A* 275 (1): 17–26. https://doi.org/10.1016/j.colsurfa.2005.09.012.

80 Iviglia, G., Strnad, S., Kleinschek, K.S. et al. (2018). New collagen-coated calcium phosphate synthetic bone filler (Synergoss®): a comparative surface analysis. *Int. J. Appl. Ceram. Technol.* 15 (4): 910–920. https://doi.org/10.1111/ijac.12854.

81 Courtenay, J.C., Johns, M.A., Galembeck, F. et al. (2017). Surface modified cellulose scaffolds for tissue engineering. *Cellulose* 24 (1): 253–267. https://doi.org/10.1007/s10570-016-1111-y.

82 Kowalchuk, R.M., Pollack, S.R., and Corcoran, T.A. (1995). Zeta potential of bone from particle electrophoresis: solution composition and kinetic effects. *J. Biomed. Mater. Res.* 29 (1): 47–57. https://doi.org/10.1002/jbm.820290108.

83 Furuya, M., Shimono, N., and Okamoto, M. (2017). Fabrication of biocomposites composed of natural rubber latex and bone tissue derived from MC3T3-E1 mouse preosteoblastic cells. *Nanocomposites* 3 (2): 76–83. https://doi.org/10.1080/20550324.2017.1352111.

84 Sakthivel, N., Socrates, R., Shanthini, G.M. et al. (2015). Silver ion impregnated composite biomaterial optimally prepared using zeta potential measurements. *Mater. Sci. Eng., C* 47: 222–229. https://doi.org/10.1016/j.msec.2014.11.018.

85 Moreira, C.D.F., Carvalho, S.M., Sousa, R.G. et al. (2018). Nanostructured chitosan/gelatin/bioactive glass in situ forming hydrogel composites as a potential injectable matrix for bone tissue engineering. *Mater. Chem. Phys.* 218: 304–316. https://doi.org/10.1016/j.matchemphys.2018.07.039.

86 Wang, Q., Jamal, S., Detamore, M.S. et al. (2011). PLGA-chitosan/PLGA-alginate nanoparticle blends as biodegradable colloidal gels for seeding human umbilical cord mesenchymal stem cells. *J. Biomed. Mater. Res. Part A* 96A (3): 520–527. https://doi.org/10.1002/jbm.a.33000.

87 Zaupa, A., Byres, N., Dal Zovo, C. et al. (2019). Cold-adaptation of a methacrylamide gelatin towards the expansion of the biomaterial toolbox for specialized functionalities in tissue engineering. *Mater. Sci. Eng., C* 102: 373–390. https://doi.org/10.1016/j.msec.2019.04.020.

88 Lin, W.-C., Lee, S.H., Karakachian, M. et al. (2009). Tuning the surface potential of gold substrates arbitrarily with self-assembled monolayers with mixed functional groups. *Phys. Chem. Chem. Phys.* 11 (29): 6199–6204. https://doi.org/10.1039/B902044F.

89 Schrems, A., Kibrom, A., Küpcü, S. et al. (2011). Bilayer lipid membrane formation on a chemically modified S-layer lattice. *Langmuir* 27 (7): 3731–3738. https://doi.org/10.1021/la104238e.

90 Sleytr, U.W.E.B. (1975). Heterologous reattachment of regular arrays of glycoproteins on bacterial surfaces. *Nature* 257 (5525): 400–402. https://doi.org/10.1038/257400a0.

91 Katzur, V., Eichler, M., Deigele, E. et al. (2012). Surface-immobilized PAMAM-dendrimers modified with cationic or anionic terminal functions: physicochemical surface properties and conformational changes after application of liquid interface stress. *J. Colloid Interface Sci.* 366 (1): 179–190. https://doi.org/10.1016/j.jcis.2011.09.029.

92 Hao, L., Fu, X., Li, T. et al. (2016a). Mediating mesenchymal stem cells responses and osteopontin adsorption via oligo(ethylene glycol)-amino mixed self-assembled monolayers. *J. Mater. Sci. Technol.* 32 (9): 966–970. https://doi.org/10.1016/j.jmst.2016.04.005.

93 Hao, L., Li, T., Zhao, N. et al. (2016b). Surface chemistry from wettability and charge for the control of mesenchymal stem cell fate through self-assembled monolayers. *Colloids Surf., B* 148: 549–556. https://doi.org/10.1016/j.colsurfb.2016.09.027.

94 Nowacka, M., Klapiszewski, Ł., Norman, M., and Jesionowski, T. (2013). Dispersive evaluation and surface chemistry of advanced, multifunctional silica/lignin hybrid biomaterials. *Cent. Eur. J. Chem.* 11 (11): 1860–1873. https://doi.org/10.2478/s11532-013-0322-4.

95 Frant, M., Stenstad, P., Johnsen, H. et al. (2006). Anti-infective surfaces based on tetraether lipids for peritoneal dialysis catheter systems. *Materialwiss. Werkstofftech.* 37 (6): 538–545. https://doi.org/10.1002/mawe.200600034.

96 Zimmermann, R., Küttner, D., Renner, L. et al. (2009). Charging and structure of zwitterionic supported bilayer lipid membranes studied by streaming current measurements, fluorescence microscopy, and attenuated total reflection Fourier transform infrared spectroscopy. *Biointerphases* 4 (1): 1–6. https://doi.org/10.1116/1.3082042.

97 Zimmermann, R., Küttner, D., Renner, L. et al. (2012). Fluidity modulation of phospholipid bilayers by electrolyte ions: insights from fluorescence microscopy and microslit electrokinetic experiments. *J. Phys. Chem. A* 116 (25): 6519–6525. https://doi.org/10.1021/jp212364q.

98 Shah, R., Eldridge, D., Palombo, E., and Harding, I. (2014). Optimisation and stability assessment of solid lipid nanoparticles using particle size and zeta potential. *J. Phys. Sci.* 25 (1): 59–75.

99 Smith, M.C., Crist, R.M., Clogston, J.D., and McNeil, S.E. (2017). Zeta potential: a case study of cationic, anionic, and neutral liposomes. *Anal. Bioanal. Chem.* 409 (24): 5779–5787. https://doi.org/10.1007/s00216-017-0527-z.

100 Morini, M.A., Sierra, M.B., and Pedroni, V.I. (2015). Influence of temperature, anions and size distribution on the zeta potential of DMPC, DPPC and DMPE lipid vesicles. *Colloids Surf., B* 131: 54–58. https://doi.org/10.1016/j.colsurfb.2015.03.054.

101 Chibowski, E. and Szcześ, A. (2016). Zeta potential and surface charge of DPPC and DOPC liposomes in the presence of PLC enzyme. *Adsorption* 22 (4): 755–765. https://doi.org/10.1007/s10450-016-9767-z.

102 Freire, J.M., Domingues, M.M., Matos, J. et al. (2011). Using zeta-potential measurements to quantify peptide partition to lipid membranes. *Eur. Biophys. J.* 40 (4): 481–487. https://doi.org/10.1007/s00249-010-0661-4.

103 Soema, P.C., Willems, G.J., Jiskoot, W. et al. (2015). Predicting the influence of liposomal lipid composition on liposome size, zeta potential and liposome-induced dendritic cell maturation using a design of experiments approach. *Eur. J. Pharm. Biopharm.* 94: 427–435. https://doi.org/10.1016/j.ejpb.2015.06.026.

104 Oyarzun-Ampuero, F.A., Rivera-Rodríguez, G.R., Alonso, M.J., and Torres, D. (2013). Hyaluronan nanocapsules as a new vehicle for intracellular drug delivery. *Eur. J. Pharm. Sci.* 49 (4): 483–490. https://doi.org/10.1016/j.ejps.2013.05.008.

105 Hirsjärvi, S., Dufort, S., Bastiat, G. et al. (2013). Surface modification of lipid nanocapsules with polysaccharides: from physicochemical characteristics to in vivo aspects. *Acta Biomater.* 9 (5): 6686–6693. https://doi.org/10.1016/j.actbio.2013.01.038.

106 Caruso, F., Rodda, E., and Furlong, D.N. (1997b). Quartz crystal microbalance study of DNA immobilization and hybridization for nucleic acid sensor development. *Anal. Chem.* 69 (11): 2043–2049.

107 Gericke, M., Höök, F., Fredriksson, C. et al. (2011). Semi-synthetic polysaccharide sulfates as anticoagulant coatings for PET, 1 - cellulose sulfate. *Macromol. Biosci.* 11 (4): 549–556. https://doi.org/10.1002/mabi.201000419.

108 Rodahl, M., Doliška, A., Stana, J. et al. (1997). Simultaneous frequency and dissipation factor QCM measurements of biomolecular adsorption and cell adhesion. *Faraday Discuss.* 107: 229–246. https://doi.org/10.1039/a703137h.

109 Höök, F., Vörös, J., Rodahl, M. et al. (2002). A comparative study of protein adsorption on titanium oxide surfaces using in situ ellipsometry, optical waveguide lightmode spectroscopy, and quartz crystal microbalance/dissipation. *Colloids Surf., B* 24 (2): 155–170. https://doi.org/10.1016/S0927-7765(01)00236-3.

110 Drescher, D.G., Drescher, M.J., and Ramakrishnan, N.A. (2009). Surface plasmon resonance (SPR) analysis of binding interactions of proteins in inner-ear sensory epithelia BT - auditory and vestibular research: methods and protocols. In: *Auditory and Vestibular Research* (ed. B. Sokolowski), 323–343. Totowa, NJ: Humana Press https://doi.org/10.1007/978-1-59745-523-7_20.

111 Jaffrezic-Renault, N., Pichat, P., Foissy, A. et al. (1986). Study of the effect of deposited platinum particles on the surface charge of titania aqueous suspensions by potentiometry, electrophoresis, and labeled-ion adsorption. *J. Phys. Chem.* 90 (12): 2733–2738. https://doi.org/10.1021/j100403a035.

112 Hollenbeck, R.G., Peck, G.E., Kildsig, D.A.N.E., and Pip, I. (1978). Application of immersional calorimetry to microcrystalline cellulose-water system. *J. Pharm. Sci.* 67 (11): 1599–1606.

113 Kramer, G. and Somasundaran, P. (2004). Fluorescence and ESR studies of the conformational behavior of oppositely charged polyelectrolytes at solid / liquid interfaces. *J. Colloid Interface Sci.* 273: 115–120. https://doi.org/10.1016/j.jcis.2004.01.009.

114 Vogt, B.D., Lin, E.K., Wu, W.I., and White, C.C. (2004). Effect of film thickness on the validity of the sauerbrey equation for hydrated polyelectrolyte films. *J. Phys. Chem. B* 108 (34): 12685–12690. https://doi.org/10.1021/jp0481005.

115 Sauerbrey, G. (1957). Wagung dunner Schichten mit Schwingquarzen. *Angew. Chem. Int. Ed. Engl.* 69: 761–761.

116 Sauerbrey, G. (1959). The use of quarts oscillators for weighing thin layers and for microweighing. *Z. Angew. Phys.* 155: 206–222.

117 Kanazawa, K.K. and Gordon, J.G. (1985). Frequency of a quartz microbalance in contact with liquid. *Anal. Chem.* 57 (8): 1770–1771. https://doi.org/10.1021/ac00285a062.

118 Martin, S.J., Granstaff, V.E., and Frye, G.C. (1991). Characterization of a quartz crystal microbalance with simultaneous mass and liquid loading. *Anal. Chem.* 63 (20): 2272–2281. https://doi.org/10.1021/ac00020a015.

119 Nomura, T. and Okuhara, M. (1982). Frequency shifts of piezoelectric quartz crystals immersed in organic liquids. *Anal. Chim. Acta* 142: 281–284. https://doi.org/10.1016/S0003-2670(01)95290-0.

120 Sedeva, I.G., Fornasiero, D., Ralston, J., and Beattie, D.A. (2010). Reduction of surface hydrophobicity using a stimulus-responsive polysaccharide. *Langmuir* 26 (20): 15865–15874. https://doi.org/10.1021/la101695w.

121 Antunes, J.C., Pereira, C.L., and Molinos, M. (2011). Layer-by-layer self-assembly of chitosan and poly(gamma-glutamic acid) into polyelectrolyte complexes. *Biomacromolecules* 12: 4183–4195. https://doi.org/10.1021/bm2008235.

122 Lundin, M., Solaqa, F., and Thormann, E. (2011). Layer-by-layer assemblies of chitosan and heparin: effect of solution ionic strength and pH. *Langmuir* 27 (12): 7537–7548. https://doi.org/10.1021/la200441u.

123 Höök, F. et al. (1998). Energy dissipation kinetics for protein and antibody – antigen adsorption under shear oscillation on a quartz crystal microbalance. *Langmuir* 7463 (21): 729–734. https://doi.org/10.1021/la970815u.

124 Höök, F., Kasemo, B., and Nylander, T. (2001). Variations in coupled water, viscoelastic properties, and film thickness of a Mefp-1 protein film during adsorption and cross-linking: a quartz crystal microbalance with dissipation monitoring, ellipsometry, and surface plasmon resonance study. *Anal. Chem.* 73 (24): 5796–5804. https://doi.org/10.1021/ac0106501.

125 Luo, Y., Liu, T., and Zhu, J. (2015). Label-free and sensitive detection of thrombomodulin, a marker of endothelial cell injury, using quartz crystal microbalance. *Anal. Chem.* 87: 11277–11284. https://doi.org/10.1021/acs.analchem.5b02447.

126 Ahola, S., Turon, X., and Osterberg, M. (2008a). Enzymatic hydrolysis of native cellulose nanofibrils and other cellulose model films: effect of surface structure. *Langmuir* 24 (20): 11592–11599. https://doi.org/10.1021/la801550j.

127 Irwin, E.F., Ho, J.E., Kane, S.R., and Healy, K.E. (2005). Analysis of interpenetrating polymer networks via quartz crystal microbalance with dissipation monitoring. *Langmuir* 21 (12): 5529–5536. https://doi.org/10.1021/la0470737.

128 Holler, F.J., Skoog, D.A., and Crouch, S. (2007). *Principles of Instrumental Analysis*, 6e. Cengage Learning.

129 Manbachi, A. and Cobbold, R.S.C. (2011). Development and application of piezoelectric materials for ultrasound generation and detection. *Ultrasound* 19 (4): 187–196. https://doi.org/10.1258/ult.2011.011027.

130 Gautschi, G. (2002). *Piezoelectric Sensorics: Force, Strain, Pressure, Acceleration and Acoustic Emission Sensors, Materials and Amplifiers*. Berlin, Heidelberg: Springer-Verlag.

131 Doliška, A. (2011). Uporaba kremenove mikrotehtnice za spremljanje adsorpcije biopolimerov. *Tekstilec* 54 (7–9): 172–180.

132 Höök, F. (1997). *Development of a Novel QCM Technique for Protein Adsorption Studies*. Chalmers University of Technology.

133 Voinova, M.V., Jonson, M., and Kasemo, B. (2002). "Missing mass" effect in biosensor's QCM applications. *Biosens. Bioelectron.* 17 (10): 835–841. https://doi.org/10.1016/S0956-5663(02)00050-7.

134 Larsson, C., Rodahl, M., and Ho, F. (2003). Characterization of DNA immobilization and subsequent hybridization on a 2D arrangement of streptavidin on a biotin-modified lipid bilayer supported on SiO_2. *Anal. Chem.* 75 (19): 8887–8894. https://doi.org/10.1021/ac034269n.

135 Lucklum, R., Behling, C., and Hauptmann, P. (2000). Gravimetric and non-gravimetric chemical quartz crystal resonators. *Sens. Actuators, B* 65 (1): 277–283. https://doi.org/10.1016/S0925-4005(99)00311-1.

136 Reimhult, E., Larsson, C., Kasemo, B., and Ho, F. (2004). Simultaneous surface plasmon resonance and quartz crystal microbalance with dissipation monitoring measurements of biomolecular adsorption events involving structural transformations and variations in coupled water. *Anal. Chem.* 76 (24): 7211–7220. https://doi.org/10.1021/ac0492970.

137 Sadman, K., Wiener, C.G., and Weiss, R.A. (2018). Quantitative rheometry of thin soft materials using the quartz crystal microbalance with dissipation. *Anal. Chem.* https://doi.org/10.1021/acs.analchem.7b05423.

138 Voinova, M.V. (1999). Viscoelastic acoustic response of layered polymer films at fluid-solid interfaces: continuum mechanics approach. *Phys. Scr.* 59: 391–396. https://doi.org/10.1238/Physica.Regular.059a00391.

139 Martin, E.J., Mathew, M.T., and Shull, K.R. (2015). Viscoelastic properties of electrochemically deposited protein/metal complexes. *Langmuir* https://doi.org/10.1021/acs.langmuir.5b00169.

140 Hiep, H.M., Endo, T., and Kerman, K. (2007). A localized surface plasmon resonance based immunosensor for the detection of casein in milk A localized

surface plasmon resonance based immunosensor for the detection of casein in milk. *Sci. Technol. Adv. Mater.* 6996. https://doi.org/10.1016/j.stam.2006.12.010.

141 Zeng, S., Baillargeat, D., Ho, H.P., and Yong, K.T. (2014). Nanomaterials enhanced surface plasmon resonance for biological and chemical sensing applications. *Chem. Soc. Rev.* 43 (10): 3426–3452. https://doi.org/10.1039/C3CS60479A.

142 Zeng, S., Yu, X., Law, W.C. et al. (2013). Chemical size dependence of Au NP-enhanced surface plasmon resonance based on differential phase measurement. *Sens. Actuators, B* 176: 1128–1133.

143 De Feijter, J.A., Benjamins, J., and Veer, F.A. (1978). Ellipsometry as a tool to study the adsorption behavior of synthetic and biopolymers at the air–water interface. *Biopolymers* 17 (7): 1759–1772. https://doi.org/10.1002/bip.1978.360170711.

144 Cuypers, P.A., Corsel, J.W., Janssen, M.P. et al. (1983). The adsorption of prothrombin to phosphatidylserine multilayers quantitated by ellipsometry*. *J. Biol. Chem.* 258 (4): 2426–2431.

145 Elschner, T., Doliška, A., Bračič, M. et al. (2015). Film formation of ω-aminoalkylcellulose carbamates - a quartz crystal microbalance (QCM) study. *Carbohydr. Polym.* 116: https://doi.org/10.1016/j.carbpol.2014.04.101.

146 Hemmersam, A.G., Foss, M., Chevallier, J., and Besenbacher, F. (2005). Adsorption of fibrinogen on tantalum oxide, titanium oxide and gold studied by the QCM-D technique. *Colloids Surf. B* 43: 208–215. https://doi.org/10.1016/j.colsurfb.2005.04.007.

147 Hemmersam, A.G., Rechendorff, K., and Foss, M. (2008). Fibronectin adsorption on gold, Ti- , and Ta-oxide investigated by QCM-D and RSA modelling. *J. Colloid Interface Sci.* 320: 110–116. https://doi.org/10.1016/j.jcis.2007.11.047.

148 Ziegler, H.S.M.M.C. (2003). Protein adsorption on surfaces : dynamic contact-angle (DCA) and quartz-crystal microbalance (QCM) measurements. *Anal. Bioanal. Chem. Res.* 53–61. https://doi.org/10.1007/s00216-002-1664-5.

149 Chandrasekaran, N., Dimartino, S., and Fee, C.J. (2013). Chemical engineering research and design study of the adsorption of proteins on stainless steel surfaces using QCM-D. *Chem. Eng. Res. Des.* 91 (9): 1674–1683. https://doi.org/10.1016/j.cherd.2013.07.017.

150 Gispert, M.P., Serro, A.P., Colac, R., and Saramago, B. (2008). Bovine serum albumin adsorption onto 316L stainless steel and alumina: a comparative study using depletion, protein radiolabeling, quartz crystal microbalance and atomic force microscopy. *Surf. Interface Anal.* 1529–1537. https://doi.org/10.1002/sia.2929.

151 Hedberg, Y., Wang, X., Hedberg, J. et al. (2013). Surface-protein interactions on different stainless steel grades: effects of protein adsorption, surface changes and metal release. *J. Mater. Sci.: Mater. Med.* 1015–1033. https://doi.org/10.1007/s10856-013-4859-8.

152 Lundin, M., Hedberg, Y., and Jiang, T. (2012). Adsorption and protein-induced metal release from chromium metal and stainless steel. *J. Colloid Interface Sci.* 366: 155–164. https://doi.org/10.1016/j.jcis.2011.09.068.

153 Andersson, M., Andersson, J., and Sellborn, A. (2005). Quartz crystal microbalance-with dissipation monitoring (QCM-D) for real time measurements of blood coagulation density and immune complement activation on artificial surfaces. *Biosens. Bioelectron.* 21: 79–86. https://doi.org/10.1016/j.bios.2004.09.026.

154 Kargl, R., Mohan, T., and Bračč, M. (2012). Adsorption of carboxymethyl cellulose on polymer surfaces: evidence of a specific interaction with cellulose. *Langmuir* 28 (31): 11440–11447. https://doi.org/10.1021/la302110a.

155 Serro, A.P., Degiampietro, K., and Colac, R. (2010). Biointerfaces adsorption of albumin and sodium hyaluronate on UHMWPE : a QCM-D and AFM study. *Colloids Surf., B* 78: 1–7. https://doi.org/10.1016/j.colsurfb.2010.01.022.

156 Bračič, M., Mohan, T., and Kargl, R. (2014). Preparation of PDMS ultrathin films and patterned surface modification with cellulose. *RSC Adv.* 4 (23): 11955–11961. https://doi.org/10.1039/C3RA47380E.

157 Bračič, M., Fras-Zemljič, L., Pérez, L. et al. (2017a). One-step noncovalent surface functionalization of PDMS with chitosan-based bioparticles and their protein-repellent properties. *Adv. Mater. Interfaces* 4 (21): 1–11. https://doi.org/10.1002/admi.201700416.

158 Bračič, M., Mohan, T., Griesser, T. et al. (2017b). Protein-repellent and antimicrobial nanoparticle coatings from hyaluronic acid and a lysine-derived biocompatible surfactant. *J. Mater. Chem. B* 5 (21): https://doi.org/10.1039/c7tb00311k.

159 Ahola, S., Salmi, J., Johansson, L. et al. (2008b). Model films from native cellulose nanofibrils. Preparation, swelling, and surface interactions. *Biomacromolecules* 9: 1273–1282.

160 Kittle, J.D., Du, X., Jiang, F. et al. (2011). Equilibrium water contents of cellulose films determined via solvent exchange and quartz crystal microbalance with dissipation monitoring. *Biomacromolecules* 12: 2881–2887. https://doi.org/10.1021/bm200352q.

161 Mohan, T., Kargl, R., Doliška, A. et al. (2011). Wettability and surface composition of partly and fully regenerated cellulose thin films from trimethylsilyl cellulose. *J. Colloid Interface Sci.* 358 (2): 604–610. https://doi.org/10.1016/j.jcis.2011.03.022.

162 Mohan, T., Niegelhell, K., Zarth, C.S.P. et al. (2014). Triggering protein adsorption on tailored cationic cellulose surfaces. *Biomacromolecules* 15 (11): 3931–3941. https://doi.org/10.1021/bm500997s.

163 Ristić, T., Mohan, T., Kargl, R. et al. (2014). A study on the interaction of cationized chitosan with cellulose surfaces. *Cellulose* 21 (4): 2315–2325. https://doi.org/10.1007/s10570-014-0267-6.

164 Breitwieser, D., Spirk, S., Fasl, H. et al. (2013). Design of simultaneous antimicrobial and anticoagulant surfaces based on nanoparticles and polysaccharides. *J. Mater. Chem. B* 1: 2022–2030. https://doi.org/10.1039/c3tb00272a.

165 Mohan, T., Ristić, T., Kargl, R. et al. (2013). Cationically rendered biopolymer surfaces for high protein affinity support matrices. *Chem. Commun.* 49 (98): 11530. https://doi.org/10.1039/c3cc46414h.

166 da Granja, C.S., Glen, K., Sandström, N. et al. (2020). A quartz crystal resonator for cellular phenotyping. *Biosens. Bioelectron.* 6: 1–12.

167 Kushiro, K., Lee, C., and Takai, M. (2016). Biomaterials science and cell – protein interactions using dynamic QCM-D analysis on SAM surfaces. *Biomater. Sci.* 989–997. https://doi.org/10.1039/c5bm00613a.

168 Lord, M.S., Whitelock, J.M., Simmons, A. et al. (2014). Fibrinogen adsorption and platelet adhesion to silica surfaces with stochastic nanotopography. *Biointerphases* 9 (4): 041002. https://doi.org/10.1116/1.4900993.

169 Şeker, Ş., Elçin, A.E., and Elçin, Y.M. (2016). Real-time monitoring of mesenchymal stem cell responses to biomaterial surfaces and to a model drug by using quartz crystal microbalance biomaterial surfaces and to a model drug by using quartz crystal. *Artif. Cells Nanomed. Biotechnol.* 1401: https://doi.org/10.3109/21691401.2015.1089255.

170 Watarai, E., Matsuno, R., Konno, T. et al. (2012). QCM-D analysis of material – cell interactions targeting a single cell during initial cell attachment. *Sens. Actuators, B* 172: 1297–1302.

171 Yongabi, D., Jooken, S., Givanoudi, S. et al. (2020). Ionic strength controls long-term cell-surface interactions – a QCM-D study of S. cerevisiae adhesion, retention and detachment. *J. Colloid Interface Sci.* 585: 583–595.

172 Orelma, H., Teerinen, T., Johansson, L.S. et al. (2012). CMC-modified cellulose biointerface for antibody conjugation. *Biomacromolecules* 13 (4): 1051–1058. https://doi.org/10.1021/bm201771m.

173 Thalla, P.K., Fadlallah, H., Liberelle, B. et al. (2014). Chondroitin sulfate coatings display low platelet but high endothelial cell adhesive properties favorable for vascular implants. *Biomacromolecules* https://doi.org/10.1021/bm5003762.

174 Kargl, R., Fadlallah, H., Liberelle, B. et al. (2015). Selective immobilization and detection of DNA on biopolymer supports for the design of microarrays. *Biosens. Bioelectron.* 68: 437–441. https://doi.org/10.1016/j.bios.2015.01.038.

175 Rawle, R.J., Johal, M.S., and Selassie, C.R.D. (2008). A real-time QCM-D approach to monitoring mammalian DNA damage using dna adsorbed to a polyelectrolyte surface. *Biomacromolecules* (II): 9–12. https://doi.org/10.1021/bm701062f.

176 Sun, L., Frykholm, K., Fornander, L.H. et al. (2014). Sensing conformational changes in DNA upon ligand binding using QCM-D. Polyamine condensation and Rad51 extension of DNA layers. *J. Phys. Chem. B* 118: 11895–11904. https://doi.org/10.1021/jp506733w.

177 Asker, D., Awad, T.S., Baker, P. et al. (2018). Non-eluting, surface-bound enzymes disrupt surface attachment of bacteria by continuous biofilm polysaccharide degradation. *Biomaterials* 167: 168–176. https://doi.org/10.1016/j.biomaterials.2018.03.016.

178 Chen, M.-y., Chen, M.j., Lee, P.f. et al. (2010). Towards real-time observation of conditioning film and early biofilm formation under laminar flow conditions using a quartz crystal microbalance. *Biochem. Eng. J.* 53 (1): 121–130. https://doi.org/10.1016/j.bej.2010.10.003.

179 Olsson, A.L.J., Van der Mei, H.C., Busscher, H.J., and Sharma, P.K. (2009). Influence of cell surface appendages on the bacterium - substratum interface measured real-time using QCM-D. *Langmuir* 25 (9): 1627–1632. https://doi.org/10.1021/la803301q.

180 Olsson, A. L. J., Wargenau, A. and Tufenkji, N. (2016) 'Optimizing bacteriophage surface densities for bacterial capture and sensing in quartz crystal microbalance with dissipation monitoring'. https://doi.org/10.1021/acsami.6b02227. *Appl. Mater. Interfaces*. 8 13698-13706.

181 Otto, K. and Elwing, H. (1999). Effect of ionic strength on initial interactions of *Escherichia coli* with surfaces, studied on-line by a novel quartz crystal microbalance technique. *J. Bacteriol.* 181 (17): 5210–5218.

182 Shan, Y. Liu L, Liu Y, et al. (2020) 'Effects of electrokinetic phenomena on bacterial deposition monitored by quartz crystal microbalance with dissipation monitoring'. https://doi.org/10.1021/acs.est.0c04347. *Environ. Sci. Technol.*

183 Tarnapolsky, A. and Freger, V. (2018) 'Modeling QCM-D response to deposition and attachment of microparticles and living cells'. https://doi.org/10.1021/acs.analchem.8b03411. *Anal. Chem.*

184 Ayela, C., Roquet, F., Valera, L. et al. (2007). Antibody – antigenic peptide interactions monitored by SPR and QCM-D A model for SPR detection of IA-2 autoantibodies in human serum ☪. *Biosens. Bioelectron.* 22: 3113–3119. https://doi.org/10.1016/j.bios.2007.01.020.

185 Caruso, F., Niikura, K., Furlong, D.N., and Okahata, Y. (1997a). 1 . Ultrathin multilayer polyelectrolyte films on gold: construction and thickness determination. *Langmuir* 7463 (10): 3422–3426. https://doi.org/10.1021/la960821a.

186 Kößlinger, C., Uttenthaler, E., Drost, S. et al. (1995). Comparison of the QCM and the SPR method for surface studies and immunological applications. *Sens. Actuators, B* 5: 107–112.

187 Reischl, M. et al. (2008). Oscillating streaming potential measurement system for macroscopic surfaces. *Rev. Sci. Instrum.* 79 (11): 2–7. https://doi.org/10.1063/1.3020699.

188 Zhang, Y., Luo, S., Tang, Y. et al. (2008). Carbohydrate - protein interactions by " clicked " carbohydrate self-assembled monolayers. *Anal. Chem.* 78 (6): 2001–2008.

189 Benbow, N.L., Webber, J.L., Karpiniec, S. et al. (2017). The influence of polyanion molecular weight on polyelectrolyte multilayers at surfaces: protein adsorption and protein–polysaccharide complexation/stripping on natural polysaccharide films on solid supports. *Phys. Chem. Chem. Phys.* 19: 23790–23801. https://doi.org/10.1039/C7CP02599H.

190 Croll, T.I., O'Connor, A.J., Stevens, G.W. et al. (2006). A blank slate? Layer-by-layer deposition of hyaluronic acid and chitosan onto various surfaces. *Biomacromolecules* 7 (5): 1610–1622. https://doi.org/10.1021/bm060044l.

191 Kujawa, P., Moraille, P., Sanchez, J. et al. (2005). Effect of molecular weight on the exponential growth and morphology of hyaluronan/chitosan multilayers: a surface plasmon resonance spectroscopy and atomic force microscopy

investigation. *J. Am. Chem. Soc.* 127 (25): 9224–9234. https://doi.org/10.1021/ja044385n.

192 Richert, L., Lavalle, P., Payan, E. et al. (2004a). Layer by layer buildup of polysaccharide films : physical chemistry and cellular adhesion aspects. *Langmuir* 9: 448–458. https://doi.org/10.1021/la035415n.

193 Mohan, T., Nagaraj, C., Nagy, B.M. et al. (2019). Nano- and micropatterned polycaprolactone cellulose composite surfaces with tunable protein adsorption, fibrin clot formation, and endothelial cellular response. *Biomacromolecules* 20: 2327–2337. https://doi.org/10.1021/acs.biomac.9b00304.

194 Strasser, S., Niegelhell, K., Kaschowitz, M. et al. (2016). Exploring nonspecific protein adsorption on lignocellulosic amphiphilic bicomponent films. *Biomacromolecules* 17: 1083–1092. https://doi.org/10.1021/acs.biomac.5b01700.

195 Gorochovceva, N., Naderi, A., Dedinaite, A. et al. (2005). Chitosan-N-poly(ethylene glycol) brush copolymers: synthesis and adsorption on silica surface. *Eur. Polym. J.* 41 (11): 2653–2662. https://doi.org/10.1016/j.eurpolymj.2005.05.021.

196 Czernohlavek, C. and Schuster, B. (2020). Formation and characteristics of mixed lipid/polymer membranes on a crystalline surface-layer protein lattice. *Biointerphases* 15 (1): https://doi.org/10.1116/1.5132390.

197 Lin, W., Xu, L., Liu, S. et al. (2020). Resistance to long-term bacterial biofilm formation based on hydrolysis-induced zwitterion material with biodegradable and self-healing properties. *Langmuir* 36 (12): 3251–3259. https://doi.org/10.1021/acs.langmuir.0c00006.

198 Endo, T., Kerman, K., Nagatani, N. et al. (2006). Multiple label-free detection of antigen-antibody reaction using localized surface plasmon resonance-based core-shell structured nanoparticle. *Anal. Chem.* 78 (18): 6465–6475. https://doi.org/10.1021/ac0608321.

199 Francesko, A., Fernandes, M.M., Ivanova, K. et al. (2016). Bacteria-responsive multilayer coatings comprising polycationic nanospheres for bacteria biofilm prevention on urinary catheters. *Acta Biomater.* 33: 203–212. https://doi.org/10.1016/j.actbio.2016.01.020.

200 Stair, J.L., Watkinson, M., and Krause, S. (2009). Sensor materials for the detection of proteases. *Biosens. Bioelectron.* 24 (7): 2113–2118. https://doi.org/10.1016/j.bios.2008.11.002.

201 Elschner, T., Reishofer, D., Kargl, R. et al. (2016). Reactive cellulose-based thin films – a concept for multifunctional polysaccharide surfaces. *RSC Adv.* 6: 72378–72385. https://doi.org/10.1039/C6RA14227C.

202 Norde, W. and Rouwendal, E. (1990). Streaming potential measurements as a tool to study protein adsorption kinetics. *J. Colloid Interface Sci.* 139 (1): 169–176. https://doi.org/10.1016/0021-9797(90)90454-V.

203 Zembala, M. and Déjardin, P. (1994). Streaming potential measurements related to fibrinogen adsorption onto silica capillaries. *Colloids Surf., B* 3 (1): 119–129. https://doi.org/10.1016/0927-7765(93)01119-C.

204 Werner, C., König, U., Augsburg, A. et al. (1999). Electrokinetic surface characterization of biomedical polymers — a survey. *Colloids Surf., A* 159 (2): 519–529. https://doi.org/10.1016/S0927-7757(99)00290-3.

205 Ethève, J. and Déjardin, P. (2002). Adsorption kinetics of lysozyme on silica at pH 7.4: correlation between streaming potential and adsorbed amount. *Langmuir* 18 (5): 1777–1785. https://doi.org/10.1021/la011224d.

206 Kawasaki, K. et al. (2003). A comparison of the adsorption of saliva proteins and some typical proteins onto the surface of hydroxyapatite. *Colloids Surf., B* 32 (4): 321–334. https://doi.org/10.1016/j.colsurfb.2003.07.001.

207 Zimmermanna, R. et al. (2007). Combined microslit electrokinetic measurements and reflectometric interference spectroscopy to study protein adsorption processes. *Biointerphases* 2 (4): 159–164. https://doi.org/10.1116/1.2814066.

208 Razzak, M.A. et al. (2017). Deciphering the interactions of fish gelatine and hyaluronic acid in aqueous solutions. *Int. J. Biol. Macromol.* 102: 885–892. https://doi.org/10.1016/j.ijbiomac.2017.04.083.

5

Methods for Analyzing the Biological and Biomedical Properties of Biomaterials

Jan Rožanc and Uroš Maver

University of Maribor, Institute of Biomedical Sciences, Faculty of Medicine, Taborska ulica 8, SI-2000 Maribor, Slovenia

5.1 Introduction

The field of biomaterials is rapidly evolving by building on cutting-edge advances in the areas of biology, chemistry, medicine, material science, and bioengineering. A biomaterial is a biological or synthetic substance (e.g. metals, ceramics, polymers, hydrogels, glasses, composites) that is designed to interact with the living tissue. Besides their chemical and physical properties, rendering them suitable for specific applications, biomaterials need to be also evaluated regarding their biological properties. These include their interaction with cells, tissues, and/or whole organisms, which should be made to assess their safety and efficacy. How cells adhere and colonize the surface of a biomaterial to initiate processes like growth, proliferation, migration, and differentiation is critical in promoting new tissue formation and regeneration. Such processes are complex and involve many physiochemical events on different scales ranging from molecular to cell organelle to tissue and system level. The evaluation of cell–material interactions is a fundamental step in assessing biocompatibility.

The "traditional" definition of biocompatibility has been challenged by recent developments in the field and the vastly increased understanding of the biological mechanisms associated with the host response. The most widely cited definition proposed back in 1986 at the *Consensus Conference on Biomaterials* defined biocompatibility as "the ability of a material to perform with an appropriate host response in a specific application" [1]. While accurate, it does not provide any information on how to evaluate or modulate biocompatibility. In 2008, an updated version was proposed, stating that biocompatibility "refers to the ability of a biomaterial to perform its desired function with respect to medical therapy, without eliciting any undesirable local or systemic effects in the recipient or beneficiary of that therapy, but generating the most appropriate beneficial cellular or tissue response in that specific situation, and optimizing the clinically relevant performance of that therapy" [2]. While this definition is more complete, it does not make any distinction

Functional Biomaterials: Design and Development for Biotechnology, Pharmacology, and Biomedicine, First Edition. Edited by Tamilselvan Mohan and Karin Stana Kleinschek.

between traditional long-lasting implants and more recent tissue-engineering (TE) products aimed at promoting integration, regeneration, and healing. To also account for this, a manifesto was written in 2011 [3], proposing two definitions, one for biocompatibility: "the ability of a material to locally trigger and guide nonfibrotic wound healing, reconstruction and tissue integration," which is more adequate for TE products, and one for biotolerability: "the ability of a material to reside in the body for long periods of time with only low degrees of inflammatory reaction," which is more suitable to describe the performance of more traditional, nondegrading or slow-degrading, implant materials.

Like all products intended for use in the human body, medical devices and biomaterials need to be evaluated for their performance and safety. Regulatory agencies require biomaterials to go through a screening process to validate biocompatibility and biotolerability, which involves a complex evaluation of *in vitro* and *in vivo* assessment. This is a well-established practice in the field, with international standard protocols providing guidelines on testing approaches and methodologies. As a starting point, evaluation of toxicity (cytotoxicity) is performed, and the results are widely used as an effective indicator of biomaterial *in vivo* toxicity potential. Other important tests include evaluation of mutagenic and carcinogenic potential. However, biocompatibility must not only be evaluated in terms of potentially harmful effects (non-toxic, nonmutagenic, and noncarcinogenic), but also in terms of desirable effects in the context of its application and function. As such, the TE scaffold should be biocompatible in terms of providing a substrate for supporting proper cellular activities (growth, extracellular matrix [ECM] deposition, desired gene expression, optimal tissue repair, and regeneration). In fact, many of such biomaterials used in regenerative medicine are developed to be "cell instructive" and have the ability to guide cell behavior and elicit specific cell response [4]. After the first screening for cytotoxicity, if the material is found nontoxic, other tests are carried out to provide general or more specific information on cellular behavior. These include assessing cell–biomaterial interactions through evaluation of cell adhesion and morphology, metabolic activity, proliferation, migration, protein and gene expression, or differentiation. There is a wide variety of tests available, and only some of them will be described here. In addition to these well-established standard testing methodologies, this chapter also briefly describes some emerging technologies such as high-throughput screening (HTS), intracellular monitoring technologies, and real-time analysis.

Ideally, materials should be tested in their final form as cell response, besides biochemical properties, it also depends also on the shape, porosity, topography, mechanical properties, all of which should be taken into account when analyzing cell–biomaterial interaction. Biomaterial-based platforms for TE and regenerative medicine are increasingly translated from 2D into 3D cell culture models, which adds another level of complexity. It is important that the protocols for analyzing cell behavior should be adequately adapted from 2D into the 3D setting, and the procedures and result interpretation should be carried out with caution. The use of 3D *in vitro* testing is becoming widely used as it provides more physiologically relevant information compared to the reductionist 2D system, which often fails

to recapitulate key features of the natural cellular microenvironment [5]. The use of advanced 3D cell culture systems has proven to be more predictive for *in vivo* tests and possibly reducing the number of animals used in research and testing, coinciding well with guiding principles of 3Rs (Replace, Reduce, Refine) [6]. Although great strides of efforts are put in replacing animal experiments whenever possible, some properties of biomaterials (e.g. sensitization, irritation, biodegradation, systemic toxicity, immune response) cannot be tested *in vitro* and require *in vivo* assessment for the final evaluation before human use. This chapter provides an overview of both *in vitro* and *in vivo* methods used to evaluate the biological and biomedical properties of biomaterials.

5.2 Fundamentals of Cell Biology as a Base for Testing

The biological cell is a basic building block of life, responsible for various functions that sustain a living organism. The human body consists of trillions of cells that structure the body, synthesize, store and transport molecules, absorb nutrients and convert them into energy, recognize and transmit signals, store and express genetic information, and have the unique ability to replicate. The size of biological cells ranges from 1 to 100 μm in diameter and is covered with phospholipid bilayer membranes and protein receptor molecules. The interior of the cell is composed of a cytosol (liquid phase) containing organelles (e.g. nucleus, mitochondria, endoplasmic reticulum, Golgi apparatus) and a cytoskeleton of microtubules (tubulins), microfilaments (actins), and intermediate filaments [7].

The "decision" of the cells which proteins to express when to divide, specialize, or die is an ongoing process that takes place in the cells by orchestrating specific gene activation in the right order and synchrony to express the right proteins required for growth, migration, proliferation, differentiation, and apoptosis [7]. The cell environment plays an essential role in this decision process. The sensitivity of cells to environmental signals can be divided into mechanical, topographical, and chemical signals that can induce a variety of cellular behaviors. The idea of how mechanical and structural signals can modulate cellular behavior arose from an understanding of the complex interplay of biochemical and mechanical signals that regulate cell growth and differentiation. The accumulation of knowledge about the modulation of the physical properties of the cell microenvironment has led to the development of intelligent biomaterials capable of interacting with cells and tissues in a direct and specific way to support and control appropriate cellular activities.

A biomaterial interacts with the adherent cells through their chemical composition and micro-/macro-structure. The combination of extrinsic and intrinsic signals derived from the nano-topology of the ECM controls the behavior of the cells (Figure 5.1). Since the cells are located *in vivo* within the ECM, which contains collagen fibrils, they react to nanostructures in a predetermined way. Major efforts are focused on the development of biomaterials that could mimic a specific microenvironment to differentiate cells in a predetermined way and trigger pathways for regeneration and tissue organization without affecting other mechanisms.

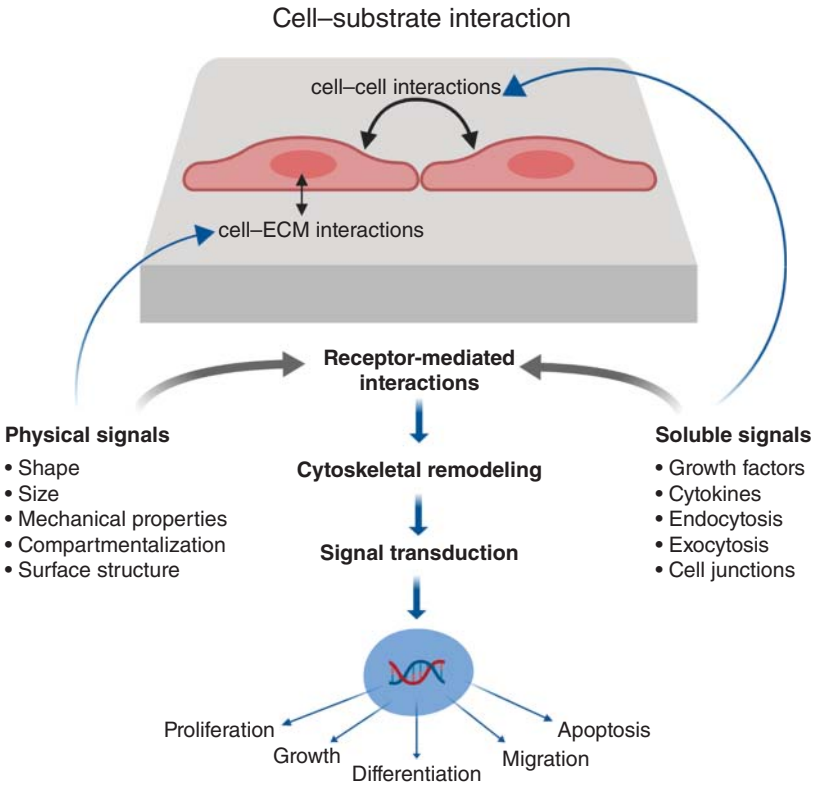

Figure 5.1 Cell–biomaterial interactions.

5.3 In Vitro Methods for Analyzing Biomaterials

To demonstrate the safety and efficiency of a biomaterial or a medical device, biocompatibility testing must be performed. The purpose of such testing is to determine if material or device is suitable for a specific (in this case in contact with the human body) use and to determine potentially harmful physiological effects. Before performing biocompatibility testing, a detailed chemical and physical characterization should be conducted.

In vitro testing is carried outside of the living body and usually utilize cell culture systems to simulate a clinical scenario. Such tests are often carried out before *in vivo* tests as they are cheaper, easier to conduct, and do not require ethical approvals for the use of laboratory animals for research. Additional advantages of *in vitro* tests include a vast range of applications, simplicity, repeatability, and a small amount of test material required.

Cells are usually harvested from human or animal sources, and their survival is maintained under defined conditions that can sustain their functionality, including organic and inorganic substances, water, and temperature. A careful selection of tissue cells from the host environment should be made and tailored for the test

application, with a clearly defined source of the cells for *in vitro* biocompatibility testing. Experimental design should also be adequate for a specific application of biomaterial and their use, as some biomaterials can be suitable for one application but not for others. Preferably the experiments should be quantitative with proper statistical tests used for evaluating significance. The following section describes various *in vitro* assays, which are also included in ISO 10993 guidelines for the biological evaluation of medical devices [8]. Such assays include cytotoxicity test, genotoxicity and carcinogenicity test, hemocompatibility test, cell–material interaction test, and other functional assays. The limitation of such *in vitro* assays is that they cannot provide translatable information on a dose–response relationship that can be extrapolated to patients and used for final risk assessment. Alternative testing methods are constantly being developed that aim to bridge the gap between *in vitro* and human environment and thus reducing the use of animals in safety evaluation testing.

5.3.1 Cytotoxicity Tests

Cytotoxicity assessment is in its essence a biocompatibility test that is required for all new biomaterials and medical devices under evaluation prior clinical use. Several organizations have developed standards and guidelines such as ISO (International Organization for Standardization), NIH (National Institute of Health), FDA (Food and Drug Administration), CEN (European Committee for Standardisation), BSI (British Standards Institute), and ASTM (American Society for Testing and Materials) to assess material biocompatibility and the tests used for evaluation. The standards and guidelines are continuously updated to keep up with the advances in the field [9]. Although these standards overlap in most parts, we will mostly refer to ISO standards for the purpose of this book chapter. The guidelines on cytotoxicity testing are described in ISO 10993-5 and provide the instructions on which test would be appropriate for given biomaterial and application under evaluation [10].

According to these guidelines, three categories of cytotoxicity testing can be performed: direct contact test [11], indirect contact test [12], and the extracts/elution test [13] (Figure 5.2). Based on the sample of use, location of the use nature of the test, an appropriate test should be chosen [10]. In the case of new biomaterials that have not been used commercially, both direct contact and elution tests should be performed [14]. Such tests utilize mammalian cell cultures (mostly mouse or human origin), which are grown in a cell culture medium, expanded to near confluency, and exposed to test material and appropriate controls. Established cell lines obtained from a reliable source such as the American Type Culture Collection (ATCC) are preferred as they allow for better reproducibility between the labs; however, primary cell cultures and organotypic models obtain from living tissue can be used to evaluate specific sensitivity if reproducibility and accuracy can be demonstrated. Based on the specific biomaterial under investigation, the appropriate choice of cell type should be considered.

Several *in vitro* cytotoxicity assays are available and can be categorized based on the evaluation criteria and read-out system. Assessment of cell morphology, cell growth, cell damage, or cellular activity can be used to determine cytotoxicity.

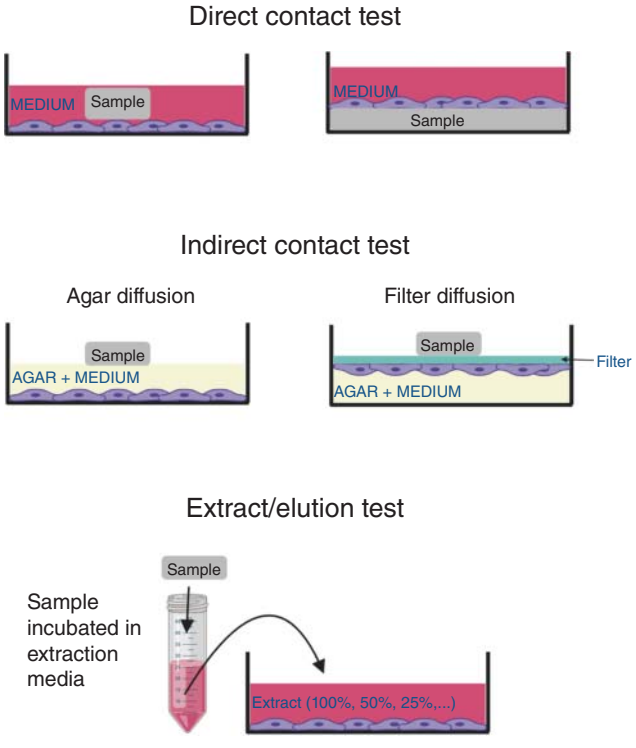

Figure 5.2 Different types of tests to evaluate cytotoxicity according to ISO 10993-5 are direct contact test, indirect contact test, and extract/elusion test.

In each independent cytotoxicity assay, appropriate controls should be included (positive, negative, and blank). When assessing new biomaterials, positive and negative controls should be chosen based on known materials that induce cytotoxicity or are known to be nontoxic. The advantages of such cytotoxicity testing are simple and inexpensive performance, easily manipulated, allows for more than one end-point investigation; it can provide quick and quantitative results and allows for the construction of a concentration–response curve. Despite being a fair predictor of biocompatibility, it should be used as a screening method and used for biocompatibility in parallel with other tests.

5.3.1.1 Direct Contact Tests

For direct contact, test biomaterials of different sizes, shapes, and physical compositions (solid, liquid, and gels) can be placed directly on the cell layer. They can be used in their original state or can be modified to achieve optimal conditions. Although standard guidelines refer to putting materials onto the cells, such physical contact can cause cell damage. Alternatively, cells can be seeded on top of the material under investigation if such material allows for cell adhesion. The cells are then incubated with the material to allow diffusion of leachable chemicals into the culture medium and contact the cell layer. Reactivity of the test sample is indicated by malformation, degeneration, and lysis of cells around the test material [10].

5.3.1.2 Indirect Contact Tests

Indirect contact tests can be applied as a filter diffusion test or an agar diffusion test. The agar diffusion test is appropriate for high-density materials such as elastomeric closures. Such a test utilizes a thin layer of nutrient-supplemented agar, which is placed over the cultured cells to protect the cells from the harmful physical effects caused by the contact with the sample. Samples are then incubated, and extractables from the sample will leach through the medium and agar to reach the cells. Similarly, in the filter diffusion test, cells are grown on a thin filter paper to near confluency and transferred upside down on to the layer of solidified agar, placing the material on the top side of the filter. After incubation, samples are removed, and cells on the filter are subjected to the analysis [10].

5.3.1.3 Extracts/Elution Tests

The extract or elution test uses extraction media to capture the leachates that may include degradation products, ions, residues, and other molecules that are extracted from the material and may affect the biological condition. The test and control materials are placed in the extraction medium (usually cell culture medium) and incubated under defined conditions (time, temperature, and surface area-to-volume ratio). The extraction should be performed under sterile conditions and used immediately without additional processing. The serial dilution of the extracts is prepared and transferred onto the cell layer and incubated (usually between 24 and 72 hours). Following incubation, the cells are examined microscopically for visible signs of toxicity in response to test and control materials and further used for other testing methods [10].

5.3.2 Cell–Material Interaction Tests

5.3.2.1 Cell Morphology and Adhesion

One of the critical points that influences the performance of biomaterials is cell adhesion. In some cases, adhesion may be undesirable, e.g. in lenses or blood contact devices, and in other cases where tissue integration is required (scaffolding for tissue generation), it plays an essential role. Both chemical (e.g. the density of functional groups) and physical (e.g. stiffness, tomography, and dimensionality) properties influence cell adhesion through the amount, orientation, and availability of protein binding domains. This availability of key protein domains – e.g. RGD (tripeptide Arg-Gly-Asp prototypic cell-binding peptide sequence), which are present in adhesion proteins such as vitronectin and fibronectin, in turn, regulates the attachment of cells to surrounding cells or the ECM [15]. In addition, transmembrane receptor proteins, known as integrins, bind to ECM proteins to promote cell anchoring and mediate cell–matrix crosstalk. Such binding of integrins plays an essential role in cell communication and regulation by triggering the activation of intracellular signaling pathways that promote cell growth, cell proliferation, migration, differentiation, and cellular repair [16].

Changes in cell adhesion can play an important role in a wide range of diseases, including cancer [17], arthritis [18], atherosclerosis [19], and osteoporosis [20].

Some biomaterials such as collagen and fibrin are able to mediate cell adhesion due to their surface binding domains directly, and other biomaterials such as pectin or alginate do not provide adhesion ligands and are therefore less susceptible to cell anchoring. Because cell anchorage is a strict requirement for the survival of most cell types, chemical modification of such materials is required to increase protein absorption and the availability of cell-binding domains [21, 22].

The simplest method to quantify cell adhesion is to calculate the percentage of attached cells with respect to all seeded cells per surface area. This is obviously dependent on the properties of biomaterials and seeding efficacy, and various strategies have been developed to improve seeding efficacy and analyze cell adhesion, such as injecting the cell suspension directly into the scaffold interior [23], using dynamic culture with agitation [24], using high-density/low volume cell suspension [25], or using uniform cell seeding devices and 3D printers [26].

Morphology assessment with different microscopy techniques is commonly used to assess shape (e.g. round, elongated, spindle, cuboidal), size, aggregation, and spreading of the cells in contact with biomaterials. Cytoskeleton organization is commonly analyzed by staining F-actin rich fibers, presence, and distribution of focal adhesion complexes, as well as mapping of integrins. Figure 5.3 shows the assessment of morphology through the staining of actin filaments of the human intestinal epithelial cell line (HUIEC) grown on silicon wafer plates coated with carboxymethyl cellulose (CMC) and poly lactic-*co*-glycolic acid (PLGA), where the clear morphological difference in cell shape and size can be observed.

Confocal microscopy is an essential tool for analyzing 3D construct as it provides a series of optical plans that can be reconstructed into a 3D image. In a 3D microenvironment, different physicochemical and structural properties of the matrix regulate cell–matrix adhesion and, therefore, the functionality of cells [27], leading to different behavior compared to cells in a 2D environment. Experiments that utilize microfabricated substrates with geometrical patterns and features of different sizes, shapes, and topographies are being used to correlate size and shape

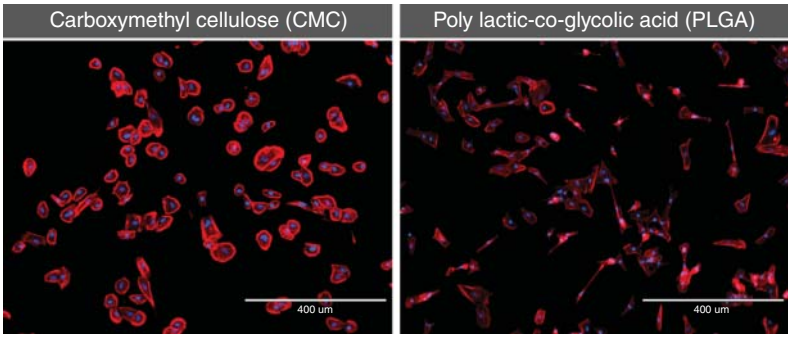

Figure 5.3 F-actin staining assay of HUIEC grown on CMC- and PLGA-coated plates. Red fluorescent color selective bicyclic peptide Phalloidin was used for staining actin filaments, and blue fluorescent color 4′,6-diamidino-2-phenylindole (DAPI) was used to visualize nuclear DNA. The scale bar represents 400 μm.

with growth or differentiation. In such experiments, individual cells are forced to adopt specific morphologies, and cellular activities are then analyzed [28, 29]. Furthermore, advances in biosensors have led to the development of aluminum nanoslit-based plasmonic biosensing chips able to simultaneously assess cell morphology and adhesion using Fano resonance [30].

5.3.2.2 Cell Viability Assay

The cell viability test is used to determine the proportion of living, healthy cells within a population. For example, a dye exclusion test such as the trypan blue test may be used to penetrate the compromised membrane of dead cells and stain them blue, whereas it does not penetrate living cells. Living and dead cells, which should be in suspension, can be distinguished by cell counting with a hemocytometer or equivalent cell counter. However, this method cannot distinguish between apoptotic and necrotic cells, so complementary assays should be used. Such tests may be difficult or even impossible for cells growing in biomaterials, and therefore the applicability of this assay is limited. When cells are grown in 3D constructs, the evaluation of living and dead cells should include an analysis of spatial distribution. For example, cells grown in central regions of 3D constructs may have lower viability than cells grown at the periphery due to limited diffusion potential and availability of nutrients and oxygen [31].

Alternatively, fluorescence-based assays (live/dead test) are used, which can distinguish between living and dead cell populations using a combination of fluorescent dyes. Calcein-AM, for example, is a cell-permeable membrane compound for staining viable cells, whereby calcein is produced by intracellular esterase to produce a strong green fluorescence. For staining dead cells, propidium iodide (PI) or ethidium homodimer (EthD-1) can be used as membrane-impermeable fluorescent dyes. By binding to the DNA of dead or dying cells, they undergo a significant increase in fluorescence intensity and produce red fluorescence. As an example, Figure 5.4 shows live/dead viability assay (Calcein-AM/PI), where authors examined the biocompatibility of osteoblast on gelatin crosslinked with genipin for potential use in dental implants. The high ratio of green-stained cells on gelatin indicates the presence of live cells, which is comparable to standard tissue culture polystyrene (TCPS) [32].

Calcein-AM and PI dyes can be used simultaneously, and incubation times should be adjusted to allow for diffusion into 3D constructs but should not exceed one hour due to possible dye-inducing cell toxicity. Fluorescence microscopy is often used to assess living and dead cells and their spatial distribution. Image analysis software is already available that allows the quantification of fluorescence microscopy data. Quantitative results can also be obtained using flow cytometry if the cells can be suspended. In addition, the fluorescence of adherent cells can be measured with special fluorescent microplate readers, which allows a "flat" model. Several commercial kits are available with constant improvements in incubation time reduction, fluorochrome availability, and dye toxicity reduction to allow continuous monitoring.

Protease biomarker assay is another assay that can quantify cell viability by detection of protease activity. The protease activity of dead or live cells can be assessed in a multiplex format using luminogenic or fluorogenic substrates. For example,

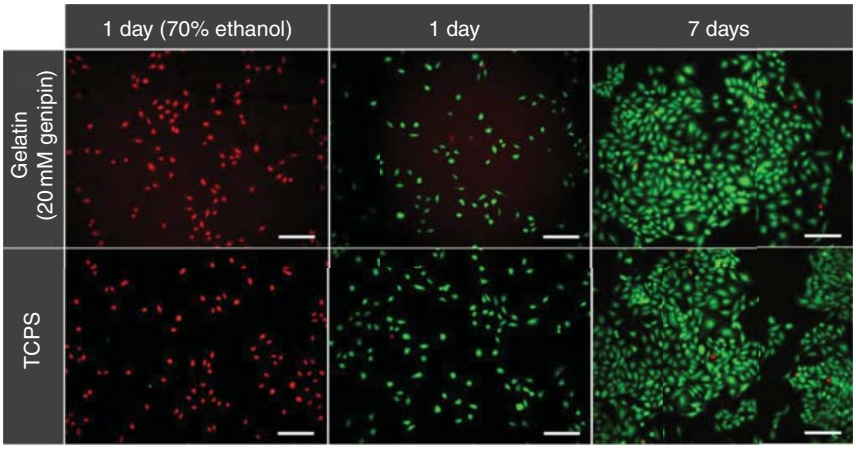

Figure 5.4 Live/dead cell viability assay of Saos-2 cells cultured on gelatin crosslinked with genipin. The cells were cultured for one and seven days. Tissue culture polystyrene was used as positive control and cells pretreated with 70% ethanol were used as a negative control. The scale bar represents 100 μm. Source: From Makita et al. [32]/Beilstein-Institut/ CC BY 4.0.

glycylphenylalanyl-aminofluorocoumarin (GF-AFC) is a cell-permeable fluorogenic protease substrate that, upon entering live cells, is being cleaved to AFC, producing a fluorescent signal proportional to the number of live cells [33]. To differentiate between viable cells and cells undergoing apoptosis (programmed cell death), several assays were developed and include detection of annexin V binding to exposed membrane lipids, caspase activation, chromatin condensation, DNA fragmentation, or cytochrome c release. For example, the TUNEL assay (terminal deoxynucleotidyl transferase [TdT] deoxyuridine triphosphate [dUTP] nick end labeling) utilizes the TdT enzyme to incorporate labeled dUTP into fragmented double-stranded DNA, resulting from the apoptotic signaling cascade. The biotinylated dUTP can then be detected with avidin-conjugated fluorochromes to assess the proportion of cells undergoing apoptosis. Figure 5.5 shows different types of assays to assess cell viability, cytotoxicity, and apoptosis.

5.3.2.3 Metabolic Activity Assay

To date, several tests to assess cell metabolic activity have been developed (Figure 5.6). One of the first assays developed to evaluate the metabolic activity of cells was the colorimetric MTT-tetrazolium salt assay [34]. In the presence of metabolic intermediates such as NADPH/NADP (nicotinamide adenine dinucleotide phosphate), NADH/NAD (nicotinamide adenine dinucleotide), FMNH/FMN (flavin mononucleotide), and FADH/FAD (flavin adenine dinucleotide), the yellow tetrazolium dye MTT (3-(4,5-dimethylthiazol-2-yl)-2,5-diphenyltetrazolium bromide) is reduced via dehydrogenases or reductases by viable cells to violet-colored formazan precipitate which is further dissolved in a colored solution

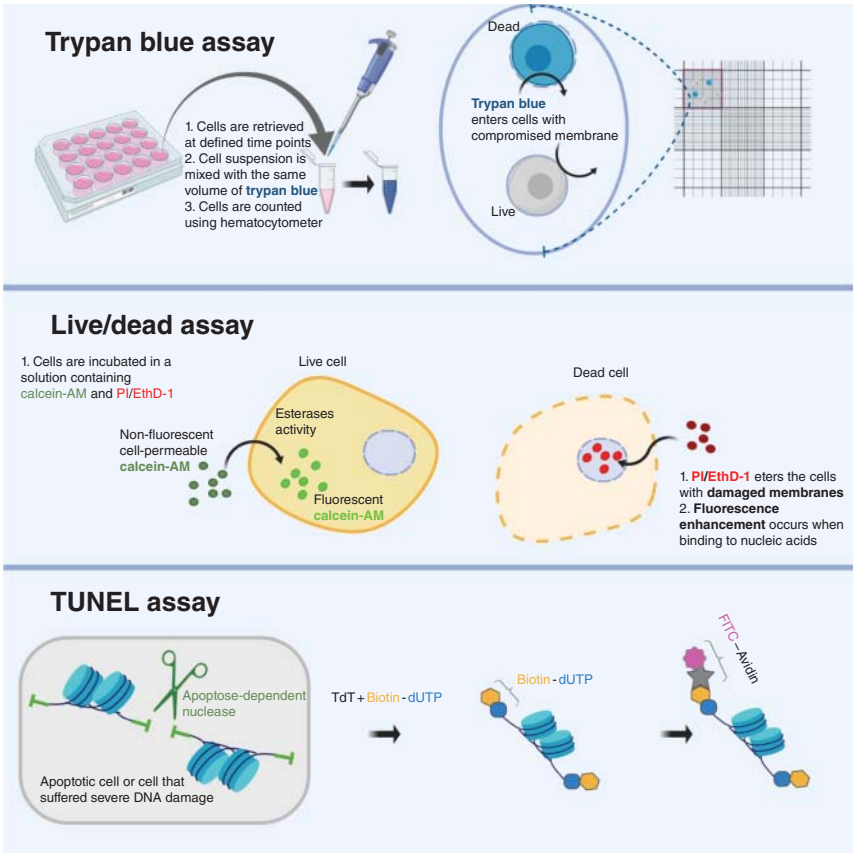

Figure 5.5 Schematic representation of some cell viability assays.

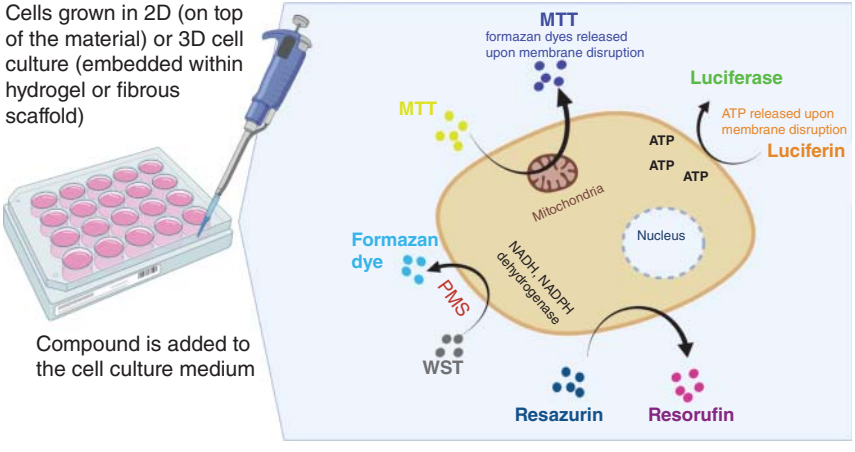

Figure 5.6 Schematic representation of some common metabolic activity assays.

by means of an organic solvent (dimethyl sulfoxide – DMSO) [35, 36]. The absorbance of the colored solution is measured with a multiwell plate reader at specific wavelengths, and the measured values are proportional to the relative amount of viable cells. The assay is destructive to the cells and can, therefore, only be used for end-point evaluation.

An alternative to MTT is the XTT test ((2-methoxy-4-nitro-5-sulfophenyl)-2H-tetrazolium-5-carboxanilide), which is a negatively charged compound compared to MTT and is not capable of penetrating cells easily [37]. It must be used in combination with PMS (1-metoxyphenazine methosulfate), which acts as an intermediate electron acceptor. The reduction step takes place outside the cells by electron transport in the plasma membrane, converting tetrazolium compounds into formazan salt, which is soluble in the culture medium and does not require an additional solubilization step, thus simplifying the assay. Resazurin (Alamar Blue) is a similar cell-permeable redox indicator, which was first described in 1945 [38], but it was only four decades later that it found application in cell culture studies [39]. Although the sensitivity of detection is superior over tetrazolium-based methods, the intense blue color of the resazurin solution and the fluorescence interference of the final product are limitations for the assay [40]. The assay is generally nontoxic and nondestructive to the cells and therefore allows continuous exposure and multiple measurements (different times), but exposure ultimately leads to cell death [41]. Resazurin can be added directly to the cells in the culture medium, followed by incubation in which metabolically active cells convert nonfluorescent resazurin to red-fluorescent resorufin, which can be quantified by excitation of the samples at 530–560 nm and reading of the emission at 590 nm in the standard equipment.

Both the resazurin reduction test and the tetrazolium-based test have certain disadvantages that have been reported [42, 43], such as sensitivity to light (handling should be carried out protected from light), long incubation times (one to four hours), susceptibility to chemical interference of reducing compounds, and a certain degree of toxicity. As mentioned earlier, appropriate controls (biomaterial in the absence of cells) should be used when biomaterials are physically present to ensure that the biomaterials do not interfere with the assay read-out by absorbing compounds. Importantly, described assays evaluate the metabolism of viable cells and do not necessarily correlate linearly with increasing cell density. Therefore, simple extrapolation to estimate the total cell count per sample should not be performed without proper validation.

An adenosine triphosphate (ATP)-based assay is an additional tool to evaluate the viability of cells through metabolic activity. Intracellular ATP is strictly regulated, and when cell viability is lost, or membrane integrity is compromised, cells immediately stop ATP synthesis after the remaining ATP has been degraded from the cytoplasm by ATPases. The quantification of ATP can be carried out using a bioluminescence-based technology in which the intensity of the emitted light is proportional to the concentration of ATP and can be measured with a standard luminescence microplate reader [44]. Although the assay is performed with light-sensitive material at the end-point, the advantage is high sensitivity (10 cells) and short incubation time (10 minutes).

5.3.2.4 Proliferation Assay

Cell proliferation is the increase in the number of cells through cell division. Cell division (cytokinesis) is a final step in the cell cycle and only occurs in healthy, proliferating cells, whereas dead, senescent, or growth-arrested cells do not proliferate. Therefore, the viability or survival of cells can be assessed by cell proliferation tests by providing information about actively dividing cells in a sample. Several methods have been developed to assess cell proliferation, ranging from simple counting of the total number of cells over time to the measurement of DNA content or DNA synthesis in replicating cells. The tests are performed using standard methods including microscopy, flow cytometry, enzyme-linked immunosorbent assays (ELISA), immunofluorescence, and high content imaging [45, 46].

For example, adherent cells seeded on biomaterials can be stained and counted under the microscope. Common fluorescent dyes can be used for opaque materials or colored dyes (e.g. eosin, hematoxylin, methylene blue, and crystal violet) for transparent materials. Defined areas are taken as representative for the whole sample, and the cells are counted under the microscope. The average number of cells is counted manually or analyzed with image processing software. However, this method is prone to distortion, as high cell density and uneven distribution can lead to inaccurate results. In addition, although 2D samples are easier to examine, 3D scaffolds require confocal microscopy and much more complex analysis. Cells can also be counted in suspension if efficient extraction of cells from the 3D construct is possible.

Quantification of total DNA is another method for assessing cell proliferation. DNA is replicated before cell division begins, and the rate of DNA synthesis is directly proportional to the rate of cell proliferation. Various types of assays can be used, such as the BrdU (5-bromo-2′-deoxyuridine) assay, in which a nucleoside-labeling agent is incorporated into the newly synthesized DNA. The incorporation of BrdU is proportional to the extent of cell division and can be detected with an anti-BrdU antibody in flow cytometry, ELISA, or IF-IC applications. An alternative to BrdU is the EdU test (5-ethynyl-2′-deoxyuridine), which directly measures the active DNA synthesis or the S-phase synthesis of the cell cycle and does not require a DNA denaturation step as in the BrdU assay, which simplifies its performance [47]. Another method for the quantification of dsDNA is PicoGreen. Cells can be lysed directly on the biomaterial, and a dye is used that binds to dsDNA with high specificity and exhibits fluorescent properties when bound. The DNA recovery step is crucial in this process and can be hindered by material–DNA interactions, especially when dealing with positively charged polymers such as chitosan, which generate strong electrostatic polymer–DNA interactions. After defined incubation time, the fluorescence is measured with a microplate fluorescence fluorometer, and the standard curve is used to correlate the fluorescence readings with the amount of DNA. Since this method is destructive, only end-point measurements can be performed.

Several variants of such assays have been developed, namely the CyQUANT cell proliferation assay, in which adherent cells are directly frozen and lysed after thawing by adding the dye and measuring the fluorescence. In addition, CyQUANT NF even eliminates the freezing step, and the dye in lysis buffer is added directly to the

adherent cells after removal of the medium, and the fluorescence of the supernatant is measured. In this way, real-time data of intact cells can be obtained from intact cells. Again, it is important to note that inefficient dye penetration may affect the results. Furthermore, different fluorescence-based assays have different sensitivities and linear ranges, which should be considered when selecting options and designing experiments.

The proliferation rate can also be assessed by the expression of cell-cycle-specific proteins. Common cell cycle proteins include proliferating cell nuclear antigen (PCNA), Ki67, and phosphohistone H3 (PH3), which can be detected by Western blot (WB), flow cytometry, ELISA, IF, and immunohistochemistry (IHC). The proliferative phase of the cell division cycle comprises the phases S, G1, G2, and M, while G0 is considered the resting phase. Ki67 is present in all phases of cell division (interphase) and is located in the nucleus, while in the M (mitosis) phase, it is found on the surface of the chromosomes. At the same time, it is excluded in the G0 phases and can, therefore, be used as a marker of cell proliferation [48]. Similarly, the PCNA gene is closely involved in the process of DNA replication and repair, the presence of which in the cell nucleus can be correlated with cell proliferation [49]. In addition, the histone H3 protein, which is the main component of chromatin, is phosphorylated only on serine-10 and serine-28 during mitosis, so that the anti-phosphohistone H3 (PHH3) antibodies can actively recognize proliferating cells [50].

It is important to note that the proliferation rates between 2D and 3D cultured cells can be very different when considering the cell type, composition, and architecture of the 3D construct. In addition, the functional properties of the cells may also be different in 3D, resulting in different responses to drugs [51]. In general, cells cultivated in 3D have shown a lower proliferation rate compared to 2D [52]. Such a reduction in the cell proliferation rate can be seen as closer to the *in vivo* scenario compared to high proliferation rates of 2D cultures where no restrictive physical barrier exists.

5.3.2.5 Cell Motility and Migration Assay

Cell migration describes the movement of cells in a body. It plays a crucial role in a variety of physiological processes and pathological conditions, as well as in scaffold-based TE. It is controlled by biochemical stimuli and cellular interactions and enables cells to change their position within the tissue or between different organs [53]. Several migration assays have been developed and used for 2D cultures, including a wound-healing assay (scratch assay) in which cells are grown to confluence. A plastic pipette tip is used to create a scratch in the middle of the monolayer. Time-lapse microscopy and image analysis software are used to track the migration dynamics of individual cells in the leading edge of the scratch [54]. The "transfilter" assay or the Boyden chamber assay is another example of cell migration studies [55]. The principle of the assay is based on two compartments separated by a porous filter through which the cells migrate. Depending on the type of cell used, a suitable pore size filter should be selected to allow active transmigration. After a certain period, the cells that have migrated through the filter are counted [56]. The sub-agarose migration assay can be used, in which agarose gels are poured into molds that have

holes in solidified gels. The chemoattractants are used to attract the cells to migrate to them [57]. Fluorescence microscopy or live dead imaging can be used for analysis. Several other migration assays have been described in the literature, which can be selected according to the specific biological problem, including the cell exclusion zone assay [58], the microcarrier bead assay [59], the spheroid migration assay [60], and the microfluidic chamber assay [61].

Tracking migration in 3D structures allows for a more comprehensive assessment similar to *in vivo* scenarios, but the equation is further complicated by several technical limitations due to the presence of material and its intrinsic properties (transparency, thickness, and autofluorescence). As mentioned earlier, confocal microscopy must be used with appropriate equipment that supports the imaging of living cells and postprocessing to track cell movement. Such an approach has been used by Harley et al. to investigate how the microarchitecture of 3D collagen glycosaminoglycan scaffolds influences cell migration behavior [62]. The migration of mouse fibroblast cells was investigated using confocal 3D time-lapse microscopy of fluorescence-labeled cells (Figure 5.7), and the authors identified that fibroblast migration, which is characterized by both motion fraction and velocity, decreases with increasing pore size of the scaffold [62].

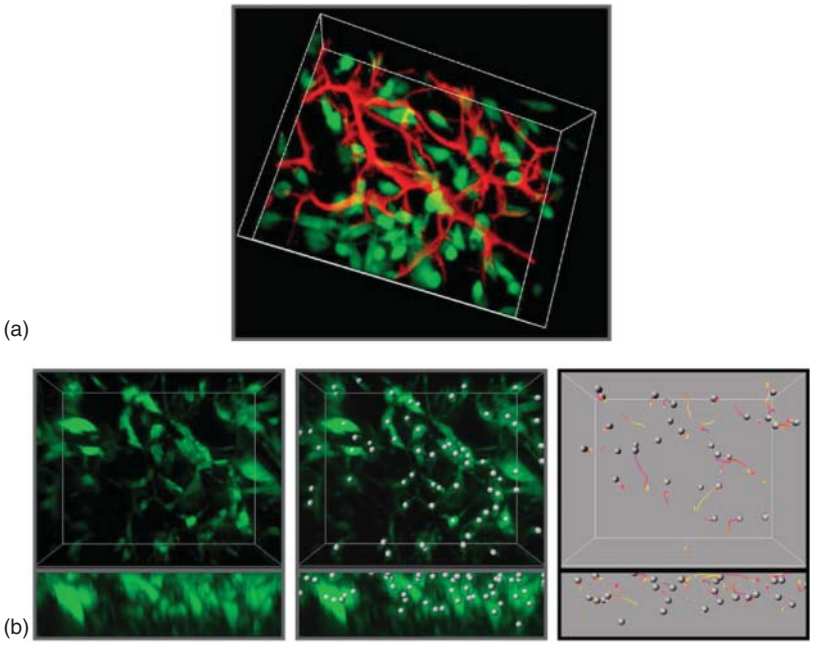

Figure 5.7 (a) 3D confocal micrograph showing the porous microstructure of CG scaffold (red) and labeled NR6 cells (green). (b) *xy* and *xz* projections (top and bottom boxes, respectively) of individual cells captured with 3D time-lapse confocal microscopy were tracked during migration in a CG scaffold. Centroids of fluorescent NR6 cells were computed (center), and individual cell tracks were generated (right). Source: From Harley et al. [62]/with permission of Elsevier.

5.3.3 Hemocompatibility Tests

Hemocompatibility testing is required for all medical devices and materials in contact with blood to assess their effects on blood and/or blood components. ISO 10993-4 provides guidelines for determining whether blood interaction testing is necessary to determine hemocompatibility [63]. In addition, the ISO guidelines also include the selection of appropriate tests that should be performed depending on the category of device or material. These include noncontact devices (e.g. *in vitro* diagnostic devices), external communication devices (e.g. blood bags, needles, catheters, guidewires, tubing, circulatory support systems, and intravascular endoscopes), and implants (e.g. stents, heart valves, vascular grafts, pacemaker leads, blood monitors) [63]. Primary and optional hemocompatibility tests are recommended for each category, including hemolysis test, coagulation, thrombosis, platelet count, and immunological tests. The hemolysis test (hematology test) is considered the primary and most meaningful test, as it measures the damage to red blood cell (erythrocyte) membranes caused by the materials or their extracts. It is one of the most frequently used screening tests, as it is inexpensive, quick, and simple to perform and provides easily interpretable quantitative results. Because erythrocytes contain hemoglobin, an oxygen transport protein, damage to the erythrocyte membrane would result in hemoglobin leakage and possibly kidney and liver injury, and the oxygen would not reach the body tissues. A detailed overview of the device examples and the corresponding test categories are listed in ISO 10993-4 [63].

The conditions for hemocompatibility testing must be as close as possible to clinical use. *In vitro* tests are preferred methods (most commonly used for screening implants or external communication devices). Still, they are not always reliable predictors of blood-to-device interaction, especially for materials with prolonged, repeated, or permanent contact with blood. *In vitro* tests are also easily repeatable and thus allow the calculation of significance. The kinetics of reactions (e.g. thrombus formation, coagulation) can be tracked over time, and systems can be evaluated in both static and dynamic configurations.

In principle, human blood is available and should be used for *in vitro* testing. However, there may be various restrictions on the use of human blood, including practical constraints and ethical issues. There are several variables that can affect the outcome of the test, including the use of anticoagulants, the method of sample collection, sample storage, age of the sample, aeration and pH, temperature, and the test testing protocol itself. Storage may reduce the quality of the blood to be used in the tests due to rapid changes in some blood characteristics [64].

In the case of animal testing, differences in the blood reactivity of the species are taken into account, and these differences may limit the predictability of a particular test in the clinical situation of humans. Although differences between species may make the evaluation of hemocompatibility difficult, the use of animals in both short- and long-term tests is considered appropriate for the evaluation of thrombosis and tissue interactions. It should be recognized that there are many challenges in evaluating the interactions of blood contact devices by *in vitro* and *in vivo* test systems and that no single model is suitable for all applications. It is therefore essential to consult vertical product standards if they are available for specific devices.

5.3.4 Genotoxicity and Carcinogenicity Testing

Genotoxicity refers to the possibility that an implant or biomaterial may directly (DNA target) or indirectly (non-DNA target) cause permanent damage to the DNA. In contrast, carcinogenicity refers to the tendency of the implant or material to induce (benign or malignant) tumors by altering the DNA. The three major genotoxic effects include gene mutation, chromosomal alteration, and DNA effects. If the *in vitro* test indicates potential genotoxicity, further evaluation is performed using the *in vivo* genotoxicity test (described later).

Assays for the evaluation of *in vitro* genotoxicity normally use mammalian cells and include the micronucleus test [65], the comet test [66], and the Ames test [67]. This assay is mainly required for devices with the permanent or extended contact time, such as implants or external communication devices. Detailed guidelines and a description of the test are given in ISO 10993-3:2014, which is currently being revised [68]. The three critical *in vitro* end-points to be evaluated include gene mutation, structural, and numerical chromosome aberration. The Ames test or reverse bacterial mutation test is normally used to assess mutagenic activity using bacteria (*Escherichia coli* or *Salmonella typhimurium*) to detect point mutations that allow the bacterial strain to grow on a selective medium. In contrast, its nonmutated parent bacteria do not grow.

Another *in vitro* assay includes mouse lymphoma tests where cells are exposed to test extracts in the presence or absence of exogenous metabolic activation [69]. After incubation, cultures are cloned in restrictive media for the mutant phenotype. Mutations are measured at the thymidine kinase locus to detect base-pair mutations, frameshift mutations, and small deletions. Since mutant colonies have a characteristic frequency of size distribution, colony measurements can be used to distinguish the type of genetic effect [69].

5.3.5 Monitoring Intracellular Activities

As already mentioned, many methods for the analysis of cell behavior were initially developed for classical 2D plastic shell cultures and only later adapted for the evaluation of biomaterial interactions in 2D and 3D microenvironments. Due to the dimensionality of biomaterials for 3D cell cultures and TE applications, monitoring of intercellular activities is a challenging task. Still, new methods for detection and quantification of intercellular properties are constantly being developed.

Intracellular activities are the result of physical and chemical changes occurring in subcellular organelles and include temperature, pH, mechanical and electrical properties, pressure, and molecular concentrations. They are crucial for the maintenance of normal cell functions and are therefore important properties that are relevant for studies on interactions between cells and biomaterials. If it is possible to reconstitute cells from the biomaterial under investigation (e.g. disassembly of polymer scaffold to separate from the cells), standard molecular analytical methods can be used to assess intracellular activities. If such recovery is not possible, miniaturized sensors and devices capable of monitoring intracellular organelles and processes can be used, making it possible to detect small variations in cell function. The two

main types of intracellular sensor systems are tethered and untethered systems [70]. In the tethered measurement, an intracellular probe (e.g. glass micropipette, nanowires, carbon nanotubes, probes for modified atomic force microscopy [AFM]) is inserted into the cell or organelles to acquire electrical or optical signals and transmit them via tethered connections to an external measuring device, which is considered destructive/invasive. On the contrary, unattached devices measure intracellular activities without damaging the cell or causing major disturbances to normal cell activities and are suitable for continuous and long-term measurements. Such sensors include nanoparticles, fluorescent proteins, and molecules, as well as unbound microelectrochemical system devices (MEMS).

Nanowires and nanotubes have been used as instruments to measure intracellular electrical activities such as ion flows and translocation of charged molecules, which play an important role in maintaining normal cell functions [71]. The nanotube is a tubular nanostructure of carbon atoms with high tensile strength and elastic modulus and exceptional carrier mobility and electrical current density, making it suitable for detecting weak signals within individual cells. Such carbon nanotubes have already been successfully used to measure electrical signals in vertebrate neurons *in vitro* and *in vivo* [72, 73].

Modified AFM probes with tips capable of penetrating cell membranes and probing intracellular structures or organelles are used [74, 75]. Beard et al. used this technique, for example, to measure the elastic moduli of the internal keratin structures of corneocytes (Figure 5.8) [76]. This enables them to create a tomographic

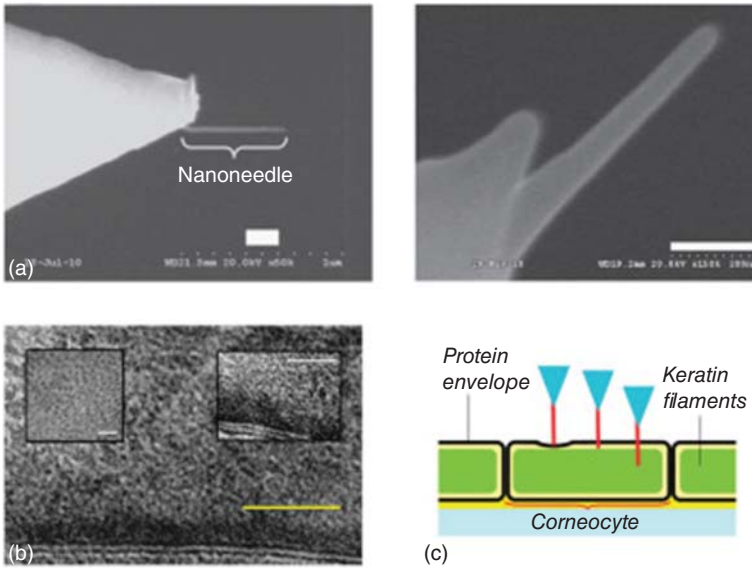

Figure 5.8 Use of nanoneedles for testing intracellular activities. (a) AFM nanoneedle under the electron microscope. (b) Nanostructure of a part of a corneocyte from stratum corneum (SC) observed by cryo-electron microscopy. (c) Schematic representation of the progressive penetration of nanoneedles on AFM probes into a monolayer of corneocytes. Source: From Beard et al. [76]/with permission of Elsevier.

profile of cellular and intercellular stiffness over a range of depths below the cell surface and to measure the mechanical properties of a nuclear membrane and nuclei directly *in situ* [76].

In contrast, untethered devices perform intracellular measurements without connection to extracellular instruments. The most commonly used are polymeric nanoparticles, nanodiamonds, gold nanoparticles, and quantum dots. The measurement is mainly based on fluorescence spectroscopy, where the nanoparticles are inherently fluorescent or conjugated with sensitive fluorescent dies [77]. Using nanodiamonds, intracellular temperature-sensing methods have been developed that allow the detection of temperature variations of only 1.8 mK (a sensitivity of 9 mK Hz-1/2), which, in combination with gold nanoparticles, allow temperature gradient control and imaging at the subcellular level of human embryonic fibroblasts [78]. Okabe et al. demonstrated the use of fluorescent polymeric nanoparticles in combination with fluorescence lifetime imaging microscopy to measure the intracellular temperature distribution across the organelles of a COS7 kidney cell [79], which opens the possibility to study the intrinsic relationship between temperature and organelle function. In addition, Korzeniowska et al. developed a chemical nanosensor using core–shell nanoparticles for the quantitative analysis of pH within living cells [80]. By observing changes in fluorescence that corresponded to the used chemical pH switch, a pH variation of only 5–6.5 was detected in living human embryonic renal cells, making it a powerful tool for monitoring the processes taking place in the cytosol [80].

Intracellular temperature mapping was also achieved with a green fluorescent protein (GFP)-based thermal nanoprobe by monitoring the fluorescence polarization anisotropy of GFP [81]. In addition, GFP coupled to the force-sensitive focal adhesion protein vinculin was used to measure local forces in the cell with piconewton (pN) sensitivity to study the regulation of focal adhesion dynamics [82]. Another method developed by Gomez-Martinez et al. evaluates pressure changes within the cell using an unbound MEMS sensor on a silicon chip small enough to be internalized by lipofection [83]. Such an approach uses two membranes separated by a vacuum gap to form a Fabry–Pérot resonator and detected pressure changes could be quantified from the intensity of the reflected light (Figure 5.9) [83].

5.3.6 Real-Time Monitoring of Cell Culture Systems

The real-time (RT) monitoring devices are constantly being improved to provide a better insight into our understanding of human physiology and tissue complexity. Such methods allow quantification of cellular responses during the growth cycle and response to external stimuli by assessing cell number, viability, and distribution in real time. By reducing the need to stain or label cells, this approach can allow nondestructive evaluation without defined end-points, giving a better overview of dynamic biological processes that took place between end-points and allowing a reduction in sample size and analysis of the transitory phenotypic response.

RT monitoring methods vary according to the parameters analyzed and can be focused on the cells themselves or the environment. The equipment usually

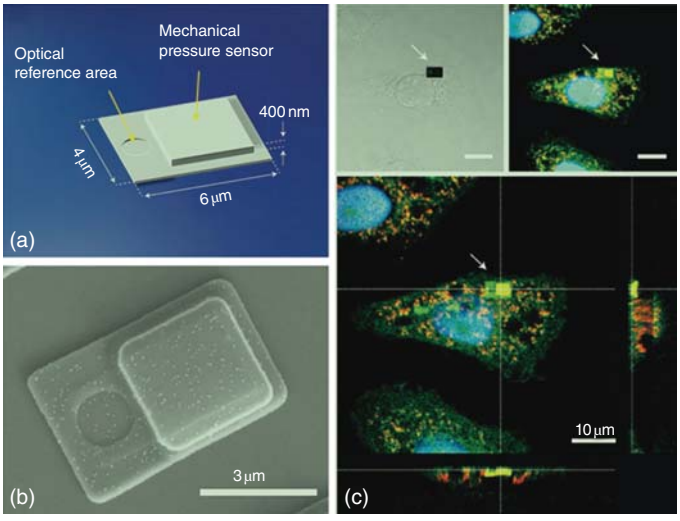

Figure 5.9 MEMS pressure sensor for intracellular pressure measurement. (a) Schematic representation of the sensor. (b) SEM image of the sensor. (c) MEMS pressure sensor internalized into cytoplasm of HeLa cells. Source: From Gómez-Martínez et al. [83]/with permission of Springer Nature.

consists of a kind of fluorescence microscope with a special chamber that reproduces incubator conditions, or the whole instrument can be placed in an existing incubator. Several commercially available systems consisting of an incubator and a cell culture monitoring system have been developed and are based on impedance, microphysiometry, or resonant waveguide grating, among others. Some of them include IncuCyte ZOOM System (Essen BioScience), BiostationCT (Nikon), Lyncee Tec (Elliot Scientific), CytoSMART (Cytosmart OMNI), JuLI stage (NanoEnTek), or xCELLigence (ACEA Biosciences) and can monitor physical and physiological parameters to analyze different types of cellular events combined (or not) with cell labeling, such as adhesion, proliferation, migration, apoptosis, and differentiation. Recent work in this field provides examples of label-free and real-time monitoring in 2D and 3D cell culture systems using impedance cell sensors [84–86], noninvasive RT assessment of cell viability in 3D tissue based on cell respiration [87], stem cell quantification and differentiation based on electrical impedance sensing [88, 89], development of a multiflow channel bioreactor to RT monitor cell dynamics in 3D cultured tissue [90], and sensor-instrumented scaffolds to study cell behavior and functions in 3D in RT [91]. Since most of the systems mentioned above were originally developed for 2D cell cultures, efforts are focused on adapting them to 3D systems, which are more similar to *in vivo* scenarios.

5.3.7 High-Throughput Screening Systems

Over the last decades, a variety of biomaterials have been developed, and the implementation of HTS methods is becoming increasingly important to identify causal

relationships between native tissue or cells and biomaterials so that they can be rationally designed to elicit the most appropriate host response. Understanding the influence of individual biomaterial properties on cell behavior is therefore important for the regulation of bioactivity. Both volume and surface properties of biomaterials define the biophysical and biochemical properties of biomaterials and include chemical composition, polarity, topography, porosity, geometry, stiffness, degradation kinetics, and erosion. This complexity of parameters makes the development of biomaterials an iterative, labor-intensive, and time-consuming process, which is a further motivation for the development of biomaterial HTS microarrays to rapidly investigate their effects [92].

Using large biomaterial libraries, combinatorial approaches for more efficient screening are used to identify the influence of different chemical, physical, and biological properties on cell behavior and to find optimal formulations that meet a specific biomedical application [93–95]. The production of 2D and 3D biomaterial microarrays can be developed in which the cells lie on or in the respective material. Analytical approaches include classical fluorescence-based read-out methods, where cells are fluorescently labeled and analyzed at a single end-point, or newer non-invasive methods that allow multiple read-outs and quantitative analysis of the cellular response over time [93–95]. However, progress in this HTS area depends on the development of appropriate analytical techniques which must be specific and sensitive enough to allow data acquisition from spatially defined locations on a micro-scale and in an automated way.

Many platforms are described in the literature for both 2D and 3D environments. For example, Dolatshahi-Pirouz et al. [96] developed a platform with a robot-assisted microarray spotter for the systematic evaluation of the fate of stem cells in various miniaturized cell-loaded gels, which enabled them to study differentiation in miniaturized 3D niches and identify those with increased differentiation potential. The results were also validated in macroscopic hydrogels to confirm the differentiation potential. In addition, Patel et al. [97] provide an overview of material properties and HTS platforms that can quickly evaluate combinatorial material libraries in 2D and 3D environments to discover material properties that influence stem cell behavior. In a further study, Kolb et al. [98] developed a microgel-based screening platform for combination tests of in situ generated proteins on the fate of stem cells in ultra-high throughput. Specialized microniches with isolated single sets of growth factors were developed. When cells were cultivated in these microniches, the fluorescence reporter indicated whether the performance of the niche was positive, followed by barcoded RNA sequencing of the differentiated cells.

5.4 In Vivo Methods for Analyzing Biomaterials

In addition to the *in vitro* tests described earlier, *in vivo* tests are carried out to confirm or disprove the results obtained *in vitro* or to supplement the toxicological end-points that can only be investigated *in vivo*. The main advantage of *in vivo* tests is the clinically relevant simulation of the real body condition. Although the results obtained

in laboratory animals cannot be directly translated to human conditions, this is currently the closest comparison before experiments on humans are started. However, such tests are expensive, time consuming, and require ethical approvals from the regulatory authorities. Several regulatory authorities have developed guidelines for the *in vivo* assessment of the biocompatibility of tissues and biological systems of materials and medical devices.

Based on the application of biomaterials, the tested substances are evaluated for the induction of an allergic reaction (sensitization), a rejection reaction (irritation), or tissue inflammation. To assess the local tissue reaction, the material can be implanted under the skin (intracutaneous reactivity) or in the bone cavity (intrabone reactivity), as required, and microscopic imaging or biochemical analysis is performed to evaluate acute or subacute toxicity to all organ systems. In addition, genotoxicity is studied to identify changes in the genetic material of cells directly exposed to the material. Cells and tissues exposed to the material are normally compared with healthy cells and tissues to identify morphological or physiological changes. Various microscopy techniques such as light microscopy, confocal microscopy, electron microscopy, and transmission electron microscopy are used for visual examination. In addition, physical tests can be carried out to assess the physical strength of the tissue (e.g. bone, teeth), and as a follow-up examination, a radiological examination can be carried out using X-rays. The comparative and time-dependent research methodology is the basis for experimental designs that use the half-life of radioactive atoms coupled to the implanted material or device to assess biodegradation.

In vivo experiments are performed in the final phase before clinical implementation, and the selection of tests is based on the properties and end-use of the biomaterial or medical device to be evaluated. It should be noted that the samples selected for *in vivo* testing should be pure, free of contamination, and sterilized according to their structure. The various animals used for *in vivo* experiments for the evaluation of medical devices include mouse, rat, pig, rabbit, sheep, cat, dog, calf, and non-human primate. The following chapters describe the evaluation of the biological properties of biomaterials by *in vivo* experiments.

5.4.1 Sensitization, Irritation, and Intracutaneous Reactivity

Sensitization or hypersensitivity occurs as a reaction of the body's immune response due to prolonged or repeated exposure to the chemicals contained in the material. It may cause an adverse local or systemic reaction, leading to irritation and inflammatory reactions. Such tests are usually performed in guinea pigs (guinea pig maximization test or Magunsson–Kligman method) or rodents (murine local lymph node test – LLNA). For example, LLNA determines the quantitative increase in lymphocytes in response to a sensitizer [99]. When a molecule acts as a skin sensitizer, it causes the epidermal Langerhans cells to transport the allergen to the draining lymph nodes, which in turn causes the T-lymphocytes to proliferate and differentiate.

The irritation test is used to assess the local inflammatory reaction of the tissue after direct contact with certain chemicals, using either the material itself or extracts

for such experiments. Although the *in vitro* test described above may provide useful information for the identification of irritants, current guidelines require confirmation of a negative *in vitro* test with an *in vivo* test. The irritation test usually includes skin, mucosal membranes, ocular, and intradermal tests. In the intradermal test, extracts of the test material must be injected intradermally together with blank samples (control), and the assessment is made on the injection side with the result for redness and swelling (erythema and edema). The primary skin irritation test involves the application of the material or extracts directly to the skin and visual assessment of redness and swelling for a specified period of time [100]. The mucosal membrane irritation test uses extracts of material rather than the material itself and includes studies of eye irritation, vaginal, and cheek pouch removal. The duration of contact should be similar to the expected clinical use of the device. Still, it is often advisable to slightly exaggerate the exposure conditions to provide a safety margin for patients. As with many assays, the final evaluation of results is often based on a comparison with the control condition. More detailed guidelines and methods for conducting such tests are described in ISO 10993-10 under "Sensitization and Irritation Tests" [101].

5.4.2 Biodegradation

Biodegradation is a biological process in the body that causes a gradual breakdown of the material. While in some cases, the degradation is intentional, in others, it is unfavorable and can lead to undesirable side effects. The biodegradation test is used to determine the tissue reaction to biodegradable materials and their biodegraded products, which can be caused by various chemical reactions, leaching, depolymerization, or physical peeling, etc. Degradation products include impurities, corrosion products, additives, and catalysts and can be leached into adjacent tissues and distant organs. *In vivo* experiments are usually necessary because it is not possible to predict the degradation rate *in vivo* accurately based on *in vitro* experiments.

For example, to assess the biodegradation of hydrogel implants, the weight loss of the implant after a certain time can be measured to determine the *in vivo* biodegradation rate [102]. In addition, tensile tests can be performed to assess the degradation of stent materials [103], or histological analyses can be performed to identify the tissue reaction [104]. While some studies can be conducted in a short time to determine the expected effect of biodegradation, other studies require a long-term assessment of degradation. For example, Amerstorfer et al. [105] evaluated the degradation of magnesium implants on bone tissue in the growing rat skeleton. They used micro-computed tomography, histological staining, and laser ablation inductively coupled plasma mass spectrometry (LA-ICP-MS) (Figure 5.10), a powerful analytical technique that allows the highly sensitive element and isotope analyses to be performed directly on solid samples [105].

5.4.3 In *V*ivo Genotoxicity

Several tests investigate genotoxicity *in vivo*, including the micronucleus test in rodents, the mammalian bone marrow cytogenetic test, the rodent dominant

Figure 5.10 LEFT: 3D (upper) and 2D (lower) μCT scans for long-term bone response implants. Middle: Histological staining to assess local tissue response. Right: LA-ICP-MS analysis showing chemical image of implanted Mg pins, from which relative mass was calculated for assessment of degradation rates. Source: From Amerstorfer et al. [105]/with permission of Elsevier.

lethal test, chromosome analysis, the mouse spot test, and the test for heritable translocation in mice. According to ISO 10993-3, *in vivo* genotoxicity is not required unless *in vitro* genotoxicity shows a genotoxic response. As with several other methods, materials dissolved in medium or extracts are used for the test. The two most commonly used *in vivo* methods are the mouse micronucleus (MN) assay [65] and the chromosome aberration test [106].

For the *in vivo* MN mouse test, young mice are used, which are treated intravenously or intraperitoneally with prepared solutions or extracts. Alternatively, an oral route of administration may be used if exposure is via the gastrointestinal tract. Assays are performed with positive and negative controls (vehicles). After the appropriate treatment time, bone marrow and/or peripheral blood is collected and analyzed MN for the presence of bone marrow. Smear preparations may be prepared and stained to assess the number of blood samples. MN or flow cytometry may be used if blood samples are involved. The number of MN is compared with the number of controls to determine whether the treatment increased the number of MN [65].

Another *in vivo* test often used to assess genotoxicity is the chromosome aberration assay [106]. Similar to the MN assay, young mice are dosed with extracts or solutions once a day for two consecutive days and sacrificed after 12–18 hours. Before sacrifice, the mice are treated with a metaphase storage agent, and bone marrow cells are removed. Slides are prepared, and metaphase cells are examined for chromosomal aberrations and compared with the negative control to determine whether the treatment has caused an increase in aberrations.

5.4.4 Systemic Toxicity

Systemic toxicity refers to a general effect caused by the material or device on the animal model, whereby leachable chemicals are absorbed in one site, spread throughout the body via the circulatory or lymphatic system, and cause a deleterious effect on the distant location. When testing medical devices, the part of the device may be implanted in the animal, or the extracts/solution may be administered.

The types of assessment can be categorized according to duration into acute, sub-acute, subchronic, and chronic toxicity. Acute toxicity is considered to be the initial screening to assess the adverse effect within 24 hours by observation of parameters such as clinical signs and symptoms and body weight. Subacute and subchronic toxicity are defined as adverse effects occurring after multiple or continuous exposure between 24 hours and 28 days and up to 90 days, respectively. Finally, adverse effects occurring during most of the life span due to repeated or continuous exposure are defined as a chronic toxicity. For rodents, such a test scenario is usually set to last six months [107].

5.4.5 Implantation

Implantation studies are the most direct means to evaluate the local tissue response to the material or device at the implantation site. Surgical implantation is performed on the appropriate clinically relevant tissue, with muscle, bone, and subcutaneous tissue is the most common, but other tissues such as the brain, tooth, or eye tissue may also be appropriate based on the intended clinical use. The pathological effects are assessed at a microscopic and gross level. Histopathological techniques are used to detect tissue necrosis, apoptosis, degeneration, inflammation, vascularization, collagen deposition, bone formation, cell proliferation, thrombus formation, and endothelialization. For short-term implantation studies (up to 12 weeks), small animals such as mice, rats, guinea pigs, and rabbits are usually used. For long-term studies (12–56 weeks), other animals with longer lifespan are also used (e.g. dogs, sheep, goats, pigs). Depending on biodegradability, absorption, and time-dependent changes in the reaction, several implant durations are required. Control materials with known reactions are implanted based on a scoring system to compare and evaluate fragmentation, degeneration, quality, and quantity of tissue ingrowth. Detailed guidelines for testing the local effect after implantation can be found in ISO 10993-6:2016 [108].

5.5 Concluding Remarks and Perspectives

The development of novel and intelligent biomaterials has been driven by the enormous increase in demand for bioalternatives that could perform the living activities of the body's organs in the absence of them. New biomaterials are constantly being developed with new applications, and the methods for analyzing their properties are constantly being improved to obtain adequate information on their safety and efficacy. There are some important considerations when evaluating the biological response. Firstly, the design of experiments for biocompatibility testing should be based on the unique properties of the biomaterial and its intended use, i.e. TE scaffold, medical devices, and prostheses. As we know, some biomaterials may be biocompatible in one application but not in another. Therefore, the design of experiments is important to determine biocompatibility and the intended or expected biological response.

Secondly, the presence of the biomaterials in the assay could interfere with classical protocols originally designed for cells grown on plastic substrates in monolayers. It is, therefore, essential to adapt and validate the protocols to ensure the quality and reproducibility of the data. Some important considerations in this regard include effective penetration of detection reagents (e.g. 3D constructs, high cell density systems), complete recovery or lysis of adherent cells, and other material-related interferences that could potentially affect the read-out of the assay and compromise results. Where possible, quantitative assays should be used, using appropriate statistical tests to determine the significance of the results

Thirdly, cell lines used for *in vitro* biocompatibility and cytotoxicity testing should be identified and suitable for the intended application. It has been shown that not all cells used in the test procedures are of the same quality [109] since different cell sources and their modifications (e.g. immortalization, knock-outs) can drastically influence the expected test results [110]. On the one hand, the use of commercial cell lines allows more controlled experiments, since they are supplied with a certificate guaranteeing certain properties. On the other hand, the use of primary human cells has many advantages since it allows researchers to draw result-oriented conclusions in relation to an actual clinical environment [111].

New developments in noninvasive continuous monitoring tests using noncytotoxic reagents and dyes that can maintain cell integrity will be appreciated. Improvements in 3D bio-imaging systems such as confocal microscopy and micro-computed tomography with increased resolution increased depth-of-field limits, and real-time monitoring capabilities will facilitate the better analysis of cells in scaffolds. HTS platforms will be an essential tool for accelerating the pace of biomaterial development in a timely and cost-effective manner, screening libraries for candidate materials, and identifying the best formulations for a given application.

The analysis of cell phenotype and differentiation, where specific biomarkers are assayed using many different techniques, constitutes in itself a very broad topic, being out of the scope of this chapter. However, phenotypic interactions must be taken into account when assessing the biological response. Cytokine analysis is now commonly used to identify the activity of different cell types in the evaluation of the biological response. Still, in many cases, this type of analysis is not sufficient to provide a complete picture or interpretation of the response.

Finally, the *in vivo* validation of *in vitro* results is necessary to evaluate the influence of a specific material in the scope of the whole organism, where various physiological effects are intertwined. Furthermore, specific parameters have to be also evaluated in *in vivo* related to a unique application of respective biomaterials under consideration. It is a common practice in the literature to make exaggerated claims based on *in vitro* results, and no follow-up testing with *in vivo* studies is presented to verify these claims and hypotheses. The *in vivo* validation of *in vitro* results must be performed if the proposed biomaterial is to be used in a clinical applications. However, the scientific community stream toward 3R (Replacement, Reduction, and Refinement) principles for *in vivo* testing and new sophisticated *in vitro* models using multiple cell types and 3D microenvironments are being developed, which may lead to a better compromise between the simplicity of

the system and biological relevance. As innovation in the field of biomaterials is expected to continue, the development of new methods for the analysis of the biological and biomedical properties of biomaterials and standardized guidelines will continue to require constant adaptations and revisions.

References

1 Williams, D.F. and Williams, D.F. (1999). *The Williams Dictionary of Biomaterials*. Liverpool University Press.
2 Williams, D.F. (2008). On the mechanisms of biocompatibility. *Biomaterials* 29 (20): 2941–2953.
3 Ratner, B.D. (2011). The biocompatibility manifesto: biocompatibility for the twenty-first century. *J. Cardiovasc. Transl. Res.* 4 (5): 523–527.
4 Custodio, C.A., Reis, R.L., and Mano, J.F. (2014). Engineering biomolecular microenvironments for cell instructive biomaterials. *Adv. Healthc. Mater.* 3 (6): 797–810.
5 Li, Y. and Kilian, K.A. (2015). Bridging the gap: from 2D cell culture to 3D microengineered extracellular matrices. *Adv. Healthc. Mater.* 4 (18): 2780–2796.
6 Flecknell, P. (2002). Replacement, reduction and refinement. *ALTEX* 19 (2): 73–78.
7 Essential, M.K. (2015). Cell biology. *Yale J. Biol. Med.* 88 (1): 100–101.
8 Use of International Standard ISO-10993 (2018). *Biological Evaluation of Medical Devices*. Standardization IOf.
9 Thrivikraman, G., Madras, G., and Basu, B. (2014). In vitro/In vivo assessment and mechanisms of toxicity of bioceramic materials and its wear particulates. *RSC Adv.* 4 (25): 12763–12781.
10 ISO 10993-5:2009 (2009). *Biological Evaluation of Medical Devices — Part 5: Tests for In Vitro Cytotoxicity*. Standardization IOf.
11 Li, W., Zhou, J., and Xu, Y. (2015). Study of the in vitro cytotoxicity testing of medical devices. *Biomed. Rep.* 3 (5): 617–620.
12 Lim, S.M., Yap, A., Loo, C. et al. (2017). Comparison of cytotoxicity test models for evaluating resin-based composites. *Hum. Exp. Toxicol.* 36 (4): 339–348.
13 Johnson, H.J., Northup, S.J., Seagraves, P.A. et al. (1985). Biocompatibility test procedures for materials evaluation in vitro. II. Objective methods of toxicity assessment. *J. Biomed. Mater. Res.* 19 (5): 489–508.
14 ISO 10993-1:2018 (2018). *Biological Evaluation of Medical Devices — Part 1: Evaluation and Testing within a Risk Management Process*. Standardization IOf.
15 Barrias, C.C., Martins, M.C.L., Almeida-Porada, G. et al. (2009). The correlation between the adsorption of adhesive proteins and cell behaviour on hydroxyl-methyl mixed self-assembled monolayers. *Biomaterials* 30 (3): 307–316.
16 Harburger, D.S. and Calderwood, D.A. (2009). Integrin signalling at a glance. *J. Cell Sci.* 122 (2): 159–163.
17 Bendas, G. and Borsig, L. (2012). Cancer cell adhesion and metastasis: selectins, integrins, and the inhibitory potential of heparins. *Int. J. Cell Biol.* 2012: 676731.

18 Veale, D.J. and Maple, C. (1996). Cell adhesion molecules in rheumatoid arthritis. *Drugs Aging* 9 (2): 87–92.

19 Galkina, E. and Ley, K. (2007). Vascular adhesion molecules in atherosclerosis. *Arterioscler. Thromb. Vasc. Biol.* 27 (11): 2292–2301.

20 Allen, M.R., Hock, J.M., and Burr, D.B. (2004). Periosteum: biology, regulation, and response to osteoporosis therapies. *Bone* 35 (5): 1003–1012.

21 Evangelista, M.B., Hsiong, S.X., Fernandes, R. et al. (2007). Upregulation of bone cell differentiation through immobilization within a synthetic extracellular matrix. *Biomaterials* 28 (25): 3644–3655.

22 Neves, S.C., Gomes, D.B., Sousa, A. et al. (2015). Biofunctionalized pectin hydrogels as 3D cellular microenvironments. *J. Mater. Chem. B* 3 (10): 2096–2108.

23 Villalona, G.A., Udelsman, B., Duncan, D.R. et al. (2010). Cell-seeding techniques in vascular tissue engineering. *Tissue Eng. Part B Rev.* 16 (3): 341–350.

24 Teixeira, G.Q., Barrias, C.C., Lourenço, A.H., and Gonçalves, R.M. (2014). A multicompartment holder for spinner flasks improves expansion and osteogenic differentiation of mesenchymal stem cells in three-dimensional scaffolds. *Tissue Eng. Part C Methods* 20 (12): 984–993.

25 Talukdar, S., Nguyen, Q.T., Chen, A.C. et al. (2011). Effect of initial cell seeding density on 3D-engineered silk fibroin scaffolds for articular cartilage tissue engineering. *Biomaterials* 32 (34): 8927–8937.

26 Reynolds, P.M., Holzmann Rasmussen, C., Hansson, M. et al. (2018). Controlling fluid flow to improve cell seeding uniformity. *PLoS One* 13 (11): e0207211.

27 Harunaga, J.S. and Yamada, K.M. (2011). Cell-matrix adhesions in 3D. *Matrix Biol.* 30 (7): 363–368.

28 Kilian, K.A., Bugarija, B., Lahn, B.T., and Mrksich, M. (2010). Geometric cues for directing the differentiation of mesenchymal stem cells. *Proc. Natl. Acad. Sci. U.S.A.* 107 (11): 4872–4877.

29 Théry, M., Pépin, A., Dressaire, E. et al. (2006). Cell distribution of stress fibres in response to the geometry of the adhesive environment. *Cell Motil.* 63 (6): 341–355.

30 Hou, H.S., Lee, K.L., Wang, C.H. et al. (2019). Simultaneous assessment of cell morphology and adhesion using aluminum nanoslit-based plasmonic biosensing chips. *Sci. Rep.* 9 (1): 7204.

31 Li, E., Chang, C.C., Zhang, Z., and Li, Q. (2016). Characterization of tissue scaffolds for time-dependent biotransport criteria – a novel computational procedure. *Comput. Methods Biomech. Biomed. Eng.* 19 (11): 1210–1224.

32 Makita, R., Akasaka, T., Tamagawa, S. et al. (2018). Preparation of micro/nanopatterned gelatins crosslinked with genipin for biocompatible dental implants. *Beilstein J. Nanotechnol.* 9: 1735–1754.

33 Niles, A.L., Moravec, R.A., Eric Hesselberth, P. et al. (2007). A homogeneous assay to measure live and dead cells in the same sample by detecting different protease markers. *Anal. Biochem.* 366 (2): 197–206.

34 Mosmann, T. (1983). Rapid colorimetric assay for cellular growth and survival: application to proliferation and cytotoxicity assays. *J. Immunol. Methods* 65 (1): 55–63.

35 Ferrari, M., Fornasiero, M.C., and Isetta, A.M. (1990). MTT colorimetric assay for testing macrophage cytotoxic activity in vitro. *J. Immunol. Methods* 131 (2): 165–172.

36 van de Loosdrecht, A.A., Beelen, R.H.J., Ossenkoppele, G.J. et al. (1994). A tetrazolium-based colorimetric MTT assay to quantitate human monocyte mediated cytotoxicity against leukemic cells from cell lines and patients with acute myeloid leukemia. *J. Immunol. Methods* 174 (1): 311–320.

37 Berridge, M.V., Herst, P.M., and Tan, A.S. (2005). Tetrazolium dyes as tools in cell biology: new insights into their cellular reduction. *Biotechnol. Annu. Rev.* 11: 127–152.

38 Twigg, R.S. (1945). Oxidation-reduction aspects of resazurin. *Nature* 155 (3935): 401–402.

39 Nakayama, G.R., Caton, M.C., Nova, M.P., and Parandoosh, Z. (1997). Assessment of the Alamar Blue assay for cellular growth and viability in vitro. *J. Immunol. Methods* 204 (2): 205–208.

40 Hamid, R., Rotshteyn, Y., Rabadi, L. et al. (2004). Comparison of alamar blue and MTT assays for high throughput screening. *Toxicol. In Vitro* 18 (5): 703–710.

41 Węsierska-Gądek, J., Gueorguieva, M., Ranftler, C., and Zerza-Schnitzhofer, G. (2005). A new multiplex assay allowing simultaneous detection of the inhibition of cell proliferation and induction of cell death. *J. Cell. Biochem.* 96 (1): 1–7.

42 van Tonder, A., Joubert, A.M., and Cromarty, A.D. (2015). Limitations of the 3-(4,5-dimethylthiazol-2-yl)-2,5-diphenyl-2H-tetrazolium bromide (MTT) assay when compared to three commonly used cell enumeration assays. *BMC. Res. Notes* 8 (1): 47.

43 O'Brien, J., Wilson, I., Orton, T., and Pognan, F. (2000). Investigation of the Alamar Blue (resazurin) fluorescent dye for the assessment of mammalian cell cytotoxicity. *Eur. J. Biochem.* 267 (17): 5421–5426.

44 Kangas, L., Gronroos, M., and Nieminen, A.L. (1984). Bioluminescence of cellular ATP: a new method for evaluating cytotoxic agents in vitro. *Med. Biol.* 62 (6): 338–343.

45 Muir, D., Varon, S., and Manthorpe, M. (1990). An enzyme-linked immunosorbent assay for bromodeoxyuridine incorporation using fixed microcultures. *Anal. Biochem.* 185 (2): 377–382.

46 Hawker, J.R. (2003). Chemiluminescence-based BrdU ELISA to measure DNA synthesis. *J. Immunol. Methods* 274 (1): 77–82.

47 Buck, S.B., Bradford, J., Gee, K.R. et al. (2008). Detection of S-phase cell cycle progression using 5-ethynyl-2′-deoxyuridine incorporation with click chemistry, an alternative to using 5-bromo-2′-deoxyuridine antibodies. *Biotechniques* 44 (7): 927–929.

48 Scholzen, T. and Gerdes, J. (2000). The Ki-67 protein: from the known and the unknown. *J. Cell. Physiol.* 182 (3): 311–322.

49 Bravo, R. (1986). Synthesis of the nuclear protein cyclin (PCNA) and its relationship with DNA replication. *Exp. Cell Res.* 163 (2): 287–293.

50 Kim, J.-Y., Jeong, H.S., Chung, T. et al. (2017). The value of phosphohistone H3 as a proliferation marker for evaluating invasive breast cancers: a comparative study with Ki67. *Oncotarget* 8 (39): 65064–65076.

51 Riedl, A., Schlederer, M., Pudelko, K. et al. (2017). Comparison of cancer cells in 2D vs 3D culture reveals differences in AKT–mTOR–S6K signaling and drug responses. *J. Cell Sci.* 130 (1): 203–218.

52 Duval, K., Grover, H., Han, L.-H. et al. (2017). Modeling physiological events in 2D vs. 3D cell culture. *Physiology (Bethesda)* 32 (4): 266–277.

53 Gallant, N.D. (2013). 3 - Quantitative assays for measuring cell adhesion and motility in biomaterials. In: *Characterization of Biomaterials* (ed. M. Jaffe, W. Hammond, P. Tolias and T. Arinzeh), 72–100. Woodhead Publishing.

54 Liang, C.-C., Park, A.Y., and Guan, J.-L. (2007). In vitro scratch assay: a convenient and inexpensive method for analysis of cell migration in vitro. *Nat. Protoc.* 2 (2): 329–333.

55 Campbell, J.J., Husmann, A., Hume, R.D. et al. (2017). Development of three-dimensional collagen scaffolds with controlled architecture for cell migration studies using breast cancer cell lines. *Biomaterials* 114: 34–43.

56 Justus, C.R., Leffler, N., Ruiz-Echevarria, M., and Yang, L.V. (2014). In vitro cell migration and invasion assays. *J. Vis. Exp.* 88: 51046.

57 Heit, B. and Kubes, P. (2003). Measuring chemotaxis and chemokinesis: the under-agarose cell migration assay. *Science's STKE* 2003 (170): Pl5.

58 Vogt, A. (2010). Advances in two-dimensional cell migration assay technologies. *Eur. Pharm. Rev.* 17 (2): 882–870.

59 Tehranirokh, M., Kouzani, A.Z., Francis, P.S., and Kanwar, J.R. (2013). Microfluidic devices for cell cultivation and proliferation. *Biomicrofluidics.* 7 (5): 051502.

60 Au-Vinci, M., Au-Box, C., and Au-Eccles, S.A. (2015). Three-dimensional (3D) tumor spheroid invasion assay. *JoVE* (99): e52686.

61 Zhang, C., Jang, S., Amadi, O.C. et al. (2013). A sensitive chemotaxis assay using a novel microfluidic device. *Biomed. Res. Int.* 2013: 373569.

62 Harley, B.A.C., Kim, H.-D., Zaman, M.H. et al. (2008). Microarchitecture of three-dimensional scaffolds influences cell migration behavior via junction interactions. *Biophys. J.* 95 (8): 4013–4024.

63 ISO 10993-4:2002 (2002). *Biological Evaluation of Medical Devices — Part 4: Selection of Tests for Interactions with Blood*. Standardization IOf.

64 Blok, S.L.J., Engels, G.E., and Oeveren, Wv. (2016). In vitro hemocompatibility testing: the importance of fresh blood. *Biointerphases* 11 (2): 029802.

65 Hayashi, M. (2016). The micronucleus test-most widely used in vivo genotoxicity test. *Genes Environ.* 38: 18.

66 Langie, S., Azqueta, A., and Collins, A. (2015). The comet assay: past, present, and future. *Front. Genet.* 6 (266): 164–171.

67 Kirkland, D., Reeve, L., Gatehouse, D., and Vanparys, P. (2011). A core in vitro genotoxicity battery comprising the Ames test plus the in vitro micronucleus

test is sufficient to detect rodent carcinogens and in vivo genotoxins. *Mutat. Res.* 721 (1): 27–73.

68 ISO 10993-3:2014 (2014). *Biological Evaluation of Medical Devices — Part 3: Tests for Genotoxicity, Carcinogenicity and Reproductive Toxicity*. Standardisation IOf.

69 Lloyd, M. and Kidd, D. (2012). The mouse lymphoma assay. *Methods Mol. Biol. (Clifton, NJ)* 817: 35–54.

70 Liu, J., Wen, J., Zhang, Z. et al. (2015). Voyage inside the cell: microsystems and nanoengineering for intracellular measurement and manipulation. *Microsyst. Nanoeng.* 1 (1): 15020.

71 Fu, T.-M., Duan, X., Jiang, Z. et al. (2014). Sub-10-nm intracellular bioelectronic probes from nanowire–nanotube heterostructures. *Proc. Natl. Acad. Sci. U.S.A.* 111 (4): 1259–1264.

72 Yoon, I., Hamaguchi, K., Borzenets, I.V. et al. (2013). Intracellular neural recording with pure carbon nanotube probes. *PLoS One* 8 (6): e65715.

73 Schrlau, M.G., Dun, N.J., and Bau, H.H. (2009). Cell electrophysiology with carbon nanopipettes. *ACS Nano* 3 (3): 563–568.

74 Liu, H., Wen, J., Xiao, Y. et al. (2014). In situ mechanical characterization of the cell nucleus by atomic force microscopy. *ACS Nano* 8 (4): 3821–3828.

75 Obataya, I., Nakamura, C., Han, N.N., and Miyake, J. (2005). Nanoscale operation of a living cell using an atomic force microscope with a nanoneedle. *Nano Lett.* 5 (1): 27–30.

76 Beard, J.D., Guy, R.H., and Gordeev, S.N. (2013). Mechanical tomography of human corneocytes with a nanoneedle. *J. Invest. Dermatol.* 133 (6): 1565–1571.

77 Ruedas-Rama, M.J., Walters, J.D., Orte, A., and Hall, E.A.H. (2012). Fluorescent nanoparticles for intracellular sensing: a review. *Anal. Chim. Acta* 751: 1–23.

78 Kucsko, G., Maurer, P.C., Yao, N.Y. et al. (2013). Nanometre-scale thermometry in a living cell. *Nature* 500 (7460): 54–58.

79 Okabe, K., Inada, N., Gota, C. et al. (2012). Intracellular temperature mapping with a fluorescent polymeric thermometer and fluorescence lifetime imaging microscopy. *Nat. Commun.* 3 (1): 705.

80 Korzeniowska, B., Woolley, R., Decourcey, J. et al. (2014). Intracellular pH-sensing using core/shell silica nanoparticles. *J. Biomed. Nanotechnol.* 10 (7): 1336–1345.

81 Donner, J.S., Thompson, S.A., Kreuzer, M.P. et al. (2012). Mapping intracellular temperature using green fluorescent protein. *Nano Lett.* 12 (4): 2107–2111.

82 Grashoff, C., Hoffman, B.D., Brenner, M.D. et al. (2010). Measuring mechanical tension across vinculin reveals regulation of focal adhesion dynamics. *Nature* 466 (7303): 263–266.

83 Gómez-Martínez, R., Hernández-Pinto, A.M., Duch, M. et al. (2013). Silicon chips detect intracellular pressure changes in living cells. *Nat. Nanotechnol.* 8 (7): 517–521.

84 Song, J.H., Lee, S.-M., and Yoo, K.-H. (2018). Label-free and real-time monitoring of human mesenchymal stem cell differentiation in 2D and 3D cell culture systems using impedance cell sensors. *RSC Adv.* 8 (54): 31246–31254.

85 Narayanan, L.K., Thompson, T.L., Shirwaiker, R.A., and Starly, B. (2018). Label free process monitoring of 3D bioprinted engineered constructs via dielectric impedance spectroscopy. *Biofabrication* 10 (3): 035012.

86 Lee, S.-M., Han, N., Lee, R. et al. (2016). Real-time monitoring of 3D cell culture using a 3D capacitance biosensor. *Biosens. Bioelectron.* 77: 56–61.

87 Mahfouzi, S.H., Amoabediny, G., Doryab, A. et al. (2018). Noninvasive real-time assessment of cell viability in a three-dimensional tissue. *Tissue Eng. Part C Methods* 24 (4): 197–204.

88 Yea, C.-H., Jeong, H.-C., Moon, S.-H. et al. (2016). In situ label-free quantification of human pluripotent stem cells with electrochemical potential. *Biomaterials* 75: 250–259.

89 Reitinger, S., Wissenwasser, J., Kapferer, W. et al. (2012). Electric impedance sensing in cell-substrates for rapid and selective multipotential differentiation capacity monitoring of human mesenchymal stem cells. *Biosens. Bioelectron.* 34 (1): 63–69.

90 Zohar, B., Blinder, Y., Epshtein, M. et al. (2019). Multi-flow channel bioreactor enables real-time monitoring of cellular dynamics in 3D engineered tissue. *Commun. Biol.* 2 (1): 158.

91 Kim, H., Kim, M.K., Jang, H. et al. (2019). Sensor-instrumented scaffold integrated with microporous spongelike ultrabuoy for long-term 3D mapping of cellular behaviors and functions. *ACS Nano* 13 (7): 7898–7904.

92 Seo, J., Shin, J.-Y., Leijten, J. et al. (2018). High-throughput approaches for screening and analysis of cell behaviors. *Biomaterials* 153: 85–101.

93 Kijun, P., Yeontaek, L., and Jungmok, S. (2018). Recent advances in high-throughput platforms with engineered biomaterial microarrays for screening of cell and tissue behavior. *Curr. Pharm. Des.* 24 (45): 5458–5470.

94 Oliveira, M.B. and Mano, J.F. (2014). High-throughput screening for integrative biomaterials design: exploring advances and new trends. *Trends Biotechnol.* 32 (12): 627–636.

95 Algahtani, M.S., Scurr, D.J., Hook, A.L. et al. (2014). High throughput screening for biomaterials discovery. *J. Control. Release* 190: 115–126.

96 Dolatshahi-Pirouz, A., Nikkhah, M., Gaharwar, A.K. et al. (2014). A combinatorial cell-laden gel microarray for inducing osteogenic differentiation of human mesenchymal stem cells. *Sci. Rep.* 4 (1): 3896.

97 Patel, A.K., Tibbitt, M.W., Celiz, A.D. et al. (2016). High throughput screening for discovery of materials that control stem cell fate. *Curr. Opin. Solid State Mater. Sci.* 20 (4): 202–211.

98 Kolb, L., Allazetta, S., Karlsson, M. et al. (2019). High-throughput stem cell-based phenotypic screening through microniches. *Biomater. Sci.* 7 (8): 3471–3479.

99 Gerberick, G.F., Ryan, C.A., Dearman, R.J., and Kimber, I. (2007). Local lymph node assay (LLNA) for detection of sensitization capacity of chemicals. *Methods (San Diego, Calif)* 41 (1): 54–60.

100 Abu Bakar, N., Othman, H., Rajab, N. et al. (2019). Primary skin irritation and dermal sensitization assay: *In vivo* evaluation of the essential oil from *Piper sarmentosum* Roxb. *Pharmacogn. Mag.* 15 (64): 352–358.

101 ISO 10993-10:2010 (2010). *Biological Evaluation of Medical Devices — Part 10: Tests for Irritation and Skin Sensitization*. Standardisation IOf.

102 Kim, J., Dadsetan, M., Ameenuddin, S. et al. (2010). In vivo biodegradation and biocompatibility of PEG/sebacic acid-based hydrogels using a cage implant system. *J. Biomed. Mater. Res. A* 95 (1): 191–197.

103 Bartosch, M., Peters, H., Koerner, A. et al. (2018). New methods for in vivo degradation testing of future stent materials. *Mater. Corros.* 69 (2): 156–166.

104 Alberti, K.A. and Xu, Q. (2015). Biocompatibility and degradation of tendon-derived scaffolds. *Regenerat. Biomater.* 3 (1): 1–11.

105 Amerstorfer, F., Fischerauer, S.F., Fischer, L. et al. (2016). Long-term in vivo degradation behavior and near-implant distribution of resorbed elements for magnesium alloys WZ21 and ZX50. *Acta Biomater.* 42: 440–450.

106 OECD (1997). Test No. 475: Mammalian Bone Marrow Chromosome Aberration Test.

107 Auletta, C.S. (2004). Current in vivo assays for cutaneous toxicity: local and systemic toxicity testing. *Basic Clin. Pharmacol. Toxicol.* 95 (5): 201–208.

108 ISO 10993-6:2016 (2016). *Biological Evaluation of Medical Devices — Part 6: Tests for Local Effects After Implantation*. Standardisation IOf.

109 Wang, K., Shindoh, H., Inoue, T., and Horii, I. (2002). Advantages of in vitro cytotoxicity testing by using primary rat hepatocytes in comparison with established cell lines. *J. Toxicol. Sci.* 27 (3): 229–237.

110 Farwell, D.G., Shera, K.A., Koop, J.I. et al. (2000). Genetic and epigenetic changes in human epithelial cells immortalized by telomerase. *Am. J. Pathol.* 156 (5): 1537–1547.

111 Czekanska, E.M., Stoddart, M.J., Ralphs, J.R. et al. (2014). A phenotypic comparison of osteoblast cell lines versus human primary osteoblasts for biomaterials testing. *J. Biomed. Mater. Res. A* 102 (8): 2636–2643.

6

Polysaccharide Thin Films – Preparation and Analysis

Carina Sampl and Stefan Spirk

Graz University of Technology, Institute of Bioproducts and Paper Technology, Inffeldgasse 23, 8010 Graz, Austria

6.1 Biopolymer Thin-Film Preparation

During the past years, biopolymer thin films have gained more and more attention. The structural and chemical inhomogeneities of biopolymer compounds such as cellulose fibers made the *in situ* evaluation of interaction processes challenging to assess [1]. To increase the knowledge of physical and chemical properties such as the swelling behavior and the interaction capacity of, e.g., cellulose, the need to develop simplified, well-defined systems arose [2, 3]. By the use of model films, the in situ evaluation of the adsorption behavior of proteins, drugs, industrially relevant compounds, etc., on cellulose surfaces became possible. The preparation of model thin films, however, is impeded by the highly complex supramolecular features of biopolymeric compounds and thus is not straightforward [3]. For cellulose, its sparse solubility [4] is the main issue with thin-film preparation, making the preparation of homogeneous, smooth films a potential challenge [3]. For the preparation of thin films, the biopolymer has to be in a dissolved or suspended form. On the example of cellulose, a suitable solvent, a derivative, or a nanocellulose suspension can be used. Model films can be prepared by two established methods, namely, Langmuir–Blodgett (LB) or Langmuir–Schaefer (LS) [5] deposition and spin coating [6].

LB films are manufactured by transferring floating organic monolayers onto solid surfaces. Combining the proper chemistry and a special instrument (a Langmuir trough) can give high-quality monomolecular assemblies exhibiting a high degree of structural order [5, 7, 8]. In 1920, Blodgett successfully transferred fatty acid monolayers from water to solid substrates such as glass slides [9]. In the early 1930, Katharine Blodgett published results on the apparatus and stearic acid monolayer formation experiments on glass substrates [10, 11]. With developments on the method itself, it had become possible to deposit more than 200 layers of material on glass and on various metal substrates [10, 11]. In the past years, the LB technique has been frequently used, and several reviews provide detailed discussions on the experimental setup, thin-film structure, morphology, etc. [12–14].

Functional Biomaterials: Design and Development for Biotechnology, Pharmacology, and Biomedicine, First Edition. Edited by Tamilselvan Mohan and Karin Stana Kleinschek.

Generally, a Langmuir monolayer is prepared by placing a known amount of organic amphiphilic molecules on the surface of an aqueous subphase. Therefore, a drop-by-drop approach is used. The applied compound spontaneously spreads onto the clean water surface, and the volatile organic solvent (such as methanol, chloroform, or benzene) evaporates within minutes. By using a floating barrier, the monolayer is compressed. Therefore, one or more movable (typically motorized) Teflon barriers are placed across the trough to vary the surface area of the monolayer [5, 7, 8, 15].

For film deposition, a suitable substrate is normally lifted and raised vertically through the compact monolayer of the organic compound at a controlled speed [16], displayed in Figure 6.1 [5], while the Langmuir monolayer is held at a constant surface pressure [15]. When adhesion to the surface is poor, a technique developed by Langmuir and Schaefer (LS) [17] can be applied. Here, a suitable substrate is placed on the liquid surface to form a monolayer of compound on it [17]. To control the nature of the deposited layers, the surface quality and the chemical composition of the substrate are of importance [7, 8, 16].

The spin coating process is widely used to apply a thin uniform film of a certain compound onto a flat substrate. It is employed, for example, in coating electrical devices and to apply coatings in the microelectronic industry for the production of photoresists [18]. In academia, spin coating is frequently used for the preparation of homogeneous thin films from biopolymer compounds to study interaction processes taking place at surfaces [19–21].

For spin coating, a solution or dispersion of a particular compound is deposited on a solid substrate. This substrate is then rapidly accelerated to a specific rotation rate, rotated for a certain duration to give a thin film (static approach). An alternative approach is to start the rotation of the substrate and to deposit the compound solution during rotation (dynamic approach). In both cases, the liquid flows radially because of the action of centrifugal force, and excess of sample solution is ejected off the edges of the substrate. Therefore, the film slowly thins out until it reaches an equilibrium thickness or until it solidifies because of the evaporation of the solvent (Figure 6.2). In the end, the final film thinning is purely caused by solvent evaporation [22].

Bornside et al. describe four stages of spin coating, deposition, spin-up, spin-off, and evaporation [23]. The stages deposition and spin-up occur very quickly; therefore, the substrate is usually brought to its final rotation rate within a fraction of

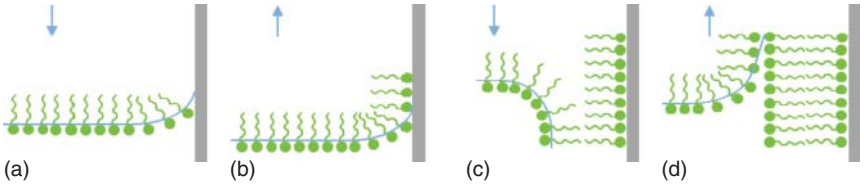

Figure 6.1 Langmuir–Blodgett deposition technique. Monolayer formation by (a) first immersion and (b) first withdrawal and multilayer build-up by (c) second immersion and (d) second withdrawal of the solid substrate (gray) [5]. Source: Adapted from Hann [5].

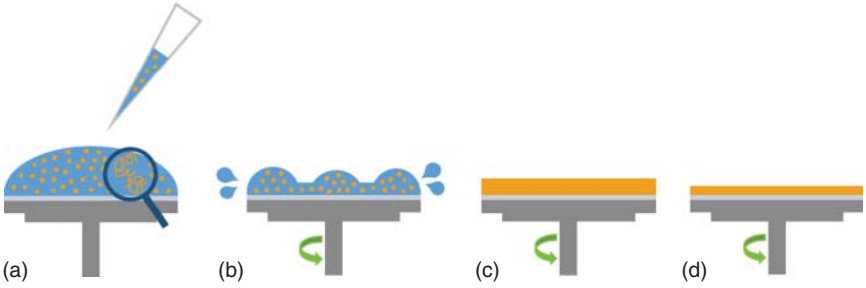

Figure 6.2 Schematic description of the spin coating process – (a) deposition of a polymer solution onto a solid substrate followed by (b) acceleration to the desired rotation speed where excess of solvent is ejected off the edges and (c) a film is formed. (d) The film turns to a solid because of complete solvent evaporation [22].

seconds [6]. The spin-off step and the evaporation step occur concurrently; during the first few seconds after spin-up, the film is several micrometers thick and the liquid phase has less time to evaporate as it is centrifuged off from the disk. Subsequently, the film thins very slowly because of solvent evaporation [6, 23, 24].

In the field of biopolymer research, spin coating and LB deposition have become the most important techniques to cast thin films. Many working groups apply these methods to deposit biopolymers such as cellulose and its derivatives [21, 25–31], starch [32, 33], or chitin [34, 35].

To prepare a biopolymer thin film by applying the presented deposition techniques, the sample needs to be dissolved/suspended in a liquid. In order to dissolve cellulose, it can be chemically modified or dissolved in a suitable solvent. There are different types of solvents in use, namely, both aqueous and non-aqueous, non-derivatizing, and derivatizing ones. One type of solvents is described by direct, non-derivatizing solvents that are divided into non-aqueous solvents – such as dimethylacetamide (DMAc/LiCl) [36] or *N*-methylmorpholine-*N*-oxide (NMMO) [37] as well as ionic liquids (IL) [38] – and aqueous solvents – such as NaOH/urea/water mixtures [39]. Further, cellulose can be modified, i.e. derivatized, to obtain a soluble cellulose derivative such as trimethylsily cellulose (TMSC), which is, after deposition onto a substrate, converted back to pure cellulose [26]. Cellulose xanthate (CX), nitrate, and carbamate (CC) are further examples for derivatized, intermediate cellulose compounds [40, 41]. Another method to directly deposit cellulose is by the use of nanocellulose suspensions consisting of cellulose nanocrystals (CNCs) or cellulose nanofibers (CNFs) [2].

The direct and indirect preparation of cellulose films using LB and LS deposition as well as spin coating is reviewed in the following section.

6.1.1 Direct Preparation of Cellulose Films

For direct deposition of cellulose thin films, nanocellulose suspensions or dissolved cellulose can be used. Well-known and frequently used cellulose suspensions consist of CNCs and CNFs. To dissolve cellulose for direct film deposition, non-derivatizing cellulose solvents are used.

6.1.1.1 Thin Films from Cellulose Solutions

Solvents for direct deposition of cellulose are described by the non-derivatizing ones, which can be divided into aqueous and non-aqueous solvents. Direct cellulose solvents can be single- or multicomponent systems involving one component that is a solid at room temperature [42].

Non-aqueous solvents such as dimethylacetamide with LiCl (DMAc/LiCl) [36] or NMMO with water [37] as well as ionic liquids (IL) [38, 43] are commonly used. On the other side, aqueous solvents such as mixtures of NaOH/urea [44, 45] and inorganic complexes such as Cuoxam (tetrammine diaqua copper hydroxide) find application [40, 42].

A disadvantage of solid cellulose thin films from direct solvents is that the solid compound from the solvent mixture will also be present in and on the resulting thin film [42] and has to be removed via a washing step with water after film deposition [2]. The LB method for film casting from direct cellulose solvents cannot be applied as this technique is based on the use of a water subphase, which is miscible with the cellulose solvents [2]. Today, the spin coating technique is the deposition method of choice when using non-derivatizing cellulose solvents [2, 3].

Dimethylacetamide with lithium chloride (DMAc-LiCl) is frequently used as a casting solvent for cellulose thin films [46, 47]. During spin coating of cellulose from DMAc/LiCl, an increased temperature of 100 °C is required because of the high boiling point of DMAc. After coating, the thin films need to be rinsed with water to remove the solid lithium chloride [3]. Thin films prepared from DMAc/LiCl and NMMO/water exhibit a certain roughness. The roughness most probably arises from the tracks and pressure marks left behind by the solid compound of the solvent mixture after rinsing [2, 48].

Aqueous solvents, such as NaOH/urea and NaOH/thiourea, also yield homogeneous thin films via spin coating. Yan et al. dissolved cellulose in NaOH/thiourea and spin coated them on mica [39]. In order to remove the solid residues from the solvent after coating, they placed the cellulose films in MilliQ (MQ) water. Atomic force microscopy (AFM) images revealed that smooth and homogeneous cellulose thin films were obtained [39].

Further, ionic liquids (IL) are a highly promising class of cellulose solvents for thin-film casting. The organic salts are regarded as “green solvents” and have attracted attention because of their unique physiochemical properties (chemical and physical stability, non-flammability, and low vapor pressure). In general, an IL is a salt whose melting point is below 100 °C, which solely consists of ions and short-living ion pairs [49].

Kargl and coworkers applied 1-ethyl-3-methyl imidazolium acetate (EmimAc) diluted with DMSO to dissolve cellulose [50]. For spin coating, they applied the cellulose solution onto a solid substrate. After spin coating, the thin films were put into an ethanol bath to precipitate the cellulose and avoid dewetting (coating method I). In coating method II, they deposited the IL–cellulose mixture on the substrate, started spin coating, and precipitated the cellulose by addition of ethanol already during the coating procedure. These procedures gave films with thicknesses ranging from the monolayer regime to hundreds of nanometers [50].

In Swatloski's group, the interaction mechanism of DMAC/LiCl and 1-butyl-3-methylimidazolium chloride [C4mim]Cl with cellulose from different sources was studied [51]. They described that the complexation of the Li ions by DMAc mobilizes the chloride ions, which interact with the cellulose hydroxyl groups. It is speculated that a high chloride concentration and the activity of the solvent are highly important in breaking the extensive hydrogen-binding network. The chloride concentration in [C4mim]Cl was found to be almost three times higher than that in traditional solvent systems, what allows for faster dissolution and the ability to dissolve cellulose in higher concentrations [51].

Pinkert et al. compared different IL in terms of synthesis, properties, and applications as well as their interaction mechanisms with cellulose [49].

6.1.1.2 Thin Films from Colloidal Nanocellulose Dispersions

Nanocellulose comes in two types, namely, CNCs and CNFs [52, 53]. Diverse approaches for production of CNCs and CNFs include top-down methods that involve enzymatic, physical, and chemical methodologies for their isolation from woody plants. Further, nanocellulose is gained from the bottom-up production of nanofibers from glucose in bacteria. In general, cellulosic materials having one dimension in the nanometer range are usually assigned to as nanocelluloses. These nanocelluloses are of unique manner as they combine important cellulose properties such as wide chemical modification capacity with the peculiar features of nanoscale materials because of their high surface area [52].

6.1.1.2.1 CNCs and its Ultrathin Films

CNCs typically consist of rodlike cellulose crystals with a width of 5–70 nm and the length between 100 nm and several micrometers [52, 54]. Water is incapable to penetrate into a cellulose crystal [53]; however, CNCs under high humidity get enveloped with an approximately 1 nm-thick layer of water on their surface [53, 55].

Typically, CNCs are obtained via acid hydrolysis using mineral acids such as sulfuric acid (64–65 wt%) or hydrochloric acid (5%) [52, 56]. Besides liquid hydrolysis, Kontturi et al. presented in 2016 a procedure using acidic vapor for hydrolysis and CNC preparation [56]. During acidic hydrolysis, glycosidic linkages between the AGUs in dislocated regions are broken and smaller cellulose fragments are obtained [57]. The sulfuric acid does not only selectively cleave the disordered segments of cellulose but simultaneously introduces sulfate half-ester groups on the CNC surface that enhance their colloidal stability [52, 53]. The dimensional diversity and the morphology of CNCs strongly depend on the source of the cellulose material and the preparation conditions [54]. Cotton and wood yield a quite narrow distribution of highly crystalline nanorods (90% crystallinity, width 5–10 nm, and length 100–300 nm) [52], and extraction from tunicates [58, 59], bacteria [60], and algae gives crystals with large polydispersity and dimensions (width 5–60 nm and length 100 nm to several micrometers) [52, 61, 62].

In 2003, the group around Edgar and Gray was the first applying spin coating to obtain smooth thin films that were stabilized by a mild heat treatment [63]. Notley

showed that a mild heat treatment after spin coating does not affect the number of sulfate groups on the CNC surface as they observed a large electrostatic component when studying the surface forces [1]. Since then, the subsequent heat treatment has become standard in the preparation of stable ultrathin films from CNCs. The introduced electrostatics from sulfated CNCs contributes to control the deposition of the cellulosic material [2].

Kontturi et al. showed that these anionic CNCs neatly disperse on a cationic TiO_2 surface and used this effect to investigate the dimensions of individual CNCs applying AFM imaging [25, 64]. Charged thin-film surfaces from CNCs can also be cast via layer-by-layer (LbL) deposition. Cranston and Gray reported on the preparation of alternating layers of sulfated CNCs and cationic polyallylamine, and Podsiadlos group introduced LbL films with embedded polyethylenimine (PEI) [65, 66]. Langmuir–Blodgett deposition for CNC thin films, however, is not possible under the general setup of an aqueous subphase as the nanocellulose suspensions are based on water as the liquid phase [2]. In 2010, however, Rojas group reported on LS films from CNCs prepared by the use of the cationic surfactant dioctadecyldimethylammonium bromide (DODA-Br) that forms a monolayer on water and complexes with CNCs that have been dispersed in the subphase [67].

6.1.1.2.2 CNFs and their Ultrathin Films

Materials based on CNFs were introduced in the early 1980 [68] and gained more and more interest in the mid-2000 because of the advancements in CNF preparation methods [69–71]. CNCs can be obtained by methods that usually comprise several operation steps, e.g. successive refining, enzymatic hydrolysis, again refining and homogenization [71], 2,2,6,6-tetramethylpiperidine-1-oxyl radical (TEMPO)-mediated oxidation followed by blending [72] or homogenization [73], quarternization, or carboxymethylation followed by homogenization [74].

Nechyporchuk et al. describe the CNF production process as a "tree" that allows to manufacture more than 50 different types of CNFs [75]. As a first step, purification is stated, followed by step 2, the mechanical pre-treatment meaning blending, refining, and grinding. The third step involves biological/chemical pre-treatment such as enzymatic hydrolysis, carboxylation, sulfonation, and quaternization. Principal mechanical treatments that include homogenization, extrusion, blending, ultrasonication, steam explosion, and ball milling comprised in step 4. As a post-treatment, chemical modification and/or fractionation can be performed in step 5. CNFs of different morphologies, surface chemistries, crystallinities, degrees of polymerization (DP), etc. are obtained by the different treatment steps and are presented in detail in Nechyporchuk publication [75].

The surface charge of CNFs can be modified by TEMPO-mediated oxidation. The oxidation involves hypochlorite oxidation of cellulose, which is catalyzed by TEMPO that allows for selective oxidation of the primary alcohol in the C-6 position of cellulose [2]. Carboxymethylated CNCs are the result of this treatment. These TEMPO-oxidized CNFs hold a high anionic charge density; however, all CNFs are at least mildly anionic because of the presence of hemicelluloses and other oxidized structures on the microfibrils [2, 76, 77].

Cellulose thin-film deposition from CNFs bears a fundamental limitation [3]. CNFs tend to form gels, even at low concentrations (1 wt%), and gels are generally not suitable for thin-film deposition [78]. An important feature of films, the thickness, cannot be controlled with spin coating if one is not free to increase the concentration of CNF suspensions because of a gelling process [2]. Kontturi and Spirk describe that even acquiring a film with full coverage from a diluted fluid suspension is not straightforward [2]. Thin-film preparation using TEMPO-oxidized CNFs has the drawback of high instability of the film after deposition. Actually, the deposited CNFs tend to redisperse because of the high surface charge density. Unfortunately, heat treatments that are applied for CNC film preparation are not able to prevent the redispersion [2]. The use of an anchoring layer turned out to be the best way to prepare thin films via spin coating. For such an anchoring layer, polyethylenimine (PEI) is the most frequently used compound [2]. LbL deposition with cationic polyelectrolytes allows for the preparation of slightly thicker films of CNFs; however, these films cannot be considered to consist of pure CNFs [2, 30].

Wågbergs group [30] carboxymethylated the CNFs and deposited them with the aid of PEI, PAH (poly(allylamine hydrochloride)), and PD (poly(diallyldimethylammonium chloride)) [30]. The thickness of the LbL deposited CNF films depends not only on the choice of the polyelectrolyte. It is strongly be controlled by electrolyte addition as salt and its concentration have an effect on the coiling of the polyelectrolyte in solution and therefore on the deposition. Variations in film thickness influences features such as transparency or color formation within the film [30].

From CNF suspensions, films in the form of nanopapers can be obtained. To produce such films, methods such as air drying [79, 80], spray coating [81], and pressurized filtration followed by hot pressing [82–84] can be used. The pressing and dense packing of such films facilitates a high level of transparency of up to 90%, enabling the preparation of optically transparent nanofiber paper [83].

6.1.2 Indirect Preparation of Cellulose Films from a Soluble Derivative

Dissolving cellulose in common solvents can be achieved by modification, i.e. derivatization of the biopolymer. TMSC is an important representative of cellulose derivatives. TMSC is often synthesized and characterized according to a model described by Kontturi et al. [26]. To synthesize the hydrophobic compound, the cellulose material is dissolved in, for example, DMAc/LiCl or ionic liquids. The silylation of cellulose is completed using compounds such as hexamethyldisilazane (HMDS) and trimethylsilyl chloride (TMSCl), which act as the reactant and catalyst, respectively [85–88]. Depending on the degree of substitution, the solubility of the TMSC can be tuned, and solvents ranging from ethanol and acetone to THF, chloroform, pentane, and toluene can be applied [89, 90]. Klemm et al. introduced TMSC as a suitable compound to produce model thin films of cellulose [91]. Thin films from TMSC solutions can be easily prepared by both LB deposition and spin coating. The casted TMSC thin films are hydrolyzed, i.e. regenerated back to cellulose by exposure to gaseous HCl (Figure 6.3) [26].

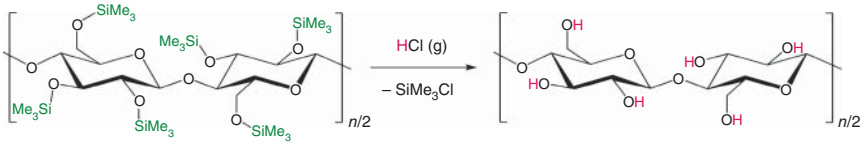

Figure 6.3 Regeneration of TMSC to cellulose by exposure to HCl vapor.

In principle, the HCl vapor penetrates into the thin film and is able to fully hydrolyze the TMSC film to cellulose without interfering much with the film morphology [92]. Schaub's method enables to provide ultrathin cellulose films of <10 nm thickness on Si wafers, glass slides, and gold coated surfaces [92]. In 2003, Kontturi et al. investigated the influence of different substrates, spin coating parameters, and solvents on the thin-film thickness, roughness, and morphology [26, 87]. Schlemmer et al. studied the effect of the substrate on the cellulose thin-film properties. They prepared regenerated TMSC films on different flexible and stiff substrates such as polyamide, polyethylene terephthalate, Cu, Al, and Ni foils as well as on silicon wafers and glass with thicknesses up to 50 nm [93]. Different studies over the past years demonstrated the tunability of the thickness of regenerated TMSC films ranging from approximately 5–740 nm [26, 93–95]. Both techniques, spin coating and LB deposition, result highly smooth TMSC-based regenerated cellulose thin films [96].

Another promising derivative for the preparation of regenerated cellulose thin films is cellulose xanthate (CX). Dissolution of cellulose via synthesis of cellulose xanthate represents the probably most important and economically most successful derivatization reaction [40]. For cellulose xanthate preparation, pulp is mixed with aqueous NaOH (18–20 wt%) to form a 5 wt% suspension. The alkali treatment is followed by the introduction of CS_2 to the reaction mixture, and sodium cellulose xanthate is produced (CX, intermediate) [41, 97]. The yellowish fibrous mass is soluble in water and dilute aqueous alkali, having a conventional DS level of about 0.5 [97]. After xanthation, the CX solution is pumped through nozzles and the resulting fibers are regenerated in an acidic bath (H_2SO_4) to give regenerated cellulose fibers [91, 98–100].

In 1965, Phifer et al. published a procedure for CX film casting and the corresponding spectroscopic results. Their characterization, however, focused on the non-regenerated CX [101].

Weißl et al. prepared regenerated cellulose thin films from CX via spin coating using different concentrations of the cellulose xanthate derivative in aqueous alkaline solutions and investigated differences in film properties [21]. In their study, they varied the HCl exposure time for regeneration and characterized the cellulose films using different surface-sensitive techniques. Similar to TMSC films, the regeneration of CX to cellulose is realized by exposure of the thin films to HCl vapor (Figure 6.4) [21].

While this procedure does not require any use of organic solvents, the solid NaOH as well as the salts formed during regeneration need to be removed by a rising step with water. The AFM images reveal the surface topography of CX

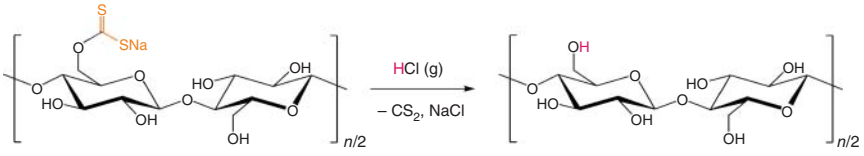

Figure 6.4 Regeneration of CX to cellulose using HCl vapor.

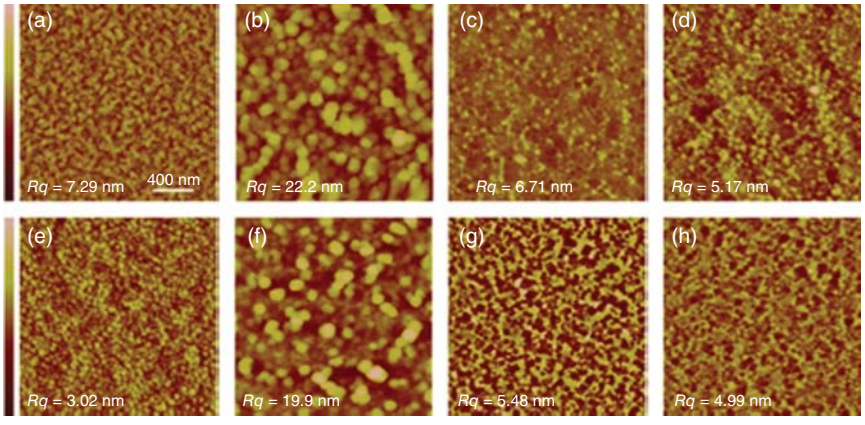

Figure 6.5 AFM images ($2 \times 2\ \mu m^2$) and the corresponding root mean square (RMS) roughness of different steps in cellulose thin-film processing with a 2.5 wt% (upper row) and a 1.5 wt% (lower row) CX solution. The images show the films directly after spin coating (a, e), after 20 min lasting exposure to the HCl atmosphere (b, f), after rinsing with deionized water (c, g), and after drying for one hours at 105 °C (d, h). The Z-scale is 100/200/50/50 nm for (a–d) and 30/150/100/50 nm for (e–h). Source: Weißl et al. [21]/Elsevier/CC BY 4.0.

films at different stages of thin-film preparation and regeneration (Figure 6.5). The CX-based regenerated cellulose thin films show smooth and homogeneous surfaces [21]. The regenerated cellulose model films can be used to study surface interaction with, e.g., proteins or industrially relevant chemicals [20, 21].

Closely related to the viscose process and the synthesis of cellulose xanthate is the CarbaCell process. The derivative cellulose carbamate (CC) is built by reaction of mercerized cellulose with urea [41] instead of CS_2. After aging, the cellulose derivative can be regenerated back to cellulose by spinning into an acidic bath (fibers) or exposure to acidic vapor using, e.g., H_2SO_4 (thin films) [102, 103].

Weißl et al. reported on the preparation of blend thin films from cellulose xanthate and cellulose carbamate via spin coating. They investigated the influence of CC on the properties of cellulose xanthate-based materials. Blend thin films prepared from solutions of different CX–CC ratios gave homogeneous all-cellulose thin films of 20–80 nm in thickness [104].

Cellulose carbamate thin films were recently used as the precursor for regenerated cellulose membranes with high transparency and separation ability. CC synthesized from cellulose pulp and urea yielded relatively dense regenerated cellulose surfaces with regular microchannels, which show a high potential for applications in water treatment [105].

6.2 Characterization of Biopolymer Thin Films

6.2.1 Surface Morphology

Today, there are several powerful techniques available to image and measure the structural features and characteristics of biopolymer thin films. The thickness and surface roughness of a film, end-to-end distances, nanostructure dimensions and distribution of sizes, polymer conformation, and spatial molecular organization describe some of them. AFM, scanning electron microscopy (SEM), and transmission electron microscopy (TEM) are the most frequently used methods.

AFM is a high-resolution type of scanning probe microscopy with resolutions in the order of fractions of a nanometer. In contrast to other microscopes, AFM does not generate an image by focusing light or electrons onto a sample surface such as optical or electron microscopies do. It is described that AFM physically "feels" the sample surface with a sharp probe. From this, a map of the height from the surface is generated [106]. An image of a surface is thereby generated by scanning across the surface of a sample using a small tip [107]. The use of a cantilever allows the tip to deflect and so to respond to height inhomogeneities on the sample surface [106, 108]. In principle, there are four common AFM operation modes; the AFM contact and tapping modes are described in Figure 6.6 [108].

The AFM contact mode was the first mode developed and is conceptually the simplest one. In this mode, the tip of the probe is in permanent contact with the sample surface. According to this, the repulsive forces between the sample and the tip may damage or change both the sample and/or the tip. However, imaging in the contact mode enables an extremely high resolution as the technique is sensitive to the nature of the sample [106]. In the AFM tapping mode, a tip that is oscillating at a certain frequency (50–500 kHz) at a tip amplitude of several tens of nanometers is used. The oscillating tip is moved toward the surface and it begins to touch or "tap" the surface. Depending on the structural features of the sample surface, the cantilever has less (bump) or more (valley) space to oscillate, and the amplitude decreases or increases, respectively [106, 110]. Both modes provide information about the sample topography. All modes are described in more detail in Refs. [106, 108, 110].

Comparing AFM to SEM, it has several advantages. With AFM, a three-dimensional surface profile is provided, while electron microscopy gives a two-dimensional projection of a sample. In AFM, only minimal sample preparation

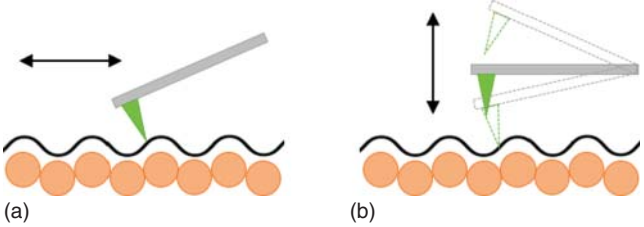

Figure 6.6 Schematic description of the (a) contact mode and the (b) tapping mode used in AFM imaging.

is needed, and it does not involve any special (pre)treatments (e.g. metal/carbon coatings) that may do damage or irreversible change to the sample. AFM has the great advantage that it can be performed in ambient air or a liquid environment, while electron microscopy usually operates under vacuum. This fact allows *in situ* studies of biological macromolecules and living organisms with AFM [106].

Further, it is possible to combine AFM imaging with techniques such as fluorescence microscopy and infrared spectroscopy, which is applied in biological sciences, polymer science [111], nanotechnology [112], and medical research [113].

A disadvantage of AFM when compared to SEM is the relatively small scanning area of max about $100 \times 100\,\mu m$, while the SEM images of an area on the order of square millimeters can be recorded [106]. The scanning speed is a limitation of conventional AFM scans. Typically, an AFM scan requires several minutes, and the slow scanning rate may lead to a drift in the image that limits the accurate measurements of distances between the topographical features on the AFM image [114–116]. To overcome the limitation of scanning speed, high-speed atomic force microscopy (HS-AFM) has been developed by optimizing all devices contained in the instrument for fast scanning and by newly developing fast and precise control techniques [117, 118]. With HS-AFM, an imaging rate of 15–25 frames per second (fps) for a scan rate of $240 \times 240\,nm^2$ with 100 lines has been reached [119]. HS-AFM typically employs the tapping mode and uses cantilevers that are much more miniaturized than the conventional ones to achieve high-resonant frequencies ($f_c = 400\,kHz$ to $1.2\,MHz$) in water [120]. HS-AFM allows for the visualization of various types of dynamic events inaccessible with other approaches such as conventional AFM. It provides a significant insight into molecular processes as in Igarashi's study, where the cellulase hydrolyzation process of crystalline cellulose fibers is visualized [121].

AFM artifacts can arise from, e.g., the use of an unsuitable tip, a poor operating environment, or by the investigated sample itself. Several artifacts are unavoidable because of the geometry of the AFM probe. With a triangular shape of a probe, measuring the steep walls of a sample is difficult because of the radius of curvature of a tip. This can cause that small obstacles on a sample surface are imaged much bigger than they are (Figure 6.7) [106, 108, 110].

Hanley et al. imaged cellulose microfibrils using AFM and TEM and evaluated the differences of the two methods [122]. They showed that the convolution of the tip and sample geometries cause distortion in certain dimensions; however, with AFM, it is possible to obtain a unique and rapid indication of the surface topography under

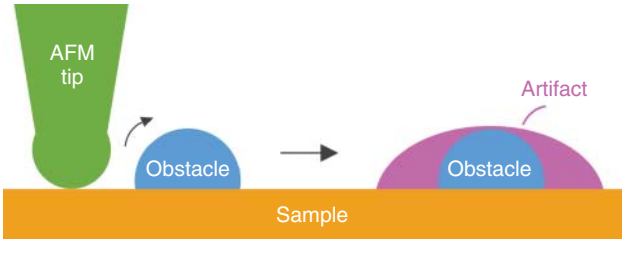

Figure 6.7 AFM artifacts can arise when imaging small convex obstacles with a dull probe.

ambient conditions [106, 122]. In a later publication, they investigated the twist of microfibrils using AFM and TEM [123]. With the tapping mode AFM, they obtained sharp images of the twist regions of the fibrils. Using TEM, they could clearly show the right-handed twist of 180° for an approximately 50 nm wide microfibril appearing at intervals of approximately 700 nm along the fiber [123]. From these publications, the advantages of both techniques such as the differences in scanning sample area can clearly be seen.

In 2015, Usov provided a detailed and consistent structural description over multiple length scales of nanocellulose, i.e. TEMPO-mediated oxidized CNFs and CNCs using AFM, Cryo-SEM, and TEM [124]. They were observing a twisting of right-handed chirality along the contour of CNFs and CNCs. This chirality was detected on the level of fibril bundles and single fibril level in CNFs. Moreover, by a statistical analysis of kink angle distribution, they concluded that the kinks in the samples do not result from alternating amorphous and crystalline regions but may originate from the processing conditions used in the preparation of the nanofibers [124].

In academia and the industry, AFM is one of the most frequently used methods to investigate biopolymer thin-film properties such as surface topography and roughness [21, 31, 93, 94, 104, 125–136]. Fast-scan AFM devices allow for studying, e.g., the degradation of cellulose in real time at high resolution. An example, where this has been demonstrated recently, was blend thin films consisting of polyhydroxybutyrate and cellulose. There, the action mode of cellulase, a cellulose-digesting enzyme cocktail, was observed in real time and the reaction kinetics could be obtained [137].

6.2.2 Thin-Film Thickness

To investigate the thickness and the roughness of biopolymer thin films, AFM is frequently used. In 2013, Kargl developed different lithographic methods for patterning of biopolymer films [138]. By the aid of a metal mask, parts of the thin film were protected and others were exposed to vapor of hydrochloric acid and regenerated to pure cellulose. This treatment resulted in hydrophobic TMSC and hydrophilic cellulose patterns of different physiochemical properties. AFM was used to determine the differences in height and roughness caused by the regeneration procedure [138].

A cheaper and faster technique to determine the thickness and roughness of a film is profilometry. Here, a diamond stylus is brought into contact with the sample and is moved laterally across the surface for a specified distance and at a certain contact force. Vertical features ranging from 10 nm to 1 μm can typically be measured by profilometry. This technique is one of the standard methods to determine the thickness of a thin film [21, 93, 104, 127, 133, 137, 139, 140].

Ellipsometry is an optical technique used to investigate dielectric properties of thin films by light reflection or transmission from samples. From change in polarization of the incident radiation, which interacts with the sample, the composition, roughness, thickness, electrical conductivity, and crystalline nature of a sample can be characterized [141]. With ellipsometry, the thickness of single and multilayers ranging from a few angstroms or tenths of nanometers can be determined [142, 143].

The most commonly used ellipsometry methods are single-wavelength and spectroscopic ellipsometry (SE). In the single-wavelength method, also called laser spectroscopy, typically a monochromatic light source in the visible spectrum, i.e. He–Ne laser, is applied, whereas in SE, a broad band light source (from the UV to IR region) is used. SE can be used to determine the complex refractive index of a material. Both methods can be performed in air at ambient conditions, and no complex sample preparation is needed. As polarized light is used and detected, normal ambient unpolarized stray light has no significant influence on the measurement. This allows us to perform real-time monitoring [141, 144].

A related method to determine the layer thickness, electron density, and surface/interface roughness is X-ray reflectivity (XRR). Here, a monochromatic beam of X-ray photons at different incident angles is used as incident radiation. The intensity of X-rays that are reflected from the sample in specular direction is recorded. The recorded intensity deviates from the incident because of the inhomogeneities within the sample. From analysis of the deviations, conclusion to, e.g., the thickness, roughness, and density of the film can be drawn. With XRR, it is possible to analyze films with thicknesses ranging from 1 nm to c. 100 nm [143]. XRR enables the investigation of lateral variation of the film thickness, indicating that a map of thickness variations over a whole sample can be provided [145].

To investigate the thickness, roughness, and density of ultrathin films, Kontturi et al. used XRR [146]. These qualities were obtained as a result from a numerical fit to the Parratt formalism, which attempts to simulate the reflectivity curve. They demonstrated that from the calculation of XRR curves (Figure 6.8), a reliable determination of the mass density for ultrathin films with certain thickness constrains can be obtained. In addition, the mass density and thickness investigations can be used to follow chemical reactions in a thin polymer film [146].

Both methods, spectroscopic ellipsometry and XRR, are based on the reflection of an incident radiation from the interfaces between the film and the underlaying sample substrate, and of course the film and air interface. For sample preparation, it is important that the sample film thickness is small enough so that the incident radiation can penetrate the bottom of the sample. During analysis of the film, the incident light/radiation should not optically, chemically, or structurally change or destabilize the sample. To obtain the best results from the analysis, the non-uniformity of the film thickness, the density, and the optical constants should be included in the evaluation. Further, it is of necessity to have a large-enough contrast between the optical constants and the electron densities of the layers and the substrate [147].

6.2.3 Elemental Composition

X-ray photoelectron spectroscopy (XPS) is a surface-sensitive technique that belongs to the family of photoemission spectroscopies and represents the most frequently used electron spectroscopy. The photoelectric effect allows us to define the elemental composition of a solid's outer surface. It is possible to identify and quantify the elemental composition of a surface, i.e. the outer 10 nm or less of a solid material with elements from Li to U. Elements present at concentrations >0.05 at% can be

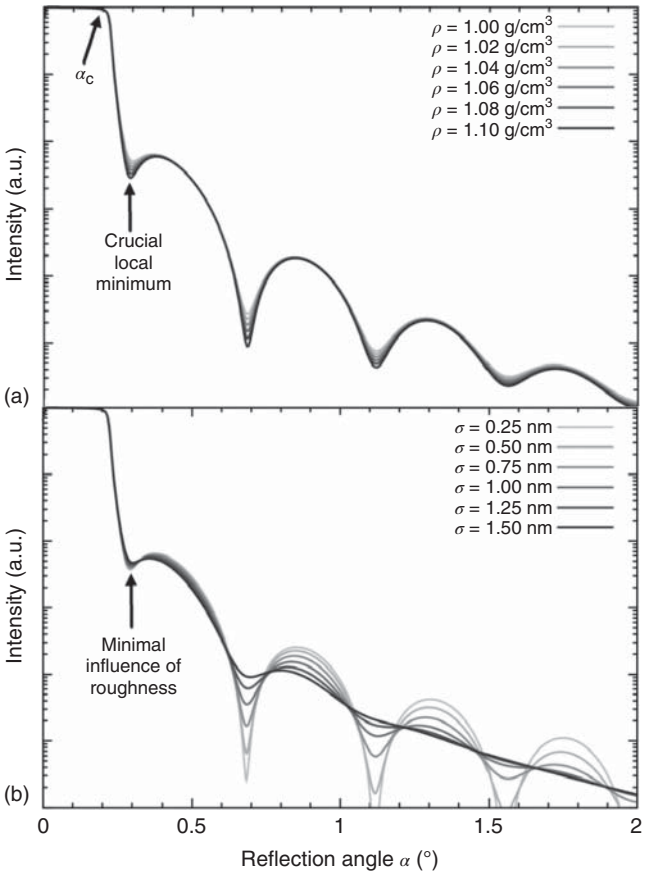

Figure 6.8 Calculated XRR curves for a structure containing 10 nm of a polystyrene-like material (C_8H_7) on a Si/SiO_x substrate. (a) Influence of mass density variation (constant roughness 0.75 nm). (b) Influence of roughness variation (constant density 1.05 g). Source: Kontturi et al. [146]/with permission of American Chemical Society.

determined. In principle, X-rays of a certain wavelength are focused on a sample surface, and photoelectrons of characteristic energies are emitted from the surface fraction (max upper 10 nm) of a solid sample and are absorbed by the detector. Before the electron beam hits the sample surface, it is focused on a concave single crystal that only reflects radiation with specific energy (wavelength) at some specific angle defined by the crystal lattice spacing (Figure 6.9). From the intensity of photoelectrons detected and the binding energy, the elemental identity, the quantity of a detected element, and the chemical state can be determined [148, 149].

Regarding sample preparation, thin solid samples prepared on glass or silicon slides can be examined; however, the XPS technique requires a vacuum environment, whereas volatile compounds cannot be examined.

In 2011, Eyley et al. published results on XPS experiments to elucidate the structure of imidazolium-grafted CNCs. The azidation of nanocrystals was confirmed by

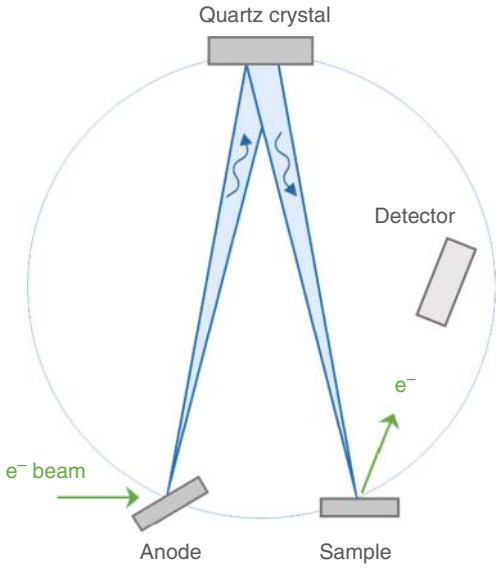

Figure 6.9 Schematic of an XPS measurement setup. Source: Adapted from [148].

the characteristic nitrogen peak and also the successful grafting reaction was validated by the presence of the two overlapping nitrogen peaks [150].

Rojas et al. studied polyelectrolyte adsorption on mica and cellulose. They used XPS to estimate the absolute amount of the adsorbed cationic polyelectrolyte [151].

Mohan et al. investigated the interaction of cationic cellulose derivatives with the ultrathin cellulose support using the quartz crystal microbalance with dissipation (QCM-D) [28]. Using the QCM-D technique, mass differences before and after adsorption can be determined. To validate the results, an analysis of the elemental composition of the surfaces by XPS was performed. The peak corresponding to elemental nitrogen, N 1s, was detected for all the treated samples (Figure 6.10b–e), whereas a lack of element N is evident in the untreated sample (Figure 6.10a) [28].

6.2.4 Functional Groups and Hydrogen-Binding Patterns

To determine the functional groups of a material, infrared (IR) spectroscopy can be used. IR spectroscopy is a versatile experimental technique based on the interaction of infrared radiation with matter. Spectra from samples in the form of liquids, solids, or gases can be relatively easily obtained. In principle, molecules absorb frequencies that are characteristic of their chemical structure. This indicates that the frequency of the absorbed radiation equals the vibration frequency of the molecule. An IR-active molecule must possess a specific feature, i.e. an electric dipole moment that changes during the molecule vibration. Heteronuclear diatomic molecules describe such molecules [153].

For IR spectroscopy, there are two main measurement principles available, Fourier transform IR (FT-IR) spectroscopy and attenuated total reflection IR (ATR-IR) spectroscopy. In FT-IR, the incoming infrared light is passed through a Michaelson interferometer, which is then transmitted through the sample before

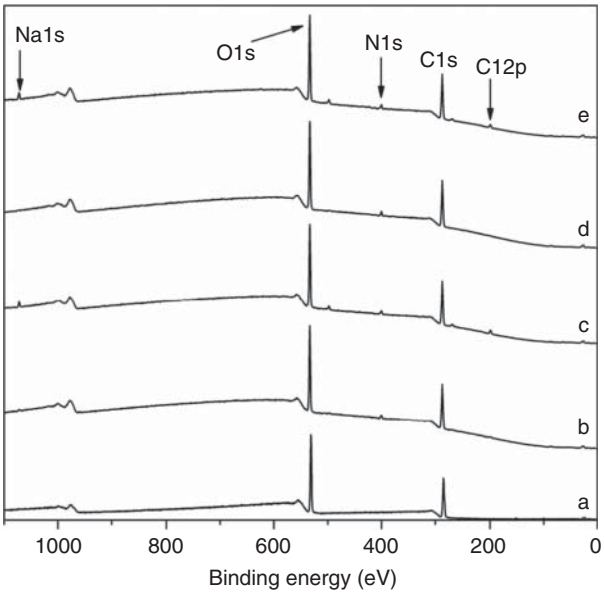

Figure 6.10 XPS spectra of cellulose surface (a) rendered with cationic cellulose derivatives adsorbed under different conditions. (b) pH 7, 1 mM NaCl, (c) pH 7, 100 mM NaCl, (d) pH 8, 1 mM NaCl, and (e) pH 8, 100 mM NaCl. Source: Mohan et al. [152]/with permission of Elsevier.

reaching the detector. The recorded signal is amplified, and high-frequency contributions get eliminated by a filter. The collected data are converted into a digital form, and further, a Fourier transformation is performed. In ATR-IR spectroscopy the phenomenon of total internal reflection (TIR) is used. A beam of infrared radiation is directed through an internal reflection element, which has a high refractive index (RI). The sample under investigation is pressed against the face of this reflection crystal, and the specific absorption of energy from the sample causes a loss in energy at the wavelength where the material absorbs. The reflected light is recorded, and a spectrum of absorbance/transmittance vs. wavenumber (cm^{-1}) can be obtained [153, 154].

A method related to IR spectroscopy is Raman spectroscopy (RS). In contrast to IR, where only elastically scattered photons are recorded (the same energy and wavelength as incident photons → Rayleigh scattering), in RS, inelastically scattered photons (the vibrational energy is exchanged → Raman scattering) are detected [155].

In a typical Raman experiment, a source of monochromatic light, i.e. a laser source for excitation in near-IR, visible, and UV spectral region or X-ray photons, is used, which interacts with the sample. The scattered photons lose energy that is specific to the vibrational coordinates of the sample. To observe a Raman band, a change in the polarizability of the sample must be caused by the molecular vibrations [155, 156].

In IR spectroscopy, mainly FT-IR and ATR-IR are used; in Raman spectroscopy, various methods such as resonance Raman spectroscopy (RRS), surface-enhanced

resonance Raman spectroscopy (SERRS), coherent anti-Stokes Raman spectroscopy (CARS), etc. are applied. Depending on the methods used, the experimental setup including lasers, detectors, and filters changes [156, 157].

In vibrational spectroscopy, IR and Raman spectroscopies are the most important and predominantly used ones and involve studying the interaction of radiation with molecules. With IR spectroscopy, it is possible to investigate molecules by causing a change in its dipole moment. In Raman spectroscopy, however, a dipole moment needs to be induced. An induced dipole moment arises as a result of the molecular polarizability, where the polarizability is the deformability of the electron cloud about the molecule via an external electric field [155].

Linear homonuclear molecules such as N_2, O_2, and H_2, for example, are exclusively Raman active as no dipole moment is present, while diatomic linear gases such as HCl and CO in contrast can only be measured by IR spectroscopy. For both techniques, no special sample preparation is needed, they are very fast and non-destructive, and a quantitative and specific identification of functional groups can be obtained. Interpretation of results is more complex in Raman spectroscopy [153–155, 157].

ATR-FTIR can also be used as a tool to investigate the crystallinity of cellulose [158]. In 1957, Tsuboi published results on infrared spectroscopy investigation of the deuteration of cellulose. It was observed that the small parts of the crystalline material in cellulose films were excluded from deuteration, while the OH groups on the disordered parts were deuterated [159].

To explore the chemical changes of a cellulose surface, Nguyen et al. applied ATR-FTIR spectroscopy to monitor the chlorination mechanism of cellulose-based membranes under different conditions [160].

In cellulose chemistry, IR spectroscopy is frequently used to control the regeneration of cellulose derivatives to pure cellulose accomplished by using HCl vapor [21, 126, 137, 139, 161, 162].

6.2.5 Wettability

The surface wetting properties of a surface, e.g. a biopolymer thin film, is of great importance in materials and surface science. Factors such as pH, temperature, humidity, charge density, and surface energy have an effect on the interaction processes of cellulose surfaces with proteins, papermaking chemicals, or lectins for example. The analysis of the surface energy and the affinity of a certain liquid toward a solid surface allow us to obtain insights into the surface properties and predict the interaction behavior. Especially, the wettability and hydrophobicity give information on material characteristics and can be determined by measuring the contact angle of a certain liquid on the sample surface. Contact angle measurements enable to calculate the surface tension for a solid sample. Regarding the water contact angle, hydrophilic surfaces easily adsorb water because of the presence of active polar functional groups (good wettability). Hydrophobic materials in contrast have little or no tendency to interact with water, and they bend the water from their surfaces (Figure 6.11) [163].

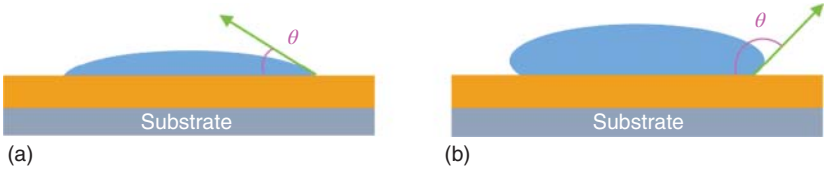

Figure 6.11 Schematic representation of (a) hydrophilic and (b) hydrophobic interactions of water molecules with a solid surface. Source: Hebbar et al. [163]/with permission of Elsevier.

The surface free energy (SFE) of a material has a vast influence on the wettability of solids by liquids. To determine the SFE, contact angle experiments using at least two different liquids, usually water and diiodomethane, are performed. With the knowledge of the surface tension of the applied liquids and the contact angles of these liquid on a certain material, the SFE can be determined. To calculate the SFE, several models are available. One of the most frequently used is the Owens, Wendt, Rabel, and Kaelble (OWRK) method, which gives the SFE – divided into its polar and disperse components [164–166].

Schlemmer et al. investigated the influence of the substrate on the cellulose thin-film properties. They spin coated the acid-labile derivative TMSC on different flexible and stiff substrates such as polyamide, polyethylene terephthalate, Cu, Al, and Ni foils as well as on silicon wafers and glass. On the synthetic and metal substrates, they obtained rather homogeneous thin films and showed that the thickness and the roughness of these films correlate with the substrate roughness and its SFE. For the TMSC layer on the Ni foil, a superhydrophobic behavior caused by the microstructuring of the substrate was observed [93].

6.2.6 Surface Charge

Zeta potential measurements enable to measure the electrokinetic potential on the surface of a material when it comes in contact with a liquid medium. Once a material comes in contact with a liquid medium, a difference in the potential between them develops, as the functional groups on its surface are reacting with the surrounding liquid [167].

Ions of opposite charge from the surrounding medium begin to arrange themselves spontaneously at the interface/surface of a solid and form a so-called electrochemical double layer (EDL). In principle, the EDL consists of a stationary and a diffuse layer. The stationary layer, also called the Stern layer, is directly formed at the surface of the sample where oppositely charged ions are strongly attracted to the surface. In the diffuse outer layer, the ions become less attracted by the surface and therefore have the ability to move within the layer (Figure 6.12) [167, 168].

In between the immobilized and the diffuse layer, a boundary termed as the shear plane can be found. This boundary defines the part of the EDL, which contributes to the overall net charge of the investigated material. The potential of a material in an ionic solution present at this shear plane is the zeta potential [167, 169].

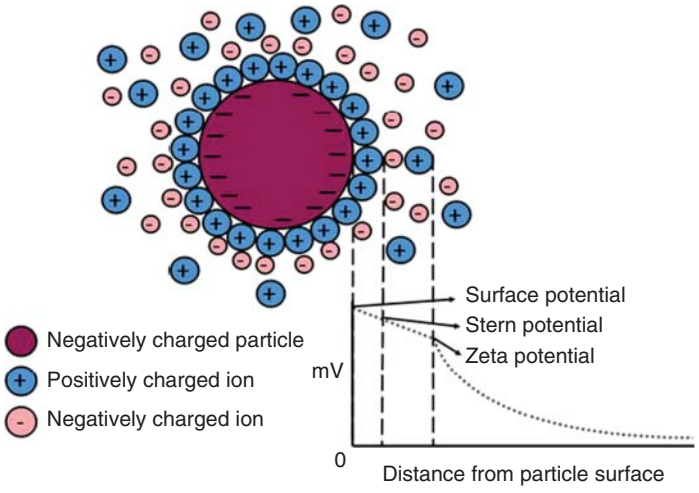

Figure 6.12 Negative-charged surface of a particle with a positively charged Stern layer and zeta potential in a dispersion medium. Source: Taqvi and Bassioni [168]/IntechOpen/ CC BY 3.0.

The zeta potential is highly dependent on the properties of the liquid medium such as the pH and the buffer ion concentration. Electrokinetic phenomena can be determined by four different measurement techniques, the streaming potential, electrophoresis, electroosmosis, and sedimentation potential. The first two, the streaming potential and the electrophoresis, are the most commonly used techniques [168].

A biomaterial zeta potential indicates its electric surface properties [170]. To investigate a thin-film system, the streaming potential method is applied, whereas to determine the zeta potential of particles, the electrophoresis method is used. In streaming the potential, a charge displacement in the electric double layer is caused by an external force shifting the liquid ionic phase tangentially against the solid thin-film surfaces [169, 171]. The temporarily bound charge carriers in the double layer will be removed by the external flow, and the potential difference can be measured between two electrodes. In the case of cellulose surfaces, the temporarily bound ions of the Stern layer consist of cations that screen the surface. In principle, large positive values of the zeta potential at a fixed pH in a certain liquid indicate a positive charge of the surface. This would mean that negatively charged particles such as anions are attracted by the surface. Lower values of zeta potential at a certain pH reflect a negative charge of a material surface that preferentially attracts positively charged entities [169].

Bai et al. investigated the surface charge properties of polyamide thin-film composite (TFC) membranes with incorporated CNCs performing zeta potential measurements [172]. Their measurements showed that the polyamide control membrane has the highest negative surface charge, represented by the highest negative zeta potential at a certain pH value (Figure 6.13). With the introduction of CNCs, the zeta potential becomes more positive, which can be explained by the reaction of the negatively charged CNCs with positive residual amino groups from the membrane.

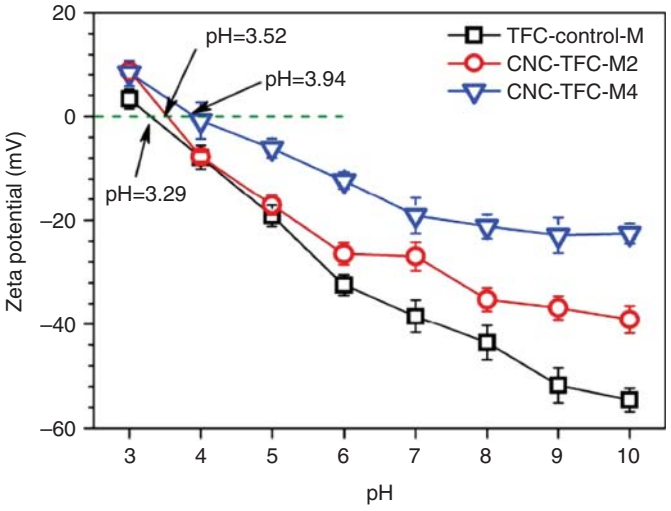

Figure 6.13 Zeta potential of the membrane surfaces as a function of solution pH. Source: Bai et al. [172]/with permission of Elsevier.

Further, they point out that unreacted compounds from membrane polymerization may still be present and interact with the incorporated CNCs. In summary, a higher CNC content in the polyamide membranes yields membrane surfaces bearing fewer negative charges [172].

Evaluating the surface charge of cellulose materials such as thin films and fibers is an essential step to predict the interaction behavior with other compounds and materials [131, 173, 174].

6.2.7 Thin-Film Structure

Scattering methods such as small-angle X-ray scattering (SAXS), wide-angle X-ray scattering (WAXS), and light scattering methods (static light scattering (SLS) and dynamic light scattering (DLS)) have become the leading techniques to characterize the dynamics and the micro- or nanoscale structure of soft-matter materials. The SAXS method has the advantage of a relatively strong signal, quick acquisition of statistically relevant data, and the experiments and results give a representative overview of the existing structure. However, scattering methods do not give information about individual particles. The need for complementary techniques with a high spatial resolution such as AFM and electron microscopy is of great importance to get a complete picture of the investigated system [175]. In principle, the material under investigation can be a solid or a liquid, and only minimal sample preparation is required.

In a SAXS experiment, a highly collimated beam of monochromatic X-rays is focused at a 90° incident angle on a sample from which the X-rays scatter. Most of the X-rays simply go through the sample without interaction. The intensity of the scattered X-rays is recorded on a flat 2D X-ray detector. The scattering pattern

allows us to draw conclusion on structural features of a sample, e.g. the size and the shape of particles [176, 177].

In SAXS, only small scattering angles are detected usually in the range of 0.1°–5°. In WAXS in contrast, a wider range of scattered angles can be detected (10°–90°), allowing us to determine very small inhomogeneities within the sample [178].

A related method is grazing incidence small-angle X-ray scattering (GISAXS), which is a versatile and frequently used analysis method to investigate micro- and nanostructured thin films and surfaces. As described before, in standard SAXS, a transmission geometry of the measurement setup is used, while in GISAXS, a reflection geometry is applied. The technique is sensitive to the morphology and alignment of nanoscale objects in the thin film and on its surface [179]. In GISAXS, a very small angle of incidence typically well below 1° (grazing incidence condition) is applied to enable a sufficient long penetration path inside the sample [176].

Krins et al. report on the formation of ZnO/SiO_2 nanocomposite thin films and present their results of in situ time-resolved GISAXS and WAXS experiments. These clearly showed the influence of the structure on thermally induced effects such as crystallization and decomposition, which take place during annealing [180].

In 2015, Ehmann et al. performed GISAXS experiments having a look on rearrangements occurring in cellulose upon regeneration and subsequent drying [181]. To study changes in situ during the ongoing regeneration of a TMSC thin film to cellulose, GISAXS was used as an instrumental method. The use of a specially designed chemical reaction chamber allowed us to determine GISAXS patterns before, during, and after the HCl treatment of the TMSC thin film. Their data show that immediately after HCl injection, the desilylation reaction was started ($t = 12$ min), represented by an increase in correlation length l_{CH}^*, until complete conversion to cellulose at $t = 28$ min (Figure 6.14). The increase in l_{CH}^* was discussed to occur because of an increase in pore size in the film or an increase in the distance between the pores, indicating densification of the film because of the rearrangements within the film. A subsequent heat treatment of the regenerated films led to a further decrease of l_{CH}^*. This was referred to interactions within and between cellulose

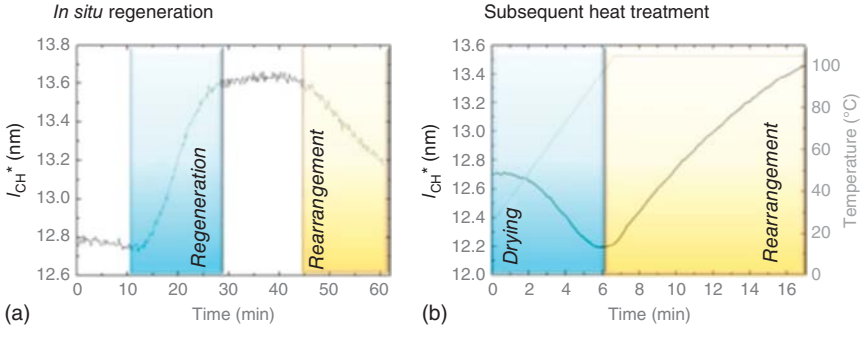

Figure 6.14 (a) Plot of the changes of the mean correlation length l_{CH}^* over time during the regeneration process, where blue indicates the TMS cleavage and the yellow area shows the pore rearrangement. (b) Subsequent temperature treatment of the regenerated cellulose film. Source: Ehmann et al. [181]/with permission of American Chemical Society.

chains, causing a collapse of capillary bridges, which led to smaller pore sizes within the cellulose film. After several minutes of heat treatment, l_{CH}^{*} started to increase again, which was most likely caused by aggregate formation and fibrillation of the cellulose [181].

6.2.8 Swelling and Adsorption Behavior

Biomolecular interactions basically describe the core of every biological phenomenon such as ligand–receptor interactions, signal transduction, and interaction of proteins and chemicals with certain biopolymer surfaces. The increasing interest to characterize such biomolecular interactions defines the need for the development of methods and techniques, allowing us to monitor these. To investigate the interaction behavior and the swelling of biopolymer substances, label-free biosensor techniques such as surface plasmon resonance (SPR) spectroscopy and QCM are frequently applied [182].

Surface plasmon resonance spectroscopy has become one of the most important techniques with a yearly impressive increase in the number of publications [183]. The SPR technique can be applied in a wide range of settings; therefore, one of the interacting partners has to be immobilized on a sensor surface [182].

The SPR technique is based on the excitation of free oscillating metal electrons, i.e. plasmons, which can be described as electromagnetic waves that propagate along a thin metal–dielectric interface [182]. In the late 1960s, Kretschmann and Raether and Otto demonstrated optical excitation of surface plasmons by means of ATR [184–186]. Today, the Kretschmann configuration is the most commonly used SPR spectroscopy configuration. In the Kretschmann configuration, the monochromatic p-polarized light (λ = 630, 670, 780, and 960 nm) falls through a prism with a high refractive index (RI) and is directed onto a thin metal film [187]. Metals, which are suitable for surface plasmon excitation, are, for example, gold, silver, and aluminum. The most widely used plasmonic SPR metal is gold in the form of a gold layer on a glass sensor substrate [188]. At a particular angle of incidence (θ), all of the incident light is reflected back through the prism to the detector. At this angle, TIR occurs. In TIR conditions, surface plasmons can be excited when the wave vector of the incident light (in plane of the surface) matches the wave vector of the surface plasmon polariton in the metallic film surface [187]. At resonance conditions (resonance angle), surface plasmons are excited by taking up the energy from the incident photons. This leads to an energy loss (lower signal), which is represented by a minimum in the SPR curve. The excitation of a plasmon resonant wave is connected to the emergence of an evanescent electromagnetic field. This evanescent field extends into the medium on either side of the metal film, which allows us to detect the change in the RI of the surrounding medium [182, 189].

When investigating a biopolymer thin film, a change in layer thickness and a change in chemical surrounding have an effect on the refractive index (RI) near the sensor surface. These factors directly influence the conditions, i.e. the angle at which the surface plasmons are excited, resulting in a shift of the angle of

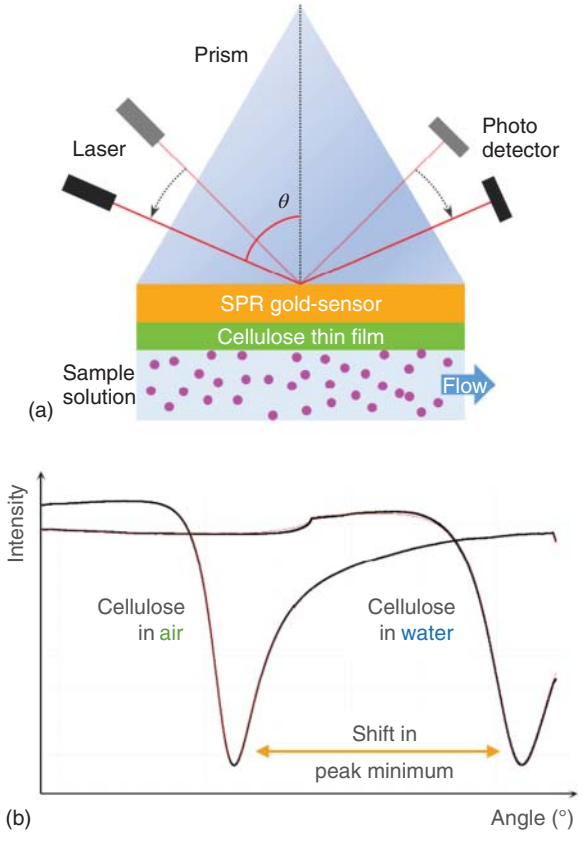

Figure 6.15 (a) Schematic description of a SPR measurement setup in the Kretschmann configuration and (b) SPR curves of a cellulose thin film measured in air and water at a temperature of 25 °C.

minimum light reflection [189]. Figure 6.15 shows a typical SPR measurement setup (Kretschmann configuration) and SPR curves of a spin-coated cellulose thin film measured in air and water. From the resulting shift in SPR angle, conclusion to the changes in thin-film thickness (from RI changes) can be drawn.

With SPR spectroscopy, it is possible to determine the physical properties of a biopolymer thin film, such as the refractive index and the layer thickness by measuring in multiple media, i.e. in liquid and air or using different laser sources, e.g. a $\lambda = 670$ nm and a 785 nm laser. Determination of the layer thickness of a model thin film and changes caused by swelling because of the use of different liquids relies on the refractive index (n)/layer thickness (d) couples to obtain a solution. As complementary methods, profilometry and AFM need to be performed in order to gain information on the initial thin-film thickness and roughness [132].

SPR spectroscopy is frequently used to study the interaction behavior of, e.g., proteins and lectins with biopolymer thin films. Niegelhell et al. investigated the adsorption behavior of industrially relevant starches toward their interaction potential with cellulose thin films from TMSC using SPR spectroscopy [19]. In Figure 6.16, the irreversible adsorption of starches having different degrees of cationization is depicted and represented by the increase in SPR angle. After the starch adsorption experiment, the surfaces were rinsed with water in order to remove the loosely bound

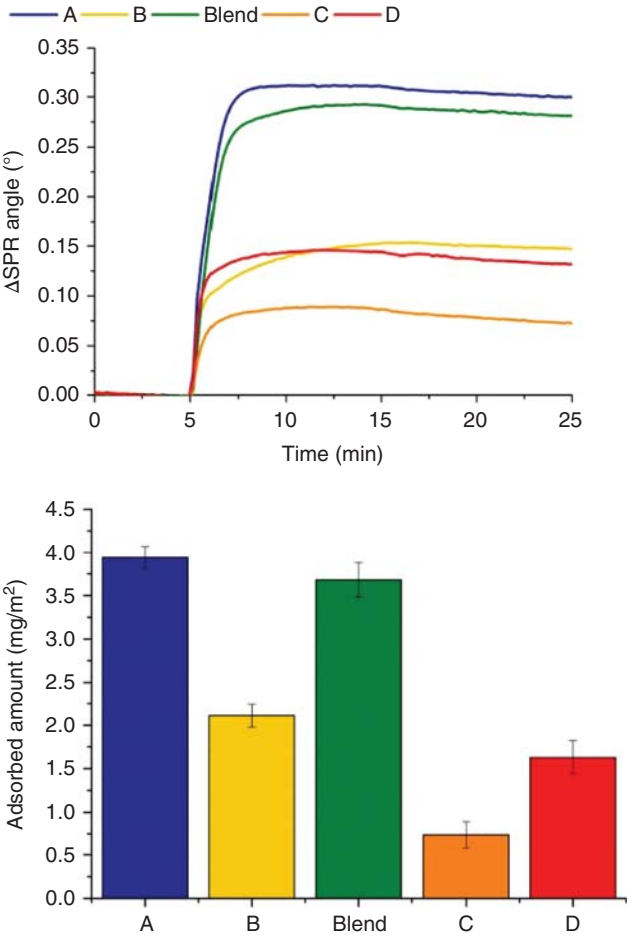

Figure 6.16 Comparison of the adsorption behavior of the different starches ($c = 1$ mg/ml, flow rate 25 µl/min) as a function of the SPR angle (left) and the corresponding adsorbed masses (right). Source: Niegelhell et al. [19]/with permission of Elsevier.

material; however, the rinsing step did not remove a significant amount of material. The authors attribute this to reorientation of the adsorbed molecules as well as to changes in refractive index, which is traceable to adsorption, desorption, or density variations. It turned out that all cationic starches adsorbed irreversibly onto cellulose. The extent of deposited mass on the surfaces depends on factors such as the degree of cationization, molecular weight, particle size, conformation of the polymer, and electrostatic interactions. They describe an additional factor influencing the adsorption behavior, namely, the negative charges of the cellulose substrate, i.e. its carboxylic groups [19].

In the recent years, a lot of studies investigating the adsorption behavior of various compounds on cellulose thin films using SPR spectroscopy and QCM-D have been published [20, 21, 127, 129, 133, 139].

The QCM-D technique, similar to the SPR spectroscopy, is used for real-time analysis of surface phenomena, including thin-film formation, interaction, and reactions with the material adsorbed. The QCM-D method is based on the inverse piezoelectric effect, i.e. the application of a voltage leads to a mechanical deformation of a material [190].

QCM-D sensors consist of a thin quartz disc located between a pair of electrodes. Applying a voltage across the electrode excites the quartz crystal to oscillate at its fundamental resonant frequency (typically around 5 MHz). The electrodes are normally coated with a layer of gold, which allows us to deposit a broad range of different materials. For evenly distributed sample films, which are thinner than the crystal, the added mass on the resonator surface is proportional to the frequency shift (Δf). The adsorbed mass can be calculated by the Sauerbrey equation. During the oscillation of the resonator, the energy dissipation (D) is an indication for the rigidity of the adsorbed material [109, 191]. For frequency and dissipation calculations for a viscoelastic film in a liquid medium, the Voigt model can be used, where the Sauerbrey equation may not be valid [109].

With QCM-D, it became possible to determine changes in the mass and rigidity of an adsorbed layer, and information on the viscoelastic properties of adsorbed layers can be gained [109]. In 2015, the importance of the nanostructure of cellulose thin films on the surface interactions and on the behavior of polysaccharide-based materials in the presence of water molecules was studied by Tammelin et al. [192]. The water uptake behavior of chemically identical cellulose thin films on the one hand from highly amorphous cellulose (prepared via spin coating) and on the other hand from more crystalline cellulose (prepared via Langmuir–Schaefer deposition) was investigated using QCM-D. Interestingly, it was shown that the nanoporous but also partly crystalline cellulose films prepared via LS deposition adsorbed a higher amount of water molecules when compared to the highly amorphous cellulose substrates. This is a very surprising result as the tightly packed crystalline regions are less permeable to water. The higher water uptake was assigned to the higher surface area generated because of the presence of nanopores within the LS films [192].

As QCM-D can be employed for a wide range of applications, the technique is frequently used in biomaterials science to study the, e.g., surface properties, adsorption behavior of proteins and polyelectrolytes, as well as the swelling behavior of biopolymer thin films [192–197].

The probably biggest difference between SPR spectroscopy and QCM-D is that in QCM-D, the adsorbed "wet mass" is measured, while in SPR spectroscopy, the "dry mass" (without liquid) is determined. In QCM-D, the resonance frequency of the sensor is dependent on the oscillation of mass including water, where the "wet-mass" is determined. Generally speaking, in SPR spectroscopy, changes in the refractive index near the metal surface are measured. Upon adsorption, the angle at which plasmons are excited changes, and this angle is used to calculate the adsorbed amount, indicating that the "dry-mass" is measured.

In 2014, Mohan et al. investigated protein adsorption on cationic cellulose surfaces applying QCM-D and SPR spectroscopy [139]. They demonstrated that the incorporation of charged species on cellulose thin films, via adsorption of

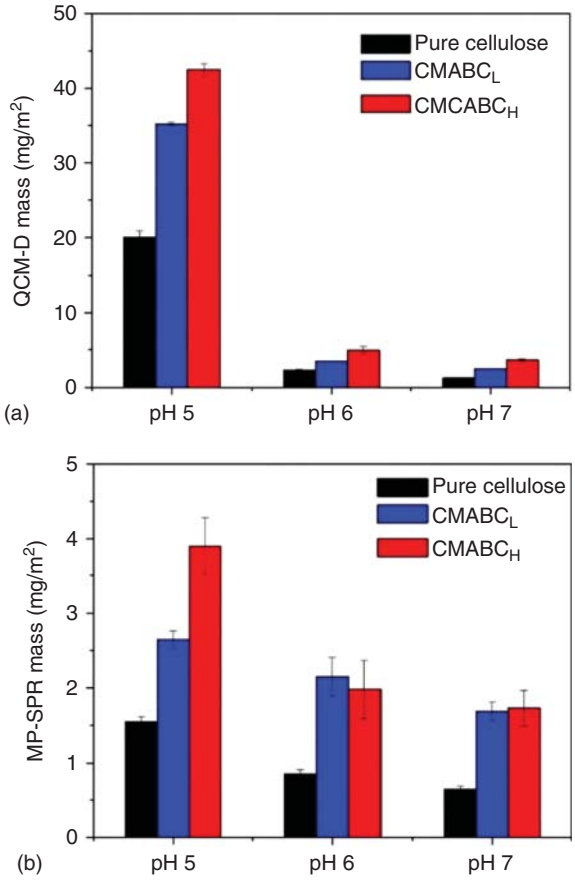

Figure 6.17 Comparison of the adsorbed fluorescein isothiocyanate (FITC)-BSA mass on cellulose and cationically rendered cellulose films at different pH values by (a) QCM-D and (b) MP-SPR. Source: Mohan et al. [139]/with permission of American Chemical Society.

cellulose-4-[*N*,*N*,*N*-trimethylammonium]butyrate chlorides with two different degrees of substitutions (CMABCL and CMABCH), allow for controlling protein adsorption of bovine serum albumin (BSA). Comparing QCM-D to SPR experiments (Figure 6.17) performed at the same conditions, QCM-D results show a much higher amount of deposited BSA on the surfaces as in QCM-D, bound water and electrolyte are also considered ("wet-mass"). Overall, they demonstrated that the trend for protein adsorption observed in QCM-D is reflected in the SPR spectroscopy study as well and therefore the comparability of the two measurement techniques [139].

6.3 Conclusion

In the past 30 years, the use of cellulose thin films has become increasingly popular, whereas the introduction of the spin coating technique boosted research in this area. In the past years, the development of new thin-film systems has brought the opportunity to adjust for film SFE, morphology, and degree of order. The main advantage of the various thin films is that the films can provide an idealized 2D model of cellulose

where interactions at the interface with a variety of species can be thoroughly studied. This involves in particular investigations into the structural aspects of cellulose and how cellulose molecules assemble in thin films and as well as their effects on water interaction and biomolecule affinity.

References

1 Notley, S.M., Eriksson, M., Wågberg, L. et al. (2006). Surface forces measurements of spin-coated cellulose thin films with different crystallinity. *Langmuir* 22 (7): 3154–3160.

2 Kontturi, E. and Spirk, S. (2019). Ultrathin films of cellulose: a materials perspective. *Front. Chem.* 7: 488.

3 Kontturi, E., Tammelin, T., and Österberg, M. (2006). Cellulose—model films and the fundamental approach. *Chem. Soc. Rev.* 35 (12): 1287–1304.

4 Medronho, B., Romano, A., Miguel, M.G. et al. (2012). Rationalizing cellulose (in)solubility: reviewing basic physicochemical aspects and role of hydrophobic interactions. *Cellulose* 19 (3): 581–587.

5 Hann, R.A. (1990). *Molecular structure and monolayer properties*. In: *Langmuir-Blodgett Films* (ed. G. Roberts), 27–32. New York, NY: Springer Science & Business Media.

6 Larson, R.G. and Rehg, T.J. (1997). *Spin coating*. In: *Liquid Film Coating: Scientific Principles and their Technological Implications* (ed. P.M. Schweizer and S.F. Kistler), 709–734. Dordrecht: Springer Science & Business Media.

7 Giles, C.H., Forrester, S.D., and Roberts, G. (1990). *Historical introduction*. In: *Langmuir-Blodgett Films* (ed. G. Roberts), 11–14. New York, NY: Springer Science & Business Media.

8 Petty, M.C. and Barlow, W.A. (1990). *Film deposition*. In: *Langmuir-Blodgett Films* (ed. G. Roberts), 93–96. New York, NY: Springer Science & Business Media.

9 Langmuir, I. (1920). The mechanism of the surface phenomena of flotation. *Trans. Faraday Soc.* 15 (June): 62–74.

10 Blodgett, K.B. (1935). Films built by depositing successive monomolecular layers on a solid surface. *J. Am. Chem. Soc.* 57 (6): 1007–1022.

11 Blodgett, K.B. and Langmuir, I. (1937). Built-up films of barium stearate and their optical properties. *Phys. Rev.* 51 (11): 964–982.

12 Knobler, C.M. and Desai, R.C. (1992). Phase transitions in monolayers. *Annu. Rev. Phys. Chem.* 43 (1): 207–236.

13 McConnell, H.M. (1991). Structures and transitions in lipid monolayers at the air-water interface. *Annu. Rev. Phys. Chem.* 42 (1): 171–195.

14 Möhwald, H. (1990). Phospholipid and phospholipid-protein monolayers at the air/water interface. *Annu. Rev. Phys. Chem.* 41 (1): 441–476.

15 Schwartz, D.K. (1997). Langmuir-Blodgett film structure. *Surf. Sci. Rep.* 27 (7): 245–334.

16 Roberts, G.G. (1985). An applied science perspective of Langmuir-Blodgett films. *Adv. Phys.* 34 (4): 475–512.

17 Langmuir, I. and Schaefer, V.J. (1938). Activities of urease and pepsin monolayers. *J. Am. Chem. Soc.* 60 (6): 1351–1360.

18 Lawrence, C.J. (1988). The mechanics of spin coating of polymer films. *Phys. Fluids* 31 (10): 2786–2795.

19 Niegelhell, K., Chemelli, A., Hobisch, J. et al. (2018). Interaction of industrially relevant cationic starches with cellulose. *Carbohydr. Polym.* 179: 290–296.

20 Sampl, C., Eyley, S., Thielemans, W. et al. (2021). Real-time adsorption of optical brightening agents on cellulose thin films. *Carbohydr. Polym.* 261: 117826.

21 Weißl, M., Niegelhell, K., Reishofer, D. et al. (2018). Homogeneous cellulose thin films by regeneration of cellulose xanthate: properties and characterization. *Cellulose* 25 (1): 711–721.

22 Hall, D.B., Underhill, P., and Torkelson, J.M. (1998). Spin coating of thin and ultrathin polymer films. *Polym. Eng. Sci.* 38 (12): 2039–2045.

23 Bornside, D.E., Macosko, C.W., and Scriven, L.E. (1989). Spin coating: one-dimensional model. *J. Appl. Phys.* 66 (11): 5185–5193.

24 Kistler, S.F. and Schweizer, P.M. (1997). *Liquid Film Coating: Scientific Principles and their Technological Implications*. Dordrecht: Springer Science & Business Media.

25 Kontturi, E., Johansson, L.-S., Kontturi, K.S. et al. (2007). Cellulose nanocrystal submonolayers by spin coating. *Langmuir* 23 (19): 9674–9680.

26 Kontturi, E., Thüne, P.C., and Niemantsverdriet, J.W. (2003). Cellulose model surfaces: simplified preparation by spin coating and characterization by X-ray photoelectron spectroscopy, infrared spectroscopy, and atomic force microscopy. *Langmuir* 19 (14): 5735–5741.

27 Kontturi, K.S., Kontturi, E., and Laine, J. (2013). Specific water uptake of thin films from nanofibrillar cellulose. *J. Mater. Chem. A* 1 (43): 13655–13663.

28 Mohan, T., Kargl, R., Doliška, A. et al. (2013). Enzymatic digestion of partially and fully regenerated cellulose model films from trimethylsilyl cellulose. *Carbohydr. Polym.* 93 (1): 191–198.

29 Mohan, T., Kargl, R., Doliška, A. et al. (2011). Wettability and surface composition of partly and fully regenerated cellulose thin films from trimethylsilyl cellulose. *J. Colloid Interface Sci.* 358 (2): 604–610.

30 Wågberg, L., Decher, G., Norgren, M. et al. (2008). The build-up of polyelectrolyte multilayers of microfibrillated cellulose and cationic polyelectrolytes. *Langmuir* 24 (3): 784–795.

31 Weißl, M., Hobisch, M.A., Johansson, L.S. et al. (2019). Cellulose carbamate derived cellulose thin films: preparation, characterization and blending with cellulose xanthate. *Cellulose* 26 (12): 7399–7410.

32 Chan, S.Y., Goh, C.F., Lau, J.Y. et al. (2019). Rice starch thin films as a potential buccal delivery system: effect of plasticiser and drug loading on drug release profile. *Int. J. Pharm.* 562: 203–211.

33 Kontturi, K.S., Tammelin, T., Johansson, L.-S., and Stenius, P. (2008). Adsorption of cationic starch on cellulose studied by QCM-D. *Langmuir* 24 (9): 4743–4749.

34 Kittle, J.D., Wang, C., Qian, C. et al. (2012). Ultrathin chitin films for nanocomposites and biosensors. *Biomacromolecules* 13 (3): 714–718.

35 Villares, A., Moreau, C., Capron, I., and Cathala, B. (2014). Chitin nanocrystal-xyloglucan multilayer thin films. *Biomacromolecules* 15 (1): 188–194.

36 Dawsey, T.R. and McCormick, C.L. (1990). The lithium chloride/dimethylacetamide solvent for cellulose: a literature review. *J. Macromol. Sci. Part C* 30 (3-4): 405–440.

37 Togawa, E. and Kondo, T. (1999). Change of morphological properties in drawing water-swollen cellulose films prepared from organic solutions. a view of molecular orientation in the drawing process. *J. Polym. Sci., Part B: Polym. Phys.* 37 (5): 451–459.

38 Rosenau, T., Potthast, A., Sixta, H., and Kosma, P. (2001). The chemistry of side reactions and byproduct formation in the system NMMO/cellulose (Lyocell process). *Prog. Polym. Sci.* 26 (9): 1763–1837.

39 Yan, L., Wang, Y., and Chen, J. (2008). Fabrication of a model cellulose surface from straw with an aqueous sodium hydroxide/thiourea solution. *J. Appl. Polym. Sci.* 110 (3): 1330–1335.

40 Liebert, T.F. (2010). *Cellulose solvents – remarkable history, bright future*. In: *Cellulose Solvents: For Analysis, Shaping and Chemical Modification* (ed. T.F. Liebert, T.J. Heinze and K.J. Edgar), 3–54. Washington, DC: American Chemical Society.

41 Woodings, C. (2001). *Regenerated Cellulose Fibres*. Cambridge, UK: Woodhead Publishing.

42 Heinze, T. and Koschella, A. (2005). Solvents applied in the field of cellulose chemistry: a mini review. *Polímeros* 15 (2): 84–90.

43 Bulota, M., Sriubaite, S., Michud, A. et al. (2021). The fiber-matrix interface in Ioncell cellulose fiber composites and its implications for the mechanical performance. *J. Appl. Polym. Sci.* 138 (17): 50306.

44 Cai, J. and Zhang, L. (2005). Rapid dissolution of cellulose in LiOH/urea and NaOH/urea aqueous solutions. *Macromol. Biosci.* 5 (6): 539–548.

45 Zhang, L., Ruan, D., and Zhou, J. (2001). Structure and properties of regenerated cellulose films prepared from cotton linters in NaOH/urea aqueous solution. *Ind. Eng. Chem. Res.* 40 (25): 5923–5928.

46 Eriksson, J., Malmsten, M., Tiberg, F. et al. (2005). Model cellulose films exposed to *H. insolens* glucoside hydrolase family 45 endo-cellulase – the effect of the carbohydrate-binding module. *J. Colloid Interface Sci.* 285 (1): 94–99.

47 Sczech, R. and Riegler, H. (2006). Molecularly smooth cellulose surfaces for adhesion studies. *J. Colloid Interface Sci.* 301 (2): 376–385.

48 Aulin, C., Ahola, S., Josefsson, P. et al. (2009). Nanoscale cellulose films with different crystallinities and mesostructures – their surface properties and interaction with water. *Langmuir* 25 (13): 7675–7685.

49 Pinkert, A., Marsh, K.N., Pang, S., and Staiger, M.P. (2009). Ionic liquids and their interaction with cellulose. *Chem. Rev.* 109 (12): 6712–6728.

50 Kargl, R., Mohan, T., Ribitsch, V. et al. (2015). Cellulose thin films from ionic liquid solutions. *Nordic Pulp Pap. Res. J.* 30 (1): 6–13.

51 Swatloski, R.P., Spear, S.K., Holbrey, J.D., and Rogers, R.D. (2002). Dissolution of cellose with ionic liquids. *J. Am. Chem. Soc.* 124 (18): 4974–4975.

52 Klemm, D., Kramer, F., Moritz, S. et al. (2011). Nanocelluloses: a new family of nature-based materials. *Angew. Chem. Int. Ed.* 50 (24): 5438–5466.

53 Kontturi, E., Laaksonen, P., Linder, M.B. et al. (2018). Advanced materials through assembly of nanocelluloses. *Adv. Mater.* 30 (24): 1703779.

54 Abdul Khalil, H.P.S., Davoudpour, Y., Islam, M.N. et al. (2014). Production and modification of nanofibrillated cellulose using various mechanical processes: a review. *Carbohydr. Polym.* 99: 649–665.

55 Niinivaara, E., Faustini, M., Tammelin, T., and Kontturi, E. (2016). Mimicking the humidity response of the plant cell wall by using two-dimensional systems: the critical role of amorphous and crystalline polysaccharides. *Langmuir* 32 (8): 2032–2040.

56 Kontturi, E., Meriluoto, A., Penttilä, P.A. et al. (2016). Degradation and crystallization of cellulose in hydrogen chloride vapor for high-yield isolation of cellulose nanocrystals. *Angew. Chem. Int. Ed.* 55 (46): 14455–14458.

57 Khodayari, A., Hirn, U., Spirk, S. et al. (2021). Recrystallization and size distribution of dislocated segments in cellulose microfibrils—a molecular dynamics perspective. *Cellulose* 28 (10): 6007–6022.

58 Favier, V., Chanzy, H., and Cavaillé, J. (1995). Polymer nanocomposites reinforced by cellulose whiskers. *Macromolecules* 28 (18): 6365–6367.

59 Petersson, L., Kvien, I., and Oksman, K. (2007). Structure and thermal properties of poly (lactic acid)/cellulose whiskers nanocomposite materials. *Compos. Sci. Technol.* 67 (11): 2535–2544.

60 Tokoh, C., Takabe, K., Fujita, M., and Saiki, H. (1998). Cellulose synthesized by Acetobacter xylinum in the presence of acetyl glucomannan. *Cellulose* 5 (4): 249–261.

61 Elazzouzi-Hafraoui, S., Nishiyama, Y., Putaux, J.-L. et al. (2008). The shape and size distribution of crystalline nanoparticles prepared by acid hydrolysis of native cellulose. *Biomacromolecules* 9 (1): 57–65.

62 Habibi, Y., Lucia, L.A., and Rojas, O.J. (2010). Cellulose nanocrystals: chemistry, self-assembly, and applications. *Chem. Rev.* 110 (6): 3479–3500.

63 Edgar, C.D. and Gray, D.G. (2003). Smooth model cellulose I surfaces from nanocrystal suspensions. *Cellulose* 10 (4): 299–306.

64 Kontturi, E. and Vuorinen, T. (2009). Indirect evidence of supramolecular changes within cellulose microfibrils of chemical pulp fibers upon drying. *Cellulose* 16 (1): 65–74.

65 Cranston, E.D. and Gray, D.G. (2006). Morphological and optical characterization of polyelectrolyte multilayers incorporating nanocrystalline cellulose. *Biomacromolecules* 7 (9): 2522–2530.

66 Podsiadlo, P., Sui, L., Elkasabi, Y. et al. (2007). Layer-by-layer assembled films of cellulose nanowires with antireflective properties. *Langmuir* 23 (15): 7901–7906.

67 Habibi, Y., Hoeger, I., Kelley, S.S., and Rojas, O.J. (2010). Development of Langmuir–Schaeffer cellulose nanocrystal monolayers and their interfacial behaviors. *Langmuir* 26 (2): 990–1001.

68 Turbak, A.F., Snyder, F.W., and Sandberg, K.R. (1983). Microfibrillated cellulose, a new cellulose product: properties, uses, and commercial potential. *J. Appl. Poly. Sci. Appl. Poly. Symp.* 37: 815–827.

69 Abe, K., Iwamoto, S., and Yano, H. (2007). Obtaining cellulose nanofibers with a uniform width of 15 nm from wood. *Biomacromolecules* 8 (10): 3276–3278.

70 Henriksson, M., Henriksson, G., Berglund, L.A., and Lindström, T. (2007). An environmentally friendly method for enzyme-assisted preparation of microfibrillated cellulose (MFC) nanofibers. *Eur. Polym. J.* 43 (8): 3434–3441.

71 Pääkkö, M., Ankerfors, M., Kosonen, H. et al. (2007). Enzymatic hydrolysis combined with mechanical shearing and high-pressure homogenization for nanoscale cellulose fibrils and strong gels. *Biomacromolecules* 8 (6): 1934–1941.

72 Saito, T., Nishiyama, Y., Putaux, J.-L. et al. (2006). Homogeneous suspensions of individualized microfibrils from TEMPO-catalyzed oxidation of native cellulose. *Biomacromolecules* 7 (6): 1687–1691.

73 Besbes, I., Vilar, M.R., and Boufi, S. (2011). Nanofibrillated cellulose from alfa, eucalyptus and pine fibres: preparation, characteristics and reinforcing potential. *Carbohydr. Polym.* 86 (3): 1198–1206.

74 Aulin, C., Johansson, E., Wågberg, L., and Lindström, T. (2010). Self-organized films from cellulose I nanofibrils using the layer-by-layer technique. *Biomacromolecules* 11 (4): 872–882.

75 Nechyporchuk, O., Belgacem, M.N., and Bras, J. (2016). Production of cellulose nanofibrils: a review of recent advances. *Ind. Crops Prod.* 93: 2–25.

76 Tanaka, R., Saito, T., Hänninen, T. et al. (2016). Viscoelastic properties of core–shell-structured, hemicellulose-rich nanofibrillated cellulose in dispersion and wet-film states. *Biomacromolecules* 17 (6): 2104–2111.

77 Tenhunen, T.-M., Peresin, M.S., Penttilä, P.A. et al. (2014). Significance of xylan on the stability and water interactions of cellulosic nanofibrils. *React. Funct. Polym.* 85: 157–166.

78 Fall, A.B., Lindström, S.B., Sundman, O. et al. (2011). Colloidal stability of aqueous nanofibrillated cellulose dispersions. *Langmuir* 27 (18): 11332–11338.

79 Aulin, C., Gällstedt, M., and Lindström, T. (2010). Oxygen and oil barrier properties of microfibrillated cellulose films and coatings. *Cellulose* 17 (3): 559–574.

80 Aulin, C., Salazar-Alvarez, G., and Lindström, T. (2012). High strength, flexible and transparent nanofibrillated cellulose–nanoclay biohybrid films with tunable oxygen and water vapor permeability. *Nanoscale* 4 (20): 6622–6628.

81 Beneventi, D., Chaussy, D., Curtil, D. et al. (2014). Highly porous paper loading with microfibrillated cellulose by spray coating on wet substrates. *Ind. Eng. Chem. Res.* 53 (27): 10982–10989.

82 Henriksson, M., Berglund, L.A., Isaksson, P. et al. (2008). Cellulose nanopaper structures of high toughness. *Biomacromolecules* 9 (6): 1579–1585.
83 Nogi, M., Iwamoto, S., Nakagaito, A.N., and Yano, H. (2009). Optically transparent nanofiber paper. *Adv. Mater.* 21 (16): 1595–1598.
84 Österberg, M., Vartiainen, J., Lucenius, J. et al. (2013). A fast method to produce strong NFC films as a platform for barrier and functional materials. *ACS Appl. Mater. Interfaces* 5 (11): 4640–4647.
85 Cooper, G.K., Sandberg, K.R., and Hinck, J.F. (1981). Trimethylsilyl cellulose as precursor to regenerated cellulose fiber. *J. Appl. Polym. Sci.* 26 (11): 3827–3836.
86 Köhler, S., Liebert, T., and Heinze, T. (2008). Interactions of ionic liquids with polysaccharides. VI. Pure cellulose nanoparticles from trimethylsilyl cellulose synthesized in ionic liquids. *J. Polym. Sci., Part A: Polym. Chem.* 46 (12): 4070–4080.
87 Kontturi, E., Thüne, P.C., and Niemantsverdriet, J.W. (2003). Novel method for preparing cellulose model surfaces by spin coating. *Polymer* 44 (13): 3621–3625.
88 Kostag, M., Köhler, S., Liebert, T., and Heinze, T. (2010). Pure cellulose nanoparticles from trimethylsilyl cellulose. *Macromol. Symp.* 294 (2): 96–106.
89 Greber, G. and Paschinger, O. (1981). Silylderivate der cellulose. *Das Papier* 35 (12): 547–554.
90 Schempp, W., Krause, T., Seifried, U., and Koura, A. (1984). Herstellung hochsubstituierter trimethylsilylcellulosen im system dimethylacetamid/lithiumchlorid. *Das Papier* 38 (12): 607–610.
91 Klemm, D., Philipp, B., Heinze, T. et al. (1998). *Comprehensive Cellulose Chemistry. Volume 1: Fundamentals and Analytical Methods*. Weinheim: Wiley-VCH Verlag GmbH.
92 Schaub, M., Wenz, G., Wegner, G. et al. (1993). Ultrathin films of cellulose on silicon wafers. *Adv. Mater.* 5 (12): 919–922.
93 Schlemmer, W., Zankel, A., Niegelhell, K. et al. (2018). Deposition of cellulose-based thin films on flexible substrates. *Materials* 11: 2433.
94 Jones, A.O.F., Resel, R., Schrode, B. et al. (2020). Structural order in cellulose thin films prepared from a trimethylsilyl precursor. *Biomacromolecules* 21 (2): 653–659.
95 Wegner, G., Buchholz, V., Ödberg, L., and Stemme, S. (1996). Regeneration, derivatization and utilization of cellulose in ultrathin films. *Adv. Mater.* 8 (5): 399–402.
96 Holmberg, M., Berg, J., Stemme, S. et al. (1997). Surface force studies of Langmuir–Blodgett cellulose films. *J. Colloid Interface Sci.* 186 (2): 369–381.
97 Klemm, D., Philipp, B., Heinze, T. et al. (1998). *Cellulose dithiocarbonate esters*. In: *Comprehensive Cellulose Chemistry*, *Volume 2: Functionalization of Cellulose* (ed. D. Klemm, B. Philipp, T. Heinze, et al.), 147–161. Weinheim: Wiley-VCH.
98 Götze, K. (1967). *Der molekulare und strukturelle Abbau der Zellulose bzw. der Alkalizellulose*. In: *Chemiefasern nach dem Viskoseverfahren* (ed. K. Götze), 356–395. Berlin, Heidelberg: Springer.

99 Götze, K. (1967). *Die Sulfidierung der Alkalizellulose und das Xanthogenat*. In: *Chemiefasern nach dem Viskoseverfahren* (ed. K. Götze), 395–420. Berlin, Heidelberg: Springer.

100 Hämmerle, F.M. (2011). The cellulose gap. *Lenzinger Ber.* 89: 12–21.

101 Phifer, L.H. (1965). Use of thin films in ultraviolet studies of cellulose xanthate. *J. Appl. Polym. Sci.* 9 (3): 1041–1053.

102 Albrecht, W., Krässinger, H., Marini, I. et al. (1984). *Lenzinger Ber.* 57.

103 Fink, H.-P., Ganster, J., and Lehmann, A. (2014). Progress in cellulose shaping: 20 years industrial case studies at Fraunhofer IAP. *Cellulose* 21 (1): 31–51.

104 Weißl, M., Rath, T., Sattelkow, J. et al. (2019). Multi-layered nanoscale cellulose/$CuInS_2$ sandwich type thin films. *Carbohydr. Polym.* 203: 219–227.

105 Zhang, S., Yu, C., Liu, N. et al. (2019). Preparation of transparent anti-pollution cellulose carbamate regenerated cellulose membrane with high separation ability. *Int. J. Biol. Macromol.* 139: 332–341.

106 Eaton, P. and West, P. (2010). *Atomic Force Microscopy*. New York: Oxford University Press.

107 Hansma, P.K., Elings, V.B., Marti, O., and Bracker, C.E. (1988). Scanning tunneling microscopy and atomic force microscopy: application to biology and technology. *Science* 242 (4876): 209–216.

108 Jandt, K.D. (2001). Atomic force microscopy of biomaterials surfaces and interfaces. *Surf. Sci.* 491 (3): 303–332.

109 Liu, G. and Zhang, G. (2013). *Basic principles of QCM-D*. In: *QCM-D Studies on Polymer Behavior at Interfaces* (ed. G. Liu and G. Zhang), 1–2. Berlin, Heidelberg: Springer.

110 Jandt, K.D. (1998). Developments and perspectives of scanning probe microscopy (SPM) on organic materials systems. *Mater. Sci. Eng. R: Rep.* 21 (5): 221–295.

111 Pollard, B. and Raschke, M.B. (2016). Correlative infrared nanospectroscopic and nanomechanical imaging of block copolymer microdomains. *Beilstein J. Nanotechnol.* 7: 605–612.

112 Bechtel, H.A., Muller, E.A., Olmon, R.L. et al. (2014). Ultrabroadband infrared nanospectroscopic imaging. *Proc. Natl. Acad. Sci. U.S.A.* 111 (20): 7191.

113 Paluszkiewicz, C., Piergies, N., Chaniecki, P. et al. (2017). Differentiation of protein secondary structure in clear and opaque human lenses: AFM – IR studies. *J. Pharm. Biomed. Anal.* 139: 125–132.

114 Lapshin, R.V. (2004). Feature-oriented scanning methodology for probe microscopy and nanotechnology. *Nanotechnology* 15 (9): 1135–1151.

115 Lapshin, R.V. (2007). Automatic drift elimination in probe microscope images based on techniques of counter-scanning and topography feature recognition. *Meas. Sci. Technol.* 18 (3): 907–927.

116 Yurov, V.Y. and Klimov, A.N. (1994). Scanning tunneling microscope calibration and reconstruction of real image: drift and slope elimination. *Rev. Sci. Instrum.* 65 (5): 1551–1557.

117 Ando, T., Kodera, N., Takai, E. et al. (2001). A high-speed atomic force microscope for studying biological macromolecules. *Proc. Natl. Acad. Sci. U.S.A.* 98 (22): 12468–12472.

118 Ando, T., Uchihashi, T., and Fukuma, T. (2008). High-speed atomic force microscopy for nano-visualization of dynamic biomolecular processes. *Prog. Surf. Sci.* 83 (7): 337–437.

119 Ando, T. (2013). *High-speed atomic force microscopy (AFM)*. In: *Encyclopedia of Biophysics* (ed. G.C.K. Roberts), 984–987. Berlin, Heidelberg: Springer.

120 Ando, T. (2014). High-speed AFM imaging. *Curr. Opin. Struct. Biol.* 28: 63–68.

121 Igarashi, K., Uchihashi, T., Koivula, A. et al. (2011). Traffic jams reduce hydrolytic efficiency of cellulase on cellulose surface. *Science* 333 (6047): 1279–1282.

122 Hanley, S.J., Giasson, J., Revol, J.-F., and Gray, D.G. (1992). Atomic force microscopy of cellulose microfibrils: comparison with transmission electron microscopy. *Polymer* 33 (21): 4639–4642.

123 Hanley, S.J., Revol, J.-F., Godbout, L., and Gray, D.G. (1997). Atomic force microscopy and transmission electron microscopy of cellulose from *Micrasterias denticulata*; evidence for a chiral helical microfibril twist. *Cellulose* 4 (3): 209.

124 Usov, I., Nyström, G., Adamcik, J. et al. (2015). Understanding nanocellulose chirality and structure–properties relationship at the single fibril level. *Nat. Commun.* 6 (1): 1–11.

125 Ganner, T., Sattelkow, J., Rumpf, B. et al. (2016). Direct-write fabrication of cellulose nano-structures via focused electron beam induced nanosynthesis. *Sci. Rep.* 6: 32451.

126 Kargl, R., Mohan, T., Bracic, M. et al. (2012). Adsorption of carboxymethyl cellulose on polymer surfaces: evidence of a specific interaction with cellulose. *Langmuir* 28: 11440–11447.

127 Mohan, T., Niegelhell, K., Nagaraj, C. et al. (2017). Interaction of tissue engineering substrates with serum proteins and its influence on human primary endothelial cells. *Biomacromolecules* 18 (2): 413–421.

128 Mohan, T., Rathner, R., Reishofer, D. et al. (2015). Designing hydrophobically modified polysaccharide derivatives for highly efficient enzyme immobilization. *Biomacromolecules* 16 (8): 2403–2411.

129 Niegelhell, K., Leimgruber, S., Grießer, T. et al. (2016). Adsorption studies of organophosphonic acids on differently activated gold surfaces. *Langmuir* 32 (6): 1550–1559.

130 Niegelhell, K., Plank, H., Stelzer, F., Kargl, R., Griesser, T., and Spirk, S. (2017). Nano- and micropatterns of cellulose - from lithography to microphase separation. *253rd ACS National Meeting & Exposition* (Vol. 253, p. CELL_255). San Francisco: American Chemical Society.

131 Ristić, T., Mohan, T., Kargl, R. et al. (2014). A study on the interaction of cationized chitosan with cellulose surfaces. *Cellulose* 21 (4): 2315–2325.

132 Sampl, C., Niegelhell, K., Reishofer, D. et al. (2019). Multilayer density analysis of cellulose thin films. *Front. Chem.* 7: 251.

133 Strasser, S., Niegelhell, K., Kaschowitz, M. et al. (2016). Exploring nonspecific protein adsorption on lignocellulosic amphiphilic bicomponent films. *Biomacromolecules* 17 (3): 1083–1092.

134 Wolfberger, A., Kargl, R., Griesser, T., and Spirk, S. (2014). Photoregeneration of trimethylsilyl cellulose as a tool for microstructuring ultrathin cellulose supports. *Molecules* 19 (10): 16266–16273.

135 Zhang, P., Chen, M., Duan, Y. et al. (2018). Real-time adsorption of exo- and endoglucanases on cellulose: effect of pH, temperature, and inhibitors. *Langmuir* 34 (45): 13514–13522.

136 Zhang, P., Ma, Y., Cui, M. et al. (2020). Effect of sugars on the real-time adsorption of expansion on cellulose. *Biomacromolecules* 21 (5): 1776–1784.

137 Niegelhell, K., Süßenbacher, M., Jammernegg, K. et al. (2016). Enzymes as biodevelopers for nano- and micropatterned bicomponent biopolymer thin films. *Biomacromolecules* 17 (11): 3743–3749.

138 Kargl, R., Mohan, T., Koestler, S. et al. (2013). Functional patterning of biopolymer thin films using enzymes and lithographic methods. *Adv. Funct. Mater.* 23 (3): 308–315.

139 Mohan, T., Niegelhell, K., Zarth, C.S.P. et al. (2014). Triggering protein adsorption on tailored cationic cellulose surfaces. *Biomacromolecules* 15 (11): 3931–3941.

140 Niegelhell, K., Süßenbacher, M., Sattelkow, J. et al. (2017). How bound and free fatty acids in cellulose films impact nonspecific protein adsorption. *Biomacromolecules* 18 (12): 4224–4231.

141 Fujiwara, H. (2007). *Introduction to spectroscopic ellipsometry*. In: *Spectroscopic Ellipsometry: Principles and Applications*, 1–2. Chichester: Wiley.

142 Fujiwara, H. (2007). *Real-time monitoring by spectroscopic ellipsometry*. In: *Spectroscopic Ellipsometry: Principles and Applications*, 328–331. Chichester: Wiley.

143 Whiteside, P.J.D., Chininis, J.A., and Hunt, H.K. (2016). Techniques and challenges for characterizing metal thin films with applications in photonics. *Coatings* 6 (3): 35.

144 Fujiwara, H. (2007). *Principles of spectroscopic ellipsometry*. In: *Spectroscopic Ellipsometry: Principles and Applications*, 89–90. Chichester: Wiley.

145 Hasche, K., Thomsen-Schmidt, P., Krumrey, M. et al. (2003). Metrological characterization of nanometer film thickness standards for XRR and ellipsometry applications. In: *Recent Developments in Traceable Dimensional Measurements II*, vol. 5190, 165–172. San Diego: International Society for Optics and Photonics.

146 Kontturi, E. and Lankinen, A. (2010). Following the kinetics of a chemical reaction in ultrathin supported polymer films by reliable mass density determination with X-ray reflectivity. *J. Am. Chem. Soc.* 132 (11): 3678–3679.

147 Kohli, S., Rithner, C.D., Dorhout, P.K. et al. (2005). Comparison of nanometer-thick films by X-ray reflectivity and spectroscopic ellipsometry. *Rev. Sci. Instrum.* 76 (2): 023906.

148 Van der Heide, P. (2012). *XPS instrumentation*. In: *X-Ray Photoelectron Spectroscopy: An Introduction to Principles and Practices* (ed. P. Van der Heide), 39. New Jersey: Wiley.

149 Van der Heide, P. (2012). *Introduction*. In: *X-Ray Photoelectron Spectroscopy: An Introduction to Principles and Practices* (ed. P. Van der Heide), 5–12. New Jersey: Wiley.

150 Eyley, S. and Thielemans, W. (2011). Imidazolium grafted cellulose nanocrystals for ion exchange applications. *Chem. Commun.* 47 (14): 4177–4179.

151 Rojas, O.J., Ernstsson, M., Neuman, R.D., and Claesson, P.M. (2000). X-ray photoelectron spectroscopy in the study of polyelectrolyte adsorption on mica and cellulose. *J. Phys. Chem. B* 104 (43): 10032–10042.

152 Mohan, T., Zarth, C., Doliska, A. et al. (2013). Interactions of a cationic cellulose derivative with an ultrathin cellulose support. *Carbohydr. Polym.* 92: 1046–1053.

153 Stuart, B. (2004). *Introduction*. In: *Infrared Spectroscopy: Fundamentals and Applications* (ed. B. Stuart), 5–7. Chichester: Wiley.

154 Stuart, B. (2004). *Experimental methods*. In: *Infrared Spectroscopy: Fundamentals and Applications* (ed. B. Stuart), 18–33. Chichester: Wiley.

155 Larkin, P. (2011). *Basic principles*. In: *Infrared and Raman Spectroscopy: Principles and Spectral Interpretation* (ed. P. Larkin), 14–16. Elsevier Inc.

156 Larkin, P. (2011). *Instrumentation and sampling methods*. In: *Infrared and Raman Spectroscopy: Principles and Spectral Interpretation* (ed. P. Larkin), 27–28. Elsevier Inc.

157 Schrader, B. (1995). *Tools for infrared and Raman spectroscopy*. In: *Infrared and Raman Spectroscopy: Methods and Applications* (ed. B. Schrader), 63–188. Weinheim: VCH.

158 Kljun, A., Benians, T., Goubet, F. et al. (2011). Comparative analysis of crystallinity changes in cellulose i polymers using ATR-FTIR, X-ray diffraction, and carbohydrate-binding module probes. *Biomacromolecules* 12: 4121–4126.

159 Tsuboi, M. (1957). Infrared spectrum and crystal structure of cellulose. *J. Poly. Sci.* 25 (109): 159–171.

160 Nguyen, T.P.N., Jun, B.-M., and Kwon, Y.-N. (2017). The chlorination mechanism of integrally asymmetric cellulose triacetate (CTA)-based and thin film composite polyamide-based forward osmosis membrane. *J. Membr. Sci.* 523: 111–121.

161 Kontturi, E., Thüne, P.C., Alexeev, A., and Niemantsverdriet, J.W. (2005). Introducing open films of nanosized cellulose—atomic force microscopy and quantification of morphology. *Polymer* 46 (10): 3307–3317.

162 Nyfors, L., Suchy, M., Laine, J., and Kontturi, E. (2009). Ultrathin cellulose films of tunable nanostructured morphology with a hydrophobic component. *Biomacromolecules* 10 (5): 1276–1281.

163 Hebbar, R.S., Isloor, A.M., and Ismail, A.F. (2017). *Contact angle measurements*. In: *Membrane Characterization* (ed. N. Hilal, A.F. Ismail, T. Matsuura and D. Oatley-Radcliffe), 219–221. Elsevier.

164 Kaelble, D.H. (1970). Dispersion-polar surface tension properties of organic solids. *J. Adhes.* 2: 66–81.

165 Owens, D.K. and Wendt, R.C. (1969). Estimation of the surface free energy of polymers. *J. Appl. Polym. Sci.* 13 (8): 1741–1747.

166 Rabel, W. (1971). Einige Aspekte der Benetzungstheorie und ihre Anwendung auf die Untersuchung und Veränderung der Oberflächeneigenschaften von Polymeren. *Farbe Lack* 77: 997–1005.

167 Paar, A. (2020). Zeta potential. https://wiki.anton-paar.com/en/zeta-potential/ (accessed 02 September 2020).

168 Taqvi, S. and Bassioni, G. (2019). *Understanding wettability through zeta potential measurements*. In: *Wettability and Interfacial Phenomena – Implications for Material Processing* (ed. R. Khanna), 3–4. IntechOpen.

169 Cai, K., Frant, M., Bossert, J. et al. (2006). Surface functionalized titanium thin films: zeta-potential, protein adsorption and cell proliferation. *Colloids Surf., B* 50 (1): 1–8.

170 Roessler, S., Zimmermann, R., Scharnweber, D. et al. (2002). Characterization of oxide layers on Ti6Al4V and titanium by streaming potential and streaming current measurements. *Colloids Surf., B* 26 (4): 387–395.

171 Delgado, A.V., Gonzalez-Caballero, F., Hunter, R.J. et al. (2005). Measurement and interpretation of electrokinetic phenomena (IUPAC technical report). *Pure Appl. Chem.* 77 (10): 1753–1805.

172 Bai, L., Liu, Y., Ding, A. et al. (2019). Fabrication and characterization of thin-film composite (TFC) nanofiltration membranes incorporated with cellulose nanocrystals (CNCs) for enhanced desalination performance and dye removal. *Chem. Eng. J.* 358: 1519–1528.

173 Bracic, M., Mohan, T., Kargl, R. et al. (2014). Preparation of PDMS ultrathin films and patterned surface modification with cellulose. *RSC Adv.* 4 (23): 11955–11961.

174 Payerl, C., Bračič, M., Zankel, A. et al. (2017). Nonspecific protein adsorption on cationically modified Lyocell fibers monitored by zeta potential measurements. *Carbohydr. Polym.* 164: 49–56.

175 Glatter, O. (2018). *Scattering Methods and their Application in Colloid and Interface Science*. Elsevier.

176 Hexemer, A. and Müller-Buschbaum, P. (2015). Advanced grazing-incidence techniques for modern soft-matter materials analysis. *IUCrJ* 2 (1): 106–125.

177 Kikhney, A.G. and Svergun, D.I. (2015). A practical guide to small angle X-ray scattering (SAXS) of flexible and intrinsically disordered proteins. *FEBS Lett.* 589 (19, Part A): 2570–2577.

178 Bauch, J. and Rosenkranz, R. (2017). *SAXS – Röntgenkleinwinkelstreuung*. In: *Physikalische Werkstoffdiagnostik: Ein Kompendium wichtiger Analytikmethoden für Ingenieure und Physiker* (ed. J. Bauch and R. Rosenkranz), 54–55. Berlin, Heidelberg: Springer.

179 Müller-Buschbaum, P. (2009). *A basic introduction to grazing incidence small-angle X-ray scattering*. In: *Applications of Synchrotron Light to Scattering and Diffraction in Materials and Life Sciences* (ed. T.A. Ezquerra, M.C.

Garcia-Gutierrez, A. Nogales and M. Gomez), 61–62. Berlin, Heidelberg: Springer.

180 Krins, N., Bass, J.D., Julián-López, B. et al. (2011). Mesoporous SiO_2 thin films containing photoluminescent ZnO nanoparticles and simultaneous SAXS/WAXS/ellipsometry experiments. *J. Mater. Chem.* 21 (4): 1139–1146.

181 Ehmann, H.M.A., Werzer, O., Pachmajer, S. et al. (2015). Surface-sensitive approach to interpreting supramolecular rearrangements in cellulose by synchrotron grazing incidence small-angle X-ray scattering. *ACS Macro Lett.* 4: 713–716.

182 de Mol, N.J. and Fischer, M.J.E. (2010). *Surface plasmon resonance: a general introduction*. In: *Surface Plasmon Resonance: Methods and Protocols* (ed. N.J. de Mol and M.J.E. Fischer), 1–7. New York: Humana Press.

183 Rich, R.L. and Myszka, D.G. (2008). Survey of the year 2007 commercial optical biosensor literature. *J. Mol. Recognit.* 21 (6): 355–400.

184 Kretschmann, E. (1969). Die Bestimmung der optischen Konstanten dünner Schichten in der Nähe der Plasmafrequenz aus Kurvenfeldern konstanter Transmission. *Z. Phys. A: Hadrons Nucl.* 221 (4): 346–356.

185 Kretschmann, E. and Raether, H. (1968). Radiative decay of non-radiative surface plasmons excited by light. *Z. Naturforsch. A* 23 (12): 2135–2136.

186 Otto, A. (1968). Excitation of nonradiative surface plasma waves in silver by the method of frustrated total reflection. *Z. Phys. A: Hadrons Nucl.* 216 (4): 398–410.

187 Gwon, H.R. and Lee, S.H. (2010). Spectral and angular responses of surface plasmon resonance based on the Kretschmann prism configuration. *Mater. Trans.* 51 (6): 1150–1155.

188 Homola, J., Yee, S.S., and Gauglitz, G. (1999). Surface plasmon resonance sensors: review. *Sens. Actuators, B* 54 (1): 3–15.

189 Marquart, A. (2021). SPR pages. https://www.sprpages.nl/ (accessed 30 April 2021).

190 Reviakine, I., Johannsmann, D., and Richter, R.P. (2011). Hearing what you cannot see and visualizing what you hear: interpreting quartz crystal microbalance data from solvated interfaces. *Anal. Chem.* 83 (23): 8838–8848.

191 Sauerbrey, G. (1959). Verwendung von Schwingquarzen zur Wägung dünner Schichten und zur Mikrowägung. *Z. Angew. Phys.* 155: 206–222.

192 Tammelin, T., Abburi, R., Gestranius, M. et al. (2015). Correlation between cellulose thin film supramolecular structures and interactions with water. *Soft Matter* 11 (21): 4273–4282.

193 Enarsson, L.-E. and Wågberg, L. (2009). Polyelectrolyte adsorption on thin cellulose films studied with reflectometry and quartz crystal microgravimetry with dissipation. *Biomacromolecules* 10 (1): 134–141.

194 Fält, S., Wågberg, L., Vesterlind, E.L., and Larsson, P.T. (2004). Model films of cellulose II – improved preparation method and characterization of the cellulose film. *Cellulose* 11 (2): 151–162.

195 Hu, G., Heitmann, J.A., and Rojas, O.J. (2009). In situ monitoring of cellulase activity by microgravimetry with a quartz crystal microbalance. *J. Phys. Chem. B* 113 (44): 14761–14768.

196 Orelma, H., Johansson, L.-S., Filpponen, I. et al. (2012). Generic method for attaching biomolecules via avidin-biotin complexes immobilized on films of regenerated and nanofibrillar cellulose. *Biomacromolecules* 13: 2802–2810.

197 Salas, C., Rojas, O.J., Lucia, L.A. et al. (2013). On the surface interactions of proteins with lignin. *ACS Appl. Mater. Interfaces* 5 (1): 199–206.

7

Biopolymer Thin Films as "Smart" Materials in Biomedical Applications

Tanja Zidarič[1] and Uroš Maver[1,2]

[1] *University of Maribor, Institute of Biomedical Sciences, Faculty of Medicine, Taborska ulica 8, 2000 Maribor, Slovenia*
[2] *University of Maribor, Faculty of Medicine, Department of Pharmacology, Taborska ulica 8, 2000 Maribor, Slovenia*

7.1 Introduction

Throughout the history, polymers have played a crucial role in humanity. Natural polymers, such as proteins, nucleic acids, and polysaccharides, are integral part of living organisms; among others, they serve as basic building blocks of cell components, represent an energy source for cell functions, and play a vital role in maintaining biological functions [1, 2]. The technological progress in polymer science over recent years has triggered remarkable achievements not only in high-tech industries, but also in the field of biomedicine, where they continue to serve as crucial components for new medical devices and therapies [3, 4]. Biopolymer-based materials have already earned their place in modern medicine to treat medical complications and diseases, as well as to improve the quality of life of patients [3]. Of particular significance to contemporary medicine is the development of artificial organs [5] and drug/implantable devices in combination with electronics (e.g. drug-eluting stents [6] and glucose biosensors [7–9]). Biomaterials interact with the biological system through their surface; therefore, it is of great importance that the used materials possess a biocompatible character (i.e. biomaterial integrates well with host tissues) [3, 10]. Unlike traditionally used implantable materials, such as metals, ceramics, and synthetic polymers, biomaterials do not raise concerns about their degradation by-products (e.g. hydrolytic product carbon dioxide, which lowers the local pH) after their administration to the body, which may cause an unwanted immunogenic response (e.g. as a result of cell and tissue necrosis) [11]. A distinct and multifaceted class of biomaterials, called biopolymers, are emerging candidates with a wide range of biomedical applications. The term "biopolymer" implies one type polymer composed of a few types of repeating units containing carbon that are used in or originate from living organisms. Referring to this broad definition, biopolymers encompass natural polymers (i.e. biomass), bio-based polymers,

Functional Biomaterials: Design and Development for Biotechnology, Pharmacology, and Biomedicine, First Edition. Edited by Tamilselvan Mohan and Karin Stana Kleinschek.

which are extracted from biomass or polymerized from bio-based monomers, and extracted polymers produced in microorganisms [12].

Bio-based polymers are made from renewable sources, which means that they are replenished by natural procedures at rates comparable or even faster compared to their rate of use. Another important (bio)polymer feature is its biodegradability, which specifies deterioration and potentially also a complete degradation of materials' chemical and physical characteristics under exposure to microorganisms (aerobic and anaerobic), as well as other processes [1, 12]. However, both terms do not go hand in hand, since biopolymers can be also formed from sustainable (bio-based) crude materials, and are nevertheless not biodegradable, or they can be synthesized from fossil fuels, and being biodegradable [1]. In addition, compared to synthetic polymers, they differ on the structural level; biopolymers are (often) complex molecular assemblies, whereas their synthetic counterparts have a simpler and more random structure. This complexity of molecular structure that enables the formation of precise and defined three-dimensional (3D) architectures is a key property, which makes biopolymers active molecules *in vivo* [13]. Nowadays, some biopolymers can directly replace synthetically developed materials in the conventional applications in food production and packaging, unfolding new opportunities for commercialization. Thus, established novel biopolymer compounds with unique properties have been under the spotlight also in the area of biotechnology and biomedicine [1]. Such applications include promising candidate molecules/materials for development of various therapeutic devices, 3D porous structures for tissue engineering, and drug-delivery systems. All mentioned can be realized due to the nonimmunogenic degradation by-products of a wide variety of base biopolymers [11]. However, there are still some crucial characteristics that limit their even wider use. These include the normal homeostatic response to the implantation injury, potential nonfavorable tissue or blood/device interactions (e.g. clot formation or other complications), and lack of biocompatibility toward target tissue cells, a limited *in vivo* functionality on the desired time-scale, including the shelf-life of implants made thereof [10, 14–16].

The main objectives of this chapter are to provide a basic insight into widely used (naturally derived) biopolymers for thin-film production in biomedical applications. Subsequently, biopolymer-based materials with different stimulus responses (e.g. temperature, pH, and redox reaction) are discussed. A substantial part is dedicated to the use of these materials in personalized medicine (e.g. bioelectronics and biosensors). A short overview of general approaches to overcome the instability of *in vivo* implantable devices is also given.

7.2 Frequently Used Biopolymers

7.2.1 Cellulose

Cellulose is the most abundant macromolecule in the biosphere and is the basic building block of the plant cell wall. Cellulose is not only found in the flora, but

Figure 7.1 Molecular structure of cellulose.

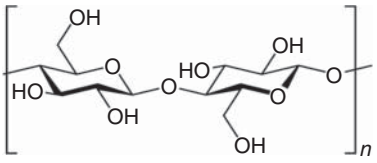

can also be produced by other living organisms such as various types of bacteria, algae, and even some species of fungi [1, 17, 18]. Plant and bacterial celluloses are chemically the same, β(1→4) linked glucans (Figure 7.1); however, they differ in polymerization degree and microfibrils forming ribbons [17, 19].

Bacterial (or microbial) cellulose is more favored than plant-based, since it can be acquired in higher purity and shows a higher degree of polymerization and crystallinity index [1, 17, 19]. Moreover, its greater tensile strength and water-holding potential compared to plant cellulose make it a more acceptable raw material for constructing high-precision acoustic speakers, high-quality paper, dessert foods [1, 20], wound dressings [19, 21–23], and even skin substitutes [24, 25]. Regardless of the source, cellulose and its derivatives have been recognized to be nontoxic in both animal and humans [26, 27].

There are three main types of cellulosic polymers that are generated by chemical alteration of cellulose for film and fiber fabrications: (i) cellulose esters (e.g. cellulose nitrate and cellulose acetate, CA), (ii) cellulose ethers (e.g. hydroxyethyl cellulose and carboxymethyl cellulose, CMC), and (iii) regenerated cellulose [1, 18]. Among the latter cellulose, ethers are extensively used in various pharmaceutical [28, 29] and biomedical applications [25, 27].

7.2.2 Starch

Similar to cellulose, starch is a naturally occurring carbohydrate polymer that is highly available in nature from diverse sources, mainly from cereals (e.g. wheat, corn, and rice) and from tubers (potato) [1, 30]. The main building blocks are two homopolymers of D-glucose, amylose, and amylopectin. Amylose (Figure 7.2a) is almost a linear polymer with α-D-(1→4) glycosidic linkages, while amylopectin

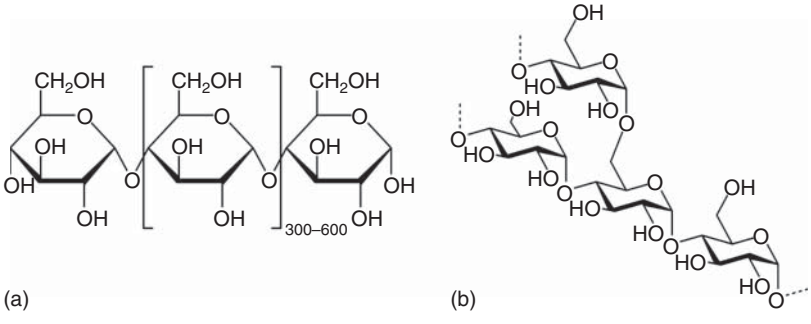

Figure 7.2 Structure of (a) amylose molecule, and (b) amylopectin molecule.

(Figure 7.2b) is a highly branched structure of short α-1, 4 chains linked by α-1, 6 bonds at branching points that occur every 24–30 glucose units [31].

Polysaccharides are known for their film-forming properties, which can be obtained owing to the diversity of available polysaccharides. Starch has been intensively investigated to achieve renewable and biodegradable films due to its wide accessibility, low cost, and its functional diversity. The amylose/amylopectin ratio defines the mechanical properties of starch films; linear amylose favors good film properties compared to branched amylopectin. Starch films contain residual water that has a significant effect on the glass transition temperature, therefore affecting the materials mechanical properties [30].

Native starch normally has a granular structure and a hydrophilic character. For the various industrial applications of starch films, the native starch must be destructurized. Because of its hydrophilic nature, the internal interactions and morphology of starch are altered by water molecules [1, 30]. Plasticizers (e.g. glycerol) can be used to overcome limitations of the destructurized process by improving the processing and flexibility of starch films. Moreover, the incorporation of plasticizers reduces the polymers' intermolecular forces, increasing the mobility of the polymer chains, enhancing mechanical properties [32–34], and affecting the water barrier property of the films [35].

The use of starch in the pharmaceutical industry is ubiquitous; it is commonly used as a copolymer and excipient in controlled drug delivery, as a drug carrier in tissue engineering scaffolds [36], as part of hydrogels [37], and as a solubility enhancer [33]. In addition, in the form of nanoparticles, it has been applied for noninvasive delivery of insulin [38, 39]. Functionalized starch films have been also proposed as part of materials for colorimetric cyanide detection [30].

7.2.3 Chitin and Chitosan

After cellulose, chitin is the second most abundant biopolymer in nature [40, 41]. It is a primary component of the cell wall of many fungal species, the exoskeleton of mollusks and crustaceans, it can be also found in the cuticle of insects, and forms the backbone of squids [40]. It is an acetylated homopolysaccharide (Figure 7.3) made up of *N*-acetyl-D-glucosamine groups linked by β(1→4) linkages. Since it is chemically related to cellulose, its insolubility and low chemical reactivity also resemble the ones of the latter [1, 40].

Chitosan, which is the most important and practical derivate of chitin, is a polysaccharide with a high content of amine and hydroxyl functionalities [38]. In

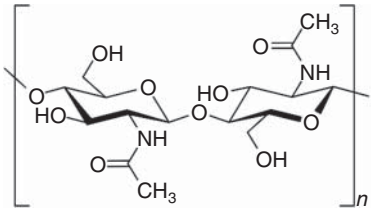

Figure 7.3 Structure of chitin molecule, showing two of *N*-acetylglucosamine units that repeat to form long chains in β(1→4)-linkage.

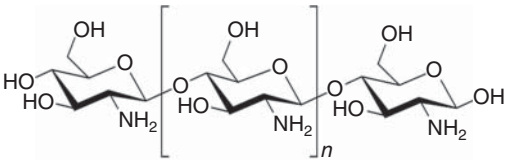

Figure 7.4 Molecular structure of completely deacetylated chitosan.

contrast to chitin, chitosan is not common in nature; however, a limited number of zygote fungi can synthesize it, and it is present in the wall of the termite queen. Chitosan (Figure 7.4) is produced on an industrial scale by partial and controlled chitin deacetylation. As a result, chitosan is a linear polysaccharide composed of randomly distributed β(1→4)-linked D-glucosamine (deacetylated unit) and N-acetyl-D-glucosamine (acetylated unit) [1, 42].

This natural amino-polysaccharide has gained progressive attention in treatment [43–45] and purification fields due to its high binding capacity, wide availability, and unique functionalities [38]. Amino and hydroxyl groups of chitosan enable absorption of anionic dyes, macromolecules, and heavy metals [41]. Beside being adsorptive, some other properties like solubility in water, high degree of shrinkage after drying, diversity of derivatives, and high polarity make chitosan a versatile and advanced biofabrication material [41, 46].

Both cationic polysaccharides and their derivatives have practical applications in different areas, among others in biotechnology, medicine, and pharmaceutical industry. The capability to control drug release of chitosan is mainly related to its swelling property, the partial dissolution or erosion in film structures, and the often-present drug–polymer interactions. Therefore, chitosan has been utilized as a tablet binder [47], and as part of unique drug-delivery vehicles [48, 49]. Chitosan also has a pronounced role in wound management due to its antibacterial activity [43, 44] and a proven positive effect on wound healing in general [50]. Different chitosan-based materials were also successfully employed in bone tissue engineering as a coating or as a source of mechanically stable scaffolds [43]. Chitosan-based wound dressings or coatings on medical implants distribute bioactive substances in two routes: (i) by conveying bioactive ingredients or (ii) by their endogenous activity [1, 43]. In addition to the aforementioned applications, chitin and especially chitosan films have been found as an important biomaterial in biosensor technology that incorporates the analyte-selective biological component [46, 51].

7.2.4 Alginate

Also called alginic acid, this anionic polysaccharide is distributed widely in cell walls of brown algae (e.g. *Laminaria* sp. and *Macrocystis* sp.). Apart from that, it is a significant component of the biofilm produced by two bacteria genera *Pseudomonas* and *Azobacter*. Structurally, alginates (Figure 7.5) are linear unbranched polymers composed of (1-4)-linked β-D-mannuronic acid (M) and α-L-guluronic (G) blocks, which are (depending on sources) sequentially distributed in either repeating or alternating blocks [52].

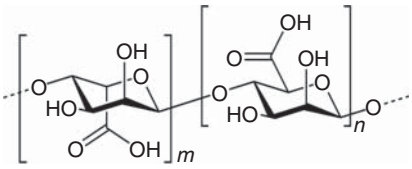

Figure 7.5 Structure of alginic acid.

Commercially, alginates for large-scale applications are refined from brown seaweeds [1], whereas bacterial ones (from *Azotobacter vinelandii*) are useful for production of micro- and nanostructures for medical applications [53]. Alginates from different species of brown seaweeds often have variations in their chemical structure. The key property of alginate is its tendency for gelation in presence of cations (commonly calcium ions, Ca^{2+}, are used). Only the G-blocks are believed to be involved in intermolecular cross-linking with divalent cations, and the gelation mechanism is known as an "egg-box" model. In the presence of Ca^{2+}, chain–chain junctions are formed between adjacent G-blocks [54, 55]. The mechanical properties of the gel can be tailored through variation of the composition sequence (i.e. M/G ratio), G-unit length, molecular weight, and concentration of the polymer in the resultant gel, as well as with the selection of cross-linking ions. Alginates with a higher ratio of G-units are prone to yield hydrogels with greater mechanical stiffness and strength compared to those with a higher M-unit ratio [56].

Sodium alginate is a widely used alginate form across a wide variety of industries, including production of stabilizers, viscosifiers, and gel-forming, film-forming, or water-binding agents [57]. Moreover, alginate is used as an ingredient in various pharmaceutical preparations for controlled drug delivery [58, 59] and for inhibition of gastric reflux (e.g. Gaviscon) [60]. The scope of its applications also includes wound management in the form of wound dressings [21, 22, 61]; when alginate merges with the wound exudates, ion exchange occurs between the Ca^{2+} of the alginate and the sodium ions (Na^{+}) in the exudates causing the formation of a gel on the surface of the wound [62].

7.2.5 Gelatin

Gelatin is a single-stranded protein obtained from collagen, which is accessible in animal connective tissue, skin, and bones, by hydrolytic degradation [1, 63–65]. It consists mainly of glycine, proline, and 4-hydroxy proline residues. The degree of hydrolytic degradation depends on the pretreatment and is affected by the temperature and pH during pretreatment, as well as by extraction time. In general, two different types of gelatin are synthesized depending on collagen sources and the extraction method, which also contributes to differences in physicochemical features. Acid treatment is especially suitable for less fully cross-linked materials (e.g. porcine skin collagen) and usually requires 10–48 hours.

On the other hand, alkaline treatment is used mainly for more complex collagen (e.g. bovine skin collagen) and is more time-consuming process (requires several weeks) in order to destroy certain chemical cross-links still present in collagen. The gelatin obtained with acid hydrolysis is known as gelatin type A. In contrast, the

one produced with alkaline hydrolysis is referred as gelatin type B. During the basic reaction conditions, the amide groups of asparagines and glutamine are hydrolyzed into carboxyl groups, thus converting many of these residues to aspartate and glutamate [1, 64, 65]. This reaction is characterized with the formation of negative charges along the backbone of gelatin type B at physiological pH, while gelatin type A is positively charged. It has been reported that the isoelectric point of gelatin can affect the biocompatibility. Gelatin type B displays better biocompatibility as compared to type A, probably due to the more rough basic treatment conditions used for its preparation [64].

Beyond its traditional use in food and cosmetic industries, gelatin has exhibited many attractive aspects for applications and improvements in the biomedical field. Among its main advantages are the low cost, abundance, high biocompatibility, biodegradability coupled with low immunogenicity, and cell-adhesive structure. All mentioned benefits make gelatin a desirable candidate to be applied for drug-delivery systems, tissue engineering, as well as for cell-based therapy [65]. Moreover, the gelling properties of gelatin can be altered by chemical cross-linking, which is an appealing approach for many researchers in developing controlled release drug-delivery vehicles [63]. Gelatin films exhibit transparency, flexibility, strength, and oxygen permeability. Since they are also characterized by rapid dissolution in gastric fluids, gelatin is still material of choice for the encapsulation of bioactive substances. Contingent on the types, gelatin can undergo polyion complexation having positive or negative-charge therapeutic agents [63, 65]. Its hydrophilic behavior and good gas barrier features make gelatin a valuable biopolymer material also for designing novel wound dressings. Its high absorptive capacity would prevent fluid accumulation in the wound by absorbing excess water and cell debris [66]. Gelatin also possesses reversible thermally responsive self-assembling properties that can contribute to additional functionalities. Recently, gelatin has been integrated into biosensing and "smart" bioelectronics applications [67].

7.2.6 Polyhydroxyalkanoates (PHA)

Polyhydroxyalkanoates (PHA) are a family of biodegradable and biocompatible polyesters of β-, γ-, δ-, and ε-hydroxy alkanoic acids that are synthesized by different bacteria (e.g. intracellular carbon sources and energy-storing granules). They are distinguished mainly by the location of the hydroxyl group in relation to the carboxyl group. Apart from that, the length of the side-alkyl chain marks them off, substituents in the side chains, and an additional methyl group at carbon atoms between the hydroxyl and the carboxyl groups [68, 69]. Majority of PHAs are synthesized from renewable materials by fermentation. Often the production, in general, is found in combination with a shortage of nitrogen (noncarbonaceous nutrient) [69]. Depending on the nature of carbon source and the metabolic differences in microorganisms, PHAs are separated in three classes: (i) short-chain length PHA (scl-PHA, carbon numbers of monomers ranging from C3 to C5), (ii) medium-chain length PHA (mcl-PHA, C6–C14), and long-chain length (lcl-PHA, >C14) [69, 70]. Of particular interest are functionalized groups in the side chain

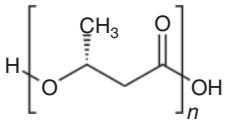

Figure 7.6 Chemical structure of poly(3-hydroxybutyrate) (PHB), the first and most widely spread polyhydroxyalkanoate (PHA).

that allow further chemical modification. Together with the length of the side chain, they influence the properties of the bioplastic (e.g. melting point, glass transition temperature, and crystallinity). Moreover, the average molecular weight and its distribution are dependent on the carbon source [69]. There are presently many commercially important PHAs available including poly(3-hydroxybutyrate) (P3HB) (Figure 7.6), poly(3-hydroxybutyrate-*co*-3-hydroxyvalerate (PHBHV), poly(3-hydroxybutyrate-*co*-4-hydroxybutyrate) (P3HB4HB), and poly(3-hydroxybutyrate-*co*-3-hydroxyhexanoate) (PHBHH*x*), which are obtained from bacterial fermentation [1].

Alteration of PHA monomers in their structures and composition has led to the development of biodegradable and biocompatible polymers with highly specific mechanical features. These are advantageous in numerous biomedical applications, including drug encapsulation, surgical sutures, wound dressings, tissue scaffolds, and various surgical and orthopedic implants. Their processable and biodegradable properties make them the standard choice for drug-delivery systems. In addition, the porosity and tunable properties (formation of films and nanoparticles) allow easy containment of bioactive substances (e.g. drugs, vaccines, steroids, and hormones) [71].

7.2.7 Polylactic Acid (PLA)

Poly(lactic acid) (PLA), also known as polylactide, belongs to the family of aliphatic polyesters, which are usually produced by the polymerization of lactic acid from renewable raw materials such as corn starch, tapioca products, or sugar cane. It is a thermoplastic, high-strength, and high-modulus polymer that is derived from 100% biodegradable and renewable polymer lactic acid (Figure 7.7) [73]. The latter exists as two stereoisomers, L- and D-lactic acid, which can be synthesized biologically

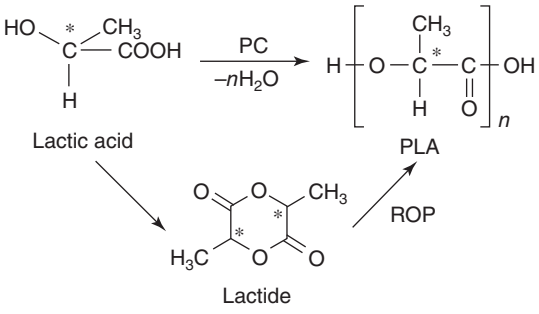

Figure 7.7 Production scheme of poly(lactic) acid (PLA) through polycondensation (PC) and ring-opening polymerization (ROP). Source: Maharana et al. [72]/with permission of Elsevier.

(fermentation of carbohydrates by lactic bacteria) or chemically (ring-opening polymerization with catalysts, ROP, or polycondensation of lactic acid, PC) [1, 72, 73].

Their thermal, mechanical, and biodegradation properties are largely dependent on the chirality of the primary monomer (L- or D-lactic acid), as well as relate to their ratio and distribution within the polymer chains. Polymers with high L-form produce crystalline products, whereas the higher D-isomers (>15%) result in an amorphous product. Similar to other polymers, the qualities of PLA depend on their molecular features and ordered structures, including crystalline thickness, crystallinity, morphology, and degree of chain orientation [1, 72]. The degree of crystallinity is the most important speed-determining factor for the biodegradation of solid polymers. Besides that, biodegradation is also influenced by solid-state morphology and primary chemical structure [72]. In general, the D- and L/D-forms degrade more rapidly than the L-form [72, 74].

PLA has become one of the most popular biopolymers in biomedical applications due to its biodegradability, biocompatibility, good mechanical strength, thermal plasticity, and potential hydrolysis in the human body. It has been used for stents, sutures, dialysis media, and also for controlled-delivery devices, such as microparticles or implants for drugs [1, 75].

7.2.8 Biopolymer Composites

Composites synergistically combine two or more phases (matrix and reinforcing component) in order to produce a new material with novel properties unique to either component alone [65]. The term "biopolymer composites" comprises materials that incorporate one or more component(s) from a biological origin, and in which at least one constituent is bio-based or biodegradable. For true biocomposites, it is desired that the matrix (i.e. primary phase with a continual character), which is polymer, be made predominantly from sustainable resources. The matrix serves as a binder of reinforcing components together, providing mechanical support, as well as directs most of the physical and chemical properties of the composite. Besides, it blends filler particles and allows for shaping products thoroughly. However, additional enhancement of selected material qualities is specified by the reinforcing component. Polymer reinforcements are typically used to improve the mechanical features of resulting biocomposite by giving the stiffness and strength to the polymer matrix. In addition to the implementation of mechanical properties, biopolymers are often blended to reduce the overall degradation time and improve the water and gas barrier properties [1, 12].

The unique combination of favorable properties of different materials has been attributed to their establishment in medical applications. In the field of tissue engineering, they are of great significance because they play a critical role through cell seeding and proliferation, and also the formation of new tissue in 3D [76]. They are also a suitable material for the development of various medical implants (e.g. stents and barrier membrane), drug- and bioactive-agent-delivery systems, and bioelectronics (e.g. biosensors, thin-film transistors, and interfaces) [1, 76, 77].

7.3 Stimuli-Responsive Biopolymer Thin Films

As the name implies, stimuli-responsive materials possess environmentally sensitive modalities within their structures that enable conformational and chemical changes in response to their environment (e.g. temperature, pH, ionic strength, and redox reactions) [27, 78, 79]. These polymers undergo reversible phase transitions involving changes in their solubility and/or in their dynamic and equilibrium swelling properties [78, 80]. The stimuli can be derived from an alteration in polymers' environment, such as temperature, pH, chemical composition, or applied mechanical force, or that can be triggered exogenously through irradiation with light or exposure to an electric and magnetic field. This stimuli-responsive behavior is playing an increasingly important part in the design of "smart" biomaterials for diverse biomedical applications, such as drug-delivery systems, diagnostics, tissue engineering, and biosensors [79]. By modifying molecular structure parameters or external conditions (e.g. pH, temperature, and redox state), the variety of structures and characteristics of stimuli-responsive biopolymers can be finely tuned [27].

7.3.1 pH-Responsive Biopolymers

The human body is a complex biological system, and it is known that pH values differ significantly not only in different tissues or organs (e.g. stomach, liver, and kidney), but also in pathophysiological states such as ischemia, infection, inflammation, and tumor development, mainly due to the different rate of glycolysis in abnormal (i.e. diseased) tissue [81]. Polymers that react to pH changes (i.e. pH-sensitive polymers) are a class of polyelectrolytes with ionizable (e.g. acidic or basic functional) groups in their backbone and side or end groups. Hence, the ionization level of the pendant group alters strongly around the pK_a, resulting in dramatic changes in their conformation. These pH-sensitive conformational changes can be formed in three different ways: (i) dissociation, (ii) destabilization (via collapse or swelling), and in the case of drug delivery, (iii) changes of partition coefficient between the bioactive agent and vehicle [78, 81]. In biomedicine, polysaccharides are an attractive source of polyelectrolytes of natural origin due to their biocompatibility, biodegradability, and similarity to native extracellular matrix (ECM). Natural polyelectrolytes include numerous anionic macromolecules, such as alginate, hyaluronic acid, and others, whereas chitosan, an N-deacetylated derivative of chitin, is the only cationic polysaccharide found in nature [78].

Their importance is related to the potential exploitation of their selective response to environments with variable pH values. For example, the pH value in tumor and inflammatory tissues is known to be acidic, and as such, differs from "healthy" cell compartments. By using layer-by-layer (LbL) films composed of pH-responsive polyelectrolytes, it is possible to create a pH-triggered drug-delivery system, as shown in Figure 7.8 [82].

The mechanism behind such drug-delivery systems relies on the embedment of a drug (or other bioactive substance) into LbL film, which is then released upon alteration in the pH through enhanced permeability of the film or decomposition

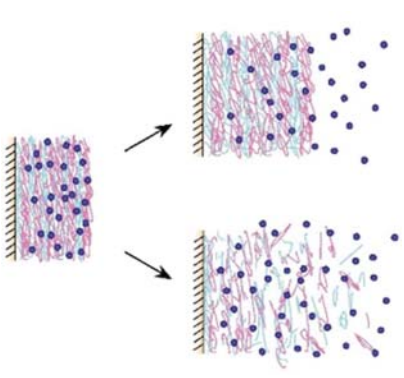

Figure 7.8 Schematic presentation of a designed pH-sensitive thin film for drug-delivery application. Source: Sato et al. [82]/with permission of Elsevier.

of the film entity. The former may lead to an accelerated diffusion of the incorporated (*in situ* entrapped) drug molecules out of the film [82, 83]. An example of such an approach was shown by Jiang and Li, who prepared biocompatible LbL films composed of poly(L-glutamic acid) (PLGA) and poly(L-lysine) (PLL). These films were used for tuning the release of antibiotic drugs, cefazolin and gentamicin [83]. This antibiotic-loaded polypeptide films showed antibacterial properties against *Staphylococcus aureus* (*S. aureus*). Authors claimed that proposed PLGA/PLL films can load both positively and negatively charged drug molecules [83]. Another example represents the approach reported by Feng et al., who constructed pH-responsive drug-delivery nanocarriers combining mesoporous silica nanoparticles (MNSs) and biocompatible polyelectrolyte LbL films composed of an alginate–chitosan mixture [84]. Both used naturally occurring polysaccharides act as pH-sensitive gatekeepers and a biocompatible shell layer. Under specific pH conditions, the negatively charged carboxylate acid groups of the alginate can form ionic bonds with the positively charged amino groups of the chitosan to produce a pH-sensitive polyelectrolyte complex [84–86]. As a proof of concept, the anticancer drug doxorubicin (DOX) was loaded into such nanocarriers, and the authors evaluated the pH-responsive *in vitro* and *in vivo* drug release. The DOX release rate was much faster in an acidic environment than under neutral and basic conditions. At lower pH values, the amino groups on chitosan become progressively ionized, leading to increased electrostatic repulsion between the DOX molecules and the ionized amino groups that may cause a rapid drug release. At the same time, the carboxylated groups on alginate become less negatively charged, which would contribute to the reduction of the electrostatic attraction between alginate and DOX and results in increased DOX release [84].

Polyelectrolytic hydrogels that are pH-sensitive are known for their ability to undergo dramatic changes that influence their volume, elasticity, and mass by slightly altering the pH of the system [87]. In the form of thin films (2D) can be used not only as drug-delivery systems but also for the development of sensors [78, 87]. Owing to their polyelectrolyte character, these hydrogels can be applied for entrapping bioactive molecules, such as enzymes and antibodies. An elegant (and also most prominent) example is the immobilization of the enzyme glucose oxidase (GO_x) [78, 88]. In the presence of glucose that diffuses into the hydrogel,

GO_x catalyzes the glucose to gluconic acid, lowering the local pH, which in turn promotes the swelling of the hydrogel that leads to volume phase transition [88]. This concept was used for designing an insulin-releasing system in response to glucose concentration [89]. The system consisted of poly(acrylic acid)-grafted porous cellulose film with immobilized GO_x; the oxidation of glucose decreases the pH in pores region, resulting in a collapse of the pH-responsive polymer. Consequently, that leads to the opening of the pores and the release of insulin [89].

7.3.2 Thermo-Sensitive Biopolymers

The temperature may act as both an external and internal (e.g. elevation of body temperature during fever) stimuli. Thermo-sensitive polymers, especially hydrogels, are the most frequently investigated class of stimuli-responsive polymeric systems [90]. This mechanism exploits a critical solution temperature at which the phase of the polymer (and hence of the solution) is changed based according to its composition [91]. Based on the origin of their thermo-sensitivity they can be classified into two groups, a lower critical solution temperature (LCST) and an upper critical solution temperature (UCST), which are temperatures below and above the phase separation of the polymeric solution. In other words, at temperatures below LCST, the system is completely miscible in all ratios; otherwise, partial liquid miscibility occurs [90, 91]. Polymers with LCST are generally more relevant for biomedical applications. They are most widely used in drug-delivery systems [90, 91] and for applications related to cell-based biochips [92]. Most of the thermo-responsive polymer systems are synthetic such as widely used poly(*N*-isopropyl acrylamide), PNIPAAm, that exhibits a LCST close to body temperature [91]. As an alternative, biomimetic approaches have been used to synthesize polypeptides, inspired by mammalian protein elastin, that possess similar thermo-responsive properties as PNIPAAm [78]. Recombinant methods have been employed to synthesize elastin-like polypeptides (ELPs), protein-based biopolymers that show thermal inverse-phase transitional behavior in response to temperature changes. They are water soluble at room temperature but precipitate above their LCST (e.g. around 40 °C) due to aggregation caused by hydrophobic interactions. Besides rapid temperature response, the ELPs have been excelling at two features: (i) reversible control of cell adhesion and (ii) nontoxic character (Figure 7.9) [78, 92].

The ability to tune the temperature behavior of ELPs, coupled with non-toxicity, has opened doors for the establishment of these materials in various medical applications, e.g. in drug- and gene-delivery systems, "smart" surface platforms for the development of bioelectronics, and in tissue engineering [92–94].

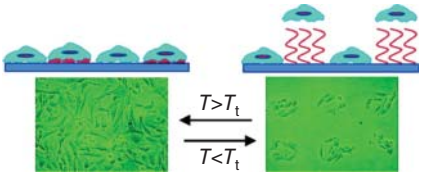

Figure 7.9 Reversibly controlled cell attachment and detachment on the thermo-responsive elastin-like polypeptide (ELP) surface. Source: Na et al. [92]/with permission of American Chemical Society.

7.3.3 Redox-Sensitive Biopolymers

Oxidative processes enable simple modification of material's behavior. Oxidants are extremely common in biological systems, and they are generally associated with inflammatory events, where reactive oxygen species (ROS) and reactive nitrogen species (RNS) can play as signaling and toxic molecules [95, 96]. Redox-sensitive biopolymers have been recognized as a fascinating class of biomedical materials for the development of sophisticated drug- and gene-delivery systems [95–97]. These materials usually contain disulfide bond(s) in the main chain, at the side chain, or in the cross-linker, which may be prone to rapid cleavage under a reductive environment via thiol–disulfide exchange reactions [97]. Thiol–disulfide reactions, which are rapid and readily reversible, are pivotal in maintaining proper biological functions of living cells, such as stabilization of protein structures, enzymatic activity, and redox cycle. Disulfide groups are frequently incorporated to provide responsiveness to conditions characteristics of the intracellular environment. Small variations in redox potential specify this environmental responsiveness, but it is remarkably affected by entropy. As a result, such materials will swell/dissolve, or alternatively shrink/harden [95].

For designing redox-sensitive drug-delivery systems in tumor tissues, one of the common strategies is the reduction of the disulfide by glutathione (GSH), specifically in tumor cells. The reason behind this approach is that the cancer environment displays a more reductive potential compared to healthy tissue due to lower oxygen partial pressure. The correlated shift in redox potential is associated with higher concentrations of reduced GSH [98]. Higher concentrations of GSH are also found in the intracellular compartments that are present in reduced form, compared to extracellular compartments, which are in the oxidized form [99, 100]. In organisms, GSH is involved in more than one physiological function. Besides acting as an antioxidant agent, it is also known as a reducing agent, especially for the disulfide bond. Proteins connected by a disulfide bond or to the protein, which has an intramolecular disulfide linkage(s), receive electrons from the GSH, resulting in oxidation of the GSH to glutathione disulfide [98]. Durney et al. [101] have described a proof-of-concept method to fabricate functional chitosan-based hydrogel thin film. The authors claimed that the proposed approach could easily confer stimuli-responsiveness to chitosan films, which have been demonstrated through a degradation response of synthesized film upon exposure to glutathione or free amino acids. Such properties expand the scope of potential utilization in biosensors and actuators [101].

7.4 Biomedical Applications of Biopolymers

7.4.1 Drug-Delivery Systems

Instead of developing new drugs or bioactive compounds (which involve additional costs), many pharmaceutical companies are keen to improve current controlled-delivery technologies. Since they are usually biocompatible and easy to

Table 7.1 Examples of biopolymers commonly used in controlled-delivery systems.

Biopolymer	Properties
Collagen and gelatin	• Very good film-forming ability • Utilized for preparation of sterile films, ophthalmic films, and sterile sponges
Chitin and chitosan	• Superior film-forming ability • Chitosan facilitates the transport of polar drugs across epithelial surfaces • Cell-binding activity; cationic polyelectrolyte structure enables binding to the negative charge to the cell surface
Alginate	• Immobilization matrices for cells and enzymes, controlled release of bioactive molecules • Excellent film-forming ability • Compatible with most water-soluble thickeners and resins
Cellulose derivates (hydroxypropyl methyl cellulose, carboxymethyl cellulose, hydroxypropyl cellulose)	• Improved the residence time of alginate films • Good compatibility with starch forming single-phase polymeric matrix film with improved mechanical and barrier properties • Used for controlled and/or delayed release of drug substances

adapt, biopolymers are the first choice for developing controlled release matrices (e.g. see Table 7.1).

In addition, compared with the traditional dosage forms, thin films have been identified as versatile alternative platforms for drug-delivery systems [102, 103]. Designing an ideal release mechanism for controlled drug and/or bioactive compounds remains the weakest link in developing such systems [104]. However, with careful design of the thin-film formulation and with the phenomenon of "smart" (i.e. stimuli-responsive) polymer materials, some advances have been made in this direction [103–105]. Thin-film formulations are useful in several aspects, including convenient administration through noninvasive routes, ease of manufacturing process, and cost-effectiveness in the development of formulations. So far, polymer films/coatings were applied mainly as tools to ameliorate biocompatibility of the underlying matrices with controlled release capability. Recently, a novel strategy of surface-mediated drug delivery has emerged, in which polymer thin film plays double role, (i) as a coating to modulate surface properties for cellular adhesion and proliferation and (ii) as a reservoir for an active therapeutic molecule [103, 105]. Polymers represent the backbone of film formulations, and they can be used alone or in composite to achieve the desired film properties. Accessibility of various polymers allows tailoring specific properties in the films [103, 106]. The kinetics of drug release from polymer vehicles depends primarily on the material used,

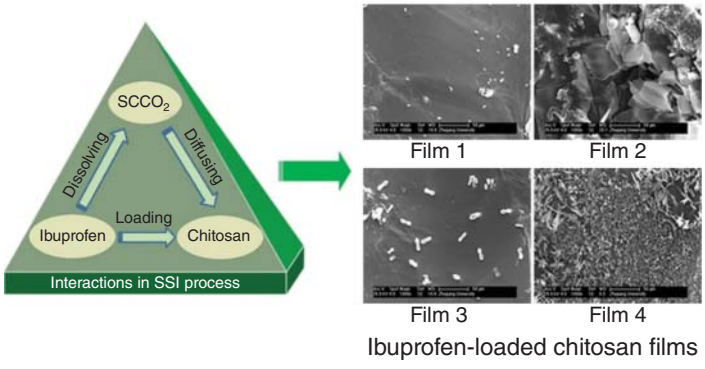

Figure 7.10 Ibuprofen-loaded chitosan film for potential oral mucosal drug-delivery system. Source: Tang et al. [107]/with permission of Elsevier.

especially its swelling properties, and the morphology of the designed system. Release mechanisms (chemical or physical) always involve diffusion. The latter is primarily reliant on the physicochemical features of used materials as well as the solvent–polymer interaction [102, 103]. For degradable drug-delivery systems, controlled release is imposed by the cleavage of the polymer bonds, regardless of the diffusion rate of the liberated therapeutic molecule [102]. The anatomical and physiological characteristics of different tissue and organs differ; thus, routes for the administration and the target sites have an important part in the development of controlled-release drug systems. Alterations in pH or temperature may cause an increase or decrease in the erosion and dissolution rates of biopolymers (such stimuli-responsiveness is described in previous section). Briefly, upon a contact with biological fluids, the polymeric films start to swell following polymer chain relaxation and consequently drug diffusion. The release of drug is directly correlated with the polymer structure; namely, the linear amorphous polymers dissolve much faster compared to cross-linked or partially crystalline polymers [102]. Tang et al. [107] have demonstrated ibuprofen-loaded chitosan films suitable for oral mucosal drug delivery (Figure 7.10), which were characterized with high water uptake and antibacterial effects. The *ex vivo* release study revealed that proposed formulations could deliver ibuprofen across the rabbit buccal mucosa in a sustained and controlled route.

While several applications of loading low-weight-molecular drugs into biopolymer thin films are often successful in their own right, some researchers believe that the success of these undertakings is case-specific limited. In such systems, it can be increasingly challenging to engineer specific release profiles, especially in terms of codelivery of multiple drugs [105].

7.4.2 Wound-Healing Materials

As mentioned several times throughout the chapter, biopolymers possess various beneficial properties, including the ability to absorb large quantities of water when

Table 7.2 Commonly used biopolymers and their biological role in wound healing.

Biopolymer	Biological role
Collagen	• Induces fibroblasts proliferation • Induces secretion of ECM components by fibroblasts • Reduces tissue contraction and scarring
Chitosan	• Induces fibroblasts and keratinocytes proliferation and migration • Antifungal, antibacterial, hemostatic, and muco-adhesive properties
Alginate	• Induces fibroblasts proliferation and migration • Stimulates monocytes • Absorbs wound exudate and maintains moist microenvironment
Cellulose	• Retention of moisture, absorption of exudates • Acidic cellulose promotes healing properties in cutaneous wounds

in the dry state and donate water when they are hydrated [108]. The latter is an ideal feature also for skin-related applications (e.g. wound treatment) since it enables the absorption of excess water and cell debris from the wound and, at the same time, keeping the moist environment, and hence, promoting the healing process [22, 109]. Moreover, in combination with an analgesic treatment, biopolymer thin films also represent an excellent platform for functional wound dressings, where a controlled and targeted delivery of pain-relieving analgesic drugs is a prerequisite [21–23, 61, 110]. Biopolymers that are widely used as wound dressing materials mainly fall into categories of polysaccharides and proteins (e.g. see Table 7.2). These biomaterials are also attractive candidates for so-called bioactive wound-healing dressings that play an active part in the wound-healing process. They have the advantage of forming part of the native tissue matrix (e.g. collagen), which are biodegradable, and some of them are actively involved in new tissue formation [109].

The dominant position as a wound-healing biomaterial among polysaccharides has alginate, which is the first choice for moderate-to-heavily exuding wounds [109]. The primary reason for its use lies in its potential to absorb 15–20 times its weight of wound fluid, which is beneficial to maintain wound exudate [111]. In addition, alginate-based wound dressings can easily be removed from the site of application, avoiding the wound reopening [109]. This is related to the swelling mechanism of calcium alginate. On contact with the wound exudate, it comes to an exchange between sodium ions (Na^+) in exudate and Ca^{2+} in the alginate, allowing the alginate to solubilize. After this ion-exchange process, the tightly bound Ca^{2+} in alginate dressing is replaced with loosely bound Na^+ that results in swollen hydrated alginate dressing [108]. Since they require moisture for functional efficacy, they are not suitable for dry wounds and those covered with hard necrotic tissue [109].

Collagen is one of the key components in the natural wound-healing process from the induction of clotting to the formation and an outward of scarred tissue [112, 113].

Collagen films have been widely used in wound treatment primarily as a barrier. Collagen-based wound dressings have a long history in the management of burn wounds and the treatment of ulcers. A combination of collagen with alginate has shown positive effects in promoting the inflammatory phase of wound healing while imparting mechanical strength, which is a feature of collagen fibrils. Collagen dressings that have attached a semi-occlusive polymer film to its outer surface are bacterial resistant as well as to further mechanical trauma, and they provide proper air and vapor permeability. As such, they reduce contraction and scarring with an increased epithelialization rate, making them the material of choice for burn care [113].

Chitosan is another natural material with a high potential in wound treatment. It is of particular interest for burn healing, due to its beneficial intrinsic properties, including hemostatic, bacteriostatic, and fungostatic activity, as well as wound-healing acceleration properties [62, 114, 115]. It stimulates cell proliferation and histoarchitectural tissue organization. As hemostat, it aids in natural blood clotting and blocks nerve endings, reducing pain. During gradual depolymerization of chitosan, released *N*-acetyl-*b*-D-glucosamine initiates fibroblast proliferation, assists in ordered collagen deposition, and stimulates the increased level of natural hyaluronic acid synthesis at the wound sites [62].

7.4.3 Bioactive Coatings for Medical Devices and Implants

Biofouling (i.e. fouling due to proteins, bacteria, etc.) is of great concern in various applications ranging from food packaging to industrial and marine equipment, and from biosensors to biomedical implants and devices. The latter are susceptible to biological erosion, bacterial colonization, and biofilm formation, which can lead to the inflammatory responses in the host. To some degree, all biomaterials interact with the surrounding tissue, and these biomaterial–tissue interactions, including both the effects of the biomaterial on host tissue and the effects of the host on the biomaterial, represent a substantial challenge associated with medical devices and implants [116]. The nature of the biofouling layer is mainly dependent on the surface of the biosensor or medical implant and the wound-healing state of the surrounding tissue [117]. Protein fouling on biological implants reduces the device's efficacy and may also result in harmful side effects, such as thrombosis. Furthermore, the subsequent formation of the protein layer on the surface of biological implants creates a culturing condition for microbial colonization, followed with biofilm formation that can lead to life-threatening infections [118, 119]. The solution to most of the undesirable effects (e.g. biomaterial-mediated inflammatory and biofouling events) lies in surface modification of the tissue–biomaterial interface. The two major strategies to prevent surface fouling are based on (i) preventing biofouling molecules from attaching or (ii) degrading them [116–118]. While protein-resistant coatings/films may also hinder bacterial attachment and subsequent biofilm formation, in order to overcome the fouling-mediated risk of bacterial infection, it is highly preferable to design coating also with bactericidal properties.

Although the immobilization of poly(ethylene glycol) (PEG) is one of the most typically used strategies to impart protein resistance to a surface, polysaccharides

(e.g. cellulose, chitosan, CMC) are also regarded as promising materials for creating antifouling surfaces [118, 119]. Mohan et al. [119] have developed functional coating based on CMC, chitosan, and partially deacetylated CA that exhibited antifouling behavior. In the field of biosensors, cellulose and its derivatives are commonly used for reducing biofouling on biosensors. Conversion of hydroxyl groups of cellulose into acetates or amines significantly decreases complement activation [117]. Ammon et al. [120] found that cellulose-based coating enables prolonged functional longevity of biosensor in undiluted blood.

Within the clinical environment, bacterial colonization and associated biofilm formation is one of the main causes of chronic infections. In general, approaches to eliminate microbial biofouling are to (i) attach biocidal nanomaterials, such as silver, copper, selenium, and titanium dioxide on the surface or (ii) incorporate commercial antibacterial agents that are concurrently released from polymer medical devices. However, the ever-growing widespread resistance of microbes toward antimicrobials emphasizes the development of "green" (i.e. biopolymer-based) strategies that mitigate the initial attachment of microbes [121]. In this regard, plant derivatives are ideal candidates due to the polydispersity of essential oils, known for their antimicrobial properties, without triggering bacterial resistance [122, 123]. Because of their intrinsic antimicrobial properties and applicability to a plethora of biomedical applications, bioactive chitosan films featuring naturally derived essential oils are emerging candidates for decreasing bacterial contamination on medical devices and implants. These natural plant and polysaccharide-based films can be used, among others, as a bioactive coating on indwelling medical devices [122, 124].

7.4.4 Bioelectronics (Biocomposites)

Over the past few years, growing demand for economical and reliable medical diagnostic and environmental surveillance has facilitated progress in fabrication, a surfeit of organic bioelectronics that allows the estimation of analytes through biochemical pathways. The idiom "bioelectronics" pinpoints to the integration of biomolecules within electronic elements to yield functional devices that recognize and interact with the analyte. These interactions produce a biological signal, which, with the aid of a transducer element, is converted into an electronic signal. This type of recognition represents one of the most advanced applications implemented in the field of biosensor technology since the introduction of bioelectronics [77, 125, 126]. The latter can be in general directed toward (i) identifying or producing a variety of bioreceptors with ameliorated sensitivity and selectivity by adapting various molecular biology approaches as well as (ii) designing new materials, which can maintain the activity of the biorecognition element and efficiently exploit the biological signal, by employing strategies from material science. Despite the progress, the most important issue in the biotechnological engineering of biosensors and implantable devices still represents the interface between living tissues and artificial human-made implantable devices. To overcome this limitation, biopolymers

present highly promising and versatile input materials due to their natural origin and their favorable interaction with living systems [125, 126].

Biosensors present analytical devices that use a biological recognition element (biochemical receptor) in order to obtain specific quantitative or semi-quantitative information, without additional separation or processing steps. In this configuration, the biochemical receptor provides specificity, whereas the transducer acts as a converter of a biological signal into a quantifiable electronic signal. The term "biosensor" is often misleading to refer to a device that measures biological molecules; the prefix "bio-" alludes to the incorporated biochemical receptor [127]. Electrochemical biosensors offer the advantages of low detection limit, specificity, simplicity of construction, and ease of operation, which make them the most extensively investigated biosensoric devices. Moreover, with the ability of miniaturization, these biosensors can be designed as lab-on-chip devices for *in vivo* monitoring. The efficient utilization of the interaction between the biorecognition unit and the analyte is the pivotal factor in biosensor development, which can be achieved through successful immobilization or attachment of a biochemical receptor to the sensor interface. Therefore, the immobilization matrix should satisfy many of the prerequisites, such as (i) protecting biochemical receptors from extreme conditions, (ii) enabling easy diffusion of the analyte to the bioreceptor, and (iii) preventing leaching of the latter out of the matrix. Aside as a platform for entrapping bioreceptor (e.g. enzyme, antibody, and whole-cell), biopolymers also provide good adhesion of as-prepared composite on electrode surface for performing electroanalytical measurements. In general, they have high permeability toward the water, enabling efficient diffusion of electrolytes across the biosensor surface. Despite that biopolymers are characterized by several beneficial properties, there are certain drawbacks, such as low mechanical strength and chemical resistance, which limit their application in biosensors development. Many of these restraints can be overcome by combining biopolymers with functional materials such as carbon-based materials, metal nanoparticles, silica, metal oxides, and conductive polymers [125].

The recent discovery of cellulose as a "smart" material paved the way to the use of cellulose as a potential candidate for biosensor fabrication. Incorporating the metal oxide into a cellulose matrix remarkably enhanced the sensor characteristics such as chemical stability, electrical conductivity, and photosensitivity [128]. Mahadeva and Kim [129] employed cellulose–tin oxide (SnO_2) hybrid nanocomposite film to design an inexpensive, flexible, and disposable glucose biosensor. Enzyme GO_x, used as a biochemical receptor, was immobilized to the cellulose–SnO_2 hybrid nanocomposite through covalent bonding between enzyme and SnO_2. The authors observed a linear correlation between GO_x activity and glucose concentration, which cover the clinically relevant values (0.5–12 mM).

Owing to its conductive ability, chitosan gained great recognition as a functional material for biosensor construction. On account of abundant amino groups, which have a strong affinity to proteins [51, 130], as well as a good film-forming ability and capacity to sustain its natural features, it is widely used as an enzyme immobilization matrix [51, 130–133]. It has been demonstrated that this biopolymer can serve

as an effective dispersant of carbon nanotubes (CNTs). For example, CNTs–chitosan (CNTs-CS) biocomposites present more attractive components as a host immobilization matrix for the biosensor fabrication [134–136]. Moreover, CNTs–CS films enable a reliable determination of nicotinamide adenine dinucleotide (NADH), which is a reduced form of the nicotinamide adenine dinucleotide (NAD+), a cofactor for a large number of dehydrogenase enzymes (>300). In such a system, CNTs provide signal transduction based on the electrooxidation of dehydrogenase cofactor NADH, while chitosan acts as a biocompatible and chemically modifiable platform for enzyme immobilization. Hence, as-prepared biocomposites have the potential to provide operational access to a large group of dehydrogenase enzymes, which encompass hundreds of members, for designing a plethora of bioelectrochemical devices [134]. Chitosan-based sensors satisfy all the key points of a reliable sensor, such as repeatability, sensitivity, recovery, and fast response [1, 133]. The most challenging task in the fabrication of a biosensor is an efficient immobilization of the bioactive molecules (e.g. enzyme and antibody) while retaining their bioactivity. Therefore, thorough research activities are being continuously pursued in the direction of developing new matrices to enhance the direct electrons transfer between the entrapped enzyme and the electrode surface. To achieve a good microenvironment for loading of enzymes and to obtain rapid electron transfer rates between the active centers of enzymes and electrons, biocomposites of chitosan and conductive polymers (e.g. polypyrrole, polyaniline, and polyacetylene) are becoming the most promising matrices for biosensing applications [130, 132, 133]. Conducting polymers, also known as "synthetic metals," have been widely used in the area of bioanalytical science due to their inherent charge properties and biocompatibility. By regulating the growth of such a polymeric matrix, various

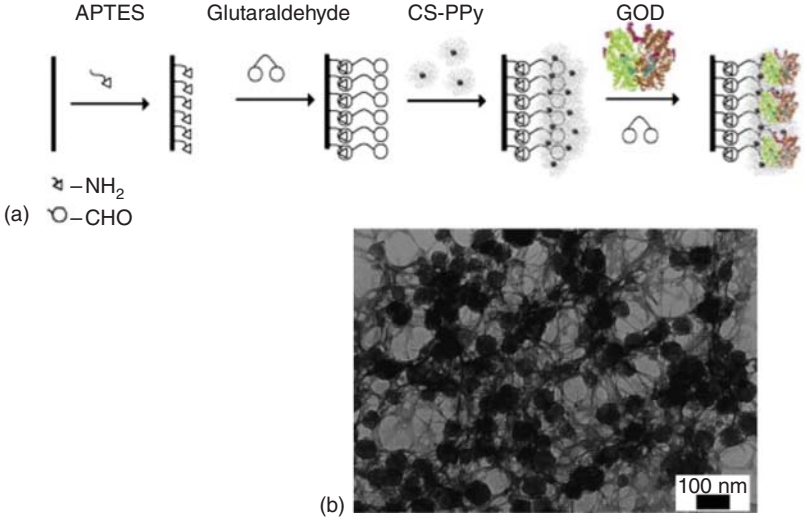

Figure 7.11 The process of fabrication of (a) an electrochemical glucose biosensor based on CS-PPy thin film, immobilized with GO_x, and (b) TEM image of the CS-PPy nanocomposites thin film. Source: Fang et al. [130]/with permission of Elsevier.

requirements can be fulfilled, including polymer layer thickness, electrical properties, and biomolecules loading. However, the poor processability of conducting polymers continues to persist as the main obstacle to their practical application, as well as present an important factor related to their potential irreproducibility. In order to overcome these limitations, conductive polymers are usually blended with chitosan [130, 132, 133, 137]. A glucose biosensor that was assembled by immobilizing GO_x on the surface of chitosan–polypyrrole (CS-PPy) nanocomposites film (Figure 7.11), offers along with rapid response and low detection limit for the glucose concentration, also improved reproducibility and the stability as a consequence of the high biocompatibility of this designed CS-PPy film [130].

7.5 Conclusions

In the past decades, clinical understanding advancements have directed notable utilization of natural materials in clinical settings. In addition to their known biocompatibility and biodegradability, naturally occurring polysaccharides and proteins allow for maximum mimicry by recapitulating the biological and physicochemical characteristics of the ECM and the existing cell recognition domains and biomolecule-binding sites. Furthermore, some of them even have inherent antibacterial and anti-inflammatory properties. The multifunctional behavior and adaptability of biopolymers to different physical states accelerate their use for a wide range of pharmaceutical and biomedical applications, from wound dressing matrices to "smart" coatings in drug-delivery systems and biosensors. Moreover, the wide variety of selection coupled with the ability to fuse biopolymers or with synthetic polymers and/or metallic compounds extends an array of strategies that can be adapted for specific functionality. The physiological compatibility and the capability to load and control release of bioactive molecules under external stimuli (e.g. pH, temperature, and redox species) have contributed to revolutionizing development not only of drug-delivery systems and wound treatment, but also the fabrication of medical implants.

Better insight into the understanding of the physical, chemical, and mechanical properties of biopolymers and biopolymers-based thin films opens new frontiers to efficiently use their advantages to make them an essential component in the desired application. With the successful mixing of biopolymers and other materials leading to the synthesis of novel functional materials that allow biocompatibility, scientific and technological society is faced with an embarrassment of richness. The future advance of biopolymer-based biomedical applications, particularly bioanalytical devices (e.g. biosensors), is driven by convergence of improvement in biopolymer-based material science and the technological progress in designing various configurations for development of controlled drug-delivery system, functional wound dressing, and (minimally or noninvasive) biosensors. Everlasting investigations on biopolymers provide new capabilities to scientists and technologists in pursuing the aim, namely creating new formulation and medical devices that will ease health care.

Acknowledgment

This research was funded by Slovenian Research Agency for Research (grant numbers: P3-0036, J3-1762, and J1-9169) and Ministry for Education, Science and Sport (grant number: C3330-19-952027).

References

1 Abhilash, M. and Thomas, D. (2017). Biopolymers for biocomposites and chemical sensor applications. In: *Biopolymer Composites in Electronics* (ed. K.K. Sadasivuni, D. Ponnamma, J. Kim, et al.), 405–435. Elsevier.
2 Nambiar, S. and Yeow, J.T. (2011). Conductive polymer-based sensors for biomedical applications. *Biosens. Bioelectron.* 26 (5): 1825–1832.
3 Vendra, V.K., Wu, L., and Krishnan, S. (2010). *Polymer Thin Films for Biomedical Applications*. Weinheim: Wiley-VCH.
4 Muskovich, M. and Bettinger, C.J. (2012). Biomaterials-based electronics: polymers and interfaces for biology and medicine. *Adv. Healthc. Mater.* 1 (3): 248–266.
5 Prokop, A. (2001). Bioartificial organs in the twenty-first century: nanobiological devices. *Ann. N. Y. Acad. Sci.* 944: 472–490.
6 Kipshidze, N.N., Tsapenko, M.V., Leon, M.B. et al. (2005). Update on drug-eluting coronary stents. *Expert Rev. Cardiovasc. Ther.* 3 (5): 953–968.
7 McGarraugh, G. (2009). The chemistry of commercial continuous glucose monitors. *Diabetes Technol. Ther.* 11 (Suppl. 1): S17–S24.
8 Liu, Z., Cho, B., Ouyang, T., and Feldman, B. (2012). Miniature amperometric self-powered continuous glucose sensor with linear response. *Anal. Chem.* 84 (7): 3403–3409.
9 Klonoff, D.C., Ahn, D., and Drincic, A. (2017). Continuous glucose monitoring: a review of the technology and clinical use. *Diabetes Res. Clin. Pract.* 133: 178–192.
10 Morais, J.M., Papadimitrakopoulos, F., and Burgess, D.J. (2010). Biomaterials/tissue interactions: possible solutions to overcome foreign body response. *AAPS J.* 12 (2): 188–196.
11 Rebelo, R., Fernandes, M., and Fangueiro, R. (2017). Biopolymers in medical implants: a brief review. *Procedia Eng.* 200: 236–243.
12 Niaounakis, M. (2014). *Biopolymers: Processing and Products*. William Andrew.
13 Mohan, S., Oluwafemi, O.S., Kalarikkal, N. et al. (2016). Biopolymers–application in nanoscience and nanotechnology. In: *Recent Advances in Biopolymers* (ed. F.K. Perveen), 47. IntechOpen Limited.
14 Anderson, J.M. (2001). Biological responses to materials. *Annu. Rev. Mater. Res.* 31 (1): 81–110.
15 Fournier, E., Passirani, C., Montero-Menei, C.N., and Benoit, J.P. (2003). Biocompatibility of implantable synthetic polymeric drug carriers: focus on brain biocompatibility. *Biomaterials* 24 (19): 3311–3331.

16 Ratner, B.D., Hoffman, A.S., Schoen, F.J., and Lemons, J.E. (2004). *Biomaterials Science: An Introduction to Materials in Medicine*. Elsevier.

17 Jonas, R. and Farah, L.F. (1998). Production and application of microbial cellulose. *Polym. Degrad. Stab.* 59 (1): 101–106.

18 Klemm, D., Heublein, B., Fink, H.P., and Bohn, A. (2005). Cellulose: fascinating biopolymer and sustainable raw material. *Angew. Chem. Int. Ed.* 44 (22): 3358–3393.

19 Czaja, W., Krystynowicz, A., Bielecki, S., and Brown, R.M. Jr., (2006). Microbial cellulose--the natural power to heal wounds. *Biomaterials* 27 (2): 145–151.

20 Yoshinaga, F., Tonouchi, N., and Watanabe, K. (1997). Research progress in production of bacterial cellulose by aeration and agitation culture and its application as a new industrial material. *Biosci. Biotechnol. Biochem.* 61 (2): 219–224.

21 Maver, T., Hribernik, S., Mohan, T. et al. (2015). Functional wound dressing materials with highly tunable drug release properties. *RSC Adv.* 5 (95): 77873–77884.

22 Maver, T., Gradisnik, L., Kurecic, M. et al. (2017). Layering of different materials to achieve optimal conditions for treatment of painful wounds. *Int. J. Pharm.* 529 (1–2): 576–588.

23 Maver, T., Mohan, T., Gradisnik, L. et al. (2019). Polysaccharide thin solid films for analgesic drug delivery and growth of human skin cells. *Front. Chem.* 7: 217.

24 Walker, M., Hobot, J., Newman, G., and Bowler, P. (2003). Scanning electron microscopic examination of bacterial immobilisation in a carboxymethyl cellulose (AQUACEL®) and alginate dressings. *Biomaterials* 24 (5): 883–890.

25 Picheth, G.F., Pirich, C.L., Sierakowski, M.R. et al. (2017). Bacterial cellulose in biomedical applications: a review. *Int. J. Biol. Macromol.* 104: 97–106.

26 Habibi, Y., Lucia, L.A., and Rojas, O.J. (2010). Cellulose nanocrystals: chemistry, self-assembly, and applications. *Chem. Rev.* 110 (6): 3479–3500.

27 Yang, J. and Li, J. (2018). Self-assembled cellulose materials for biomedicine: a review. *Carbohydr. Polym.* 181: 264–274.

28 Kamel, S., Ali, N., Jahangir, K. et al. (2008). Pharmaceutical significance of cellulose: a review. *Express Polym. Lett.* 2 (11): 758–778.

29 Shukla, R.K. and Tiwari, A. (2011). Carbohydrate molecules: an expanding horizon in drug delivery and biomedicine. *Crit. Rev. Ther. Drug Carrier Syst.* 28 (3): 255–292.

30 Isaad, J., El Achari, A., and Malek, F. (2013). Bio-polymer starch thin film sensors for low concentration detection of cyanide anions in water. *Dyes Pigm.* 97 (1): 134–140.

31 Avella, M., De Vlieger, J.J., Errico, M.E. et al. (2005). Biodegradable starch/clay nanocomposite films for food packaging applications. *Food Chem.* 93 (3): 467–474.

32 Krogars, K., Heinamaki, J., Karjalainen, M. et al. (2003). Enhanced stability of rubbery amylose-rich maize starch films plasticized with a combination of sorbitol and glycerol. *Int. J. Pharm.* 251 (1–2): 205–208.

33 Lourdin, D., Coignard, L., Bizot, H., and Colonna, P. (1997). Influence of equilibrium relative humidity and plasticizer concentration on the water content and glass transition of starch materials. *Polymer* 38 (21): 5401–5406.

34 Krogars, K., Heinamaki, J., Karjalainen, M. et al. (2003). Development and characterization of aqueous amylose-rich maize starch dispersion for film formation. *Eur. J. Pharm. Biopharm.* 56 (2): 215–221.

35 Sothornvit, R. and Krochta, J.M. (2001). Plasticizer effect on mechanical properties of β-lactoglobulin films. *J. Food Eng.* 50 (3): 149–155.

36 Geresh, S., Gdalevsky, G.Y., Gilboa, I. et al. (2004). Bioadhesive grafted starch copolymers as platforms for peroral drug delivery: a study of theophylline release. *J. Control. Release* 94 (2–3): 391–399.

37 Van Soest, J., De Wit, D., and Vliegenthart, J. (1996). Mechanical properties of thermoplastic waxy maize starch. *J. Appl. Polym. Sci.* 61 (11): 1927–1937.

38 Sonia, T.A. and Sharma, C.P. (2012). An overview of natural polymers for oral insulin delivery. *Drug Discov. Today* 17 (13–14): 784–792.

39 Jain, A.K., Khar, R.K., Ahmed, F.J., and Diwan, P.V. (2008). Effective insulin delivery using starch nanoparticles as a potential trans-nasal mucoadhesive carrier. *Eur. J. Pharm. Biopharm.* 69 (2): 426–435.

40 Kumar, M.R. (1999). Chitin and chitosan fibres: a review. *Bull. Mater. Sci.* 22 (5): 905.

41 Salehi, E., Daraei, P., and Shamsabadi, A. (2016). A review on chitosan-based adsorptive membranes. *Carbohydr. Polym.* 152: 419–432.

42 Guibal, E. (2004). Interactions of metal ions with chitosan-based sorbents: a review. *Sep. Purif. Technol.* 38 (1): 43–74.

43 Finsgar, M., Uzunalic, A.P., Stergar, J. et al. (2016). Novel chitosan/diclofenac coatings on medical grade stainless steel for hip replacement applications. *Sci. Rep.* 6: 26653.

44 Rafique, A., Mahmood Zia, K., Zuber, M. et al. (2016). Chitosan functionalized poly(vinyl alcohol) for prospects biomedical and industrial applications: a review. *Int. J. Biol. Macromol.* 87: 141–154.

45 Huang, X., Sun, Y., Nie, J. et al. (2015). Using absorbable chitosan hemostatic sponges as a promising surgical dressing. *Int. J. Biol. Macromol.* 75: 322–329.

46 Suginta, W., Khunkaewla, P., and Schulte, A. (2013). Electrochemical biosensor applications of polysaccharides chitin and chitosan. *Chem. Rev.* 113 (7): 5458–5479.

47 Nunthanid, J., Laungtana-Anan, M., Sriamornsak, P. et al. (2004). Characterization of chitosan acetate as a binder for sustained release tablets. *J. Control. Release* 99 (1): 15–26.

48 Gupta, K.C. and Ravi Kumar, M.N. (2000). Drug release behavior of beads and microgranules of chitosan. *Biomaterials* 21 (11): 1115–1119.

49 Kofuji, K., Ito, T., Murata, Y., and Kawashima, S. (2000). The controlled release of a drug from biodegradable chitosan gel beads. *Chem. Pharm. Bull. (Tokyo)* 48 (4): 579–581.

50 Kojima, H., Nakatsubo, N., Kikuchi, K. et al. (1998). Detection and imaging of nitric oxide with novel fluorescent indicators: diaminofluoresceins. *Anal. Chem.* 70 (13): 2446–2453.

51 Teepoo, S., Dawan, P., and Barnthip, N. (2017). Electrospun chitosan-gelatin biopolymer composite nanofibers for horseradish peroxidase immobilization in a hydrogen peroxide biosensor. *Biosensors (Basel)* 7 (4): 47.

52 Usov, A.I. (1999). Alginic acids and alginates: analytical methods used for their estimation and characterisation of composition and primary structure. *Russ. Chem. Rev.* 68 (11): 957–966.

53 Remminghorst, U. and Rehm, B.H.A. (2006). Bacterial alginates: from biosynthesis to applications. *Biotechnol. Lett.* 28: 1701–1712. https://doi.org/10.1007/s10529-006-9156-x.

54 Donati, I., Holtan, S., Morch, Y.A. et al. (2005). New hypothesis on the role of alternating sequences in calcium-alginate gels. *Biomacromolecules* 6 (2): 1031–1040.

55 Lee, K.Y. and Mooney, D.J. (2012). Alginate: properties and biomedical applications. *Prog. Polym. Sci.* 37 (1): 106–126.

56 Kaklamani, G., Cheneler, D., Grover, L.M. et al. (2014). Mechanical properties of alginate hydrogels manufactured using external gelation. *J. Mech. Behav. Biomed. Mater.* 36: 135–142.

57 Ertesvåg, H. and Valla, S. (1998). Biosynthesis and applications of alginates. *Polym. Degrad. Stab.* 59 (1–3): 85–91.

58 Christensen, B. (2011). Alginates as biomaterials in tissue engineering. In: *Carbohydrate Chemistry: Chemical and Biological Approaches*, vol. 37 (ed. A.P. Rauter and T.K. Lindhorst), 227–258. Royal Society of Chemistry.

59 Goh, C.H., Heng, P.W.S., and Chan, L.W. (2012). Alginates as a useful natural polymer for microencapsulation and therapeutic applications. *Carbohydr. Polym.* 88 (1): 1–12.

60 Bor, S., Kalkan, I.H., Celebi, A. et al. (2019). Alginates: from the ocean to gastroesophageal reflux disease treatment. *Turk. J. Gastroenterol.* 30 (Suppl. 2): 109–136.

61 Maver, T., Maver, U., Pivec, T. et al. (2018). *Polysaccharide Based Wound Care Materials*, SpringerBriefs in Molecular Science, 9–24. Springer.

62 Paul, W. and Sharma, C.P. (2004). Chitosan and alginate wound dressings: a short review. *Trends Biomater. Artif. Organs* 18 (1): 18–23.

63 Deshmukh, K., Ahamed, M.B., Deshmukh, R. et al. (2017). Biopolymer composites with high dielectric performance: interface engineering. In: *Biopolymer Composites in Electronics* (ed. K.K. Sadasivuni, D. Ponnamma, J. Kim, et al.), 27–128. Elsevier.

64 Van Vlierberghe, S., Graulus, G.-J., Samal, S.K. et al. (2014). Porous hydrogel biomedical foam scaffolds for tissue repair. In: *Biomedical Foams for Tissue Engineering Applications* (ed. P.A. Netti), 335–390. Elsevier.

65 Su, K. and Wang, C. (2015). Recent advances in the use of gelatin in biomedical research. *Biotechnol. Lett.* 37 (11): 2139–2145.

66 Ulubayram, K., Cakar, A.N., Korkusuz, P. et al. (2001). EGF containing gelatin-based wound dressings. *Biomaterials* 22 (11): 1345–1356.

67 Peng, X., Liu, Y., Bentley, W.E., and Payne, G.F. (2016). Electrochemical fabrication of functional gelatin-based bioelectronic interface. *Biomacromolecules* 17 (2): 558–563.

68 Steinbüchel, A. and Valentin, H.E. (1995). Diversity of bacterial polyhydroxyalkanoic acids. *FEMS Microbiol. Lett.* 128 (3): 219–228.

69 Zinn, M., Witholt, B., and Egli, T. (2001). Occurrence, synthesis and medical application of bacterial polyhydroxyalkanoate. *Adv. Drug Deliv. Rev.* 53 (1): 5–21.

70 Kumar, A., Srivastava, J.K., Mallick, N., and Singh, A.K. (2015). Commercialization of bacterial cell factories for the sustainable production of polyhydroxyalkanoate thermoplastics: progress and prospects. *Recent Pat. Biotechnol.* 9 (1): 4–21.

71 Butt, F.I., Muhammad, N., Hamid, A. et al. (2018). Recent progress in the utilization of biosynthesized polyhydroxyalkanoates for biomedical applications - review. *Int. J. Biol. Macromol.* 120 (Pt. A): 1294–1305.

72 Maharana, T., Mohanty, B., and Negi, Y. (2009). Melt–solid polycondensation of lactic acid and its biodegradability. *Prog. Polym. Sci.* 34 (1): 99–124.

73 Garlotta, D. (2001). A literature review of poly (lactic acid). *J. Polym. Environ.* 9 (2): 63–84.

74 da Silva, D., Kaduri, M., Poley, M. et al. (2018). Biocompatibility, biodegradation and excretion of polylactic acid (PLA) in medical implants and theranostic systems. *Chem. Eng. J.* 340: 9–14.

75 Sawalha, H., Schroën, K., and Boom, R. (2008). Mechanical properties and porosity of polylactide for biomedical applications. *J. Appl. Polym. Sci.* 107 (1): 82–93.

76 Park, S.-B., Lih, E., Park, K.-S. et al. (2017). Biopolymer-based functional composites for medical applications. *Prog. Polym. Sci.* 68: 77–105.

77 Das, T. and Prusty, S. (2017). Biopolymer composites in field-effect transistors. In: *Biopolymer Composites in Electronics* (ed. K.K. Sadasivuni, D. Ponnamma, J. Kim, et al.), 219–229. Elsevier.

78 Mano, J.F. (2008). Stimuli-responsive polymeric systems for biomedical applications. *Adv. Eng. Mater.* 10 (6): 515–527.

79 Stuart, M.A., Huck, W.T., Genzer, J. et al. (2010). Emerging applications of stimuli-responsive polymer materials. *Nat. Mater.* 9 (2): 101–113.

80 Zhao, L., Mitomo, H., and Yosh, F. (2008). Synthesis of pH-sensitive and biodegradable CM-cellulose/chitosan polyampholytic hydrogels with electron beam irradiation. *J. Bioact. Compat. Polm.* 23 (4): 319–333.

81 Liu, J., Huang, Y., Kumar, A. et al. (2014). pH-sensitive nano-systems for drug delivery in cancer therapy. *Biotechnol. Adv.* 32 (4): 693–710.

82 Sato, K., Yoshida, K., Takahashi, S., and Anzai, J. (2011). pH- and sugar-sensitive layer-by-layer films and microcapsules for drug delivery. *Adv. Drug Deliv. Rev.* 63 (9): 809–821.

83 Jiang, B. and Li, B. (2009). Tunable drug loading and release from polypeptide multilayer nanofilms. *Int. J. Nanomed.* 4: 37–53.

84 Feng, W., Nie, W., He, C. et al. (2014). Effect of pH-responsive alginate/chitosan multilayers coating on delivery efficiency, cellular uptake and biodistribution of mesoporous silica nanoparticles based nanocarriers. *ACS Appl. Mater. Interfaces* 6 (11): 8447–8460.

85 Yuan, W., Dong, H., Li, C.M. et al. (2007). pH-controlled construction of chitosan/alginate multilayer film: characterization and application for antibody immobilization. *Langmuir* 23 (26): 13046–13052.

86 Zhao, Q., Han, B., Wang, Z. et al. (2007). Hollow chitosan-alginate multilayer microcapsules as drug delivery vehicle: doxorubicin loading and in vitro and in vivo studies. *Nanomedicine* 3 (1): 63–74.

87 White, E.M., Yatvin, J., Grubbs, J.B. III, et al. (2013). Advances in smart materials: stimuli-responsive hydrogel thin films. *J. Polym. Sci., Part B: Polym. Phys.* 51 (14): 1084–1099.

88 Tokarev, I. and Minko, S. (2009). Stimuli-responsive hydrogel thin films. *Soft Matter* 5 (3): 511–524.

89 Ito, Y., Casolaro, M., Kono, K., and Imanishi, Y. (1989). An insulin-releasing system that is responsive to glucose. *J. Control. Release* 10 (2): 195–203.

90 Bawa, P., Pillay, V., Choonara, Y.E., and du Toit, L.C. (2009). Stimuli-responsive polymers and their applications in drug delivery. *Biomed. Mater.* 4 (2): 022001.

91 Pattanashetti, N.A., Heggannavar, G.B., and Kariduraganavar, M.Y. (2017). Smart biopolymers and their biomedical applications. *Procedia Manuf.* 12: 263–279.

92 Na, K., Jung, J., Kim, O. et al. (2008). "Smart" biopolymer for a reversible stimuli-responsive platform in cell-based biochips. *Langmuir* 24 (9): 4917–4923.

93 Kelley, E.G., Albert, J.N.L., Sullivan, M.O., and Epps, T.H. (2013). Stimuli-responsive copolymer solution and surface assemblies for biomedical applications. *Chem. Soc. Rev.* 42 (17): 7057–7071.

94 McDaniel, J.R., Macewan, S.R., Dewhirst, M., and Chilkoti, A. (2012). Doxorubicin-conjugated chimeric polypeptide nanoparticles that respond to mild hyperthermia. *J. Control. Release* 159 (3): 362–367.

95 Lallana, E. and Tirelli, N. (2013). Oxidation-responsive polymers: which groups to use, how to make them, what to expect from them (biomedical applications). *Macromol. Chem. Phys.* 214 (2): 143–158.

96 Song, C.-C., Du, F.-S., and Li, Z.-C. (2014). Oxidation-responsive polymers for biomedical applications. *J. Mater. Chem. B* 2 (22): 3413–3426.

97 Meng, F., Hennink, W.E., and Zhong, Z. (2009). Reduction-sensitive polymers and bioconjugates for biomedical applications. *Biomaterials* 30 (12): 2180–2198.

98 Urbánek, T., Jäger, E., Jäger, A., and Hrubý, M. (2019). Selectively biodegradable polyesters: nature-inspired construction materials for future biomedical applications. *Polymers* 11 (6): 1061.

99 Quinn, J.F., Whittaker, M.R., and Davis, T.P. (2017). Glutathione responsive polymers and their application in drug delivery systems. *Polym. Chem.* 8 (1): 97–126.

100 Ling, X., Tu, J., Wang, J. et al. (2018). Glutathione-responsive prodrug nanoparticles for effective drug delivery and cancer therapy. *ACS Nano* 13 (1): 357–370.

101 Durney, A.R., Kawaguchi, S., Pennamon, G., and Mukaibo, H. (2014). Polymeric hydrogel thin film synthesis via diffusion through a porous membrane. *Mater. Lett.* 133: 171–174.

102 Pal, K., Paulson, A.T., and Rousseau, D. (2009). Biopolymers in controlled-release delivery systems. In: *Modern Biopolymer Science* (ed. S. Kasapis, I.T. Norton and J.B. Ubbink), 519–557. Elsevier.

103 Karki, S., Kim, H., Na, S.-J. et al. (2016). Thin films as an emerging platform for drug delivery. *Asian J. Pharm. Sci.* 11 (5): 559–574.

104 Wroblewska-Krepsztul, J., Rydzkowski, T., Michalska-Pozoga, I., and Thakur, V.K. (2019). Biopolymers for biomedical and pharmaceutical applications: recent advances and overview of alginate electrospinning. *Nanomaterials (Basel)* 9 (3): 140.

105 Zelikin, A.N. (2010). Drug releasing polymer thin films: new era of surface-mediated drug delivery. *ACS Nano* 4 (5): 2494–2509.

106 Renukuntla, J., Vadlapudi, A.D., Patel, A. et al. (2013). Approaches for enhancing oral bioavailability of peptides and proteins. *Int. J. Pharm.* 447 (1–2): 75–93.

107 Tang, C., Guan, Y.-X., Yao, S.-J., and Zhu, Z.-Q. (2014). Preparation of ibuprofen-loaded chitosan films for oral mucosal drug delivery using supercritical solution impregnation. *Int. J. Pharm.* 473 (1–2): 434–441.

108 Smith, A.M., Moxon, S., and Morris, G. (2016). Biopolymers as wound healing materials. In: *Wound Healing Biomaterials* (ed. M.S. Ågren), 261–287. Elsevier.

109 Boateng, J.S., Matthews, K.H., Stevens, H.N., and Eccleston, G.M. (2008). Wound healing dressings and drug delivery systems: a review. *J. Pharm. Sci.* 97 (8): 2892–2923.

110 Maver, T., Smrke, D., Kurečič, M. et al. (2018). Combining 3D printing and electrospinning for preparation of pain-relieving wound-dressing materials. *J. Sol-Gel Sci. Technol.* 88 (1): 33–48.

111 Jones, V. (1999). Alginate dressings and diabetic foot lesions. *Diabet. Foot* 2: 8–15.

112 Mian, M., Beghe, F., and Mian, E. (1992). Collagen as a pharmacological approach in wound healing. *Int. J. Tissue React.* 14: 1–9.

113 Chattopadhyay, S. and Raines, R.T. (2014). Collagen-based biomaterials for wound healing. *Biopolymers* 101 (8): 821–833.

114 Wittaya-areekul, S. and Prahsarn, C. (2006). Development and in vitro evaluation of chitosan–polysaccharides composite wound dressings. *Int. J. Pharm.* 313 (1–2): 123–128.

115 Sezer, A.D., Hatipoglu, F., Cevher, E. et al. (2007). Chitosan film containing fucoidan as a wound dressing for dermal burn healing: preparation and in vitro/in vivo evaluation. *AAPS PharmSciTech* 8 (2): E94–E101.

116 Kazmierska, K.A. and Ciach, T. (2009). Bioactive coatings for minimally invasive medical devices: surface modification in the service of medicine. *Recent Pat. Biomed. Eng.* 2 (1): 1–14.

117 Wisniewski, N. and Reichert, M. (2000). Methods for reducing biosensor membrane biofouling. *Colloids Surf., B* 18 (3–4): 197–219.

118 Banerjee, I., Pangule, R.C., and Kane, R.S. (2011). Antifouling coatings: recent developments in the design of surfaces that prevent fouling by proteins, bacteria, and marine organisms. *Adv. Mater.* 23 (6): 690–718.

119 Mohan, T., Kargl, R., Tradt, K.E. et al. (2015). Antifouling coating of cellulose acetate thin films with polysaccharide multilayers. *Carbohydr. Polym.* 116: 149–158.

120 Ammon, H., Ege, W., Oppermann, M. et al. (1995). Improvement in the long-term stability of an amperometric glucose sensor system by introducing a cellulose membrane of bacterial origin. *Anal. Chem.* 67 (2): 466–471.

121 Dobosz, K.M., Kolewe, K.W., and Schiffman, J.D. (2015). Green materials science and engineering reduces biofouling: approaches for medical and membrane-based technologies. *Front. Microbiol.* 6: 196.

122 Rieger, K.A., Eagan, N.M., and Schiffman, J.D. (2015). Encapsulation of cinnamaldehyde into nanostructured chitosan films. *J. Appl. Polym. Sci.* 132 (13): 41739.

123 Zodrow, K.R., Tousley, M.E., and Elimelech, M. (2014). Mitigating biofouling on thin-film composite polyamide membranes using a controlled-release platform. *J. Membr. Sci.* 453: 84–91.

124 Rieger, K.A. and Schiffman, J.D. (2014). Electrospinning an essential oil: cinnamaldehyde enhances the antimicrobial efficacy of chitosan/poly(ethylene oxide) nanofibers. *Carbohydr. Polym.* 113: 561–568.

125 Sawant, S. (2017). Development of biosensors from biopolymer composites. In: *Biopolymer Composites in Electronics* (ed. K.K. Sadasivuni, D. Ponnamma, J. Kim, et al.), 353–383. Elsevier.

126 Willner, I. and Katz, E. (2006). *Bioelectronics: From Theory to Applications.* Wiley.

127 Igarzabal, C.I.A., Martinelli, M., Brunetti, V., and Strumia, M.C. (2015). Adaptation of biopolymers to specific applications. In: *Surface Modification of Biopolymers* (ed. V.K. Thakur and A.S. Singha), 84–112. Wiley.

128 Kim, J.-H., Mun, S., Ko, H.-U. et al. (2014). Disposable chemical sensors and biosensors made on cellulose paper. *Nanotechnology* 25 (9): 092001.

129 Mahadeva, S.K. and Kim, J. (2011). Conductometric glucose biosensor made with cellulose and tin oxide hybrid nanocomposite. *Sens. Actuators, B* 157 (1): 177–182.

130 Fang, Y., Ni, Y., Zhang, G. et al. (2012). Biocompatibility of CS–PPy nanocomposites and their application to glucose biosensor. *Bioelectrochemistry* 88: 1–7.

131 Shan, C., Yang, H., Han, D. et al. (2010). Graphene/AuNPs/chitosan nanocomposites film for glucose biosensing. *Biosens. Bioelectron.* 25 (5): 1070–1074.

132 Du, Z., Li, C., Li, L. et al. (2009). Simple fabrication of a sensitive hydrogen peroxide biosensor using enzymes immobilized in processable polyaniline nanofibers/chitosan film. *Mater. Sci. Eng., C* 29 (6): 1794–1797.

133 Sharma, A. and Kumar, A. (2016). Study of structural and electro-catalytic behaviour of amperometric biosensor based on chitosan/polypyrrole nanotubes-gold nanoparticles nanocomposites. *Synth. Met.* 220: 551–559.

134 Zhang, M., Smith, A., and Gorski, W. (2004). Carbon nanotube– chitosan system for electrochemical sensing based on dehydrogenase enzymes. *Anal. Chem.* 76 (17): 5045–5050.

135 Li, W., Yuan, R., Chai, Y., and Chen, S. (2010). Reagentless amperometric cancer antigen 15-3 immunosensor based on enzyme-mediated direct electrochemistry. *Biosens. Bioelectron.* 25 (11): 2548–2552.

136 Liu, Y., Wang, M., Zhao, F. et al. (2005). The direct electron transfer of glucose oxidase and glucose biosensor based on carbon nanotubes/chitosan matrix. *Biosens. Bioelectron.* 21 (6): 984–988.

137 Ates, M. (2013). A review study of (bio)sensor systems based on conducting polymers. *Mater. Sci. Eng., C* 33 (4): 1853–1859.

8

Biopolymer-Based Nanofibers – Synthesis, Characterization, and Application in Tissue Engineering and Regenerative Medicine

Merin S. Thomas[1,2], Prasanth K. S. Pillai[2], Sabu Thomas[2,3,4], and Laly A. Pothen[2,5]

[1] *Mahatma Gandhi University, Mar Thoma College, Department of Chemistry, Kuttapuzha P.O., Tiruvalla, Kerala 689103, India*
[2] *Mahatma Gandhi University, International and Interuniversity Centre for Nanoscience and Nanotechnology, School of Energy Materials, Priyadarsini Hills P.O., Kottayam, Kerala 686560, India*
[3] *Mahatma Gandhi University, School of Chemical Sciences, School of Energy Materials, Priyadarsini Hills P.O., Kottayam, Kerala 686560, India*
[4] *Mahatma Gandhi University, School of Energy Materials, School of Energy Materials, Priyadarsini Hills P.O., Kottayam, Kerala 686560, India*
[5] *Mahatma Gandhi University, C.M.S. College, Department of Chemistry, Kottayam, Kerala 686001, India*

8.1 Introduction

Natural polymers, especially polysaccharides, proteins, etc., due to their numerous applications in packaging, food, paper, textile, medicine, and agriculture, are very significant in controlling the drift of modern industrial economies [1, 2]. Scientists hold new strategies that include different polymerization techniques, such as nanoscience/nanotechnology, which allows a very good control of the molecular architecture of polymeric molecules to be transformed into smart bio-based nanostructures for different advanced applications, including packaging, food, paper, and textile industries; medicine; agriculture, etc. [3]. The emergence of nanomaterials from different renewable feedstock has lifted the research outcome in many areas of technology. Nanomaterials such as nanowires, nanorods, nanofibers, nanotubes, and nanosheets are highly important because of the numerous applications in the above mentioned applications and in controlling the drift of modern industrial economies [4–6]. The exceptional surface-to-volume ratio (aspect ratio), the fast-absorbing ability of biomolecules, and high porosity possessed by nanofibers from natural polymers have escalated their demand [7].

The different properties such as biodegradability, biocompatibility, renewability, low toxicity, and sustainability escalated the utilization of biopolymers for more advanced research studies [8]. For example, biopolymers derived

Functional Biomaterials: Design and Development for Biotechnology, Pharmacology, and Biomedicine, First Edition. Edited by Tamilselvan Mohan and Karin Stana Kleinschek.

from polysaccharides (starch, cellulose, chitin, and chitosan) and proteins (soy protein, wheat protein, casein, and gelatin) are natural in origin and the most sustainable substitute for producing green materials in the near future. For example, environmental compatibility would be enhanced as no environmental burdens would be introduced because of their use. In addition, the utilization of renewable resources provides an incentive to extend non-renewable petrochemical supplies. In this chapter, we highlight the uniqueness of different nanofibers obtained from different polysaccharides for various biomedical applications.

8.2 Different Strategies of Nanofiber Development

8.2.1 Drawing

Drawing is a method adopted to produce single nanofibers (Figure 8.1). In this technique, each fiber is pulled out from a previously deposited polymer solution droplet, accompanied by evaporation of the solvent, leading to solidification of the fiber [10].

8.2.2 Template Synthesis

In this method, the nanofibers are produced within the pores of a nanoporous membrane under pressure. Nanoporous filtration membrane acts as a template. Nanofibers are produced when the polymer is extruded through these nanopores under pressure (Figure 8.2) [12].

8.2.3 Phase Separation

Three-dimensional networks of nanofiber scaffolds can be prepared by this method, in which the phase separation of a polymer solution is achieved either thermally or by using a non-solvent (Figure 8.3). For removing the solvent, the membrane is then freeze-dried, resulting in the formation of a porous structure [14].

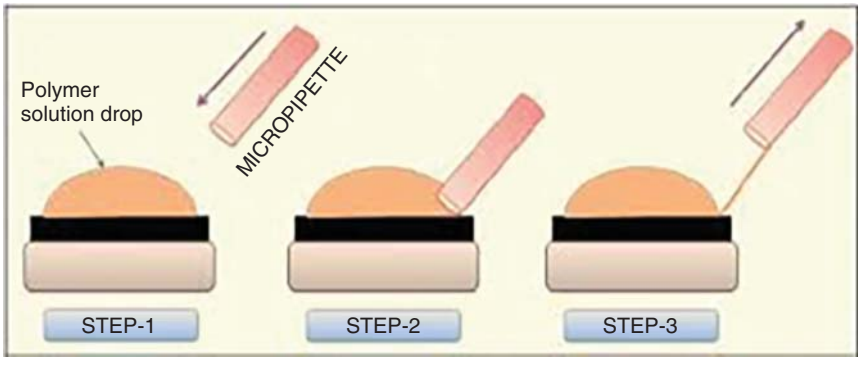

Figure 8.1 Schematic representation of nanofiber formation by drawing. Source: Garg et al. [9]/with permission of Taylor & Francis.

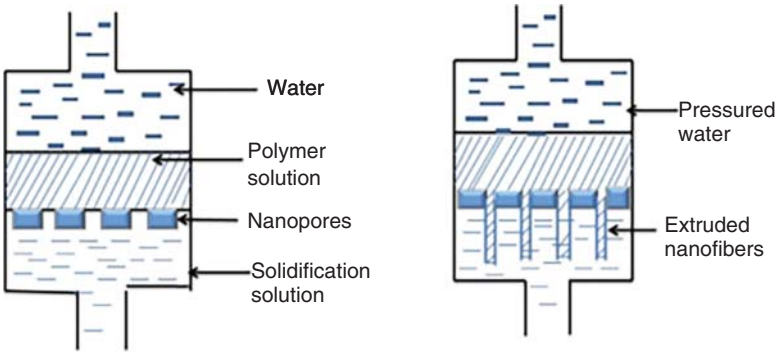

Figure 8.2 Schematic representation of nanofiber formation by template synthesis. Source: Patil et al. [11]/with permission of Elsevier.

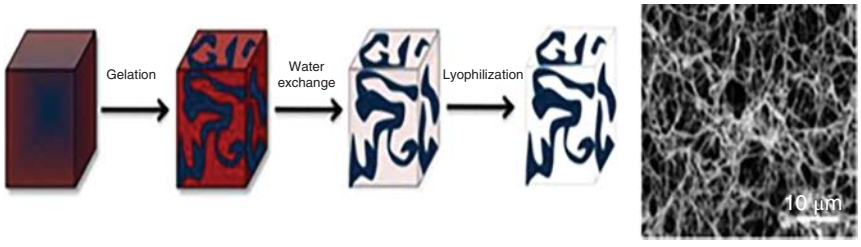

Figure 8.3 Schematic representation of nanofiber formation by phase separation. Source: Wade et al. [13]/with permission of Elsevier.

8.2.4 Self-Assembly

Stable ordered nanostructures can be prepared by the self-assembly method, which employs non-covalent bonding interactions such as hydrogen bonding (Figure 8.4) [15, 16].

8.2.5 Electrospinning

It is the most widely used, simple, versatile method for the fabrication of nanofibers that use the application of electric field for nanofiber production. By using this technique, layered, porous nanofiber structures can be produced (Figure 8.5).

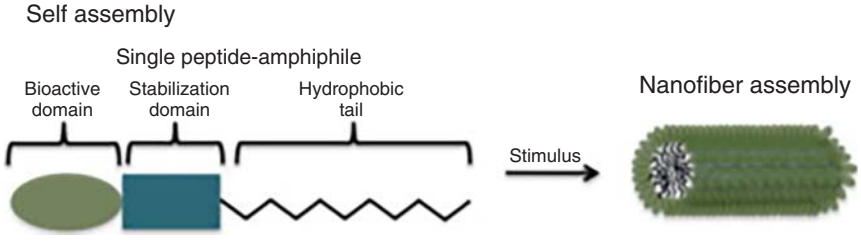

Figure 8.4 Schematic representation of nanofiber formation by self-assembly. Source: Wade and Burdick [13]/with permission of Elsevier.

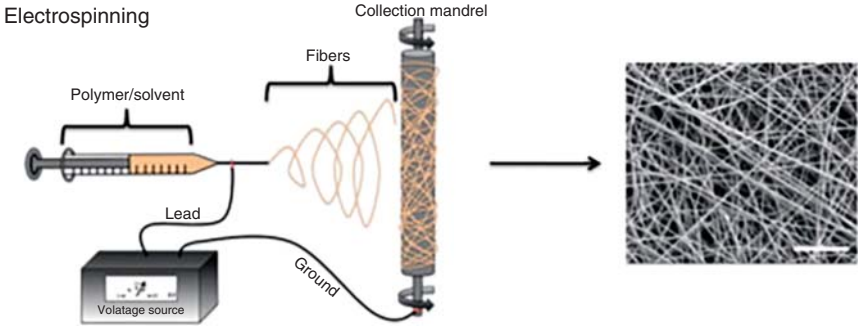

Figure 8.5 Schematic representation of nanofiber formation by electrospinning. Source: Wade and Burdick [13]/with permission of Elsevier.

8.2.5.1 Advantages of Electrospun Nanofibers

The assembly of nanofibers produced by the electrospinning method can be used for a wide range of applications because of their morphology, aspect ratio, and inter/intrafibrous porosity. The potential applications of the electrospun fibers include biomedical applications (tissue engineering, wound healing, drug delivery, and enzyme immobilization), environmental protection (water purification and air filtration), affinity membranes, nanobiosensors, electronic/optical, food science (packaging applications and preparation of edible films), and protective clothing fields. Electrospinning is a simple, cost-effective, versatile technique for the fabrication of nanofibers. In addition to this, it is easy to handle, and the membranes fabricated by this process have unique properties because of its structural and functional characteristics such as submicron scale to nanoscale.

8.3 Biopolymers

Biopolymers are natural in origin, and the nanofibers from biopolymers possess properties such as high surface area and high porosity, which allow its use in the fabrication of three-dimensional structures that simulate the extracellular matrix (ECM). Electrospinning is the most suitable method for the fabrication of nanofibers. However, most of the biopolymers exhibit low spinnability, and this limits its application. This can be overcome by the use of polymers as a co-spinning agent.

8.3.1 Chitosan Nanofibers

Chitosan, a linear biopolymer, is obtained by the deacetylation of chitin present in the exoskeletons of arthropods, in the endoskeletons of cephalopods, and in the cell walls and ECM of certain fungi, yeasts, and algae [17]. The reactive amino groups and the hydroxyl group in its structure help the chelating action of chitosan for metal ions to bind to biomolecules, mammalian cells, and microbial cells. Chitosan

is polycationic in nature and favors its dissolution in acidic media, and this helps the electrospinning of chitosan. Chitosan nanofibers can be prepared by using electrospinning technology. Ohkava et al. [18] prepared the electrospun fibers of chitosan. They found that trifluoroacetic acid (TFA) was the most suitable solvent for electrospinning of chitosan as the amino groups of chitosan form salts with TFA, decreasing the strong interactions in chitosan [19]. The chitosan nanofibers were also prepared by dissolving chitosan in TFA and dichloromethane [20] and acetic acid [21]. Min et al. prepared chitosan nanofibers by the subsequent deacetylation of electrospun membranes obtained by the electrospinning of chitin dissolved in 1,1,1,3,3,3-hexafluoro-2-propanol (HFIP) [22]. Some electrospinning parameters used in different literature studies are summarized in Table 8.1.

8.3.2 Cellulose Nanofibers

Cellulose is the most abundant natural biopolymer. It is obtained from plants. The hydrophilicity biodegradability, biocompatibility, and low toxicity make its use in multiple applications, including biomedical applications [29, 30], environmental applications [31], cloth-protectant applications [32], as affinity membranes [33, 34], and among others [35]. Cellulose acetate is the most important derivative of cellulose used for nanofiber applications. Electrospun composite nanofibers from native cotton cellulose loaded with different hydroxyapatite concentrations were prepared by Ao and coworkers [29] for bone tissue engineering applications. Recently, cellulose nanofibers were prepared via electrospinning of cellulose solution by Otsuka et al. [36]. Lee et al. [37] found that the mixture of dimethylformamide (DMF)/acetone can be used to fabricate very smooth, bead-free cellulose acetate nanofibers in the proper concentration of the polymer.

Table 8.1 Electrospinning parameters used in different research studies.

Polymers	Feeding rate	Voltage power (kV)	Distance to collector (cm)	References
PLGA/chitosan/PVA	0.2 (ml/h)	15	10	[23]
Chitosan–polyethylene oxide containing bioactive silver nanoparticles	1 (ml/h)	21	10	[24]
Chitosan dissolved in concentrated acetic acid solution	20 (μl/min)	40		[21]
Ti_3C_2Tz/chitosan nanofibers	—	20–25	10–14	[25]
Hydroxyapatite-containing chitosan nanofibers	1.2 (ml/h)	15	15	[26]
Chitosan/poly (vinyl alcohol) nanofibers	0.13 (ml/h)	16	20	[27]
Core–shell polyurethane/chitosan nanofibers	0.2 (ml/h)	15	12	[28]

8.4 Characterization Techniques

8.4.1 Morphological Analysis

Imaging techniques such as scanning electron microscopy (SEM), transmission electron microscopy (TEM), atomic force microscopy (AFM), etc., were used for the morphological evaluation of the structure and represent an essential part of characterization of the most materials, including nanofibers. These imaging techniques are used for the visualization of various places of the nanofibrous sample. Therefore, the obtained images provide the useful information to compare the local structures within the whole sample. Imaging methods also play a key role in the evaluation of *in vitro* biomedical experiments, depicting the cell cultivation process on various synthetic substrates.

8.4.2 Scanning Electron Microscopy (SEM)

The basic feature of a nanofiber such as the fiber diameter and the pore size can be visualized using SEM analysis. For the electrospun nanofibers, SEM analysis provides a clear picture regarding the surface morphology. Thomas et al. [38] studied the morphology of the PLA/nanochitosan composite fibers by field emission scanning electron microscopy (FESEM) analysis (Figure 8.6). They explained that the secondary porous structure developed during the electrospinning process was due to the evaporative cooling of the solvent on the surface of the fibers and the condensation of water vapor present in the atmosphere on the fiber surface.

8.4.2.1 Transmission Electron Microscopy (TEM)

The surface morphology of nanoscale structures can be analyzed using TEM analysis (Figure 8.7). Jatoi et al. [39] generated silver nanoparticles (AgNPs) on the surface of cellulose nanofibers by thermal treatment and DMF as reducing agents. TEM images

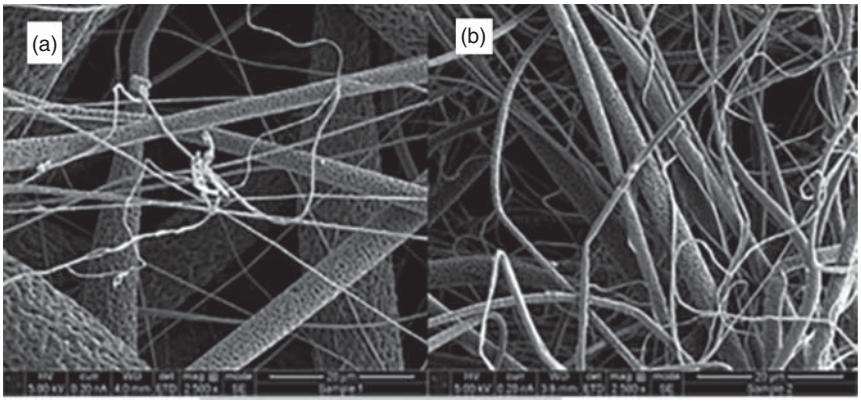

Figure 8.6 Field emission scanning electron microscopy (FESEM) images of (a) neat polylactic acid (PLA) and (b) PLA loaded with chitosan. Source: Thomas et al. [38]/with permission of John Wiley & Sons.

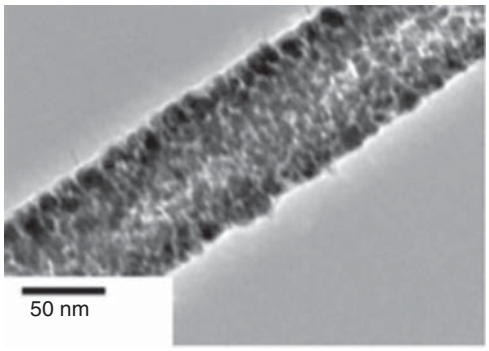

Figure 8.7 Transmission electron microscopy (TEM) images of cellulose nanofibers with AgNPs. Source: Wahab et al. [39]/with permission of Elsevier.

showed the cellulose nanofibers highly decorated with spherical metallic AgNPs and very good spatial distribution of AgNPs.

Liu et al. [40] studied the electrochemical behavior and microstructure evolution of carbon nanofibers (CNFs) during Na^+ and K^+ insertions using a nanoscale battery setup inside a TEM. The CNFs are hollow and consist of a bilayer wall with an outer layer of disordered-carbon (d-C) enclosing an inner layer of crystalline-carbon (c-C). The sodiation and potassiation responses of c-C and d-C were compared. Longitudinal cracks are frequently observed near the c-C/d-C interface during sodiation and potassiation. An *in situ* TEM study of amorphous Si (a-Si)-coated CNFs was conducted to further evaluate the mechanical confinement effect on sodiation and potassiation.

8.4.2.2 Atomic Force Microscopy (AFM)

In AFM, the surface characterization was done by analyzing the sample surface with the probe of AFM, moving in close proximity of the sample. By using this method, a three-dimensional image can be constructed for the sample. AFM is widely used for successful characterization of individual fibers as well as for the accurate measurement of fiber diameter. Zhang et al. [41] performed surface morphology imaging on the electrospun cholesteryl-succinyl silane (CSS) nanofibers using AFM. The analysis was done using a Digital Instrument Nanoscope IIID AFM in air at room temperature. They performed both the AFM deflection and three-dimensional (3D) imaging of the CSS fibers in the contact mode. From AFM analysis **(**Figure 8.8**),** they found that the CSS fibers displayed swollen diameters ranging from 370 to 600 nm. Bead-like structures 800 nm in width and 900 nm in height were also observed. They suggested that the bead-like morphology is due to the weak chain entanglement of small molecules of lipids in solutions.

8.4.3 Mechanical Characterization

8.4.3.1 Nanotensile Test

It was found to be the most challenging experiment to perform because direct handling of the fiber is required. In addition to this, the right specimen gripping is necessary to prevent the fiber from slipping from grips or breaking at the grips. The use

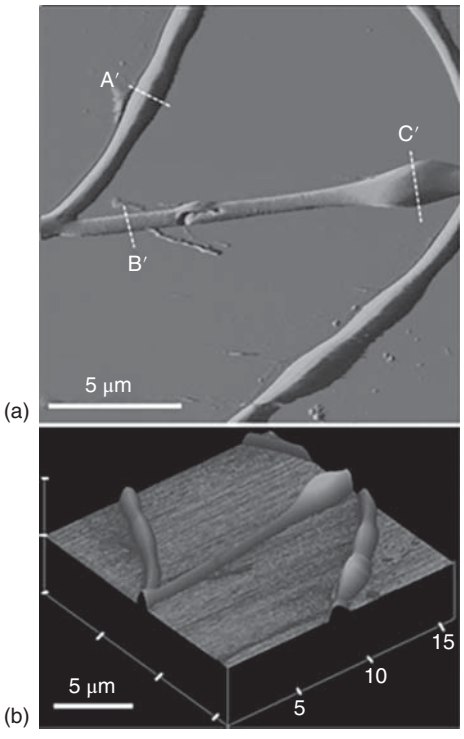

Figure 8.8 AFM images of the electrospun cholesteryl-succinyl silane (CSS) nanofibers. (a) A representative AFM deflection image with a data scale of 50 nm. (b) The 3D AFM image. Source: Zhang et al. [41]/with permission of AIP Publishing LLC.

of conventional mechanical grips is not adequate because of the small size of the samples. Another problem is related to the misalignment of the fibers between sample axis and loading direction, which may result in unwanted bending moment, and this may lead to premature sample failure.

8.4.3.2 Nanoindentation

Nanoindentation is the most convenient and simple methods to perform the mechanical characterization. Here, the sample can be prepared for testing by simply depositing nanofibers on a hard and flat substrate, with sufficient adhesion between the substrate and the nanomaterials. Nanoindentation of nanofibers has not been widely studied because of the difficulty in probing the curved surface of the fiber. The mechanical properties of single-composite fibers of polymethylmethacrylate fibers reinforced with nanocellulose obtained via electrospinning studied by nanoindentation method showed a modest increase in the mechanical properties with increasing cellulose nano crystals (CNC) content, up to 17% [42].

8.5 Applications

8.5.1 Tissue Engineering

The necessary requirement for the tissue engineering scaffold is that it should resemble with the native ECM. The biodegradability and biocompatibility of biopolymers

help for degradation of the scaffold after the formation of a new ECM. A wide range of natural polymers have been utilized as nanofibrous scaffolding materials for bone, cartilage, ligament, and skeletal muscle tissue engineering, including hydroxyapatite [43], chitin, chitosan [44], cellulose [45], and soy protein [46]. Tan et al. [47] prepared electrospun cellulose acetate butyrate/polyethylene glycol (CAB/PEG) composite nanofibers for tissue engineering applications. They reported that with the increase in hydrophilicity, the swelling ability of the composite nanofiber increases by twofold with more rapid biodegradation. The cell viability assay results revealed that the nanofibers are non-toxic and have better cell attachment compared to pure CAB nanofibers. Chakraborty et al. [48] fabricated non-woven nanofibrous cellulose acetate scaffolds (CAS) with average fiber diameters from 300 to 600 nm diameters via electrospinning and found that the higher aspect ratio, higher swelling abilities, higher porosity, and moderate degradation rates of the scaffolds imparted better mechanical and chemical properties to the scaffolds. The cell viability tests carried out by MTT assay analysis gave best results of cell viability and provided a viable surface for potential bone tissue engineering applications.

Xu et al. [49] introduced chitosan island-structured polylactic acid by electrospinning method and found that the island-like surface topology surfaces were more favorable for the spread of cells and can be used for improving the interface of tissue engineering scaffolds.

8.5.2 Drug Delivery

The high surface-to-volume ratio and porosity of polymeric nanofibers makes them an ideal carrier for the discharge of bioactive molecules and compounds such as drugs, herbal extracts, etc. These nanofibers resulted in enhanced drug loading capacity, mass transfer properties, and cell attachment. Electrospinning process can be employed for the encapsulation of drug into the nanofibrous membrane. The texture, degradation, and high aspect ratio make them excellent carriers for therapeutic agents. Drugs can easily be loaded into the polymer solution before the electrospinning process. The controlled release of any drug or biomolecule added to the precursor polymer solution can be regulated by the degradation rate of the polymer shell. Chitosan nanofibrous structures have been proven to be useful in drug release applications as well. Chitosan possess hypocholesterolemic and hypolipidemic activities [50]. Along with these properties, chitosan has antimicrobial, antiviral, and antitumor activity and can be used for drug delivery [51], tissue engineering [52], and in dentistry [53]. Ibuprofen-loaded poly(lactideco-glycolide)/poly(ethylene glycol)-*g*-chitosan (PLGA/PEG-*g*-Cs) electrospun membranes for controlled drug delivery applications was reported by Jiang et al. [54]. The presence of PEG-*g*-Cs significantly toned-down the burst release of drug from PLGA-electrospun membrane. Toshkova et al. [55] fabricated nanofibrous implants containing quaternized chitosan, poly(L-lactide-*co*-D,L-lactide), and the antitumor drug doxorubicin by electrospinning. The implants efficiently inhibited the Graffi tumor growth, and the introduction of these implants increased the animal survival rate.

Cellulose and cellulose derivatives have been widely used as potential candidates for pharmaceutical applications. The electrospun fiber mats of cellulose and cellulose derivatives are used as drug delivery vehicles with useful and controllable dissolution properties. Hydroxypropyl cellulose (HPC) is a cellulose ether having both water solubility and organic solubility. The HPC nanofibers alone or in conjugation with either poly(vinyl alcohol) (PVA) or poly(vinyl pyrrolidone) (PVP) were used for the delivery of the drug diclofenac sodium, utilized to relieve pain (inflammation) and joint stiffness caused by arthritis [56]. Kumar et al. [57] fabricated polylactic acid and hydroxypropyl cellulose (PLA-HPC) fibers by electrospinning for drug delivery applications.

8.5.3 Wound Healing

Wound healing is very closely related to the tissue regeneration mechanism, and it involves a number of symbiotic phases involving cellular and matrix components, such as homeostasis, inflammation, migration, proliferation, and maturation, for the reconstruction of lost or damaged tissue. The essential requirement for a material to be wound dressing is its antimicrobial activities [58]. Chitosan possesses good antimicrobial activity because of its positive charge. The polycationic nature of chitosan makes it possible to interact with the negatively charged microbial cell membranes, leading to the disruption of the microbial membrane and subsequently the leakage of proteinaceous and other intracellular constituents [58–61]. Chitosan is also used as sponges and bandages for the treatment of wounds because of its biocompatible and biodegradable nature. However, the applications are limited because of its insolubility in water and low reactivity [62]. Ignatova et al. [63] prepared electrospun non-woven nanofibrous hybrid mats based on chitosan and PLA for wound dressing applications. They found that nanofibers containing cross-linked chitosan or quaternized chitosan exhibits higher antibacterial activity against *Staphylococcus aureus* and *Escherichia coli* than the corresponding solvent-cast films and very effective in suppressing the adhesion of pathogenic bacteria *S. aureus*. Li et al. [64] produced electrospun poly(lactic acid)/chitosan core–shell structure nanofibers and found that it possesses good cell adhesion and proliferation capacity and can be used for tissue engineering and wound healing applications. Goh et al. [65] developed antibacterial poly(lactic acid)/chitosan nanofibers decorated with cerium, copper, or silver-doped bioactive glasses with excellent antibacterial properties and bioactivity. A schematic representation of the healing process is given in Figure 8.9.

Xu et al. [67] fabricated chitosan/PLA/PEG hydrogel nanofibers for wound dressing by solution blowing method. They suggested that the prepared nanofibers ensure the advantages of both hydrogel and nanofiber mats for wound dressing, such as the ability to absorb excess exudates, creating a moist wound healing environment, allowing gas exchange, and possessing excellent antibacterial activity against *E. coli* bacteria. To improve the wound dressing capacity of cellulose and its derivatives, several biomolecules have been incorporated within it. Cellulose acetate (CA) functionalized with antibiotics, nanoparticles, plant extracts, proteins, antimicrobial peptide-electrospun dressings, etc., has been used for the treatment

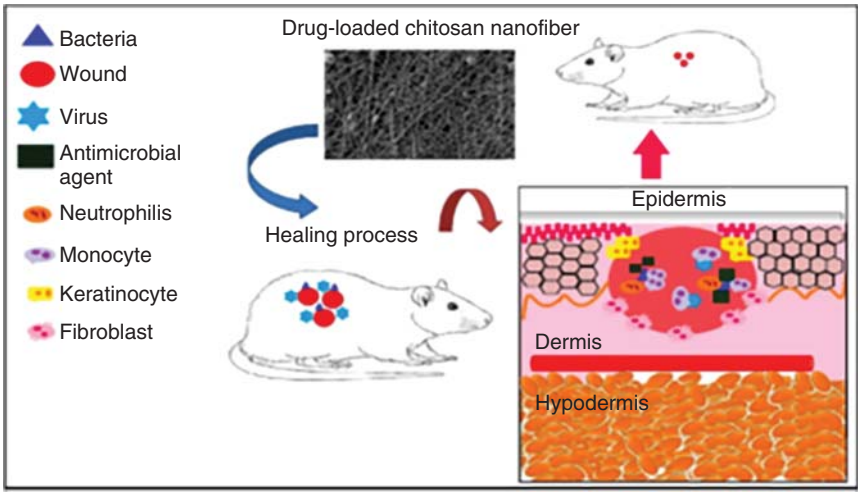

Figure 8.9 Representation of the healing process in a wound rat model. Source: Kalantari et al. [66]/with permission of Elsevier.

of skin wounds. Antibacterial electrospun nanofibers of polyurethane, CA, and zein incorporated with streptomycin sulfate showed hydrophilicity, excellent cell attachment, proliferation, and blood clotting ability, together with good antimicrobial features [68]. Ahn et al. [69] developed plant-based biomimetic cellulose/soy protein nanofibrous scaffolds using rotary jet spinning. The properties of this nanofibrous matrix mimic native ECM in skin and exhibit high water-retaining capability for enhanced wound healing. The presence of plant-based materials in wound dressing accelerates *in vitro* dermal fibroblast proliferation, spreading, and migration.

8.5.4 Biosensors

Biosensors are used for sensing analytes such as DNA, enzyme, proteins, RNA, dopamine, cholesterol, and many other biomolecules that use specific biochemical reactions mediated by a biological recognition [70]. Electrospun fibers can be used as biosensors because of their large surface area and porous structure that make them detect with a wide response. Li et al. [71] studied the dependence of fiber diameter on the sensing performance of sensors developed by the integration of functional nanomaterials with optical micro/nanofibers (OMNFs). According to their view, the refractive index sensitivity can be significantly increased and the biosensing ability of the sensor using an OMNF of 1.0 μm possesses high sensitivity as well as good mechanical robustness. They found that the ultra-high sensitivity makes this sensor suitable for small-molecule detection and trace element assays. Teepoo et al. [72] prepared electrospun chitosan–gelatin biopolymer composite nanofibers for horseradish peroxidase immobilization in a hydrogen peroxide biosensor. They found that horseradish peroxidase immobilization on chitosan–gelatin composite biopolymer nanofibers had advantages of fast response,

excellent reproducibility, and high stability. The electrospun fibers of chemically modified form of cellulose, cellulose acetate [73], are widely used as biosensors including optical/colorimetric and electrochemical sensors because of their high thermal stability, biocompatibility, and biodegradability.

8.6 Conclusions

This chapter gives an overview of the preparation and applications of different biopolymer nanofibers that have been extensively used in a wide range of biomedical applications. The properties of these functional materials are extremely dependent on their synthetic pathways and their uniqueness of the structure, which can be altered using different modification reactions. Chitosan and cellulose are the most used polysaccharides for nanofiber preparation. Although several techniques are available for the preparation of nanofibers, it was found that electrospinning is very effective in structuring the architecture of different natural polymers and in terms of cost perspective to produce materials for biomedical applications. The right kind of modification architecture will improve its prospects as a substrate for making materials that can be used for biomedical, structural, and other industrial applications.

References

1 Kraśniewska, K., Galus, S., and Gniewosz, M. (2020). Biopolymers-based materials containing silver nanoparticles as active packaging for food applications–a review. *Int. J. Mol. Sci.* 21 (3): 698.

2 Moohan, J., Stewart, S.A., Espinosa, E. et al. (2020). Cellulose nanofibers and other biopolymers for biomedical applications. A review. *Appl. Sci.* 10 (1): 65.

3 Mondal, S. (2017). Preparation, properties and applications of nanocellulosic materials. *Carbohydr. Polym.* 163: 301–316.

4 Dasgupta, N., Ranjan, S., and Ramalingam, C. (2017). Applications of nanotechnology in agriculture and water quality management. *Environ. Chem. Lett.* 15 (4): 591–605.

5 Duncan, T.V. (2011). Applications of nanotechnology in food packaging and food safety: barrier materials, antimicrobials and sensors. *J. Colloid Interface Sci.* 363 (1): 1–24.

6 Ismail, A.F., Hilal, N., Jaafar, J., and Wright, C. (2019). *Nanofiber Membranes for Medical, Environmental, and Energy Applications*. CRC Press.

7 Barhoum, A., Pal, K., Rahier, H. et al. (2019). Nanofibers as new-generation materials: from spinning and nano-spinning fabrication techniques to emerging applications. *Appl. Mater. Today* 17: 1–35.

8 Lu, Y., Sun, Q., She, X. et al. (2013). Fabrication and characterisation of α-chitin nanofibers and highly transparent chitin films by pulsed ultrasonication.

Carbohydr. Polym. 98 (2): 1497–1504. https://doi.org/10.1016/j.carbpol.2013.07.038.

9 Garg, T., Rath, G., and Goyal, A.K. (2015). Biomaterials-based nanofiber scaffold: targeted and controlled carrier for cell and drug delivery. *J. Drug Targeting* 23 (3): 202–221.

10 Ondarcuhu, T. and Joachim, C. (1998). Drawing a single nanofibre over hundreds of microns. *EPL* 42 (2): 215.

11 Patil, J.V., Mali, S.S., Kamble, A.S. et al. (2017). Electrospinning: a versatile technique for making of 1D growth of nanostructured nanofibers and its applications: an experimental approach. *Appl. Surf. Sci.* 423: 641–674.

12 Martin, C.R. (1995). Template synthesis of electronically conductive polymer nanostructures. *Acc. Chem. Res.* 28 (2): 61–68.

13 Wade, R.J. and Burdick, J.A. (2012). Engineering ECM signals into biomaterials. *Mater. Today* 15 (10): 454–459.

14 Morie, A., Garg, T., Goyal, A.K., and Rath, G. (2016). Nanofibers as novel drug carrier–an overview. *Artif. Cells Nanomed. Biotechnol.* 44 (1): 135–143.

15 Hartgerink, J.D., Beniash, E., and Stupp, S.I. (2002). Peptide-amphiphile nanofibers: a versatile scaffold for the preparation of self-assembling materials. *Proc. Natl. Acad. Sci. U.S.A.* 99 (8): 5133–5138.

16 Zhang, S. (2003). Fabrication of novel biomaterials through molecular self-assembly. *Nat. Biotechnol.* 21 (10): 1171.

17 Muzzarelli, R.A.A. and Muzzarelli, C. (2005). Chitosan chemistry: relevance to the biomedical sciences. In: *Polysaccharides I*, 151–209. Springer.

18 Ohkawa, K., Cha, D., Kim, H. et al. (2004). Electrospinning of chitosan. *Macromol. Rapid Commun.* 25 (18): 1600–1605.

19 Hasegawa, M., Isogai, A., Onabe, F. et al. (1992). Characterization of cellulose–chitosan blend films. *J. Appl. Polym. Sci.* 45 (11): 1873–1879.

20 Torres-Giner, S., Ocio, M.J., and Lagaron, J.M. (2008). Development of active antimicrobial fiber-based chitosan polysaccharide nanostructures using electrospinning. *Eng. Life Sci.* 8 (3): 303–314.

21 Geng, X., Kwon, O.H., and Jang, J. (2005). Electrospinning of chitosan dissolved in concentrated acetic acid solution. *Biomaterials* 26 (27): 5427–5432. https://doi.org/10.1016/j.biomaterials.2005.01.066.

22 Min, B.-M., Lee, S.W., Lim, J.N. et al. (2004). Chitin and chitosan nanofibers: electrospinning of chitin and deacetylation of chitin nanofibers. *Polymer* 45 (21): 7137–7142.

23 Duan, B., Yuan, X., Zhu, Y. et al. (2006). A nanofibrous composite membrane of PLGA–chitosan/PVA prepared by electrospinning. *Eur. Polym. J.* 42 (9): 2013–2022.

24 Kohsari, I., Shariatinia, Z., and Pourmortazavi, S.M. (2016). Antibacterial electrospun chitosan–polyethylene oxide nanocomposite mats containing bioactive silver nanoparticles. *Carbohydr. Polym.* 140: 287–298.

25 Mayerberger, E.A., Street, R.M., McDaniel, R.M. et al. (2018). Antibacterial properties of electrospun Ti 3 C 2 T z (MXene)/chitosan nanofibers. *RSC Adv.* 8 (62): 35386–35394.

26 Frohbergh, M.E., Katsman, A., Botta, G.P. et al. (2012). Electrospun hydroxyapatite-containing chitosan nanofibers crosslinked with genipin for bone tissue engineering. *Biomaterials* 33 (36): 9167–9178.

27 Sanchez-Alvarado, D., Guzmán-Pantoja, J., Páramo-García, U. et al. (2018). Morphological study of chitosan/poly (vinyl alcohol) nanofibers prepared by electrospinning, collected on reticulated vitreous carbon. *Int. J. Mol. Sci.* 19 (6): 1718.

28 Maleknia, L., Dilamian, M., Pilehrood, M.K. et al. (2018). Preparation, process optimization and characterization of core-shell polyurethane/chitosan nanofibers as a potential platform for bioactive scaffolds. *Res. Pharm. Sci.* 13 (3): 273.

29 Ao, C., Niu, Y., Ximu Zhang, X. et al. (2017). Fabrication and characterization of electrospun cellulose/nano-hydroxyapatite nanofibers for bone tissue engineering. *Int. J. Biol. Macromol.* 97: 568–573.

30 Xu, W., Zhang, D., Cai, J. et al. (2020). One-pot fabrication of cellulose-collagen fibrous networks for potential use as wound dressing: from characterization to first evaluation of cytocompatibility. *BioResources* 15 (2): 2501–2511.

31 Zhang, D., Wei, X., Cai, J. et al. (2020). Citric acid-incorporated cellulose nanofibrous mats as food materials-based biosorbent for removal of hexavalent chromium from aqueous solutions. *Int. J. Biol. Macromol.* 149: 459–466.

32 Baji, A., Agarwal, K., and Oopath, S.V. (2020). Emerging developments in the use of electrospun fibers and membranes for protective clothing applications. *Polymers* 12 (2): 492.

33 Choi, H.Y., Bae, J.H., Hasegawa, Y. et al. (2020). Thiol-functionalized cellulose nanofiber membranes for the effective adsorption of heavy metal ions in water. *Carbohydr. Polym.* 234: 115881.

34 Ma, Z., Kotaki, M., and Ramakrishna, S. (2005). Electrospun cellulose nanofiber as affinity membrane. *J. Membr. Sci.* 265 (1–2): 115–123.

35 Liu, Y., Wang, Q., Yuan, L. et al. (2020). Synergistic enhancement of cytotoxicity against cancer cells by incorporation of rectorite into the paclitaxel immobilized cellulose acetate nanofibers. *Int. J. Biol. Macromol.* 152: 672–680.

36 Otsuka, I., Njinang, C.N., and Borsali, R. (2017). Simple fabrication of cellulose nanofibers via electrospinning of dissolving pulp and tunicate. *Cellulose* 24 (8): 3281–3288.

37 Lee, H., Nishino, M., Sohn, D. et al. (2018). Control of the morphology of cellulose acetate nanofibers via electrospinning. *Cellulose* 25 (5): 2829–2837.

38 Thomas, M.S., Pillai, P.K.S., Faria, M. et al. (2020). Polylactic acid/nano chitosan composite fibers and their morphological, physical characterization for the removal of cadmium (II) from water. *J. Appl. Polym. Sci.* 137 (34): 48993.

39 Jatoi, A.W., Kim, I.S., and Ni, Q.Q. (2019). A comparative study on synthesis of AgNPs on cellulose nanofibers by thermal treatment and DMF for antibacterial activities. *Mater. Sci. Eng., C* 98: 1179–1195.

40 Liu, Y., Fan, F., Wang, J. et al. (2014). In situ transmission electron microscopy study of electrochemical sodiation and potassiation of carbon nanofibers. *Nano Lett.* 14 (6): 3445–3452.

41 Zhang, J., Cohn, C., Qiu, W. et al. (2011). Atomic force microscopy of electrospun organic-inorganic lipid nanofibers. *Appl. Phys. Lett.* 99 (10): 103702.

42 Dong, H., Strawhecker, K.E., Snyder, J.F. et al. (2012). Cellulose nanocrystals as a reinforcing material for electrospun poly (methyl methacrylate) fibers: formation, properties and nanomechanical characterization. *Carbohydr. Polym.* 87 (4): 2488–2495.

43 Nezafati, N., Faridi-Majidi, R., Pazouki, M., and Hesaraki, S. (2019). Synthesis and characterization of a novel freeze-dried silanated chitosan bone tissue engineering scaffold reinforced with electrospun hydroxyapatite nanofiber. *Polym. Int.* 68 (8): 1420–1429.

44 Tao, F., Cheng, Y., Shi, X. et al. (2020). Applications of chitin and chitosan nanofibers in bone regenerative engineering. *Carbohydr. Polym.* 230: 115658.

45 Krüger, M., Spee, B., Walther, A. et al. (2019). Nanofibrillar cellulose as an enzymatically and flow driven degradable scaffold for three-dimensional tissue engineering. *J. Eng. Sci. Med. Diagn. Ther.* 2 (4): 041001. (8 pages).

46 Chuysinuan, P., Pengsuk, C., Lirdprapamongkol, K. et al. (2019). Enhanced structural stability and controlled drug release of hydrophilic antibiotic-loaded alginate/soy protein isolate core-sheath fibers for tissue engineering applications. *Fibers Polym.* 20 (1): 1–10.

47 Tan, H.-L., Kai, D., Pasbakhsh, P. et al. (2020). Electrospun cellulose acetate butyrate/polyethylene glycol (CAB/PEG) composite nanofibers: a potential scaffold for tissue engineering. *Colloids Surf., B* 188: 110713.

48 Chakraborty, P.K., Adhikari, J., and Saha, P. (2019). Facile fabrication of electrospun regenerated cellulose nanofiber scaffold for potential bone-tissue engineering application. *Int. J. Biol. Macromol.* 122: 644–652.

49 Xu, T., Yang, H., Yang, D., and Zhong-Zhen, Y. (2017). Polylactic acid nanofiber scaffold decorated with chitosan Islandlike topography for bone tissue engineering. *ACS Appl. Mater. Interfaces* 9 (25): 21094–21104.

50 Domard, A. and Domard, M. (2001). Chitosan: structure-properties relationship and biomedical applications. *Polym. Biomater.* 2: 187–212.

51 Ngwuluka, N.C., Ochekpe, N.A., and Aruoma, O.I. (2016). Functions of bioactive and intelligent natural polymers in the optimization of drug delivery. In: *Industrial Applications for Intelligent Polymers and Coatings*, 165–184. Springer.

52 Ran, J., Jiang, P., Sun, G. et al. (2017). Comparisons among Mg, Zn, Sr, and Si doped nano-hydroxyapatite/chitosan composites for load-bearing bone tissue engineering applications. *Mater. Chem. Front.* 1 (5): 900–910.

53 Özdoğan, A.I., Akca, G., and Şenel, S. (2018). Development and in vitro evaluation of chitosan based system for local delivery of atorvastatin for treatment of periodontitis. *Eur. J. Pharm. Sci.* 124: 208–216.

54 Jiang, H., Fang, D., Hsiao, B. et al. (2004). Preparation and characterization of ibuprofen-loaded poly (lactide-co-glycolide)/poly (ethylene glycol)-g-chitosan electrospun membranes. *J. Biomater. Sci., Polym. Ed.* 15 (3): 279–296.

55 Toshkova, R., Manolova, N., Gardeva, E. et al. (2010). Antitumor activity of quaternized chitosan-based electrospun implants against Graffi myeloid tumor. *Int. J. Pharm.* 400 (1–2): 221–233.

56 El-Newehy, M.H., El-Naggar, M.E., Alotaiby, S. et al. (2018). Green electrospining of hydroxypropyl cellulose nanofibres for drug delivery applications. *J. Nanosci. Nanotechnol.* 18 (2): 805–814.

57 Kumar, M., Dagmar, W., Böttcher, F.L.O.R.I.A.N. et al. (2017). PLA-HPC fibrous membranes for temperature-responsive drug release. In: *Nano Hybrids and Composites*, 18, 34–41. Trans Tech Publ.

58 Kong, M., Chen, X.G., Xing, K., and Park, H.J. (2010). Antimicrobial properties of chitosan and mode of action: a state of the art review. *Int. J. Food Microbiol.* 144 (1): 51–63.

59 Rabea, E.I., Badawy, M.E.-T., Stevens, C.V. et al. (2003). Chitosan as antimicrobial agent: applications and mode of action. *Biomacromolecules* 4 (6): 1457–1465.

60 Shahid, M. and Mohammad, F. (2013). Green chemistry approaches to develop antimicrobial textiles based on sustainable biopolymers—a review. *Ind. Eng. Chem. Res.* 52 (15): 5245–5260.

61 Shahidi, F., Arachchi, J.K.V., and Jeon, Y.-J. (1999). Food applications of chitin and chitosans. *Trends Food Sci. Technol.* 10 (2): 37–51.

62 Zargar, V., Asghari, M., and Dashti, A. (2015). A review on chitin and chitosan polymers: structure, chemistry, solubility, derivatives, and applications. *ChemBioEng Rev.* 2 (3): 204–226.

63 Ignatova, M., Manolova, N., Markova, N., and Rashkov, I. (2009). Electrospun non-woven nanofibrous hybrid mats based on chitosan and PLA for wound-dressing applications. *Macromol. Biosci.* 9 (1): 102–111.

64 Li, Y., Chen, F., Nie, J., and Yang, D. (2012). Electrospun poly(lactic acid)/chitosan core-shell structure nanofibers from homogeneous solution. *Carbohydr. Polym.* 90 (4): 1445–1451. https://doi.org/10.1016/j.carbpol.2012.07.013.

65 Goh, Y.-f., Akram, M., Alshemary, A., and Hussain, R. (2016). Antibacterial polylactic acid/chitosan nanofibers decorated with bioactive glass. *Appl. Surf. Sci.* 387: 1–7.

66 Kalantari, K., Afifi, A.M., Jahangirian, H., and Webster, T.J. (2018). Biomedical applications of chitosan electrospun nanofibers as a green polymer–review. *Carbohydr. Polym.*

67 Xu, X.-l., Zhou, G.-q., Li, X.-j. et al. (2016). Solution blowing of chitosan/PLA/PEG hydrogel nanofibers for wound dressing. *Fibers Polym.* 17 (2): 205–211.

68 Unnithan, A.R., Gnanasekaran, G., Sathishkumar, Y. et al. (2014). Electrospun antibacterial polyurethane–cellulose acetate–zein composite mats for wound dressing. *Carbohydr. Polym.* 102: 884–892.

69 Ahn, S., Chantre, C.O., Gannon, A.R. et al. (2018). Soy protein/cellulose nanofiber scaffolds mimicking skin extracellular matrix for enhanced wound healing. *Adv. Healthcare Mater.* 7 (9): 1701175.

70 Zhang, X., Guo, Q., and Cui, D. (2009). Recent advances in nanotechnology applied to biosensors. *Sensors* 9 (2): 1033–1053.

71 Li, K., Zhou, W., and Zeng, S. (2018). Optical micro/nanofiber-based localized surface plasmon resonance biosensors: fiber diameter dependence. *Sensors* 18 (10): 3295.

72 Teepoo, S., Dawan, P., and Barnthip, N. (2017). Electrospun chitosan-Gelatin biopolymer composite nanofibers for horseradish peroxidase immobilization in a hydrogen peroxide biosensor. *Biosensors* 7 (4): 47.

73 Baharifar, H., Honarvarfard, E., Malek-kheili, M.H. et al. (2017). The potentials and applications of cellulose acetate in biosensor technology. *Nanomed. Res. J.* 2 (4): 216–223. https://doi.org/10.22034/nmrj.2017.04.002.

9

Formation of Polysaccharide-Based Nanoparticles and Their Biomedical Application

Thomas Elschner

Institute of Plant and Wood Chemistry, Technische Universität Dresden, Pienner Straße 19, D-01737 Tharandt, Germany

9.1 Introduction

Nanoparticles are generally defined as solid, colloidal particles in the range of 10–1000 nm in diameter [1]. Within this chapter, the focus is on spherical polymer particles. The formation of micelles, polymersomes, or the coating of metal particles is not the subject of this summary. Therefore, the review of Wen and Oh (2014) about polysaccharide-based nanomaterials, including self-assembled micelles, crosslinked microgels/nanogels, three-dimensional hydrogels, and fibrous meshes, can be considered [2]. Polysaccharide-based nanoparticles are predestinated for an application in medicine and pharmacy. On one hand, natural biopolymers are superior to metals or other synthetic polymers due to the low concerns regarding toxicity, biodegradability, and physiological stability. On the other hand, polysaccharide-based nanoparticles may decrease uptake by the mononuclear phagocyte system compared to other types of nanoparticles, i.e. the accumulation on the target is favored since the immune defense is less active against the particles [3]. Moreover, the bioadhesion of polysaccharides, in particular to mucosal surfaces, is extended. Hydroxyl-, amine-, or carboxyl groups of polysaccharide-based nanoparticles allow biomedical multifunctionality by further derivatization. In this chapter, the self-assembly of hydrophobic polysaccharide derivatives is in spotlight. Esters, ethers, acetals, and deoxy derivatives of dextran and cellulose may provide hydrophobicity, functionality, or reactivity.

9.2 Nanoparticle Formation

For the preparation of nanomaterials, two different strategies are generally applied. On one hand, the top-down approach includes lithography and milling techniques. On the other hand, the biomimetic bottom-up strategy is based on self-assembly of molecules to supramolecular structures [4]. The latter method is

Functional Biomaterials: Design and Development for Biotechnology, Pharmacology, and Biomedicine, First Edition. Edited by Tamilselvan Mohan and Karin Stana Kleinschek.

of particular interest in order to yield nanoparticles from dissolved biopolymers. Polysaccharide-based nanoparticles have been reviewed several times [5–7] presenting preparation techniques such as covalent crosslinking, ionic crosslinking, and polyelectrolyte complexation. While most of the summaries are focused on water-soluble, natural polysaccharides, this chapter will highlight self-assembly of hydrophobically modified polysaccharides. In field of pharmacy, these nanoparticles were classified as aggregates or drug conjugates of amphiphilic polysaccharide derivatives [8].

The preparation of nanoparticles from polymer solutions was reviewed by Rao and Geckeler (2011) [9] and comprises the salt-out method as well as the supercritical fluid technology [10]. Moreover, the preparation methods of organic nanoparticles including polymer particles were reviewed by Horn and Rieger (2001) [11]. However, for the preparation of polysaccharide-based nanoparticles, there are three techniques established, namely nanoprecipitation by dropping, dialysis, and emulsification–evaporation. Dropping technique and dialysis are often summarized as nanoprecipitation or solvent displacement (Figure 9.1). The formation of nanoparticles by solvent displacement can be explained by the nucleation of macromolecules due to concentration fluctuations caused by the interdiffusion of solvent and nonsolvent [13]. Although the process of nanoparticle formation is not fully understood, the nanoprecipitation by dropping technique takes most likely place by the nucleation-and-aggregation mechanism. The nuclei are formed initially by the contact of hydrophobic material with water at the millisecond timescale and subsequently undergo an aggregation to primary nanoparticles at the second time scale. Dialysis and inverse dropping technique (water in polymer solution) are based on a slow nanoprecipitation by the nucleation-and-growth mechanism [14].

9.2.1 Nanoprecipitation by Dropping Technique

9.2.1.1 Methodology

The nanoprecipitation method [15] is based on interfacial deposition of a polymer after displacement of a solvent, miscible with water. The preparation is carried out by dropping technique, i.e. stepwise mixing of a dissolved hydrophobic material with water. Nonpolar polymer chains become separated as droplets or particles

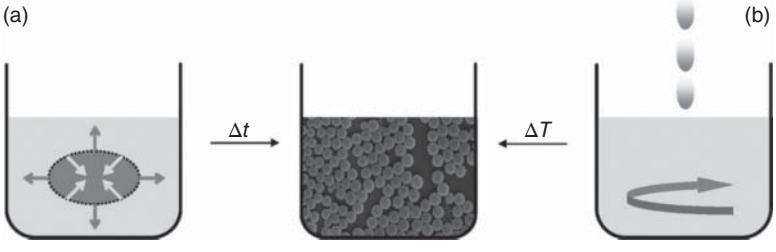

Figure 9.1 Schematic presentation of nanoprecipitation methods applying dialysis (a) and the dropping technique under stirring (b). Source: Hornig et al. [12]/with permission of the Royal Society of Chemistry.

in the solution with increasing polarity. Due to the increasing turbidity of the solution during nanoprecipitation, the formation of particles is called "Ouzo"effect. High initial concentration of the polymer solution causes the formation of nano- and microparticles (non-"Ouzo" region). Below a certain polymer concentration ("Ouzo" boundary), there is the formation of nanoparticles only [16]. In practice, the boundary is observed at the critical overlapping concentration c*. Beyond c* entanglements between the polymer chains lead to a broad particle size distribution due to the formation of nanoparticles, microparticles, or macroscopic aggregates. C* is determined by the crossing of two linear fits from concentration-reduced viscosity plots (Figure 9.2).

After the first step of nanoprecipitation, the particles formed are existent in a water–solvent mixture. Therefore, solvents that are easy to remove by evaporation, e.g. acetone or tetrahydrofuran (THF), are chosen. Moreover, the purification of the particle suspension by dialysis is an option.

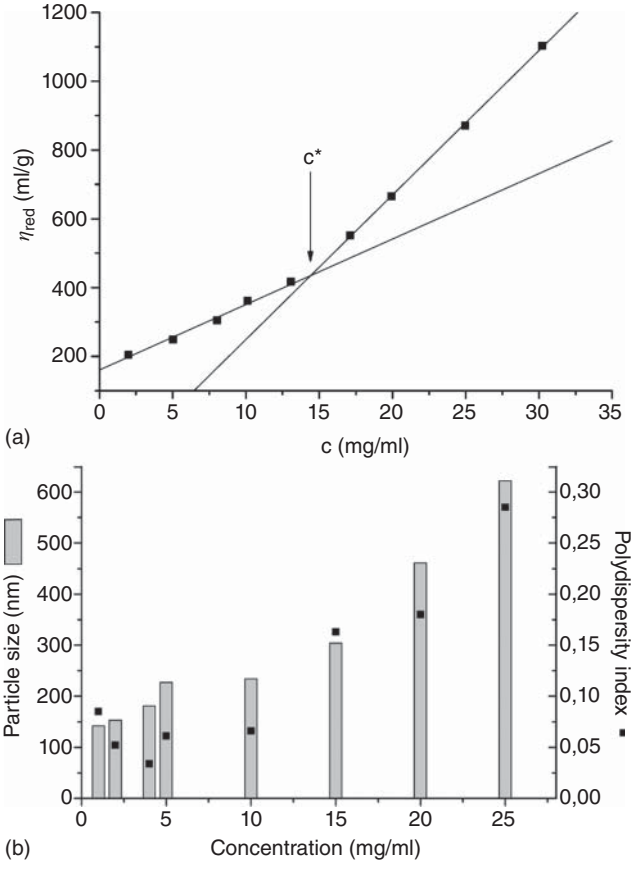

Figure 9.2 Plot of the reduced viscosity vs. the concentration of cellulose acetate; c* indicates critical overlapping concentration (a). Particle size and polydispersity index of nanoparticles obtained by dialysis depending on the concentration of cellulose acetate (b). Source: Hornig and Heinze [17]/with permission of American Chemical Society.

9.2.1.2 Examples

One of the first polysaccharide-based nanoparticle suspensions was prepared by nanoprecipitation of hydroxypropyl methyl cellulose phthalate in acetone/water [15]. An amount of 2.4% of progesterone was encapsulated in the nanoparticles with a mean diameter of 250 ± 25 nm.

A detailed study about nanoparticle formation of cellulose esters by dropping technique yielded bean-shaped morphologies [17]. Mainly, nanoparticles from cellulose acetate with different degree of substitution (DS) values were prepared in acetone by dropwise addition of water to the polymer solution or vice versa. If the acetone solution of the polymer was dropped into water, small particles and large precipitates in the millimeter scale occurred (high polydispersity index, PDI). Dropping water into acetone solution leads to nanoprecipitation without aggregation due to the slow increase of water content in the mixture (PDI < 0.1). In more detailed studies, the diameter of cellulose acetate particles depending on the ratio of water and acetone was investigated. The size of the final particles increased with increasing amount of added water until a certain water/acetone ratio was reached [13]. Moreover, the concentration of the polymer solution and the rate of water addition were varied. However, it was difficult to show regular trends. The dropping technique using acetone/water was also adapted for the preparation of nanoparticles from ibuprofen dextran esters [18]. The particles possessed a spherical shape and a z-average mean diameter of about 70–350 nm as determined by DLS.

Beside the slow particle formation by strictly speaking inverse dropping technique, very hydrophobic derivatives self-assemble into very uniform particles by the nucleation-and-aggregation mechanism. Cellulose stearoyl esters were shaped into nanospheres by dropping a polymer solution (THF) into water (Figure 9.3) [19]. A modification of the procedure, i.e. dropping without stirring or pouring, leads to similar particle sizes of around 200 nm (PDI < 0.1) if polymer solutions of 5 mg/ml were applied. The authors observed a shrinkage of up to 35% due to the release of THF accompanied by further crystallization of polymer chains via stearoyl groups. Extended studied with cellulose stearoyl-, lauroyl-, and caproyl ester showed a temperature-responsive crystalline structure of nanoparticles [20].

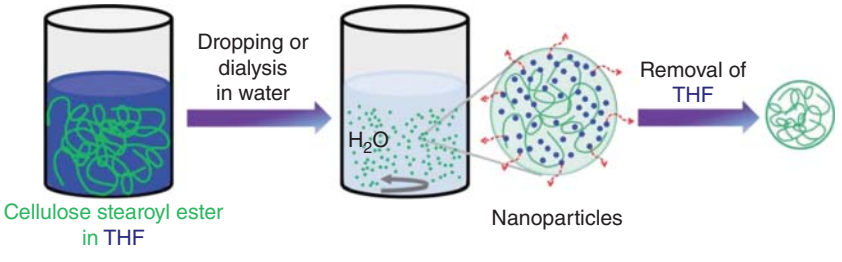

Figure 9.3 Schematic illustration for the nanoprecipitation of cellulose stearoyl ester. Source: Geissler et al. [19]/with permission of the Royal Society of Chemistry.

9.2.2 Dialysis

9.2.2.1 Methodology

For dialysis, the polymer is dissolved and placed into a dialysis tube surrounded by a precipitating medium. The procedure is based on the passive transport of small molecules through a semipermeable membrane (osmosis) enabling slow mixing of the polymer solution with the nonsolvent available at the outer side of the membrane. The displacement of the solvent inside the membrane is followed by the progressive aggregation of polymer due to a loss of solubility and the formation of homogeneous suspensions of nanoparticles [9]. The properties of the particles are influenced by type and concentration of polymer, difference between the dielectric constant values of the solvent/nonsolvent pair ($\Delta\varepsilon$), temperature, and "molecular weight cut off" (MWCO) of the membrane [21]. For instance, the particle size of poly(phenylacetylene) (PPA) gets smaller with decreasing polymer concentration, MWCO, and temperature. A decrease in $\Delta\varepsilon$ leads to formation of bigger and spherical particles, but an increase of $\Delta\varepsilon$ results in sponge-like structures (Figure 9.4). For polysaccharide derivatives in particular, the hydrophobic–hydrophilic balance, arising from DS and nature of the substituent, has to be considered.

9.2.2.2 Examples

In 2005, Liebert and Hornig et al. started extensive studies regarding the particle formation of dextran esters by dialysis from *N*,*N*-dimethylacetamide (DMA) solutions against water (Figure 9.5). Dextran propionate pyroglutamate derivatives could be shaped into spherical particles possessing a diameter of about 300 nm [23]. Dextran furoate pyroglutamate was formed into particles of 250–500 nm in diameter, depending on molecular weight and DS values [22, 24, 25]. Products with low DS values were propionylated or acetylated to improve the particle formation. Dialysis procedure was also applied for the preparation of nanospheres from ibuprofen- and naproxen dextran esters [18]. Depending on the DS value and the substituent, particle sizes between 100 and 450 nm were measured by DLS. Photochromic dextran esters of 2-methoxycinnamic acid, [(4-methyl-2-oxo-2Hchromen-7-yl)oxy]acetic

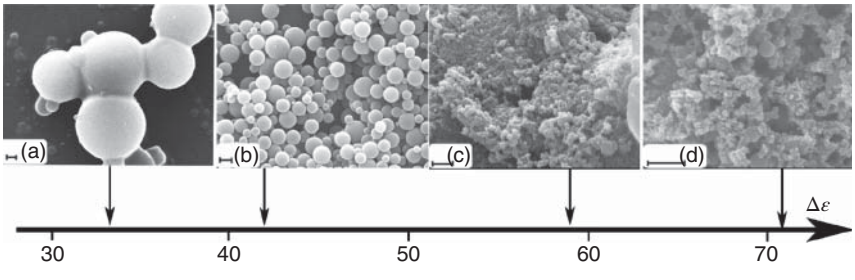

Figure 9.4 Dependence of particle morphology from $\Delta\varepsilon$ of solvent pair: (a) DMF/hexane, (b) DMF/H_2O, (c) acetone/H_2O, (d) THF/H_2O. Source: Chronopoulou et al. [21]/with permission of American Chemical Society.

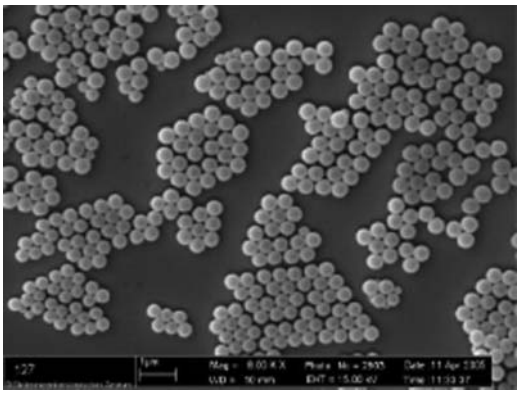

Figure 9.5 SEM images of dextran furoate pyroglutamate nanospheres. Source: Hornig et al. [22]/with permission of John Wiley & Sons.

acid, and azobenzene-4-carboxylic acid could be shaped into nanospheres with a diameter in the range from 90 to 300 nm [26, 27].

In addition to dextran esters, cellulose esters could be shaped into nanospheres by dialysis. Nanoparticles of cellulose stearoyl esters were obtained by dialysis of a polymer solution in THF against water. The average size of the particles was found to be larger compared to those obtained by dropping technique [19]. Nanospheres of less hydrophobic cellulose esters, e.g. acetates, were yielded by dialysis from DMA solutions against water [17, 28]. Reactive polysaccharide derivatives, namely carbonates [29], tosylates, azides, and NHS-esters, are interesting to enable postmodifications on nanoparticles. Dextran alkyl carbonates, dissolved in DMA, were shaped into nanospheres by dialysis against water, and different particle diameters in the range from 150 to 600 nm were observed [30]. A similar approach leads to nanoparticles of xylan phenyl carbonate [31]. Moreover, reactive nanoparticles were prepared from (perpropionylated) tosyl dextran and deoxy-azido tosyl dextran [32]. Tosylated polysaccharides are predestinated to form deoxyamino derivatives, e.g. aminocelluloses, which could be assembled into nanoparticles, too [33, 34]. Nanospheres of the NHS ester of cellulose acetate phthalate, prepared by dialysis, were found to be reactive with amine-functionalized compounds in aqueous phase. After a reaction with fluorescent dyes or ethanolamine the covalent bonding was spectrometrically proofed [28].

9.2.3 Emulsification–Evaporation

9.2.3.1 Methodology

The emulsification–evaporation process can be used for preparation of hydrophobic nanoparticles dispersed in water. Anton et al. (2008) reviewed theoretical and practical aspects of the preparation of nanoemulsions and the formation of nanoparticles [35]. The loading of nanoparticles with water-soluble drugs can be performed by double-emulsion solvent evaporation technique. Following this method, a first emulsion was obtained by sonication of an aqueous solution containing the drug (low volume) with an immiscible organic solvent, e.g. ethyl acetate or dichloromethane, containing the hydrophobic polymer (Figure 9.6). The first

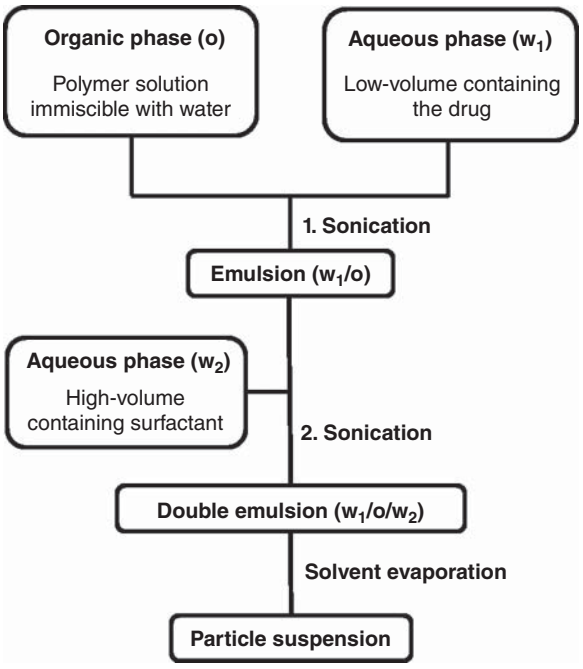

Figure 9.6 Schematic diagram of the nanoparticle formation by double-emulsion solvent evaporation technique.

(w_1/o) emulsion is dispersed by a second sonication step in an external aqueous phase containing a surfactant. The organic solvent is removed by evaporation from the double emulsion (w_1/o/w_2) to yield solid particles. Subsequent centrifugation and redispersion in water might be necessary to remove the surfactant. The intensity and duration of the second sonication step is crucial for the particle formation. Sensitive drugs, such as peptides and proteins, can be preserved by a gentle sonication in the first step [36]. An interesting option of the emulsion–evaporation process is the inverse miniemulsion system. The polysaccharide (e.g. hyaluronic acid or hydroxylethyl starch) is dissolved in the aqueous phase and sonicated with a solution of organic solvent (e.g. cyclohexane) with surfactant. Subsequently, the polysaccharide is cross-linked by a diisocyanate, and particles can be isolated into an aqueous phase [37]. The emulsification–evaporation technique yields very small and uniformly distributed particles in short time with excellent reproducibility. While solvent displacement methods are limited to polymer concentrations below c*, this procedure allows high concentrations to prepare large amounts of nanoparticles very efficiently [13].

9.2.3.2 Examples

A prominent example is the nanoparticle formation of acetal-derivatized dextran [38, 39]. This material is degraded under mildly acid conditions (pH 5.5) and thus predestinated for drug-delivery systems. For emulsion formation dichloromethane (solvent) and polyvinyl alcohol (surfactant) were used. The particles were loaded with 3.7% ovalbumin by double-emulsion technique and possessed an average

diameter of 230 ± 93 nm as determined by DLS. Pyrene was encapsulated by single-emulsion technique with a loading of 3.6% (particle diameter: 258 ± 70 nm).

A similar emulsification–evaporation procedure was carried out by Wondraczek et al. [13]. Cellulose esters, e.g. acetates, acetate propionate, butyrate, were formed into nanoparticles by single-emulsion technique applying dichloromethane and polyvinyl alcohol. The obtained highly uniform particles possessed z-average diameters of about 200–250 nm and a PDI below 0.1.

A comprehensive study about the formation of ethyl cellulose (EC) nanoparticles was carried out by Bozic et al. [40]. EC nanoparticles were obtained by single-emulsion technique with ethyl acetate as chlorine-free organic solvent. The influence of different polysaccharide-based surfactants, i.e. carboxymethyl cellulose CMC (ionic), hydroxyethyl cellulose (nonionic), and methyl cellulose (amphiphilic) with different molecular weights, was studied by scanning electron microscopy (SEM), dynamic light scattering (DLS), zeta potential measurements, Fourier-transform infrared spectroscopy (FTIR), rheology, and tensiometry. High-molecular-weight polysaccharides increased the viscosity of emulsions leading to less favorable mixing resulting in semi-spherical microscale particle sizes. Lower-molecular CMC and methyl cellulose took less space in the aqueous solvent, their small hydrodynamic volume led to favorable mixing efficiency resulting in smooth spherical nanoparticles (Figure 9.7). Surface-active polysaccharides interacted with EC and new supramolecular structures were formed, i.e. the

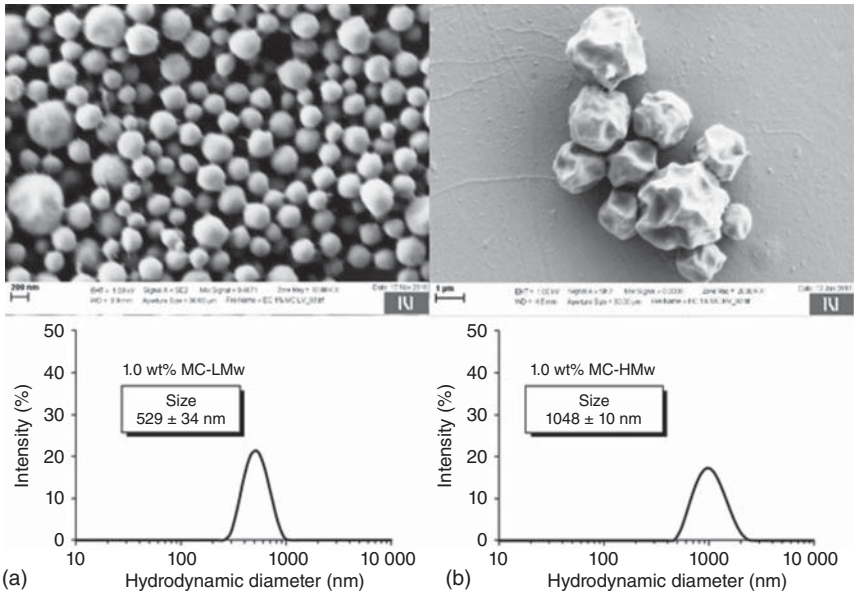

Figure 9.7 FE-SEM images of ethyl cellulose particles prepared in the presence of methyl cellulose (MC) at the concentration of 1 wt% as surfactant; (a) low-molecular-weight MC, (b) high-molecular-weight (MC). Source: Božič et al. [40]/with permission from Springer Nature/CC BY 4.0.

surfactants were integrated into the EC particle surface by intra- and intermolecular hydrogen bonds.

Recently, dextran amino acid ester particles derived from N-protected *S*-trityl-L-cysteine were formed into nanoparticles by emulsification–evaporation technique using chloroform as organic solvent and dextran as surfactant [41]. The particles possessed an average dry diameter of 325 ± 118 nm.

9.2.4 Miscellaneous Nanoparticle Formation

Last but not least, there are unconventional examples encouraging to think outside the box. The preparation of pure cellulose nanoparticles with diameters of 100–200 nm could be performed by dialysis of trimethylsilyl cellulose dissolved in DMA or THF against water. As confirmed by FTIR spectroscopy, the silyl groups are completely removed during this process [42, 43]. The preparation of polysaccharide composite nanoparticles was carried out by dropping a solution of cellulose acetate in THF into an aqueous solution containing a water-soluble polysaccharide derivative. The particle formation was performed by stirring and sonication with subsequent evaporation of the organic solvent. Functionalization of cellulose acetate nanoparticles with hydroxyethyl cellulose, CMC, low-molecular-weight chitosan, and amino cellulose enabled the control of particle size, charge, effective zeta potential, and stability [44].

9.3 Interaction with Cells

9.3.1 Cellular Uptake

Polysaccharides are predestinated for nanoparticulate drug or gene carriers due to their inherent biocompatibility and biodegradability. Moreover, they are nontoxic and tunable for therapeutic application and cellular mechanism. Nanoparticles may enter living cells by several endocytic pathways or by passive penetration of the plasma membrane. The cellular uptake of polysaccharide nanoparticles by endocytosis was reviewed by Salatin and Khosroushahi [45] including the explanation of main pathways such as phagocytosis (cell eating) and pinocytosis (cell drinking), which can be further subdivided into macropinocytosis, clathrin-mediated endocytosis, caveolin-mediated endocytosis, and clathrin-caveolin-independent endocytosis (Figure 9.8). In brief, the cellular uptake is influenced by characteristics of nanoparticles including size, shape, and surface chemistry. For example, the uptake of particles increases with decreasing size due to the higher specific surface area being in contact with the cell membrane. An analogous explanation is used for an elongated particle shape which can interact more efficiently with the cell membrane, compared to a nanosphere. However, the cellular uptake of spheric cellulose nanoparticles was found to be superior to rod-like cellulose nanocrystals of comparable size. Confocal microscopy revealed the incorporation of cellulose nanospheres into human fibroblasts without attachment of a receptor selective

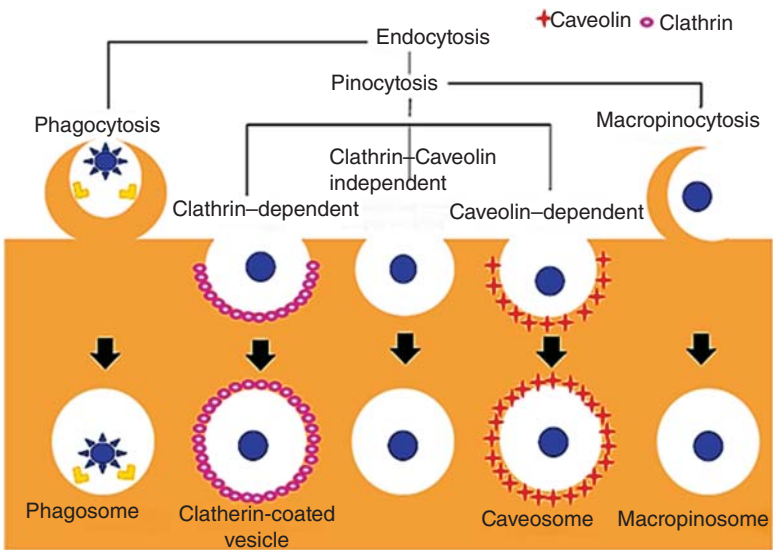

Figure 9.8 Scheme for the main pathways of nanoparticle endocytosis. Source: Salatin and Yari Khosroushahi [45]/John Wiley & Sons/CC BY 4.0.

molecule, as it is necessary for cellulose nanocrystals [46]. A fast cellular uptake of cellulose nanospheres possessing an average diameter of 80–260 nm was observed without transfection reagents.

9.3.2 Nanospheres of Organo-Soluble 6-Deoxy-6-(ω-Aminoalkyl) Amino Cellulose Carbamates

Amino cellulose particles with sizes from 80 to 200 nm were very stable, nontoxic, and possessed primary amino groups that were accessible for further modifications in aqueous suspension. For instance, particles could be labeled with rhodamine B isothiocyanate without any change in size, stability, and shape as proofed by photocorrelation spectroscopy, zeta potential measurements, SEM, and fluorescence spectroscopy [33]. Confocal laser scanning microscopy revealed the uptake of these nanoparticles in human foreskin fibroblasts BJ1-hTERT and breast carcinoma MCF-7 cells without utilization of any transfection reagent. Nanospheres of 6-deoxy-6-(2-aminoethyl)amino (AEA) and 6-deoxy-6-(2-bis[*N*′,*N*′-(2-aminoethyl)]-aminoethyl)amino (BAEA) cellulose carbamate with an average diameter of 80–120 nm possessed significant antimicrobial activity with moderate cell compatibility [47]. An antibacterial activity against *Staphylococcus aureus* and *Klebsiella pneumoniae* of the particles was found, in a similar range like a solution of a parent aminocellulose. However, the particles exhibited an improved biocompatibility as studied with HaCaT cells. The lower toxicity of the nanoparticles compared to the solution of the amino cellulose could not be satisfactorily explained up to now.

9.4 Release Mechanisms

As discussed in Section 9.5, polysaccharide nanoparticles can be applied in cancer and inflammation treatment as well as theranostics. However, internal and external triggers for on-demand release, such as pH value, redox potential, temperature, enzymes, or light, have to be considered and were reviewed by Yang et al. (Figure 9.9) [8]. One feature of hydrophilic polysaccharide chains is their enzyme-responsive behavior. The overexpression of hyaluronidase in tumor microenvironments promotes the degradation of hyaluronic-acid-based nanomaterials [8, 48]. Moreover, polysaccharide chains can be reactive oxygen species (ROS)-responsive, i.e. they are oxidatively depolymerized [49–52].

In addition to the ROS-cleavable polysaccharide backbone, hydrophobic moieties (substituents) may possess ROS-sensitivity. Due to a low concentration of endogenous ROS, short lifetime (<200 ns), and restricted diffusion range (<20 nm) [53], light-triggered ROS-generators have been an attractive research field [8]. For instance, the particle-forming pullulan lipoic acid ester acts as ROS scavenger and was combined with a chlorin e6 moiety generating ROS to induce DOX release [53]. Light-responsive polysaccharide nanoparticles could be obtained by installing photosensitive *o*-nitrobenzyl succinate groups [54, 55]. Cleavable linkages to the polysaccharide backbone were designed to be pH- and redox-responsive. pH-sensitive derivatives are for instance acetals or hydrazones. Disulfide- and boronic acid-based cross-linkers are redox- and pH-sensitive, respectively [8].

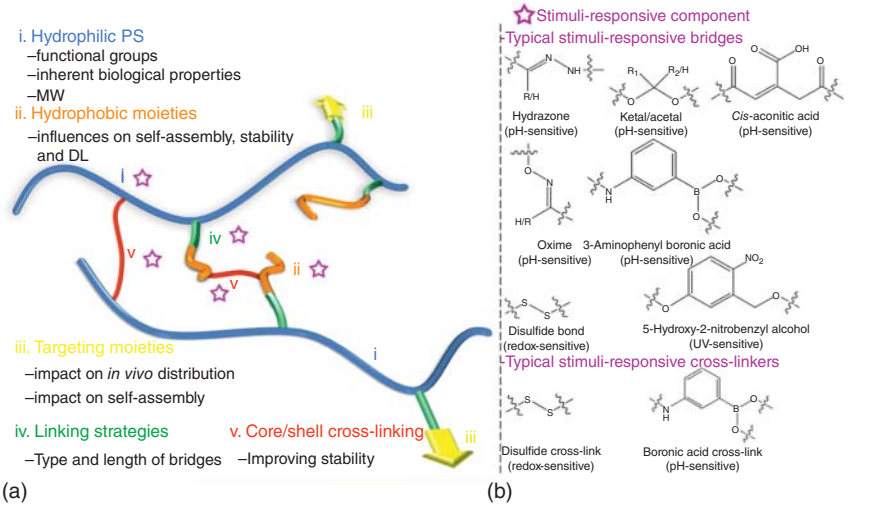

Figure 9.9 (a) Structural features of amphiphilic polysaccharide derivatives: i. hydrophilic PS chains; ii. hydrophobic moieties; iii. targeting moieties; iv. linking strategies; v. cross-linking strategies. Stimuli-responsive components can exist in parts i, ii, iv, and v; (b) Typical stimuli-responsive linkers and cross-linkers Source: Yang et al. [8]/with permission of Elsevier.

9.5 Examples in Therapeutics and Diagnostics

Due to the wide spread of dextran in medicine and pharmacy, this polysaccharide is also extensively used for nanoparticles. One example is intracellular pH measurement by means of dextran-based nanospheres. Dextran was hydrophobized by propionylation and labeled with sulforhodamine B and fluorescein applying the corresponding acid chloride or isothiocyanate, respectively. Human fibroblasts were loaded with these nanoparticles to enable ratiometric pH measurements in the cells by fluorescence spectroscopy. The ratio of sensor- and reference dye can be varied to tune the dynamic range and the sensitivity of the nanosensors [56].

Acetylated dextran is an acid-sensitive material obtained from the conversion of the biopolymer with 2-methoxypropene [38]. The hydrophobic derivative could be shaped into nanoparticles loaded with ovalbumin. Due to release of protein under mildly acidic conditions, the particles are predestinated for immunotherapy. Within a study, B3Z cells were used to quantify MHC I (major histocompatibility complex class I) presentation from BMDCs (bone-marrow-derived dendritic cells) after incubation with ovalbumin-loaded particles. The tailoring of acetylated dextran could improve the MHC I presentation efficiency, and thus, the nanomaterial is superior to PLGA- or iron oxide particles [39].

Recently, functional dextran amino acid ester particles derived from N-protected *S*-trityl-L-cysteine were found to be nontoxic for lung epithelial cells. The particles are a carrier for the BOC-protected mitotic kinesin Eg5 inhibitor STLC, and the potential of this material as a drug-delivery vehicle is under investigation [41]. Research on the improvement of chemotherapy with dextran-based nanoparticles is focused on the controlled delivery of doxorubicin (DOX) and paclitaxel (PTX). For instance, the lipoic acid ester of dextran forms nanoparticles in water. The core could be cross-linked by dithiothreitol (DTT). In cancer cells, de-cross-linking is triggered by a high concentration of glutathione (GSH) tripeptides inducing the release of DOX to the cell nucleus (Figure 9.10) [57]. Another example is the utilization of folic acid ester of dextran. The drug targeting of DOX-loaded nanoparticles is performed by folate receptors, which are overexpressed in many cancer cells [58]. Moreover, these two principles based on lipoic acid and folic acid derivatives were combined in one nanoparticle to enable PTX release [59]. Nanoparticles based on the deoxycholic acid ester showed a pH-dependent release of DOX, i.e. there was an increased release with decreasing pH value. Moreover, the *in vitro* cellular uptake revealed that nanoparticles based on a polysaccharide from *Angelica sinensis* were internalized into HepG2 cells through ASGPR-mediated endocytosis, resulting in a higher antiproliferation effect than DOX-loaded dextran-based nanoparticles [60].

Finally, nanoparticles of carboxymethyl dextran (CMD) are applicable for release of DOX under hypoxic conditions present in tumor tissues. The 2-nitroimidazole derivative of CMD is hypoxia-responsive since 2-nitroimidazole converts to hydrophilic 2-aminoimidazoles through a series of reductive processes, and the release rate of DOX is remarkably increased [3, 61]. A similar approach is based on CMD with a BHQ3 moiety (black hole quencher 3). The release of DOX takes place under hypoxic conditions throughout the cleavage of the azo bond in BHQ3 [62].

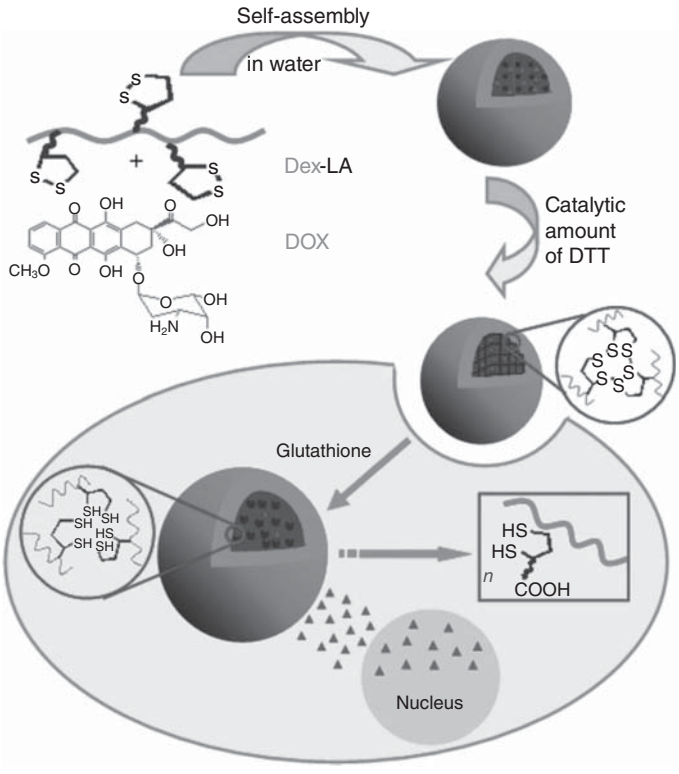

Figure 9.10 Schematic illustration of formation and effect mechanism of multifunctional dextran nanoparticles. Source: Li et al. [57]/with permission of John Wiley & Sons.

References

1 Kreuter, J. (1994). Drug targeting with nanoparticles. *Eur. J. Drug Metab. Pharmacokinet.* 19 (3): 253–256.

2 Wen, Y. and Oh, J.K. (2014). Recent strategies to develop polysaccharide-based nanomaterials for biomedical applications. *Macromol. Rapid Commun.* 35 (21): 1819–1832.

3 Swierczewska, M., Han, H.S., Kim, K. et al. (2016). Polysaccharide-based nanoparticles for theranostic nanomedicine. *Adv. Drug Delivery Rev.* 99: 70–84.

4 Shimomura, M. and Sawadaishi, T. (2001). Bottom-up strategy of materials fabrication: a new trend in nanotechnology of soft materials. *Curr. Opin. Colloid Interface Sci.* 6 (1): 11–16.

5 Liu, Z., Jiao, Y., Wang, Y. et al. (2008). Polysaccharides-based nanoparticles as drug delivery systems. *Adv. Drug Delivery Rev.* 60 (15): 1650–1662.

6 López-López, E.A., Hernández-Gallegos, M.A., Cornejo-Mazón, M. et al. (2015). *Polysaccharide-based nanoparticles*. In: *Food Nanoscience and Nanotechnology* (ed. H. Hernández-Sánchez and G.F. Gutiérrez-López), 59–68. Cham: Springer International Publishing.

7 Khan, W., Abtew, E., Modani, S. et al. (2018). Polysaccharide based nanoparticles. *Isr. J. Chem.* 58 (12): 1315–1329.

8 Yang, X., Shi, X., D'Arcy, R. et al. (2018). Amphiphilic polysaccharides as building blocks for self-assembled nanosystems: molecular design and application in cancer and inflammatory diseases. *J. Controlled Release* 272: 114–144.

9 Rao, J.P. and Geckeler, K.E. (2011). Polymer nanoparticles: preparation techniques and size-control parameters. *Prog. Polym. Sci.* 36 (7): 887–913.

10 Zu, Y., Wang, D., Zhao, X. et al. (2011). A novel preparation method for camptothecin (CPT) loaded folic acid conjugated dextran tumor-targeted nanoparticles. *Int. J. Mol. Sci.* 12 (7): 4237–4249.

11 Horn, D. and Rieger, J. (2001). Organic nanoparticles in the aqueous phase—theory, experiment, and use. *Angew. Chem. Int. Ed.* 40 (23): 4330–4361.

12 Hornig, S., Heinze, T., Becer, C.R. et al. (2009). Synthetic polymeric nanoparticles by nanoprecipitation. *J. Mater. Chem.* 19 (23): 3838–3840.

13 Wondraczek, H., Petzold-Welcke, K., Fardim, P. et al. (2013). Nanoparticles from conventional cellulose esters: evaluation of preparation methods. *Cellulose* 20 (2): 751–760.

14 Vitale, S.A. and Katz, J.L. (2003). Liquid droplet dispersions formed by homogeneous liquid–liquid nucleation: "The Ouzo Effect". *Langmuir* 19 (10): 4105–4110.

15 Fessi, H., Puisieux, F., Devissaguet, J.P. et al. (1989). Nanocapsule formation by interfacial polymer deposition following solvent displacement. *Int. J. Pharm.* 55 (1): R1–R4.

16 Aubry, J., Ganachaud, F., Cohen Addad, J.-P. et al. (2009). Nanoprecipitation of polymethylmethacrylate by solvent shifting: 1. Boundaries. *Langmuir* 25 (4): 1970–1979.

17 Hornig, S. and Heinze, T. (2008). Efficient approach to design stable water-dispersible nanoparticles of hydrophobic cellulose esters. *Biomacromolecules* 9 (5): 1487–1492.

18 Hornig, S., Bunjes, H., and Heinze, T. (2009). Preparation and characterization of nanoparticles based on dextran–drug conjugates. *J. Colloid Interface Sci.* 338 (1): 56–62.

19 Geissler, A., Biesalski, M., Heinze, T. et al. (2014). Formation of nanostructured cellulose stearoyl esters via nanoprecipitation. *J. Mater. Chem. A* 2 (4): 1107–1116.

20 Zhang, K., Geissler, A., and Heinze, T. (2015). Reversibly crystalline nanoparticles from cellulose alkyl esters via nanoprecipitation. *Part. Part. Syst. Char.* 32 (2): 258–266.

21 Chronopoulou, L., Fratoddi, I., Palocci, C. et al. (2009). Osmosis based method drives the self-assembly of polymeric chains into micro- and nanostructures. *Langmuir* 25 (19): 11940–11946.

22 Hornig, S., Heinze, T., Hesse, S. et al. (2005). Novel nanoparticles based on dextran esters with unsaturated moieties. *Macromol. Rapid Commun.* 26 (24): 1908–1912.

23 Liebert, T., Hornig, S., Hesse, S. et al. (2005). Nanoparticles on the basis of highly functionalized dextrans. *J. Am. Chem. Soc.* 127 (30): 10484–10485.

24 Hornig, S., Liebert, T., and Heinze, T. (2007). Structure design of multifunctional furoate and pyroglutamate esters of dextran by polymer-analogous reactions. *Macromol. Biosci.* 7 (3): 297–306.

25 Hornig, S. and Heinze, T. (2007). Nanoscale structures of dextran esters. *Carbohydr. Polym.* 68 (2): 280–286.

26 Wondraczek, H. and Heinze, T. (2008). Efficient synthesis and characterization of new photoactive dextran esters showing nanosphere formation. *Macromol. Biosci.* 8 (7): 606–614.

27 Wondraczek, H., Kotiaho, A., Niemi, M. et al. (2013). Studies on the structure of coumarin-modified dextran nanoparticles by fluorescence spectroscopy. *Carbohydr. Polym.* 97 (1): 45–51.

28 Schulze, P., Gericke, M., Scholz, F. et al. (2016). Incorporation of hydrophobic dyes within cellulose acetate and acetate phthalate based nanoparticles. *Macromol. Chem. Phys.* 217 (16): 1823–1833.

29 Elschner, T. and Heinze, T. (2015). Cellulose carbonates: a platform for promising biopolymer derivatives with multifunctional capabilities. *Macromol. Biosci.* 15 (6): 735–746.

30 Wondraczek, H., Elschner, T., and Heinze, T. (2011). Synthesis of highly functionalized dextran alkyl carbonates showing nanosphere formation. *Carbohydr. Polym.* 83 (3): 1112–1118.

31 Gericke, M., Gabriel, L., Geitel, K. et al. (2018). Synthesis of xylan carbonates – An approach towards reactive polysaccharide derivatives showing self-assembling into nanoparticles. *Carbohydr. Polym.* 193: 45–53.

32 Heinze, T., Michealis, N., and Hornig, S. (2007). Reactive polymeric nanoparticles based on unconventional dextran derivatives. *Eur. Polym. J.* 43 (3): 697–703.

33 Nikolajski, M., Wotschadlo, J., Clement, J.H. et al. (2012). Amino-functionalized cellulose nanoparticles: preparation, characterization, and interactions with living cells. *Macromol. Biosci.* 12 (7): 920–925.

34 Obst, M. and Heinze, T. (2016). Simple synthesis of reactive and nanostructure forming hydrophobic amino cellulose derivatives. *Macromol. Mater. Eng.* 301 (1): 65–70.

35 Anton, N., Benoit, J.-P., and Saulnier, P. (2008). Design and production of nanoparticles formulated from nano-emulsion templates—a review. *J. Controlled Release* 128 (3): 185–199.

36 Bilati, U., Allémann, E., and Doelker, E. (2003). Sonication parameters for the preparation of biodegradable nanocapsules of controlled size by the double emulsion method. *Pharmaceut. Develop. Technol.* 8 (1): 1–9.

37 Kang, B., Opatz, T., Landfester, K. et al. (2015). Carbohydrate nanocarriers in biomedical applications: functionalization and construction. *Chem. Soc. Rev.* 44 (22): 8301–8325.

38 Bachelder, E.M., Beaudette, T.T., Broaders, K.E. et al. (2008). Acetal-derivatized dextran: an acid-responsive biodegradable material for therapeutic applications. *J. Am. Chem. Soc.* 130 (32): 10494–10495.

39 Broaders, K.E., Cohen, J.A., Beaudette, T.T. et al. (2009). Acetalated dextran is a chemically and biologically tunable material for particulate immunotherapy. *Proc. Natl. Acad. Sci. U.S.A.* 106 (14): 5497.

40 Božič, M., Elschner, T., Tkaučič, D. et al. (2018). Effect of different surface active polysaccharide derivatives on the formation of ethyl cellulose particles by the emulsion-solvent evaporation method. *Cellulose* 25 (12): 6901–6922.

41 Bratuša, A., Elschner, T., Heinze, T. et al. (2019). Functional dextran amino acid ester particles derived from N-protected S-trityl-L-cysteine. *Colloids Surf., B* 181: 561–566.

42 Köhler, S., Liebert, T., and Heinze, T. (2008). Interactions of ionic liquids with polysaccharides. VI. Pure cellulose nanoparticles from trimethylsilyl cellulose synthesized in ionic liquids. *J. Polym. Sci., Part A: Polym. Chem.* 46 (12): 4070–4080.

43 Kostag, M., Köhler, S., Liebert, T. et al. (2010). Pure cellulose nanoparticles from trimethylsilyl cellulose. *Macromol. Symp.* 294 (2): 96–106.

44 Kulterer, M.R., Reichel, V.E., Kargl, R. et al. (2012). Functional polysaccharide composite nanoparticles from cellulose acetate and potential applications. *Adv. Funct. Mater.* 22 (8): 1749–1758.

45 Salatin, S. and Yari Khosroushahi, A. (2017). Overviews on the cellular uptake mechanism of polysaccharide colloidal nanoparticles. *J. Cell. Mol. Med.* 21 (9): 1668–1686.

46 Liebert, T., Kostag, M., Wotschadlo, J. et al. (2011). Stable cellulose nanospheres for cellular uptake. *Macromol. Biosci.* 11 (10): 1387–1392.

47 Wiegand, C., Nikolajski, M., Hipler, U.-C. et al. (2015). Nanoparticle formulation of AEA and BAEA cellulose carbamates increases biocompatibility and antimicrobial activity. *Macromol. Biosci.* 15 (9): 1242–1251.

48 Chao, K.L., Muthukumar, L., and Herzberg, O. (2007). Structure of human hyaluronidase-1, a hyaluronan hydrolyzing enzyme involved in tumor growth and angiogenesis. *Biochemistry* 46 (23): 6911–6920.

49 Schweikert, C., Liszkay, A., and Schopfer, P. (2002). Polysaccharide degradation by Fenton reaction- or peroxidase-generated hydroxyl radicals in isolated plant cell walls. *Phytochemistry* 61 (1): 31–35.

50 Liu, P., Yue, C., Sheng, Z. et al. (2014). Photosensitizer-conjugated redox-responsive dextran theranostic nanoparticles for near-infrared cancer imaging and photodynamic therapy. *Polym. Chem.* 5 (3): 874–881.

51 Park, W., Bae, B.C., and Na, K. (2016). A highly tumor-specific light-triggerable drug carrier responds to hypoxic tumor conditions for effective tumor treatment. *Biomaterials* 77: 227–234.

52 Jeong, D., Bae, B.C., Park, S.J. et al. (2016). Reactive oxygen species responsive drug releasing nanoparticle based on chondroitin sulfate–anthocyanin nanocomplex for efficient tumor therapy. *J. Controlled Release* 222: 78–85.

53 Seo, E.H., Lee, C.-S., and Na, K. (2015). Photomediated reactive oxygen species-generable nanoparticles for triggered release and endo/lysosomal escape of drug upon attenuated single light irradiation. *Adv. Healthcare Mater.* 4 (18): 2822–2830.

54 Meng, L., Huang, W., Wang, D. et al. (2013). Chitosan-based nanocarriers with pH and light dual response for anticancer drug delivery. *Biomacromolecules* 14 (8): 2601–2610.

55 Ye, Z., Guo, J., Wu, D. et al. (2015). Photo-responsive shell cross-linked micelles based on carboxymethyl chitosan and their application in controlled release of pesticide. *Carbohydr. Polym.* 132: 520–528.

56 Hornig, S., Biskup, C., Gräfe, A. et al. (2008). Biocompatible fluorescent nanoparticles for pH-sensoring. *Soft Matter* 4 (6): 1169–1172.

57 Li, Y.-L., Zhu, L., Liu, Z. et al. (2009). Reversibly stabilized multifunctional dextran nanoparticles efficiently deliver doxorubicin into the nuclei of cancer cells. *Angew. Chem. Int. Ed.* 48 (52): 9914–9918.

58 Tang, Y., Li, Y., Xu, R. et al. (2018). Self-assembly of folic acid dextran conjugates for cancer chemotherapy. *Nanoscale* 10 (36): 17265–17274.

59 Huang, L., Chaurasiya, B., Wu, D. et al. (2018). Versatile redox-sensitive pullulan nanoparticles for enhanced liver targeting and efficient cancer therapy. *Nanomed. Nanotechnol. Biol. Med.* 14 (3): 1005–1017.

60 Zhang, Y., Cui, Z., Mei, H. et al. (2019). *Angelica sinensis* polysaccharide nanoparticles as a targeted drug delivery system for enhanced therapy of liver cancer. *Carbohydr. Polym.* 219: 143–154.

61 Thambi, T., Deepagan, V.G., Yoon, H.Y. et al. (2014). Hypoxia-responsive polymeric nanoparticles for tumor-targeted drug delivery. *Biomaterials* 35 (5): 1735–1743.

62 Son, S., Rao, N.V., Ko, H. et al. (2018). Carboxymethyl dextran-based hypoxia-responsive nanoparticles for doxorubicin delivery. *Int. J. Biol. Macromol.* 110: 399–405.

10

Advanced Methods for Design of Scaffolds for 3D Cell Culturing

Boštjan Vihar[1,3], Marko Milojević[1], Luka Banovic[3], and Uroš Maver[1,2]

[1] *University of Maribor, Institute of Biomedical Sciences, Faculty of Medicine, Taborska Ulica 8, 2000 Maribor, Slovenia*
[2] *University of Maribor, Department of Pharmacology, Faculty of Medicine, Taborska Ulica 8, 2000 Maribor, Slovenia*
[3] *IRNAS – Institute for development of advanced applied systems, Ltd., Limbuška cesta 76b, 2000 Maribor, Slovenia*

10.1 Introduction

Developing new methods for artificial fabrication of organ or tissue models, which mimic the native organism more closely, would be a significant achievement in biomedical research, as well as would provide a great boost for the development of novel patient treatment options. Organ and tissue transplantation has become an important tool in regenerative medicine, saving thousands of patients every year. In the EU alone, organ transplants have increased by more than 30% over the past decade, totaling at over 31 000 transplants in the year 2013 and 34 000 in 2017 [1–3]. Despite the rise of donations and improved efficiency in their uptake and transfer, the demand for organs remains far greater than the available supply. Thus, approximately 63 000 patients remained on waiting lists in 2013, which dropped to about 60 000 by the end of 2017 [1–3]. Nevertheless, even if a match is found and a patient receives a new organ, which is then successfully transplanted, the risk of rejection remains high, and patients are bound by lifelong immunosuppressive therapy that is always related with some serious unwanted effects [4–6] and significantly reduces life quality of the patient. The concept of engineering a tissue or organ for the specific need of a patient would therefore provide an enormous improvement for the mentioned challenges, as it would increase supply and (when patient's own cells are used as source material) compatibility of transplants. Certain successfully engineered structures [7–10] are already within preclinical and clinical trials for transplantation [11], and many more are in early testing stages. However, currently used structures are limited in their size, shape, as well as cell density and do not fully recapitulate the functionality of complex tissues. Besides sufficient quantities of transplants with improved histocompatibility, tissue engineering also

Functional Biomaterials: Design and Development for Biotechnology, Pharmacology, and Biomedicine, First Edition. Edited by Tamilselvan Mohan and Karin Stana Kleinschek.

promises new applications in other areas. Of particular value is the production of *in vitro* tissue models that can be used for more accurate disease models, assessing the pharmacology, and/or toxicology of drugs and cosmetics, while reducing the need for animal testing [11]. In combination with microfluidic and organ-on-a-chip devices, new insights into physiology, tissue development, or regeneration can be gained. By linking several miniaturized tissue models, even systemic body reactions can be investigated [11]. A new and increasingly important aspect of tissue engineering is also the prospect of cellular agriculture and the culturing of animal products such as meat without the negative effects of livestock farming, such as animal suffering, greenhouse gas emissions, and excessive use of land, water, as well as antibiotics [12–14].

10.2 General Considerations in Tissue Engineering

To reconstruct the shape and function of native tissues *in vitro* and create new models that can be used for research, restoration, or even augmentation of their *in vivo* counterparts [11, 15], one needs to consider some general limitations [11, 15, 16]:

- Availability of appropriate and viable cell sources.
- Substrates with suitable bio-physicochemical properties.
- Cell heterogeneity, distribution, and precise spatial positioning.
- Cell–substrate interactions [17, 18].
- Nutrient diffusion and consequent limits in size, requirements for the implementation of a vascular system [19, 20].

10.2.1 3D Cell Culture

Before tissue engineering became a practical method, two-dimensional (2D) cell culture was widely used in biological research and has already proven to be an invaluable tool in the past decades [16]. It is essentially performed by incubating a cell suspension in a nutrient-rich medium under physiological conditions (typically 37 °C and 5% CO_2 and high humidity). The cells adhere to their substrate and gradually multiply until they reach confluence, after which further growth is stopped by contact inhibition [21, 22]. While the traditional approach to cell cultivation has provided tremendous insights for cell biology, neuroscience, oncology, etc., it has not been possible to fully recapture the complex three-dimensional (3D) environment of cells *in vivo* [16, 23–26], which limits the usefulness of 2D cell culture for advanced applications. The flat attachment surface does not support vertical growth and cell attachment, which prevents the cells from assuming their native morphology (except perhaps in epithelial cells), forcing the cells into a base–apical polarity that extends laterally with minimal height. Similarly, the culture vessels do not mimic other features of the native cell environment, such as surface roughness, hardness, elasticity, or permeability, and there are no chemical signals through which the cells typically interact with their environment. In addition, the method

described is associated with limitations in nutrient uptake and waste removal that are only possible via the apical surface of the cells [16].

Successful *in vitro* tissue cultivation requires the cultivation of cells in three dimensions (3D) with the appropriate spatial distribution and without the shortcomings of traditional 2D cell culture. This requires structural support *in vivo* by the extracellular matrix (ECM) [16]. In addition to this support, the ECM plays a role in the proliferation, differentiation, and migration of cells in the tissue. Since the ECM is produced by the cells themselves, it is an active environment that contributes to the emerging properties of the tissue. The function, composition, and proportion of the total volume of the ECM vary according to tissue type, ranging from epithelial tissues with very little ECM to connective tissues, where the ECM can make up the largest part of the total volume [27]. The successful establishment of complex *de novo* tissue constructs requires new platforms that extend cell culture into the third dimension. This has led to the development of two main approaches: scaffold-based and scaffold-free tissue engineering [16].

10.2.2 Scaffold-Free Tissue Engineering

Instead of implementing cells into a matrix with a predesigned shape to determine the final form, cells are densely accumulated in 3D and stimulated to form their own ECM [16, 28]. Most commonly, such cell aggregates are formed in a spherical shape and are hence termed spheroids. However, other forms are experimented with as well. Spheroids can be arranged using a single or several cell types [29], and several approaches have already demonstrated successful spheroid formation. These include hanging-drop [30] approaches, microfluidics [31], liquid overlay [32], rotating flask [33], spinner flask [34], magnetic assembly [35, 36], and acoustic assembly [37]. The main advantage of scaffold-free tissue engineering is high cell density within the structure. However, it is often limited with its maximal reachable size. On the other hand, the spheroid formation can be combined with additive manufacturing or other scaffold-based approaches to overcome its shortcomings. Mironov et al. have demonstrated an approach where spheroids are extruded through a nozzle into a support matrix, which keeps them in place and allows self-assembly of larger tissue constructs during incubation [38]. By depositing the spheroids in appropriate shapes, biomimetic geometries such as blood vessels were established [38]. Alternatively, Ayan et al. established an aspiration-based system, which picks up individual spheroids from a reservoir and places them at a target position [39]. By sourcing spheroids from various containers, this method allows the assembly of highly heterogeneous tissue constructs. Similarly, LaBarge et al. demonstrated that the same principle can be used for the transfer of several spheroids simultaneously, increasing fabrication speed [40].

10.2.3 Scaffold-Based Tissue Engineering

The second and more commonly used approach is incorporating cells into ECM substitutes – commonly referred to as *scaffolds* – a 3D environment, which holds cells

in place, provides structural support, and often emulates the physiological properties of the native ECM. Today many different techniques are used and continuously developed for scaffold fabrication. Many are based on industrial and rapid prototyping methods (i.e. additive manufacturing), which have evolved to become compatible with biological or biocompatible materials and can take place at physiological conditions (e.g. low temperatures, pressures, and absence of toxic compounds) [28]. In general, the advantages of using scaffolds include improved control over the shape and spatial cell arrangement, as well as the possibility of implementing growth factors and other modulatory compounds. In combination with imaging techniques, such as magnetic resonance imaging (MRI) or X-ray tomography, digital fabrication allows precise reconstruction of damaged or missing tissues and organs [21]. 3D bioprinting *in situ* could, therefore, become a real possibility, where advanced wound dressings are printed directly onto the injured site. Some studies have already shown progress in this area, by inkjet printing stem cells to treat burn wounds [41] and bone reconstruction by laser-assisted bioprinting of hydroxyapatite (HA) particles onto the skulls of mice [42]. Ideally, a scaffold should sufficiently mimic physical, chemical, and biological tissue-specific properties of the native ECM [11, 28, 43], including

- Structural and mechanical properties that are retained post-fabrication and during incubation under cell culture conditions, providing stable cell support, as well as necessary mobility.
- Porosity, roughness, and surface energy for sufficient cell attachment and diffusion of nutrients, waste products, growth factors, and other molecules.
- Biocompatibility such that the main components or their degradation products do not cause unwanted effects, but rather stimulate desired ones, such as proliferation and correct differentiation.
- Controlled degradation that matches cell growth and cellular ECM production.

In the end, the scaffold should be completely replaced by healthy tissue, which resembles its *in vivo* counterpart. In addition to fulfilling the above-mentioned criteria, scaffolding components should be available from sustainable and low-cost sources, allowing scalable production of scaffolds and *in vitro* engineered tissues. Fulfilling all mentioned requirements simultaneously is enormously difficult, as optimizing one parameter can diminish another. For example, a high elastic modulus may require a higher molecular density, which in turn impacts degradation times [28], and inks exhibiting appropriate chemical environments, such as alginate-based hydrogels [44–47], may be prone to osmotic swelling [48] etc.

10.2.4 Definitions and General Terminology

Before delving into the technical details of this chapter, it is important to clarify some definitions. As young, rapidly developing, and interdisciplinary fields of research, tissue engineering, and its supporting technologies such as 3D bioprinting, have been described multiple times, from several perspectives and with inconsistent use [49, 50]. Hence, determining a unified nomenclature with clear definitions has

become necessary. Here we will use the terminology, as compiled and determined by Groll et al. in 2016 and later extended by Ramos and Moroni [49, 50]:

- Tissue engineering: "*The use of physical, chemical, biological, and engineering processes to control and direct the aggregate behavior of cells*." [51]
- Regenerative medicine: "*Application of tissue science, tissue engineering, and related biological and engineering principles that restore the structure and function of damaged tissues and organs*." [52]
- Biofabrication: "*Automated generation of biologically functional products with structural organization from living cells, bioactive molecules, biomaterials, cell aggregates such as micro-tissues, or hybrid cell-material constructs, through Bioprinting or Bioassembly and subsequent tissue maturation processes*." [50]
- Bioprinting: "*The use of computer-aided transfer processes for patterning and assembling living and non-living materials with a prescribed 2D or 3D organization in order to produce bioengineered structures serving in regenerative medicine, pharmacokinetic and basic cell biology studies*." [53]
- Bioassembly: "*Fabrication of hierarchical constructs with a prescribed 2D or 3D organization through automated assembly of pre-formed cell-containing fabrication units generated via cell-driven self-organization or through preparation of hybrid cell-material building blocks, typically by applying enabling technologies, including microfabricated molds or microfluidics*." [50]
- Bioinks: "*A formulation of cells suitable for processing by an automated biofabrication technology that may also contain biologically active components and biomaterials*." [54]
- Biomaterial inks: "*Materials that can be printed and subsequently seeded with cells after printing, but not directly formulated with cells*." [54]

10.3 Building Scaffolds

Today several approaches for scaffold fabrication are in use, exploiting different mechanisms of cell and material arrangement as well as phase transition principles between liquid and solid form. The most popular approaches are based on additive manufacturing (e.g. 3D bioprinting) and were summarized in some excellent reviews on the topic [11, 28, 43, 55]. However, as the technology is developing rapidly and there are several possible ways of categorizing its applications and configurations (e.g. solidification mechanism, scaffold shape, etc.), the classifications vary in structure and comprehensiveness. Here we will attempt to describe scaffold preparation in a broad manner and classify the approaches based on the mechanism by which a scaffold is formed, leaving the mechanical aspects of the technologies mostly aside. For example, microextrusion-based techniques exploit different mechanisms for dispensing the ink through the nozzle (e.g. pneumatic, mechanical piston, or screw based) [28], which have their advantages and disadvantages. However, the properties of the ink and the process of scaffold construction (the domain of interest in this chapter) stay more or less the same, regardless. Our aim

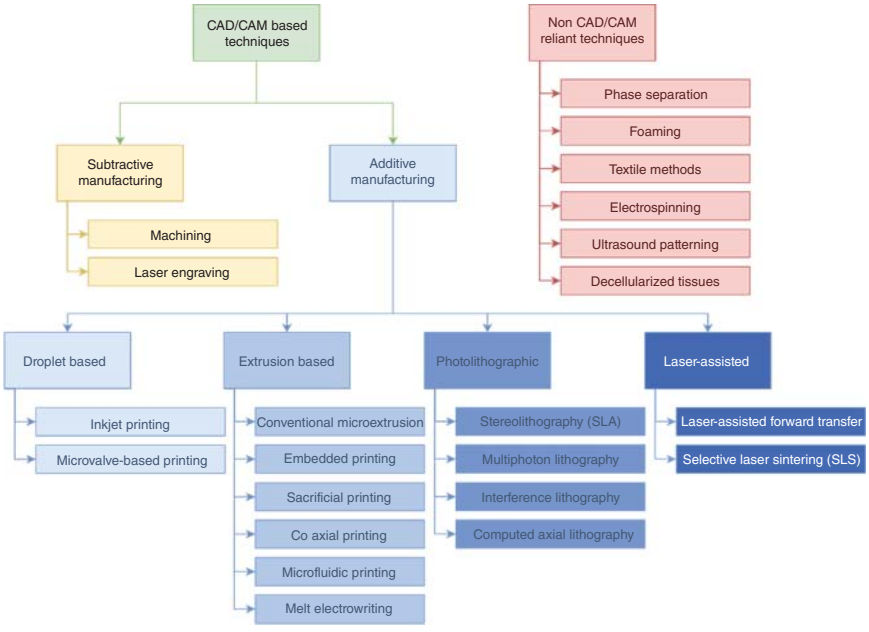

Figure 10.1 Classification of scaffold preparation approaches. Compared to common classifications, which focus on 3D bioprinting processes – in this chart additive manufacturing, here we attempt to structure scaffold manufacturing methods in a broader sense as further described later.

here is to give a comprehensive overview of the possibilities, but due to a large number of papers available, we might unintentionally miss out on certain (more "exotic") scaffolding approaches. The described techniques are summarized in Figure 10.1.

10.3.1 Techniques Without Computer-Aided Design and Manufacturing

The main two groups of scaffold preparation that we can distinguish are methods that rely on computer-aided design and manufacturing (CAD/CAM) and methods that do not. While the first group of methods has become very popular in recent years, the latter group is more heterogeneous and encompasses approaches that are not necessarily related. These include phase separation, foaming combined with freeze drying, methods more common in the textile industry, decellularization, etc. Scaffolds that are obtained using the mentioned techniques are showcased in Figure 10.2. What most of these approaches have in common is that they rely mostly on the inherent properties of the starting material and its behavior during processing conditions. Consequently, they typically allow less control over the anisotropic properties of the internal architecture.

10.3.1.1 Phase Separation

Phase separation is a process of preparing porous structures by separating a polymer solution into two phases, one with a high polymer concentration and another with

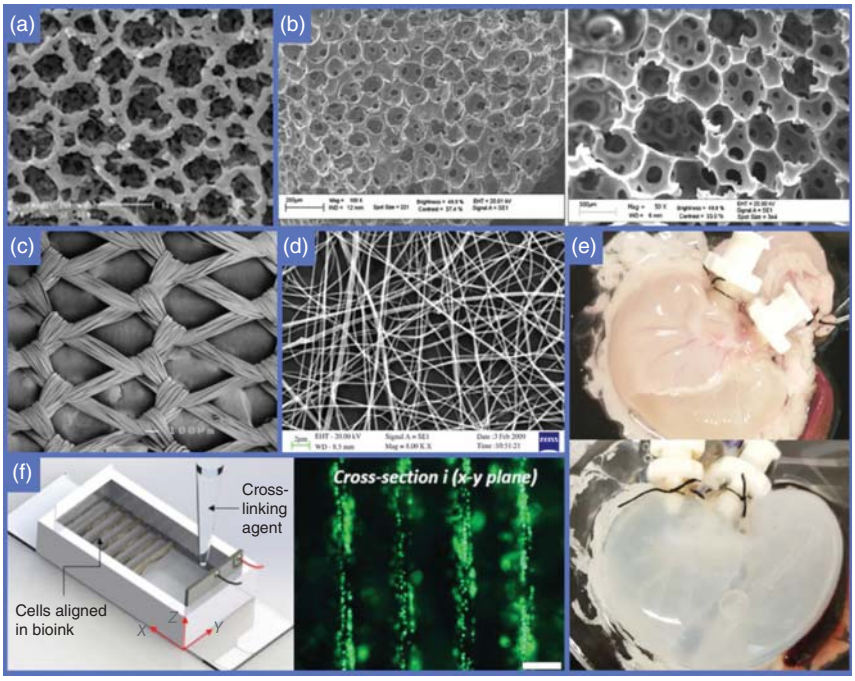

Figure 10.2 Scaffold fabrication approaches without the aid of computer-aided design and manufacturing. (a) A scanning electron micrograph of PVDF scaffolds prepared by phase separation. Source: From Abzan et al. [56]/with permission of Elsevier. (b) SEM images of PVA scaffolds prepared by using classical gas foaming (right) or microfluidic gas foaming (left). Source: Reproduced from Colosi et al. [57]/with permission of American Chemical Society. (c) Woven PLGA scaffold. Source: Reproduced from Chen et al. [58]/with permission of Elsevier. (d) Scanning electron micrograph of electrospun polyethylene oxide fibers. Source: Reproduced from Bhardwaj and Kundu [59]/with permission of Elsevier. (e) Scaffold preparation using decellularization of a rat stomach before (upper image) and after (lower image) detergent enzymatic treatment. Source: Reproduced from Zambaiti et al. [60]/with permission of Springer Nature. (f) Scaffold fabrication using standing waves with ultrasound patterning of bioink. On the right, a microscopic image is shown using a live/dead assay with living cells colored green. Source: Reproduced from Chansoria et al. [61]/with permission IOP Publishing Ltd/reproduced from Zambaiti et al. [60]/with permission of Springer Nature.

a low polymer concentration. After stabilization (e.g. by freezing), subsequent removal of the polymer-poor phase, one phase is left with a porous structure, which can be used as a scaffold for tissue engineering [56, 62]. Several different mechanisms of phase separation are reported in literature, including emulsification [57], thermally induced phase separation [63], and selective sublimation [64]. The most appropriate approach for a specific application depends primarily on the selection of materials and their properties, which has advantages and disadvantages in regard to the intended use. For example, emulsification-based approaches typically require the use of organic solvents to remove the oil phase in the later stages of the process [57].

10.3.1.2 Foaming

Foaming is the process of trapping gaseous bubbles inside the preferred scaffolding material, for example, an aqueous solution of a polymer. Typically, a hydrophobic gas (e.g. N_2, Ar, or hexafluoroethane) is dispersed within the medium, and the obtained foam is rapidly stabilized (e.g. by freeze-drying and subsequent cross-linking) [57]. The described approach is suitable for creating highly porous structures, but allows little control over bubble size, which translates to a broad distribution of pore sizes. Alternative approaches to foaming include chemical reactions [65] and supercritical CO_2 [66]. An improved approach to gas foaming has been demonstrated by Colosi et al. using a microfluidic approach to produce gas bubbles with highly homogeneous sizes [57].

10.3.1.3 "Textile" Methods

Textile meshes have already found use as implants in regenerative medicine, such as surgical procedures to treat herniae, pelvic floor dysfunctions, and even as vascular grafts and heart valve repair [67]. Using appropriate materials and fiber preparation methods, weaving represents a viable option for scaffold fabrication [58, 68, 69]. Creating a textile mesh is typically a two-step process, composed of fiber formation and assembly, with many possibilities available for both steps, depending on the source material and desired scaffold structure. Processes which have been used in fiber formation for tissue engineering include electrospinning (further described later), wet spinning, microfluidic spinning, interfacial complexation, and collection of naturally occurring fibers such as silk [68]. Similarly, several options are available for scaffold formation, using weaving, knitting, or braiding [68]. By designing the pattern, the anisotropic directionality of mechanical and topographical properties can be controlled, making such scaffolds especially suitable for engineering connective tissues [69].

10.3.1.4 Electrospinning

Electrospinning is a process of creating fibers by accelerating a polymer solution in an electric field. As the solution body extends between the conductive nozzle and collector, the solvent evaporates rapidly, leaving behind a fiber in nanometer-to-micrometer diameters [59, 62, 63], which can be adjusted by solution composition, voltage, and nozzle to collector distance. Electrospinning has become a very popular technique for creating fibers, as it is compatible with a wide range of synthetic as well as natural polymers, including polycaprolactone (PCL), polylactic acid (PLA), silk fibroin, collagen, and fibrinogen [59, 63]. The technique, however, also has certain disadvantages, as it is difficult to create larger, 3D structures, and the scaffold fabrication process is slow and is not suitable for use with bioinks.

10.3.1.5 Ultrasound Patterning

A very exciting technique for scaffold fabrication was demonstrated by Chansoria et al. using ultrasound-assisted biofabrication for creating aligned three-dimensional cellular constructs [61]. In their article, they described an experimental set-up where a bioink composed of alginate and human adipose stem cells (hASCs) is placed

inside a chamber with an ultrasonic actuator and exposed to standing waves, which imposes a stable alignment on the bioink, which is then stabilized by cross-linking. By adjusting the placement of the actuators, more complex lattice shapes can be produced for higher control of ink distribution and porosity. In addition, the technique is compatible with 3D bioprinting to form more complex shapes.

10.3.1.6 Decellularized Tissues and Organs

Scaffolds derived from native tissues and organs seem especially suitable for tissue engineering, as they already exhibit the ideal bio-physicochemical properties for 3D cell culture. Through the improvement of decellularization strategies, cells can be removed from the tissue while leaving the architecture and composition of the ECM intact [60, 70, 71]. Such scaffolds have already been used in the engineering of several tissues and organs, including bladder, artery, esophagus, or skin [70]. A study by Ott et al. has demonstrated successful decellularization of the whole heart, its successful repopulation with cells, and restoration of function [71]. Furthermore, Noor et al. have succeeded in deconstructing decellularized cardiac tissue to develop a bioink for 3D printing, which was used to fabricate *de novo* cardiac tissue with basic functionality [72].

Clearly, in terms of biomimicry, chemical, and structural properties, decellularized tissues seem the superior source of scaffolds for tissue engineering. They will likely be used as a guiding model for other approaches to scaffold fabrication. However, they also have a major drawback. Animal-derived tissue sources are problematic in terms of supply, ethical, environmental, and other aspects of livestock farming [12, 13]. A viable alternative could come from decellularized plant tissues, which have been successfully used as scaffolds for both *in vitro* and *in vivo* applications in animal models [73–76]. Plant-derived, decellularized tissue scaffolds exhibit good biocompatibility and proangiogenic function [75], can even be used to induce basic cardiac function *in vitro* [76], and are a significantly more sustainable resource. On the other hand, due to their mechanical properties and internal architecture, such scaffolds are limited in their use for tissue engineering of soft and movable structures.

10.4 Computer-Aided Design and Manufacturing

When scaffold fabrication requires control in terms of shape and dimensions that go beyond the possibilities of most methods mentioned earlier (e.g. for precise reconstruction of a bone defect), CAD/CAM techniques represent a feasible and increasingly popular option. The process typically has several steps, including design of the desired shape, its translation to a robotic toolpath, and optimization of fabrication parameters, such as tool selection, speed, base materials, and environmental conditions. The manufacturing process is commonly executed using machines with computer numerical control (CNC), which allows the movement of manufacturing tools in several spatial directions. In this sense, two categories can be distinguished: subtractive manufacturing, where a shape is created by removing material from a

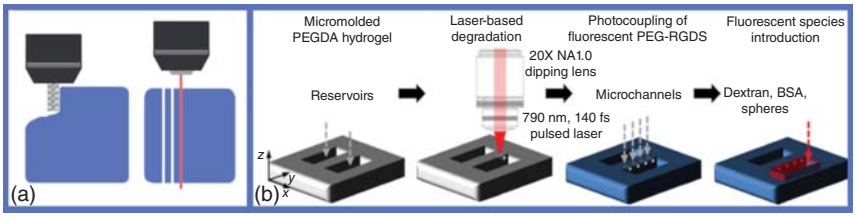

Figure 10.3 Subtractive manufacturing approaches. (a) Shows two possible approaches to subtractive manufacturing, machining (left), and laser ablation (right). (b) By integrating image-guided laser control with laser degradation, Heintz et al. created channel structures within PEGDA hydrogels. Source: Heintz et al. [77]/with permission of John Wiley & Sons.

piece of raw material; and additive manufacturing, which functions by depositing or solidifying material in subsequent layers, attaching each new layer to the previous one.

10.4.1 Subtractive Manufacturing

Subtractive manufacturing techniques (Figure 10.3), such as laser ablation or machining, allow processing of bulk materials with a broad range of structural properties, from soft materials, such as hydrogels [78] and polymers, to metals and ceramics [79]. While subtractive manufacturing does not provide control over the internal architecture and chemistry of the scaffold, it can still be a viable option for the preparation of products, especially when used in combination with other scaffold preparation approaches, especially nonautomated techniques, like those described earlier. Though without automation, the Pelling group has demonstrated carving as a viable option of forming scaffolds from plant-derived materials [73–75].

Subtractive manufacturing methods for scaffold fabrication have also been demonstrated on softer structures. Shahriari et al. reported successful growth of peripheral nerves in agarose hydrogel scaffolds prepared by CNC machining and knife cutting [78]. Instead of removing the material mechanically, Heintz et al. showed that using laser degradation, 3D networks of microchannels can be created within poly(ethylene glycol) diacrylate (PEGDA) hydrogels, with biomimetic architecture and size [77].

10.4.2 Additive Manufacturing

As mentioned earlier, additive manufacturing is commonly referred to as 3D printing, and usually works as a bottom-up approach, where the material is applied or solidified in a single layer at a time, with each subsequent layer supported by and bonded to the previous one. This type of build-up allows great control over the internal architecture, porosity and, by changing the material during the process, continuous adjustment of the chemical composition. Consequently, additive manufacturing provides researchers with more flexibility and allows the fabrication of complex scaffolds, which would be significantly more difficult to create by other means. Many

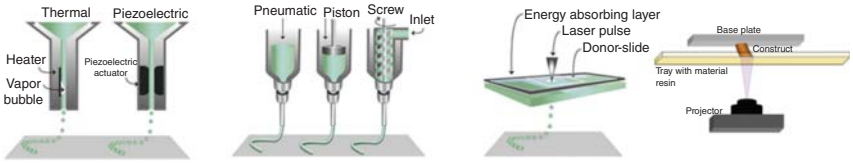

Figure 10.4 General overview over common approaches to additive manufacturing of scaffolds for tissue engineering. From left to right: inkjet based, extrusion based, laser-assisted forward transfer, and stereolithography. Source: Pedde et al. [69]/with permission of John Wiley & Sons.

approaches and mechanisms of creating structures through additive manufacturing have been developed over the years, each suitable for a specific application. In terms of scaffold fabrication for tissue engineering and regenerative medicine, every technique has certain advantages and disadvantages, which will be discussed in more detail later. A schematic of the four main groups of additive manufacturing techniques for scaffold fabrication is summarized in Figure 10.4.

10.4.2.1 Droplet-Based Techniques

Droplet-based 3D bioprinting includes methods and approaches of depositing (bio)inks for tissue engineering in the form of droplets [55]. By exploiting various possible drive and ink "feeding" mechanisms, this class of methods is very diverse. However, we will focus on three main subcategories, namely inkjet-based, microvalve based, and laser-assisted bioprinting (Figure 10.5).

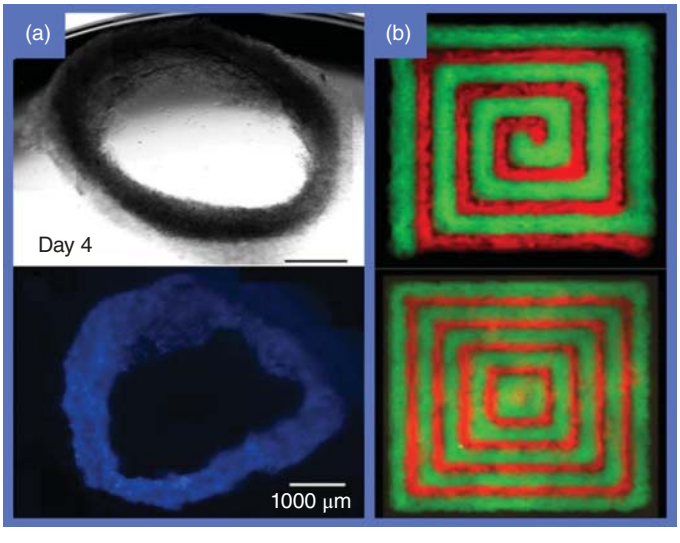

Figure 10.5 Droplet-based techniques. (a) 3D Silk fibroin scaffolds printed with sacrificial alginate. Source: Reproduced from Compaan et al. [80]/with permission of American Chemical Society. (b) Precisely ordered scaffolds prepared by two-component inkjet printing. Source: Reproduced from Zimmermann et al. [81]/with permission of IOP Publishing.

10.4.2.2 Inkjet Bioprinting

The first inkjet bioprinting applications deployed commercial, paper printers, adapted for bioink deposition [28]. Generally speaking, inkjet printing is the process of placing small droplets of liquid phase materials with high volumetric precision in defined arrays on a target substrate [82]. It is typically classified into two main categories: continuous or drop-on-demand inkjet printing, distinguished by the physical process by which drops are generated [83]. Continuous inkjet printing (CIJ) describes a technique where a continuous jet of material is ejected through a nozzle and breaks into discrete drops as a consequence of surface tension [83]. In drop-on-demand (DoD) printing, on the other hand, individual droplets are generated when required, using thermal, piezoelectric, or electrostatic driving mechanisms [83]. Inkjet printing allows high-speed deposition (up to $10\,000\,s^{-1}$) of subnanoliter droplets and shows high cell viability after deposition. Therefore, deploying modified commercial inkjet printers offers a cost-effective solution [28, 69]. On the other hand, these techniques are limited to the use of liquid inks and are prone to clogging [28, 69]. Being limited by the range of compatible material viscosities, scaffold size is an important limitation for inkjet bioprinted scaffolds. Nevertheless, promising new approaches and workarounds for inkjet bioprinting show the potential to increase the range of compatible materials and applications. Compaan et al. demonstrated two-step inkjet bioprinting of silk fibroin bioinks with alginate as a sacrificial material. Printing onto a platform, submerged into a $CaCl_2$ cross-linking solution each layer at a time, thick, 3D scaffolds were successfully fabricated. After cross-linking the silk fibroin, alginate is dissolved, leaving behind silk-based fibroblast scaffolds [80]. Zimmermann et al. have demonstrated successful 3D printing by joining two piezoelectric pipettes for high precision droplet dispensing of reactive hydrogel precursors onto the same position, where a hydrogel is formed by mixing of the two components [81]. Using the described approach, multicomponent fabrication processes can be designed, which facilitate high precision, printing speed, viability, and control over matrix mechanics.

10.4.2.3 Microvalve-Based Bioprinting

In contrast to inkjet printing, where the material is accelerated by a pulsed mechanism, microvalve-based bioprinting characterizes techniques where droplets are generated by controlled opening and closing of a valve, allowing (bio)ink to escape from a container under a set pressure [84]. Similar to inkjet printing, it is compatible with a relatively narrow range of materials in terms of viscosity and is prone to clogging [84]. Compared to inkjet printing, it is somewhat slower (up to 1000 droplets/s) and less precise. However, it is compatible with the inks of a broader spectrum of viscosities [55]. Regardless, microvalve-based bioprinting has found valuable applications, e.g. in high-throughput screening toxicology analysis, fabrication of tissue spheroids, as well as *in vitro* tissue models of bladder, lungs, and skin [55, 84].

10.4.2.4 Extrusion-Based Techniques

"Conventional" microextrusion is the most widely used approach to 3D bioprinting. Its working principle is very straight forward: (Bio)ink, which is contained in a

syringe, or similarly shaped cartridge, is extruded through a nozzle and deposited to a target surface while changing its relative position in the X, Y, and Z dimensions. The basic fabrication procedure can be distilled into the following parts:

- Computer-aided design (CAD) of target structures.
- "Slicing" the model into individual layers and generating a sequence of coordinate positions with movement and (optionally) extrusion rates.
- Printing preparation, including (bio)ink assembly, as well as mounting of the cartridge and fixation of a substrate, onto which the printing will occur.
- Printing: typically, scaffolds are fabricated from the bottom-up, depositing each new layer on top of the previous one.

A substantial part of its functionality is derived from fused deposition modeling (FDM), which has become widely adopted, especially since the first open-source licenses for hardware and software became available [85–87]. Consequently, the technology has become low cost, easy to use, and built with commonly available components. In addition, microextrusion bioprinting is highly customizable, allowing the integration of several fabrication heads with multiple materials and deposition parameters. Of all mentioned approaches, extrusion bioprinting is compatible with the broadest range of (bio)inks, gelation principles, and cross-linking mechanisms [28, 43, 55, 88]. It is also highly adaptable and has already been used in many important contributions to tissue engineering and regenerative medicine, further discussed later. Despite its versatility, microextrusion bioprinting also has certain disadvantages. The minimum width of the deposited filament is limited with the inner diameter of the nozzle, typically in the range of 100 μm in diameter [89] and the consequent shear stress, which is higher in narrower nozzles and is harmful to cells [28]. In addition, the geometrical complexity of target scaffolds is typically limited to structures where each successive layer receives structural support from the previous one. Nevertheless, the development of new materials, fabrication procedures, and hardware are providing solutions and workarounds for the mentioned challenges. The different approaches to extrusion-based bioprinting are shown in Figure 10.6.

10.4.2.5 Freeform Embedded Bioprinting

Scaffold fabrication requires a balance between ink fluidity, which facilitates extrusion and reduces shear stress on cells on one side, and ink stability after deposition of the material for high shape fidelity of the designed scaffold [28]. The extent and duration of the liquid to solid transition significantly limit the control over scaffold geometry and shape fidelity. However, improvements are possible by adjusting the ink properties and process parameters. One possible approach to enhancing the geometrical range of microextrusion manufactured scaffolds is printing into a support bath [90, 95, 96]. Freeform reversible embedding of suspended hydrogels (FRESH), as termed by Hinton et al., is performed by 3D printing (typically) hydrogels into a dense suspension of a finely granulated secondary hydrogel. The support bath allows fluent gliding of a fine nozzle (e.g. gauge needle) while providing structural support to the deposited material. Additionally, the support bath provides a gentle

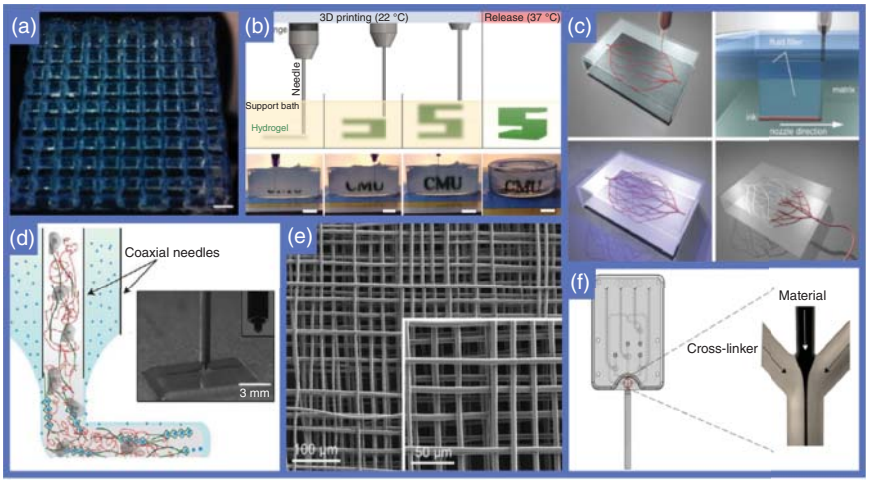

Figure 10.6 Scaffolds fabricated by microextrusion bioprinting. (a) A "woodpile" scaffold created using conventional microextrusion. Source: Reproduced from Irvine et al. [88]/Springer Nature/CC BY. (b) The process of freeform bioprinting by reversed embedding in suspended hydrogels (FRESH). Source: Reproduced from Hinton et al. [90]/American Association for the Advancement of Science/CC BY 4.0. (c) Sacrificial bioprinting in a biocompatible matrix used to create a network of perfusable channels. Source: Reproduced from Wu et al. [91]/with permission of John Wiley & Sons. (d) A schematic of coaxial printing, showing simultaneous extrusion of hydrogel and cross-linking solution. Source: Reproduced from Colosi et al. from [92]/with permission of John Wiley & Sons. (e) A well-defined lattice structure composed of microfibers, created using melt electrowriting (MEW). Source: Reproduced from Brown et al. [93]/with permission of John Wiley & Sons. (f) A microfluidic extrusion nozzle with focusing capabilities. Source: Reproduced from Dickman et al. [94]/with permission of John Wiley & Sons.

cross-linking environment, allowing bonding of a successive layer to the previous one and stabilizing the structure before releasing it [90]. The described technique is compatible with various support bath compositions, cross-linking mechanisms, and significantly improves resolution as well as shape fidelity of a scaffold and allows the manufacturing of physiologically relevant shapes [90, 95, 96].

10.4.2.6 Sacrificial Bioprinting

Building on embedded bioprinting, the scaffolding and placeholder material can also be swapped. Thus, instead of printing scaffolds into a support bath and releasing them afterward, a sacrificial material can be deposited into a scaffold matrix and evacuated after curing. This is especially useful for fabricating scaffolds with complex and interconnected channel systems, an important building block for the engineering of tubular tissue components, especially vasculature, which is one of the critical challenges for the engineering of large, functional *in vitro* tissue models [91, 97, 98]. To obtain perfusable channels, successful extraction of sacrificial ink is necessary, which, especially for the use of interconnected networks, requires appropriate rheological properties. Wu et al. used a Pluronic F127 ink, with optimized shear-thinning characteristics to support smooth flow during deposition

and stability during curing, but transitioned to a liquid below the critical micelle temperatures, allowing its complete removal [91]. Štumberger and Vihar used a similar approach using xanthan hydrogel as the sacrificial ink in gelatin or alginate matrices [98]. In addition to the above-described method, Kolesky et al. successfully 3D printed a self-supporting sacrificial scaffold (Pluronic F127-Thrombin) inside a custom-built container and filled the empty spaces with liquid gelatin–fibrinogen bioink. After curing, the structure was cooled to liquefy and remove the sacrificial ink, followed by incubation [97]. Their study demonstrated that the process is sufficiently mild to sustain the survival of cells in the used inks. In a breakthrough study, Skylar-Scott et al. demonstrated sacrificial bioprinting-assembled organoid matrices, which exhibit high cell density, self-healing, and viscoplastic behavior [99]. Utilizing the sacrificial writing into functional tissue (SWIFT) method, sacrificial gelatin ink was printed into a bed of cardiac tissue spheroids, suspended in a collagen–matrigel matrix. Following spheroid fusion, the researchers obtained a perfusable cardiac tissue, which exhibited synchronous beating over a seven-day period [99].

10.4.2.7 Core–Shell Bioprinting

Sacrificial printing shows enormous promise, especially for fabricating dense tissues with integrated vasculature. For applications where loose or porous scaffolds with directional perfusion are required, other approaches may be beneficial. A possible and convenient method to fabricating perfusable scaffolds is employing coaxial nozzles, which can also be used in a conventional extrusion-based set-up. Nozzles of varying diameters are aligned on the same axis, such that a wider nozzle encloses a narrower one [46]. By extruding different inks through separate compartments of a coaxial nozzle, a "core" and "shell" are deposited, hence the name core–shell bioprinting. Gao et al. demonstrated a single-step process of fabricating stable channels within the 3D printing of cell-laden structures [47]. Simultaneously extruding an alginate hydrogel from the shell compartment and $CaCl_2$ from the core compartment of the nozzle, the gel was cross-linked at the interface, creating a hollow, yet stable filament [47]. By spatially controlling deposition, woodpile structures were successfully fabricated. While the nozzle design using long and narrow compartments is expected to facilitate high shear stress on cells, the approach has been successfully deployed using alginate and decellularized ECM bioinks with endothelial progenitor cells [100]. A typical coaxial set-up contains a hollow needle, aligned within a wider hollow needle. In a proof-of-concept study, Attalla et al. report a modified set-up, where materials can be extruded in multiple layers along the same axis and provide a protocol for optimizing the flow rate of individual components [45].

10.4.2.8 Multicomponent and Microfluidic Bioprinting

In addition to highly complex internal geometries, native tissues also exhibit precisely structured, spatially specific cellular and ECM composition. To achieve relevant biomimicry, the process of biofabrication requires not only spatial control over deposition but also spatial control over the chemical composition of the scaffold. Extrusion-based 3D bioprinters have early adopted multiextruder configuration, allowing consecutive change of (bio)inks within the printed scaffold [28, 38].

However, sequential deposition of discrete units of material cannot fully recapitulate the bio-physicochemical gradients of native tissues. An elegant solution for this problem could be extruding multiple materials through the same nozzle. In addition to changing component ratios during ink deposition, specific interactions between components could be exploited to achieve new and improved existing scaffold functionality. Liu et al. demonstrated this type of set-up by integrating a CNC stage with an array of 7 bioink reservoirs, which are pneumatically driven and routed to a single printhead [101]. By individually controlling the valves in sequence or simultaneously, structures with complex internal gradients and hierarchical composition were 3D printed, including complex cell-laden structures and bioelectric circuits [101]. Its own respective field for miniaturization complex biological and chemical experiments, synthesis, mixing, lamination, encapsulation, etc. is microfluidics [102]. Allowing work with small quantities of material and adjusting its properties "on-the-fly" create a powerful tool, also for microfabrication and 3D bioprinting. Using microfluidic bioprinting, Dickman et al. demonstrated the fabrication of respiratory and intestinal tissue constructs containing smooth muscle cells that mimic the native contractile function in response to normal physiological triggers, as well as diseased behavior as a response to fibrosis trigger transforming growth factor beta (TGF-β) [94]. The development of new microfluidic chips and nozzles for "on-the-fly" controlled bioprinting will generate new possibilities for the fabrication of geometrically and bio-chemically heterogeneous scaffolds, with advanced functionality and biomimicry. Colosi et al. and Costantini et al. reported the fabrication of scaffolds using microfluidic printing heads with a core–shell nozzle [92, 103].

10.4.2.9 Melt Electrowriting

As described earlier, electrospinning is a useful tool for fabricating meshes of ultrafine fibers as scaffolds for tissue engineering. In a static set-up, the electrostatically drawn polymer jet deposits fibers over a relatively large area and in a chaotic manner [93]. Fibers electrospun from solution are also restricted in the number of layers, which can be collected on the same surface area, limiting scaffold thickness [93]. However, by deploying melt electrospinning, while laterally translating the collector in X and Y directions, fiber deposition can be controlled much more precisely. By adjusting voltage, distance, and motion velocity, Brown et al. report a direct melt electrowriting (MEW) process that allows consistent and reproducible deposition of submicron PCL filaments, constructing 3D scaffolds suitable for biomedical applications [93]. By optimizing the writing parameters, the thickness of the filament can be controlled using the same nozzle [104], hence enabling the process adaptation to other polymers [93]. The fabrication conditions of MEW do not allow fabrication using bioinks. Nevertheless, the MEW process shows a lot of promise for high-resolution 3D-printed scaffolds with submicron thick filaments, which can be used in combination with other bioprinting techniques, producing scaffolds with advanced composition and functionality. de Ruijter et al. reported the fabrication of composite scaffolds, by simultaneous MEW of PCL and extrusion bioprinting using GelMA bioinks and pluronic-based hydrogels [105].

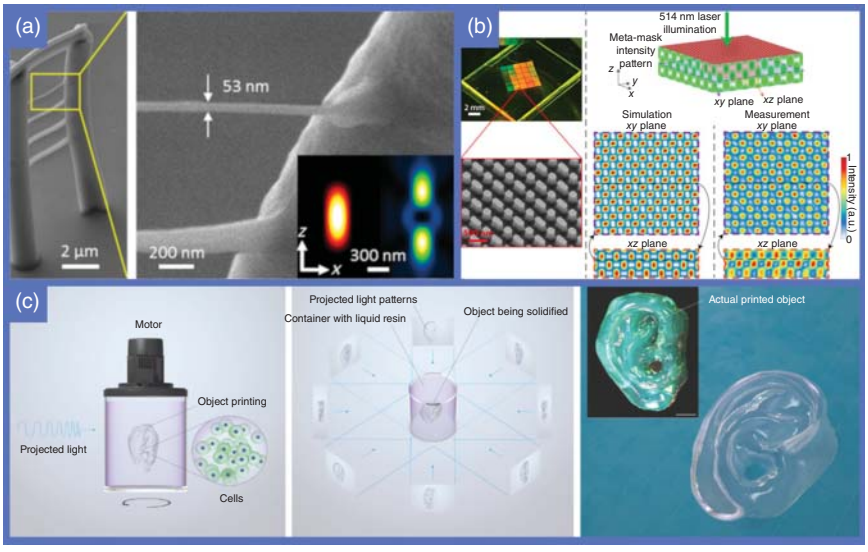

Figure 10.7 Photolithographic bioprinting methods. (a) Micro- and nanostructures fabricated using multiphoton STED lithography. Source: Reproduced from Klar et al. [106]/with permission of IOP Publishing. (b) Interference lithography. Sample structures (left) and a schematic showing pattern generation. Source: Reproduced from Kamali et al. [107]/with permission of Proceedings of the National Academy of Sciences. (c) Volumetric bioprinting using computed axial lithography. Source: Reproduced from Bernal et al. [108]/with permission of John Wiley & Sons.

10.4.2.10 Photopolymerization

This section describes several approaches to additive manufacturing using light as a mechanism to create solid objects from typically liquid sources through photopolymerization – the process of extending polymer chains by adding reactive monomers. The term "laser-assisted techniques" is in literature often used to describe processes that are used to create and deposit discrete bio-ink droplets by laser pulses, aimed at a membrane [28, 43, 55], and are further described in a separate category below. Examples of techniques exploiting photopolymerization are shown in Figure 10.7.

10.4.2.10.1 Stereolithography (SLA)

Conventional stereolithography is a process of forming 3D objects by selective solidification of a photosensitive material using targeted irradiation with light, which causes the formation of reactive species, e.g. free radicals or ions [109, 110]. In turn, a chemical chain reaction is induced, which bonds smaller molecules into a stable, cross-linked polymer. As the monomers are typically not sufficient to start the reaction, photoinitiators are added into the solution. Shapes are then produced by UV light in a single-photon process, which allows producing several centimeter-sized structures in high resolution [109, 110]. Different sources of irradiation and consequent set-ups are used, including focused light beams and mask-based set-ups [109]. With the development of microelectronics and processes, new and more

convenient methods for irradiation can be used, such as light-emitting diode (LED) displays [111] or digital micromirror devices (DMD)[112], extending the range of useful wavelengths and compatible materials. The SLA process takes place in a narrow plane of light focus, where the ink is exposed to light. The first polymerized layer is bonded onto a target platform, which is moved away from the light source, as each subsequent layer is solidified. SLA allows rapid fabrication of extraordinarily complex structures in high resolution, which is very advantageous for tissue engineering and regenerative medicine [110, 113]. On the other hand, it is quite limited in the use of biocompatible materials and cell friendliness of the process. Monomers, photoinitiators, and later on, degradation products, are often toxic to cells [114]. Thus, improving the cell friendliness of the process and the involved materials is an important focus of stereolithographic biofabrication [115]. One approach in this regard is reducing the toxicity of photoresists and monomeric components. Heller et al. demonstrated that using vinyl ester as monomers is a viable option for creating stereolithographic scaffolds for tissue engineering, compared, for example, to acrylates or methacrylates [116]. Torgersen et al. composed an excellent review of biocompatible chemicals for stereolithographic biofabrication [115]. Another important factor that impacts cell viability during the lithographic process is the incident light, its exposure, intensity, and wavelength. In this regard, multiphoton polymerization represents a major improvement in SLA biofabrication.

10.4.2.10.2 Multiphoton Lithography

To begin the polymerization reaction in a conventional SLA set-up, a photon with a specific wavelength needs to be absorbed by the photoinitiator to shift toward the appropriate energy state, which allows the process to unfold. However, the photoinitiator can also be sufficiently excited if it simultaneously absorbs two or more photons with longer wavelengths [109]. The probability for this to occur depends on the incident light intensity and is, for example, high in the focal region of a focused laser [117]. Hence, the term for this fabrication is two-photon or even multiphoton lithography (MPL), often also referred to as direct laser writing (DLW). Exploiting this phenomenon causes polymerization solely in the focal region and significantly increases writing resolution, which reaches the sub-micron, even nanometer range [106, 109, 118]. However, there is a trade-off between resolution, numerical aperture (NA), and working range of the objective [119, 120]. For biological applications, multiphoton excitation systems with low NA objectives are preferably used [121]. Using this approach, Non-Bulbar Dermal Sheath (NBDS) cells were successfully cultivated on pentaerythritol triacrylate (PETA) – bisphenol A glycidyl methacrylate (BisGMA) scaffolds, exhibiting marginal cytotoxicity and development toward bone-like ECM production [122]. In 2019, an important breakthrough study by Dobos et al. demonstrated successful scaffold fabrication using a bioink, composed of Thiol–Gelatin–Norbornen (Gel-NB) and mouse L929 fibroblasts, which survived such printing process and showed positive proliferative capacity [123].

10.4.2.10.3 Interference Lithography

Typical layer-by-layer approaches to additive manufacturing are limited in throughput and may result in mechanical anisotropies [124], which is an important drawback for scaling and standardization of the technology. However, by exploiting the quantum properties of photons, solutions could be on the horizon. A recent article by Kamali et al. proposed the concept of large-scale metasurface-assisted 3D lithography. The approach is aimed at rapid photo-lithography-based fabrication of complex periodical structures, which are the result of light interference patterns induced by metasurface masks, which provide orthogonal polarizations, resulting in exotic 3D patterns [107]. This technique is still a proof of concept and has not yet been translated into biofabrication or tissue engineering. However, it could be an exceptionally fast and scalable method for printing high-resolution scaffolds.

10.4.2.10.4 Computed Axial Lithography – Volumetric Bioprinting

Recently, a new light-based approach to additive manufacturing has been proposed capable of fabricating 3D structures with exceptional speed, without anisotropic effects [124, 125]. The technique was inspired by computed tomography (CT) image reconstruction, and intensity-modulated radiation therapy (IMRT) functions by projecting 2D images at consecutive angles through a rotating container filled with photosensitive resin. The consequent superposition of exposures results in a sufficient energy dose to polymerize the material within a bound 3D geometry [124, 125]. The described computed axial lithography (CAL) or volumetric additive manufacturing holds immense promise for the fast generation of complex structures and has already been successfully implemented for 3D bioprinting applications using photoresponsive gelatin hydrogels [108]. Using a bioink composed of gelatin methacryloyl (gelMA) and either articular-cartilage-resident chondroprogenitor cells (ACPCs), endothelial colony-forming cells (ECFCs), or mesenchymal stem cells (MSCs), respectively, Bernal et al. successfully fabricated cell-laden structures. The images were projected at a wavelength of 405 nm, resulting in >85% cell viability and the production of relevant ECM proteins [108].

10.4.2.11 Laser-Assisted Bioprinting

In this section, techniques (Figure 10.8) will be discussed, which require the use of lasers but do not fall into the categories of lithography or engraving.

10.4.2.11.1 Laser-Assisted Forward Transfer

In most review articles, laser-assisted techniques are classified into a separate group [28, 43, 55]. However, the further described laser-induced forward transfer (LIFT) for 3D biofabrication is typically used for droplet-based scaffold manufacturing; hence in this text, laser-assisted techniques are ordered into this category. In LIFT 3D bioprinting, a pulsed laser beam is focused on an energy-absorbing substrate (typically a thin layer of ink deposited on a transparent slide or membrane), causing local vaporization, followed by a pressure rise, which propels a droplet of ink toward

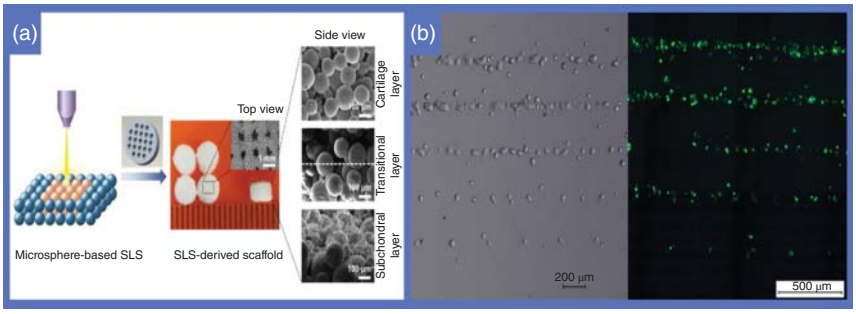

Figure 10.8 Laser-assisted bioprinting techniques. (a) Basic principle (left) and sample scaffolds (right) created using selective laser sintering. Source: Reproduced from Du et al. [126]/with permission of Elsevier. (b) Single-cell bioprinting using laser-assisted forward transfer. Source: Reproduced from Guillotin et al. [127]/with permission of Elsevier.

a collector [28, 43, 55]. As the laser beam absorption is highly localized and short termed, the technique is compatible with bioinks with high post-printing viability [128], whereas avoiding nozzles eliminates the possibility of clogging [28, 55]. In addition, LIFT has been demonstrated to facilitate the use of bioinks with high cell densities and a broader range of viscosities (1–300 $mPas^{-1}$) than other droplets-based techniques, such as inkjet printing (3–12 $mPas^{-1}$) or microvalve-based printing (1–200 $mPas^{-1}$) [28]. The resolution of laser-assisted bioprinting depends on the inherent properties of the bioink, such as layer thickness, viscosity, surface tension, and the set-up parameters, such as substrate wettability, ink-to-surface distance, and laser fluence [129]. In their study, Guillotin et al. report successful LIFT bioprinting of individual cells encapsulated in an alginate-based bioink [127], though accurate positioning can be difficult [28]. An important milestone for *in vivo* bioprinting was reached by Keriquel et al. who showcased the use of LIFT for depositing nano-HA [42] and later on bioinks composed of stromal cells with collagen and HA directly onto deletions in the calvaria of mice [130], stimulating bone regeneration.

10.4.2.11.2 Selective Laser Sintering

Similar to most additive manufacturing techniques, selective laser sintering (SLS) is a layer-by-layer fabrication process. Successive layers of powdered material such as metals, ceramics, or plastics are fused by a focused laser [131]. Requiring high energies of the incident beam, the process would be highly destructive for cells; thus, it does not fit directly into the category of 3D bioprinting. Nevertheless, SLS produced structures do find use in tissue engineering and regenerative medicine, especially for the manufacturing of hard tissue replacements, implants, or surgical guides [132, 133].

In addition to SLS, where sintering occurs in successive, individually shaped layers, bulk material can be sintered under high temperatures or pressures. This can be useful for finishing additive manufactured objects, which contain powdered materials held together by binding agents. Combining SLA techniques with

subsequent sintering has shown promising results in the fabrication of highly precise ceramic scaffolds, which find applications in bone or dental reconstruction [10, 79, 134].

With high mechanical strength, metals and ceramics typically find applications as scaffolds for replacement of "hard tissues," such as bone or cartilage, to provide structural support. However, not only the scaffolds need to have the appropriate shape and sufficient structural strength but also they should closely mimic the mechanical properties of the target tissue, have good biocompatibility, and allow sufficient mass transport [135, 136]. To match these properties, highly porous and chemically heterogeneous scaffolds are required [136]. SLS can be a suitable technique to achieve these results, as Du et al. demonstrated by fabricating hybrid HA-PCL scaffolds [126].

10.5 Challenges and Future Outlook

The number of biofabrication techniques has grown and evolved significantly over the past few years, and researchers are demonstrating the successful fabrication of increasingly complex tissue models. This can be presumed to increase even further with more research groups as well as companies entering the field. Ng et al. report that since the year 2001, when a single scientific publication was published for bioprinting, the number has increased to 50 publications per year in 2019 [43]. IDTechEx estimates show that the global bioprinting market will reach US$1.9 billion by 2028 [137]. It should be noted, though, that applications that will successfully tackle the challenges of tissue engineering and regenerative medicine will require additional development of accurate and reliable tools [138].

Currently scalable, yet spatially accurate and biochemically heterogeneous tissue constructs, which exhibit full functionality, cannot be achieved by any single biofabrication strategy. While light-assisted techniques such as lithography or LIFT offer the highest spatial resolution, and volumetric techniques offer fast manufacturing of large, complex structures, these can be produced using a homogeneous (bio)ink, selected from a narrow range of materials. Also, the long-term effects of irradiation and degradation products require further studies. Extrusion-based bioprinting allows fabrication of human-scale tissue scaffolds with integrated biochemical and cellular gradients, selecting from a broad range of materials. However, it is also the most limited technique in terms of resolution.

The above-described fabrication techniques are continually refined to reduce the extent of their limitations. To rapidly build large, fully functional, and personalized tissues or complete organs, a viable direction seems to develop hybrid methods, which combine advantages of several scaffold fabrication approaches. Efforts have already been made in this direction, for example, by combining MEW with microextrusion [105] or microextrusion with droplet-based techniques [139]. In this regard, it will be crucial to consider parallel development of fabrication techniques with novel (bio)inks, which will, in addition to exhibiting ECM-like properties,

be appropriately "printable." In terms of composition, decellularized ECMs are excellent guides for the design of new scaffolding materials for the engineering of specific tissue types. A good example of using decellularized ECM as source material for a bioink design was demonstrated by Noor et al. who 3D printed a miniature version of the human heart [72].

Another aspect of biofabrication worth noting is the emergence of 4D bioprinting. The concept is based on the idea that the fabricated scaffold continues to change over time, adapting its functionality according to time and external triggers, such as chemical cues and temperature, and has been extensively reviewed by Gao et al. [140].

At the moment, some of the main challenges in tissue engineering remain to be solved, including effective vascularization, improved control over scaffold resolution, shape fidelity, and anisotropic properties in terms of mechanics and biochemical composition. However, progress is made rapidly, and we can be optimistic about the future. Current advances and the state of organ manufacturing are further discussed in Chapter 17.

References

1 European Commission (2014). Journalist Workshop on Organ donation and transplantation Recent Facts & Figures.

2 European Commission (2017). Study on the uptake and impact of the EU Action Plan on Organ Donation and Transplantation (2009–2015) in the EU Member States.

3 European Commission (2018). Infographic: Organs, Blood, Tissues & Cells in the EU.

4 Frohn, C., Fricke, L., Puchta, J.C., and Kirchner, H. (2001). The effect of HLA-C matching on acute renal transplant rejection. *Nephrol. Dial. Transplant.* 16 (2): 355–360.

5 Cippa, P.E., Schiesser, M., Ekberg, H. et al. (2015). Risk stratification for rejection and infection after kidney transplantation. *Clin. J. Am. Soc. Nephrol.* 10 (12): 2213–2220.

6 Lai, X.Q., Chen, G.D., Qiu, J. et al. (2014). Recipient-related risk factors for graft failure and death in elderly kidney transplant recipients. *PLoS One* 9 (11): e112938.

7 Tunchel, S., Blay, A., Kolerman, R. et al. (2016). 3D printing/additive manufacturing single titanium dental implants: a prospective multicenter study with 3 years of follow-up. *Int. J. Dent.*

8 Lee, J.S., Hong, J.M., Jung, J.W. et al. (2014). 3D printing of composite tissue with complex shape applied to ear regeneration. *Biofabrication* 6 (2): 024103.

9 Teng, Y.D., Lavik, E.B., Qu, X. et al. (2002). Functional recovery following traumatic spinal cord injury mediated by a unique polymer scaffold seeded with neural stem cells. *Proc. Natl. Acad. Sci. U.S.A.* 99 (5): 3024–3029.

10 Chen, T.-H., Ghayor, C., Siegenthaler, B. et al. (2018). Lattice microarchitecture for bone tissue engineering from calcium phosphate compared to titanium. *Tissue Eng. Part A* 24 (19–20): 1554–1561.

11 Khademhosseini, A. and Langer, R. (2016). A decade of progress in tissue engineering. *Nat. Protoc.* 11 (10): 1775–1781.

12 Ben-Arye, T. and Levenberg, S. (2019). Tissue engineering for clean meat production. *Front. Sustain. Food Syst.* 3: 46.

13 Post, M.J. (2012). Cultured meat from stem cells: challenges and prospects. *Meat Sci.* 92 (3): 297–301.

14 Stephens, N., Di Silvio, L., Dunsford, I. et al. (2018). Bringing cultured meat to market: technical, socio-political, and regulatory challenges in cellular agriculture. *Trends Food Sci. Technol.* 78: 155–166.

15 Khademhosseni, A., Vacanti, J.P., and Langer, R. (2009). Progress in tissue engineering. *Sci. Am.* 300 (5): 64–71.

16 Romo-Morales, A. and Przyborski, S. (2017). An introduction to the third dimension for routine cell culture. *Technology Platforms for 3D Cell Culture: A User's Guide*, p. 1.

17 Bell, S., Redmann, A.L., and Terentjev, E.M. (2019). Universal kinetics of the onset of cell spreading on substrates of different stiffness. *Biophys. J.* 116 (3): 551–559.

18 Engler, A.J., Sen, S., Sweeney, H.L., and Discher, D.E. (2006). Matrix elasticity directs stem cell lineage specification. *Cell* 126 (4): 677–689.

19 Dew, L., MacNeil, S., and Chong, C.K. (2015). Vascularization strategies for tissue engineers. *Regenerat. Med.* 10 (2): 211–224.

20 Song, H.G., Rumma, R.T., Ozaki, C.K. et al. (2018). Vascular tissue engineering: progress, challenges, and clinical promise. *Cell Stem Cell* 22 (3): 340–354.

21 Hatton, G.B., Madla, C.M., Gaisford, S. et al. (2018). Medical applications of 3D printing. In: *3D Printing of Pharmaceuticals* (ed. W. Jamróz, J. Szafraniec, M. Kurek and R. Jachowicz), 163–182. Springer.

22 Abercrombie, M. (1970). Contact inhibition in tissue culture. *In Vitro* 6 (2): 128–142.

23 Mattei, G., Giusti, S., and Ahluwalia, A. (2014). Design criteria for generating physiologically relevant *in vitro* models in bioreactors. *Processes* 2 (3): 548–569.

24 Elliott, N.T. and Yuan, F. (2011). A review of three-dimensional *in vitro* tissue models for drug discovery and transport studies. *J. Pharm. Sci.* 100 (1): 59–74.

25 Edmondson, R., Broglie, J.J., Adcock, A.F. et al. (2014). Three-dimensional cell culture systems and their applications in drug discovery and cell-based biosensors. *Assay Drug Dev. Technol.* 12 (4): 207–218.

26 Breslin, S. and O'Driscoll, L. (2013). Three-dimensional cell culture: the missing link in drug discovery. *Drug Discovery Today* 18 (5–6): 240–249.

27 Alberts, B., Johnson, A., Lewis, J. et al. (2002). The extracellular matrix of animals. In: *Molecular Biology of the Cell*, 4e (ed. B. Alberts, A. Johnson, J. Lewis, et al.). Garland Science.

28 Murphy, S.V. and Atala, A. (2014). 3D bioprinting of tissues and organs. *Nat. Biotechnol.* 32 (8): 773–785.

29 Yu, Y., Moncal, K.K., Li, J.Q. et al. (2016). Three-dimensional bioprinting using self-assembling scalable scaffold-free "tissue strands" as a new bioink. *Sci. Rep.* 6: 28714.

30 Ware, M.J., Colbert, K., Keshishian, V. et al. (2016). Generation of homogenous three-dimensional pancreatic cancer cell spheroids using an improved hanging drop technique. *Tissue Eng. Part C Methods* 22 (4): 312–321.

31 Gong, X., Lin, C., Cheng, J. et al. (2015). Generation of multicellular tumor spheroids with microwell-based agarose scaffolds for drug testing. *PLoS One* 10 (6): e0130348.

32 Costa, E.C., Gaspar, V.M., Coutinho, P., and Correia, I.J. (2014). Optimization of liquid overlay technique to formulate heterogenic 3D co-cultures models. *Biotechnol. Bioeng.* 111 (8): 1672–1685.

33 Ingram, M., Techy, G.B., Saroufeem, R. et al. (1997). Three-dimensional growth patterns of various human tumor cell lines in simulated microgravity of a NASA bioreactor. *In Vitro Cell. Dev. Biol.-Anim.* 33 (6): 459–466.

34 Santo, V.E., Estrada, M.F., Rebelo, S.P. et al. (2016). Adaptable stirred-tank culture strategies for large scale production of multicellular spheroid-based tumor cell models. *J. Biotechnol.* 221: 118–129.

35 Haisler, W.L., Timm, D.M., Gage, J.A. et al. (2013). Three-dimensional cell culturing by magnetic levitation. *Nat. Protoc.* 8 (10): 1940–1949.

36 Parfenov, V.A., Mironov, V.A., van Kampen, K.A. et al. (2020). Scaffold-free and label-free biofabrication technology using levitational assembly in high magnetic field. *Biofabrication* 12 (4): 045022.

37 Sriphutkiat, Y., Kasetsirikul, S., and Zhou, Y.F. (2018). Formation of cell spheroids using standing surface acoustic wave (SSAW). *Int. J. Bioprint.* 4 (1).

38 Mironov, V., Visconti, R.P., Kasyanov, V. et al. (2009). Organ printing: tissue spheroids as building blocks. *Biomaterials* 30 (12): 2164–2174.

39 Ayan, B., Heo, D.N., Zhang, Z. et al. (2020). Aspiration-assisted bioprinting for precise positioning of biologics. *Sci. Adv.* 6 (10): eaaw5111.

40 LaBarge, W., Morales, A., Pretorius, D. et al. (2019). Scaffold-free bioprinter utilizing layer-by-layer printing of cellular spheroids. *Micromachines (Basel)* 10 (9): 570.

41 Skardal, A., Mack, D., Kapetanovic, E. et al. (2012). Bioprinted amniotic fluid-derived stem cells accelerate healing of large skin wounds. *Stem Cells Transl. Med.* 1 (11): 792–802.

42 Keriquel, V., Guillemot, F., Arnault, I. et al. (2010). *In vivo* bioprinting for computer- and robotic-assisted medical intervention: preliminary study in mice. *Biofabrication* 2 (1): 014101.

43 Ng, W.L., Chua, C.K., and Shen, Y.-F. (2019). Print me an organ! Why we are not there yet. *Prog. Polym. Sci.* 97: 101145.

44 Saunders, R.E. and Derby, B. (2014). Inkjet printing biomaterials for tissue engineering: bioprinting. *Int. Mater. Rev.* 59 (8): 430–448.

45 Attalla, R., Puersten, E., Jain, N., and Selvaganapathy, P.R. (2018). 3D bioprinting of heterogeneous bi- and tri-layered hollow channels within gel scaffolds

using scalable multi-axial microfluidic extrusion nozzle. *Biofabrication* 11 (1): 015012.

46 Milojevic, M., Vihar, B., Banovic, L. et al. (2019). Core/shell printing scaffolds for tissue engineering of tubular structures. *J. Vis. Exp.* 151: e59951.

47 Gao, Q., He, Y., Fu, J.Z. et al. (2015). Coaxial nozzle-assisted 3D bioprinting with built-in microchannels for nutrients delivery. *Biomaterials* 61: 203–215.

48 Davidovich-Pinhas, M. and Bianco-Peled, H. (2010). A quantitative analysis of alginate swelling. *Carbohydr. Polym.* 79 (4): 1020–1027.

49 Ramos, T. and Moroni, L. (2020). Tissue engineering and regenerative medicine 2019: the role of biofabrication-A year in review. *Tissue Eng. Part C Methods* 26 (2): 91–106.

50 Groll, J., Boland, T., Blunk, T. et al. (2016). Biofabrication: reappraising the definition of an evolving field. *Biofabrication* 8 (1): 013001.

51 Editorial board of Mary Ann Liebert, Inc. (2007). Advancing tissue science and engineering: a foundation for the future a multi-agency strategic plan. *Tissue Eng.* 13 (12): 2825–2826.

52 U.S. Department of Health and Human Services (2020). *A New Vision—A Future for Regenerative Medicine*. Washington, DC.

53 Guillemot, F., Mironov, V., and Nakamura, M. (2010). Bioprinting is coming of age: report from the International Conference on Bioprinting and Biofabrication in Bordeaux (3B'09). *Biofabrication* 2 (1): 010201.

54 Groll, J., Burdick, J.A., Cho, D.W. et al. (2018). A definition of bioinks and their distinction from biomaterial inks. *Biofabrication* 11 (1): 013001.

55 Vijayavenkataraman, S., Yan, W.C., Lu, W.F. et al. (2018). 3D bioprinting of tissues and organs for regenerative medicine. *Adv. Drug Delivery Rev.* 132: 296–332.

56 Abzan, N., Kharaziha, M., Labbaf, S., and Saeidi, N. (2018). Modulation of the mechanical, physical and chemical properties of polyvinylidene fluoride scaffold via non-solvent induced phase separation process for nerve tissue engineering applications. *Eur. Polym. J.* 104: 115–127.

57 Colosi, C., Costantini, M., Barbetta, A. et al. (2013). Morphological comparison of PVA scaffolds obtained by gas foaming and microfluidic foaming techniques. *Langmuir* 29 (1): 82–91.

58 Chen, G., Sato, T., Ohgushi, H. et al. (2005). Culturing of skin fibroblasts in a thin PLGA-collagen hybrid mesh. *Biomaterials* 26 (15): 2559–2566.

59 Bhardwaj, N. and Kundu, S.C. (2010). Electrospinning: a fascinating fiber fabrication technique. *Biotechnol. Adv.* 28 (3): 325–347.

60 Zambaiti, E., Scottoni, F., Rizzi, E. et al. (2019). Whole rat stomach decellularisation using a detergent-enzymatic protocol. *Pediatr. Surg. Int.* 35 (1): 21–27.

61 Chansoria, P., Narayanan, L.K., Schuchard, K., and Shirwaiker, R. (2019). Ultrasound-assisted biofabrication and bioprinting of preferentially aligned three-dimensional cellular constructs. *Biofabrication* 11 (3): 035015.

62 Kurimoto, R., Niiyama, E., and Ebara, M. (2016). Fibrous materials. In: *Biomaterials Nanoarchitectonics* (ed. M. Ebara), 267–278. Amsterdam, Netherlands: Elsevier Inc.

63 Holzwarth, J.M. and Ma, P.X. (2011). Biomimetic nanofibrous scaffolds for bone tissue engineering. *Biomaterials* 32 (36): 9622–9629.

64 Zhao, F., Yin, Y.J., Lu, W.W. et al. (2002). Preparation and histological evaluation of biomimetic three-dimensional hydroxyapatite/chitosan-gelatin network composite scaffolds. *Biomaterials* 23 (15): 3227–3234.

65 Kucharska, M., Butruk, B., Walenko, K. et al. (2012). Fabrication of in-situ foamed chitosan/β-TCP scaffolds for bone tissue engineering application. *Mater. Lett.* 85: 124–127.

66 Ji, C., Annabi, N., Hosseinkhani, M. et al. (2012). Fabrication of poly-DL-lactide/polyethylene glycol scaffolds using the gas foaming technique. *Acta Biomater.* 8 (2): 570–578.

67 Akbari, M., Tamayol, A., Bagherifard, S. et al. (2016). Textile technologies and tissue engineering: a path toward organ weaving. *Adv. Healthc. Mater.* 5 (7): 751–766.

68 Tamayol, A., Akbari, M., Annabi, N. et al. (2013). Fiber-based tissue engineering: progress, challenges, and opportunities. *Biotechnol. Adv.* 31 (5): 669–687.

69 Pedde, R.D., Mirani, B., Navaei, A. et al. (2017). Emerging biofabrication strategies for engineering complex tissue constructs. *Adv. Mater.* 29 (19): 1606061.

70 Uygun, B.E., Soto-Gutierrez, A., Yagi, H. et al. (2010). Organ reengineering through development of a transplantable recellularized liver graft using decellularized liver matrix. *Nat. Med.* 16 (7): 814–820.

71 Ott, H.C., Matthiesen, T.S., Goh, S.K. et al. (2008). Perfusion-decellularized matrix: using nature's platform to engineer a bioartificial heart. *Nat. Med.* 14 (2): 213–221.

72 Noor, N., Shapira, A., Edri, R. et al. (2019). 3D printing of personalized thick and perfusable cardiac patches and hearts. *Adv. Sci.* 6 (11): 1900344.

73 Hickey, R.J., Modulevsky, D.J., Cuerrier, C.M., and Pelling, A.E. (2018). Customizing the shape and microenvironment biochemistry of biocompatible macroscopic plant-derived cellulose scaffolds. *ACS Biomater. Sci. Eng.* 4 (11): 3726–3736.

74 Campuzano, S. and Pelling, A.E. (2019). Scaffolds for 3D cell culture and cellular agriculture applications derived from non-animal sources. *Front. Sustain. Food Syst.* 3: 38.

75 Modulevsky, D.J., Lefebvre, C., Haase, K. et al. (2014). Apple derived cellulose scaffolds for 3D mammalian cell culture. *PLoS One* 9 (5): e97835.

76 Gershlak, J.R., Hernandez, S., Fontana, G. et al. (2017). Crossing kingdoms: using decellularized plants as perfusable tissue engineering scaffolds. *Biomaterials* 125: 13–22.

77 Heintz, K.A., Bregenzer, M.E., Mantle, J.L. et al. (2016). Fabrication of 3D biomimetic microfluidic networks in hydrogels. *Adv. Healthc. Mater.* 5 (17): 2153–2160.

78 Shahriari, D., Shibayama, M., Lynam, D.A. et al. (2017). Peripheral nerve growth within a hydrogel microchannel scaffold supported by a kink-resistant conduit. *J. Biomed. Mater. Res. A* 105 (12): 3392–3399.

79 Ioannidis, A., Bomze, D., Hammerle, C.H.F. et al. (2020). Load-bearing capacity of CAD/CAM 3D-printed zirconia, CAD/CAM milled zirconia, and heat-pressed lithium disilicate ultra-thin occlusal veneers on molars. *Dent. Mater.* 36: e109–e116.

80 Compaan, A.M., Christensen, K., and Huang, Y. (2016). Inkjet bioprinting of 3D silk fibroin cellular constructs using sacrificial alginate. *ACS Biomater. Sci. Eng.* 3 (8): 1519–1526.

81 Zimmermann, R., Hentschel, C., Schron, F. et al. (2019). High resolution bio-printing of multi-component hydrogels. *Biofabrication* 11 (4): 045008.

82 Singh, M., Haverinen, H.M., Dhagat, P., and Jabbour, G.E. (2010). Inkjet printing-process and its applications. *Adv. Mater.* 22 (6): 673–685.

83 Daly, R., Harrington, T.S., Martin, G.D., and Hutchings, I.M. (2015). Inkjet printing for pharmaceutics - a review of research and manufacturing. *Int. J. Pharm.* 494 (2): 554–567.

84 Ng, W.L., Lee, J.M., Yeong, W.Y. et al. (2017). Microvalve-based bioprinting - process, bio-inks and applications. *Biomater. Sci.* 5 (4): 632–647.

85 Jones, R., Haufe, P., Sells, E. et al. (2011). RepRap – the replicating rapid prototyper. *Robotica* 29 (1): 177–191.

86 Banović, L. and Vihar, B. (2018). Development of an extruder for open source 3D bioprinting. *J. Open Hardw.* 2 (1).

87 Cohen, D.L., Malone, E., Lipson, H., and Bonassar, L.J. (2006). Direct freeform fabrication of seeded hydrogels in arbitrary geometries. *Tissue Eng.* 12 (5): 1325–1335.

88 Irvine, S.A., Agrawal, A., Lee, B.H. et al. (2015). Printing cell-laden gelatin constructs by free-form fabrication and enzymatic protein cross-linking. *Biomed. Microdev.* 17 (1): 16.

89 Holzl, K., Lin, S.M., Tytgat, L. et al. (2016). Bioink properties before, during and after 3D bioprinting. *Biofabrication* 8 (3): 032002.

90 Hinton, T.J., Jallerat, Q., Palchesko, R.N. et al. (2015). Three-dimensional printing of complex biological structures by freeform reversible embedding of suspended hydrogels. *Sci. Adv.* 1 (9): e150075.

91 Wu, W., DeConinck, A., and Lewis, J.A. (2011). Omnidirectional printing of 3D microvascular networks. *Adv. Mater.* 23 (24): H178–H183.

92 Colosi, C., Shin, S.R., Manoharan, V. et al. (2016). Microfluidic bioprinting of heterogeneous 3D tissue constructs using low-viscosity bioink. *Adv. Mater.* 28 (4): 677–684.

93 Brown, T.D., Dalton, P.D., and Hutmacher, D.W. (2011). Direct writing by way of melt electrospinning. *Adv. Mater.* 23 (47): 5651–5657.

94 Dickman, C.T.D., Russo, V., Thain, K. et al. (2020). Functional characterization of 3D contractile smooth muscle tissues generated using a unique microfluidic 3D bioprinting technology. *FASEB J.* 34 (1): 1652–1664.

95 Bhattacharjee, T., Zehnder, S.M., Rowe, K.G., and Jain, S. (2015). Writing in the granular gel medium. *Sci. Adv.* 1 (8): e1500655.

96 Highley, C.B., Rodell, C.B., and Burdick, J.A. (2015). Direct 3D printing of shear-thinning hydrogels into self-healing hydrogels. *Adv. Mater.* 27 (34): 5075–5079.

97 Kolesky, D.B., Homan, K.A., Skylar-Scott, M.A., and Lewis, J.A. (2016). Three-dimensional bioprinting of thick vascularized tissues. *Proc. Natl. Acad. Sci. U.S.A.* 113 (12): 3179–3184.

98 Stumberger, G. and Vihar, B. (2018). Freeform perfusable microfluidics embedded in hydrogel matrices. *Materials (Basel)* 11 (12): 2529.

99 Skylar-Scott, M.A., Uzel, S.G.M., Nam, L.L., and Ahrens, J.H. (2019). Biomanufacturing of organ-specific tissues with high cellular density and embedded vascular channels. *Sci. Adv.* 5 (9): eaaw2459.

100 Gao, G., Lee, J.H., Jang, J. et al. (2017). Tissue engineered bio-blood-vessels constructed using a tissue-specific bioink and 3D coaxial cell printing technique: a novel therapy for ischemic disease. *Adv. Funct. Mater.* 27 (33): 1700798.

101 Liu, W., Zhang, Y.S., Heinrich, M.A., and De Ferrari, F. (2017). Rapid continuous multimaterial extrusion bioprinting. *Adv. Mater.* 29 (3): 1604630.

102 Whitesides, G.M. (2006). The origins and the future of microfluidics. *Nature* 442 (7101): 368–373.

103 Costantini, M., Testa, S., Mozetic, P. et al. (2017). Microfluidic-enhanced 3D bioprinting of aligned myoblast-laden hydrogels leads to functionally organized myofibers *in vitro* and *in vivo*. *Biomaterials* 131: 98–110.

104 Hrynevich, A., Elci, B.S., Haigh, J.N., and McMaster, R. (2018). Dimension-based design of melt electrowritten scaffolds. *Small* 14 (22): e1800232.

105 de Ruijter, M., Ribeiro, A., Dokter, I. et al. (2019). Simultaneous micropatterning of fibrous meshes and bioinks for the fabrication of living tissue constructs. *Adv. Healthc. Mater.* 8 (7): e1800418.

106 Klar, T.A., Wollhofen, R., and Jacak, J. (2014). Sub-Abbe resolution: from STED microscopy to STED lithography. *Phys. Scr.* T162: 014049 1, 014049 10.

107 Kamali, S.M., Arbabi, E., Kwon, H., and Faraon, A. (2019). Metasurface-generated complex 3-dimensional optical fields for interference lithography. *Proc. Natl. Acad. Sci. U.S.A.* 116 (43): 21379–21384.

108 Bernal, P.N., Delrot, P., Loterie, D. et al. (2019). Volumetric bioprinting of complex living-tissue constructs within seconds. *Adv. Mater.* 31 (42): e1904209.

109 Bártolo, P.J. (2011). Stereolithographic processes. In: *Stereolithography: Materials, Processes and Applications* (ed. P.J. Bártolo), 1–36. Boston, MA: Springer US.

110 Melchels, F.P., Feijen, J., and Grijpma, D.W. (2010). A review on stereolithography and its applications in biomedical engineering. *Biomaterials* 31 (24): 6121–6130.

111 Zheng, X., Deotte, J., Alonso, M.P. et al. (2012). Design and optimization of a light-emitting diode projection micro-stereolithography three-dimensional manufacturing system. *Rev. Sci. Instrum.* 83 (12): 125001.

112 Z. Wang, Z. Tian, X. Jin, J.F. Holzman, F. Menard, K. Kim (2017). Visible light-based stereolithography bioprinting of cell-adhesive gelatin hydrogels. *2017 39th Annual International Conference of the IEEE Engineering in Medicine and Biology Society (EMBC)*.

113 Han, X.X., Courseaus, J., Khamassi, J. et al. (2018). Optimized vascular network by stereolithography for tissue engineered skin. *Int. J. Bioprint.* 4 (2).

114 Bail, R., Patel, A., Yang, H. et al. (2013). The effect of a Type I photoinitiator on cure kinetics and cell toxicity in projection-microstereolithography. *Procedia CIRP* 5: 222–225.

115 Torgersen, J., Qin, X.-H., Li, Z. et al. (2013). Hydrogels for two-photon polymerization: a toolbox for mimicking the extracellular matrix. *Adv. Funct. Mater.* 23 (36): 4542–4554.

116 Heller, C., Schwentenwein, M., Russmueller, G. et al. (2009). Vinyl esters: low cytotoxicity monomers for the fabrication of biocompatible 3D scaffolds by lithography based additive manufacturing. *J. Polym. Sci., Part A: Polym. Chem.* 47 (24): 6941–6954.

117 Juodkazis, S., Mizeikis, V., Seet, K.K. et al. (2005). Two-photon lithography of nanorods in SU-8 photo-resist. *Nanotechnology* 16 (6): 846–849.

118 Stocker, M.P., Li, L., Gattass, R.R., and Fourkas, J.T. (2011). Multiphoton photo-resists giving nanoscale resolution that is inversely dependent on exposure time. *Nat. Chem.* 3 (3): 223–227.

119 Burmeister, F., Zeitner, U.D., Nolte, S., and Tünnermann, A. (2012). High numerical aperture hybrid optics for two-photon polymerization. *Opt. Express* 20 (7): 7994–8005.

120 Chu, W., Tan, Y., Wang, P. et al. (2018). Centimeter-height 3D printing with femtosecond laser two-photon polymerization. *Adv. Mater. Technol.* 3 (5): 1700396.

121 Nguyen, A.K. and Narayan, R.J. (2017). Two-photon polymerization for biological applications. *Mater. Today* 20 (6): 314–322.

122 J. Heitz, C. Plamadeala, M. Wiesbauer, P. Freudenthaler, R. Wollhofen, J. Jacak, S. Puthukodan, T.A. Klar, A. Weth, W. Baumgartner, (2016). Three-dimensional photonic structures on transparent substrates fabricated by two-photon polymerization for use as cell substrates and for wetting experiments. *2016 18th International Conference on Transparent Optical Networks (ICTON)*.

123 Dobos, A., Van Hoorick, J., Steiger, W. et al. (2019). Thiol-gelatin-norbornene bioink for laser-based high-definition bioprinting. *Adv. Healthc. Mater.* 9: 1900752.

124 Kelly, B.E., Bhattacharya, I., Heidari, H. et al. (2019). Volumetric additive manufacturing via tomographic reconstruction. *Science* 363 (6431): 1075–1079.

125 Loterie, D., Delrot, P., and Moser, C. (2020). High-resolution tomographic volumetric additive manufacturing. *Nat. Commun.* 11 (852): 1–6.

126 Du, Y., Liu, H., Yang, Q. et al. (2017). Selective laser sintering scaffold with hierarchical architecture and gradient composition for osteochondral repair in rabbits. *Biomaterials* 137: 37–48.

127 Guillotin, B., Souquet, A., Catros, S. et al. (2010). Laser assisted bioprinting of engineered tissue with high cell density and microscale organization. *Biomaterials* 31 (28): 7250–7256.

128 Hopp, B., Smausz, T., Kresz, N. et al. (2005). Survival and proliferative ability of various living cell types after laser-induced forward transfer. *Tissue Eng.* 11 (11–12): 1817–1823.

129 Guillemot, F., Souquet, A., Catros, S., and Guillotin, B. (2010). Laser-assisted cell printing: principle, physical parameters versus cell fate and perspectives in tissue engineering. *Nanomedicine* 5 (3): 507–515.

130 Keriquel, V., Oliveira, H., Remy, M. et al. (2017). In situ printing of mesenchymal stromal cells, by laser-assisted bioprinting, for *in vivo* bone regeneration applications. *Sci. Rep.* 7: 1778.

131 Kruth, J.P., Mercelis, P., Van Vaerenbergh, J. et al. (2005). Binding mechanisms in selective laser sintering and selective laser melting. *Rapid Prototyp. J.* 11 (1): 26–36.

132 Drstvenšek, I., Brajlih, T., and Tomažič, T. (2013). Additive manufacturing in practical use. *J. Trends Dev. Mach.* 17 (1): 9–16.

133 de Wild, M., Schumacher, R., Mayer, K. et al. (2013). Bone regeneration by the osteoconductivity of porous titanium implants manufactured by selective laser melting: a histological and micro computed tomography study in the rabbit. *Tissue Eng. Part A* 19 (23–24): 2645–2654.

134 Schmidleithner, C., Malferarri, S., Palgrave, R. et al. (2019). Application of high resolution DLP stereolithography for fabrication of tricalcium phosphate scaffolds for bone regeneration. *Biomed. Mater.* 14 (4): 045018.

135 Singh, R., Lee, P.D., Dashwood, R.J., and Lindley, T.C. (2013). Titanium foams for biomedical applications: a review. *Mater. Technol.* 25 (3–4): 127–136.

136 Hollister, S.J. (2005). Porous scaffold design for tissue engineering. *Nat. Mater.* 4 (7): 518–524.

137 Tsao, N. (2018). 3D Bioprinting 2018–2028: Technologies, Markets, Forecasts (17 March 2020). https://www.idtechex.com/en/research-report/3d-bioprinting-2018-2028-technologies-markets-forecasts/592 (accessed 24 March 2020).

138 Gomes, M.E., Rodrigues, M.T., Domingues, R.M.A., and Reis, R.L. (2017). Tissue engineering and regenerative medicine: new trends and directions-A year in review. *Tissue Eng. Part B Rev.* 23 (3): 211–224.

139 Kim, B.S., Lee, J.S., Gao, G., and Cho, D.W. (2017). Direct 3D cell-printing of human skin with functional transwell system. *Biofabrication* 9 (2): 025034.

140 Gao, B., Yang, Q., Zhao, X. et al. (2016). 4D bioprinting for biomedical applications. *Trends Biotechnol.* 34 (9): 746–756.

11

Methods and Challenges in the Fabrication of Biopolymer-Based Scaffolds for Tissue Engineering Application

Daniela Ivanov

"Petru Poni" Institute of Macromolecular Chemistry, 41A Grigore Ghica Voda Alley, 700487, Iasi, Romania

11.1 Introduction

Extracellular matrix (ECM) has tissue-specific dynamic composition with dissimilar internal and external macro- to nano-structural multiscale architecture, biological, and mechanical characteristics. This is why tissue engineering as originally stated is "*an interdisciplinary field which applies the principles of engineering and life sciences*," from material sciences, cell biology, biotechnology, and chemistry [1].

Contemporary concept of scaffolding in tissue engineering is to mimic, at least partially, the structure and functions of native ECM [2]. The scaffold's efficiency is associated with its biodegradability upon implantation, ideally at a rate matching that of the new ECM regeneration, cyto- and tissue compatibility and bioactivity [3, 4], microstructure with porosity, pore size and pore size distribution for efficient nutrient and metabolite diffusion, vascularization, and new tissue formation and remodeling without significantly compromising mechanical properties, surface properties [5], mechanical stability providing rigidity, stiffness, and elasticity [6], easy to fabricate into precise desired shape, and structural and biochemical stability upon sterilization [7]. It becomes clear the ideal scaffolds *features* should be different for each tissue type, hard or soft tissues. There are some key factors in controlling the potential of an engineered scaffold to mimic the native tissue as accurately as possible. First, material selection in scaffold construct is strongly related to the native tissue mechanical properties. Potential materials include natural and synthetic biocompatible and eventually biodegradable polymers, ceramics, metals, and combinations of these materials, such as reinforced polymeric composites, each of them with specific chemical, physical, and mechanical properties. Scaffold surface, as the interface for cell and native tissues, plays a key role in guiding cell behavior; a large surface area and an appropriate surface energy (hydrophilicity/hydrophobicity balance) favor cell attachment and growth, and the surrounding fluids ability to interact along the surface; moreover, for a better interaction, the biomaterial surface could be eventually modified with bioactive molecules. Another important issue is the macro- and

Functional Biomaterials: Design and Development for Biotechnology, Pharmacology, and Biomedicine, First Edition. Edited by Tamilselvan Mohan and Karin Stana Kleinschek.

microstructure of the materials. Highly porous biomaterials with interconnected pores are desirable for the easy diffusion of nutrients to and waste products to/from the scaffold and for vascularization. Moreover, the interconnected porous structures will substantially affect the final mechanical properties. The surface area/volume ratio of porous scaffolds depends on the density and average diameter of the pores; the dimensional characteristics of specific cells dictate the minimum pore size and interconnectivity type. Generally, micro- and mesopores promote cell adhesion and favor scaffold degradation at controllable rates, whereas macropores support tissue ingrowth and vascularization [8]. After selecting the most appropriate biomaterial for scaffold fabrication, it is quite important to select an adequate processing technique with high levels of control over the macro- and microstructural architecture. The selection of the most appropriate processing method must meet some key requirements, such as process accuracy and reproducibility – the obtained scaffolds have to present consistent pore size and interconnectivity and should not suffer any physical–chemical variations when produced by the same method. Moreover, the processing conditions must not alter the properties of the biomaterials, and any cytotoxic additive used during the process must be totally removed [9].

Conventional techniques (polymer melt-based processing or solution-based processing, gas foaming, freeze drying, solvent casting or particulate leaching, and their combinations) usually result in macro- to microstructured bioscaffolds, whereas electrospinning and advanced techniques (UV or laser polymerizable systems–stereolithography and selective laser sintering [SLS], and nozzle-based deposition–fused deposition, and 3D bioprinting) allow the fabrication of more precise micro- to nanostructure organized scaffolds. The fabrication of biomimetic hybrid 3D scaffolds by combining micro- and nanotechnologies is a promising approach to design 3D anisotropic scaffolds that better replicates the anatomical structures of native extracellular matrices [10, 11].

Hybrid scaffolds, generally consisting of 3D microprinted pores and electrospun nanofibers, provide the necessary topography and the architecture needed for more efficient tissue ingrowth. Such 3D scaffolds improve cell entrapment and proliferation, promote cell differentiation, and favor tissue regeneration. In order to replicate the spatial gradient of composition, properties, and functions typical to targeted biological tissues, scaffolds with spatially distributed gradients have also been developed [12, 13]. The successful scaffold implantation requires the biomimetic structure to be seeded with corresponding type of cells and charged with specific growth factors. Both the top-down and the bottom-up approaches have been used for the design of tissue-engineered *in vitro* implantable scaffolds. Hence, in top-down strategies, specifically designed scaffolds have been seeded with cells and cultured on to mimic the tissue to be replaced in terms of structure, composition, and mechanical properties. On the other hand, the bottom-up approach supposes the construction of modular scaffolds, obtained through both microencapsulation and microfabrication techniques, as well as employing traditional cell culture strategies, to create a more biomimetic scaffold [14].

This chapter briefly describes some of the most representative biopolymer fabrication techniques to produce the various types of 3D scaffolds with each characteristic,

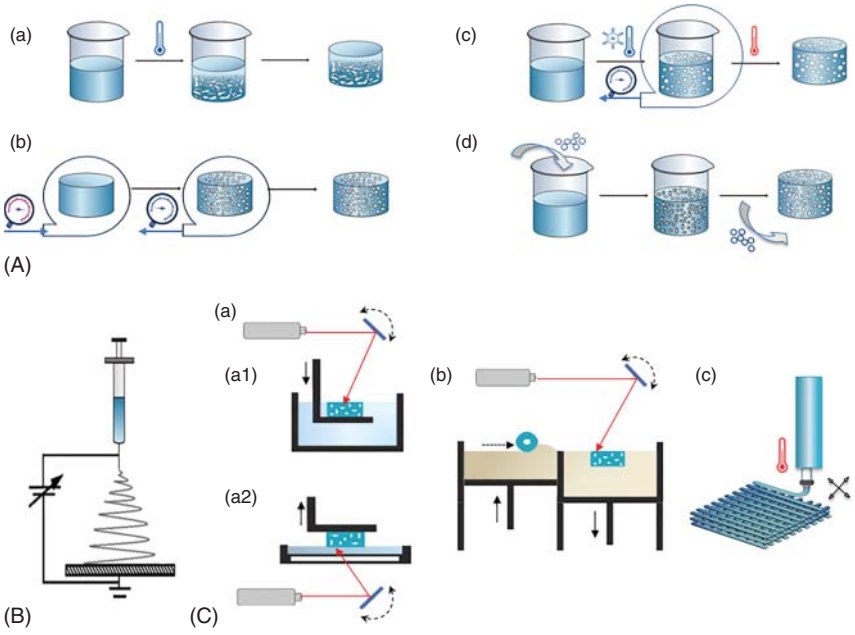

Figure 11.1 Schematic representation of the common techniques for scaffold fabrication. (A) Conventional methods: (a) phase separation, (b) gas foaming, (c) freeze drying, and (d) solvent casting/particulate leaching. (B) Electrospinning. (C) Advanced fabrication methods: (a) stereolithography: (a1) top-down approach and (a2) bottom-up approach; (b) selective laser sintering; (c) fused deposition modeling.

advantages and limitations or shortcomings, specifying their related potential applications (summarized in (Figure 11.1) and Table 11.1). Biopolymer composites scaffold fabrication and applications in tissue engineering can be found elsewhere [81].

11.2 Conventional Methods for 3D Scaffold Engineering

11.2.1 Fluid-Based Technologies

11.2.1.1 Melt-Based Processing – Melt Molding

Melt-based processing is used to produce solid implants of biodegradable biomaterials [82]. These conventional techniques are simple, easy to scale up, and cost effective. Orthopedic fixation devices (plates, rods, and screws) are often obtained using extrusion or injection-molding methods. Melt-based methods involve the use of molds to produce complex 3D scaffolds of any desired shape by modifying the mold geometry. Melt-based techniques typically use solid polymers, without solvents, being useful in fabricating scaffolds from insoluble polymers in organic solvents [83].

The selection of a melt-based processing method strongly depends on the thermoplastic or thermosetting nature of the initial polymeric material. For thermoplastic

Table 11.1 Fabrication methods with their advantages, limitations, and related possible clinical applications.

Fabrication method	Suitable biomaterials	Advantages	Limitations/ disadvantages	Targeted clinical applications	Selected references
		Conventional methods for 3D porous scaffolds			
		Fluid-based technologies			
Melt-based processing – melt molding	Synthetic polymers; polymer composites	Macro-shape control; independent control of porosity and pore size	High processing temperature and/or pressure; association with other conventional methods	Bone; cartilage; peripheral nerve; intestine; blood vessel	[15–22]
		Solution-based processing			
Phase separation	Natural and synthetic polymers	Potential for drug-delivery applications; bioactive molecules protected from solvents; anisotropic microstructure	Residual solvents; limited pore sizes; difficult to control precisely scaffold morphology	Osteochondral; nerves; pulmonary alveoli	[23–26]
Gas foaming	Synthetic polymers	Control over porosity and pore size; free of organic solvents needed	Inadequate pore interconnectivity; limited pore sizes; limited mechanical property	Cartilage; heart; lung	[27–30]
Freeze drying	Natural and synthetic polymers; polymer composites	Pore interconnectivity; high controlled porosity; unidirectional orientated microstructure	Lower porosity and pore size than most other procedures; long processing time	Skin; adipose tissue; nerves; arterial; muscles; tendon; bone, cartilage, and osteochondral	[31–38]
Solvent casting/particulate leaching	Natural and synthetic polymers; polymer composites	High porosity control; independent control of porosity and pore size and geometry; minimal material needed for procedure; minimal steps; simple procedure	Inadequate pore interconnectivity; produces thin membranes with a dense surface skin; harmful residual solvents/porogens; possible acidic polymer degradation affecting cell viability; poor mechanical strength	Cartilage	[39–42]

		Textile technologies for 3D scaffold engineering			
Electrospinning	Natural and synthetic polymers – advantage of material versatility	Control over porosity, pore size, and fiber diameter; simple setup, versatility, productivity, relative low cost	Uneven pore size; limited control porosity; poor mechanical integrity; most cytotoxic solvents; pore sizes decrease with fiber thickness – relatively poor cellular infiltration	Liver tissue; articular cartilage; bone; ligaments and tendons; vascular grafts, cardiac patches; muscles; soft tissues (cornea and corneal components, skin, nerves)	[43–53]
		Hydrogel scaffolds fabrication			
Physical or/and chemical cross-linking hydrogels	Natural and synthetic materials	Immediate implantable; minimal processing necessary	Limited mechanical properties; limited porosity; harmful polymerization by-products; limited material choice	Bone	[54, 55]
In situ polymerization	Functionalized natural and synthetic polymers	Injectable application	Poor mechanical properties	Bone; cartilage	[56–59]
		Self-assembly methods			
Self-assembly	Peptides, polymers	Laminated layers constructs	Difficult to construct thick constructs	Liver	[44, 60]
Cell sheet engineering	Polymers and cells	Laminated layers of cell-seeded constructs	Difficult to construct thick constructs	Corneal epithelium and endothelium, vessel endothelium, myocardial tissue, and tracheal epithelium; injectable applications	[61, 62]

(*continued*)

Table 11.1 (Continued)

Fabrication method	Suitable biomaterials	Advantages	Limitations/ disadvantages	Targeted clinical applications	Selected references
		Microsphere-based scaffolds fabrication			
	Biopolymers and synthetic polymers; inorganic materials	Good mechanical strength and stability, high porosity and pore interconnectivity may be arthroscopically implanted; allow for controlled release of bioactive molecules; sintering easy quick fabrication and large-scale production of complicated designs	Depending on microsphere fabrication method: poor size control; solvent toxicity; complex and expensive process; denaturation of biopolymers due to high temperature and loss in bioactivity	Bone; cartilage; skin; heart; liver; neural tissue	[63–65]
		Advanced fabrication methods – solid freeform fabrication – rapid prototyping			
Stereolithography	Photopolymers	Rapid fabrication; very high resolution; smooth finish surface	Expensive; support system needed	Bone; tendon; trachea	[66–68]
Selective laser sintering (SLS)	Heat-resistant polymers and composites	High mechanical strength; complex structure; fine resolution	High temperature required; processing and postprocessing expensive and time consuming	Bone; heart; skin	[69–73]

Fused deposition modeling (FDM)	Limitation on materials (thermoplastics)	Low cytotoxicity; relatively inexpensive	Requires support structure for overhangs and complex shapes; postprocessing may be necessary; low-resolution	Bone	[74–76]
3D printing 3D bioprinting	Wide variety of materials; deposition of material and/or cells	Highly defined porosity and architecture; accurate repeatability; allows incorporation of bioactive molecules and cells; automation, reproducibility, and ability to print specific shapes	Time-consuming process	Cornea and corneal components; liver tissue engineering; bone; articular cartilage	[43–45, 77]
Indirect rapid prototyping	Wide range of biomaterials or combination	Good for prototyping; material versatility casting once mold is obtained	Low accuracies/resolution; mold required for casting; long time production	Bone–ligament complex; bone; arterial tissue	[78–80]

polymers, that are first melted in fabrication method, the softening temperature and the thermal stability of the polymer dictates the processing method, beside the geometry and size of the finished product. Injection molding, similar to die casting used for metals, is usually used for processing thermoplastic polymers. Extrusion is another method for thermoplastic materials, supposing a simple injection molding through an open-ended die. Blow-molding process is frequently used to obtain products with thin walls, similar to blowing glass containers. Thermosetting polymers, usually prepared as linear chains, normally in liquid state, are further cured in a mold, resulting in polymeric product. Usual, thermosetting polymers are processed by compression molding, injection molding – also called reaction injection molding. Curing reaction of thermoset polymers takes place under pressure in the heated mold, as long as the reaction requires completing. Casting is a method used for both thermoplastic and thermosetting polymers. In this method liquid polymer (molten polymers or polymer solutions) is poured into a not heated mold that further physically (cooling) or chemically (polymerization) solidifies to form a rigid product with detailed shape and dimensions of the mold cavity.

Melt-based scaffold fabrication techniques are usually combined with some other methods to generate porous structures in the processed scaffolds for tissue engineering. One of these methods is particulate leaching, which involves the dispersion of a porogen within the polymeric material, that is leached out after curing, and produces a porous scaffold. Porogens particles can also be bonded together to ensure the pore interconnectivity. As main disadvantage, beside the need of possible cytotoxic porogens, this method requires long processing time. Gas-foaming method has been also used to avoid the shortcomings associated with residual porogen and/or solvent in scaffold fabrication, by dispersing gas bubbles throughout the polymeric material, to generate porous structures. As limitation, gas foaming can be applied only to hydrophobic polymers for the limited solubility of CO_2 in hydrophilic polymers. However, the main shortcoming of these methods consists in poor pores interconnectivity and the formation of external skin layer. To overcome the disadvantages associated with porogens and gas foaming, melt blending of two immiscible thermoplastic polymers in a two-phase material continuous structure has been proposed; hence, one polymer acts as a porogen generating an interconnected porous structure in the other polymer.

11.2.1.1.1 Compression Molding

Compression molding is a straightforward melt-molding method where pressure is applied in a mold shaped in the form of the desired defect geometry to compact a polymer powder while being heated and reduce the admitted air. The mold is heated above the melting temperature (for semicrystalline polymers) or, respective, temperature of glass transition of the polymeric material (for amorphous polymers). This method provides, beside the advantages of melt molding, a greater capability to incorporate in polymer material bioactive agents or porogens, when processed at relatively low temperatures. As advantage, compression molding produces scaffolds of high density and low material shrinkage and swelling after demolding [84]. Moreover, as compared to injection molding or extrusion, the process involves

low flow stress and smaller deformation; hence the structure is expected to be more robust. Furthermore, complex 3D scaffolds can be obtained [85]. Porous scaffolds for tissue-engineering applications have been fabricated by combining compression-molding method with several conventional pore-generating techniques.

11.2.1.1.2 Injection Molding

Polymer injection molding is an effective and versatile net-shaped melt-molding method, suitable especially for high precision and repeatability processing of 3D shapes with complex architecture and narrow dimensional tolerances. From this perspective, injection molding represents an almost ideal manufacturing method to create 3D scaffolds of high porosity and interconnectivity [15, 86]. Nowadays, orthopedic devices (plates, rods, and screws) are often obtained using injection-molding method [87]. Moreover, injection molding might allow the sterilization of parts produced with polymeric materials that are not heavily contaminated, avoiding further sterilization techniques that might damage the polymers [88]. The first porous scaffold produced by injection molding was reported in 2001 by Gomes and coworkers. A foamed structure was produced using a blowing agent [89]. Later, more pore-generating co-techniques have been developed.

11.2.1.1.3 Extrusion

Extrusion is a high-volume, melt-processing method used to obtain continuous products with a determined cross-sectional profile, defined by a die. Extrusion generally determines the orientation of polymer chain, increasing the strength and modulus of elasticity of polymer product. Extrusion methods can be applied for melt blending of the polymers, using a mixture of polymers as a premixing stage. The field of tissue engineering has recently gained interest in thermoplastic polymer extrusion to produce biocompatible porous polymer scaffold, especially in the obtaining of tubular porous scaffolds [90].

11.2.1.2 Solution-Based Processing

11.2.1.2.1 Phase Separation

Thermally induced phase-separation technique is based on the concentration gradient to separate two phases of polymeric solutions of two different concentrations, one of rich concentration and the other with lean concentration. The gradient in the concentration is created by modifying solution temperature that is quickly dropped to separate the two phases of the solution [91]. The fabrication of porous scaffolds using phase separation relies on many parameters including solvent type, polymer concentration, quenching temperature, and aging time. Phase-separation techniques are compatible with a wide range of materials, scalable, and relatively low cost.

Phase separation can be achieved as a solid–liquid phase separation by lowering the temperature to induce solvent crystallization from a polymer solution (solid-phase formation in a liquid phase). After the removal of the solvent crystals by sublimation or solvent exchange, the porous scaffold is formed, with solvent

crystals acting as porogen. Oriented tubular scaffold with anisotropic mechanical properties similar to fibrillar tissues, with high porosity and oriented open microtubules, can be obtained using a novel phase-separation technique. It consists in growing oriented rod-like crystals in a polymer solution. After the removal of these rod crystals, a parallel array of microtubules is generated [92].

Liquid–liquid phase separation of a thermodynamically unstable polymer solution can be induced by lowering the temperature under upper critical solution temperature, leading to the formation of a bi-continuous structure, polymer rich respective polymer poor phases. The fabrication process begins with the dissolution of the polymer into a suitable solvent, followed by bioactive molecules addition. Subsequently, the temperature of the polymer solution is lowered, leading to the quenching of liquid–liquid phase of the two-phase solid system. In the final stage, the solvents are removed from the system [93], and the highly porous scaffold with an open-pore structure is formed. After the solvents removal, porous scaffolds with the incorporated biomolecules are obtained [94–96]. However, the pores generated using this technique are reported to be not large enough and often not uniformly distributed, making the method not suitable for tissue-engineering applications [97]. Liquid–liquid phase separation confronts the same drawbacks of emulsification and freeze-drying techniques. One of the advantages of this method is that it can be combined with other scaffold synthesis techniques, like particulate-leaching technique or rapid prototyping (RP), for preparing nanofibrous scaffolds [98].

11.2.1.2.2 Gas Foaming

To overcome the inconveniences related in using organic solvents and chemical porogens, a technique using gas, termed blowing agent, as a porogen, has been developed. The gas in the foaming process can be introduced either chemically or physically. Chemical blowing agents are chemicals that take part in a reaction or decompose, giving off gases in the process. Physical blowing agents are gases that do not react chemically in the foaming process and are therefore inert to the polymer forming the matrix. Often, physical blowing agents are volatile liquids that evaporate and make the foam expand; pressurized gases such as inert gases – argon or nitrogen – or air can be directly injected into the foaming medium [99].

Gas foaming by **chemical reaction** exploits the generation of a blowing hydrophobic gas *in situ* the aqueous solution containing a biopolymer and a surfactant. This approach is applicable exclusively to hydrophilic biopolymers since a certain number of reactions are available for the generation of hydrophobic gases; the converse does not hold true. As a consequence, this method is applicable for the production of scaffolds made of hydrophilic materials.

Scaffolds obtained with this method have inhomogeneous morphology with wide pore sizes dispersity and reduced interpore connections, since it is difficult to finely dose the volume of the gas evolved and that effectively remains entrapped within the foam [100].

An evolution of the chemical blowing approach that avoids the development of salts as side products and permits dosing the amount of gas introduced is based on the use of **physical blowing agents**. The ratio between volume of gas infiltrated

and scaffold pore volume is not insignificant and can be achieved only by tuning the rheological properties of the liquid phase of the foam. A typical gas-foaming process supposes the inflation of gas molecules (e.g. nitrogen, helium, and carbon dioxide) under high pressure, in order to dissolve into a polymer solution or melt. A subsequent deflation process lets the gas return to ambient pressure, releasing gas molecules from the polymer matrix. During the process, gas molecules tend to minimize their free energy and form clusters, and pores are subsequently formed, with the diffusion of gas molecules, causing a significant expansion of the polymer volume, and finally creating a highly porous structure [101].

Different processing parameters influence the gas foaming, including molecular mass of the polymer and the type of gas used. Polymers with a relatively low molecular mass (low intrinsic viscosity) result in scaffolds with high porosity because of more homogeneous distribution of gas molecules. However, gas foaming usually generates not interconnected closed pores. Carbon dioxide has been found to be a better foaming agent, compared to nitrogen and helium, as it formed more porous structure, supposing as a result from higher intermolecular interactions with carbonyl groups of commonly used polymers. The supercritical gas-foaming corresponding process uses supercritical CO_2 to obtain microcellular foams. The main requirement in this case is that CO_2 has to dissolve, in a sufficient amount, in the polymer (excluding the use of polymers with a low affinity for CO_2). Compared to traditional foaming, supercritical CO_2-based technique is characterized by larger mass transfer coefficients and tunability of the CO_2 dissolved in the polymer; moreover, this process does not require any solvent [102, 103].

Advantages of gas-foaming technique include ease of fabrication, simplicity of necessary devices, and the possibility to produce a large amount of foam in one preparation that can be casted in molds of anatomically size shaped scaffolds; subsequent steps involving cross-linking and purification are simple and versatile. The main disadvantages of the method are related to the poor control over the porous structure, characterized by wide pore dimension and interconnect distributions and the limited kinetic stability that affects all operations being performed.

To improve the porosity and pore interconnectivity between pores in the gas-foaming method, this technique has been combined with the salt-leaching method. The hybrid technique in the first step creates a mixture of the polymer with a porogen, where, in a high-pressure environment, the polymer and gas are allowed to mix. The pressure is subsequently decreased to the ambient pressure, while the gas creates pores within the structure. Scaffold structures produced using the hybrid method were able to support cellular functions critical for tissue regeneration [99, 104].

Microfluidics that operate liquid or gaseous flows at microscale offers new opportunities to generate monodisperse bubbles templates at micro-scales, corresponding to the regime of scaffold pores. Foams at this length scale stay wet and are spontaneously and rapidly ordered into crystalline structures. Different microfluidic systems have been used for obtaining monodisperse foams, including co-flowing of liquids and gas streams, flow-focusing devices, cross-flowing, and T-junction [105, 106]. Foam templating using microfluidics overcomes the drawbacks of

conventional gas foaming, offering the opportunity to finely tune the dimension of pores and their interconnectivity in the scaffolds, eventually independent from the other, hence better responding to the morphological need required by a particular cell type. The monodisperse nature of the bubbles extends considerably the foam stability, which can be collected continuously as it is produced. The main drawback of microfluidic foaming is the low production rate that limits the scaffold production only to small samples [107].

11.2.1.2.3 Freeze Drying

Freeze drying, also known as ice templating or lyophilization, consists of dehydration process where a material solution is freezed to extremely low temperature in the first step and, in the next step the surrounding pressure is lowered, causing the frozen solvent to sublime. The initial solution is maintained so that polymerization can take place. By lowering the temperature of the solution, the solvent is separated in a negative pressure environment, causing the solvent to sublime, leaving a porous network in the solid polymeric structure. The porosity of the structure can be controlled by tuning the pH of the solution and freezing rate. However, the process is time consuming, and pore sizes formed have relatively small sizes [108]. The advantages of this technique are using water as solvent and the absence of any solid porogen, like in solvent casting and particulate leaching. Furthermore, the process can be combined with other techniques, such as gas foaming and salt leaching, to improve the properties of scaffolds [109]. In addition, no heat is required during the process, so any kind of additives such as protein, drug, or growth factor, sensitive to high temperature can be loaded [110].

First, a raw polymer is dissolved into a suitable solvent, then water is added to the polymeric solution, and the two liquids are mixed until an emulsion is obtained. Further, before the two phases separate, the emulsion is cast into a suitably shaped mold and quickly frozen, usually by immersion into liquid nitrogen. The frozen emulsion is freeze-dried in the next step to remove the water and the solvent, leaving a solidified, porous interconnected structure. Emulsification and freeze drying represent faster preparation steps compared to solvent-casting and particulate-leaching method, though they require the use of solvents. Moreover, as limitation, pore size is relatively small and porosity is often irregular. Freeze drying by itself represents a usually employed technique for the fabrication of natural and synthetic polymer scaffolds [111]. The ability of producing aligned structure with interconnected pores is significant especially with applications for anisotropic tissue with hierarchical structure, such as bone. In addition, the aligned structure can improve mechanical properties of a scaffold without changing composition, by intrinsic or extrinsic control method [112].

11.2.1.2.4 Solvent Casting and Particulate Leaching

Solvent casting is one of the simplest techniques for production of polymer scaffolds. In this process, an organic solvent is used to dissolve a polymer and, subsequently, the solvent is allowed to evaporate to generate the scaffold. The process can be accomplished in two different ways. One, where a mold of desired shape is dipped

in a solution of polymer and is maintained for suitable time to draw the solution, resulting in a layer of polymer formation on the mold that is, in a further step, processed for fabricating the scaffold. Another way is to pour the polymer solution into a mold and keep until the solvent evaporates and the mold is filled with a layer of polymeric slurry. To enhance the strength and integrity of the scaffold, certain binders are added to the polymeric solution [113].

One major drawback of this technique is the need for possible toxic solvents; therefore, proper attention is required for their complete removal by proper drying of the scaffold under vacuum post processing.

Particulate leaching is one of the most widely used techniques to fabricate scaffolds for tissue-engineering applications. Briefly, porogen salt is first ground into particles of the desired size and transferred into a mold; a polymer solution in a solvent is then cast into the salt-filled mold. After the solvent evaporation, the salt crystals are leached away with water to generate the pores in the scaffold. The method is quite simple and can be achieved by a proper dimensional manage of pore size by controlling the quantity, shape, and size of the selected porogen. However, certain critical variables such as pore shape and interpore openings are not controlled. One of the drawbacks is the lack of control over the interconnectivity of the pores inside the scaffold structure [114]. Mikos et al. described the hybrid solvent-casting/particulate-leaching method for the first time to fabricate porous scaffold for bone tissue engineering [115]. In this method, a porous agent is dispersed in appropriate solvent and then processed by casting or by freeze drying.

To ameliorate the previously mentioned shortcomings, another method is the use of melt polymer solutions for the solvent-casting stage, instead of using a polymer solution in harsh organic solvents. The melt-molding step supposes mixing a thermally stabile polymer powder with salt particles and then melting the mixture [40]. The melting step avoids the need for organic solvents, preventing the contamination of the scaffold with residual solvent. Another attempt to create better pores interconnectivity is using a method where salt particles are partially merged. This technique involves merging salt particles by moisture or by heating, hence significantly reducing the probability of isolated particles remaining in the polymer mixture [40].

11.2.2 Textile Technologies for 3D Scaffold Engineering

Textile technologies allow for scale-up and production at an industrial scale and offer a superior control over the material design in terms of size, shape, porosity, and fiber orientation. With various kinds of knitting and weaving techniques, textile engineering can provide a sheer infinite number of fabric designs. In this context, textile-engineering techniques offer versatile tools to obtain a wide variety of 3D patterns incorporating laces of woven and knitted fabrics. These platform technologies involve not only design and production of woven and knitted materials, but also manufacture of nonwoven fabrics via the electrospinning method. Moreover, the manufacturing process confers a high degree of reproducibility, and the already-present textile manufacturing systems can accelerate the translation of the research prototype into manufacturable product.

Textiles have been used in medical field from simple bandages to implantable devices used in surgery. Nonimplantable medical textiles comprise wound dressings, bandages, pressure garments, prosthetics, etc. Sutures, vascular grafts, artificial ligaments, skin grafts, and tissue-specific scaffolds [116] are implantable medical textiles that are referred to as "biotextiles" [117, 118]. Along the new developments in biomedical engineering, today's sutures are made of various kinds of bioactive, biocompatible, and/or bioresorbable materials. Other implantable products include vascular grafts, hernia repair meshes, artificial skin, ligament prostheses, heart meshes, and artificial heart devices in which textile and tissue-engineering approaches have been combined [119]. Given that textile engineering provides a quasi-unlimited number of different designs and patterns of fabrics, it is possible to generate numerous scaffolds patterned after distinct configurations and with a variety of mechanical properties.

11.2.2.1 Woven, Knitted, and Braided Methods

Conventional textile manufacturing methods, e.g. weaving, knitting, and braiding, allow precise tuning of the mechanical strength of final products – a necessary requirement for the biomedical scaffolds that should be robust enough to maintain the physiological load.

Woven textiles consist of two sets of parallel yarns interlacing with angles. These provide stiffness and strength, high tenacity, excellent structural stability, and anisotropy. Because of their lack of elasticity, they can hold shape in time without losing the original form. The most advanced medical devices for cardiovascular or orthopedic applications are the main candidates of the strength and manufacturing flexibility of woven scaffolds. A variety of geometric possibilities of woven polymer materials are developed to create finer fabrics that meet the performance and functional requirements for reparative applications, such as vascular grafts, heart valves, ligament repair, and tendon reinforcement [116].

Knitted fabrics are obtained by interconnecting yarns that are formed into loops. Knitted textiles have lower stiffness compared with woven textiles, but they present similar structural stability and strength. Knitted textiles can also present mechanical properties between axial and transverse directions, emphasizing their anisotropic features, making this technique the technology of choice for applications, such as cardiac constructs [120] or creating artificial muscles with enhanced strain [121]. Varied knitting methods include warp knitting [122], weft knitting [123], and circular knitting [124], in many different configurations, with extra strength without increasing thickness, flexible mesh with high conformability. Common applications of knitted scaffolds include surgical meshes for reconstructive and cosmetic surgery and hernia repair [125], and also urogynecologic replacements [126].

Braided textiles are obtained by intertwining three or more strands of yarns in precise ways [127]. Braided fabrics possess softness, compression, expandability, and fatigue resistance. They can maintain their structural composition without affecting flexibility. For implantable replacements, braided designs can allow a material to degrade partially over time or maintain a precise geometry [128]. Common braided medical applications include sutures and sewing threads, tubes and tubing reinforcement, catheters, and tendon/ligament fixation [129].

11.2.2.2 Nonwoven Methods: Electrospinning

Fiber-based technologies have been very appealing for scaffold fabrication because of their large surface-area-to-volume ratio, early commercial availability, and the ease of fabrication by industrial processes [130].

Textile fibers in scaffold fabrication were first reported by Mikos et al. [131]. The process was initially described in multiple steps, including the formation of a material of nonbonded fibers embedded in a polymer matrix, further thermal treatment of the matrix, and finally, selective dissolution of the matrix. The nonbonded fibrous mesh is obtained by isolating fibers from a thicker multilamellar material, subsequently either immerged into another polymer solution, hence ensuring the fibers are immiscible in the second polymer solution, or the fibers are placed in a mold and the other polymer solution is allowed to fill the remaining mold volume. After the solvent evaporates, the mixture is heated above the melting point of the polymer that comprises the fiber network to form welded points at the crosspoints of the fiber mesh. Finally, the nonfiber polymer is selectively dissolved using a solvent that is immiscible with the fiber network. The resulting fiber matrix is finally vacuum dried to completely remove solvents [131]. Two prominent drawbacks of the fiber-bonding technique include the inability to control pore size and the need for harsh solvents. As previously mentioned, harsh solvents and inadequate pore size could render the scaffold ineffectual for tissue-engineering purposes.

Electrospinning is a versatile technique used to produce continuous fibers from submicro- to nanosizes in diameter. In a classical electrospinning process, the polymers are dissolved in a solvent and extruded through a needle under a high electrostatic charge that affects the surface tension of the polymer solution, leading to a thin jet pulled toward a grounded or negatively charged collector of different shape. Subsequently, the solvent evaporates as the jet moves toward the collector, resulting in the formation of micro- or nanofibers. The type of collector used is essential to control the orientation of fibers during electrospinning. The individual fibers produced are not cross-linked to each other, so often an alternative method is required to form a stable scaffold. In the last years, there has been increasing interest in melt electrospinning; instead of using solvents to dissolve the polymer, the polymer is heated into its viscous phase to allow to be extruded through the needle. This process allows an even better control of the fiber architecture, compared with solvent-based electrospinning. However, the fibers formed are generally larger in diameter and the range of polymers that can be used is more limited [132–134]. The parameters chosen during electrospinning process greatly influence the collected fibers [135]. These parameters are typically classified into three categories: polymer parameters, polymer solution parameters, and parameters of the apparatus. The type of polymer used and its physical properties such as molecular mass and the molecular mass distribution greatly affect the fibers. Solution properties include polymer solution viscosity, polymer concentration, conductivity, and surface tension. Important apparatus parameters are applied voltage, distance from syringe needle tip to collector, type of collector, the type of needle used, flow rate, and the ambient conditions during electrospinning [136–138].

Aligning nanofibers is useful for a variety of applications. When fibers are used to impart additional mechanical integrity, control of the alignment influences the degree of structural support the fibers provide. In the area of tissue engineering, aligned fibers can serve as a physical guide for cellular growth, affect cell adhesion, and modulate cellular patterns [139]. They are particularly useful to regenerate tissues that require directional recruitment and assembly of cells, e.g. in neural tissue engineering.

Centrifugal electrospinning is another modified electrospinning method that also produces highly aligned nanofibers. This process involves loading a spinneret and nozzle onto a circular disk that is attached to a rotating axle; a metallic cylindrical shell is then placed around the disk and grounded to serve as the collector. Centrifugal action on the polymer solution provides a uniform distribution of stress, stretching the polymer into a long fiber. This process also permits the processing of lower-molecular-weight polymer solutions.

Coaxial or core–shell electrospinning is another common modification to the traditional electrospinning technique to obtain nanofibrous scaffolds. The fibers can be spun from different polymers and polymeric combinations, and a variety of material (synthetic or natural polymers) can be placed in the core, all aimed at efficient scaffold formation. Biomolecules can be encapsulated as the core; polymer shell surrounding has the property of tunable biodegradability, depending on its composition that allows the release of biochemical agents over a favorable time period. The ability to optimize the release of the molecules in right time promotes more efficacious behavior of the biomolecules [140, 141].

11.2.3 Hydrogel Scaffolds Fabrication

Hydrogels are composed of a hydrophilic polymer, either covalent or noncovalent bonded (ionic interaction, hydrogen bonding, or molecular entanglement). Hydrogels can absorb large amounts of water and swell, being soft and elastic. The cross-linked structure of hydrogels allows them to retain their 3D shape and swell without dissolving; the higher the cross-linking density, the lower the swelling. Both chemical and radiative cross-linking have been used in hydrogels fabrication [142, 143]. Hydrogel scaffolds exhibit high flexibility, hydrophilicity, biocompatibility, and degradability along limited mechanical properties, difficulty of purification, and sometimes immunogenicity (depending on the polymer source). Their applications include injectable materials able to adapt the form of the damaged tissue. Synthetic polymers used for hydrogels bring tunable and responsive physicochemical features like modulus, water affinity, and degradation rate, along potential cytotoxicity and lack of cell adhesion. Both natural and synthetic hydrogels, according to their structure, could be amorphous or semi-crystalline. According to their response to environmental stimuli, hydrogels could be conventional and smart (intelligent). “Smart” hydrogels reversely modify their swelling behavior or structure in response to stimuli including light, pH, pressure, temperature, ionic strength, electric, or magnetic field, making them interesting for the production of 4D scaffolds such as artificial muscles and self-regulating drug-delivery systems.

Hydrogels represent important biomaterials for scaffolds applications due to the ability of tailoring the mechanical properties, preventing bacterial invasion, and adhering or suspending of cells [144]. Their appropriate rheological properties (dependent on cross-linking) are essential to maintain construct shape without compromising cell (cytocompatibility) or include bioactive moiety and related function. Hydrogels are currently used in cell-entrapped scaffolds, bone regeneration, cartilage healing, wound dress, and drug or growth factor delivery [145].

Injectable hydrogels are highly attractive, especially as injectable fillers of soft and hard tissues, promoting a good integration into the defect site and avoiding open surgeries with hard recovery. The high water content of the hydrogels makes them easy to manipulate for the delivery of cells and growth factors. Usually, the hydrogel precursors are injected into the wound site in a solution-to-gelation transition due to physical or chemical stimuli and cross-linking reactions [146]. The most common physical cross-linking methods for *in situ* hydrogelation reactions include thermal gelation, ionic interactions, physical self-assembly, or photopolymerization [147–149].

Apart from their use as injectable fillers, or in bioprinting technologies, different processing methods can be used for turning hydrogels into highly porous scaffolds with superior mechanical properties, including solvent casting and particulate leaching, freeze drying, phase separation, gas foaming, electroforming, and polymer blending [150–152]. These techniques have been proposed based on different natural and synthetic polymers depending on their particular chemistry, molecular mass, solubility, and hydrophilicity or hydrophobicity [153].

11.2.4 Self-Assembly Methods

Self-assembly technique involves an autonomous organization of components into patterns or structures. Such a structure can be constructed by ionic bonds or complex, noncovalent interactions, such as hydrogen bonding and/or π stacking, van der Waals forces, electrostatic forces, and hydrophobic interactions [154]. Self-assembly is used for the preparation of 3D scaffolds for tissue regeneration [155, 156]. Scaffolds prepared via self-assembly can also be used in engineering nerve tissue and cartilage tissue [157, 158]. In most assemblies, molecules arrange themselves in a manner that results in the fabrication of various structures by the bottom-up method without any external support.

Self-assembly processes mimic the native formation of extracellular matrices and the self-assembled nanofiber-based structures have been investigated for different tissue-engineering applications [159]. However, nanofibrous structures formed by polymer self-assembly are usually short in length and weak in mechanical properties, which result in difficulties in offering adequate structural cues to cells. Besides, the complex mechanisms involved make it difficult to control the nanofibrous structures formed by self-assembly. Amphiphilic peptide sequence is a common method for the fabrication of 3D nanofibrous structures for tissue engineering like self-assembled rod-like architectures. By modifications in polymer chemistry, a variety of self-assemblies including layered and lamellar

structures and by its reversibility properties provides flexibility to the system. Therefore, the self-assembly technique shows designing potential novel scaffolds for tissue- engineering applications [160]. In aqueous solution, the hydrophobic and hydrophilic domains within these peptides interact based on weak noncovalent bonds resulting in distinct fast-recovering hydrogel. Instead of peptides, synthetic polymer nanofibers are also prepared by self-assembly of diblock polymers [161]. Self-assembly shows several advantages over electrospinning because it produces the much thinner nanofiber with very thin diameter [162]. The amino acid residues used for self-assembly may be chemically modified by the addition of bioactive moieties. Other advantage of this technique is to avoid the use of organic solvent and reduce the cytotoxicity because it is carried out in aqueous salt solution or physiological media. Main disadvantage of this technique is its complicated and elaborated process [134]. Mimicking the ECM, a viscoelastic network consisting of nanofibrous proteins, might be the best way to develop next generation of materials with control over cell adhesion, migration, proliferation, and differentiation [163].

Layer-by-layer (LbL) assembly is an alternative to self-assembled monolayer assembly. LbL assembly represents a highly versatile and also simple multilayer self-assembly technique; multilayer coatings can be fabricated, with controlled architectures and compositions, from extensive choices of materials for biomedical applications. Various LbL assembly biomaterials have been prepared from different materials, including polyelectrolytes, biomolecules, and colloids, with remarkable physical, chemical, and biological properties and functions appropriate in the field of tissue engineering [164]. Typically, the LbL assembly process includes the sequential interaction of complementary molecules absorbed on a substrate surface, driven by multiple electrostatic and/or nonelectrostatic interactions [165, 166]. The technologies for LbL assembly can be classified into five main categories: immersion, spinning, spraying, electromagnetic-driven, and fluidic assembly. The proper choice of assembly process is crucial for fabrication and successful applications of the nanostructured assembly. Between the adsorption steps corresponding to each layer deposition, steps of washing and drying are usually introduced to avoid contamination of the next solution, to elute the loose molecules, and stabilize the formed layers. These sequential deposition and washing steps are repeated until the desired number of deposition layers is achieved. Fine control of composition, thickness, and topography can be tuned by adjusting the assembly parameters related to solution properties, such as concentration, ionic strength, and pH, and also process parameters, such as temperature, time, and drying conditions. Various building blocks used for LbL assembly include, but are not limited to, natural polymers, synthetic polymers, peptides, and polymer gels.

11.2.5 Microsphere-Based Scaffolds Fabrication

Conventionally, microspheres or microparticles, rigid in shape, were used as vehicles for controlled-release kinetics of loaded drugs or bioactive molecules, due to the ease of fabrication, and the ability to control their physicochemical properties and morphology. Recently, microspheres have been also used in obtaining tissue-engineering

scaffolds, where microspheres act as supporting matrices and play an important role in drug release and cell entrapping, targeting regeneration and repair of a variety of tissues. Moreover, microsphere approach of anisotropic scaffold design has received attention and is intensively used in bioactive substances delivery applications, in a controlled and specific site-targeting manner [167].

Microsphere size, ranging from 1 to 1000 μm in diameter, is a primary factor governing the kinetic release of loaded drugs, being determined by polymer degradation rate. Microsphere fabrication using traditional methods such as emulsion or spraying techniques generates, though reproducible, often poorly controllable microsphere sizes and size distribution. Furthermore, the control over microsphere sizes dramatically influences spatial control over pore sizes and scaffold porosity.

There are two types of microspheres containing scaffolds, microsphere-based scaffolds and microsphere-incorporating scaffolds [168, 169]. In the former, microspheres themselves act as the building blocks of the scaffold, via a bottom-up approach, linked by chemical cross-linking, or cohesive forces, as either injectable or heat/solvent sintered scaffolds. Microsphere-based scaffolds can be processed as either injectable (as liquid suspension, colloids, or gels) or sintered as a macroscopic scaffold that may be implanted even arthroscopically. Microspheres and microsphere-based 3D scaffolds were obtained by polymerization in two- or multiphase systems, using different methods like particle aggregation, oil-in-water dispersion, solvent vapor treatment, solvent/nonsolvent sintering, and SLS. In principle, microspheres/microparticles are generated during or after polymerization, aggregation, coalescence, or crosslinking. Microsphere-based scaffolds can be fabricated by random packing, directed assembly – involves cohesive forces such as electrostatic forces, hydrophobic interactions, or magnetic forces, and RP – allows layer-by-layer assembly of microspheres via computer-aided design (CAD).

In microsphere-incorporating scaffolds, the microspheres represent one component of the scaffold, microspheres being dispersed into a continuous phase, such as solid polymers or hydrogels.

This type of scaffolds is generally fabricated in a multistep process, via a top-down approach, separately obtaining the bulk scaffold matrix and microspheres, and in the next step, loading the matrix with microspheres to the final scaffold. Microspheres generate pores and provide mechanical strength, beside controlling the drug release. Despite their several advantages, this approach presents numerous challenges such as the control over biomolecule delivery, cell infiltration and viability, and clinical handling.

11.3 Advanced Fabrication Methods – Solid Freeform Fabrication

RP, also known as additive manufacturing or 3D printing technology, refers to processes of creating a three-dimensional (3D) object of almost any shape or

geometry, through successive deposition and processing of biomaterial layers, using computer-controlled machines, based on 2D cross-sectional data obtained from slicing a CAD model of the original object. Furthermore, biomimetic cell-encapsulated scaffolds can be obtained in predefined patterns using appropriate advanced methods using both biomaterials and cells, with a cell-level resolution. Standard terminology for additive manufacturing ISO/ASTM52900-15 defines seven categories of processes, based on photopolymerization–stereolithography, powder bed fusion–SLS, material extrusion–fused deposition modeling (FDM), material jetting, binder jetting, sheet lamination, and directed energy deposition. Most representative processes for scaffold fabrication are presented.

11.3.1 Stereolithography

Stereolithography (SLA) also known as optical fabrication, photo-solidification, or resin printing, is a technology that utilizes liquid polymers contained in a vat (or tank) selectively cured by a concentrated beam of UV light or a laser to form the designed scaffold [170]. Upon exposure to the UV radiation, the photopolymer is polymerized to form the corresponding layer. This process is further repeated, overlaying the previous layer for the next layer, until the entire scaffold structure has been fabricated. The process can be achieved by two approaches, top-down and bottom-up. The top-down approach consists of placing the radiation beam above the vat and the construct is built facing up. The bottom-up technique supposes placing the radiation beam under the resin vat, while the scaffold is built facing upside down. The bottom-up approach is generally used in desktop printers, while the top-down is mainly used in industrial systems. SLA technology generally falls into two categories: laser direct writing [171] and mask image projection [172].

The advantage of SLA is the reuse of the uncured photopolymer for another print. In addition, because of the use of lasers, more defined scaffolds of high resolution can be made [173]. Photopolymerization is successfully applied to scaffolds fabrication, enabling the replication of accurate 3D models of specific anatomical parts of a certain patient, based on data acquired by computer scans. SLA photopolymerization processes are excellent in producing parts with fine details and a smooth surface finish. The disadvantage of this technique is that the photopolymers are often not biodegradable once cured and cross-linked. In addition, photoinitiators are often toxic and generate free radicals that may be detrimental if not fully removed from the final structure. SLA was also used in combination with electrospinning to fabricate highly aligned neural scaffolds [174]. This technique was used to overcome the limitations of high-resolution scaffolds without compromising mechanical properties. SLA technology provides an opportunity to print complex and defined scaffolds, where intricacies in the morphology of the scaffold may affect cellular differentiation and alignment as described for neural cells earlier.

Recently, multiphoton processing was employed for *in vivo* experiments by engineering artificial cartilage constructs that may be successfully implemented for tissue-engineering scaffolding [175]. Two-photon lithography system was able to print retinal cell grafts seeded with human-induced pluripotent stem cell

and restore vision to patients with retinal degenerative disease [176]. With the advancements in SLA technologies such as two-photon 3D printing, the method can be applicable to a plethora of diseases.

11.3.2 Selective Laser Sintering

SLS, a powder-based RP technology, works by fusing together biopolymer powder particles, layer by layer, using a high-energy laser [177]. The interaction of the high-energy laser and the powdered polymer causes the polymer particles to partially fuse together. After a layer is complete, the device bed is moved down and a new layer of powder is placed on top of the previous layer, and the process is repeated [178]. The degree to which the particles are fused together controls the porosity of the finished object. If the lasers achieve full melting of the particles, the process is referred to as selective laser melting. The advantage of SLS over other additive manufacturing techniques is that unsintered powder supports each layer, and it does not require support material or a separate feeder when forming complex structures. However, due to the mechanism by which SLS forms objects, different powders will respond differently to the same set of printing parameters (e.g. hatching distance, laser strength, and scan speed). This has led to the development of an improved approach for handling biopolymer powders involving the formation of microspheres of different desired materials, to get powder that responds evenly to printing parameters. As a result, increased control over the porosity of the scaffolds is achieved [179].

11.3.3 Nozzle-Based Deposition Techniques

11.3.3.1 Fused Deposition Modeling

FDM is a popular form of additive manufacturing. In this technique, the material is extruded from a heated nozzle close to its melting point onto a platform. The process starts with a CAD file that is then sliced into layers upon exporting to the STL format [180]. This communicates with the printing head, relaying the parameters for extruded materials (e.g. printing speed, nozzle temperature) and the platform (e.g. platform temperature, the thickness of each layer) [181]. The semi-molten material is extruded from the nozzle, which moves in the XY plane to a desired location above the platform. A constant feed of material is obtained by two rollers that feed material from the feedstock to the nozzle, which can be in a filament form or powder form. Upon the completion of a layer, the platform moves downward in the Z-axis at a predetermined distance [182]. The process is repeated until the desired 3D object is formed [183]. Altering the manufacturing variables such as the nozzle diameter, nozzle temperature, feed rate, and print speed can lead to finely tuned control over the object formed. However, these parameters are dependent upon the material being printed. The use of heat to provide a semi-molten polymer to form structures can pose a problem for cell printing with FDM. This can be alleviated by using multiple printing heads to extrude different materials sequentially or simultaneously. One of the limitations of FDM has always been the optimal printing resolution. A recent

advancement has been made by adopting principles from a form of electrospinning, specifically melt electrospinning writing (MEW), which allows for small-diameter fibers to be formed by adding a high electrical potential to a polymer melt, increasing the microporosity and effectiveness of FDM-manufactured scaffolds. FDM combined with gas foaming was used to develop a hierarchical scaffold with macropores and micropores scaffolds [184].

11.3.3.2 3D Printing and 3D Bioprinting

Direct 3D printing: The original 3D printer was first developed in the 1990s by the Massachusetts Institute of Technology (MIT), and it utilized the technology of an inkjet printer [185]. Through this process, instead of printing in the x–y plane in a fashion similar to an ordinary inkjet printer, a height-adjustable platform was added with the capabilities to print in the z-plane, thus allowing structures to be fabricated in all dimensions. During the development of a 3D printing device, MIT was able to maintain the workings of an ordinary 2D inkjet printer by use of a printer cartridge where, instead of ink, the cartridge contained a binder solution that was automatically deposited at the desired spot on a powder bed instead of a sheet of paper. These binder solutions are the reason that direct 3D printing is sometimes referred to as "binder jetting" or "drop on powder." These methodologies have improved over the years but all follow a similar process where a powder bed, containing the sifted homogenized material of interest, is initially spread onto the build platform and then leveled with an automated roller. Once leveled, the binder solution is dispensed from the ink nozzle to a specified position on the powder bed dictated by the CAD design and printing parameters. Upon solidification of the first layer, the excess powder is then removed and the build platform is then lowered to allow for a new, fresh bed of powder to be deposited and leveled. This process is repeated until the final structure has been fabricated. The advantage of this method of printing is the versatility of utilizing different powders and binder solutions to fabricate a defined scaffold with various properties such as mechanical strength, porosity, and biocompatibility. The different combinations of powder bed materials and binder solutions ensure that scaffolds can be tailored to specific purposes that may include the recruitment and differentiation of specific cell types. However, one problem with using direct 3D printing technology is that some binder solutions use toxic organic solvents that if not removed completely can be cytotoxic to cells and detrimental to the tissue-engineering process. Another disadvantage of this type of 3D printing is the postprocessing time that may be required, such as heat treatment to enhance the durability of the final structure [186].

3D-Bioplotter printing: In a similar manner to direct 3D printing, 3D-Bioplotter printing or bio-printing has garnered much attention due to its ability to print scaffolds with cell-laden gels. The printing process uses a nozzle extrusion system to extrude soluble materials that have been chemically or thermally treated in a layer-by-layer format. In this system, the ink cartridge contains "bioink" rather than a binder solution used in direct 3D printing. With a CAD design programmed into the printer, the printer has the ability to print different subsets of stem cells

in designated positions for enhanced tissue engineering. In addition to cells, drugs can also be incorporated into the bioinks. 3D-Bioplotter printing utilizes a pneumatic pressurized air system to dispense the bioink in a layer-by-layer fashion. When printing cell-laden gels, nozzle diameter and pressure must be calibrated because excess shear stress generated in the nozzle decreases cell viability [187]. The 3D-Bioplotter technology provides researchers with a versatile and convenient tool to manufacture ready-to-implant scaffolds with high mechanical strength, interconnectivity, porosity, biodegradability, and the ability to achieve higher rates of attachment, differentiation, and proliferation for enhanced tissue regeneration.

Four-dimensional (4D) printing emerged as the next generation of fabrication techniques. Use of intelligent materials that change properties, produce an electrical current, become bioactive, or perform an intended function in response to an external stimulus, ensures the production of dynamic 3D structures, which is now called 4D printing [188]. Introduction of the fourth dimension, time, in addition to the 3D arrangement gives both spatial and temporal control over the fabricated product. Therefore, 4D printing overcomes one of the major drawbacks of 3D printing and produces structures that are biomimetically dynamic. 4D-printed product can change its shape, function, or other physical or chemical properties in response to the aforementioned stimuli types, eliminating the need for external devices or methods for postprocessing, and reduce the production duration, and in some cases, may also aid in the application process [189].

11.3.4 Indirect Rapid Prototyping

Indirect 3D printing or indirect solid freeform fabrication takes advantage of both conventional scaffolding methods and 3D printing capabilities. The basis of indirect 3D printing consists of using a 3D printer to create a negative mold into which the desired scaffold material is cast and allowed to harden. The mold is then removed to retrieve the formed structure [190]. Using 3D printing to generate the mold allows for scaffolds to be fabricated from conventional techniques with the added advantage of microarchitecture [191]. Also, noncompatible materials for direct 3D printing can be combined seamlessly with indirect 3D printing [190]. One main advantage of indirect 3D printing is that structures with microarchitecture can be fabricated from a wide variety of materials without the use of potentially damaging solvents and materials. Furthermore, since mold materials such as plasters are compatible with many scaffold materials, optimization and new, specialized equipment are not required when investigating potential scaffold materials. However, the additional step of negative mold generation and demolding increases fabrication times, which may deter use in patient-specific applications [192]. Viscous polymer-casting solutions limit the intricacy of microarchitecture because incomplete saturation of the void space results in scaffold deformations [193]. Indirect 3D printing offers researchers a user-friendly method to fabricate 3D scaffolds for tissue engineering, but casting solution accessibility and time-intensive mold fabrication limit the application of this technique.

11.4 Conclusions and Future Perspectives

3D scaffold fabrication is an emerging multidisciplinary field. Efforts are being made to design and select the most appropriate materials to achieve the desired properties of a scaffold. By careful selection of biomaterials and key scaffold characteristics, novel techniques have been developed to produce complex architectures with desired properties for soft- and hard-tissue-engineering applications. These scaffolds should be fabricated so that to regenerate and mimic both the anatomical structure and function of the original soft tissue have to be repaired. Although many types of scaffolds have been designed and obtained, there are only few of them that are able to successfully pass the clinical trials and enter the market.

A critical opinion suggests that conventional scaffold concept that had persisted for 30-year history of tissue engineering represents the wrong approach [194]. Conventionally, a scaffold designates a temporary support necessary to facilitate the building of a construct and that is subsequently disassembled and eliminated, without playing any active role at building activity. Instead, it is suggested and argued that it be replaced with template concept, capable to selectively target the appropriate cells using a combination of molecular and mechanical signals, since the signaling ability toward targeted cells does not exclusively rely on chemistry [195]. The architecture of templates for tissue engineering has been switching toward hybrid macro- and nanoscale structures, and hydrogel-based tissues, tissue-derived, or tissue-mimicking components. These include biomimetic hydrogels [196] and injectable peptide-based hydrogels [154]. It is important to avoid undesirable host responses, according to the basic principles of biocompatibility. The template biomaterial should be compatible with the processing methods that simultaneously pattern both the material and living cells, or injectable if desired, with the appropriate rheological properties.

In this respect, an emerging concept in tissue engineering is to get inspiration from natural processes and products as the most advanced models of smart technology. The development of the last generation of biomaterials aims at the biologically inspired design principles in nano- to micro- to macro-scale hybrid structures by synthetic routes that allow the obtaining of hierarchically controlled and dynamic supramolecular assembly, such as 4D bioprinting and functionalities of building blocks, eventually using adaptive self-assembling, self-shaping, or self-healing polymer components.

References

1 Langer, R. and Vacanti, J. (1993). Tissue engineering. *Science* 260: 920–926.
2 Caddeo, S., Boffito, M., and Sartori, S. (2017). Tissue engineering approaches in the design of healthy and pathological in vitro tissue models. *Front. Bioeng. Biotechnol.* 5: 40.
3 Hutmacher, D.W. (2000). Scaffolds in tissue engineering bone and cartilage. *Biomaterials* 21: 2529–2543.

4 Obrien, F.J. (2011). Biomaterials & scaffolds for tissue engineering. *Mater. Today* 14: 88–95.

5 Khan, Y., Yaszemski, M.J., Mikos, A.G., and Laurencin, C.T. (2008). Tissue engineering of bone: material and matrix considerations. *J. Bone Joint Surg. Am.* 90 (Suppl. 1): 36–42.

6 Richbourg, N.R., Peppas, N.A., and Sikavitsas, V.I. (2019). Tuning the biomimetic behavior of scaffolds for regenerative medicine through surface modifications. *J. Tissue Eng. Regen. Med.* 13: 1275–1293.

7 Dai, Z., Ronholm, J., Tian, Y. et al. (2016). Sterilization techniques for biodegradable scaffolds in tissue engineering applications. *J. Tissue Eng.* 7. https://doi.org/10.1177/2041731416648810.

8 Mourino, V. and Boccaccini, A.R. (2012). Bone tissue engineering therapeutics: controlled drug delivery in three-dimensional scaffolds. *J. R. Soc. Interface* 7: 209–227.

9 Dolcimascolo, A., Calabrese, G., Conoci, S., and Parenti, R. (2019). Innovative biomaterials for tissue engineering. In: *Biomaterial-supported Tissue Reconstruction or Regeneration* (ed. M. Barbeck, O. Jung, R. Smeets and T. Koržinskas). IntechOpen. https://doi.org/10.5772/intechopen.83839.

10 Dvir, T., Timko, B.P., Kohane, D.S., and Langer, R. (2011). Nanotechnological strategies for engineering complex tissues. *Nat. Nanotechnol.* 6: 13–22.

11 Panseri, S., Cunha, C., Lowery, J. et al. (2008). Electrospun micro- and nanofiber tubes for functional nervous regeneration in sciatic nerve transections. *BMC Biotechnol.* 8: 39.

12 McCullen, S.D., Autefage, H., Callanan, A. et al. (2012). Anisotropic fibrous scaffolds for articular cartilage regeneration. *Tissue Eng.* 18: 2073–2083.

13 Vaquette, C. and Cooper-White, J. (2013). A simple method for fabricating 3-D multilayered composite scaffolds. *Acta Biomater.* 9: 4599–4608.

14 Nichol, J.W. and Khademhosseini, A. (2009). Modular tissue engineering: engineering biological tissues from the bottom up. *Soft Matter* 5: 1312–1319.

15 Ghosh, S., Viana, J.C., Reis, R.L., and Mano, J.F. (2008). Development of porous lamellar poly(L-lactic acid) scaffolds by conventional injection molding process. *Acta Biomater.* 4: 887–896.

16 Allaf, R.M., Rivero, I.V., Abidi, N., and Ivanov, I.N. (2013). Porous poly (ε-caprolactone) scaffolds for load-bearing tissue regeneration: solventless fabrication and characterization. *J. Biomed. Mater. Res. B Appl. Biomater.* 101: 1050–1060.

17 Thomson, R.C., Yaszemski, M.J., Powers, J.M., and Mikos, A.G. (1995). Fabrication of biodegradable polymer scaffolds to engineer trabecular bone. *J. Biomater. Sci. Polym. Ed.* 7: 23–38.

18 Shokrolahi, F., Mirzadeh, H., Yeganeh, H., and Daliri, M. (2011). Fabrication of poly(urethane urea)-based scaffolds for bone tissue engineering by a combined strategy of using compression moulding and particulate leaching methods. *Iran. Polym. J.* 20: 645–658.

19 Lee, J., Shen, Y.-K., Bai, C.-Y., and Hung, J.-H. (2011). Study on novel porous nasal scaffold using injection molding and particle leaching. In: *2010 International Conference on Nanotechnology and Biosensors*, 62–66. Hong Kong, China: IACSIT Press.

20 Lee, S.H., Kim, B.S., Kim, S.H. et al. (2004). Thermally produced biodegradable scaffolds for cartilage tissue engineering. *Macromol. Biosci.* 4: 802–810.

21 Wu, L., Zhang, H., Zhang, J., and Ding, J. (2005). Fabrication of three-dimensional porous scaffolds of complicated shape for tissue engineering. I. Compression molding based on flexible rigid combined mold. *Tissue Eng.* 11: 1105–1114.

22 Widmer, M.S., Gupta, P.K., Lu, L. et al. (1998). Manufacture of porous biodegradable polymer conduits by an extrusion process for guided tissue regeneration. *Biomaterials* 19: 1945–1955.

23 He, L., Zuo, Q., Shi, Y., and Xue, W. (2014). Microstructural characteristics and crystallization behaviors of poly(L-lactide) scaffolds by thermally induced phase separation. *J. Appl. Polym. Sci.* 131: 39436.

24 Heijkants, R.G.J.C., van Calck, R.V., De Groot, J.H. et al. (2004). Design, synthesis and properties of a degradable polyurethane scaffold for meniscus regeneration. *J. Mater. Sci. Mater. Med.* 15: 423–427.

25 Yang, F., Murugan, R., Ramakrishna, S. et al. (2004). Fabrication of nano-structured porous PLLA scaffold intended for nerve tissue engineering. *Biomaterials* 25: 1891–1900.

26 Liu, X. and Ma, P.X. (2009). Phase separation, pore structure, and properties of nanofibrous gelatin scaffolds. *Biomaterials* 30: 4094–4103.

27 Harris, L.D., Kim, B.S., and Mooney, D.J. (1998). Open pore biodegradable matrices formed with gas foaming. *J. Biomed. Mater. Res.* 42: 396–402.

28 Mei, J.-C., Wu, A.Y.K., Wu, P.-C. et al. (2014). Three-dimensional extracellular matrix scaffolds by microfluidic fabrication for long-term spontaneously contracted cardiomyocyte culture. *Tissue Eng. Part A* 20: 2931–2941.

29 Wang, C.-C., Yang, K.-C., Lin, K.-H. et al. (2011). A highly organized three-dimensional alginate scaffold for cartilage tissue engineering prepared by microfluidic technology. *Biomaterials* 32: 7118–7126.

30 Sun, Y.-S., Peng, S.-W., Lin, K.-H., and Cheng, J.-Y. (2012). Electrotaxis of lung cancer cells in ordered three-dimensional scaffolds. *Biomicrofluidics* 6: 14102–14114.

31 Fereshteh, Z. (2018). Freeze-drying technologies for 3D scaffold engineering. In Functional 3D tissue engineering scaffolds. In: *Materials, Technologies and Applications* (ed. Y. Deng and J. Kuiper), 151–174. Woodhead Publishing https://doi.org/10.1016/C2015-0-05681-7.

32 Jiang, L.B., Su, D.H., Liu, P. et al. (2018). Shape-memory collagen scaffold for enhanced cartilage regeneration: native collagen versus denatured collagen. *Osteoarthr. Cartil.* 26: 1389–1399.

33 Del Bakhshayesh, A.R., Mostafavi, E., Alizadeh, E. et al. (2018). Fabrication of three-dimensional scaffolds based on nano-biomimetic collagen hybrid constructs for skin tissue engineering. *ACS Omega* 3: 8605–8611.

34 Stratton, S., Shelke, N.B., Hoshino, K. et al. (2016). Bioactive polymeric scaffolds for tissue engineering. *Bioact. Mater.* 1: 93–108.

35 Basile, P., Dadali, T., Jacobson, J. et al. (2008). Freeze-dried tendon allografts as tissue-engineering scaffolds for Gdf5 gene delivery. *Mol. Ther.* 16: 466–473.

36 Wangkulangkul, P., Jaipaew, J., Puttawibul, P., and Meesane, J. (2016). Constructed silk fibroin scaffolds to mimic adipose tissue as engineered implantation materials in postsubcutaneous tumor removal. *Mater. Des.* 106: 428–435.

37 Lin, C.Y., Li, L.T., and Su, W.T. (2014). Three dimensional chitosan scaffolds influence the extracellular matrix expression in Schwann cells. *Mater. Sci. Eng. C* 42: 474–478.

38 Dragusin, D.-M., Van Vlierberghe, S., Dubruel, P. et al. (2012). Novel gelatin-PHEMA porous scaffolds for tissue engineering applications. *Soft Matter* 8: 9589–9602.

39 Murphy, W.L., Dennis, R.G., Kileny, J.L., and Mooney, D.J. (2002). Salt fusion: an approach to improve pore interconnectivity within tissue engineering scaffolds. *Tissue Eng.* 8: 43–52.

40 Reignier, J. and Huneault, M.A. (2006). Preparation of interconnected poly(ε-caprolactone) porous scaffolds by a combination of polymer and salt particulate leaching. *Polymer* 47: 4703–4717.

41 Antunes, J.C., Oliveira, J.M., Reis, R.L. et al. (2010). Novel poly(L-lactic acid)/hyaluronic acid macroporous hybrid scaffolds: characterization and assessment of cytotoxicity. *J. Biomed. Mater. Res. A* 94A: 856–869.

42 Yan, L.-P., Oliveira, J.M., Oliveira, A.L. et al. (2012). Macro/microporous silk fibroin scaffolds with potential for articular cartilage and meniscus tissue engineering applications. *Acta Biomater.* 8: 289–301.

43 Ahearne, M., Fernández, Pérez, J., Masterton, S. et al. (2020). Designing scaffolds for corneal regeneration. *Adv. Funct. Mater.* 30 (44): 1908996.

44 da Silva Morais, A., Vieira, S., Zhao, X. et al. (2020). Advanced biomaterials and processing methods for liver regeneration: state-of-the-art and future trends. *Adv. Healthc. Mater.* 9 (5): 1901435.

45 Zhao, Z., Fan, C., Chen, F. et al. (2020). Progress in articular cartilage tissue engineering: a review on therapeutic cells and macromolecular scaffolds. *Macromol. Biosci.* 20: e1900278.

46 Reneker, D.H. and Chun, I. (1996). Nanometre diameter fibres of polymer, produced by electrospinning. *Nanotechnology* 7: 216–223.

47 Liu, Z.T., Zhang, X.-I., Jiang, Y., and Zeng, B.-F. (2010). Four-strand hamstring tendon autograft versus LARS artificial ligament for anterior cruciate ligament reconstruction. *Int. Orthop.* 34: 45–49.

48 Burns, J.P. and Snyder, S.J. (2009). Biologic patches for management of irreparable rotator cuff tears. *Tech. Shoulder Elbow Surg.* 10: 11–21.

49 Inui, A., Kokubu, T., Makino, T. et al. (2010). Potency of double-layered poly L-lactic acid scaffold in tissue engineering of tendon tissue. *Int. Orthop.* 34: 1327–1332.

50 Shikinami, Y., Kawabe, Y., Yasukawa, K. et al. (2010). A biomimetic artificial intervertebral disc system composed of a cubic three-dimensional fabric. *Spine J.* 10: 141–152.

51 Heim, F., Durand, B., and Chakfe, N. (2010). Textile for heart valve prostheses: fabric long-term durability testing. *J. Biomed. Mater. Res. B* 92: 68–77.

52 Inada, Y., Morimoto, S., Takakura, Y., and Nakamura, T. (2004). Regeneration of peripheral nerve gaps with a polyglycolic acid-collagen tube. *Neurosurgery* 55: 640–646.

53 Zhang, X., Reagan, M.R., and Kaplan, D.L. (2009). Electrospun silk biomaterial scaffolds for regenerative medicine. *Adv. Drug Deliv. Rev.* 61: 988–1006.

54 Zhao, L., Weir, M.D., and Xu, H.H. (2010). An injectable calcium phosphate-alginate hydrogel-umbilical cord mesenchymal stem cell paste for bone tissue engineering. *Biomaterials* 31: 6502–6510.

55 Hartwell, R., Leung, V., Chavez-Munoz, C. et al. (2011). A novel hydrogel collagen composite improves functionality of an injectable extracellular matrix. *Acta Biomater.* 7: 3060–3069.

56 Sivashanmugam, A., Kumar, R.A., Priya, M.V. et al. (2015). An overview of injectable polymeric hydrogels for tissue engineering. *Eur. Polym. J.* 72: 543–565.

57 Park, H., Choi, B., Hu, J., and Lee, M. (2013). Injectable chitosan hyaluronic acid hydrogels for cartilage tissue engineering. *Acta Biomater.* 9: 4779–4786.

58 Townsend, J.M., Zabel, T.A., Feng, Y. et al. (2018). Effects of tissue processing on bioactivity of cartilage matrix-based hydrogels encapsulating osteoconductive particles. *Biomed. Mater.* 13: 034108.

59 Zhang, W., Wang, X., Wang, S. et al. (2011). The use of injectable sonication-induced silk hydrogel for VEGF165 and BMP-2 delivery for elevation of the maxillary sinus floor. *Biomaterials* 32: 9415–9424.

60 Loo, Y., Zhang, S., and Hauser, C.A. (2012). From short peptides to nanofibers to macromolecular assemblies in biomedicine. *Biotechnol. Adv.* 30: 593–603.

61 Nishida, K., Yamato, M., Hayashida, Y. et al. (2004). Corneal reconstruction with tissue engineered cell sheets composed of autologous oral mucosal epithelium. *N. Engl. J. Med.* 351: 1187–1196.

62 Shimizu, T., Yamato, M., Kikuchi, A., and Okano, T. (2003). Cell sheet engineering for myocardial tissue reconstruction. *Biomaterials* 24: 2309–2316.

63 Huang, W., Li, X., Shi, X., and Lai, C. (2014). Microsphere based scaffolds for bone regenerative applications. *Biomater. Sci.* 2: 1145–1153.

64 Singh, M., Sandhu, B., Scurto, A. et al. (2010). Microsphere-based scaffolds for cartilage tissue engineering: using subcritical CO_2 as a sintering agent. *Acta Biomater.* 6: 137–143.

65 Chen, W.H. and Tong, Y.W. (2012). PHBV microspheres as neural tissue engineering scaffold support neuronal cell growth and axon–dendrite polarization. *Acta Biomater.* 8: 540–548.

66 Lee, J.W., Kang, K.S., Lee, S.H. et al. (2011). Bone regeneration using a microstereolithography-produced customized poly(propylene fumarate)/diethyl

fumarate photopolymer 3D scaffold incorporating BMP-2 loaded PLGA microspheres. *Biomaterials* 32: 744–752.

67 Park, J.H., Jung, J.W., Kang, H.W. et al. (2012). Development of a 3D bellows tracheal graft: mechanical behavior analysis, fabrication and an in vivo feasibility study. *Biofabrication* 4: 035004.

68 Li, X., He, J., Bian, W. et al. (2014). A novel silk-TCP-PEEK construct for anterior cruciate ligament reconstruction: an off-the shelf alternative to a bone-tendon-bone autograft. *Biofabrication* 6: 015010.

69 Keriquel, V., Guillemot, F., Arnault, I. et al. (2010). In vivo bioprinting for computer- and robotic-assisted medical intervention: preliminary study in mice. *Biofabrication* 2: 014101.

70 Zieber, L., Or, S., Ruvinov, E., and Cohen, S. (2014). Microfabrication of channel arrays promotes vessel-like network formation in cardiac cell construct and vascularization in vivo. *Biofabrication* 6: 024102.

71 Tarafder, S., Balla, V.K., Davies, N.M. et al. (2013). Microwave-sintered 3D printed tricalcium phosphate scaffolds for bone tissue engineering. *J. Tissue Eng. Regen. Med.* 7: 631–641.

72 Killat, J., Reimers, K., Choi, C.Y. et al. (2013). Cultivation of keratinocytes and fibroblasts in a three-dimensional bovine collagen-elastin matrix (Matriderm®) and application for full thickness wound coverage in vivo. *Int. J. Mol. Sci.* 14: 14460–14474.

73 Gaebel, R., Ma, N., Liu, J. et al. (2011). Patterning human stem cells and endothelial cells with laser printing for cardiac regeneration. *Biomaterials* 32: 9218–9230.

74 Hong, J.M., Kim, B.J., Shim, J.H. et al. (2012). Enhancement of bone regeneration through facile surface functionalization of solid freeform fabrication-based three-dimensional scaffolds using mussel adhesive proteins. *Acta Biomater.* 8: 2578–2586.

75 Jensen, J., Rolfing, J.H., Le, D.Q. et al. (2014). Surface-modified functionalized polycaprolactone scaffolds for bone repair: in vitro and in vivo experiments. *J. Biomed. Mater. Res. A* 102: 2993–3003.

76 Costa, P.F., Vaquette, C., Zhang, Q. et al. (2014). Advanced tissue engineering scaffold design for regeneration of the complex hierarchical periodontal structure. *J. Clin. Periodontol.* 41: 283–294.

77 Mandrycky, C., Wang, Z., Kim, K., and Kim, D.-H. (2016). 3D bioprinting for engineering complex tissues. *Biotechnol. Adv.* 34: 422–434.

78 Park, C.H., Rios, H.F., Jin, Q. et al. (2012). Tissue engineering bone-ligament complexes using fiber-guiding scaffolds. *Biomaterials* 33: 137–145.

79 Wang, J., Jiang, B., Guo, W., and Zhao, Y.-M. (2019). Indirect 3D printing technology for the fabrication of customised β-TCP/chitosan scaffold with the shape of rabbit radial head – an in vitro study. *J. Orthop. Surg. Res.* 14: 102.

80 Uchida, T., Ikeda, S., Oura, H. et al. (2008). Development of biodegradable scaffolds based on patient-specific arterial configuration. *J. Biotechnol.* 133: 213–218.

81 Simionescu, B.C. and Ivanov, D. (2016). Natural and synthetic polymers for designing composite materials. In: *Handbook of Bioceramics and Biocomposites* (ed. I.V. Antoniac), 233–286. Switzerland: Springer International Publishing.

82 Carter, P. and Bhattarai, N. (2013). Bioscaffolds: fabrication and performance. In: *Engineered Biomimicry* (ed. A. Lakhtakia and R.J. Martin-Palma), 161–188. Elsevier Inc.

83 Zhu, N. and Chen, X. (2013). Biofabrication of tissue scaffolds. In: *Advances in Biomaterials Science and Biomedical Applications* (ed. R. Pignatello). InTech. 316328.

84 Jing, D., Wu, L., and Ding, J. (2006). Solvent-assisted room-temperature compression molding approach to fabricate porous scaffolds for tissue engineering. *Macromol. Biosci.* 6: 747–757.

85 Yao, D., Smith, A., Nagarajan, P. et al. (2006). Fabrication of polycaprolactone scaffolds using a sacrificial compression-molding process. *J. Biomed. Mater. Res. B Appl. Biomater.* 77: 287–295.

86 Kramschuster, A. and Turng, L.-S. (2010). An injection molding process for manufacturing highly porous and interconnected biodegradable polymer matrices for use as tissue engineering scaffolds. *J. Biomed. Mater. Res. B Appl. Biomater.* 92: 366–376.

87 Agrawal, C.M., Niederauer, G.G., and Athanasiou, K.A. (1995). Fabrication and characterization of PLA-PGA orthopedic implants. *Tissue Eng.* 1: 241–252.

88 Kőnig, C., Ruffieux, K., Wintermantel, E., and Blaser, J. (1997). Autosterilization of biodegradable implants by injection molding process. *J. Biomed. Mater. Res.* 38: 115–119.

89 Gomes, M.E., Ribeiro, A.S., Malafaya, P.B. et al. (2001). A new approach based on injection moulding to produce biodegradable starch-based polymeric scaffolds: morphology, mechanical and degradation behaviour. *Biomaterials* 22: 883–889.

90 Liebschner, M.A.K. and Wettergreen, M.A. (2003). Optimization of bone scaffold engineering for load bearing applications. In: *Topics in Tissue Engineering* (ed. N. Ashammakhi and P. Ferretti), 1–39. University of Oulu.

91 Sachlos, E. and Czernuszka, J.T. (2003). Making tissue engineering scaffolds work. Review on the application of solid freeform fabrication technology to the production of tissue engineering scaffolds. *Eur. Cell. Mater.* 5: 29–40.

92 Ma, P.X. and Zhang, R. (2001). Microtubular architecture of biodegradable polymer scaffolds. *J. Biomed. Mater. Res.* 56: 469–477.

93 Mikos, A.G.L., Lu, L., Temenoff, J.S., and Temmser, J.K. (2004). Synthetic bioresorbable polymer scaffolds. In: *An Introduction to Material in Medicine* (ed. B.D. Ratner, A.S. Hoffman, F.J. Schoen and J.E. Lemons), 743. New York: Elsevier/Academic Press.

94 Hua, F.J.K.G.E., Lee, J.D., Son, Y.K., and Lee, D.S. (2002). Macroporous poly(L-lactide) scaffold 1. Preparation of a macroporous scaffold by liquid–liquid phase separation of a PLLA–dioxane–water system. *J. Biomed. Mater. Res.* 2: 161–167.

95 Sachlos, E. and Czernuszka, J.T. (2003). Making tissue engineering scaffolds work. Review on the application of solid free from fabrication technology to the production of tissue engineering scaffolds. *Eur. Cell. Mater.* 5: 29–39.

96 Subia, B., Kundu, J., and Kundu, S. (2010). *Biomaterial Scaffold Fabrication Techniques for Potential Tissue Engineering Applications*. IntechOpen Access Publisher.

97 Zhang, R. and Ma, P.X. (2001). Processing of polymer scaffolds: phase separation. In: *Methods of Tissue Engineering* (ed. A. Atala and R. Lanza), 715. San Diego, CA: Academic Press.

98 Smith, L.A., Beck, J.A., Ma, P.X. et al. (2007). Nanofibrous scaffolds and their biological effects. *Nanotechnol. Life Sci.* 9: 188–215.

99 Dehghani, F. and Annabi, N. (2011). Engineering porous scaffolds using gas-based techniques. *Curr. Opin. Biotechnol.* 22: 661–666.

100 Barbetta, A., Gumiero, A., Pecci, R. et al. (2009). Gas-in-liquid foam templating as a method for the production of highly porous scaffolds. *Biomacromolecules* 10: 3188–3192.

101 Barbetta, A., Rizzitelli, G., Bedini, R. et al. (2010). Porous gelatin hydrogels by gas-in-liquid foam templating. *Soft Matter* 6: 1785–1792.

102 Whitea, L.J., Hutter, V., Tai, H. et al. (2012). The effect of processing variables on morphological and mechanical properties of supercritical CO_2 foamed scaffolds for tissue engineering. *Acta Biomater.* 8: 61–71.

103 Song, C., Luo, Y., Liu, Y. et al. (2020). Fabrication of PCL scaffolds by supercritical CO_2 foaming based on the combined effects of rheological and crystallization properties. *Polymers* 12: 780.

104 Huang, Y. and Mooney, D.J. (2005). Gas foaming to fabricate polymer scaffolds in tissue engineering. In: *Scaffolding in Tissue Engineering* (ed. P.X. Ma and J. Elisseeff), 155–165. Boca Raton, FL: CRC Press.

105 Martinez, C.J. (2009). Bubble generation in microfluidic devices. *Bubble Sci. Eng. Technol.* 1: 40–52.

106 Garstecki, P., Fuerstman, M.J., Stone, H.A., and Whitesides, G.M. (2006). Formation of droplets and bubbles in a microfluidic T-junction – scaling and mechanism of break-up. *Lab Chip* 6: 437–446.

107 Marmottant, P. and Raven, J.P. (2009). Microfluidics with foams. *Soft Matter* 5: 3385–3388.

108 Mandal, B.B. and Kundu, S.C. (2008). Non-bioengineered silk gland fibroin protein: characterization and evaluation of matrices for potential tissue engineering applications. *Biotechnol. Bioeng.* 100: 1237–1250.

109 Alizadeh, M., Abbasi, F., Khoshfetrat, A.B., and Ghaleh, H. (2013). Microstructure and characteristic properties of gelatin/chitosan scaffold prepared by a combined freeze-drying/leaching method. *Mater. Sci. Eng. C* 33: 3958–3967.

110 Asuncion, M.C., Goh, J.C., and Toh, S.L. (2016). Anisotropic silk fibroin/gelatin scaffolds from unidirectional freezing. *Mater. Sci. Eng. C* 67: 646–656.

111 Simionescu, B.C., Neamtu, A., Balhui, C. et al. (2013). Macroporous structures based on biodegradable polymers – candidates for biomedical application. *J. Biomed. Mater. Res. A* 101: 2689–2698.

112 Nelson, I. and Naleway, S.E. (2019). Intrinsic and extrinsic control of freeze casting. *J. Mater. Res. Technol.* 8: 2372–2385.

113 Murphy, C., Haugh, M., and O'Brien, F. (2010). The effect of mean pore size on cell attachment, proliferation and migration in collagen–glycosaminoglycan scaffolds for bone tissue engineering. *Biomaterials* 31: 461–466.

114 Kim, B.S., Yang, S.S., and Lee, J. (2014). A polycaprolactone/cuttlefish bone-derived hydroxyapatite composite porous scaffold for bone tissue engineering. *J. Biomed. Mater. Res. Part B Appl. Biomater.* 102: 943–951.

115 Mikos, A.G., Thorsen, A.J., Czerwonka, L.A. et al. (1994). Preparation and characterization of poly(L-lactic acid) foams. *Polymer* 35: 1068–1077.

116 Rajendran, S. and Anand, S. (2002). Developments in medical textiles. *Text. Prog.* 32: 1–42.

117 Ramakrishna, S. (2001). *Textile Scaffolds in Tissue Engineering*. Boca Raton, FL: CRC Press.

118 Dattilo, P.P. Jr., King, M.W., Cassill, N.L., and Leung, J.C. (2002). Medical textiles: application of an absorbable barbed bi-directional surgical suture. *J. Text. Apparel Technol. Manage.* 2: 1–5.

119 Sumanasinghe, R.D. and King, M.W. (2003). New trends in biotextiles – the challenge of tissue engineering. *J. Text. Apparel Technol. Manage.* 3: 1–13.

120 Boublik, J., Park, H., Radisic, M. et al. (2005). Mechanical properties and remodeling of hybrid cardiac constructs made from heart cells, fibrin, and biodegradable, elastomeric knitted fabric. *Tissue Eng.* 11: 1122–1132.

121 Maziz, A., Concas, A., Khaldi, A. et al. (2017). Knitting and weaving artificial muscles. *Sci. Adv.* 3 (1): e1600327.

122 Moutos, F.T., Freed, L.E., and Guilak, F. (2007). A biomimetic three-dimensional woven composite scaffold for functional tissue engineering of cartilage. *Nat. Mater.* 6: 162–167.

123 Almeida, L.R., Martins, A.R., Fernandes, E.M. et al. (2013). New biotextiles for tissue engineering: development, characterization and in vitro cellular viability. *Acta Biomater.* 9: 8167–8181.

124 Ellä, V., Annala, T., Länsman, S. et al. (2011). Knitted polylactide 96/4 L/D structures and scaffolds for tissue engineering: shelf life, in vitro and in vivo studies. *Biomatter* 1: 102–113.

125 Coda, A., Lamberti, R., and Martorana, S. (2012). Classification of prosthetics used in hernia repair based on weight and biomaterial. *Hernia* 16: 9–20.

126 Zou, H., Zhi, Y.L., Chen, X. et al. (2010). Mesenchymal stem cell seeded knitted silk sling for the treatment of stress urinary incontinence. *Biomaterials* 31: 4872–4879.

127 Chellamani, K., Sudharsan, J., and Sathish, J. (2013). Medical textiles using braiding technology. *J. Acad. Ind. Res.* 2: 21–26.

128 Du, G.-W. and Ko, F.K. (1993). Unit cell geometry of 3-D braided structures. *J. Reinf. Plast. Compos.* 12: 752–768.

129 Barber, J.G., Handorf, A.M., Allee, T.J., and Li, W.-J. (2011). Braided nanofibrous scaffold for tendon and ligament tissue engineering. *Tissue Eng. Part A* 19: 1265–1274.

130 Freed, L.E., Vunjak-Novakovic, G., Biron, R.J. et al. (1994). Biodegradable polymer scaffolds for tissue engineering. *Nat. Biotechnol.* 12: 689–693.

131 Mikos, A.G., Bao, Y., Cima, L.G. et al. (1993). Preparation of poly(glycolic acid) bonded fiber structures for cell attachment and transplantation. *J. Biomed. Mater. Res.* 27: 183–189.

132 Brown, T.D., Dalton, P.D., and Hutmacher, D.W. (2011). Direct writing by way of melt electrospinning. *Adv. Mater.* 23: 5651–5657.

133 Li, D. and Xia, Y.N. (2004). Electrospinning of nanofibers: reinventing the wheel? *Adv. Mater.* 16: 1151–1170.

134 Ma, Z., Kotaki, M., Inai, R., and Ramakrishna, S. (2005). Potential of nanofiber matrix as tissue-engineering scaffolds. *Tissue Eng.* 11: 101–109.

135 Beachley, V. and Wen, X. (2010). Polymer nanofibrous structures: fabrication, biofunctionalization, and cell interactions. *Prog. Polym. Sci.* 35: 868–892.

136 Reneker, D.H., Yarin, A.L., Fong, H., and Koombhongse, S. (2000). Bending instability of electrically charged liquid jets of polymer solutions in electrospinning. *J. Appl. Phys.* 87: 4531–4547.

137 Spivak, A.F., Dzenis, Y.A., and Reneker, D.H. (2000). A model of steady state jet in the electrospinning process. *Mech. Res. Commun.* 27: 37–42.

138 Srinivasan, G. and Reneker, D.H. (1995). Structure and morphology of small-diameter electrospun aramid fibers. *Polym. Int.* 36: 195–201.

139 Cooper, A., Bhattarai, N., and Zhang, M. (2011). Fabrication and cellular compatibility of aligned chitosan–PCL fibers for nerve tissue regeneration. *Carbohydr. Polym.* 85: 149–156.

140 Nguyen, T.T.T., Chung, O.H., and Park, J.S. (2011). Coaxial electrospun poly(lactic acid)/chitosan (core/shell) composite nanofibers and their antibacterial activity. *Carbohydr. Polym.* 86: 1799–1806.

141 Yu, D.G., Williams, G.R., Gao, L.D. et al. (2012). Coaxial electrospinning with sodium dodecylbenzene sulfonate solution for high quality polyacrylonitrile nanofibers. *Colloids Surf. A: Physicochem. Eng. Asp.* 396: 161–168.

142 Hoffman, A.S. (2012). Hydrogels for biomedical applications. *Adv. Drug Deliv. Rev.* 64: 18–23.

143 El-Sherbiny, I.M. and Yacoub, M.H. (2013). Hydrogel scaffolds for tissue engineering, progress and challenges. *Global Cardiol. Sci. Pract.* 38: 1–27.

144 Schmedlen, R.H., Masters, K.S., and West, J.L. (2002). Photocrosslinkable polyvinyl alcohol hydrogels that can be modified with cell adhesion peptides for use in tissue engineering. *Biomaterials* 23: 4325–4332.

145 Guadalupe, E., Ramos, D., Shelke, N.B. et al. (2015). Bioactive polymeric nanofiber matrices for skin regeneration. *J. Appl. Polym. Sci.* 132: 41879–41889.

146 Nguyen, K.T. and West, J.L. (2002). Photopolymerizable hydrogels for tissue engineering applications. *Biomaterials* 23: 4307–4314.

147 Burke, S.A., Ritter-Jones, M., Lee, B.P., and Messersmith, P.B. (2007). Thermal gelation and tissue adhesion of biomimetic hydrogels. *Biomed. Mater.* 2: 203–210.

148 Silva, S.S., Popa, E.G., Gomes, M.E. et al. (2013). Silk hydrogels from non-mulberry and mulberry silkworm cocoons processed with ionic liquids. *Acta Biomater.* 9: 8972–8982.

149 Silva, S.S., Motta, A., Rodrigues, M.T. et al. (2008). Novel genipin-cross-linked chitosan/silk fibroin sponges for cartilage engineering strategies. *Biomacromolecules* 9: 2764–2774.

150 Ribeiro, V., Pina, S., Costa, J.B. et al. (2019). Enzymatically crosslinked silk fibroin-based hierarchical scaffolds for osteochondral regeneration. *ACS Appl. Mater. Interfaces* 11: 3781–3799.

151 De France, K.J., Xu, F., and Hoare, T. (2018). Structured macroporous hydrogels: progress, challenges, and opportunities. *Adv. Healthc. Mater.* 7: 1700927.

152 Dhandayuthapani, B., Yoshida, Y., Maekawa, T., and Kumar, D.S. (2011). Polymeric scaffolds in tissue engineering application: a review. *Int. J. Polym. Sci.* 2011. Article ID: 290602.

153 Drury, J.L. and Mooney, D.J. (2003). Hydrogels for tissue engineering: scaffold design variables and applications. *Biomaterials* 24: 4337–4351.

154 Aida, T., Meijer, E.W., and Stupp, S.I. (2012). Functional supramolecular polymers. *Science* 335: 813–817.

155 Zhang, S. (2003). Fabrication of novel biomaterials through molecular self-assembly. *Nat. Biotechnol.* 21: 1171–1178.

156 Zhang, S. (2002). Emerging biological materials through molecular self-assembly. *Biotechnol. Adv.* 20: 321–339.

157 Holmes, T.C., de Lacalle, S., Su, X. et al. (2000). Extensive neurite outgrowth and active synapse formation on self-assembling peptide scaffolds. *Proc. Natl. Acad. Sci. U.S.A.* 97: 6728–6733.

158 Kisiday, J., Jin, M., Kurz, B. et al. (2002). Self-assembling peptide hydrogel fosters chondrocyte extracellular matrix production and cell division: implications for cartilage tissue repair. *Proc. Natl. Acad. Sci. U.S.A.* 99: 9996–10001.

159 Wade, R.J. and Burdick, J.A. (2014). Advances in nanofibrous scaffolds for biomedical applications: from electrospinning to self-assembly. *Nano Today* 9: 722–742.

160 Hartgerink, J.D., Beniash, E., and Stupp, S.I. (2002). Peptide-amphiphile nanofibers: a versatile scaffold for the preparation of self-assembling materials. *Proc. Natl. Acad. Sci. U.S.A.* 99: 5133–5138.

161 Liu, G.J., Qiao, L.J., and Guo, A. (1996). Diblock copolymer nanofibers. *Macromolecules* 29: 5508–5510.

162 Ma, P.X. (2008). Biomimetic materials for tissue engineering. *Adv. Drug Deliv. Rev.* 60: 184–198.

163 Jun, H.-W., Paramonov, S.E., and Hartgerink, J.D. (2006). Biomimetic self-assembled nanofibers. *Soft Matter* 2: 177–181.

164 Zhang, S., Xing, M., and Li, B. (2018). Biomimetic layer-by-layer self-assembly of nanofilms, nanocoatings, and 3D scaffolds for tissue engineering. *Int. J. Mol. Sci.* 19: 1641.

165 Costa, R.R. and Mano, J.F. (2014). Polyelectrolyte multilayered assemblies in biomedical technologies. *Chem. Soc. Rev.* 43: 3453–3479.

166 Borges, J. and Mano, J.F. (2014). Molecular interactions driving the layer-by-layer assembly of multilayers. *Chem. Rev.* 114: 8883–8942.

167 Singh, M., Morris, C.P., Ellis, R.J. et al. (2008). Microsphere-based seamless scaffolds containing macroscopic gradients of encapsulated factors for tissue engineering. *Tissue Eng. Part C* 14: 299–309.

168 Gupta, V., Khan, Y., Berkland, C.J. et al. (2017). Microsphere-based scaffolds in regenerative engineering. *Annu. Rev. Biomed. Eng.* 19: 135–161.

169 Brown, J.L., Nair, L.S., and Laurencin, C.T. (2008). Solvent/non-solvent sintering: a novel route to create porous microsphere scaffolds for tissue regeneration. *J. Biomed. Mater. Res. Part B Appl. Biomater.* 86: 396–406.

170 Dhariwala, B., Hunt, E., and Boland, T. (2004). Rapid prototyping of tissue-engineering constructs, using photopolymerizable hydrogels and stereolithography. *Tissue Eng.* 10: 1316–1322.

171 Hribar, K.C., Soman, P., Warner, J. et al. (2014). Light-assisted direct-write of 3D functional biomaterials. *Lab Chip* 14: 268–275.

172 Cui, H., Nowicki, M., Fisher, J.P., and Zhang, L.G. (2017). 3D Bioprinting for organ regeneration. *Adv. Healthc. Mater.* 6: 1601118.

173 Cooke, M.N., Fisher, J.P., Dean, D. et al. (2003). Use of stereolithography to manufacture critical-sized 3D biodegradable scaffolds for bone ingrowth. *J. Biomed. Mater. Res. B* 64: 65–69.

174 Lee, S.J., Nowicki, M., Harris, B., and Zhang, L.G. (2017). Fabrication of a highly aligned neural scaffold via a table top stereolithography 3D printing and electrospinning. *Tissue Eng. Part A* 23: 491–502.

175 Ronca, A. and Ambrosio, L. (2017). Polymer based scaffolds for tissue regeneration by stereolithography. *Adv. Biomater. Dev. Med.* 4: 1–15.

176 Worthington, K.S., Wiley, L.A., Kaalberg, E.E. et al. (2017). Two-photon polymerization for production of human iPSC-derived retinal cell grafts. *Acta Biomater.* 55: 385–395.

177 Shirazi, S.F.S., Gharehkhani, S., Mehrali, M. et al. (2015). A review on powder-based additive manufacturing for tissue engineering: selective laser sintering and inkjet 3D printing. *Sci. Technol. Adv. Mater.* 16: 033502.

178 Olakanmi, E.O., Cochrane, R.F., and Dalgarno, K.W. (2015). A review on selective laser sintering/melting (SLS/SLM) of aluminium alloy powders: processing, microstructure, and properties. *Prog. Mater. Sci.* 74: 401–477.

179 Du, Y., Liu, H., Shuang, J. et al. (2015). Microsphere-based selective laser sintering for building macroporous bone scaffolds with controlled microstructure and excellent biocompatibility. *Colloids Surf. B Biointerfaces* 135: 81–89.

180 Gu, B.K., Choi, D.J., Park, S.J. et al. (2016). 3-Dimensional bioprinting for tissue engineering applications. *Biomater. Res.* 20: 12.

181 Zein, I., Hutmacher, D.W., Tan, K.C., and Teoh, S.H. (2002). Fused deposition modeling of novel scaffold architectures for tissue engineering applications. *Biomaterials* 23: 1169–1185.

182 Leigh, S.J., Bradley, R.J., Purssell, C.P. et al. (2012). A simple, low-cost conductive composite material for 3D printing of electronic sensors. *PLoS One* 7: e49365.

183 Korpela, J., Kokkari, A., Korhonen, H. et al. (2013). Biodegradable and bioactive porous scaffold structures prepared using fused deposition modeling. *J. Biomed. Mater. Res. B* 101: 610–619.

184 Zhou, C., Yang, K., Wang, K. et al. (2016). Combination of fused deposition modeling and gas foaming technique to fabricated hierarchical macro/microporous polymer scaffolds. *Mater. Des.* 109: 415–424.

185 Sachs, E.M., Haggerty, J.S., Cima, M.J., and Williams, P.A. (1993). Three-dimensional printing techniques. US5204055A Patent, filed 09 April 1993 and issue 23 August 1994.

186 Do, A.-V., Khorsand, B., Geary, S.M., and Salem, A.K. (2015). 3D Printing of scaffolds for tissue regeneration applications. *Adv. Healthc. Mater.* 4: 1742–1762.

187 Ozbolat, I.T., Chen, H., and Yu, Y. (2014). Development of "Multi-arm Bioprinter" for hybrid biofabrication of tissue engineering constructs. *Rob. Comput. Integr. Manuf.* 30: 295–304.

188 Tamay, D.G., Dursun Usal, T., Alagoz, A.S. et al. (2019). 3D and 4D printing of polymers for tissue engineering applications. *Front. Bioeng. Biotechnol.* 9: 164.

189 Yang, Q., Gao, B., and Xu, F. (2020). Recent advances in 4D bioprinting. *Biotechnol. J.* 15: e1900086.

190 Taboas, J.M., Maddox, R.D., Krebsbach, P.H., and Hollister, S.J. (2003). Indirect solid free form fabrication of local and global porous, biomimetic and composite 3D polymer-ceramic scaffolds. *Biomaterials* 24: 181–194.

191 Hernandez-Cordova, R., Mathew, D.A., Balint, R. et al. (2016). Indirect three-dimensional printing: a method for fabricating polyurethane-urea based cardiac scaffolds. *J. Biomed. Mater. Res. A* 104: 1912–1921.

192 Chia, H.N. and Wu, B.M. (2015). Recent advances in 3D printing of biomaterials. *J. Biol. Eng.* 9: 4.

193 Lee, J.Y., Choi, B., Wu, B., and Lee, M. (2013). Customized biomimetic scaffolds created by indirect three-dimensional printing for tissue engineering. *Biofabrication* 5: 045003.

194 Williams, D.F. (2004). Benefit and risk in tissue engineering. *Mater. Today* 7: 24–29.

195 Williams, D.F. (2019). Challenges with the development of biomaterials for sustainable tissue engineering. *Front. Bioeng. Biotechnol.* 7: 127.

196 Patterson, J., Martino, N.M., and Hubbell, J.A. (2010). Biomimetic materials in tissue engineering. *Mater. Today* 13: 14–22.

12

Solvent-Casting Approach for Design of Polymer Scaffolds and Their Multifunctional Applications

Blessy Joseph[1], Cintil Jose[2], Sagarika V. Kavil[3], Nandakumar Kalarikkal[1], and Sabu Thomas[1,4]

[1] *International and Inter University Centre for Nanoscience and Nanotechnology, Mahatma Gandhi University, Kottayam 686560 Kerala, India*
[2] *Newman College Rd, Mangattukavala, Thodupuzha 685584 Kerala, India*
[3] *Indian Institutes of Science Education and Research (IISER), Tirupati 517507 Andhra Pradesh, India*
[4] *School of Energy Materials, Mahatma Gandhi University, Kottayam 686560 Kerala, India*

12.1 Introduction

Skin is one of the vital protective parts of the human body. It serves as an important barrier against pathogens and prevents any mechanical, thermal, or chemical stress. The repair and renewal of tissue after an injury is essential as the restoration of the damaged part of the skin. Tissue engineering is an important interdisciplinary field which mainly focuses on the production of engineered tissues for the repair and replacement of damaged tissues or organs [1]. Tissue-engineering scaffolds play a major role in the regeneration of tissues. Isolated cells need a surface for attachment, to replicate, migrate, and function, since those cells are unable to form new tissues on their own. That is, they require the presence of a supporting material that can act as a template for cell growth. To mimic their natural extracellular matrices, three-dimensional scaffolds are often used as this supporting material [2]. In the past few years, increasing attention has been paid to nanocomposites made of biopolymers and bioactive materials as scaffolds for application in tissue engineering [3–5]. Scaffolds can facilitate the organization of cells into a three-dimensional architecture, direct cell behavior, and finally result in the formation of organ-specific tissue. Scaffolds play a crucial role in tissue engineering because they represent an alternative to the conventional implantation of organs and tissues. The main goal of scaffolds is to provide appropriate base for tissue growth and cell proliferation [6]. A wide variety of nanocomposites are currently being explored for use as porous scaffolds for many tissue-engineering strategies. Nanocomposites scaffolds may prove necessary for reconstruction of multitissue organs, tissues interfaces, and structural tissues including bone, cartilage, tendons, ligaments, and muscles [7]. Scaffold fabrication methods aim at the production of highly porous and interconnected pore structures. To fabricate such tissue scaffolds, a number of fabrication techniques have

Functional Biomaterials: Design and Development for Biotechnology, Pharmacology, and Biomedicine, First Edition. Edited by Tamilselvan Mohan and Karin Stana Kleinschek.

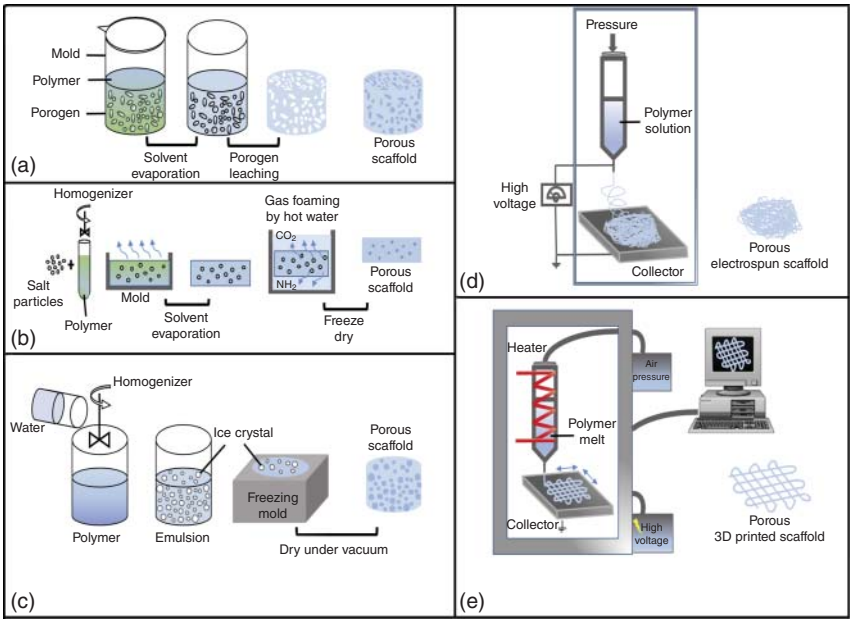

Figure 12.1 Common scaffold fabrication techniques. (a) Porogen leaching, (b) Gas foaming, (c) Freeze-drying, (d) Solution electrospinning, (e) Melt electrowriting and 3-D printing. Source: Abbasi [8]/Elsevier/CC BY 4.0.

been developed. Polymer scaffolds with various geometries, such as porous scaffolds and fibrous matrices, have been prepared by using different processing techniques, including particulate leaching (PL), freeze drying, rapid prototyping (RP), phase separation, and electrospinning, as shown in Figure 12.1 [8].

This chapter intends to give a brief description about the solvent-casting (SC) process with major focus on biomedical applications. Other applications of solvent-cast films are also discussed. In this study, we outline the scientific and technical challenges associated with the fabrication and characterization of solvent-cast scaffolds. It is worthy to note that the interplay between polymer and solvent affects the morphology, porosity, and overall quality of polymer films.

12.2 Solvent-Casting Technology

Solvent casting is used for the preparation of films containing nanocomposite scaffolds. This method is widely used because of low costs, shorter preparation time, and most importantly easy variation in reaction conditions. This method is called as "solvent casting" because the polymer is completely soluble in the solvent which ensures uniform distribution, hence fulfilling one of the ideal scaffold properties. The choice of solvent is the key factor as it can influence the polymer surface structure, which includes surface heterogeneity, reorientation of the surface crystal segment, swelling behavior, and deformation rates which may

influence the application of scaffold in tissue engineering [9, 10]. Solvent casting is a conventional and rapid technique for the fabrication of free-standing films. Here polymer is dissolved in an appropriate solvent, like water or chloroform (CF). Additionally, plasticizers can also be added based on the specific requirement. The solution is degassed and then poured into glass Petri dish, flat plate, or molds made of polytetrafluoroethylene (PTFE) or polycarbonate (PC). Then the sample is kept for drying in oven or at room temperature. The dried films are then peeled off from the glass plate and stored in vacuum-sealed covers. The drying step is crucial in several properties of the films and can be performed in an oven or a convection chamber or even at room temperature. This manufacturing method is suitable for heat-sensitive drugs due to the rather low temperature used to eliminate the solvents in comparison with other temperature-dependent extrusion techniques. The schematic representation of solvent-casting technique is shown in Figure 12.2.

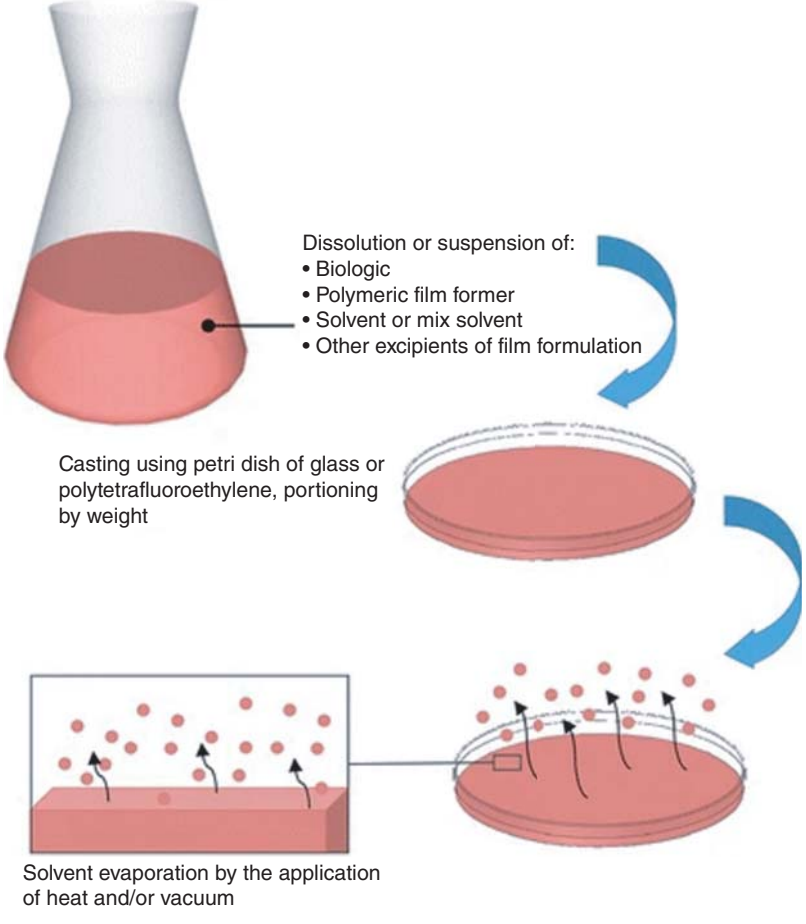

Figure 12.2 Schematic representation of solvent-casting process. Source: Montenegro-Nicolini and Morales [11]/with permission of Springer Nature.

12.2.1 Solvent Casting/Particulate Leaching

Solvent casting/particulate leaching (SC/PL) is a casting technique that has been widely used to fabricate 3D porous polymer scaffolds for tissue-engineering applications. The technique uses porogens, substances that can be dispersed into a molded structure and subsequently dissolved once the structure has set, resulting in the creation of pores. Salt (sodium chloride) is the most commonly used particulate (also called porogen) because it is easily available and very easy to handle. Briefly, this technique involves producing a suspension of polymer composites in a solvent. Salt particles are ground and sieved into small particles, and those of the desired size (most researchers used 100–200 μm range particles) are transferred into a mold. A polymer suspension is then cast into the salt-filled mold. The solvent is then removed by evaporation in air and/or in vacuum. After the evaporation of the solvent, the salt crystals are leached away by immersion in water to form a porous structure, as schematically shown in Figure 12.3 [12]. In this technique, the pore size can be controlled by the size of the porogen particles, and the porosity can be controlled by the salt/polymer composite ratio.

SC/PL technique is easy to carry out in the laboratory and flexible to be combined with other fabrication techniques due to its simplicity and low cost. For example, combined modified compression molding and conventional particulate-leaching to fabricate complexly shaped 3D porous scaffolds has been reported. Briefly, a polymer–particulate mixture was first prepared by the conventional solvent-casting method and then compressively molded in a specially designed flexible–rigid combined mold which facilitates shaping and mold release during the fabrication process. The molding was carried out at a moderate temperature, above the glass transition temperature and below the flow temperature of these amorphous

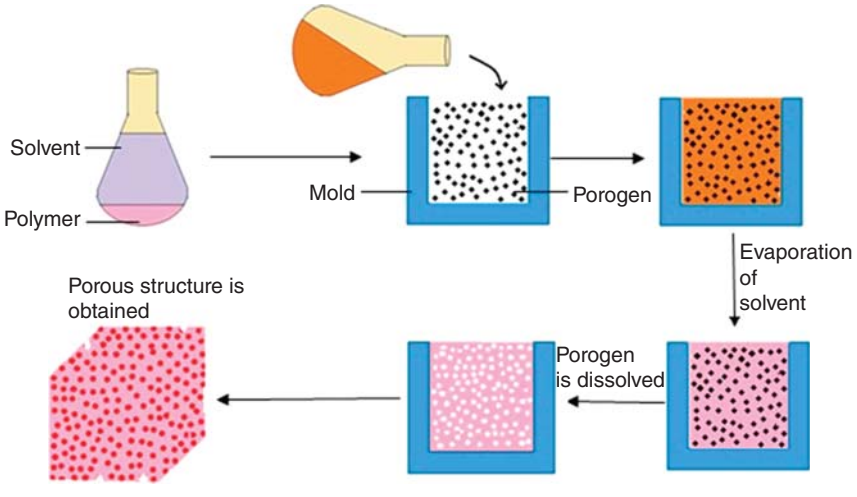

Figure 12.3 The schematic diagram of solvent-casting particulate-leaching techniques. (a) Density of PLA scaffolds in different solvents (HFIP/DCM/CF). (b) Porosity of PLA scaffolds in different solvents (HFIP/DCM/CF). Source: Sampath et al. [12]/MDPI/CC BY 4.0.

polymers. A porous scaffold was then obtained after particulate leaching. Highly interconnected and uniformly distributed pores both in the bulk and on the external surface of the polylactic acid (PLA) and poly(lactic-*co*-glycolic acid) (PLGA) auricle-shaped scaffolds were observed, and the porosity could exceed 90% [13].

One of the main benefits of this technique is that the produced scaffold is of high porosity and with the capability of tuning the pore size, which makes it appropriate for the development and growth of the 3D cell [14]. Other researchers have also applied this technique in the scaffold fabrication for different purposes, such as the combination of natural polymers [15, 16] or the integration of bioactive compounds into the scaffold [17, 18]. One of the drawbacks of this fabrication technique is its time consumption since it only uses thin membranes. Layers of porous sheets allow only a defined number of pore networks between them and may, therefore, limit its suitability to use because of the limited porous size [17].

12.2.1.1 Effect of Solvents on Solvent Casting

Solvent will inevitably affect the final physical properties of PLA/hyaluronic acid porous scaffold when varieties of SC/PL technique were used [19]. The most commonly used solvents are acetone, chloroform, and methylene chloride [20–24]. It was hypothesized that polymer/solvent interactions may affect the microstructure and physical properties of the resulting scaffolds. Polymer chains that are extended in solvent may entangle to a greater degree than aggregated bulky chains. This may increase the stiffness of the resulting tissue scaffold and alter the permeability. However, the differing rates of solvent evaporation may also dictate or contribute to observed differences in scaffold morphology.

Choudhury et al. prepared PLA porous scaffolds, using NaCl as porogen in three different solvents, i.e. 1,1,1,3,3,3-hexafluoro-2-propanol (HFIP), dichloromethane (DCM), and chloroform (CF) by SC/PL method [25]. The morphology, structure, and thermal behavior of the PLA scaffolds for porosity measurement were evaluated. PLA/CF scaffold depicted higher porosity factor (93%) along with enhanced water uptake capacity (220%) as against PLA/HFIP scaffold (75%). However, PLA/DCM scaffolds illustrated more thermal stability as compared with PLA/HFIP and PLA/CF scaffold. Figure 12.4 elaborates the density of PLA scaffolds in different solvents. As evident from Figure 12.4, with increase in density, there is a steady decrease in porosity of PLA/HFIP scaffolds; further, PLA/CF depicted the higher porosity in terms of last density, and hence the PLA scaffold followed the increase in proportionality, i.e. porosity is inversely proportional to density. The PLA/DCM scaffolds represented a stiffer base as compared to PLA/chloroform or PLA/HFIP scaffolds. Also, when ensured for permeability, the PLA/DCM depicted lower permeability and rugged morphology as compared to the other two. However, with similar content of porogen loading, the PLA/DCM scaffold showed highest porosity as compared to PLA/DCM and PLA/HFIP scaffolds, a factor that benefits the requirements in bone-tissue engineering. Hence, chloroform was suggessted as a better solvent to meet the homogeneity requirements of the scaffold due to its lower vapor pressure and slower evaporation time. Also, the cost-effectiveness

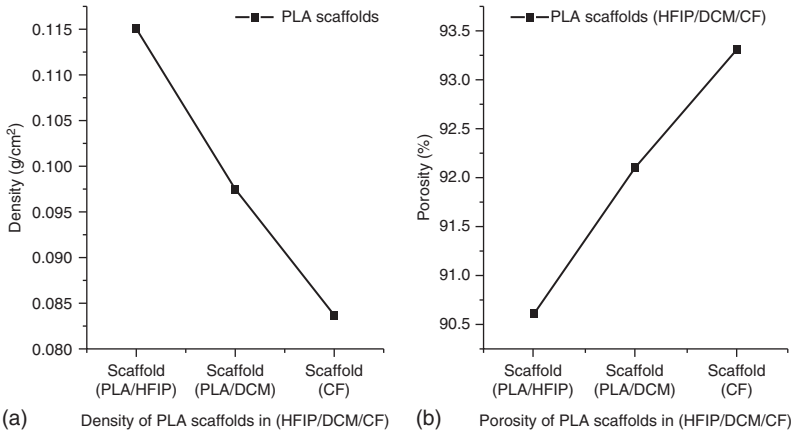

Figure 12.4 Density of PLA scaffolds in different solvents. Source: Choudhury et al. [25]/American Scientific Publishers/CC BY 4.0.

makes chloroform a preferred solvent along with its simplicity in hazards while handling the chemical [25].

Wanga et al. prepared hydroxyapatite/polymer scaffolds with proper biomechanical properties and stable 3D porous structure by combining gas foaming with SC/PL technique, in which novel solid H_2O_2 was used as a porogen [26]. During the manufacturing process, they found that the porosity, compressive strength, and microstructure of the composites are varied from each other, while different solvents (DCM, acetone, chloroform, and 1,4-dioxane) were used. Porosities of the specimens increase from $72 \pm 5\%$ to $87 \pm 5\%$ in accordance with the increase of boiling point from 39.75 to 101.32 °C, while compressive strength decreased (4.8 ± 0.7 to 0.5 ± 0.3 MPa). Interactions of hydroxyapatite (HA)/solvent and PLA/solvent together with evaporation dynamic tests of different solvents were investigated. The results show that the evaporation rate of the solvents is the most important factor affecting the final properties of the scaffolds.

12.2.1.2 Characterization of Solvent Cast Scaffolds

The complete characterization of scaffold structure and properties is essential to design scaffolds with optimal characteristics for numerous applications. For tissue-engineering applications, besides scaffold morphology and mechanical and surface properties, biological characterization of scaffolds by suitable cell-culture methods is also required. Depending on the final application, scaffold requirements include matching the structural and mechanical properties with those of the recipient tissue and optimization of the micro-environment to support cell integration, adhesion and growth, issues that have become known as structural and surface compatibility of biomaterials [27].

12.2.1.2.1 Morphology and Porosity

Scanning electron microscopy (SEM), micro-computed tomography (m-CT), and confocal laser scanning microscopy are used to visualize and subsequently quantify

scaffold structures [28–31]. In particular, m-CT has been widely used as an essential scaffold characterization tool with the potential to significantly enhance the understanding of pore structures in porous material in the millimeter-to-micrometer range [32, 33].

Porosity assessment via porosimetry is based on the study of the flow of gases or liquids (or both), across a porous structure. This method, therefore, is only suitable for the detection of open pores that allow fluid transport. Consequently, standard porosimetry methods cannot be used to assess total pore volume. Liquid intrusion methods (e.g. mercury intrusion porosimetry) are based on the pressurized penetration of a liquid into a porous structure and are capable of determining the total pore volume exposed to the outside of a structure. As with flow porosimetry, closed pores are hidden from the test. Other strategies used for scaffold characterization include gas pycnometry, gravimetry, and gas adsorption [34–37].

Highly porous scaffolds (Figure 12.5) were fabricated by Sola et al. using polymethyl methacrylate (PMMA) and polyurethane (PU) [38]. The scaffolds showed a highly interconnected geometry, as shown in Figure 12.5, and the porosity ranged from 82.1% to 91.3% for PU scaffolds and 84.3% to 87.4% for PMMA scaffolds. The polymer-to-salt (NaCl) ratio was taken as 1 : 4 for both polymers. Scaffolds were prepared using fine-grained (S2) and coarse-grained (S3) NaCl, and compared with samples made of NaCl that was not sieved (S1). The improved interconnectivity in samples containing sieved salts with respect to the samples containing unsieved salt was related to the shape of the S2 and S3 salt particles that were more spherical with respect to the strictly cubic geometry of S1. It was observed that when the salt content increased, the structural continuity deteriorated.

12.2.1.2.2 Mechanical Characterization of Scaffolds

Clearly, understanding the correlation between pore structure, porosity, and scaffold mechanical properties is crucial in the process of optimization of scaffold architecture. In most of the cases, compressive mechanical testing is used to measure the mechanical strength of a scaffold. It can be considered that scaffolds for bone regeneration should have a minimum compressive strength of 2 MPa and a minimum modulus of 50 MPa, which are at the low range of properties for trabecular bone [39].

In the engineering of soft tissues, scaffolds with high elasticity and strength coupled with controllable biodegradable properties are necessary. To fulfill such design, researchers tried two kinds of biodegradable polyurethane ureas, namely poly(ester urethane)urea (PEUU) and poly(ether ester urethane)urea (PEEUU) from polycaprolactone (PCL), polycaprolactone-*b*-polyethylene glycol-*b*-polycaprolactone, 1,4-diisocyanatobutane, and putrescine. PEUU and PEEUU were further fabricated into scaffolds by thermally induced phase separation using dimethyl sulfoxide (DMSO) as a solvent. The effect of polymer solution concentration, quenching temperature, and polymer type on pore morphology and porosity was investigated. Scaffolds were obtained with open and interconnected pores having sizes ranging from several millimeters to more than 150 mm and porosities of 80–97%. By changing the polymer solution concentration or quenching temperature, scaffolds with random or oriented tubular pores could be obtained. The PEUU scaffolds were

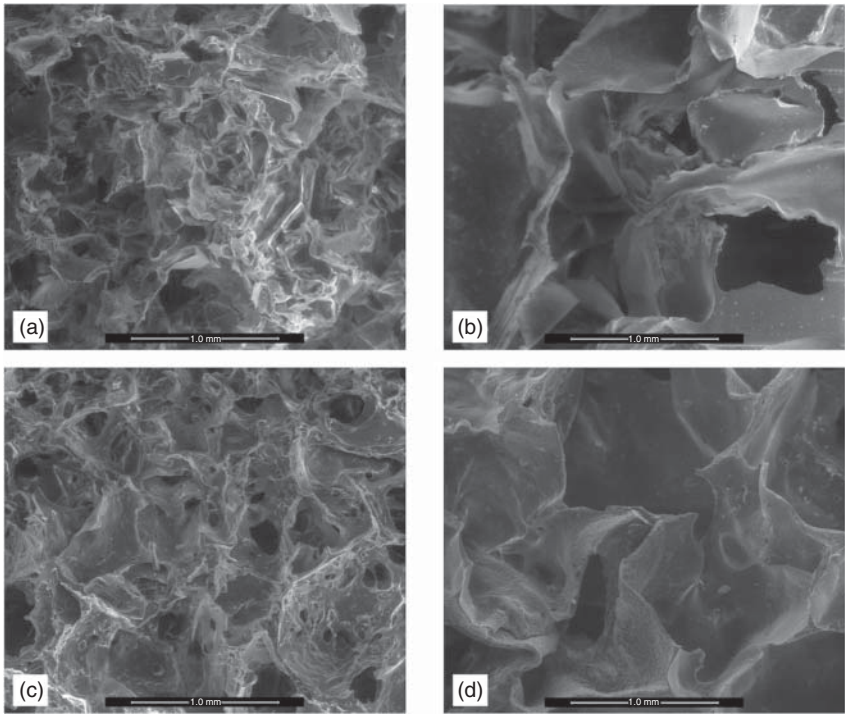

Figure 12.5 Microstructure of the optimized scaffolds: PMMA-S2 (a), PMMA-S3 (b), PU-S2 (c), and PU-S3 (d). Scale bar: 1 mm. Source: Sola et al. [38]/with permission of Elsevier.

flexible with breaking strains of 214% and higher and tensile strengths of approximately 1.0 MPa, whereas the PEEUU scaffolds generally had lower strengths and breaking strains. Scaffold degradation in aqueous buffer was related to the porosity and polymer hydrophilicity. Smooth muscle cells were filtration seeded in the scaffolds, and it was shown that both scaffolds supported cell adhesion and growth, with smooth muscle cells growing more extensively in the PEEUU scaffold. Figure 12.6 represents typical tensile stress–strain curves for PEUU scaffolds [40]. These biodegradable and flexible scaffolds demonstrate potential for future application as cell scaffolds in cardiovascular tissue-engineering or other soft-tissue applications.

12.2.1.2.3 Wettability Studies of Solvent Cast Films

Surface wettability is a measure of the surface energy of a material and is an important parameter that affects biological response to a material. It affects cell behavior on biomaterials like cell growth, protein adsorption, and platelet adhesion. Usually, good cell adhesion is observed on surfaces that are moderately hydrophilic, whereas poor cell attachment is seen on highly hydrophobic surfaces. Wettability is usually expressed in terms of contact angle. Generally, higher contact angles imply higher hydrophobicity and vice versa. Ammann et al. compared the wettability of PCL films fabricated by solvent casting, spin coating, and melt press [41]. The solvent-cast film exhibited highest roughness thus being highly hydrophobic having contact angle

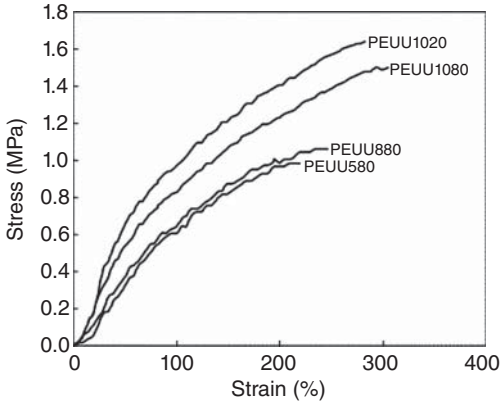

Figure 12.6 Typical tensile stress–strain curves for poly(ester urethane)urea (PEUU) scaffolds. Source: Guan et al. [40]/with permission of Elsevier.

about 104.1°. This was contrary to the results obtained by Deng et al. who observed that gelatin/zein nanofibrous film fabricated by electrospinning had a hydrophobic surface (water contact angle of 118.0°), while the solvent-casted gelatin/zein film had a hydrophilic surface (water contact angle of 53.5°) [42].

12.2.1.2.4 Biological Characterization of Scaffolds

The scaffolds designed for tissue engineering should be biocompatible and degradable. The scaffolds act as template that supports the growth and adhesion of cells and further their proliferation. So an ideal scaffold is one that necessarily mimics the native extracellular matrix (ECM) as well as promotes complete regeneration. The scaffold should provide structural support for the cells to reside and provide bioactive cues for the cells to interact with their microenvironment. Another important consideration is that the scaffold should degrade as regeneration is achieved. The interaction of cells with the scaffolds can be analyzed *in vitro* by culturing cells on the scaffolds and evaluating their cell viability after predetermined intervals. PCL films doped with PLGA was fabricated by solvent casting [43]. The adhesion and growth of osteoblasts on the PCL surface analyzed by laser scanning confocal microscopy revealed excellent attachment of osteoblasts on the polymer surface.

Vascular smooth muscle cells cultured on PEUU and PEEUU scaffolds were quantified by measuring the MTT absorbance of the seeded scaffolds (Figure 12.7). The relative cell number in the PEUU scaffold did not change from one to seven days ($p^{1/4}$ 0 : 42), whereas the cell number in PEEUU scaffolds at seven days was significantly higher than at one day ($p^{1/4}$ 0 : 03). Comparing the cell number in PEUU and PEEUU scaffolds, there was no significant difference at day 1 ($p^{1/4}$ 0 : 11). However, by day 7, the PEEUU scaffolds had significantly higher cell numbers ($p^{1/4}$ 0 : 01). Electron micrographs showed that both scaffold surfaces covered were populated with cells that had started to spread after one day. By seven days, the cells had formed dense confluent layers on the surface. The cellular ingrowth was examined by hematoxylin and eosin (H&E) staining. Smooth muscle cells were uniformly distributed in the scaffolds and generally retained a rounded morphology after one day of culture. Cells at seven days were spread and had a slightly higher density in PEEUU scaffolds.

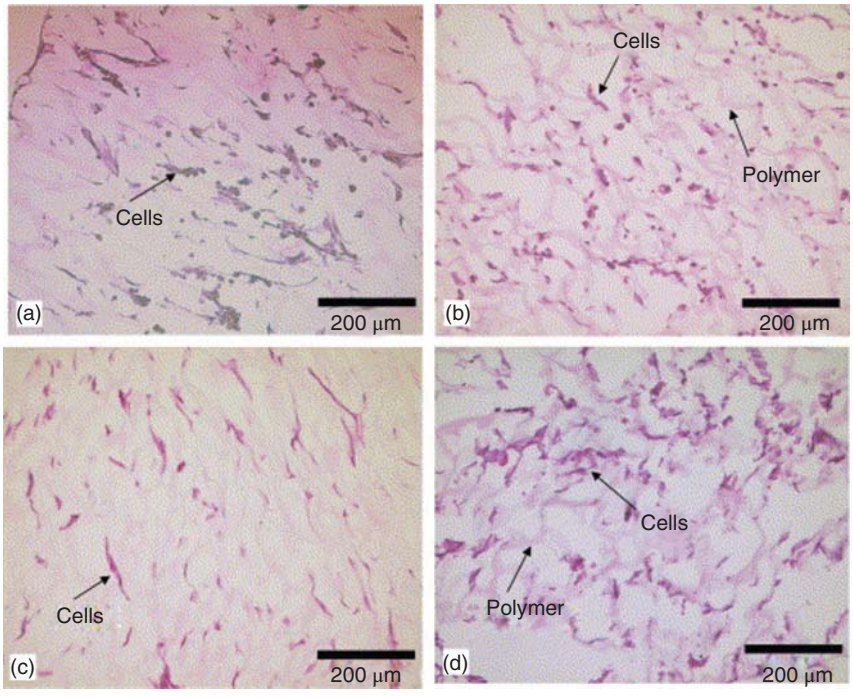

Figure 12.7 Hematoxylin and eosin (H&E) staining of vascular smooth muscle cells in the cross-section of PEUU (a, c) and PEEUU (b, d) scaffolds after one day (a, b) and seven days (c, d) of culture. Source: Guan et al. [40]/with permission of Elsevier.

A single solvent-based film-casting process for fabricating porous polymer films was developed by Hossain et al. [44]. Figure 12.8 shows the schematic diagram of methodology used for the preparation of porous PLA films.

Here concentrated PLA/chloroform solution (20 wt%) and fresh chloroform solvent were mixed at various ratios and three types of films PLA1 (1 : 2 v/v), PLA2 (1 : 3 v/v), and PLA3 (1 : 4 v/v) were produced. After incubation of the films with cells, PLA surface was covered by cells as seen in Figure 12.9a,b. After three days, the cells showed well-spread morphology with lamellipodia extending onto the porous surface as seen in Figure 12.9c. After eight days, the PLA surface was completely covered by cells. The viability of G63 cells on PLA films was evaluated using Alamar Blue assay. PLA1 showed higher cell viability than PLA2 and PLA3, which could be due to their smaller pore size (Figure 12.9d).

Antibacterial activity is required to protect the damaged skin in case of injury and to prevent bacterial adherence. Polymer films are usually loaded with biomaterials or metal/metal oxide nanoparticles like gold, silver, and zinc oxide in order to impart antibacterial activity. Mandapalli et al. compared the antibacterial activity of various polymer films. He showed that chitosan films loaded with gold nanoparticles (AuNPs) inhibited the growth of *Escherichia coli* bacteria similar to the control used tetracycline antibiotic [45]. Blank films of chitosan and zein also

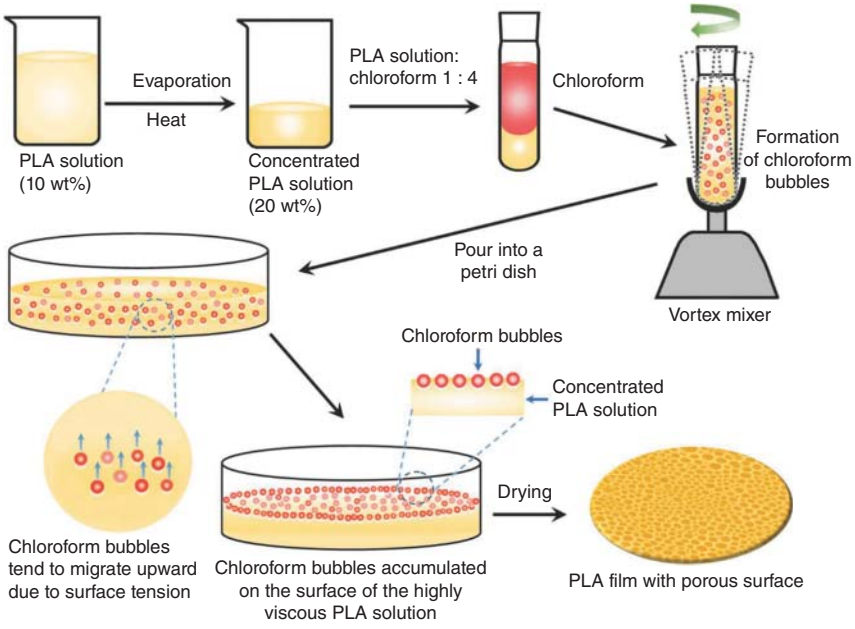

Figure 12.8 Schematic diagram showing methodology used for the preparation of porous PLA films. Source: Hossain et al. [44]/with permission of John Wiley & Sons.

showed antibacterial activity, whereas blank PCL film did not show inhibition zone against any bacteria.

Nano-biocomposite, based on PLA, surfactant-modified cellulose nanocrystals, and silver nanoparticles (Ag) to be applied for fresh food antimicrobial active packaging, was designed by Fortunati et al. Silver nanoparticles (Ag) were synthesized by selective reduction of silver nitrate ($AgNO_3$) in the presence of polyvinylpyrrolidone (PVP). Antibacterial studies were evaluated on two types of bacterial strains namely, *E. coli* and *Staphylococcus aureus*. The antibacterial activity was greater on *E. coli* than on *S. aureus* cells [46].

12.2.2 Surface Modification of Solvent Casted Films

Surface properties are of importance in certain applications such as tissue engineering. Several techniques have been used to modify the surface properties of solvent-cast films without affecting their bulk properties. The surface properties like wettability and biocompatibility need to be improved prior to application to meet the desired requirements. Several studies showed that tuning the surface properties affects the durability and functionality of materials. Chemical methods for modification involve aminolysis, grafting functional monomers or polymers, and incorporation of functional groups using plasma, radiation, etc. Plasma treatment has gained widespread importance due to its relatively simple process that is clean, solvent-free, fast, and environment friendly. Surface modification by plasma treatment is achieved using different gases such as air, oxygen, nitrogen, argon, and

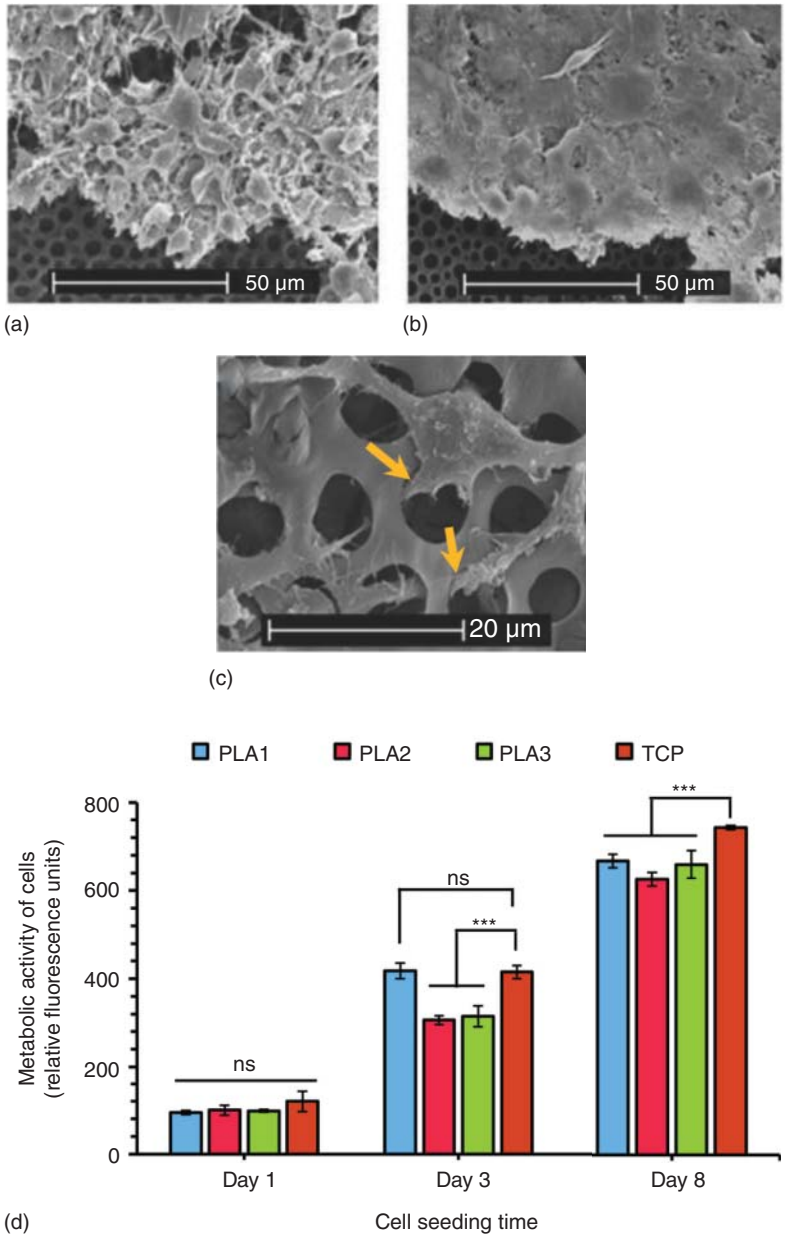

Figure 12.9 SEM micrographs of MG63 cell morphology: (a) after three days incubation, (b) eight days incubation, and (c) cells at day 3 are seen to attach and extend lamellipodia through the larger pores (≈6.4 µm). (d) Bar chart representing metabolic activity of MG63 cells measured using Alamar blue assay after one, three, and eight days of cell seeding (seeding density 40 000 cells/cm^2) on PLA porous films having different pore sizes and tissue culture plate (TCP) was used as a positive control. Source: Hossain et al. [44]/with permission of John Wiley & Sons.

Table 12.1 Different surface modification techniques employed in solvent-cast films.

Matrix used	Modification used	Property achieved	References
Polyvinyl alcohol	Dipping with chitosan solution	Hydrophobic surface	[48]
Poly-L-lactide (PLLA)	Oxygen (O_2) and tetra fluorocarbon (CF_4) plasma	Hydrophilic with O_2 plasma and hydrophobic with CF_4 plasma	[49]
Polyhydroxyalkanoates (PHA)	Oxygen plasma treatment and insulin-immobilization	Increased cell proliferation	[50]
Poly(lactic) acid	Induced photo polymerization process	Improved wettability	[51]
Zein	Atmospheric cold plasma (ACP)	Increased wettability Enhanced mechanical and thermal properties	[52]

helium. Surface-treated polymers have found widespread use in textiles, biomedical applications, electronics, water treatment, and energy industries [47]. Different strategies used for surface modification of solvent-cast films are listed in Table 12.1.

12.2.3 Degradation of Solvent Cast Films

Biodegradable polymers have a high potential for applications as medical implant materials. The biodegradation process is a biological activity of living organisms to decompose the complex structure of organic compounds to nontoxic products with lower-molecular weights. The end products of the biodegradation process can be used as an energy and nutritional source for anabolism of nonproducing organisms [53, 54]. Many factors such as microbial activity, polymer composition, molecular weight, crystallinity, temperature, moisture, pH, nutrient content, and oxygen can affect the biodegradation process [55, 56]. In addition, the surface area of polymeric materials can have an effect on the biodegradation rate where a lower surface area can restrict the microbial growth [57]. Petroleum polymers contribute to nondegradable waste materials, and it would therefore be desirable to produce ecofriendly degradable materials. Biodegradation of polyhydroxybutyrate (PHB) in the presence of oligomer hydrolase and PHB depolymerase gave 3-hydroxybutyric acid which could be oxidized to acetyl acetate. Biodegradation of PHB studies showed a significant decrease in the molecular weight (M_w), number-average molecular weight (M_n), and the dispersity (M_w/M_n) for all the film formulations. Nanofibers of PHB and its composites showed faster degradation compared to other films and displayed complete degradation after three weeks. Such changes were due to the growth of microorganisms that secreted PHB depolymerase enzyme

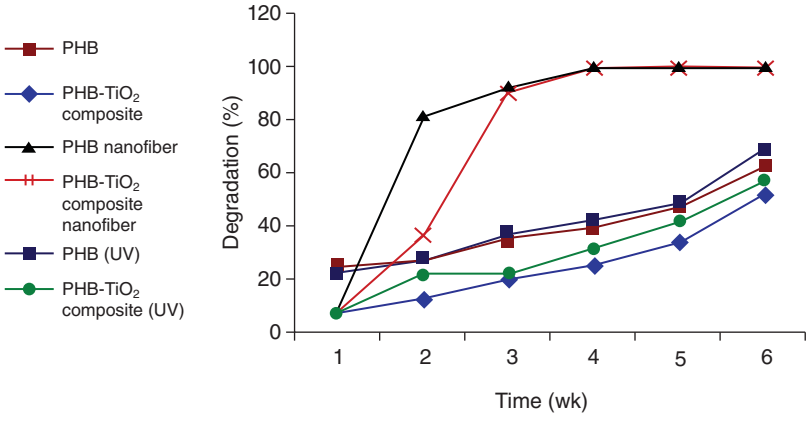

Figure 12.10 The degradation percentage of PHB films up to six weeks. Source: Altaee et al. [54]/Springer Nature/CC BY 4.0.

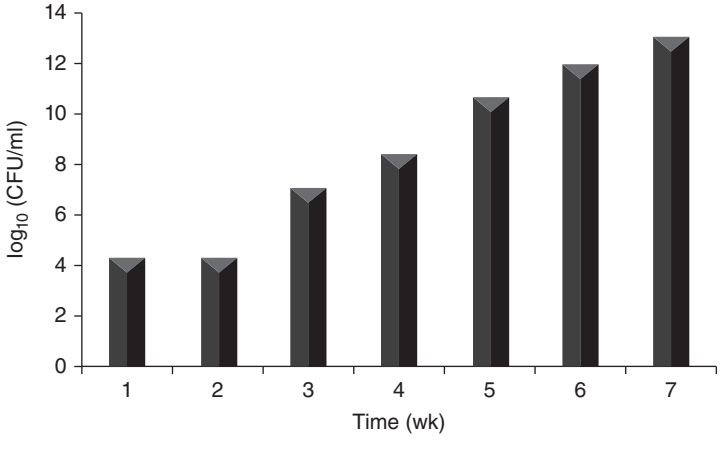

Figure 12.11 The microbial number in soil at the buried site for different PHB films. Source: Altaee et al. [54]/Springer Nature/CC BY 4.0.

which led to the biopolymer films degradation. Figures 12.10 and 12.11 show the degradation behavior of PHB films.

With a view to the potential of chitosan in the regeneration of nerve tissue, the influence of *n* degree of deacetylation (DDA) on the growth and health of olfactory ensheathing cells (OECs) was investigated [58]. There was a linear increase in OEC proliferation as the DDA increased from 72% to 85%. Variation in degradation for solvent-cast films of different commercial chitosan samples with different DDAs, as measured by weight loss from original is given in Figure 12.12.

12.2.4 Porosity of Solvent Cast Films

Porous membranes are utilized in many scientific fields due to their applicability in varying applications, such as surface coating, separation sciences, biosensors,

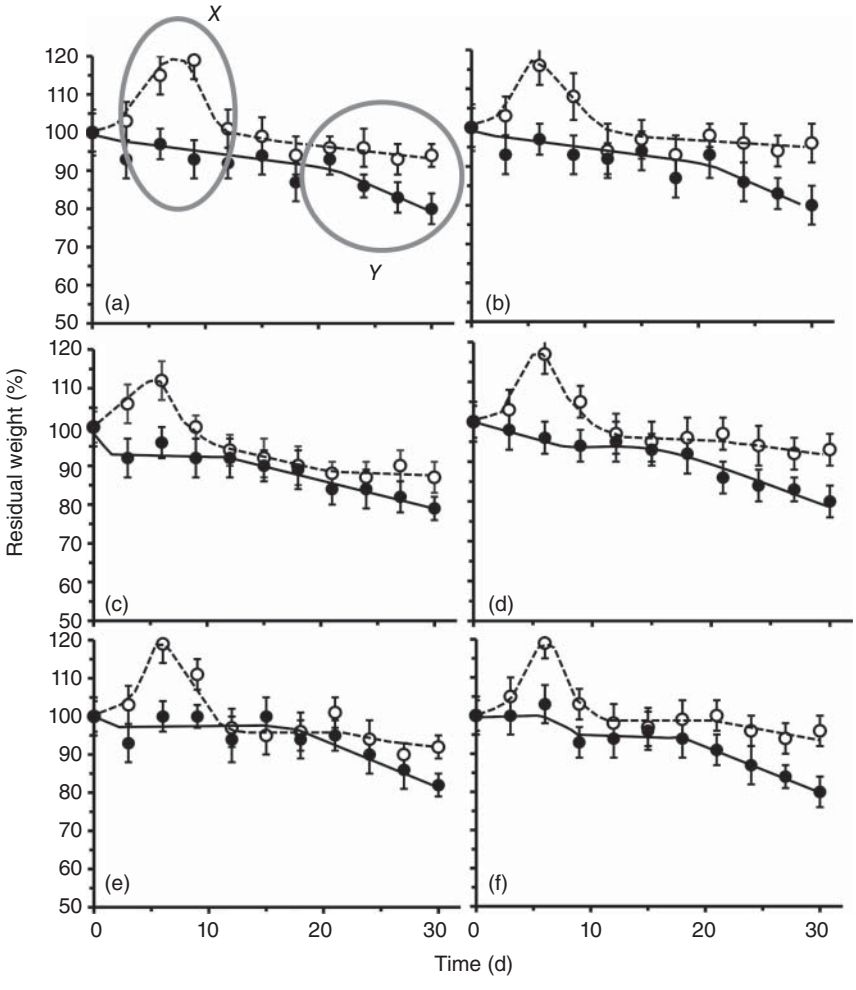

Figure 12.12 Variation in degradation for solvent-cast films of different commercial chitosan samples with different DDAs, as measured by weight loss from original (%): (a) 72%; (b) 73%; (c) 75%; (d) 77%; (e) 79%; and (f) 85% DDA (37 °C, pH 7.4, 120 rpm; white circle: abiotic degradation in phosphate buffered saline (PBS) and black circle: biotic degradation in PBS with 2% w/v lysozyme). Source: Foster et al. [58]/PLOS/CC BY 4.0.

optoelectronic devices, biomedical devices, and tissue-engineering applications. Fabrication of porous structures from either polymer or metal or ceramics with diverse pore sizes (from nano-to-micrometer range) has been explored extensively. For example, nano, micro, and macroporous polymer films have proven to be suitable for gas separation, biosensing, and drug-release applications, and metal and ceramic films have been utilized as thermal barrier coatings [44, 58, 59].

By considering a mixture of poly(methyl methacrylate)–tetrahydrofuran–water (PMMA–THF–H_2O), Pervin et al. report an experimental approach to tune the distribution of pores in polymer films formed via evaporation-induced phase

separation (EIPS) [59]. They showed that the drying-induced composition and microstructural changes that occur due to the evaporation of the solvent (THF) and the nonsolvent (H_2O) delineate the ultimate polymer film morphology. The temporal evolution of the microstructure, the phase behavior, and the change in the composition of the PMMA–THF–H_2O mixture at air–solution (top surface) and solution–substrate (bottom surface) interfaces is monitored to provide insights into the origin of the pore distribution in the final polymer films. The effects of various parameters such as nonsolvent and polymer concentration in the casting solution, casting solution thickness, relative humidity, and temperature on the final film morphology are investigated to correlate how the composition path (CP) change under various conditions ultimately dictates the film morphology. Depending on the change in the composition of the polymer solution (evolution of CP) and the water/PMMA ratio at the time of phase separation, the morphology of the final film formed varies as – (i) nonporous, i.e. dense film, (ii) a film with pores only at the bottom surface, (iii) an asymmetric film, i.e. films with a top dense layer (nonporous) supported by porous sublayers, (iv) a porous film with uniform pores distributed across the entire film thickness, and (v) a film with pores only at the top surface. Figure 12.13 shows the average porosity of the film (a) and average pore diameter and (b) of the film surface in contact with the glass substrate obtained under different experimental conditions [59].

Hossain et al. showed that with increase in volume of solvent used (chloroform), the pore size increased. Here the pores were generated only on the top surface of the PLA film, while the bottom surface was seen to be fairly smooth (with no visible porosity) [44].

12.2.5 Advantages and Disadvantages of Solvent Cast Films

The oldest technology in plastic films manufacturing, the continuous solvent-cast process was developed more than hundred years ago driven by the needs of the emerging photographic industry [60]. In the years after 1950, new film-extrusion techniques of thermoplastic polymers became the dominant production method for plastic films and the importance of solvent-cast technique has declined. Nowadays, the solvent-cast technology is becoming increasingly attractive for the production of films with extremely high-quality requirements. The advantages of this technology include uniform thickness distribution, maximum optical purity, and extremely low haze. The optical orientation is virtually isotropic and the films have excellent flatness and dimensional stability. The cast film can be processed in-line with an optical coating design. The tremendous growth of new liquid crystal display (LCD) applications has incited the development of new materials and improved processes for solvent-casting and -coating techniques.

However, solvent-casting technique has four main disadvantages. First, this technique usually involves organic solvents which are not favorable for tissue-engineering applications due to potential harmful influences on cells and tissues. Organic solvents also in many cases preclude the possibility of adding pharmacological agents to the scaffold during the fabrication. Second, certain critical variables such as pore shape and interpore openings are still not well controlled in

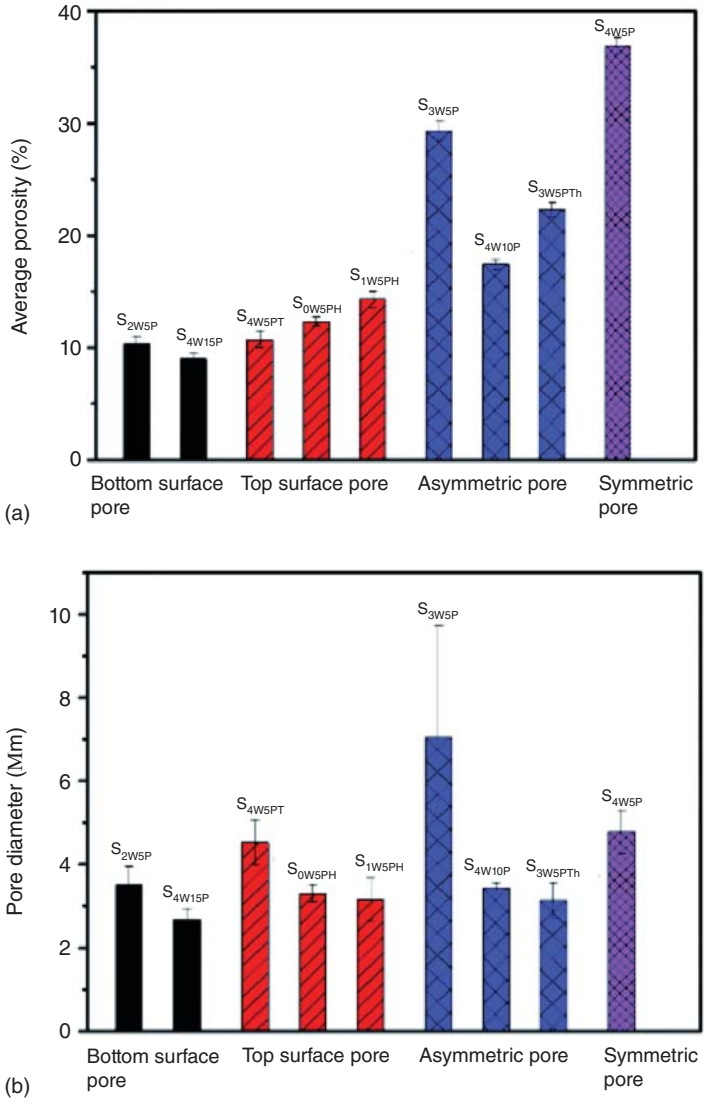

Figure 12.13 Average porosity of the film (a) and average pore diameter (b) of the film surface in contact with the glass substrate obtained under different experimental conditions. Source: Pervin et al. [59]/Royal Chemical Society/CC BY 3.0.

this technique. Third, when applying this technique to polymer/ceramic composite scaffolds, the polymer–organic solvent solutions may coat the bioactive ceramic surfaces, hinder their exposure to the scaffold surface, and decrease their direct contact with osteogenic cells that are crucial for osseointegration. The last but not the least, if nanophase ceramic particles were used to make nanocomposite scaffolds in this technique, nanoparticles may interfere the porogen-leaching process, which will result in residual porogen particles in the final tissue-engineering products.

12.2.6 Applications of Solvent-Cast Films

A variety of natural and synthetic polymers have been used to fabricate tissue-engineering scaffolds. These materials must be inherently biocompatible, biodegradable, and highly cell adhesive. Additionally, the polymers must be porous and mechanically stable and exhibit a three-dimensional (3D) structure that can be obtained via facile manufacturing processes. Aliphatic polyesters, such as PCL, PLA, polyglycolic acid, and related copolymers, are most extensively used in biodegradable scaffolds because of these polymers' excellent biocompatibility, biodegradability, bioresorbability, and mechanical strength. Most importantly, they are used as scaffolds, some other applications are discussed later [60].

12.2.6.1 Photographic Application

The largest areas of solvent-cast films are produced for photographic use. About 300 million square meters of cellulose triacetate film base are used every year for 35 mm amateur films, movie films, and other film types. The market is rapidly declining since 2002 because of the fierce competition of digital photography.

12.2.6.2 Liquid Crystal Display (LCD) Applications

Optical polarizers are based on polyvinylalcohol films cast from an aqueous solution [60]. This film is stretched and doped with iodine or organic dyes to provide the polarizing function. The polyvinyl alcohol polarizing layer is usually protected against mechanical and other environmental effects using materials such as cellulose triacetate films having very low birefringence [61]. The fastest-growing area of solvent-cast films with more than 20% growth per year is the production of cellulose triacetate film for manufacturing polarizers for liquid crystal (LC) displays. The quality requirements are much higher than for photographic tri acetate cellulose (TAC) film base. A recent application is the use of LC displays for televisions (TVs) (up to 62 in. screen). This will rapidly increase the use of cellulose triacetate-based solvent-cast film in the near future. Polycarbonate is used for several specialty films, some of them designed for optical purposes. Two sets of LCD panels were made using solvent-cast polyimide (PI) films prepared using two different precursors, polyamic acid (PAA) and prepolymerized polyimide (PI) solution [62]. For LCD panel with PAA-type polyimide film functioning as alignment layer, the luminance decreased sharply on voltage removal. In case of LCD panel with PI-type polyimide film, a slow change was only observed demonstrating that the residual charges remained on PI film for longer period. In such situations, the displayed image gets retained even after the voltage is switched off which is undesirable in case of LCD. However, in PAA-type film, higher ionic conductivity was achieved, allowing the residual charges to dissipate along the film; thus, there is less chance of causing sticky image.

12.2.6.3 Other Optical Applications

Cellulose diacetate, soluble in acetone, is converted to films by means of solvent coating mainly in thicknesses between 14 and 200 μm. Since about 1950, big volumes have been used for applications such as print lamination, graphic arts, windows in

food stuff boxes, photographical sleeves, goggles, and visors. The advantages of this film type are high gloss levels, excellent transparency, and a good balance between moisture resistance and water permeability. That makes it an ideal film especially for the combination together with paper or carton.

12.2.6.4 Electrical and Electronic Applications

Other advantages of cast film technology are important for electrical and electronic applications. Electrical properties that are stable at high temperatures over the long term can only be achieved with polymers with high or no melting temperatures. Processing of highly purified and filtered polymers with high glass transition temperatures, high bulk resistivity, and a low dissipation factor is possible. It is often not feasible to produce these films using thermoplastic manufacturing methods. In some cases, a soluble polymer such as poly(amide carboxylic) is cast from solutions in dimethylacetamide to form a film, which is subsequently cross-linked with acetic anhydride during the casting process. Typical products are base materials for flexible printed circuits, insulation films, wrappings, capacitors, etc. Polymers such as polycarbonates and polyimides are used for these purposes. Consumption of this type of film is increasing with the growth of the electronic industry and the development of new, more sophisticated electronic devices. The field of flexible and stretchable electronic devices has been highly explored during the recent years. Solvent casting was used to transfer graphene patterns from a rigid or flexible substrate onto a polymeric film surface. The process involved preparation of graphene-based patterns or films on the molds, casting of polymer solution on the graphene patterns formed on the mold surface, peeling of films after drying, thus transferring the pattern from mold to the polymer film surface [63]. The graphene patterns were highly conductive and stable, thus offering great promise in the field of stretchable electronics.

12.2.6.5 High-Temperature Applications

Depending on the temperature requirements and the chemical composition of the polymer, cast film techniques can be used for release films. Polyimides, cellulose triacetate, and others are the typical raw materials. Another emerging area is the application of high-temperature resistive films for LCDs and as substrate materials for organic light emitting diode (OLED) displays. Feasible trial films have been made on the basis of polyether sulfone, polycarbonate, cyclic polyolefins, polyarylates, and polyimides [60].

12.3 Conclusions

Solvent-cast technology is considered as a versatile tool for the production of polymer or biomaterial films. Solvent casting enables tunability of various characteristics like mechanical properties, barrier properties, and optical properties of the film through the variation of processing parameters such as solvent-casting time and temperature. However, in many cases, the toxicity associated with organic solvents that remain in the casted polymer even after long-aging times poses severe

environmental concern. Hence, the choice of cost-effective and nontoxic solvent is a major factor that needs attention while using the approach of solvent casting. Much more theoretical and experimental insights into the structure–property relationships of solvent-cast films along with in-depth understanding of their biological interactions are necessary to explore their potential in various applications.

References

1 Parveen, S., Krishnakumar, K., and Sahoo, S.K. (2006). New era in health care: tissue engineering. *J. Stem Cells Regen. Med.* 1: 8–24. https://doi.org/10.46582/jsrm.0101003.

2 Deluzio, T.G., Seifu, D.G., and Mequanint, K. (2013). 3D scaffolds in tissue engineering and regenerative medicine: beyond structural templates? *Pharm. Bioprocess.* https://doi.org/10.4155/pbp.13.21.

3 Hutmacher, D.W. (2000). Scaffolds in tissue engineering bone and cartilage. *Biomaterials* https://doi.org/10.1016/S0142-9612(00)00121-6.

4 Quirk, R.A., Davies, M.C., Tendler, S.J.B., and Shakesheff, K.M. (2000). Surface engineering of poly(lactic acid) by entrapment of modifying species. *Macromolecules* https://doi.org/10.1021/ma9916133.

5 Goldstein, A.S., Juarez, T.M., Helmke, C.D. et al. (2001). Effect of convection on osteoblastic cell growth and function in biodegradable polymer foam scaffolds. *Biomaterials* https://doi.org/10.1016/S0142-9612(00)00280-5.

6 Shea, L.D., Wang, D., Franceschi, R.T., and Mooney, D.J. (2000). Engineered bone development from a pre-osteoblast cell line on three-dimensional scaffolds. *Tissue Eng.* https://doi.org/10.1089/10763270050199550.

7 Liu, C., Xia, Z., and Czernuszka, J.T. (2007). Design and development of three-dimensional scaffolds for tissue engineering. *Chem. Eng. Res. Des.* https://doi.org/10.1205/cherd06196.

8 Abbasi, N., Hamlet, S., Love, R.M., and Nguyen, N.-T. (2020). Porous scaffolds for bone regeneration. *J. Sci.: Adv. Mater. Devices* 5: 1–9. https://doi.org/10.1016/j.jsamd.2020.01.007.

9 Li, C., Vepari, C., Jin, H.J. et al. (2006). Electrospun silk-BMP-2 scaffolds for bone tissue engineering. *Biomaterials* https://doi.org/10.1016/j.biomaterials.2006.01.022.

10 Nie, H. and Wang, C.-H. (2007). Fabrication and characterization of PLGA/HAp composite scaffolds for delivery of BMP-2 plasmid DNA. *J. Controlled Release* 120: 111–121. https://doi.org/10.1016/j.jconrel.2007.03.018.

11 Montenegro-Nicolini, M. and Morales, J.O. (2017). Overview and future potential of buccal mucoadhesive films as drug delivery systems for biologics. *AAPS PharmSciTech* https://doi.org/10.1208/s12249-016-0525-z.

12 Sampath, U., Ching, Y., Chuah, C. et al. (2016). Fabrication of porous materials from natural/synthetic biopolymers and their composites. *Materials (Basel)* 9: 991. https://doi.org/10.3390/ma9120991.

13 Liu, H. and Webster, T.J. (2007). Bioinspired nanocomposites for orthopedic applications. In: *Nanotechnology for the Regeneration of Hard and Soft Tissues* (ed. T.J. Webster), 1–51. World Scientific https://doi.org/10.1142/9789812779656_0001.

14 Eltom, A., Zhong, G., and Muhammad, A. (2019). Scaffold techniques and designs in tissue engineering functions and purposes: a review. *Adv. Mater. Sci. Eng.* https://doi.org/10.1155/2019/3429527.

15 Fonseca-Santos, B. and Chorilli, M. (2017). An overview of carboxymethyl derivatives of chitosan: their use as biomaterials and drug delivery systems. *Mater. Sci. Eng., C* https://doi.org/10.1016/j.msec.2017.03.198.

16 Jahed, E., Khaledabad, M.A., Almasi, H., and Hasanzadeh, R. (2017). Physicochemical properties of *Carum copticum* essential oil loaded chitosan films containing organic nanoreinforcements. *Carbohydr. Polym.* https://doi.org/10.1016/j.carbpol.2017.02.022.

17 Agrawal, P., Sonali, Singh, R.P. et al. (2017). Bioadhesive micelles of D-α-tocopherol polyethylene glycol succinate 1000: synergism of chitosan and transferrin in targeted drug delivery. *Colloids Surf., B* 152: 277–288. https://doi.org/10.1016/j.colsurfb.2017.01.021.

18 Preethi Soundarya, S., Sanjay, V., Haritha Menon, A. et al. (2018). Effects of flavonoids incorporated biological macromolecules based scaffolds in bone tissue engineering. *Int. J. Biol. Macromol.* https://doi.org/10.1016/j.ijbiomac.2017.09.014.

19 Athanasiou, K.A., Schmitz, J.P., and Agrawal, C.M. (1998). The effects of porosity on in vitro degradation of polylactic acid-polyglycolic acid implants used in repair of articular cartilage. *Tissue Eng.* https://doi.org/10.1089/ten.1998.4.53.

20 Agrawal, C.M., McKinney, J.S., Lanctot, D., and Athanasiou, K.A. (2000). Effects of fluid flow on the in vitro degradation kinetics of biodegradable scaffolds for tissue engineering. *Biomaterials* https://doi.org/10.1016/S0142-9612(00)00112-5.

21 Agrawal, C., McKinney, J., Huang, D., and Athanasiou, K. (2008). The use of the vibrating particle technique to fabricate highly porous and permeable biodegradable scaffolds. In: *Synthetic Bioabsorbable Polymers for Implants*, vol. 1396, 99–114. ASTM Special Technical Publication https://doi.org/10.1520/stp15303s.

22 Lu, L., Peter, S.J., Lyman, M.D. et al. (2000). In vitro and in vivo degradation of porous poly(D,L-lactic-*co*-glycolic acid) foams. *Biomaterials* https://doi.org/10.1016/S0142-9612(00)00047-8.

23 Ochi, K., Chen, G., Ushida, T. et al. (2003). Use of isolated mature osteoblasts in abundance acts as desired-shaped bone regeneration in combination with a modified poly-D,L-lactic-*co*-glycolic acid (PLGA)-collagen sponge. *J. Cell. Physiol.* 194: 45–53. https://doi.org/10.1002/jcp.10185.

24 Thomson, R.C., Mikos, A.G., Beahm, E. et al. (1999). Guided tissue fabrication from periosteum using preformed biodegradable polymer scaffolds. *Biomaterials* https://doi.org/10.1016/S0142-9612(99)00103-9.

25 Choudhury, M., Mohanty, S., and Nayak, S. (2015). Effect of different solvents in solvent casting of porous scaffolds – in biomedical and tissue engineering applications. *J. Tissue Sci. Eng.* https://doi.org/10.4172/2157-7552.1000142.

26 Wang, Y., Fan, H.S., Wen, X.T. et al. (2007). Effect of solvent on porous PLA/HA scaffolds preparation using novel solid H_2O_2 porogen. *Key Eng. Mater.* 342–343: 49–52. https://doi.org/10.4028/www.scientific.net/KEM.342-343.49.

27 Ramakrishna, S., Mayer, J., Wintermantel, E., and Leong, K.W. (2001). Biomedical applications of polymer-composite materials: a review. *Compos. Sci. Technol.* 61: 1189–1224. https://doi.org/10.1016/S0266-3538(00)00241-4.

28 Brunke, O., Odenbach, S., and Beckmann, F. (2005). Quantitative methods for the analysis of synchrotron-μCT datasets of metallic foams. *EPJ Appl. Phys.* https://doi.org/10.1051/epjap:2004203.

29 Cooper, D.M.L., Turinsky, A.L., Sensen, C.W., and Hallgrímsson, B. (2003). Quantitative 3D analysis of the canal network in cortical bone by micro-computed tomography. *Anat. Rec. Part B* https://doi.org/10.1002/ar.b.10024.

30 Otsuki, B., Takemoto, M., Fujibayashi, S. et al. (2006). Pore throat size and connectivity determine bone and tissue ingrowth into porous implants: three-dimensional micro-CT based structural analyses of porous bioactive titanium implants. *Biomaterials* https://doi.org/10.1016/j.biomaterials.2006.08.013.

31 Tjia, J.S. and Moghe, P.V. (1998). Analysis of 3-D microstructure of porous poly(lactide-glycolide) matrices using confocal microscopy. *J. Biomed. Mater. Res.* https://doi.org/10.1002/(SICI)1097-4636(199823)43:3<291::AID-JBM10>3.0.CO;2-J.

32 Botchwey, E.A., Dupree, M.A., Pollack, S.R. et al. (2003). Tissue engineered bone: measurement of nutrient transport in three-dimensional matrices. *J. Biomed. Mater. Res. Part A* https://doi.org/10.1002/jbm.a.10111.

33 Grimm, M.J. and Williams, J.L. (1997). Measurements of permeability in human calcaneal trabecular bone. *J. Biomech.* https://doi.org/10.1016/S0021-9290(97)00016-X.

34 Chor, M.V. and Li, W. (2007). A permeability measurement system for tissue engineering scaffolds. *Meas. Sci. Technol.* https://doi.org/10.1088/0957-0233/18/1/026.

35 Kohles, S.S., Roberts, J.B., Upton, M.L. et al. (2001). Direct perfusion measurements of cancellous bone anisotropic permeability. *J. Biomech.* https://doi.org/10.1016/S0021-9290(01)00082-3.

36 Haugen, H., Will, J., Köhler, A. et al. (2004). Ceramic TiO_2-foams: characterisation of a potential scaffold. *J. Eur. Ceram. Soc.* 24: 661–668. https://doi.org/10.1016/S0955-2219(03)00255-3.

37 Shimko, D.A. and Nauman, E.A. (2007). Development and characterization of a porous poly(methyl methacrylate) scaffold with controllable modulus and permeability. *J. Biomed. Mater. Res. Part B* https://doi.org/10.1002/jbm.b.30605.

38 Sola, A., Bertacchini, J., D'Avella, D. et al. (2019). Development of solvent-casting particulate leaching (SCPL) polymer scaffolds as improved three-dimensional supports to mimic the bone marrow niche. *Mater. Sci. Eng., C* 96: 153–165. https://doi.org/10.1016/j.msec.2018.10.086.

39 Schumacher, M., Deisinger, U., Ziegler, G., and Detsch, R. (2010). Indirect rapid prototyping of biphasic calcium phosphate scaffolds as bone substitutes: influence of phase composition, macroporosity and pore geometry on mechanical properties. *J. Mater. Sci. – Mater. Med.* https://doi.org/10.1007/s10856-010-4166-6.

40 Guan, J., Fujimoto, K.L., Sacks, M.S., and Wagner, W.R. (2005). Preparation and characterization of highly porous, biodegradable polyurethane scaffolds for soft tissue applications. *Biomaterials* https://doi.org/10.1016/j.biomaterials.2004.10.018.

41 Ammann, K.R., Li, M., Hossainy, S., and Slepian, M.J. (2019). The influence of polymer processing methods on polymer film physical properties and vascular cell responsiveness. *ACS Appl. Bio Mater.* 2: 3234–3244. https://doi.org/10.1021/acsabm.9b00175.

42 Deng, L., Kang, X., Liu, Y. et al. (2018). Characterization of gelatin/zein films fabricated by electrospinning vs solvent casting. *Food Hydrocolloids* 74: 324–332. https://doi.org/10.1016/j.foodhyd.2017.08.023.

43 Tang, Z.G., Callaghan, J.T., and Hunt, J.A. (2005). The physical properties and response of osteoblasts to solution cast films of PLGA doped polycaprolactone. *Biomaterials* https://doi.org/10.1016/j.biomaterials.2005.04.013.

44 Hossain, K.M.Z., Felfel, R.M., Ogbilikana, P.S. et al. (2018). Single solvent-based film casting method for the production of porous polymer films. *Macromol. Mater. Eng.* https://doi.org/10.1002/mame.201700628.

45 Mandapalli, P.K., Labala, S., Chawla, S. et al. (2017). Polymer–gold nanoparticle composite films for topical application: evaluation of physical properties and antibacterial activity. *Polym. Compos.* https://doi.org/10.1002/pc.23885.

46 Fortunati, E., Rinaldi, S., Peltzer, M. et al. (2014). Nano-biocomposite films with modified cellulose nanocrystals and synthesized silver nanoparticles. *Carbohydr. Polym.* 101: 1122–1133. https://doi.org/10.1016/j.carbpol.2013.10.055.

47 Nemani, S.K., Annavarapu, R.K., Mohammadian, B. et al. (2018). Surface modification of polymers: methods and applications. *Adv. Mater. Interfaces* 5: 1801247. https://doi.org/10.1002/admi.201801247.

48 Jayasekara, R., Harding, I., Bowater, I. et al. (2004). Preparation, surface modification and characterisation of solution cast starch PVA blended films. *Polym. Test.* https://doi.org/10.1016/S0142-9418(03)00049-7.

49 Mattioli, S., Kenny, J.M., and Armentano, I. (2012). Plasma surface modification of porous PLLA films: analysis of surface properties and in vitro hydrolytic degradation. *J. Appl. Polym. Sci.* https://doi.org/10.1002/app.36827.

50 Kang, I.K., Choi, S.H., Shin, D.S., and Yoon, S.C. (2001). Surface modification of polyhydroxyalkanoate films and their interaction with human fibroblasts. *Int. J. Biol. Macromol.* https://doi.org/10.1016/S0141-8130(00)00165-3.

51 Janorkar, A.V., Metters, A.T., and Hirt, D.E. (2004). Modification of poly(lactic acid) films: enhanced wettability from surface-confined photografting and increased degradation rate due to an artifact of the photografting process. *Macromolecules* https://doi.org/10.1021/ma049056u.

52 Dong, S., Guo, P., Chen, Y. et al. (2018). Surface modification via atmospheric cold plasma (ACP): improved functional properties and characterization of zein film. *Ind. Crops Prod.* 115: 124–133. https://doi.org/10.1016/j.indcrop.2018.01.080.

53 Braunegg, G., Lefebvre, G., and Genser, K.F. (1998). Polyhydroxyalkanoates, biopolyesters from renewable resources: physiological and engineering aspects. *J. Biotechnol.* https://doi.org/10.1016/S0168-1656(98)00126-6.

54 Altaee, N., El-Hiti, G.A., Fahdil, A. et al. (2016). Biodegradation of different formulations of polyhydroxybutyrate films in soil. *SpringerPlus* https://doi.org/10.1186/s40064-016-2480-2.

55 Boopathy, R. (2000). Factors limiting bioremediation technologies. *Bioresour. Technol.* https://doi.org/10.1016/S0960-8524(99)00144-3.

56 Bernard, M. (2014). Industrial potential of polyhydroxyalkanoate bioplastic: a brief review. *USURJ Univ. Sask. Undergrad. Res. J.* https://doi.org/10.32396/usurj.v1i1.55.

57 Tokiwa, Y., Calabia, B.P., Ugwu, C.U., and Aiba, S. (2009). Biodegradability of plastics. *Int. J. Mol. Sci.* https://doi.org/10.3390/ijms10093722.

58 Foster, L.J.R., Ho, S., Hook, J. et al. (2015). Chitosan as a biomaterial: influence of degree of deacetylation on its physiochemical, material and biological properties. *PLoS One* https://doi.org/10.1371/journal.pone.0135153.

59 Pervin, R., Ghosh, P., and Basavaraj, M.G. (2019). Tailoring pore distribution in polymer films via evaporation induced phase separation. *RSC Adv.* https://doi.org/10.1039/c9ra01331h.

60 Siemann, U. (2005). Solvent cast technology – a versatile tool for thin film production. *Prog. Colloid Polym. Sci.* https://doi.org/10.1007/b107336.

61 Greener, J., Lei, H., Elman, J., and Chen, J. (2005). Optical properties of solvent-cast polarizer films for liquid-crystal displays: a viscoelastic modeling framework. *J. Soc. Inf. Disp.* https://doi.org/10.1889/1.2121067.

62 Kim, T.Y., Kim, W.J., Lee, T.H. et al. (2007). Electrical conduction of polyimide films prepared from polyamic acid (PAA) and pre-imidized polyimide (PI) solution. *eXPRESS Polym. Lett.* https://doi.org/10.3144/expresspolymlett.2007.60.

63 Uz, M., Jackson, K., Donta, M.S. et al. (2019). Fabrication of high-resolution graphene-based flexible electronics via polymer casting. *Sci. Rep.* https://doi.org/10.1038/s41598-019-46978-z.

13

Freeze-Casted Biomaterials for Regenerative Medicine

Selestina Gorgieva[1,2], Silvo Hribernik[1,2], Alenka Ojstršek[1,2], and Manja Kurečič[1,2]

[1] University of Maribor, Faculty of Mechanical Engineering, Institute of Engineering Materials and Design, Smetanova ulica 17, 2000 Maribor, Slovenia
[2] University of Maribor, Faculty of Electrical Engineering and Computer Science, Institute of Automation, Koroška cesta 46, 2000 Maribor, Slovenia

This chapter will give a background in freeze-casting principles and parameters, while the emphasis will be given on the freeze-casted scaffolds, based on biopolymers (nanocellulose, gelatin, and composites thereof), used in regenerative medicine. Site-specific control over the porosity enables processing of scaffold with different properties in different regions and formation of functionally graded construct, which can more closely mimic the cells niche giving the expected mechanistic and biochemical clues for regeneration processes. As such, freeze-casting in all its variations (unidirectional, bidirectional, electrical or magnetic fields assisted, etc.) has big success in material science research, yet progress in commercialization is yet to be seen, mainly due to stringent medical device regulations.

13.1 Introduction

The mechanism behind freezing of colloids is highly ubiquitous in nature and well introduced in many disciplines and (bio)physics, chemistry, biology, pharmacy, food engineering, material science, medicine, and even mathematics. In frozen state, the molecular motions are slowed down to the point where most of activity stops, preserving cells, tissues, and even whole organisms, for years. As such, it is a perfect tool, intensively used in food storage and cryopreservation of cells and bacteria. Also, it can supplement in water-cleaning process, as molecules, particles, bacteria, cells, and impurities can be easily condensed and rejected by ice crystals in formation.

At freezing, the apparently single, homogeneous solutions or dispersions undergo phase separation, which concentrate water (or other solvents or dispersants)-lean phase, out of liquid-rich phase, aiding removal of solvent/dispersant (e.g. ice) phase by means of sublimation or washing. This ultimately leaves behind a templated material construct with isotropic or anisotropic microstructure. Such process may

Functional Biomaterials: Design and Development for Biotechnology, Pharmacology, and Biomedicine, First Edition. Edited by Tamilselvan Mohan and Karin Stana Kleinschek.

facilitate processing or rather complex structures, being hardly processable through traditional processing routes.

Nowadays, the freeze-casting count as environmental friendly processing technique; it is rather simple process, where a material suspension is frozen and then sublimated, leaving behind an unique porous architecture as a replica of frozen solvent crystals formed at freezing stage [1]. It is a versatile, shape-forming technique, which offers optimal control over the pores' size and distribution, percentage of porosity, and morphology of pores. This processing route is extensively investigated in recent years for the fabrication of ceramics-, metals-, polymers-, biomacromolecules-, and carbon-based materials, endowing them with novel, distinct physic/mechanical attributes, thus making them widely applicable. According to recently established repository for freeze-casting experimental data, available through the web interface *FreezeCasting.net* [2], near history of freeze-casting dates back to 1954, when was used by NASA as material processing technique. Next prominent research in this area was work of Mahler, using the freeze-casting for processing of silica fibers out of aqueous polysilicic acid [3]. From the start of new century, the freeze-casting was again put in focus of many material scientist, which uncover the versatility of this processes, which in turn broaden its applicability. Freeze-casting has seen a surge of interest over the past two decades, as can be anticipate from Figure 13.1, in technical application, as fuel cell electrodes [4], dye-sensitized solar cell electrodes [5], stretchable circuits [6], lithium ion battery electrodes [7], metallic foams [8], graphene monoliths [9], ultrafiltration membranes [10, 11], and biomedical applications, in processing of biomaterials [12], scaffolds [13], pharmaceuticals [14], etc.

13.1.1 Principle of Freeze-Casting

Freeze-casting, also known as freeze-drying, lyophilization, cryodesiccation, or ice-templating, presents segregation-induced templating of a solution, suspension, or gel phase, where under specific conditions, the assembling of a second phase (polymeric, particulate) occurs, triggered by the progressive concentration increase in the intercrystal space. This yields fine, porous structures with a wide range of morphologies as a replicate to structure of ice crystals being formed at freezing stage. In general, freeze-casting proceed through main steps, depicted in Figure 13.2, which are formulation of (liquid) colloid, freezing (solidification) under temperature and pressure manipulation, removal of solvent/dispersant phase by sublimation, and posttreatment (e.g. densification).

The first and very essential step is the preparation of colloid or solution, containing solid material (metal, ceramic, carbon material, polymer, and hybrids thereof in the form of nano-particles, fibers, tubes, plates, or sheets [16]) as main body of structure in development, the freezing agent, and additives. Due to feasibility, environmental friendliness, and cost-effectiveness, the water is most often used as solvent or dispersant; in such case, thee freeze-casting equalize with ice-templating process. Beside water, the organic solvents are next choice for materials not soluble in water (e.g. for casting of traditional ceramic suspensions and preceramic polymer solutions [17]),

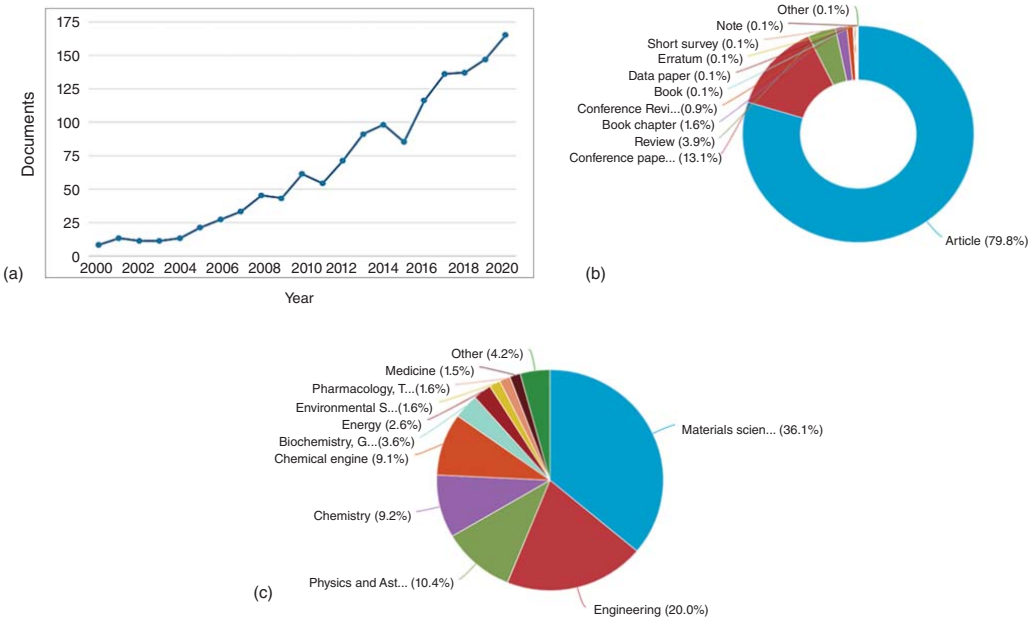

Figure 13.1 Documents by (a) year, (b) type, and (c) subject area, according to Scopus search engine, using single keyword "freeze-casting." Total of 1386 results were obtained.

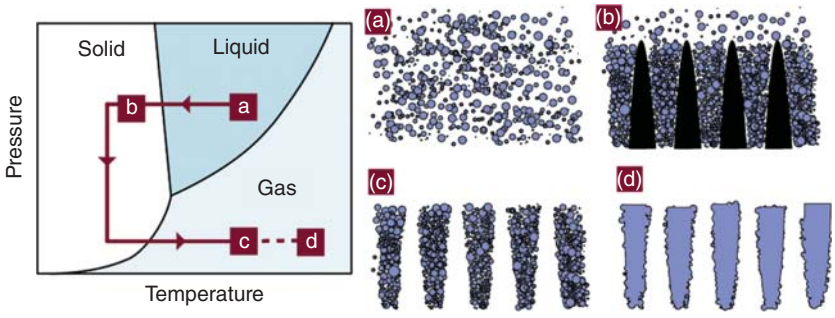

Figure 13.2 Schematic diagram of the freeze-casting principles. (a) Suspension, (b) freezing, (c) Sublimation, and (d) sintering. Source: Deville et al. [15]/Taylor & Francis/CC BY 3.0.

such as dimethyl sulfoxide, cyclooctane, cyclohexane, dioxane, dimethyl carbonate, and *tert*-butyl alcohol. The crosslinkers [18], binders, dispersants, and plasticizers are often added as accessional additives to facilitate the processing as well as improving the stability of final porous construct. Other additives that may also interfere with the solvent, promoting morphology changes during solidification are glycerol, ethylene glycol, propylene glycol, methanol, ethanol, dimethyl sulfoxide, and acrylamide.

Next step, being crucial in pores form and shaping, is the freezing step. When solvent is rapidly freezed (e.g. upon immersion into liquid nitrogen), the structure of dissolved or dispersed material can be preserved, yet, after sublimation, the powder-like material is obtain, rather than upstructured solid material. Opposite, the slower freezing procedure, followed by sublimation allows formation of ice templates, as sublimation step avoids formation of a liquid/vapor interface and thus the creation of a capillary pressure that can deform or collapse the porous structure [19]. The speed of solidification, promoting the states between particle entrapment and rejection, is possible to manipulated by chemical (solvents, additives, and salts) or physical (temperature, velocity, mold surface and shape, and external force fields) means.

When water is used as a solvent or dispersant, the temperature reduction below freezing point allows the formation of ice crystals and their nucleation, where the liquid molecules start to cluster, and arrange within define crystalline structure. This hardly occurs at theoretical freezing point since large energy barrier needs to be overcome to bring the water molecules closer than they are in liquid water. Moreover, the nucleation of ice presents the most significant and in the same time uncontrolled variable in processes closely related to freezing, such as freeze-casting. According to Morris and Acton [20], the ice nucleation in undercooled liquids may occur by two distinct processes. First and more frequent is heterogeneous (or facilitated) processes, which is catalyzed by a solid or liquid substrate (including impurities and containers) in contact with the water, which allows clusters of water molecules to take up configurations that can promote ice formation. During heterogeneous nucleation, the nucleation site can be a physical disturbance, impurity, presence of salt, or

even roughness of the mold or freezing container. The second, much less frequent type is homogeneous nucleation, which occurs in absence of nucleation site. In such case, the ice crystals nucleate simultaneously, without any predefined nucleation site, and no favorable location. In consequence, the ice arrangements are random, with short-range alignments. Conditions required for homogeneous nucleation are rare, as, practically, completely pure water (having freezing temperature of ~−40 °C) does not exist.

During freezing step, the dispersed particles are expelled from the newly formed solid, stacking between the ice crystals, which interact with dispersed particles by short-range thermomolecular forces induced by van der Waals or electrostatic interactions [21]. According to single-particle model, the suspended particle will be rejected by the solidification front only if interfacial free energies satisfy this following thermodynamical condition:

$$\Delta\gamma_0 = \gamma_{ps} - (\gamma_{pl} + \gamma_{sl}) > 0 \tag{13.1}$$

where γ_{ps}, γ_{pl}, and γ_{sl} are the interfacial free energies associated with the particle–solid, particle–liquid, and solid–liquid interfaces, respectively. This energy balance facilitates the analysis of systems where suspended particles experience the repulsive (F_R) and attractive (F_A) forces with respect to the advancing freezing front arising due to interparticle van der Waals interactions at the liquid–solid interface and viscous drag, respectively.

$$F_R = 2\pi r\Delta\gamma_0(\alpha_0 d)n \tag{13.2}$$

$$F_A = 6\pi\eta v r^2 d \tag{13.3}$$

where r is the radius of the solid particle, v is the freezing front velocity, α_0 is the mean distance between molecules in the liquid phase, d is the thickness of the liquid layer between the solid–liquid interface and the particle (i.e. the distance between the ice front and the particle), η is the dynamic viscosity of the liquid, and n is an empirical correction factor for the repulsive forces that generally range from 1 to 4.

Third step following the freezing is sublimation, i.e. solid–gas transition, or direct vaporization of structured ice, bypassing the liquid phase, which occurs at atmospheric or reduced pressure. This process, also known as lyophilization, consists of primary and secondary drying that occurs due to water vapor concentration gradient between the drying front and the condensate. The sublimation of water occurs below its triple point (temperature of 0.0098 °C and pressure of 611 Pa).

13.1.2 Special Types of Freeze-Casting

The microstructure of freeze-casted construct is controlled by several independent or interconnected, structural, kinetic, and thermodynamic factors, which are divided between internal and external types [22]. The internal acts in a way to alter the repulsive and attractive forces that a particle experiences when interacting with the freezing front, impacting the morphology of the ice crystals and consequently the pore size and shape. Their effect is distributed to whole suspension, and as such is hardly possible to obtain complex microstructures in absence of the

second, external type of factors. The most dominant internal factors are composition of freezing system (nature of solvent-single or cosolvent, proportion and concentration of additive and impurities, geometry of particles and their aspect ratio) and the operational conditions (freezing temperature, cooling rate, and temperature gradient) [16]. The external factors (including freezing surface, assisting external magnetic, electric or acoustic fields, and thermal radiation) affect the freezing process, by application of exterior/additional forces or energies, altering the entire microstructure rather than individual pore size and shape.

The generation of diverse ice morphologies translate into myriad of microstructures and macroarchitectures, including isotropic porous, honeycomb of fish-bone-like, anisotropic: lamellar, radial, nacre-mimetic, and many more. They are accomplished by different means of freezing, including unidirectional, bidirectional, radial, radial-concentric freezing, dynamic, random, and freeze–thawing. Among most conventional is unidirectional freezing, where suspension starts freezing under a single temperature gradient. Cooling is applied to one end of a colloidal suspension, allowing formation of planar freezing front as advancing interface between solidified solvent crystals and liquid suspension. This causes nucleation of ice to occur randomly, resulting in the formation of microscale crystallites. Their preferential orientation is direction of freezing, forming a small-scale lamellar structure [23]. In contrary, at bidirectional freezing, the nucleation and growth of ice crystals are guided by dual temperature gradients allowing ice propagation in both directions. In this case, the large-sized single-domain aligned lamellar structures are formed [24]. At radial, or radial concentric freeze casting, suspension is exposed to two temperature gradients, resulting in longitudinally and radially aligned porosity.

Zhao et al. recently presented example of different nucleation patterns directly affected by the chemistry of molds surface [25]; the rich designability of surface wettability patterns was harnessed to process bulk materials with bioinspired complex architectures. Same study proposed the possible mechanism for controlling freeze-casted structures by surface wettability, where ice crystals "nucleate successively" from the hydrophilic to the hydrophobic region. In consequence, the colloidal particles aligned, causing preferential growth of ice crystals being restricted by them, ultimately forming an aligned microstructure.

Beside presented examples of intrinsic control over the freeze-casting processes, external factors, such as exposure to magnetic, electric, and acoustic fields, as well as light irradiation may further manipulate freezing process, through their effect on chemical states of suspension media or solid particles during or after solidification.

13.1.2.1 Magnetic Freeze-Casting

Magnetic freeze-casting relies on the use of magnetic fields to manipulate matter during the solidification of colloidal suspensions. Although water is a diamagnetic material, its magnetic susceptibility is relatively small, and weak magnetic fields have a minimal effect. According to Tang et al. [26], the magnetic fields weaken the hydrogen bonds between clusters of water molecules, leading to the growth

of smaller ice crystals, and hence decreased pore sizes (in diamagnetic slurries). Magnetic fields generated by permanent magnets arranged in a variety of spatial orientations can produce scaffolds with different microstructural patterns when used in the freeze-casting of magnetic particles or other building blocks, functionalized with magnetic nanoparticles. Recent research into magnetic freeze-casting has demonstrated the utility of diverse types of magnets and magnet-positioning techniques, including rotating magnets, to control field strength and produce freeze cast structures of various tailored forms including helical scaffolds, uniform scaffolds, and functionally graded materials.

13.1.2.2 Electric Freeze-Casting

The effect of the electrostatic field on ice crystal growth was observed during directional freezing of aqueous, ceramic slurries. It was found that even weak electric fields can cause the ceramic particles to move, which can form the gradient porous structure after freeze-casting and sintering, as well as increase of compressive strength along the electrostatic field direction, comparing to conventional freeze-casting [26]. The electric field can be also used to control the growth path of ice crystals, by affecting the temperature gradient, where the electric fields oriented perpendicular to the freezing direction can produce long-range alignment of lamellar walls through the formation of angled ice crystals, while applying electric fields parallel to the solidification direction, producing scaffolds with bilayer dense/porous regions. Both electric and magnetic require extremely high field strengths (20.0 kV/m and 80.0 kOe, respectively) and do not easily scale to cover large areas or volumes, which limits the viability of these techniques to manufacture larger samples. Also, they require use of electrically conductive and/or ferromagnetic materials, which restricts material choice.

13.1.2.3 Ultrasound and Acoustic Freeze-Casting

Recent work combines freeze-casting with ultrasound directed self-assembly, to fabricate bioinspired materials that mimic the concentric rings of natural materials such as osteons and Liesegang rings [13]. The ultrasound-directed self-assembly allows organizing user-specified patterns of micro/nanoparticles dispersed in a liquid medium using the acoustic radiation force associated with a standing ultrasound wave field, working independently from material properties. The acoustic radiation force creates a standing pressure wave, while regions of high and low pressure can be imparted in freeze-casting processes. As particles are driven to low-pressure regions of the standing wave, the resulting scaffolds exhibit a distribution of alternating dense/porous rings. Next novel approach utilizing external tuning of freeze-casting is light irradiation, which drives the reactions and rearrangement between polymeric building blocks in the obtained frozen state. Same was utilized in work of Obmann et al. [27], where porous polysilazane-derived ceramics were formed, combining freeze-casting of a liquid preceramic polymer with a photo-induced thiol-ene “click” reaction, occurring at low temperature ($<-10\,^{\circ}C$).

13.2 Freeze-Casted Scaffolds for Regenerative Medicine

Porous scaffold are the major components in regenerative medicine and tissue engineering. Same have prominent role as coherently structured matrices, which can regulate cell behavior, starting from initial attachment to proliferation and differentiation at latter stage, by delivering the unique combination of physicochemical and mechanical cues for residing cells and allowing proper exchange of nutrients and metabolic waste [19]. By presenting a synthetic cellular niche, scaffolds should closely mimic the native extracellular matrix (ECM) in term of morphology (shape, microstructure, porosity, and pattern), topography, biomechanical characteristics, as well as the composition. Fate, efficiency, and safety of scaffold constructs when implanted into biological environment to large extent depend on above-mentioned properties, where the microstructuring (% porosity, pore size, and interconnectivity) is among most influential. High porosity and large pores were found important at stage of cell infiltration and colonization. On the other hand, the open and interconnected pores were beneficial for growth, proliferation, and migration of the cells, the ECM production, and vascularization. The microporosity was required for efficient cell adhesion and spreading, and micromechanics, facilitating the initial mechanical strength between the scaffold and the tissue [28].

Several processing techniques have been utilized in fabrication of scaffolds. Among them, solvent evaporation technique [29], using organic solvents or noncytotoxic porogens (i.e. salt, wax, sugar, and gelatin), showed relatively limited control over sample thickness and pore interconnectivity, diminishing its applicability. Similar limitations were recognized using techniques, based on self-organization of nanofibers in (nano)lamellar structures or 3D printing, using layer-by-layer processing [30], the latter being particularly difficult for generation of pores with dimension of few 10 μm, required for cells proliferation. On the contrary, scaffolds with large surface area for cell's fixation and excellent porosity are developed by different spinning and knitting processes [31]. Freeze-casting appears to be a promising technique, allowing porosity manipulation by freezing temperature, temperature gradient [32], speed of freezing [33], number of lyophilization steps after the freezing [34, 35], etc. Porosity of scaffolds can be additionally influenced by additives as acetic acid, EtOH [36], metal tubes [37], or even oriented crossing of heat [38]. Involving compulsory displacement of polymeric precursor into a nonfrozen microphase and concentration of polymeric gel in the pore walls [39], these processes allow modulation of porosity, pore-wall surfaces biochemistry, and degradation rates [40].

The structure–property–processing correlation for directionally freeze-casted scaffolds is critical for optimal scaffold design. In study of Divakar et al. [41], collagen scaffolds were obtained by freeze-casting of collagen solutions, applying three different cooling rates (10, 1, and 0.1 °C/min) and two freezing directions (longitudinal and radial). Scanning electron spectroscopy (SEM) microscopy (Figure 13.3) identified aligned, regular pores in longitudinally frozen scaffolds, while those in radially frozen ones exhibit greater variations in pore geometry and alignment. The porosity parameters, i.e. lamellar spacing, pore area, and cell

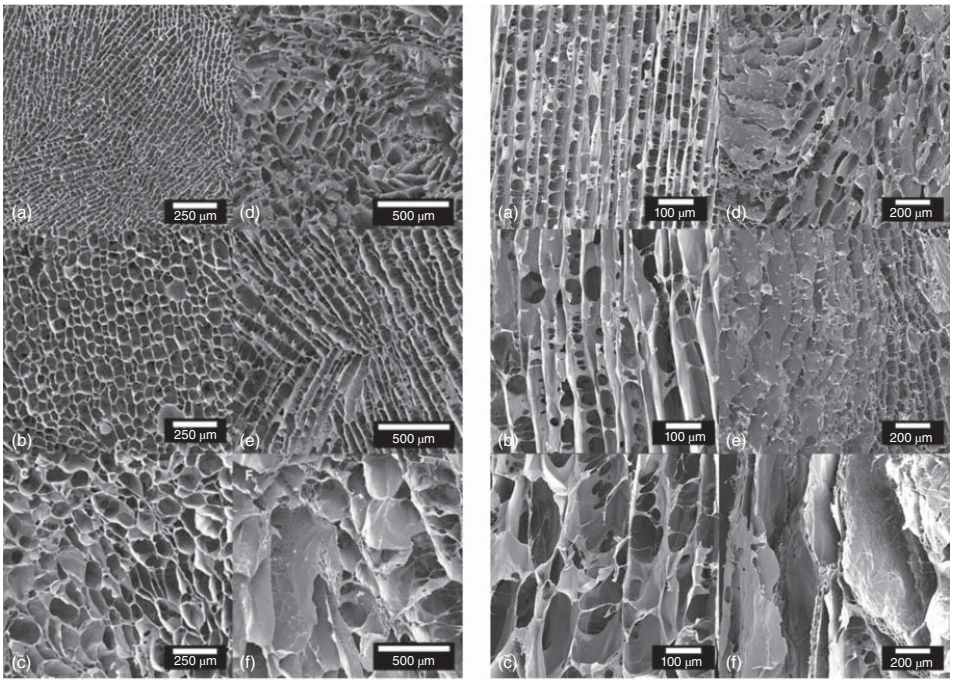

Figure 13.3 SEM micrographs of transverse (a) and longitudinal (b) cross-sections in the upper region of scaffolds freeze-cast longitudinally (A: 10 °C/min, B: 1 °C/min, C: 0.1 °C/min) and radially (D: 10 °C/min, E: 1 °C/min, F: 0.1 °C/min). Source: From Divakar et al. [41]/with permission of Elsevier.

wall thickness, were found to increase with decreasing cooling rate. The freezing direction influences mechanical strength, where longitudinally and radially frozen scaffolds possess higher mechanical strength when loaded parallel rather than perpendicular to the ice-crystal growth direction. In conclusion, such scaffold profile was found ideal for tissue regeneration applications.

The use of unidirectional freeze-casting to impart aligned porous structures has been conducted in various established biomaterial systems including bioactive polymers, ceramics, or complex building blocks, such as multiwall carbon nanotubes, graphene sheets, ceramic nanofibers and nanosheets, and metallic nanowires. The biocompatible polymers represent major domain of implantable biomaterials, where freeze-casting technology is largely applied. They include collagen, chitin, gelatin, polylactic acid (PLA), poly(lactide-*co*-glycolide) (PLGA), poly(2-hydroxyethyl methacrylate) (poly(HEMA)), agarose, sericin, alginate, cellulose, etc.

13.2.1 (Nano)cellulose Scaffolds

Semi-crystalline nanofibrils and crystalline cellulose nanocrystals have been growing in importance over the last decade as abundant and renewable nanomaterials that combine a lightness, large surface areas, high strength and flexibility, low thermal expansion coefficients, proven biocompatibility, biodegradability, the chemical inertness, and OH^- groups abundance for chemical modifications [42]. Due to all above, this nanomaterial, when shaped within diverse forms and compositions (nanocomposites/hybrids, nano-additives, nano sensors, and nano-filters), becomes profoundly investigated and already applied in diverse technical and (bio)medical applications. Formation of self-standing foams/porous solids by freeze casting, out of cellulose nanoparticles as single components, is highly dependent of length/diameter aspect of cellulose nanoparticles, their concentration, as well as freezing speed. During the freezing of nanocellulose suspensions, as already mentioned, the ice crystals gradually grew in the direction of the temperature gradient, generating ice patterns parallel to freezing front, simultaneously squeezing, and expelling the nanoparticles into the space between ice crystals. Being constrained, and at certain concentration level, the cellulose nanoparticles re-aligned and self-assembled into compact pore walls, where strong hydrogen bonds and van der Waals forces keep them together at lyophilization stage [43]. Even possible, the single-component cellulose nanoparticles are not investigated as scaffolding systems, as they lack important biochemical cues, crucial for cellular recognition and positive immunological response [44]; therefore, they are often combined with amino acids, peptides, or proteins [45].

In the work of Gorgieva et al. [46], the cellulose nanofibrils were combined with protein-gelatin, using the freeze-casting process, supplemented with carbodiimide crosslinking chemistry. Highly porous scaffolds with diverse morphologies were processed using identical freezing regime and different components' ratio, as depicted on micrographs in Figure 13.4. It was found that in the absence of cellulose nanofibrils, the scaffold with the relatively large pore size (~200 μm) on top side was formed, while addition of 50% gelatin reduces the pore size more than twice.

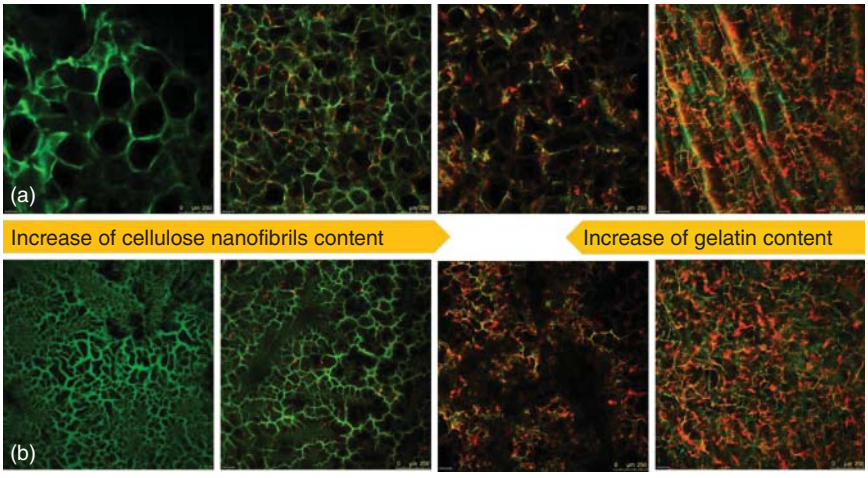

Figure 13.4 Fluorescence micrographs of the scaffolds' top (a) and bottom (b) surface prepared from combination of cellulose nanofibrils and gelatin. Green and red spectral mappings were used for imaging of the fluorescein isothiocyanate (FITC)-labeled gelatin component and rhodamine B isothiocyanate (RBITC)-labeled cellulose nanofibrils content, respectively. Source: Reproduced from Gorgieva et al. [46]/with permission of Elsevier.

Dominant presence of cellulose nanofibrils induces unidirectional, close to parallel, lamellae-like alignment of pore walls due to intensive hydrogen bonding in cellulose nanoparticle-rich segment. Instead, the freezing plate-exposed surface remained isotropic in all cases, with pore sizes of ~50 μm, sufficient to allow diffusion of nutrients and wastes. Scaffolds were further seeded with mesenchymal stem cells, where Ca deposition in five weeks' study was demonstrated as marker for osteogenic differentiation.

In another work of Gorgieva and Hribernik [47], the bacterial-originated cellulose was combined with gelatin, using a successive periodate oxidation, freeze-casting/carbodiimide crosslinking procedure in the formation of membrane-like scaffold. The micrographs in Figure 13.5 demonstrate anisotropic structuring due to the presence of dense bacterial cellulose membrane and porous gelatin component. Intention was to build the barrier membrane, which can stop proliferation of gingival cells and allow inclusion of periodontal cells, as required by guided tissue regeneration (GTR) procedure. Fluorescent microscopy images were preprocessed for data demonstrating distribution of pore size and wall thickness. It was found that size of pore generated within the gelatin phase during unidirectional freeze-casting process follows a certain relation, i.e. it is larger on top than bottom, increases with reduction in the gelatin concentration, and is smaller in case when oxidized bacterial cellulose is underlying the gelatin phase. Same study identified that presence of nanofibrillar, bacterial cellulose membrane arrests the progression of freezing front from freezing plate-contacting surface to sample top surface, at the same time enlarging the time frame for ice crystals growth. Such procedure results in the formation of homogeneous pores, whose size ranges between 30 and 100 μm (i.e. above size threshold for

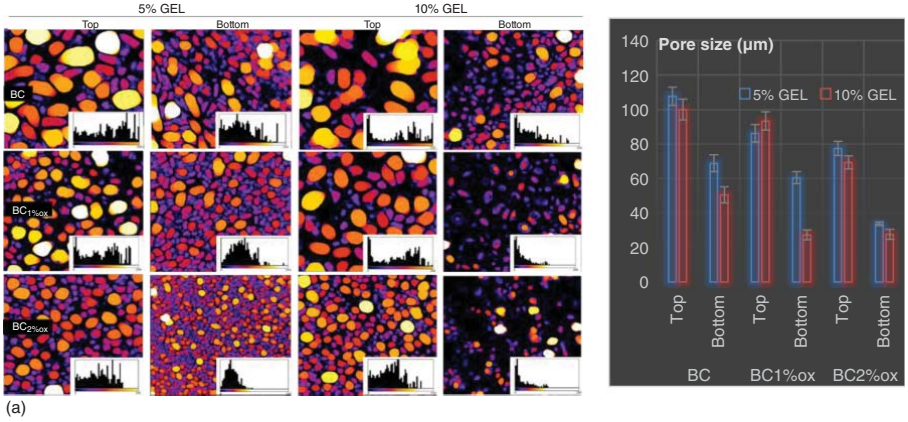

Figure 13.5 Color-coded images of bacterial cellulose–gelatin membranes, emphasizing pores (a) and pore walls (b). The image insets are respective histograms demonstrating normalized distributions of pore size and pore wall thicknesses within top and bottom of membranes (*x* axis: 0–200 μm, *y* axis: count) without and with 5% and 10% gelatin and (non)oxidized bacterial cellulose. Mean/standard deviation (SD) data of pore size and pore wall thickness are presented next to respective (a, b) image sets. Source: Gorgieva and Hribernik [47]/MDPI/CC BY 4.0.

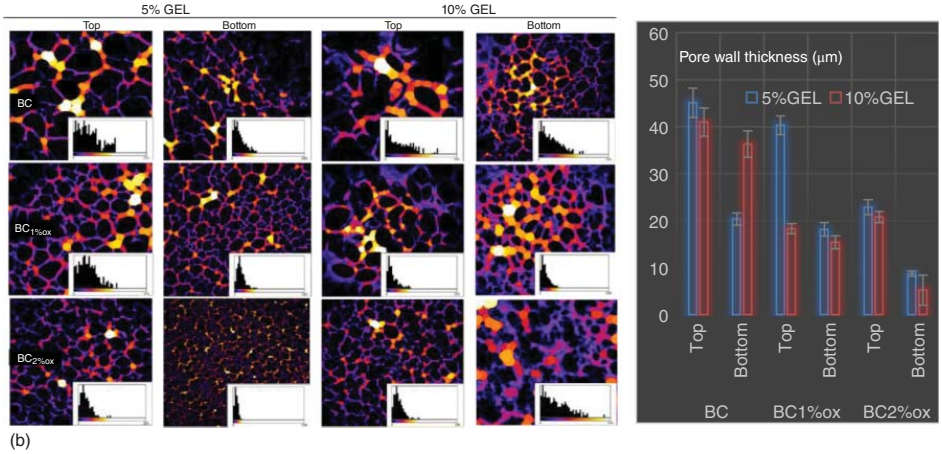

Figure 13.5 (*Continued*)

cell trafficking), according to [48], depending on preparation conditions (preoxidation of bacterial cellulose and different concentration of gelatin used).

13.2.2 Gelatin Scaffolds

Gelatin chronology as biomaterial dates back to ~1970s; even its benefits to health may have been recognized in the Middle Ages (~1150). Originating from ECM protein, the collagen, gelatin has attracted substantial research interest over recent years and consequently biomedical applications regarding tissue regeneration. Its merits such as desirable cellular response, engagement with the cell-adhesion-promoting Arg–Gly–Asp (RGD) sequences, its nonimmunogenicity and noncytotoxicity, biodegradability and bioresorbability, and finally its immense capacity for modifying at the level of amino acids make this protein one of the most exploited in biomaterials fabrication.

Subjecting the gelatin solutions to freezing under directional thermal gradient results in directional ice templating. Same was utilized in work of Gorgieva and Kokol [49], where porous gelatin cryogels were processed by spatiotemporal and temperature-controlled (−12 and −16 °C) freeze-casting procedure, followed by zero-length crosslinking, utilizing the media (100% phosphate buffered saline [PBS] or 20/80% PBS/EtOH mixture) and time variations (1–24 hours). Resulting gradient microporosity was influenced by crosslinkers' concentration and ethanol addition. The SEM data (Figure 13.6) reveal appearance of thin, nonporous, skin-like surface near the top of scaffolds, which was assigned to the interfacial tension caused by solvent evaporation. As skin formation is a common feature and often a problem in case of pharmaceutical formulations, the one hypothesis is that skin is formed due to nonsufficient freezing, which allows nonfrozen solution to be expelled at the surface [50]. Even so, the visible contours of pore wall appear as micropits, which may be attributed to the phenomenon known as "syneresis." In contrary, the bottom surface was full of pore openings with a dimension of ~20 μm, while disclosed pores are observed in cross-section images showing an interconnected pore system and pore size gradient as an important feature (from 100 μm near bottom up to 1000 μm near top surface). Such a structure with different pore-size domains originated from the gradient in velocity of water crystals growth, being mostly dependent on freezing end temperature and the distance from the cooling plate [49].

Fluorescence microscopy images of same samples (Figure 13.7) reveal distinct features (shape of pores and their cross-points) within scaffolds microstructure in function of preparation parameters, i.e. from round, and radially organized to isotropic pores with smaller dimensions. The introduction of ethanol in crosslinking medium enlarges the pore wall thickness due to denaturation effect and induction of closer interaction between gelatin molecules. On the other hand, decrease in crosslinker concentration allows higher swelling and thus, round-shaped pores with higher dimensions were identified.

Combining freeze-drying and gel-casting using gelatin is a promising tool in the production of porous ceramics, as the same enables the scaffolds with dense walls excluding apparent tiny pores or defects, giving rise to well-tailored microstructure

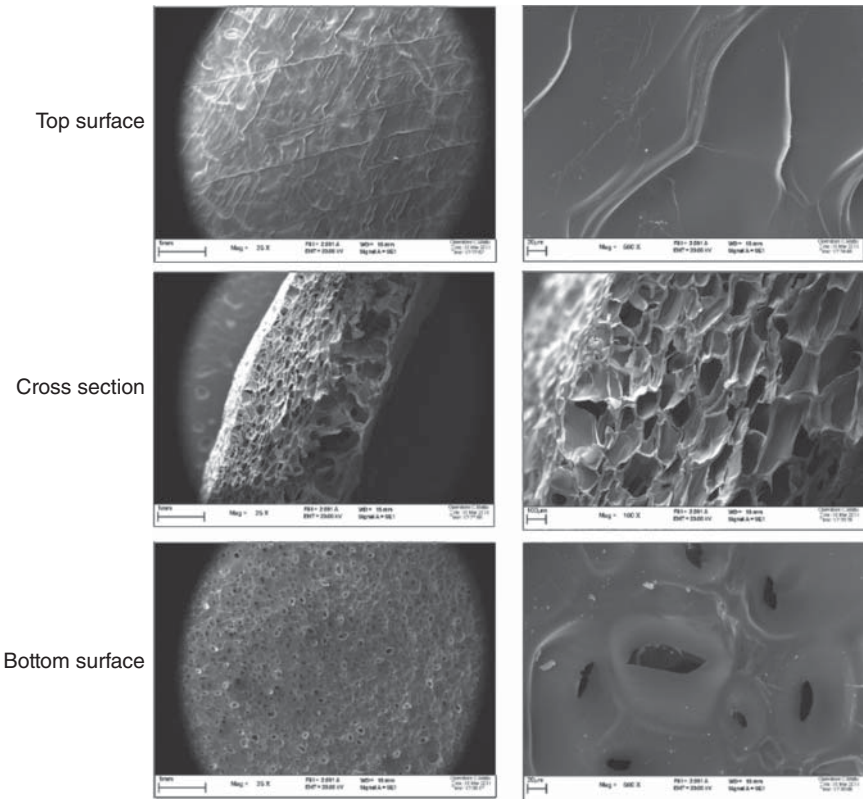

Figure 13.6 SEM images of unidirectionally frozen 10% gelatin samples, with contact plate freezing set at −12 °C.

with enhanced mechanical properties. Thus, it also improves the micro-morphology of scaffolds, thereby addressing the lowered strength of the scaffolds. In the work of Wang et al. [51], the gelatin was infiltrated into boron carbide ceramic scaffolds, and unidirectionally oriented, nacre-like architectures were obtained through gelation–freeze-drying technique. The study indicates the possibility of adjusting both the microstructure and mechanical properties of ceramic scaffolds by varying the concentrations of gelatin, providing type of composite scaffolds as bioinspired materials.

The effect of porosity in similar type of gelatin scaffolds (out of 10% solution, unidirectional freezing, and carbodiimide crosslinked chemistry) was inspected by Podlipec et al. [52], where the molecular mobility, rather than porosity profile (the average wall thickness and pore size), was found to most strongly correlate with growth of L929 fibroblasts, which did not exclude the effect of microstructure, but point at more influencing factors than porosity.

Gelatin was also used as a coating on polypropylene mesh, forming a composite after O_2 plasma activation of synthetic mesh (used in hernia treatment) and freeze-casting process [53]. Obtained micrographs (Figure 13.8) depict the

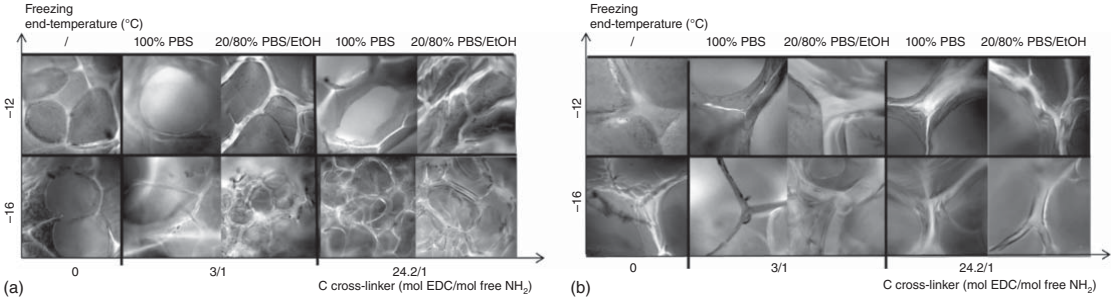

Figure 13.7 Fluorescence microscopy images of cross-sections (a) and cross-points (b) from differently frozen (at −12 °C and −16 °C) scaffolds being post-crosslinked for 24 hours with different concentration of crosslinker (1-ethyl-3-[3-dimethylaminopropyl]carbodiimide hydrochloride [EDC]), 100% PBS, or 20/80% PBS/EtOH as reaction media. Source: Reproduced from Gorgieva and Kokol [49]/with permission of John Wiley & Sons.

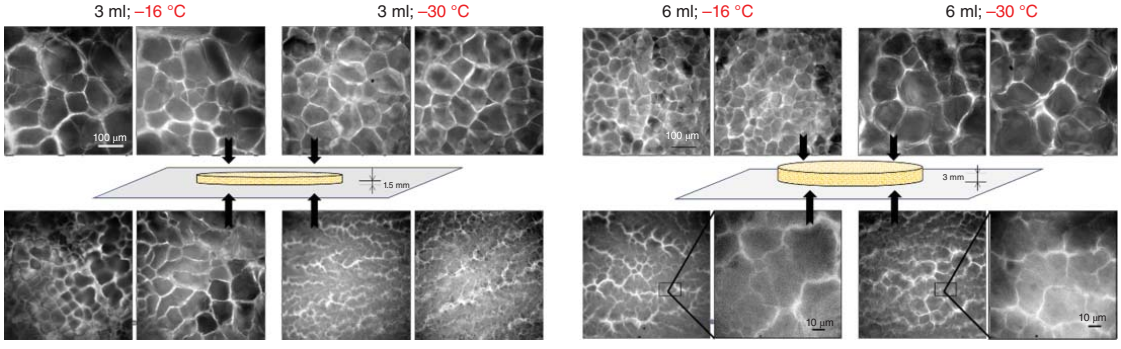

Figure 13.8 Fluorescent microscopy images depicting FITC-labeled gelatin component of polypropylene mesh–gelatin composites. Composites contain two different volumes (3 and 6 ml) of 10% gelatin solution and are exposed to different, unidirectional freezing end temperatures (−16 and −30 °C). Both the air-exposed side and cooling plate-exposed side are presented, referring to the relative position of composite surface with freezing plate surface. Source: From Gorgieva [54]/with permission of American Chemical Society.

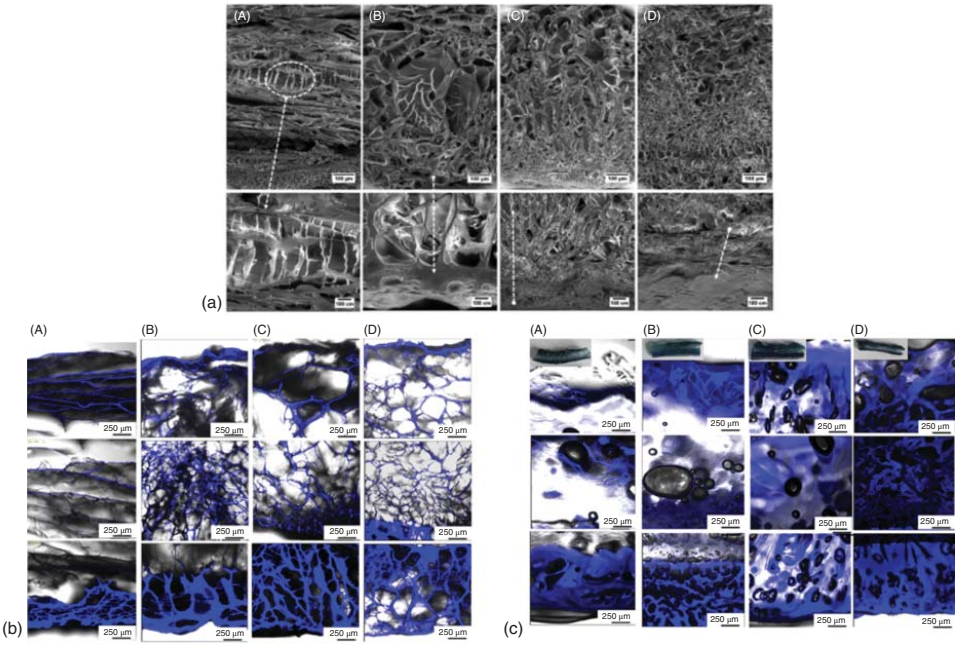

Figure 13.9 SEM (a) and fluorescent microscopy images from cross-sections of dry (b) and in wet membranes (c) with different chitosan/gelatin weight ratio, from 1/1 (A) to 1/20 (D), after crosslinking with 0.5 wt% genipin. Upper insets (c) are photographs from respective wet membranes. Source: Reproduced from Gorgieva et al. [55]/with permission Elsevier.

differences in the microstructuring of gelatin phase when different volumes of 10% gelatin (3 and 6 ml) and different freezing temperatures during unidirectional freezing (−16 and −30 °C) were applied [53].

Uniformity of pores in term of shape, on both the freezing plate contacting surface and the air expose surface, results from the knitting pattern of polypropylene mesh itself, over which the gelatin was casted. The presence of polypropylene mesh influences the temperature gradients throughout the sample, forming the pores between 50 μm (when frozen at −16 °C) and ∼100 μm (at −30 °C). Irrespective of preparation conditions, the all polypropylene–gelatin composites were found not cytotoxic toward human-adipose-derived stem cells (ASC) as a relevant cell source for treating abdominal hernias [55].

Gelatin–chitosan bilayer membranes were prepared by successive solvent– and freeze–casting procedures and genipin crosslinking chemistry [55], with potential use in GTR. The inspection of cross-sections by SEM (Figure 13.9a) demonstrates composition-dependent microstructure formed at identical freezing conditions, yet different solution composition. Herein, dense skin was observed on bottom segment of all samples, irrespective of composition, as a result of lyophilization process. The composite A, having dominant chitosan presence, mostly differs among the samples, due to specific, sheet-like, anisotropic structuring, parallel freezing plates surface, which was similarly as in nanocellulose addition, was to assigned close molecular arrangement and intensive H-bonding of the carbohydrate (chitosan) component. The gelatin fraction increase contributes to scaffold density and homogeneity. The fluorescent microscopy images in both dry and wet states (Figure 13.9b,c) were obtained, utilizing the developed fluorescence signal from (genipin) crosslinking products. Composite with lowest gelatin content (A) demonstrates layered structure, parallel to freezing surface, while increase of gelatin component induces the formation of isotropic system and interconnected porosity. The exposure to phosphate buffer saline causes significant swelling (Figure 13.9c), which deteriorates the pores to large extent, especially in sample A due to lack of interconnections between layers. Data extracted from the images reveal pores with diameter up to 130 μm. It was concluded that at same freezing conditions, the composition did not affect the pore sizes significantly, while pore wall thickness was increased with gelatin content.

13.3 Summary and Outlook

As the human body itself possesses highly graded organization, the gradients in pore size and architecture of scaffolds overall become focus domain in scaffolds (material) research, being of particular importance when formation of multiple tissue and tissue interfaces is of interest. The freeze–casting found profound role in processing of scaffold materials out of solutions or particulate matter, allowing formation of architecturally complex structures. The cellular templating, resulting from freeze-casting processes, can be endowed with vast morphologies, and as such is a logical route toward the design of nature-inspired synthetic materials. The recent development of this procedure allows use, not only of solutions or dispersions, but also building

blocks with low dimensions (nanoparticles, nanotubes), the latter developing and thus feeding the development and performance of freeze-casting technology itself. Identifying new routes for manipulation with freezing process as external magnetic or electrical fields enlarges the length scale on which controlled variation of structure parameters (pore size, geometry, and directional heterogeneity) is enabled. Such procedure can easily go ahead with other manufacturing procedures, or simply supplement their capacity in forming complex, and hierarchically ordered scaffolding systems. By combining freeze-casting with electrospraying, electrospinning, extrusion, tape-casting, or additive manufacturing during the solidification process, other forms, then monoliths, such as beads, microspheres, fibers, meshes, films, and membranes can be shaped, drawing inspiration from functional biological systems.

References

1 Deville, S. (2010). Freeze-casting of porous biomaterials: structure, properties and opportunities. *Materials (Basel)* 3: 1913–1927. https://doi.org/10.3390/ma3031913.

2 Scotti, K.L. and Dunand, D.C. (2018). Freeze casting – a review of processing, microstructure and properties via the open data repository, FreezeCasting.net. *Prog. Mater. Sci.* 94: 243–305.

3 Mahler, W. and Bechtold, M.F. (1980). Freeze-formed silica fibres. *Nature* 285: 27–28. https://doi.org/10.1038/285027a0.

4 Du, Y., Hedayat, N., Panthi, D. et al. (2018). Freeze-casting for the fabrication of solid oxide fuel cells: a review. *Materialia* 1: 198–210.

5 Khaleghi, E., Olevsky, E., and Meyers, M. (2009). Uniaxial freezing, freeze-drying, and anodization for aligned pore structure in dye-sensitized solar cells. *J. Am. Ceram. Soc.* 92: 1487–1491. https://doi.org/10.1111/j.1551-2916.2009.03038.x.

6 Fassler, A. and Majidi, C. (2013). 3D structures of liquid-phase GaIn alloy embedded in PDMS with freeze casting. *Lab Chip* 13: 4442–4450. https://doi.org/10.1039/c3lc50833a.

7 Huang, C. and Grant, P.S. (2018). Coral-like directional porosity lithium ion battery cathodes by ice templating. *J. Mater. Chem. A* 6: 14689–14699. https://doi.org/10.1039/c8ta05049j.

8 Jo, H., Kim, M.J., Choi, H. et al. (2016). Morphological study of directionally freeze-cast nickel foams. *Metall. Mater. Trans. E* 3: 46–54. https://doi.org/10.1007/s40553-016-0068-y.

9 Wang, C., Chen, X., Wang, B. et al. (2018). Freeze-casting produces a graphene oxide aerogel with a radial and centrosymmetric structure. *ACS Nano* 12: 5816–5825. https://doi.org/10.1021/acsnano.8b01747.

10 Gorgieva, S., Vogrinčič, R., and Kokol, V. (2019). The effect of membrane structure prepared from carboxymethyl cellulose and cellulose nanofibrils for cationic dye removal. *J. Polym. Environ.* 27: 318–332. https://doi.org/10.1007/s10924-018-1341-1.

11 Liu, Y., Zhu, W., Guan, K. et al. (2018). Freeze-casting of alumina ultra-filtration membranes with good performance for anionic dye separation. *Ceram. Int.* 44: 11901–11904. https://doi.org/10.1016/j.ceramint.2018.03.160.

12 Wegst, U.G.K., Schecter, M., Donius, A.E., and Hunger, P.M. (2010). Biomaterials by freeze casting. *Philos. Trans. R. Soc. London, Ser. A* 368: 2099–2121. https://doi.org/10.1098/rsta.2010.0014.

13 Ogden, T.A., Prisbrey, M., Nelson, I. et al. (2019). Ultrasound freeze casting: fabricating bioinspired porous scaffolds through combining freeze casting and ultrasound directed self-assembly. *Mater. Des.* 164: 107561. https://doi.org/10.1016/j.matdes.2018.107561.

14 Szepes, A., Ulrich, J., Farkas, Z. et al. (2007). Freeze-casting technique in the development of solid drug delivery systems. *Chem. Eng. Process. Process Intensif.* 46: 230–238. https://doi.org/10.1016/j.cep.2006.06.004.

15 Deville, S., Meille, S., and Seuba, J. (2015). A meta-analysis of the mechanical properties of ice-templated ceramics and metals. *Sci. Technol. Adv. Mater.* 16: 43501.

16 Yang, J., Yang, W., Chen, W., and Tao, X. (2020). An elegant coupling: freeze-casting and versatile polymer composites. *Prog. Polym. Sci.* 109: 101289.

17 Naviroj, M., Voorhees, P.W., and Faber, K.T. (2017). Suspension- and solution-based freeze casting for porous ceramics. *J. Mater. Res.* 32: 3372–3382. https://doi.org/10.1557/jmr.2017.133.

18 Gorgieva, S. and Kokol, V. (2015). Processing of gelatin-based cryogels with improved thermomechanical resistance, pore size gradient, and high potential for sustainable protein drug release. *J. Biomed. Mater. Res. Part A* 103: https://doi.org/10.1002/jbm.a.35261.

19 Lavoine, N., Bergström, L., and Bergström, B. (2017). Nanocellulose-based foams and aerogels: processing, properties, and applications. *J. Mater. Chem. A*. https://doi.org/10.1039/c7ta02807e.

20 John Morris, G. and Acton, E. (2013). Controlled ice nucleation in cryopreservation – a review. *Cryobiology* 66: 85–92.

21 Saint-Michel, B., Georgelin, M., Deville, S., and Pocheau, A. (2017). Interaction of multiple particles with a solidification front: from compacted particle layer to particle trapping. *Langmuir* 33: 5617–5627. https://doi.org/10.1021/acs.langmuir.7b00472.

22 Nelson, I. and Naleway, S.E. (2019). Intrinsic and extrinsic control of freeze casting. *J. Mater. Res. Technol.* 8: 2372–2385.

23 Zhang, H., Hussain, I., Brust, M. et al. (2005). Aligned two- and three-dimensional structures by directional freezing of polymers and nanoparticles. *Nat. Mater.* 4: 787–793. https://doi.org/10.1038/nmat1487.

24 Yan, L., Wu, J., Zhang, L. et al. (2017). Pore structures and mechanical properties of porous titanium scaffolds by bidirectional freeze casting. *Mater. Sci. Eng., C* 75: 335–340. https://doi.org/10.1016/j.msec.2016.12.044.

25 Zhao, N., Li, M., Gong, H., and Bai, H. (2020). Controlling ice formation on gradient wettability surface for high-performance bioinspired materials. *Sci. Adv.* 6 (31), eabb4712. https://doi.org/10.1126/sciadv.abb4712.

26 Tang, Y., Qiu, S., Miao, Q., and Wu, C. (2016). Fabrication of lamellar porous alumina with axisymmetric structure by directional solidification with applied electric and magnetic fields. *J. Eur. Ceram. Soc.* 36: 1233–1240. https://doi.org/10.1016/j.jeurceramsoc.2015.12.012.

27 Obmann, R., Schörpf, S., Gorsche, C. et al. (2019). Porous polysilazane-derived ceramic structures generated through photopolymerization-assisted solidification templating. *J. Eur. Ceram. Soc.* 39: 838–845. https://doi.org/10.1016/j.jeurceramsoc.2018.11.045.

28 Pina, S., Ribeiro, V.P., Marques, C.F. et al. (2019). Scaffolding strategies for tissue engineering and regenerative medicine applications. *Materials (Basel)* 12: 1824.

29 Mikos, A.G., Bao, Y., Cima, L.G. et al. (1993). Preparation of poly(glycolic acid) bonded fiber structures for cell attachment and transplantation. *J. Biomed. Mater. Res.* 27: 183–189. https://doi.org/10.1002/jbm.820270207.

30 Zhang, S. (2003). Fabrication of novel biomaterials through molecular self-assembly. *Nat. Biotechnol.* 21: 1171–1178. https://doi.org/10.1038/nbt874.

31 Dvir, T., Timko, B.P., Kohane, D.S., and Langer, R. (2011). Nanotechnological strategies for engineering complex tissues. *Nat. Nanotechnol.* 6: 13–22. https://doi.org/10.1038/nnano.2010.246.

32 Liu, X., Rahaman, M.N., Fu, Q., and Tomsia, A.P. (2012). Porous and strong bioactive glass (13-93) scaffolds prepared by unidirectional freezing of camphene-based suspensions. *Acta Biomater.* 8: 415–423. https://doi.org/10.1016/j.actbio.2011.07.034.

33 Van Vlierberghe, S., Dubruel, P., Lippens, E. et al. (2009). Correlation between cryogenic parameters and physico-chemical properties of porous gelatin cryogels. *J. Biomater. Sci., Polym. Ed.* 20: 1417–1438. https://doi.org/10.1163/092050609X12457418905508.

34 Kasper, J.C. and Friess, W. (2011). The freezing step in lyophilization: physico-chemical fundamentals, freezing methods and consequences on process performance and quality attributes of biopharmaceuticals. *Eur. J. Pharm. Biopharm.* 78: 248–263. https://doi.org/10.1016/j.ejpb.2011.03.010.

35 Mao, J.S., Zhao, L.G., Yin, Y.J., and Yao, K.D. (2003). Structure and properties of bilayer chitosan-gelatin scaffolds. *Biomaterials* 24: 1067–1074.

36 Schoof, H., Apel, J., Heschel, I., and Rau, G. (2001). Control of pore structure and size in freeze-dried collagen sponges. *J. Biomed. Mater. Res.* 58: 352–357.

37 Brouwer, K.M., van Rensch, P., Harbers, V.E.M. et al. (2011). Evaluation of methods for the construction of collagenous scaffolds with a radial pore structure for tissue engineering. *J. Tissue Eng. Regener. Med.* 5: 501–504. https://doi.org/10.1002/term.397.

38 Davidenko, N., Gibb, T., Schuster, C. et al. (2012). Biomimetic collagen scaffolds with anisotropic pore architecture. *Acta Biomater.* 8: 667–676.

39 Dainiak, M.B., Allan, I.U., Savina, I.N. et al. (2010). Gelatin-fibrinogen cryogel dermal matrices for wound repair: preparation, optimisation and in vitro study. *Biomaterials* 31: 67–76. https://doi.org/10.1016/j.biomaterials.2009.09.029.

40 Savina, I.N., Dainiak, M., Jungvid, H. et al. (2009). Biomimetic macroporous hydrogels: protein ligand distribution and cell response to the ligand architecture

in the scaffold. *J. Biomater. Sci., Polym. Ed.* 20: 1781–1795. https://doi.org/10.1163/156856208X386390.

41 Divakar, P., Yin, K., and Wegst, U.G.K. (2019). Anisotropic freeze-cast collagen scaffolds for tissue regeneration: how processing conditions affect structure and properties in the dry and fully hydrated states. *J. Mech. Behav. Biomed. Mater.* 90: 350–364. https://doi.org/10.1016/j.jmbbm.2018.09.012.

42 Gorgieva, S., Vogrinčič, R., and Kokol, V. (2015). Polydispersity and assembling phenomena of native and reactive dye-labelled nanocellulose. *Cellulose* 22: 3541–3558. https://doi.org/10.1007/s10570-015-0755-3.

43 Du, L., Yu, Z., Wang, J. et al. (2020). Analyzing the film formation mechanism of cellulose nanoparticles (CNPs) based on the fast freeze-drying morphology. *Cellulose* 27: 6921–6933. https://doi.org/10.1007/s10570-020-03164-z.

44 Gorgieva, S. (2020). Bacterial cellulose as a versatile platform for research and development of biomedical materials. *Processes* 8: 624. https://doi.org/10.3390/pr8050624.

45 Lin, N. and Dufresne, A. (2014). Nanocellulose in biomedicine: current status and future prospect. *Eur. Polym. J.* 59: 302–325. https://doi.org/10.1016/j.eurpolymj.2014.07.025.

46 Gorgieva, S., Girandon, L., and Kokol, V. (2017). Mineralization potential of cellulose-nanofibrils reinforced gelatine scaffolds for promoted calcium deposition by mesenchymal stem cells. *Mater. Sci. Eng., C* 73: 478–489. https://doi.org/10.1016/j.msec.2016.12.092.

47 Gorgieva, S. and Hribernik, S. (2019). Microstructured and degradable bacterial cellulose–gelatin composite membranes: mineralization aspects and biomedical relevance. *Nanomaterials* 9. https://doi.org/10.3390/nano9020303.

48 Koshy, S.T., Ferrante, T.C., Lewin, S.A., and Mooney, D.J. (2014). Injectable, porous, and cell-responsive gelatin cryogels. *Biomaterials* 35: 2477–2487. https://doi.org/10.1016/j.biomaterials.2013.11.044.

49 Esfandiary, R., Gattu, S.K., Stewart, J.M., and Patel, S.M. (2016). Effect of freezing on lyophilization process performance and drug product cake appearance. *J. Pharm. Sci.* 105: 1427–1433. https://doi.org/10.1016/j.xphs.2016.02.003.

50 Wang, Y., Liu, Q., Zhang, B. et al. (2020). Gelatin tailored pore structure and mechanical properties of freeze-cast porous boron carbide ceramics. *Ceram. Int.* 47: 2897–2902. https://doi.org/10.1016/j.ceramint.2020.09.111.

51 Podlipec, R., Gorgieva, S., Jurašin, D. et al. (2014). Molecular mobility of scaffolds' biopolymers influences cell growth. *ACS Appl. Mater. Interfaces* 6: 15980–15990. https://doi.org/10.1021/am5037719.

52 Gorgieva, S., Modic, M., Dovgan, B. et al. (2015). Plasma-activated polypropylene mesh-gelatin scaffold composite as potential implant for bioactive hernia treatment. *Plasma Processes Polym.* 12: 237–251. https://doi.org/10.1002/ppap.201400125.

53 Gorgieva, S. (2014). Effect of gelatine scaffolds fabrication as polypropylene mesh coat on implant biocompatibility, Doctoral thesis. University of Maribor, Faculty of Mechanical Engineering, Slovenia.

54 Zhao, J. and Xu, J.J. (2018). Experimental study on application of polypropylene hernia of fat stem cells in rats. *Eur. Rev. Med. Pharmacol. Sci.* 22: 6156–6161. https://doi.org/10.26355/eurrev_201809_15957.

55 Gorgieva, S., Vuherer, T., and Kokol, V. (2018). Autofluorescence-aided assessment of integration and μ-structuring in chitosan/gelatin bilayer membranes with rapidly mineralized interface in relevance to guided tissue regeneration. *Mater. Sci. Eng., C* 93: 226–241. https://doi.org/10.1016/J.MSEC.2018.07.077.

14

Polysaccharide-Based Stimuli-Responsive Nanofibrous Materials for Biomedical Applications

Manja Kurečič[1,2], Beste Elveren[2], and Selestina Gorgieva[1,2]

[1] *University of Maribor, Faculty of Electrical Engineering and Computer Science, Institute of Automation, Koroška cesta 46, 2000 Maribor, Slovenia*
[2] *University of Maribor, Faculty of Mechanical Engineering, Institute of Engineering Materials and Design, Smetanova ulica 17, 2000 Maribor, Slovenia*

14.1 Introduction

All living organisms are active toward a variety of environmental changes called stimuli, such as light, heat, sound, chemical, or mechanical contact, to which they react in a rapid, reversible, and repeated manner. Response to stimulus is a basic process of living systems. The ability to react or to adapt to the environmental changes is called stimuli responsiveness [1]. Stimuli-responsive materials (SRMs) also known as "smart" materials, with the ability to respond and change according to specific stimuli, have recently gained significant interest and are presenting one of the most rapidly evolving classes of materials. SRMs are defined as materials designed with one or more properties that can significantly change upon stimuli in a controlled fashion [2]. The most common external stimuli and consequent material responses are presented in Figure 14.1. Smart materials respond with changes in their internal structure and intrinsic properties such as color, shape, stiffness, viscosity, energy absorption capacity, damping, or optical properties like transparency or opacity [2]. There are numerous publications dealing with development of synthetic and naturally occurring materials with stimuli-responsive properties [4]. The responsiveness of smart polymers can be an inherent property, or it can be due to the presence of additives, as in composite materials [5]. Commonly, these changes are reversible when the stimulus is removed and can be repeated many times.

Polymers, which respond to their environment by changing their physical and/or chemical properties, like shape, solubility, surface characteristics, and molecular assembly, are referred to as stimuli-responsive polymers (or smart/intelligent polymers) [6]. Stimuli alter the levels of various interaction energies, thus altering molecular interactions and hydrophilic–hydrophobic balance in these materials, leading to reversible changes in their microstructure [7].

According to the abundance of possible responses and stimuli, the far most studied and understood response is to temperature. Thermoresponsive polymers

Functional Biomaterials: Design and Development for Biotechnology, Pharmacology, and Biomedicine, First Edition. Edited by Tamilselvan Mohan and Karin Stana Kleinschek.

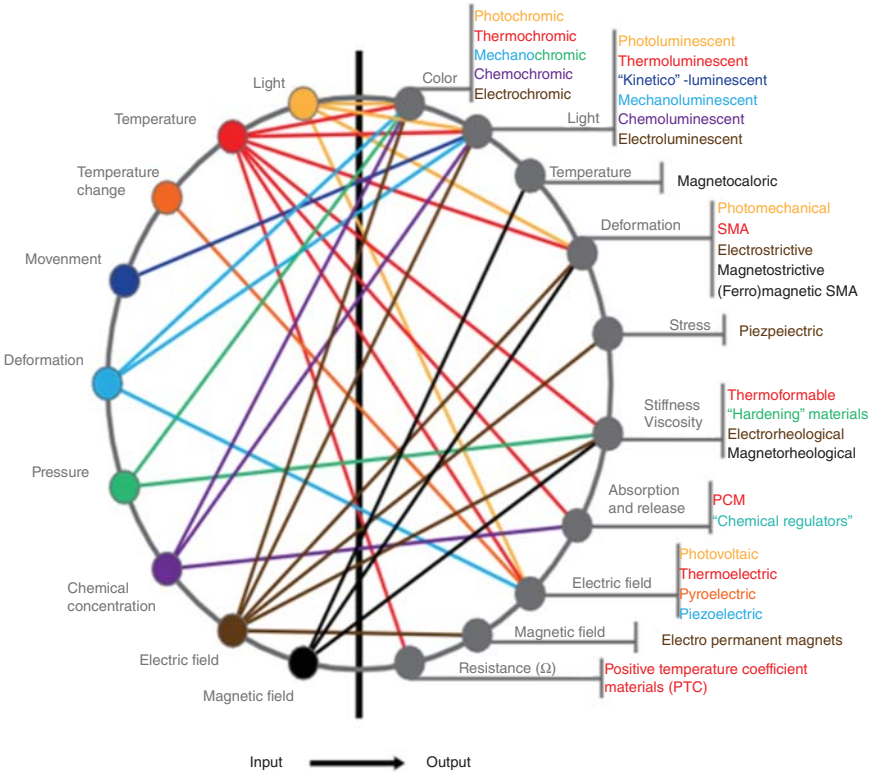

Figure 14.1 Graph of the transition phenomena connecting stimulus and response. Source: Esther et al. [3]/with permission of Agnese Piselli.

undergo a reversible coil-to-globule transition in water after which the chains collapse and aggregate into bigger globules when passing to above its lower critical solution temperature (LCST) [8]. Critical solution temperature can be defined as a critical temperature at which the polymeric solution shows a phase separation, which moves from the isotropic state to the anisotropic state [9]. The most studied polymer system in biomedical applications is the temperature-responsive smart polymer poly(*N*-isopropyl acrylamide), or PNIPAAm. PNIPAAm exhibits LCST at ~32 °C, which is close to the human body temperature. PNIPAAm chains are subjected to reversible phase transition above the LCST, going from swollen hydrated state to a shrunken dehydrated state, losing about 90% of its volume [10]. For individual polymer chains, the thermoreversible behavior can be thermodynamically controlled by adjusting the polymer composition, shifting the LCST to higher or lower temperature by copolymerization with a hydrophilic or hydrophobic monomer, respectively [6, 11].

The pH is the most commonly used trigger and modulator for the release of drugs in medicine. pH-responsive polymers are a series of stimuli-responsive polymers that can respond to external pH change by effecting the physical and chemical nature. The mechanism of pH-responsive polymers can be defined as polyelectrolytes that contain, in their polymer chain, either weak acidic groups or basic groups that favor protonation or deprotonation depending on the surround

pH values. The acceptance and release of protons of functional groups depending on the pH are associated with their pK_a value [12].

14.2 Stimuli Responsiveness in Polysaccharides

It is known that polysaccharides are intrinsically biocompatible due to resemblance of their structure with many body components. From the viewpoint of polyelectrolytes, polysaccharides can be divided into polyelectrolytes and nonpolyelectrolytes. In polyelectrolyte group, we have positively charged (e.g. chitosan) and negatively charged polysaccharides (e.g. alginate, heparin, hyaluronic acid [HA], pectin, etc.) [13]. Polysaccharides with their unique structure are able to work as SRMs due to their chain conformation, dependent on pH, ions, temperature, and concentration of certain molecules. Therefore, polysaccharides, either in neat or modified form, respond to physiological changes triggered by pH, temperature, light, sounds, ions, solvent composition, pressure, electric and magnetic fields, antigens, and enzymes. The outcomes of their responses may be alterations in phases, shapes, optics, mechanics, electric fields, surface energies, recognition, reaction rates, and permeation rates (Table 14.1) [14]. Due to the presence of various functional groups

Table 14.1 Polysaccharides and their responses.

Polysaccharide	Stimuli
Gellan gum	Temperature, ions, pH
Carrageenan	pH, temperature (with other polysaccharides and metallic particles), ions
Chitosan	Ions, pH, electric field, surfactants, light (grafted with anthracene), temperature (grafted with poly(*N*-isopropylacrylamide) – PNIPAAm, or poly(ethylene oxide) – PEO, or poly(propylene oxide) – PPO, or block copolymers – PEO-PPO-PEO), redox (if thiolated), magnetic (with magnetite – Fe_3O_4), and specific molecules such as dynamic Schiff bases
Scleroglucan	pH, ions
Alginate	Ions, pH, electrical field, surfactant, light (grafted with anthracene), temperature (grafted with PNIPAAm), redox (if thiolated), magnetic (with Fe_3O_4)
Agar	Ions, pH
Chondroitin sulfate	Ions, pH, colon enzymes
Cellulose ethers	Ions, pH, temperature
Guar gum	Ions, pH, temperature
Heparin	Ions, pH, redox (if thiolated)
Hyaluronic acid	Ions, pH, electrical field, surfactant, light (grafted with anthracene), temperature (grafted with PNIPAAm), redox (by itself and if thiolated)
Pectin	Ions, pH, colon enzymes
Xanthan gum	Ions, pH, temperature

Source: Ngwuluka [14]/with permission of Elsevier.

on macromolecular chains, they can be easily modified chemically, thus offering the possibility of obtaining newer polysaccharide derivatives [15].

14.3 Nanofibrous Materials and Electrospinning

Nanofibrous materials can be defined as materials formed from nanofibers with a fiber diameter in nanometer range, possessing properties such as high surface area-to-mass ratio and high density of pores [16]. These unique properties offer them possibilities in different application areas. Due to their unique structure, they are mimicking important features of the native extracellular matrix, showing great promise to restore functions or achieve favorable responses for tissue regeneration [17]. The production of nanofibrous materials is done by several techniques and among them, electrospinning is recognized as one of the most efficient [18]. Electrospinning technique is suitable for the production of pure biopolymer nanofibers and in composition with several additives such as nanoparticles, therapeutic agents, drugs, natural extracts, and dyes, holding promise for different biomedical applications, like tissue engineering, drug delivery, for sensor applications, as well as food processing and microelectronics [19, 20].

Electrospinning is a spinning technique that exploits electrostatic forces for the formation and design of fine fibers from polymer solutions or melts [18]. Formed nanofibers have the diameter from few nano- to few micro-meters with theoretically infinitive length, distinguished also by large active surface area compared to fibers formed by conventional spinning process [21]. The basic electrospinning setup is assembled from power supply (source of electric voltage – few 1000 V), dosing unit (usually needle with syringe), and grounded collecting surface (Figure 14.2).

By looking closer at the polymer solution's path between the dosing unit and the collecting surface, when exposed to an electric field, the path can be divided into four areas. The first area, located right next to the tip of the spinning nozzle, is an area where the polymer Taylor cone formation takes place. Geometry of cone is governed by the ratio of surface tension to electrostatic repulsion. The second region is the

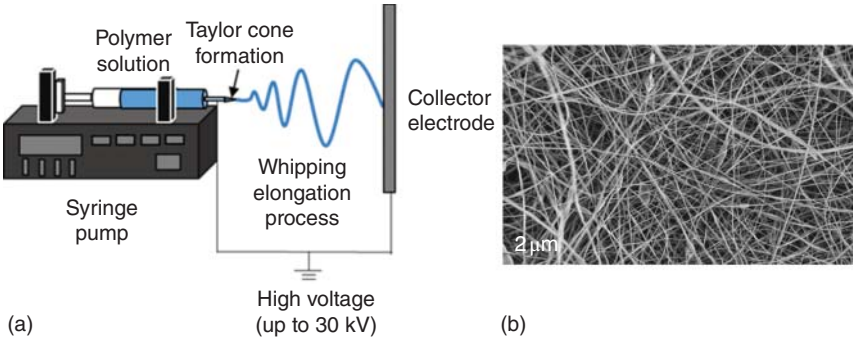

Figure 14.2 (a) Needle electrospinning set-up and (b) scanning electron microscopy (SEM) image of cellulose acetate nanofibers (5 wt% CA).

region of the stable jet, followed by the region of jet instability, due to exposure to numerous forces, stretching the polymer jet and thereby thinning the fiber diameter. This is also the zone of polymers transformation from liquid to solid. The last area of the jet's path is the collecting electrode, where the formed nanofibers are deposited (Figure 14.3).

14.3.1 Taylor Cone Formation

When the spinning solution is pushed through the spinning nozzle of the dosing unit, a spherically shaped droplet is formed at the tip of the nozzle due to the action of surface tension forces. When the polymer solution is exposed to electrical voltage, the droplet is charged and, in addition to the surface tension forces, electrostatic repulsive forces begin to act, causing stress inside the droplet due to the influence of an electric field. By increasing the electric voltage, the forces of the electric field start to strengthen, affecting the electrostatics of the reflecting force in the droplet, allowing the droplet to stretch into a conical shape, called the Taylor cone. Upon formation of the polymer solution into a Taylor cone shape, the surface tension forces and the electrostatic repulsive forces in a droplet are in equilibrium. The tip of the Taylor cone acts as a trigger surface for spinning jet formation (see Figure 14.4) [23, 24].

14.3.2 Polymer Jet Formation

As the electrical voltage increases, we arrive at a critical point where the balance between forces of surface tension and electrostatic forces is disturbed and a charged polymer jet is formed at the top of the conical droplet. The diameter of the jet decreases with increasing jet's traveling distance toward the collecting electrode. During the journey to the collecting surface, the polymer jet is firstly stable and

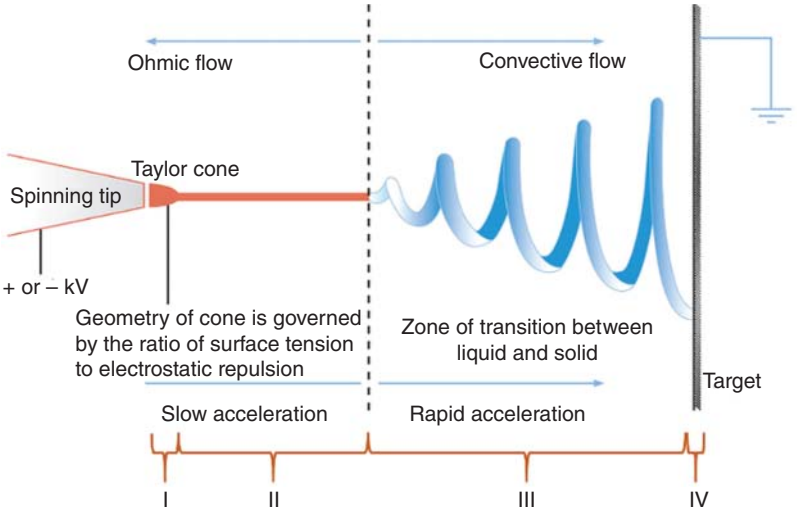

Figure 14.3 Spinning solution's path in electrospinning process. Source: Joanna Gatford, Wikipedia [22]/CC BY 3.0.

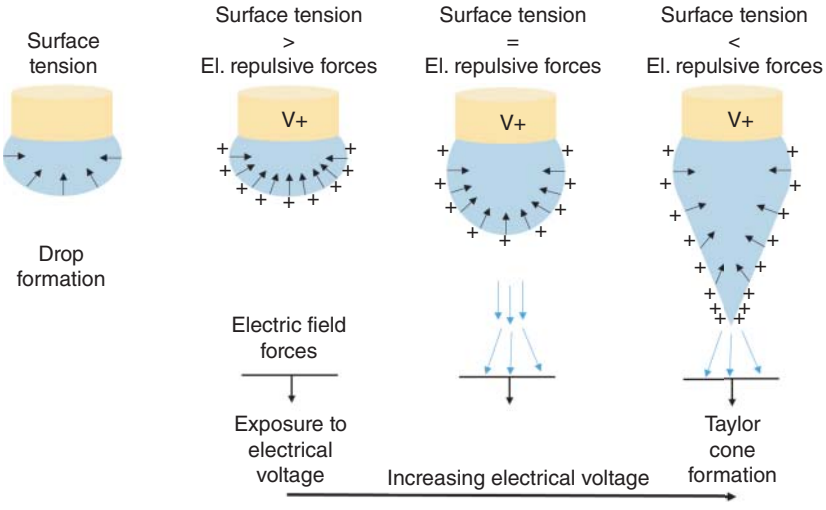

Figure 14.4 Schematic presentation of drop formation and formation of Taylor cone.

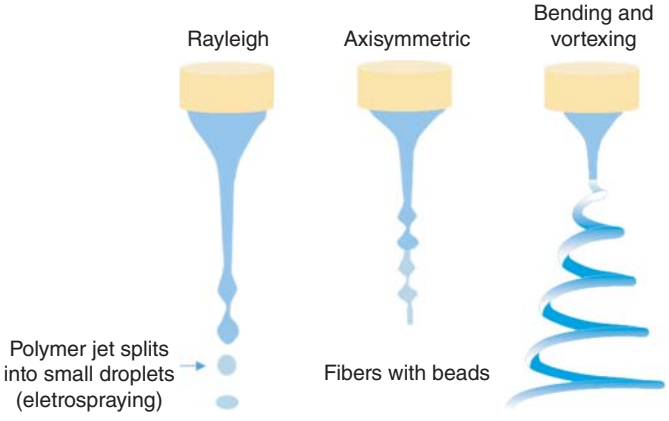

Figure 14.5 Schematic presentation of polymer jet instabilities.

then becomes unstable due to exposure to a number of forces causing three types of physical jet instability. These instabilities affect the diameter, geometry, and morphology of the formed nanofibers [24, 25].

- *Rayleigh instability* occurs when the electric field is weak. In this region of instability, the polymer jet splits into small droplets. The critical value of the surface charge in a polymer jet is called the Rayleigh limit.
- *Axisymmetric instability* is caused by a change in the surface charge density. As a result of this instability, fibers with beads or, e.g. pearls on a string are formed.
- *Bending instability and vortexing* occur under the influence of a strong electric field. In this instability, due to the uneven distribution of the charge, a dipole moment is created perpendicular to the polymer jet, which causes the jet to bend and consequently swirl (Figure 14.5).

14.3.3 Parameters Affecting Electrospinning Process

Morphology and size of electrospun nanofibers are determined by the combination of different parameters affected by solution composition, as well as process and ambient parameters (Table 14.2). Several major parameters need to be controlled and optimized in order to fabricate high-quality electrospun materials. Ideally, electrospun fibers will display consistent diameter, be free of surface defects and beads, and be continuous and collectable [18]. The relationship between fiber morphology and electrospinning parameters is not universal for each type of biopolymer and solvent [26]. By using different electrospinning technologies as well as changing parameters, versatile types of fibers (porous, hollow, core–shell structured, nanocomposite, etc.) and fibrous structures (nonwoven, aligned fiber, multilayered, etc.) can be formed.

Although polysaccharides are very attractive excipients for nanofiber production, it has generally not been possible to achieve high polysaccharide contents in nanofibers. Typically, the formation of electrospun polysaccharide fibers is dependent on the degree of their chain entanglements, the viscosity of the solution, and requires weak shear thinning properties to favor the breakdown of the liquid jet when pulled and extended by the electric field [27]. In case of charged polysaccharides, the chains will repel each other due to their repulsive electrostatic interactions [28]. To obtain nanofibers, the polymer jet must remain unbroken until it reaches the collector plate; therefore, a combination with another uncharged polymer will lower the repelling forces between the polysaccharide chains, and thus enable nanofiber formation. For a number of polysaccharides, the most commonly used copolymers are poly(ethylene oxide) and poly(vinyl alcohol), as nonionogenic, linear, water-soluble, and flexible polymers, showing significant improvement in the spinnability [27–29].

Kurečič et al. [30] reported on the effect of polymer and solvent concentration on cellulose acetate (CA) nanofiber's morphology. They observed beaded morphology with biconcave-shaped disk, connected with very fine strings (Figure 14.6a–d) at lower polymer concentration. A rather low solution viscosity influences the polymer jets in the electrospinning chamber in a way to disintegrate the jet into droplets and to increase the effect of surface tension (electrospraying). This phenomenon is described well by Roemhild et al. [31] in the case of needleless electrospinning. The first step in the formation of the hollow sphere is the formation of a polymer skin during the Taylor cone formation by evaporation of solvent. After the polymer droplet ejects from the electrode, the droplet is disrupted by evaporation of trapped solvent on a pathway to the collecting electrode, which causes the formation of biconcave-shaped discs. By increasing the CA concentration to 15 and 17 wt%, more uniform and smooth fibers are formed, with an average fiber diameter of 237 ± 130 and 312 ± 212 nm, respectively (histogram in Figure 14.6e–h). Formation of smooth nanofibers is attributed to the increase in solutions' viscosity, indicating a larger number of chain entanglements affecting the stabilization of the polymer jet. Stabilization of the polymer jet is connected with the formation of the internal structure, enabling the jet initiation and elongation [32].

Table 14.2 Effects of solution, process, and ambient parameters on nanofiber morphology.

	Polymer solution parameters	
Viscosity (depends on the polymer concentration and molecular weight of the polymer)	Low	– Micro/nanoparticle (electrospraying) – Fibers with beads
	Ideal	– Uniform fibers – Thin fibers
	High	– No fibers, the polymer jet cannot branch off from the Taylor cone
Molecular weight (entanglement of polymer chains affect the continuity of the polymer jet)	Low	– Fibers with beads
	Ideal	– Uniform fibers – Thin fibers
	High	– Microfibers in the form of spiral strip
Concentration (affects the spinning solution viscosity)	Low	– Micro/nanoparticles – Fibers with beads
	Ideal	– Uniform fibers – Thin fibers
	High	– Microfibers in the form of spiral strip
Surface tension (depends on the solvent composition)	Low	– Uniform fibers – Thin fibers
	High	– Fibers with beads
Conductivity (depends on the polymer and solvent used and addition of salts)	Low	– Fibers with beads
	High	– Uniform fibers – Thin fibers
	Process parameters	
Electric voltage (depends on the concentration of polymer solution and the distance between electrodes)	Low	– No fibers, unable to form Taylor cone and jet
	High	– Thinner fibers due to splitting of the origin jet into smaller jets

Dosing speed (affects the time for solution to polymerize and fibers drying time)	Low	– Uniform fibers – Thin fibers
	High	– Fibers with beads – Fibers with large diameter
Electrode distance (affects the fibers drying/solvent evaporation)	Short	– Wet fibers – Fused fibers
	Ideal	– Uniform fibers – Thin fibers
	Long	– Fibers with beads
Nozzle size	Increasing the nozzle diameter affects the diameter of formed fibers, which is proportionally increased	
Nozzle shape (affects the final fiber morphology and product properties)	Needle electrospinning	– Single needle – Multineedle – Coaxial – Triaxial
	Needleless electrospinning	– Wire with knots – Cone – Spiral coil – Round – Cylinder – Disc
	Ambient parameters	
Temperature	High	– By increasing the temperature thinner fibers are formed
Humidity	Low	– Increase in solvent evaporation rate
	High	– Thicker fibers due to the neutralization of jet's charge – Porous fibers

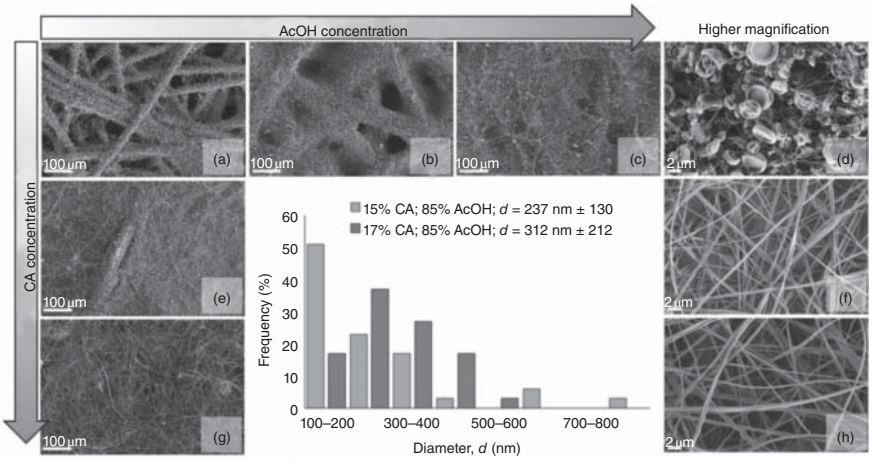

Figure 14.6 Effect of polymer and solvent concentration of nanofiber morphology. SEM images [(a) 12% CA; 75% AcOH; (b) 12% CA; 80% AcOH; (c) 12% CA; 85% AcOH; (d) 12% CA; 85% AcOH (higher magnification); (e) 15% CA; 75% AcOH; (f) 15% CA; 85% AcOH (higher magnification); (g) 17% CA; 75% AcOH; (h) 17% CA; 85% AcOH (higher magnification)] and diameter distribution histogram of 17% CA; 85% AcOH and 15% CA; 85% AcOH electrospun nanofibers. Source: From Kurečič et al. [30]/with permission of Springer Nature.

14.4 Needleless Electrospinning

Despite the enormous application potential, needle electrospun nanofibers meet difficulties in broad applications in practice, due to the lack of an economic and efficient way to scale up the electrospinning process [33]. Needleless electrospinning has emerged as a new electrospinning mode showing ability to produce nanofibers on large scales [34]. Needleless electrospinning is featured as electrospinning of nanofibers directly from an open liquid surface on which numerous polymer jets are formed simultaneously, without the influence of capillary effect that is normally associated with needle-like nozzles [18, 35]. The first needleless electrospinning system was patented in 1979, and it is used a ring as spinneret for electrostatic production of fiber fleece [36]. In 2005, a horizontal rotating cylinder was invented as a generator of multiple jets from liquid surface, for mass electrospinning of nanofibers, and this technique was rapidly commercialized by Elmarco Co. with a brand name "Nanospider™" [37].

By comparing technology of needle and needleless electrospinning, the main advantage of this technology is initiation of Taylor cones and solution jets naturally in the optimal position, next to each other, on the surface of the rotating spinning electrode emerging from the polymer solution. The waves of an electrically conductive liquid self-organize on a mesoscopic scale and finally form Taylor cones and polymer jets when the applied electric field intensity is above a critical value (Figure 14.7) [38, 39]. Polymer jet initiation and resulting fiber morphology are highly influenced by the electric field intensity profile around the spinneret and in the electrospinning zone, governed by the applied voltage and the shape of the needleless spinneret [30].

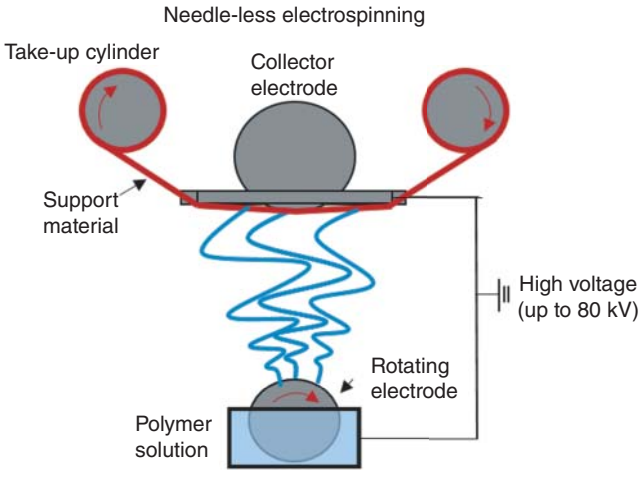

Figure 14.7 Needleless electrospinning set-up.

The rotating needleless electrospinning setup uses mechanical forces to assist in the jet initiation from the surface of the polymer, while in the case of stationary needleless electrospinning the initiation of jet occurs from the liquid surface with the use of external forces, such as magnetic fields, gravity, and the flow of gases [40]. The rotation of spinneret has two functions: loading the polymer solution onto electrospinning sites and enabling electrospinning of loaded solution into nanofibers [41]. Formation of polymer jets in needleless electrospinning has been proposed as four steps [42]:

(1) Formation of polymer solution's thin layer on the spinneret surface due to its partial immersion in the solution and rotation
(2) By spinneret rotation the perturbation occurs on the solution layer, inducing the formation of conical spikes on the solution surface
(3) By applying the high voltage, the conical spikes concentrate electric forces and intensifying the perturbations to form Taylor cones
(4) By increasing the voltage, numerous polymer jets are distributed over the electrode surface with certain periodicity and stretched out from Taylor cones. This process is driven by a high electric field and enormous number of solution filaments is generated from the roller surface, resulting in fibers on the collecting electrode (Figure 14.8).

14.5 Electrospinning Techniques for Preparation of Stimuli-Responsive Nanofibers

14.5.1 Blend Electrospinning

Blend electrospinning is a conventional electrospinning technique that allows exploitation of the favorable characteristics from two polymers or mixing of active agents with polymer solutions. In this relatively simple technique, the

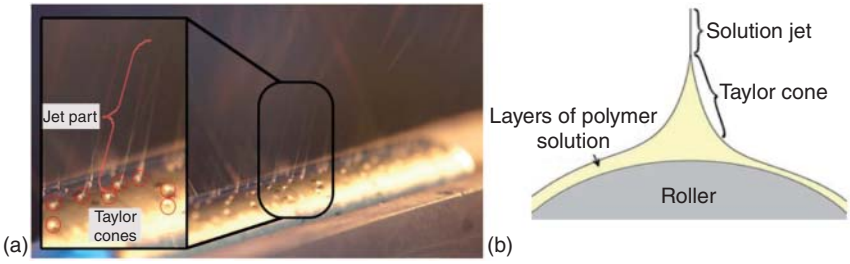

Figure 14.8 Formation of Taylor cones and polymer jets on a rotating electrode. (a) Formation of Taylor cones and polymer jets on rotating electrode, (b) scheme interpretation of Taylor cone and polymer jet. Source: Yalcinkaya et al. [43]/with permission of SAGE Publications.

drug/biomolecules are dispersed or dissolved in the polymer solution, resulting in the development of nanofibers with drug/biomolecules dispersed throughout the fibers [44]. Blend electrospinning has been tested for a wide range of substances such as antibiotics, cytostatic, and anti-inflammatory drugs. The technology is especially useful for the delivery of small molecules. Blend electrospinning was successfully used for encapsulation of antimicrobial peptides. Utilization of blend electrospinning for delivery of proteins is problematic due to harsh environment during encapsulation [45]. Although this method is simple in contrast with other electrospinning methods, the solvents used for the dispersion of bioactive molecules can lead to protein denaturation or loss of biological activity. In addition, the inherent charge of the biomolecules can often result in their migration on the jet surface and thereby result in their distribution on the surface of the nanofibers rather than the encapsulated matrix [44]. Blend electrospinning can be used to develop nanofibers with burst release, while coaxial and emulsion electrospinning can be used to generate core–shell nanofibers that can assist in sustained drug release [45].

14.5.2 Coaxial Electrospinning

A coaxial electrospinning setup allows the encapsulation of bioactive agents into the polymer nanofibers developing core–shell matrices [46]. It uses a dual-solution feed system allowing injection of inner fluid – nonpolymeric Newtonian liquid or even powder (core) and outer fluid – polymer solution (shell) to spinneret (Figure 14.9) [48]. Under high voltage, the electrospinning liquid is drawn out from spinneret forming Taylor cone with a core–shell structure, allowing the formation and collection of core–shell fibers [49].

In the process of coaxial electrospinning, spinning parameters have a high impact on the formation of a coaxial jet, and furthermore, affect the properties of the collected fiber. Low fluid viscosity makes it difficult for the core layer to follow the bending and vortexing action of the shell fluid, and therefore perfect core–shell nanofibers with uniform structure are unattainable. When the shell fluid of a polymer matrix has a very high concentration, the efficient coaxial electrospinning is also difficult. For the preparation of coaxial composite nanofibers with superior morphology, a common approach is to reduce the concentration of the

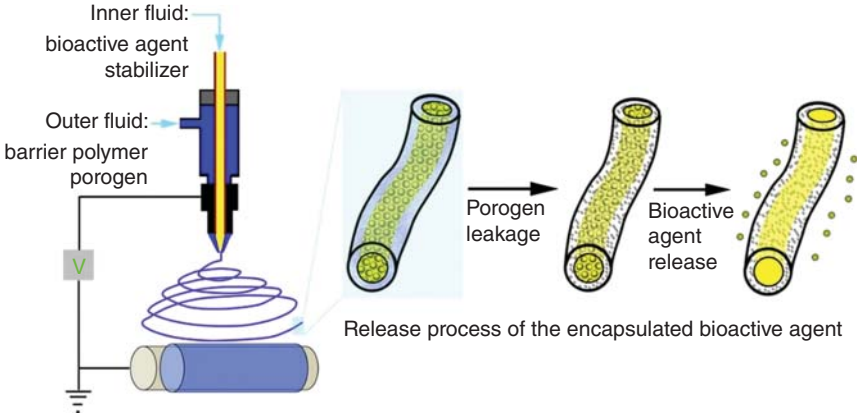

Figure 14.9 Schematic presentation of core–shell electrospinning. Source: Jiang et al. [47]/with permission of Elsevier.

electrospinning solution to be as low as possible. However, a high enough chain-entangling density in the working solution is necessary to prevent capillary breakup and Rayleigh instability, which is the principal factor for producing thinner nanofibers with uniform structures [50].

Core–shell structured nanofibers made by coaxial electrospinning have many applications in bio-medicine, optoelectronic devices, and absorption filtration. In the field of medicine, they can preserve unstable biological reagents or viruses effectively, to prevent the decomposition of unstable compounds. Core–shell structured nanofibers also serve as molecular drug slow-release materials. By adjusting the shell's thickness of the nanofibers, the drug-release rate can be controlled [50]. The main advantages of the process are the possibility of core/shell nanofiber formation from miscible and immiscible polymers, the high loading capacity of bioactive molecules, the sustained release from fibers, and a less harsh process enabling the delivery of susceptible compounds [51].

14.5.3 Emulsion Electrospinning

In comparison with coaxial electrospinning, emulsion electrospinning is a method for production of core–shell fibers, using an ordinary single-nozzle spinning setup (Figure 14.10). It is a modification of the blend electrospinning process based on the mixing of immiscible solvents. The dispersed drops in the emulsion form the core in the electrospun fibers, and the continuous polymer becomes the shell [51]. This technique is used for incorporation of functional additives (e.g. food bioactive compounds, enzymes, peptides, flavonoids, proteins, and drugs) into biodegradable polymer fibers, forming core–shell structures [46]. The application of emulsion nanofiber system has been reported to result in the sustained release, good bioactivity, and effectiveness of encapsulated drugs after delivery and release, and to simplify the metabolism, proliferation, and differentiation of cells [52].

Emulsion-based systems are useful for encapsulating, protecting, and releasing valuable ingredients consisting of oil, surfactant/cosurfactant, and water. Emulsion

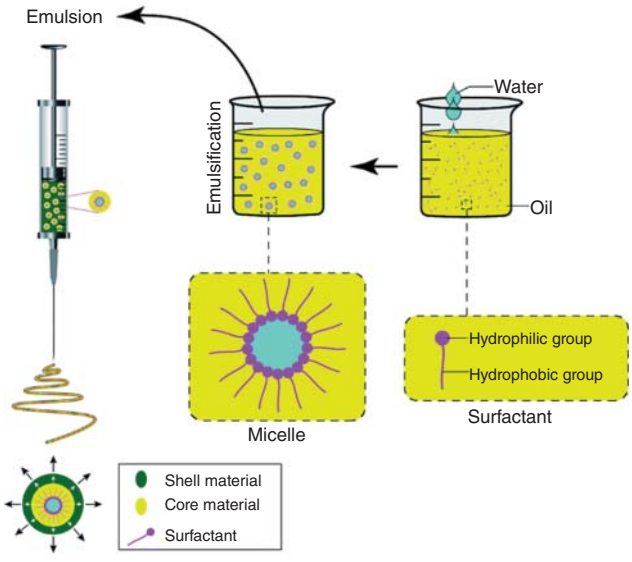

Figure 14.10 Schematic presentation of emulsion electrospinning. Source: Nikmaram et al. [52]/Royal Society of Chemistry/CC BY 3.0.

systems can be categorized into oil-in-water (O/W) and water-in-oil (W/O) emulsions, depending on the organization of oil and water phases. In an O/W emulsion, oil droplets are dispersed in the continuous water phase, while W/O emulsions are dispersions of aqueous droplets in the oil phase. The substance that makes up the droplets in an emulsion is referred to as the "dispersed phase," while the surrounding liquid substance is called "continuous phase" [52].

During the emulsion electrospinning process, the solvent from the region close to the surface evaporates more quickly than the central part of the polymer jet, resulting in a rapid increase in the viscosity of the outer layer compared to that of the inner layer. Subsequently, the inward movement of emulsion droplets is induced from the surface to the center, and the droplets are simultaneously condensed and stretched into elliptical shapes in the axial direction of nanofibers under the force of a high-voltage electric field [53].

However, both coaxial and emulsion electrospinning have several disadvantages in the current setup. The main limitation is the productivity of the method associated with the needle-based process and the rapid burst release of embedded functional additives. Therefore, there have been already some attempts to upgrade the emulsion electrospinning in needleless technique (e.g. needleless emulsion electrospinning) [51].

14.6 Stimuli-Responsive Polysaccharide-Based Nanofibrous Materials for Wound Dressings Application

Electrospinning, as a technique for production of nanofibers with high ratio of active surface area to volume, is particularly attractive for biomedical applications, taking

advantage to increase drug loading and cell attachment attributes. This technique is attractive in a variety of biomedical applications such as drug release, tissue engineering, and wound dressings for its high loading efficiency, flexibility in surface functionalities, versatility of drug incorporation, simple procedure, feasible massive production, wide range of usable polymers, and low cost [6]. In addition, electrospun nanofibers can reduce the burst release of drug *in vitro* to some extent, regulated via selecting different polymer matrix. Moreover, electrospun nanofibers can encapsulate different drugs, from antibiotics, anticancer, to anti-inflammatory [54, 55]. By combining electrospinning technology with SRMs, "smart" nanofibrous materials can be produced [56, 57]. Such materials can effectively control or manage the delivery of drugs from nanofibers not only *in vitro* but also *in vivo* conditions [58] (Figure 14.11).

Nanofiber-based drug-delivery systems are widely applicable for specific drug release, according to the target location and timing, to achieve the desired

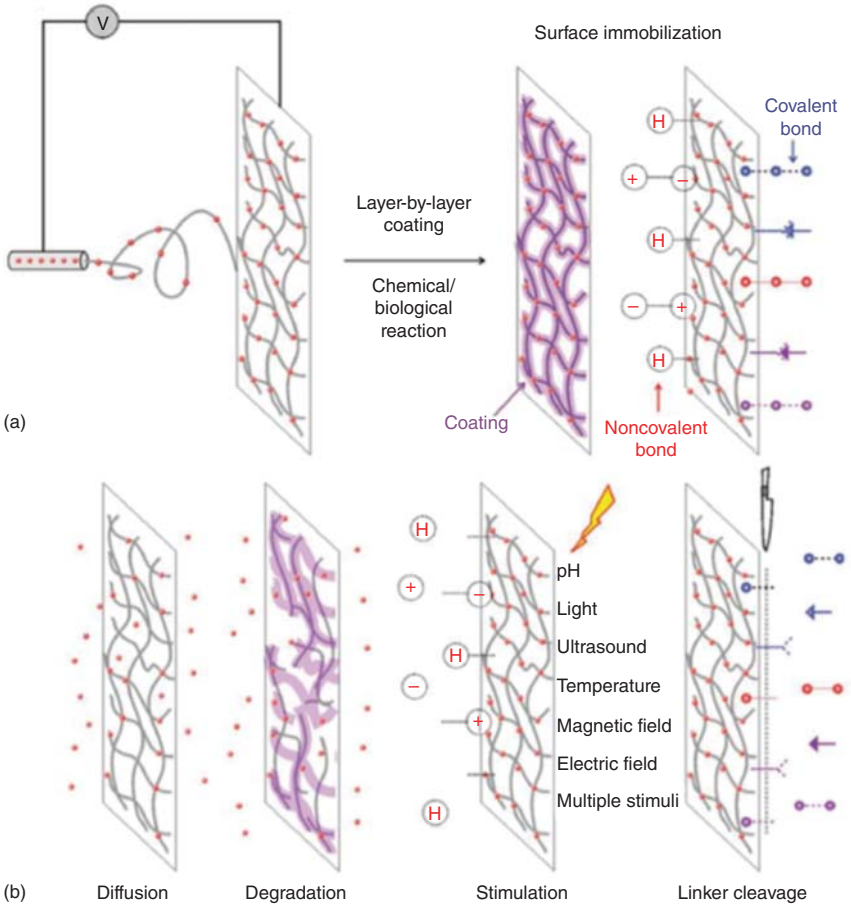

Figure 14.11 Loading and release of drugs from electrospun nanofibers: (a) different loading methods and (b) their release mechanisms. Source: Gao et al. [58]/with permission of Royal Society of Chemistry.

therapeutic effects [59]. Kajdič et al. prepared a review paper on various types of nanofibers from the latest available literature, based on their composition and drug-release properties, where only few examples can be found dealing with polysaccharide-based nanofibers. Namely, Li et al. reported on the preparation of thermosensitive drug-delivery system prepared by blend electrospinning. The first criterion for developing an effective delivery system is to ensure the excess release of the encapsulated drug into the physiological environment. In their study, they reported on the use of thermosensitive polymer poly(di(ethylene glycol)methyl ether methacrylate) (PDEGMA), having similar thermoresponsive properties as *N*-isopropylacrylamide (NIPPAM), in combination with ethyl cellulose (EC) to prepare "smart" nanofibrous materials. As a model drug, they used ketoprofen (KET). *In vitro* drug-release studies showed that KET was released over a prolonged time period with the fibers having different profiles at 25 and 37 °C, reflecting their thermosensitive properties (Figure 14.12). Furthermore, the materials were found to have good biocompatibility toward L929 fibroblasts [60].

Khorshidi et al. developed an antibiotic-loaded electrospun materials with improved drug delivery via acoustic stimulation. Ultrasonication with ultrasonic stimuli at 15 W/cm^2 intensity increased drug release from material due to disturbance of ionic crosslinking of alginate network. These alginate nanofibers revealed three times more drug-release properties with ultrasonic stimuli and endowed higher percentages of bacterial DNA synthesis inhibition in both in *Escherichia coli* and *Staphylococcus aureus*, enhancing bactericidal and bacteriostatic activities of antibiotics [61].

Slemming-Adamsen et al. reported on the preparation of thermoresponsive drug release from PNIPAAm/gelatin nanofibers in the presence of the crosslinking agents 1-ethyl-3-(3-dimethyl-aminopropyl)-1-carbodiimide hydrochloride (EDC)

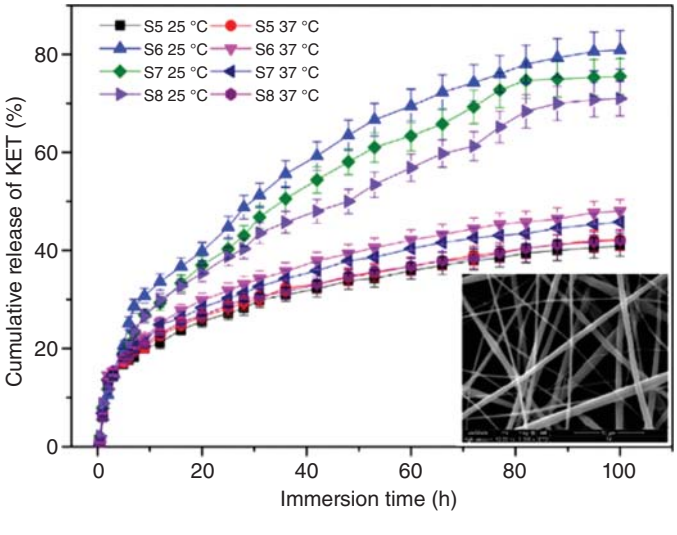

Figure 14.12 *In vitro* release profile of KET upon different environment temperature. Source: From Li et al. [60]/with permission of Elsevier.

and *N*-hydroxysuccinimide (NHS) and described a straightforward approach for encapsulating and releasing drugs. *In situ* EDC/NHS crosslinked PNIPAM–gelatin nanofibers show dynamically and reversibly swelling/deswelling properties. When an anticancer drug doxorubicin (DOX) was loaded, the fibers were able to release DOX evidently on demand of a temperature rise, and the released DOX could effectively lower the viability of human cervical cancer Hela cells [62] (Figure 14.13).

Devarayan and Kim reported on the development of an eco-friendly, reversible pH sensor based on electrospun cellulose nanofibers functionalized with a natural pigment from red cabbage (RC) [63], while Pakolpakçıl et al. reported on the use of RC in preparation of pH sensoric nanofibrous mat from mixture of alginate and polyvinyl alcohol (PVA) [64]. In Figure 14.14 are presented results of prepared CA nanofibrous mats with halochromic behavior for the purpose of monitoring wound healing upon pH change. Nanofibrous mats exhibited color change upon exposure to different pH conditions [63].

Behnaz et al. fabricated pH-sensitive composite nanofibers using chitosan (CS), polyethylene oxide (PEO), and graphite oxide (GO) using glyoxal as a crosslink agent and DOX model drug (Figure 14.15). The π–π stacking interaction between DOX and GO with fine pores of nanofibrous scaffolds exhibited higher drug loading (98%) and controlled release of the DOX-loaded PEO/CS/GO nanofibers. The results of DOX release from nanofibrous scaffolds at pH 5.3 and 7.4 indicated strong pH dependence. The hydrogen-bonding interaction between GO and DOX could be unstable under acidic conditions, which resulted in faster drug-release rate in pH 5.3. Thus, the prepared nanofibrous scaffold offers as a novel formulation for treatment of lung cancer [65].

Schoolaert et al. reported on the fast-responding and user-friendly biocompatible, halochromic nanofibrous sensors, successfully fabricated by incorporating the halochromic dyes Methyl Red and Rose Bengal inside a chitosan/poly(ε-caprolactone) nanofibrous matrix. The commonly applied dye-doping technique frequently suffers from dye-leaching, which not only reduces the sensor's sensitivity over time but can also induce adverse effects. Therefore, in this work, dye immobilization is accomplished by covalent dye modification of chitosan before blend electrospinning. It is shown that efficient dye immobilization with minimal dye leaching is achieved within the biomedical relevant pH region, without significantly affecting the halochromic behavior of the dyes. Moreover, the nanofibers show high and reproducible pH sensitivity by providing an instantaneous color change in response to change in pH in aqueous medium and when exposed to acidic or basic gases. The results stated within this work are of particular interest for natural (bio)polymers for which covalent modification combined with electrospinning provides a universal method for versatile dye functionalization of large area nanofibrous membranes with proper dye immobilization [66].

Kurečič et al. reported the preparation of multifunctional bio-based nanofibrous mats containing the commonly used pain reducing local anesthetic benzocaine (BZC) and the *in situ* pH-detecting dye bromocresol green (BCG), by using large-scale needleless electrospinning. Such material can serve as a dual

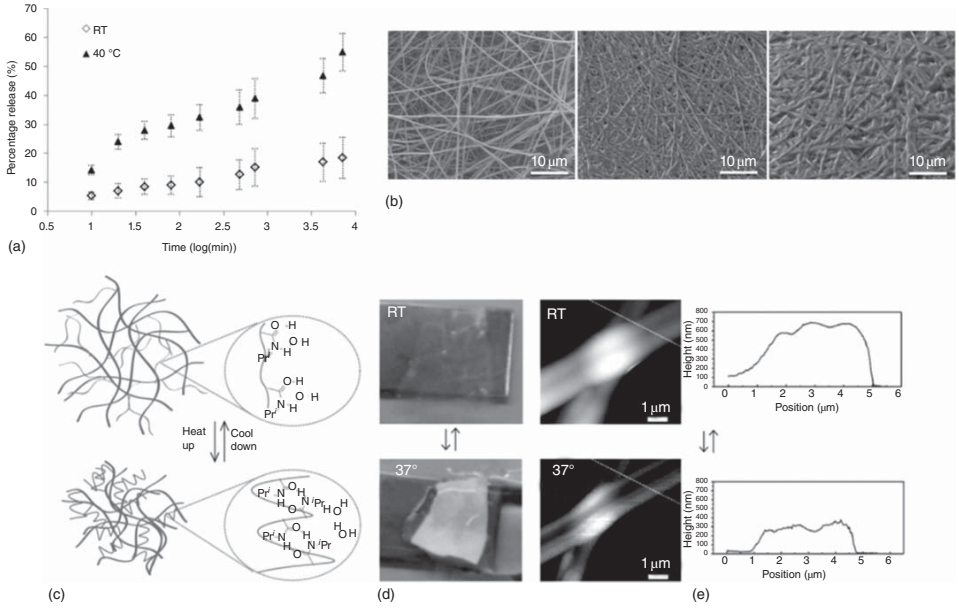

Figure 14.13 PNIPAAm/gelatin nanofibers with loaded DOX and their release profile upon different temperature; swelling/deswelling mechanism. (a) DOX release profiles; effect of temperature, (b) SEM images of DOX loaded nanofibers before and after swelling/deswelling. Source: From Slemming-Adamsen et al. [62]/with permission of John Wiley & Sons.

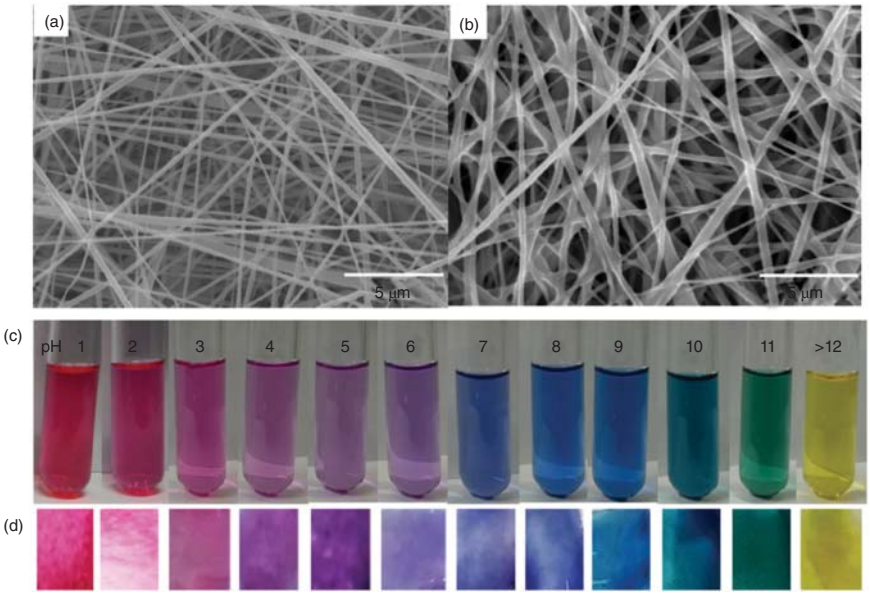

Figure 14.14 (a) SEM images of prepared CA/RC nanofibers, regenerated CA/RC nanofibers (b). Color schemes of (c) RC extract solution and (d) CA/RC regenerated nanofibrous mats at pH 1–14. Source: From Devarayan and Kim [63]/with permission of Elsevier.

nano-carrier system for wound-healing applications, especially in the treatment of infected wounds. BZC and BCG were introduced into CA-based nanofibers using a single-step blend needleless electrospinning process. Results from the *in vitro* drug-release studies showed a pH dependent (i.e. controllable) release of BZC and confirmed the expected maximum drug-release rate at pH 9.0, which would correspond clinically to the pH of an infected wound. The accompanying color change of the nanofibrous mats, provided through the encapsulated BCG (from yellow to blue), is noticeable within a few seconds after the pH changes from acidic to alkaline (Figure 14.16). Due to their rapid coloration (noticeable within a few seconds) upon pH change and response of non-steroid anti-inflammatory drugs (NSAID), the use of the developed materials in actual clinical settings could enable potential patients, as well as treating physicians, a faster response to complications during wound treatment [30].

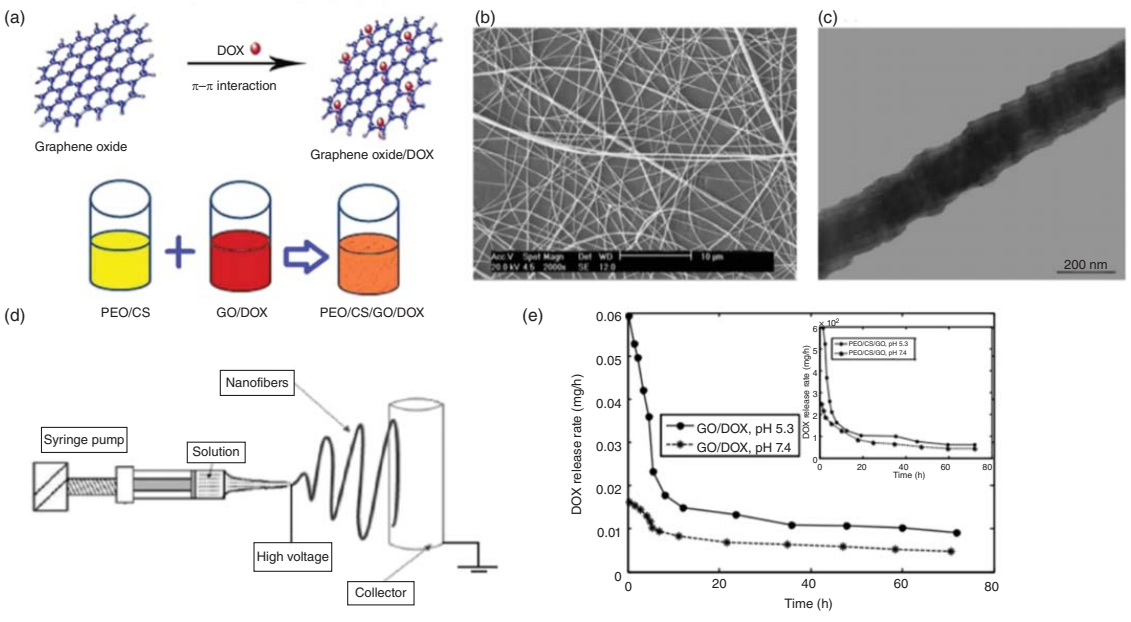

Figure 14.15 Scheme of PEO/CS/GO/DOX nanofiber preparation and release profile of DOX upon different pH environment (a) polymer solution preparation scheme, (b) SEM images of formed electrospun nanofibers, (c) SEM images of morphology of EO/CS/GO/DOX nanofibers, (d) scheme of electrospinning process, (e) DOX release profiles; effect of pH. Source: From Ardeshirzadeh et al. [65]/with permission of Elsevier.

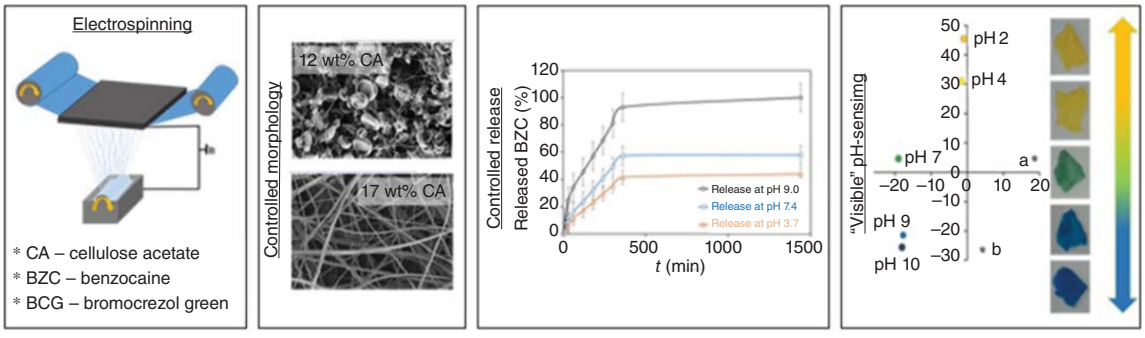

Figure 14.16 Prepared CA nanofibers and their release profile combined with color change upon different pH. Source: From Kurečič et al. [30]/with permission of Springer Nature.

14.7 Conclusions

SRMs with their ability to respond and change upon a certain stimulus are gaining significant interest in many application fields, not only as stimuli-responsive polymers, but also as composite materials. Beside well-known synthetic-responsive polymers, polysaccharides, with their intrinsic biocompatibility and structural resemblance with many body components, are finding applications in biomedical field, especially as nanofibrous materials. Electrospinning, as a technique for production of nanofibrous materials, with their porous structure and large active surface area, is taking advantage of drug loading and cell attachment attributes. The production of nanofibers is far from an easy method, due to variety of parameters affecting the spinning process (formation of Taylor cone, polymer jet instability, fiber diameter, etc.). Formation of uniform and defect-free nanofibers can be tuned with polymer solution parameters as well as process and ambient parameters. Stimuli-responsive polysaccharide-based nanofibrous materials are reported as drug-delivery systems, for specific targeted location and timed drug release as well as pH sensors for wound-healing monitoring and lately as multifunctional materials with combined properties of simultaneous wound monitoring and healing.

References

1 Bronzino, J.D. and Peterson, D.R. (2015). *The Biomedical Engineering Handbook: Four Volume Set*, 4e. CRC Press https://doi.org/10.1201/b18423.

2 Rebouillat, S. and Pla, F. (2019). A review: on smart materials based on some polysaccharides; within the contextual bigger data, insiders, "improvisation" and said artificial intelligence trends. *J. Biomater. Nanobiotechnol.* 10 (2): 41–77.

3 Esther, L., Piselli, A., Faucheu, J. et al. (2014). Smart materials: development of new sensory experiences through stimuli responsive materials. In: *5th STS Italia Conference A Matter of Design: Making Society Through Science and Technology* (ed. C. Coletta, S. Colombo, P. Magaudda, et al.), 367–382. STS Italia.

4 El-Sherbiny, I.M., Khalil, I.A., and Ali, I.H. (2018). Updates on stimuli-responsive polymers: synthesis approaches and features. In: *Polymer Gels*, 129–146. Springer.

5 Shafranek, R.T., Millik, S.C., Smith, P.T. et al. (2019). Stimuli-responsive materials in additive manufacturing. *Prog. Polym. Sci.* 93: 36–67.

6 Wei, M., Gao, Y., Li, X., and Serpe, M.J. (2017). Stimuli-responsive polymers and their applications. *Polym. Chem.* 8 (1): 127–143.

7 Teotia, A., Sami, H., and Kumar, A. (2015). Thermo-responsive polymers: structure and design of smart materials. In: *Switchable and Responsive Surfaces and Materials for Biomedical Applications* (ed. Z. Zhang), 3–43. Elsevier.

8 Futscher, M.H., Philipp, M., Müller-Buschbaum, P., and Schulte, A. (2017). The role of backbone hydration of poly(*N*-isopropyl acrylamide) across the volume phase transition compared to its monomer. *Sci. Rep.* 7 (1): 1–10.

9 Chatterjee, S. and Hui, C.-L. (2019). Review of stimuli-responsive polymers in drug delivery and textile application. *Molecules* 24 (14): 2547.

10 Zhang, K., Zhu, X., Jia, F. et al. (2013). Temperature-activated nucleic acid nanostructures. *J. Am. Chem. Soc.* 135 (38): 14102–14105.

11 Tauer, K., Gau, D., Schulze, S. et al. (2009). Thermal property changes of poly(*N*-isopropylacrylamide) microgel particles and block copolymers. *Colloid. Polym. Sci.* 287 (3): 299.

12 Reyes-Ortega, F. (2014). pH-responsive polymers: properties, synthesis and applications. In: *Smart Polymers and Their Applications*, 45–92. Elsevier.

13 Muntimadugu, E., Ickowicz, D.E., Domb, A.J., and Khan, W. (2013). Polysaccharide biomaterials. *Isr. J. Chem.* 53 (9–10): 787–794.

14 Ngwuluka, N.C. (2018). Responsive polysaccharides and polysaccharides-based nanoparticles for drug delivery. In: *Stimuli Responsive Polymeric Nanocarriers for Drug Delivery Applications*, vol. 1 (ed. A.S.H. Makhlouf and N.Y. Abu-Thabit), 531–554. Elsevier.

15 Laha, B., Maiti, S., Sen, K.K., and Jana, S. (2019). Nanoscale polysaccharide-based particles for the delivery of therapeutic molecules. In: *Green Synthesis, Characterization and Applications of Nanoparticles* (ed. A.K. Shukla and S. Iravani), 347–368. Elsevier.

16 Lim, C.T. (2017). Nanofiber technology: current status and emerging developments. *Prog. Polym. Sci.* 70: 1–17.

17 Wang, X., Ding, B., and Li, B. (2013). Biomimetic electrospun nanofibrous structures for tissue engineering. *Mater. Today* 16 (6): 229–241.

18 Mishra, R.K., Mishra, P., Verma, K. et al. (2019). Electrospinning production of nanofibrous membranes. *Environ. Chem. Lett.* 17 (2): 767–800.

19 Thenmozhi, S., Dharmaraj, N., Kadirvelu, K., and Kim, H.Y. (2017). Electrospun nanofibers: new generation materials for advanced applications. *Mater. Sci. Eng., B* 217: 36–48.

20 Bhattarai, R.S., Bachu, R.D., Boddu, S.H., and Bhaduri, S. (2019). Biomedical applications of electrospun nanofibers: drug and nanoparticle delivery. *Pharmaceutics* 11 (1): 5.

21 Luo, C., Stoyanov, S.D., Stride, E. et al. (2012). Electrospinning versus fibre production methods: from specifics to technological convergence. *Chem. Soc. Rev.* 41 (13): 4708–4735.

22 Wikipedia. Electrospinning. https://en.wikipedia.org/wiki/Electrospinning (accessed 09 April 2022).

23 Garg, K. and Bowlin, G.L. (2011). Electrospinning jets and nanofibrous structures. *Biomicrofluidics* 5 (1): 013403.

24 Haider, S., Haider, A., Alghyamah, A.A. et al. (2019). Electrohydrodynamic processes and their affecting parameters. In: *Electrospinning and Electrospraying-Techniques and Applications* (ed. S. Haider and A. Haider), 3–21. IntechOpen.

25 Šimko, M. and Lukáš, D. (2016). Mathematical modeling of a whipping instability of an electrically charged liquid jet. *Appl. Math. Modell.* 40 (21–22): 9565–9583.

26 Angel, N., Guo, L., Yan, F. et al. (2020). Effect of processing parameters on the electrospinning of cellulose acetate studied by response surface methodology. *J. Agric. Food Res.* 2: 100015.

27 Shekarforoush, E., Faralli, A., Ndoni, S. et al. (2017). Electrospinning of xanthan polysaccharide. *Macromol. Mater. Eng.* 302 (8): 1700067.

28 Mirtič, J., Balažic, H., Zupančič, Š., and Kristl, J. (2019). Effect of solution composition variables on electrospun alginate nanofibers: response surface analysis. *Polymers (Basel)* 11 (4): 692.

29 Guo, M.Q., Hu, X., Wang, C., and Ai, L. (2017). Polysaccharides: structure and solubility. In: *Solubility of Polysaccharides* (ed. Zhenbo Xu), 7–21. Intech Open.

30 Kurečič, M., Maver, T., Virant, N. et al. (2018). A multifunctional electrospun and dual nano-carrier biobased system for simultaneous detection of pH in the wound bed and controlled release of benzocaine. *Cellulose* 25 (12): 7277–7297.

31 Roemhild, K., Niemz, F., Mohan, T. et al. (2016). The cellulose source matters – hollow semi spheres or fibers by needleless electrospinning. *Macromol. Mater. Eng.* 301 (1): 42–47.

32 Rošic, R., Pelipenko, J., Kristl, J. et al. (2013). Physical characteristics of poly(vinyl alcohol) solutions in relation to electrospun nanofiber formation. *Eur. Polym. J.* 49 (2): 290–298.

33 Lin, T. (2012). Needleless electrospinning: a practical way to mass production of nanofibers. *J. Text. Sci. Eng.* 2 (6): 3.

34 Wei, L., Sun, R., Liu, C. et al. (2019). Mass production of nanofibers from needleless electrospinning by a novel annular spinneret. *Mater. Des.* 179: 107885.

35 Niu, H. and Lin, T. (2012). Fiber generators in needleless electrospinning. *J. Nanomater.* 2012: 1–13.

36 Simm, W., Gosling, C., Bonart, R., and Falkai, B.V. (1979). Fibre fleece of electrostatically spun fibres and methods of making same. US4143196A. https://patents.google.com/patent/US4143196A/en.

37 Jirsak, O.S., Sanetrnik, F., Lukas, D., et al. (2009) Method of nanofibres production from a polymer solution using electrostatic spinning and a device for carrying out the method. US7585437B2. https://patents.google.com/patent/US7585437B2/en.

38 Niu, H., Lin, T., and Wang, X. (2009). Needleless electrospinning. I. A comparison of cylinder and disk nozzles. *J. Appl. Polym. Sci.* 114 (6): 3524–3530.

39 Poshina, D.N., Khadyko, I.A., Sukhova, A.A. et al. (2020). Needleless electrospinning of a chitosan lactate aqueous solution: influence of solution composition and spinning parameters. *Technologies* 8 (1): 2.

40 Nagam Hanumantharao, S. and Rao, S. (2019). Multi-functional electrospun nanofibers from polymer blends for scaffold tissue engineering. *Fibers* 7 (7): 66.

41 Wang, X., Niu, H., Wang, X., and Lin, T. (2012). *Needleless Electrospinning of Uniform Nanofibers Using Spiral Coil Spinnerets*, vol. 2012. London, GBR: Hindawi Limited https://doi.org/10.1155/2012/785920.

42 Wang, X., Niu, H., Lin, T., and Wang, X. (2009). Needleless electrospinning of nanofibers with a conical wire coil. *Polym. Eng. Sci.* 49 (8): 1582–1586.

43 Yalcinkaya, B., Callioglu, F.C., and Yener, F. (2014). Measurement and analysis of jet current and jet life in roller electrospinning of polyurethane. *Text. Res. J.* 84 (16): 1720–1728.

44 Shahriar, S., Mondal, J., Hasan, M.N. et al. (2019). Electrospinning nanofibers for therapeutics delivery. *Nanomaterials (Basel)* 9 (4): 532.

45 Buzgo, M., Mickova, A., Rampichova, M., and Doupnik, M. (2018). Blend electrospinning, coaxial electrospinning, and emulsion electrospinning techniques. In: *Core-Shell Nanostructures for Drug Delivery and Theranostics* (ed. M.L. Focarete and A. Tampieri), 325–347. Elsevier.

46 Iacob, A.-T., Drăgan, M., Ionescu, O.-M. et al. (2020). An overview of biopolymeric electrospun nanofibers based on polysaccharides for wound healing management. *Pharmaceutics* 12 (10): 983.

47 Jiang, H., Wang, L., and Zhu, K. (2014). Coaxial electrospinning for encapsulation and controlled release of fragile water-soluble bioactive agents. *J. Controlled Release* 193: 296–303.

48 Yarin, A. (2011). Coaxial electrospinning and emulsion electrospinning of core–shell fibers. *Polym. Adv. Technol.* 22 (3): 310–317.

49 Begum, H. and Khan, K. (2017). Study on the various types of needle based and needleless electrospinning system for nanofiber production. *Int. J. Text. Sci.* 6: 110–117.

50 Li, C., Li, Q., Ni, X. et al. (2017). Coaxial electrospinning and characterization of core-shell structured cellulose nanocrystal reinforced PMMA/PAN composite fibers. *Materials (Basel)* 10 (6): 572.

51 Buzgo, M., Filova, E., Staffa, A.M. et al. (2018). Needleless emulsion electrospinning for the regulated delivery of susceptible proteins. *J. Tissue Eng. Regener. Med.* 12 (3): 583–597.

52 Nikmaram, N., Roohinejad, S., Hashemi, S. et al. (2017). Emulsion-based systems for fabrication of electrospun nanofibers: food, pharmaceutical and biomedical applications. *RSC Adv.* 7 (46): 28951–28964.

53 Zhang, C., Feng, F., and Zhang, H. (2018). Emulsion electrospinning: fundamentals, food applications and prospects. *Trends Food Sci. Technol.* 80: 175–186.

54 Sill, T.J. and von Recum, H.A. (2008). Electrospinning: applications in drug delivery and tissue engineering. *Biomaterials* 29 (13): 1989–2006.

55 Hu, X., Liu, S., Zhou, G. et al. (2014). Electrospinning of polymeric nanofibers for drug delivery applications. *J. Controlled Release* 185: 12–21.

56 Rogina, A. (2014). Electrospinning process: versatile preparation method for biodegradable and natural polymers and biocomposite systems applied in tissue engineering and drug delivery. *Appl. Surf. Sci.* 296: 221–230.

57 Yu, D., Chian, W., Wang, X. et al. (2013). Linear drug release membrane prepared by a modified coaxial electrospinning process. *J. Membr. Sci.* 428: 150–156.

58 Gao, S., Tang, G., Hua, D. et al. (2019). Stimuli-responsive bio-based polymeric systems and their applications. *J. Mater. Chem. B* 7 (5): 709–729.

59 Kajdič, S., Planinšek, O., Gašperlin, M., and Kocbek, P. (2019). Electrospun nanofibers for customized drug-delivery systems. *J. Drug Delivery Sci. Technol.* 51: 672–681.

60 Li, H., Liu, K., Sang, Q. et al. (2017). A thermosensitive drug delivery system prepared by blend electrospinning. *Colloids Surf., B* 159: 277–283.

61 Khorshidi, S. and Karkhaneh, A. (2018). On-demand release of ciprofloxacin from a smart nanofiber depot with acoustic stimulus. *J. Biosci.* 43 (5): 959–967.

62 Slemming-Adamsen, P., Song, J., Dong, M. et al. (2015). *In situ* cross-linked PNIPAM/gelatin nanofibers for thermo-responsive drug release. *Macromol. Mater. Eng.* 300 (12): 1226–1231.

63 Devarayan, K. and Kim, B.-S. (2015). Reversible and universal pH sensing cellulose nanofibers for health monitor. *Sens. Actuators, B* 209: 281–286.

64 Pakolpakçıl, A., Karaca, E., and Becerir, B. (2018). Investigation of a natural pH-indicator dye for nanofibrous wound dressings. *IOP Conf. Ser.: Mater. Sci. Eng.* 460 (1): 5. https://doi.org/10.1088/1757-899X/460/1/012020.

65 Ardeshirzadeh, B., Anaraki, N.A., Irani, M. et al. (2015). Controlled release of doxorubicin from electrospun PEO/chitosan/graphene oxide nanocomposite nanofibrous scaffolds. *Mater. Sci. Eng., C* 48: 384–390.

66 Schoolaert, E., Steyaert, I., Vancoillie, G. et al. (2016). Blend electrospinning of dye-functionalized chitosan and poly(ε-caprolactone): towards biocompatible pH-sensors. *J. Mater. Chem. B* 4 (26): 4507–4516.

15

Cells Responses to Surface Geometries and Potential of Electrospun Fibrous Scaffolds

Urszula Stachewicz

AGH University of Science and Technology, Faculty of Metals Engineering and Industrial Computer Science, al. Mickiewicza 30, Kraków 30-059, Poland

15.1 Introduction

Combining scaffolds, cells, and biologically active molecules into functional tissues is the key element of tissue-engineering approaches. The goal of tissue engineering is to assemble functional constructs that restore, maintain, or improve damaged tissues or whole organs. The most important is the design of scaffolds that is eventually controlling the cells' responses. Generally, groups of cells make and secrete their support structures called the extracellular matrix (ECM). This matrix, or scaffold, does more than just support the cells; it also acts as a relay station for various signaling molecules. Thus, cells receive messages from many sources that become available from the local environment. Each signal can start a chain of responses that determine what happens to the cell. By understanding how individual cells respond to signals, interact with their environment, and organize into tissues and organisms, researchers have been able to manipulate these processes to mend damaged tissues or even create new ones.

Electrospun fibers are one of the most commonly applied in tissue engineering, as their structures remind cells' ECM, and thus are commonly studied and used in many tissue culture products [1]. The number of published research on using electrospun fibers is increasing every year. As the electrospun fibrous scaffold has a very large surface-area-to-volume ratio, such modifications and controlled surface and bulk properties will be extremely useful to generate new nanostructured materials with novel functionality for biomedical applications. Tissue engineers aim to recapitulate developmental processes *in vitro*, but this is a challenging task when those processes are not well understood, in particular cell responses to substrate properties. Many fundamental studies are performed on polymer film or grooved film structure [2]. The generation of tension by actin stress fibers is known to be necessary for the formation of focal adhesions [3]. The focal adhesion is important for contact guidance and the formation of actin stress fibers. Therefore, surface

Functional Biomaterials: Design and Development for Biotechnology, Pharmacology, and Biomedicine, First Edition. Edited by Tamilselvan Mohan and Karin Stana Kleinschek.

properties in biomaterials are one of the most influential parameters in cells, and a lot of effort in tissue engineering is focused on surface modifications with roughness [4, 5], by generally changing the architecture of scaffolds [6, 7], or designing antibacterial or antimicrobial properties [8]. The dynamic cell–material interaction is a complex process, controlling not only cells' fate but also their adhesion and differentiation [9], by specific surface properties including topography [10], potential, and charge [11, 12]. Each type of cell has its unique characteristics including how cells respond to surface charge [13]. This peculiar property allows us to design and adapt biomaterials surfaces to a specific application. Surface charge determines the amount, type, and refolding degree of absorbed proteins and thus the following cell adhesion process [14].

The surface of a cell is composed of thousands of different lipids, proteins, and carbohydrates, all intricately (and dynamically) arranged in three dimensions on multiple length scales. This complexity presents both a challenge and an opportunity to materials scientists and chemists working on bioactive interfaces. The protein adsorption is strongly related to so-called RGD motif, which is the tripeptide Arg–Gly–Asp consisting of arginine, glycine, and aspartate. RGD sequence is in ECM proteins. Cell adhesion proteins called integrins recognize and bind to this sequence, which is found within many matrix proteins, including fibronectin, fibrinogen, vitronectin, osteopontin, and several other adhesive ECM proteins. During cell–substrate or cell–cell interactions, integrins recognize the RGD proteins within the ligands causing the binding reactions [15].

Cells must nevertheless exert a tractive force on the substrate via filopodia as the leading and trailing edges of cells were often extended along the top of the ridges or the floor of the grooves. Filopodial guidance by the failure of lamellipodia to reach adjacent ridges, becoming effectively trapped in the groove, may contribute to inhibition of lateral spreading. Cell alignment resulted from anisotropic cell spreading as cells extended and retracted lamellipodia preferentially along the direction of the patterns. Similarly, the alignment of the cells is observed on the aligned scaffolds, which was verified with 3D imaging using advanced microscopy techniques such as 3D tomography based on dual beam: scanning electron microscopy and focus ion beam (FIB-SEM) [16]. Additionally, the pore shape and size restrict cell proliferation which we verified for both cases – random and aligned electrospun scaffolds [7]. The current state of applying polymer fibers in tissue engineering still lacks fundamental understanding, which can be clarified by advanced microscopy and surface characterization techniques.

15.2 Electrospinning

Scaffolds used in the regeneration processes have not only supporting function but also importantly help in cells' signaling path [17]. Scaffold geometry is critical in tissue engineering, enabling building complex tissues [6]. Cells need to first develop suitable morphology and physical features such as filopodia in the *in vitro* conditions and can reorganize materials properties, such as topography [18, 19],

mechanical strength [20], and surface potential [21, 22], to facilitate their growth. Pore size or voids between fibers affect mostly cell proliferation inside the scaffolds and metabolic circulation [23, 24]. Therefore, the shape and morphology of the scaffolds are crucial in controlling cell behavior, development, and proliferation [25]. Apart from many other methods used to produce scaffolds for tissue engineering, we focus here on electrospinning.

The electrospinning technology platform can indeed offer the versatility and unique nanostructure features beyond most existing technologies [26]. Electrospun scaffolds showed great promise and potential for many biomedical applications, such as tissue engineering, wound dressing, immobilized enzymes, and controlled delivery of drugs [27]. Successful creation of fibrous scaffolds must start with the proper selection of materials, a judicious and realistic fabrication pathway, and possible post modification with a functional reagent. The polymer material selection plays a key role in the fabrication of scaffolds. Many desirable properties can be achieved by polymer mixing (natural and/or synthetic polymers), copolymerization, or a hybrid of materials and processing techniques [28, 29]. Multicomponent mixtures can be miscible or immiscible, containing different phases (liquid or solid). Several newly developed innovative electrospinning methods have been described, including oriented scaffolds, multilayer electrospinning, mixing electrospinning, fabrication of dual-porosity scaffolds, two-phase electrospinning, and fabrication of core–shell fibers [30].

As mentioned previously, the surface area of produced electrospun fibers is large; therefore, they easily find application in tissue engineering for artificial skin or cartilage, drug delivery or bone scaffolds, and in biodegradable bandages [26, 27, 31, 32]. Electrospun fibers mimic ECM that plays an important role in adhesion and proliferation of osteoblasts. Natural ECM is built of fibers with a diameter in the range of 50–300 nm and plays an important role in cell activities and functions. Moreover, proper communication between cells through ECM allows the proper function of tissues and organs. Cells, after adhesion to the substrates, create focal adhesion points, vinculins, and stress fibers, which allow cell movement, and cell migration is recognized by filopodia formation. Importantly, ECM is able to control cell proliferation and thereby their division [33]. Nanofibers are used for cell culture as scaffolds not only to support cells but also to control cell shapes, functions, proliferation, and differentiation [6]. Apart from tissue-engineering applications, nanofibers are used in gene therapies to transfer DNA to cells. In the chemical industry often they are used in filtration processes or are integrated with textiles or in composites for reinforcements [34–36]. Nanofibers have a complex 3D structure, and their size and shape can be controlled [37]. Often, they are used in membranes and standard air filters, increasing the cleaning performance due to the large surface area and porosity above 90%. Nanofibers are easily modified with additional functionalities such as antibacterial or antimicrobial properties [38].

The electrospinning itself is a process that uses an electric field to draw the polymer solution while solvents are evaporating [39, 40], see the schematics in Figure 15.1. In electrospinning, we apply charge at the liquid jet–air interface during the expulsion of the polymer solution so that spinning with a negative

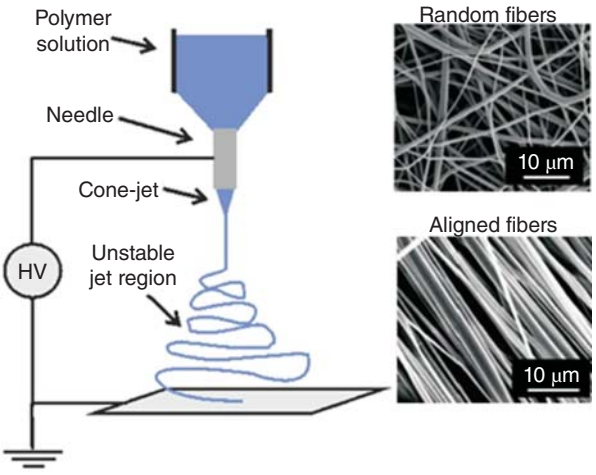

Figure 15.1 Schematic of electrospinning process with the examples of random and aligned fibers in the produced membranes shown in the SEM micrographs.

polarity causes accumulation of the negative charge at the surface of the liquid jet, whereas the positive charge accumulates at the liquid jet surface when spinning with a positive polarity [41]. Manipulation of the polarity of the applied voltage used during electrospinning changes not only the chemical functionality of electrospun nanofibers [42, 43], but also the mechanical properties of produced fibers [44]. Therefore, the wetting effects on electrospun fibers produced with positive or negative charges are different as we previously showed on PA6 fibers characterized by different surface chemistry [41, 45].

Electrospinning is one of the most commonly used methods to produce polymer fibers in nano- and macrosizes, but it is also possible to produce ribbons [46] having large surface-area-to-volume ratio [47]. Different types of collectors used in electrospinning allow controlling distance between fibers and pore sizes [48, 49] together with the controlled fiber diameter [50]. Noteworthy, electrospun nanofibers have specific mechanical and surface properties that vary from those produced by conventional fibers, e.g. by extrusion or injection molding. Another concept is coaxial electrospinning where we are able to mix polymers and produce a well-defined core–shell structure of fibers.

Stretching of the jet reduces fibers' diameter [51] and controlling of applied charges allow the reorientation of molecules in polymer chains according to their electronegativity. Additionally, the stretching of polymer chains aligns them along the main axis of produced fibers [52], which increases their mechanical performance. There are many parameters influencing nanofibers morphology during electrospinning. These parameters can be controlled during solution preparation: viscosity, conductivity, surface tension, and dielectric constant, a polymer used, and its molecular weight, the concentration of the polymer in the solution, and choice of solvent. Polymer solutions with low concentration produce droplets (electrospray) instead of fibers. High polymer concentration increases the viscosity of a solution, making it difficult to push it through tiny nozzles and often causing

drying droplets at the nozzles or blocking the nozzle before electrospinning starts. Low-concentration solutions are responsible also for the formation of beads on electrospun fibers. If the molecular weight is low (below 60 kDa), beads occur more often on polymer fibers [53]. Other sets of parameters can be controlled via the electrospinning setup. These include applied voltage, type of collector, nozzle diameter, the distance between a nozzle and a counter electrode, and flow rate [54–56]. To obtain a stable electrospinning process, the flow rate has to be adjusted according to applied voltage and distance between the needle and collecting electrode. Increasing this distance increases the space for the jet to travel and stretch, so the solvent has more time to evaporate, producing smaller diameter nanofibers [52]. Apart from that, environmental conditions, e.g. humidity, temperature, gas, and type of atmosphere, have a huge influence on electrospinning. By changing humidity we can control nanofibers morphology [57].

Electrospun nanofibers have good mechanical properties (tensile strength, elastic modulus, and extension) compared to polymer films made out of the same polymer or fibers produced with conventional polymer-processing methods. Significant improvement of mechanical properties is observed for nanofibers with a diameter smaller than 100 nm [58–62], which is related to polymer chains alignment or confinement in the direction of stretching in the electric field along the main axis. In nanofibers with a smaller diameter, the fraction of aligned polymers is usually higher and the solvent evaporation is more rapid during electrospinning, causing freezing of the polymer chains alignment. This is an excellent example of a structure–properties relationship, showing the improved mechanical properties via an increased Young's modulus of nanofibers with an increased fraction of aligned polymer chains [60]. Aligning fibers at the macroscopic level is performed by using a drum or parallel-plate collectors. A parallel-plate collector consists of two metal plates with an adjustable gap, where the aligned fibers are deposited. Here alignment depends mainly on the gap distance. The degree of alignment in the case of a rotating drum collector depends on its speed and drum diameter, and is most often used to obtain specific fibers' arrangements [63].

For a large production rate of nanofibers surface-free electrospinning (or also called needleless electrospinning) is usually used, where voltage is applied to the rotating drum or wire with a thin layer of polymer solution [64–66]. When the voltage is applied, a polymer solution surface starts perturbating, causing droplets formation that transfer into cone-jet spinning, like in the case of a single nozzle presented in Figure 15.1. Needleless electrospinning allows mass production of nanofibers. Currently, in the market, there are a few producers of needleless electrospinning equipment [64, 67–70].

15.3 Surface Geometry and Typical Cell Responses

PMMA scaffolds were prepared in the form of nanofibers, microfibers, and ribbons and were compared with spin-coated films to verify the geometrical effect on cells, see Figure 15.2. In this study, osteoblasts were used to observe how cells integrate with fibers and change their shapes [46]. The surface roughness of electrospun

scaffolds, often correlated with fiber diameter [71], is considered as a key parameter to enhance the interactions of the cell with fibers. Importantly, surface roughness affects the wetting properties of the membranes [72–74]. Microfibers exhibit a higher contact angle above nanofibers [46], which is reflected with further cell interaction with them. In the case of nanofibers, the distances between fibers are limited to what facilitates more spreading of cells on the top of the surface in comparison to microfibers. The diameter of fiber exceeding 3 μm provided the right geometry and enough spacing for cell migration inside the 3D scaffold structure, which was initiated by filopodia attachments to underneath fibers. The 3D structure is preferable by osteoblast [75], while fibroblast spreads on top [76].

The SEM micrographs of fibroblasts in Figure 15.3 show their behavior in three types of electrospun meshes: on hydrophobic polystyrene (PS) with an average diameter of approximately 5 μm, hydrophilic nylon 6 (PA6) nanofibers with the

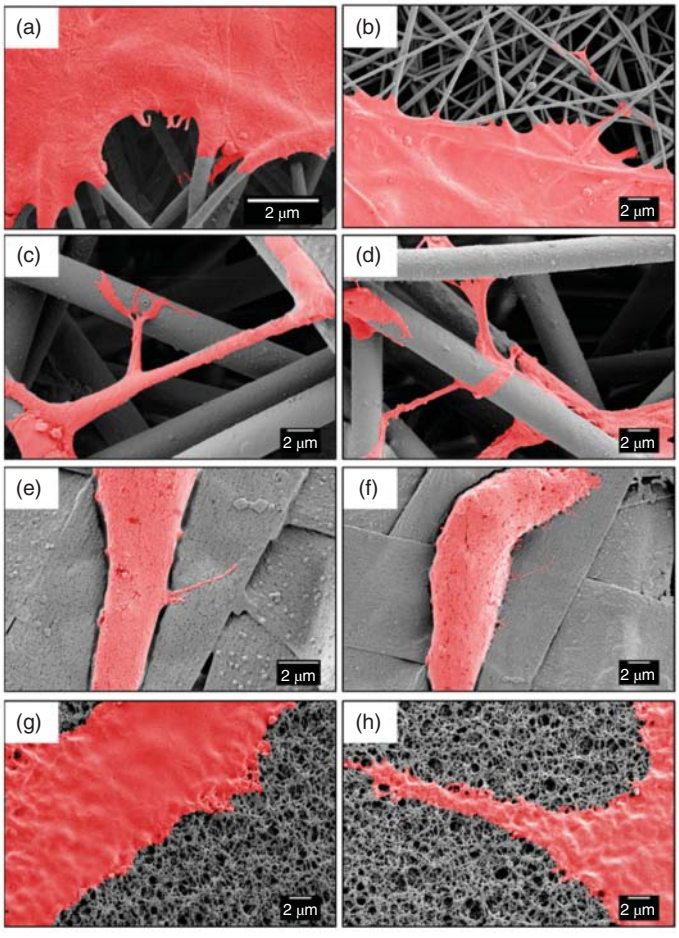

Figure 15.2 SEM micrographs showing cell attachment to a different type of scaffold, after three days: (a, b) nanofibers, (c, d) microfibers, (e, f) ribbons, and (g, f) film; cells are colored in red. Source: Ura et al. [46]/MDPI/CC BY 4.0.

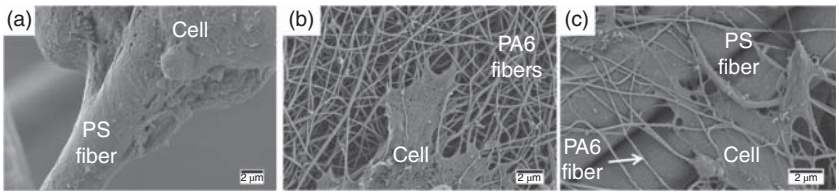

Figure 15.3 SEM micrographs focused on cell–fiber attachment after the third day of cell culture on (a) PS microfibers, (b) PA6 nanofibers, and (c) hierarchical PS-PA6 composite meshes. Source: Krysiak et al. [76]/MDPI/CC BY 4.0.

diameter of 100 nm, and composite PS-PA6 combining micro- and nanofibers. Spreading and cells anchoring to scaffolds are crucial for tissue development [77, 78]. When PA6 nanofibers are added to PS meshes the surface roughness decreases [71, 76], which favors fibroblasts attachment [79, 80], spreading, and migration [81]. PA6 nanofibers are hydrophilic which eventually enhances cell development, their flattening, and proliferation [82, 83]. Controlling of surface properties of the fiber network by mixing hydrophilic/hydrophobic properties of polymers can be done through surface roughness of nanofibers. Simultaneous electrospinning of two different polymers with different surface properties and mechanical properties can be performed with the two-nozzle set-up [76].

The proliferation and attachment of cells strongly depend on scaffolds geometry [84]. The deeper penetration into electrospun scaffolds by cells is controlled with pore size [7] allowing enhanced material integration with the living systems. The arrangement of electrospun fibers often defines the pore size, and it is possible to control via collecting drums used during electrospinning. Several types of collectors have been used to increase the size of the pore such as ice drum by introducing low-temperature electrospinning [49, 85]. Electrospinning in cryogenic conditions allows ice crystals formation in between fibers, which are subsequently removed by freeze-drying, creating large voids between electrospun fibers. Also using the collector with various patterns and holes increased the formation of voids between electrospun fibers [48]. Using a similar principle, the salt crystals are used in electrospinning too [86, 87]. Also, the self-organization of electrospun fibers in electrospinning allows us to obtain the honeycomb-like structures or 3D foams with the wide pore gradient range, which is dependent on electrospinning time [88–90]. Foam-like structure is also obtained, while electrospun fibers are directly deposited in fluids, such as water or oil [91–93]. Other foamy structures can be also done with electrospun fibers following a few postprocessing steps [94, 95]. The introduced additional voids between electrospun fibers give more 3D structure to scaffolds and facilitate cell infiltration inside, which is an important step for tissue regeneration processes.

The integration of cells with electrospun fibers requires also 3D visualization which enables the understanding of cell development. The commonly used confocal microscopy is often limited to cell observation mainly; however, so-called dual or cross beam microscopy, FIB-SEM, and “slice and view” tomography allow the material and cell visualization in 3D reconstructions at the same time [16]. The interaction between resident cells and electrospun nanofibers is critical in determining resultant cell proliferation and activity in orthopedic tissue scaffolds. The

use of techniques to evaluate cell–nanofiber interactions is crucial in understanding scaffold function, with visualization promising unparalleled access to spatial information on such interactions. 3D tomography FIB-SEM was used to examine electrospun scaffolds to understand the features responsible for (osteoblast-like MC3T3-E1 and UMR106) cell behavior and resultant scaffold function. 3D imaging of cell–nanofiber interactions within a range of electrospun poly(D,L-lactide-*co*-glycolide acid) (PLGA) nanofiber scaffold architectures indicated a coherent interface between osteoblasts and fiber surfaces, promoting osteoblast filopodia formation for successful cell growth. Coherent cell–nanofiber interfaces were demonstrated throughout a randomly organized and aligned nanofiber network. The penetration depth of cells into aligned fibers scaffolds was much smaller, 4 μm, compared to randomly deposited fibers reaching 7 μm The sizes of fibers, around 1 μm, using other 3D imaging techniques such as microcomputer tomography (μCT), could not be applied to visualize the cell–scaffold interconnections [96].

15.4 Surface Potential Importance and Typical Cell Responses

Understanding the effect of surface charge is key to designing biomaterials for specific tissue-engineering applications. However, the current knowledge on surface charge and its potential impact on cell–material interaction is still rather limited. The surface potential of materials in contact with liquids is described by ζ potential, depending on the functional groups at the surface promoting the formation of the electrical double layer (Stern–Graham and Gouy–Chapman diffuse layer). The ζ potential is typically measured at the shear plane between the two layers [97]. The isoelectric point (IEP) defines the pH value where the ζ potential is zero and is used to describe protein adsorption [98]. Protein adsorptions control cell responses and cell–biomaterial electrostatic interactions related to cell adhesion and focal adhesion formation [99, 100]. The integration of cells with the scaffolds is further responsible for cell development increase for osteoblasts – collagen formation – and is crucial for bone mineralization process, hence, of the calcium phosphate crystallization too [101]. The surface charge of biomaterials is often controlled via chemical modifications [102] on many biopolymers applied in tissue engineering [103].

As previously mentioned, the electrospinning with positive and negative voltage polarities allows controlling surface potential on polymer fibers used as scaffolds in tissue-engineering applications. The successfully produced scaffolds from polyvinylidene fluoride (PVDF) and polycaprolactone (PCL) showed for PVDF(−) with the surface potential of −95 m in comparison to PVDF(+) with surface potential reaching −173 mV and in the case of PCL(+) and PCL(−) it was a few hundred of mV, which was directly measured using Kelvin probe force microscopy (KPFM) [11, 104]. These measurements were also repeated for two morphologies of PCL fibers, porous and smooth, and films showing similar differences, as shown in Figure 15.4. Importantly, the obtained results are correlated with the ζ potential

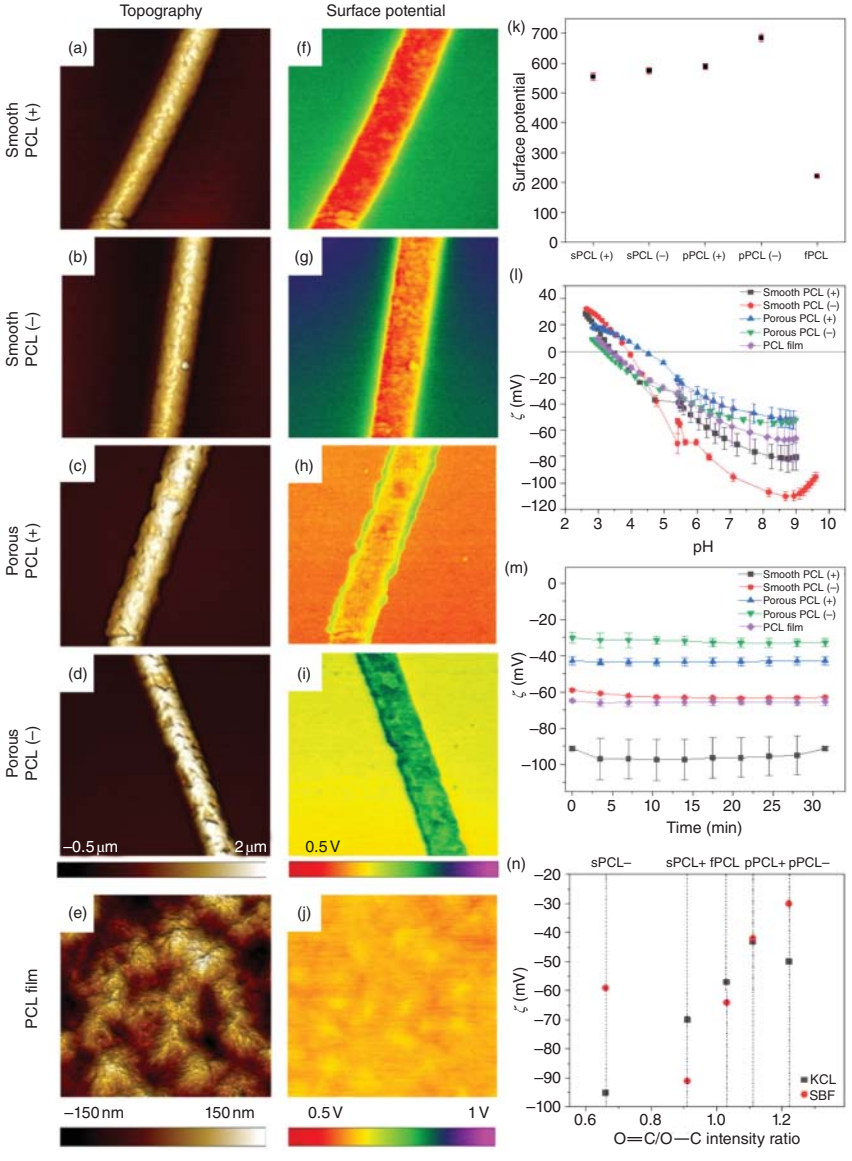

Figure 15.4 KPFM results showing (a–e) surface topography, (f–j) map of the surface potential for the smooth PCL(+) and PCL(–), the porous PCL(+) and the PCL(–) fibers and the PCL film, (k) the graph of the surface potential measured with the KPFM, (l) titration curves measured in the function of pH in KCL solution, (m) ζ in the function of time in the SBF solution in pH 7.4, and (n) ARXPS surface chemistry showing close to the linear relation of the O=C/O–C intensity ratio and the measured ζ potential. Source: Metwally et al. [105]/Elsevier/CC BY 4.0.

data defining the charges interactions in liquids such as simulated body fluids (SBF), see Figure 15.4l.

The surface potential varies according to the polymers used and voltage polarity applied in such a single-step electrospinning approach. This innovative and facile way of fibers production regulates the interfacial properties to enhance cell adhesion and filopodia formation on fibrous tissue scaffolds for possible bone regeneration, as indicated in SEM micrographs presented in Figure 15.5. Tuning surface chemistry by altering voltage polarity during electrospinning allowed to double the surface potential on fibers up to 145 mV for PCL(−). The obtained surface potential on PCL fibers is directly correlated with surface chemistry analyzed at the grazing angle by X-ray photoelectron microscopy (XPS), showing lower oxygen content at PCL fiber surfaces, produced with negative voltage polarity, PCL(−), see Figure 15.4n. The fibers with controlled surface potential create well-engineered scaffolds that are able to increase significantly cell proliferation that was visualized with fluorescence microscopy, and filopodia formation on positively charged fibers, investigated with high-resolution SEM.

We have proved that the surface potential of electrospun fibers regulates not only specific biological functions, anchoring, and proliferation of cells but also stimulates cells for collagen production for further remineralization processes, see Figure 15.5. The surface potential of PVDF(−) scaffolds was very similar to the one reported for osteoblast-like cells MG63 potential of −60 mV that was used in our cell culture study. Importantly, adjusting the surface potential of the scaffolds gives enormous possibilities to tune the mineralization process without any presence of hydroxyapatite or tricalcium phosphate incorporated in the scaffolds, to start the nucleation process of collagen mineralization notably within seven days of cell culture. To a great degree surface potential of scaffolds has the ability to control many cell processes. This is seen through the high-resolution 3D images of the detailed morphology of cells filopodia formed on PCL fibers, Figure 15.6. Through a simple and efficient approach to alter voltage polarity during electrospinning, it was possible to achieve stable surface potential over a long time. The results have a great impact on the development of scaffold interfaces to enhance bio-integration in many biomaterials applied in tissue engineering.

15.5 Conclusions

Surface properties of materials used in tissue-engineering scaffolds are the key to enhance the integration of the cell with the biomaterials. Electrospinning is a versatile method that allows the scaffolds' production by applying positive- and negative-voltage electrical polarity to the nozzle. The changing polarity of the applied voltage enables control of the molecular orientation of the chemical functional groups in the polymer's chains in the fibers, which affects the surface potential. Adding also the geometrical effect to electrospun fibers by changing the porosity of fibers and creating a hierarchical structure intensifies the integration and

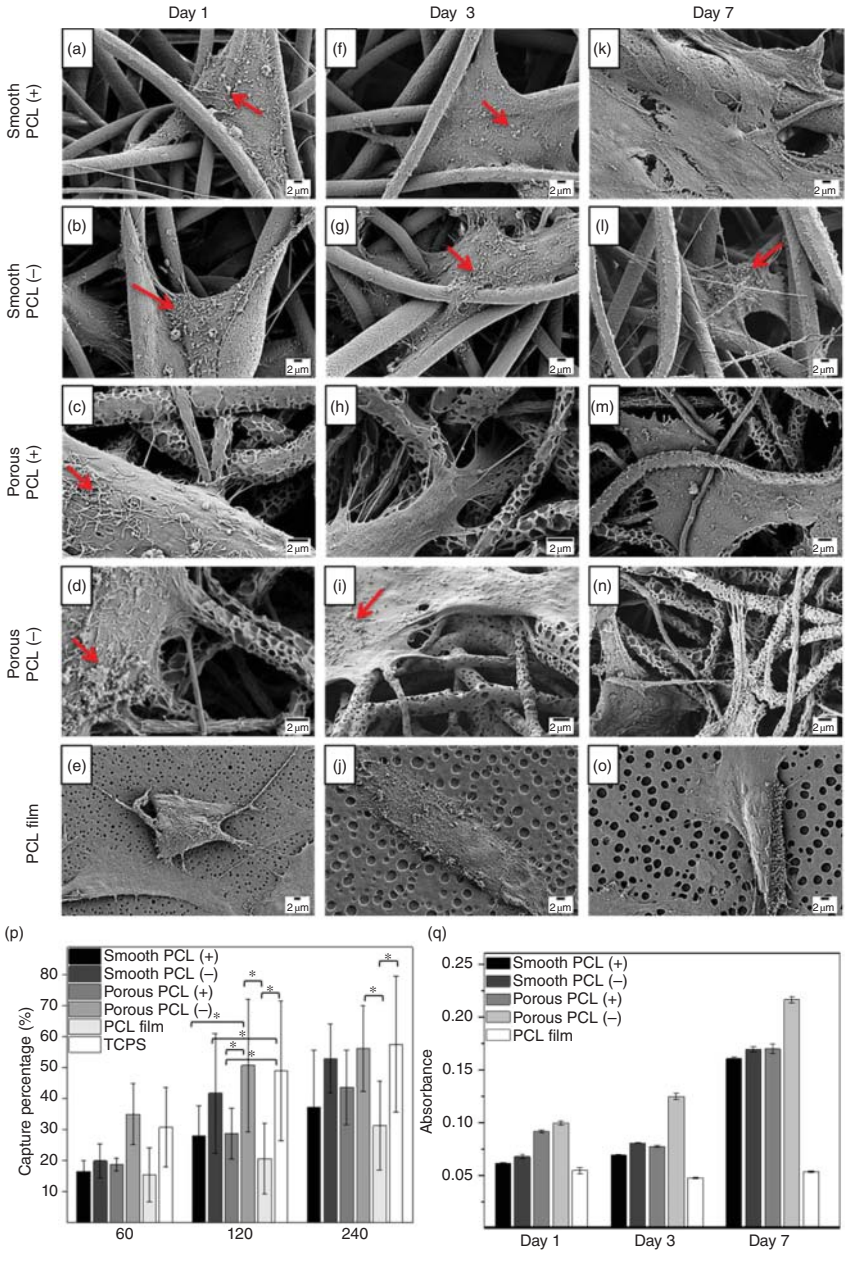

Figure 15.5 SEM micrographs of cells growing on smooth, porous PCL fibers and after: (a–e) one day, (f–j) three days, and (k–o) seven days of culture (red arrows indicate collagen fibrils). (p) Graph of the capture percentage of the cells adhered after one, two, and four hours and (q) Sirius Red absorbance indicating collagen formation after one, three, and seven days of cell culture on the smooth PCL(+), PCL(–), the porous PCL(+), and the PCL(–) and the PCL film. Statistical significance was calculated with a one-way ANOVA followed by a post hoc Tukey test with significance level $p < 0.05$. In (q) the significant difference among all the tested groups is displayed. Source: Reproduced from Metwally et al. [105]/Elsevier/ CC BY 4.0.

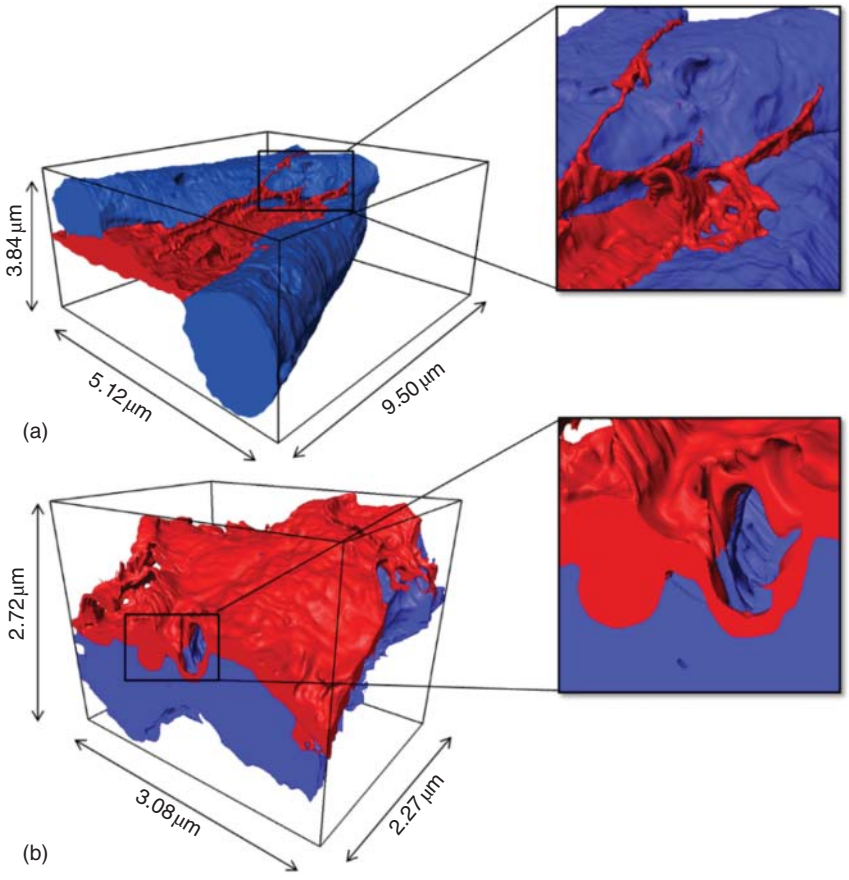

Figure 15.6 3D reconstructions from FIB-SEM tomography of cell interaction with the scaffolds after three days of culture: (a) cell attached to the smooth PCL(–) scaffold, growing between the fibers with zoom-in on long filopodia overlapping the fibers and (b) cell growing on top of the fibers with zoom-in on cell internalizing the pores on the surface of the porous PCL(–) scaffold. The voxel size of the 3D reconstructions was $10 \times 10 \times 30$ and $5 \times 5 \times 15$ nm^3 for the smooth and the porous PCL(–) scaffolds, respectively. Cells in red and fibers in blue. Source: Metwally et al. [105]/Elsevier/CC BY 4.0.

anchoring of the cell to scaffolds. The combination of both high surface electrical potential and surface topography is enhanced by pores, and increased roughness determines cell proliferation and adhesion. Paying attention to these parameters in the design scaffolds results in a faster regeneration process such as collagen and calcium mineralization in bone tissue. Electrospun scaffolds demonstrate high potential in tissue engineering as their surface properties can be tuned in single-step manufacturing method, thereby reducing postprocessing steps and the cost associated with their production.

Acknowledgments

This book chapter was written on studies correlated with the funding from the OPUS 17 project grant provided by the National Science Centre in Poland, No. 2019/33/B/ST5/01311.

References

1 Xue, J., Wu, T., Dai, Y., and Xia, Y. (2019). Electrospinning and electrospun nanofibers: methods, materials, and applications. *Chem. Rev.* 119 (8): 5298–5415. https://doi.org/10.1021/acs.chemrev.8b00593.

2 Teixeira, A.I., Abrams, G.A., Bertics, P.J. et al. (2003). Epithelial contact guidance on well-defined micro- and nanostructured substrates. *J. Cell Sci.* 116 (Pt. 10): 1881–1892. https://doi.org/10.1242/jcs.00383.

3 Chrzanowska-Wodnicka, M. and Burridge, K. (1996). Rho-stimulated contractility drives the formation of stress fibers and focal adhesions. *J. Cell Biol.* 133 (6): 1403–1415. https://doi.org/10.1083/jcb.133.6.1403.

4 Anselme, K., Bigerelle, M., Noel, B. et al. (2000). Qualitative and quantitative study of human osteoblast adhesion on materials with various surface roughnesses. *J. Biomed. Mater. Res.* 49 (2): 155–166. https://doi.org/10.1002/(sici)1097-4636(200002)49:2<155::Aid-jbm2>3.0.Co;2-j.

5 Satoshi, M. and Kunitaka, A. (2017). Effect of nanometer scale surface roughness of titanium for osteoblast function. *AIMS Bioengineering* 4 (1): 162–170. https://doi.org/10.3934/bioeng.2017.1.162.

6 Stevens, M.M. and George, J.H. (2005). Exploring and engineering the cell surface interface. *Science* 310 (5751): 1135–1138. https://doi.org/10.1126/science.1106587.

7 Stachewicz, U., Szewczyk, P.K., Kruk, A. et al. (2019). Pore shape and size dependence on cell growth into electrospun fiber scaffolds for tissue engineering: 2D and 3D analyses using SEM and FIB-SEM tomography. *Mater. Sci. Eng. C Mater. Biol. Appl.* 95: 397–408. https://doi.org/10.1016/j.msec.2017.08.076.

8 Goudouri, O.M., Kontonasaki, E., Lohbauer, U., and Boccaccini, A.R. (2014). Antibacterial properties of metal and metalloid ions in chronic periodontitis and peri-implantitis therapy. *Acta Biomater.* 10 (8): 3795–3810. https://doi.org/10.1016/j.actbio.2014.03.028.

9 Kuo, Y.C. and Rajesh, R. (2017). Nerve growth factor-loaded heparinized cationic solid lipid nanoparticles for regulating membrane charge of induced pluripotent stem cells during differentiation. *Mater. Sci. Eng. C Mater. Biol. Appl.* 77: 680–689. https://doi.org/10.1016/j.msec.2017.03.303.

10 Dvir, T., Timko, B.P., Kohane, D.S., and Langer, R. (2011). Nanotechnological strategies for engineering complex tissues. *Nat. Nanotechnol.* 6 (1): 13–22. https://doi.org/10.1038/nnano.2010.246.

11 Metwally, S., Karbowniczek, J.E., Szewczyk, P.K. et al. (2019). Single-step approach to tailor surface chemistry and potential on electrospun PCL fibers for tissue engineering application. *Adv. Mater. Interfaces* 6 (2): 1801211. https://doi.org/10.1002/admi.201801211.

12 Li, J., Mou, X., Qiu, J. et al. (2015). Surface charge regulation of osteogenic differentiation of mesenchymal stem cell on polarized ferroelectric crystal substrate. *Adv. Healthc. Mater.* 4 (7): 998–1003. https://doi.org/10.1002/adhm.201500032.

13 Grosse, C. and Schwan, H.P. (1992). Cellular membrane potentials induced by alternating fields. *Biophys. J.* 63 (6): 1632–1642. https://doi.org/10.1016/S0006-3495(92)81740-X.

14 Mariani, E., Lisignoli, G., Borzi, R.M., and Pulsatelli, L. (2019). Biomaterials: foreign bodies or tuners for the immune response? *Int. J. Mol. Sci.* 20 (3): https://doi.org/10.3390/ijms20030636.

15 Ruoslahti, E. (1996). RGD and other recognition sequences for integrins. *Annu. Rev. Cell Dev. Biol.* 12: 697–715. https://doi.org/10.1146/annurev.cellbio.12.1.697.

16 Stachewicz, U., Qiao, T., Rawlinson, S.C.F. et al. (2015). 3D Imaging of cell interactions with electrospun PLGA nanofiber membranes for bone regeneration. *Acta Biomater.* 27: 88–100. https://doi.org/10.1016/j.actbio.2015.09.003.

17 Hughes-Brittain, N.F., Qiu, L., Wang, W. et al. (2012). Photoembossing of surface relief structures in polymer films for biomedical applications. *J. Biomed. Mater. Res. B* 102 (2): 214–220. https://doi.org/10.1002/jbm.b.32997.

18 Lee, J.-W., Lee, K.-B., Jeon, H.-S., and Park, H.-K. (2011). Effects of surface nano-topography on human osteoblast filopodia. *Anal. Sci.* 27 (4): 369–374. <Go to ISI>://WOS:000289744200004.

19 Xue, F., Janzen, D.M., and Knecht, D.A. (2010). Contribution of filopodia to cell migration: a mechanical link between protrusion and contraction. *Int. J. Cell Biol.* 2010: 507821. https://doi.org/10.1155/2010/507821.

20 Wala, J., Maji, D., and Das, S. (2017). Influence of physico-mechanical properties of elastomeric material for different cell growth. *Biomed. Mater.* 12 (6): 065002. https://doi.org/10.1088/1748-605x/aa7e81.

21 do Nascimento, R.M., de Carvalho, V.R., Govone, J.S. et al. (2017). Effects of negatively and positively charged Ti metal surfaces on ceramic coating adhesion and cell response. *J. Mater. Sci. Mater. Med.* 28 (2): 33. https://doi.org/10.1007/s10856-017-5848-0.

22 Metwally, S. and Stachewicz, U. (2019). Surface potential and charges impact on cell responses on biomaterials interfaces for medical applications. *Mater. Sci. Eng. C Mater. Biol. Appl.* 104. https://doi.org/10.1016/j.msec.2019.109883.

23 Sosnowski, S., Wozniak, P., and Lewandowska-Szumiel, M. (2006). Polyester scaffolds with bimodal pore size distribution for tissue engineering. *Macromol. Biosci.* 6 (6): 425–434. https://doi.org/10.1002/mabi.200600003.

24 Lowery, J.L., Datta, N., and Rutledge, G.C. (2010). Effect of fiber diameter, pore size and seeding method on growth of human dermal fibroblasts in electrospun poly(ε-caprolactone) fibrous mats. *Biomaterials* 31 (3): 491–504. https://doi.org/10.1016/j.biomaterials.2009.09.072.

25 Perez, R.A. and Mestres, G. (2016). Role of pore size and morphology in musculo-skeletal tissue regeneration. *Mater. Sci. Eng. C Mater. Biol. Appl.* 61: 922–939. https://doi.org/10.1016/j.msec.2015.12.087.

26 Kumbar, S.G., James, R., Nukavarapu, S.P., and Laurencin, C.T. (2008). Electrospun nanofiber scaffolds: engineering soft tissues. *Biomed. Mater.* 3 (3): 034002. <Go to ISI>://MEDLINE:18689924.

27 Agarwal, S., Wendorff, J.H., and Greiner, A. (2008). Use of electrospinning technique for biomedical applications. *Polymer* 49 (26): 5603–5621. https://doi.org/10.1016/j.polymer.2008.09.014.

28 Kolbuk, D., Sajkiewicz, P., Maniura-Weber, K., and Fortunato, G. (2013). Structure and morphology of electrospun polycaprolactone/gelatine nanofibres. *Eur. Polym. J.* 49 (8): 2052–2061. https://doi.org/10.1016/j.eurpolymj.2013.04.036.

29 Denis, P., Dulnik, J., and Sajkiewicz, P. (2015). Electrospinning and structure of bicomponent polycaprolactone/gelatin nanofibers obtained using alternative solvent system. *Int. J. Polym. Mater. Polym. Biomater.* 64 (7): 354–364. https://doi.org/10.1080/00914037.2014.945208.

30 Yoon, J., Yang, H.S., Lee, B.S., and Yu, W.R. (2018). Recent progress in coaxial electrospinning: new parameters, various structures, and wide applications. *Adv. Mater. (Deerfield Beach, Fla.)* 30 (42): e1704765. https://doi.org/10.1002/adma.201704765.

31 Agarwal, S., Greiner, A., and Wendorff, J.H. (2009). Electrospinning of manmade and biopolymer nanofibers-progress in techniques, materials, and applications. *Adv. Funct. Mater.* 19 (18): 2863–2879. https://doi.org/10.1002/adfm.200900591.

32 Doshi, J. and Reneker, D.H. (1995). Electrospinning process and applications of electrospun fibers. *J. Electrostat.* 35 (2–3): 151–160. <Go to ISI>://WOS:A1995RP03900002.

33 Rosso, F., Giordano, A., Barbarisi, M., and Barbarisi, A. (2004). From cell-ECM interactions to tissue engineering. *J. Cell. Physiol.* 199 (2): 174–180. https://doi.org/10.1002/jcp.10471.

34 Bhardwaj, N. and Kundu, S.C. (2010). Electrospinning: a fascinating fiber fabrication technique. *Biotechnol. Adv.* 28 (3): 325–347. https://doi.org/10.1016/j.biotechadv.2010.01.004.

35 Sill, T.J. and von Recum, H.A. (2008). Electrospinning: applications in drug delivery and tissue engineering. *Biomaterials* 29 (13): 1989–2006. https://doi.org/10.1016/j.biomaterials.2008.01.011.

36 Hohman, M.M., Shin, M., Rutledge, G., and Brenner, M.P. (2001). Electrospinning and electrically forced jets. II. Applications. *Phys. Fluids* 13 (8): 2221–2236. <Go to ISI>://WOS:000169868400010.

37 Stepanyan, R., Subbotin, A., Cuperus, L. et al. (2014). Fiber diameter control in electrospinning. *Appl. Phys. Lett.* 105 (17): 173105. https://doi.org/10.1063/1.4900778.

38 Thavasi, V., Singh, G., and Ramakrishna, S. (2008). Electrospun nanofibers in energy and environmental applications. *Energ. Environ. Sci.* 1 (2): 205–221. https://doi.org/10.1039/b809074m.

39 Hohman, M.M., Shin, M., Rutledge, G., and Brenner, M.P. (2001). Electrospinning and electrically forced jets. I. Stability theory. *Phys. Fluids* 13 (8): 2201–2220. <Go to ISI>://WOS:000169868400009.

40 Theron, S.A., Zussman, E., and Yarin, A.L. (2004). Experimental investigation of the governing parameters in the electrospinning of polymer solutions. *Polymer* 45 (6): 2017–2030. https://doi.org/10.1016/j.polymer.2004.01.024.

41 Stachewicz, U., Stone, C.A., Willis, C.R., and Barber, A.H. (2012). Charge assisted tailoring of chemical functionality at electrospun nanofiber surfaces. *J. Mater. Chem.* 22 (43): 22935–22941. https://doi.org/10.1039/C2JM33807F.

42 Szewczyk, P.K., Gradys, A., Kim, S.K. et al. (2020). Enhanced piezoelectricity of electrospun polyvinylidene fluoride fibers for energy harvesting. *ACS Appl. Mater. Interfaces* 12 (11): 13575–13583. https://doi.org/10.1021/acsami.0c02578.

43 Busolo, T., Ura, D.P., Kim, S.K. et al. (2019). Surface potential tailoring of PMMA fibers by electrospinning for enhanced triboelectric performance. *Nano Energy* 57: 500–506. https://doi.org/10.1016/j.nanoen.2018.12.037.

44 Ura, D.P., Rosell-Llompart, J., Zaszczynska, A. et al. (2020). The role of electrical polarity in electrospinning and on the mechanical and structural properties of As-spun fibers. *Materials* 13: 4169. https://doi.org/10.3390/ma13184169.

45 Stachewicz, U. and Barber, A.H. (2011). Enhanced wetting behavior at electrospun polyamide nanofiber surfaces. *Langmuir* 27 (6): 3024–3029. https://doi.org/10.1021/la1046645.

46 Ura, D.P., Karbowniczek, J.E., Szewczyk, P.K. et al. (2019). Cell integration with electrospun PMMA nanofibers, microfibers, ribbons, and films: a microscopy study. *Bioengineering* 6 (2): 41. https://www.mdpi.com/2306-5354/6/2/.41.

47 Fetz, A.E., Fantaziu, C.A., Smith, R.A. et al. (2019). Surface area to volume ratio of electrospun polydioxanone templates regulates the adsorption of soluble proteins from human serum. *Bioengineering* 6 (3): 78. https://www.mdpi.com/2306-5354/6/3/78.

48 Vaquette, C. and Cooper-White, J.J. (2011). Increasing electrospun scaffold pore size with tailored collectors for improved cell penetration. *Acta Biomater.* 7 (6): 2544–2557. https://doi.org/10.1016/j.actbio.2011.02.036.

49 Simonet, M., Stingelin, N., Wismans, J.G.F. et al. (2014). Tailoring the void space and mechanical properties in electrospun scaffolds towards physiological ranges. *J. Mater. Chem. B* 2 (3): 305–313. https://doi.org/10.1039/c3tb20995d.

50 Pham, Q.P., Sharma, U., and Mikos, A.G. (2006). Electrospinning of polymeric nanofibers for tissue engineering applications: a review. *Tissue Eng.* 12 (5): 1197–1211. https://doi.org/10.1089/ten.2006.12.1197.

51 Reneker, D.H., Yarin, A.L., Zussman, E., and Xu, H. (2007). Electrospinning of nanofibers from polymer solutions and melts. *Adv. Appl. Mech.* 41: 43–195. https://doi.org/10.1016/s0065-2156(07)41002-x.

52 Rutledge, G.C. and Fridrikh, S.V. (2007). Formation of fibers by electrospinning. *Adv. Drug Deliv. Rev.* 59 (14): 1384–1391. https://doi.org/10.1016/j.addr.2007.04.020.

53 Fong, H., Chun, I., and Reneker, D.H. (1999). Beaded nanofibers formed during electrospinning. *Polymer* 40 (16): 4585–4592. https://doi.org/10.1016/s0032-3861(99)00068-3.

54 Tan, S.H., Inai, R., Kotaki, M., and Ramakrishna, S. (2005). Systematic parameter study for ultra-fine fiber fabrication via electrospinning process. *Polymer* 46 (16): 6128–6134. https://doi.org/10.1016/j.polymer.2005.05.068.

55 Haider, A., Haider, S., and Kang, I.-K. (2016). A comprehensive review summarizing the effect of electrospinning parameters and potential applications of nanofibers in biomedical and biotechnology. *Arabian J. Chem.* https://doi.org/10.1016/j.arabjc.2015.11.015.

56 Huang, C.B., Chen, S.L., Lai, C.L. et al. (2006). Electrospun polymer nanofibres with small diameters. *Nanotechnology* 17 (6): 1558–1563. https://doi.org/10.1088/0957-4484/17/6/004.

57 Casper, C.L., Stephens, J.S., Tassi, N.G. et al. (2004). Controlling surface morphology of electrospun polystyrene fibers: effect of humidity and molecular weight in the electrospinning process. *Macromolecules* 37 (2): 573–578. https://doi.org/10.1021/ma0351975.

58 Liu, Y., Chen, S., Zussman, E. et al. (2011). Diameter-dependent modulus and melting behavior in electrospun semicrystalline polymer fibers. *Macromolecules* 44 (11): 4439–4444. https://doi.org/10.1021/ma200262z.

59 Camposeo, A., Greenfeld, I., Tantussi, F. et al. (2013). Local mechanical properties of electrospun fibers correlate to their internal nanostructure. *Nano Lett.* 13 (11): 5056–5062. https://doi.org/10.1021/nl4033439.

60 Arinstein, A., Burman, M., Gendelman, O., and Zussman, E. (2007). Effect of supramolecular structure on polymer nanofibre elasticity. *Nat. Nanotechnol.* 2 (1): 59–62. https://doi.org/10.1038/nnano.2006.172.

61 Pai, C.-L., Boyce, M.C., and Rutledge, G.C. (2011). Mechanical properties of individual electrospun PA 6(3)T fibers and their variation with fiber diameter. *Polymer* 52 (10): 2295–2301. https://doi.org/10.1016/j.polymer.2011.03.041.

62 Knapczyk-Korczak, J., Ura, D.P., Gajek, M. et al. (2020). Fiber-based composite meshes with controlled mechanical and wetting properties for water harvesting. *ACS Appl. Mater. Interfaces* 12 (1): 1665–1676. https://doi.org/10.1021/acsami.9b19839.

63 Li, D., Wang, Y.L., and Xia, Y.N. (2003). Electrospinning of polymeric and ceramic nanofibers as uniaxially aligned arrays. *Nano Lett.* 3 (8): 1167–1171. https://doi.org/10.1021/nl0344256.

64 Bhattacharyya, I., Molaro, M.C., Braatz, R.D., and Rutledge, G.C. (2016). Free surface electrospinning of aqueous polymer solutions from a wire electrode. *Chem. Eng. J.* 289: 203–211. https://doi.org/10.1016/j.cej.2015.12.067.

65 Forward, K.M. and Rutledge, G.C. (2012). Free surface electrospinning from a wire electrode. *Chem. Eng. J.* 183: 492–503. https://doi.org/10.1016/j.cej.2011.12.045.

66 Kostakova, E., Meszaros, L., and Gregr, J. (2009). Composite nanofibers produced by modified needleless electrospinning. *Mater. Lett.* 63 (28): 2419–2422. https://doi.org/10.1016/j.matlet.2009.08.014.

67 Niu, H.T., Lin, T., and Wang, X.G. (2009). Needleless electrospinning. I. A Comparison of cylinder and disk nozzles. *J. Appl. Polym. Sci.* 114 (6): 3524–3530. https://doi.org/10.1002/app.30891.

68 Dubsky, M., Kubinova, S., Sirc, J. et al. (2012). Nanofibers prepared by needleless electrospinning technology as scaffolds for wound healing. *J. Mater. Sci. Mater. Med.* 23 (4): 931–941. https://doi.org/10.1007/s10856-012-4577-7.

69 Ali, U., Niu, H., Khurshid, M.F. et al. (2019). Electrospinning behavior of needleless spinneret with a popular mace shape. *J. Text. Inst.* 110 (3): 349–357. https://doi.org/10.1080/00405000.2018.1480456.

70 Partheniadis, I., Nikolakakis, I., Laidmae, I., and Heinamaki, J. (2020). A mini-review: needleless electrospinning of nanofibers for pharmaceutical and biomedical applications. *Processes* 8 (6). https://doi.org/10.3390/pr8060673.

71 Szewczyk, P.K., Ura, D.P., Metwally, S. et al. (2019). Roughness and fiber fraction dominated wetting of electrospun fiber-based porous meshes. *Polymers* 11 (1): 17. https://doi.org/10.3390/polym11010034.

72 Stachewicz, U., Bailey, R.J., Zhang, H. et al. (2015). Wetting hierarchy in oleophobic 3D electrospun nanofiber networks. *ACS Appl. Mater. Interfaces* 7 (30): 16645–16652. https://doi.org/10.1021/acsami.5b04272.

73 McHale, G. (2007). Cassie and Wenzel: were they really so wrong? *Langmuir* 23 (15): 8200–8205. https://doi.org/10.1021/1a7011167.

74 Cassie, A.B.D. and Baxter, S. (1944). Wettability of porous surfaces. *Trans. Faraday Soc.* 40: 546–551. https://doi.org/10.1039/tf9444000546.

75 Kaniuk, L., Krysiak, Z.J., Metwally, S., and Stachewicz, U. (2020). Osteoblasts and fibroblasts attachment to poly(3-hydroxybutyric acid-co-3-hydrovaleric acid) (PHBV) film and electrospun scaffolds. *Mater. Sci. Eng. C Mater. Biol. Appl.* 110. https://doi.org/10.1016/j.msec.2020.110668.

76 Krysiak, Z.J., Gawlik, M.Z., Knapczyk-Korczak, J. et al. (2020). Hierarchical composite meshes of electrospun PS microfibers with PA6 nanofibers for regenerative medicine. *Materials* 13 (8). https://doi.org/10.3390/ma13081974.

77 Tuzlakoglu, K., Bolgen, N., Salgado, A.J. et al. (2005). Nano- and micro-fiber combined scaffolds: a new architecture for bone tissue engineering. *J. Mater. Sci. Mater. Med.* 16 (12): 1099–1104. https://doi.org/10.1007/s10856-005-4713-8.

78 Knight, E. and Przyborski, S. (2015). Advances in 3D cell culture technologies enabling tissue-like structures to be created in vitro. *J. Anat.* 227 (6): 746–756. https://doi.org/10.1111/joa.12257.

79 Kunzler, T.P., Drobek, T., Schuler, M., and Spencer, N.D. (2007). Systematic study of osteoblast and fibroblast response to roughness by means of surface-morphology gradients. *Biomaterials* 28 (13): 2175–2182. https://doi.org/10.1016/j.biomaterials.2007.01.019.

80 Dalby, M.J., Riehle, M.O., Johnstone, H.J.H. et al. (2002). Polymer-demixed nanotopography: control of fibroblast spreading and proliferation. *Tissue Eng.* 8 (6): 1099–1108. https://doi.org/10.1089/107632702320934191.

81 Oliveira, S.M., Song, W., Alves, N.M., and Mano, J.F. (2011). Chemical modification of bioinspired superhydrophobic polystyrene surfaces to control cell attachment/proliferation. *Soft Matter* 7 (19): 8932–8941. https://doi.org/10.1039/C1SM05943B.

82 Oliveira, S.M., Alves, N.M., and Mano, J.F. (2014). Cell interactions with superhydrophilic and superhydrophobic surfaces. *J. Adhes. Sci. Technol.* 28 (8–9): 843–863. https://doi.org/10.1080/01694243.2012.697776.

83 Anselme, K., Ploux, L., and Ponche, A. (2010). Cell/material interfaces: influence of surface chemistry and surface topography on cell adhesion. *J. Adhes. Sci. Technol.* 24 (5): 831–852. https://doi.org/10.1163/016942409X12598231568186.

84 Wu, S.L., Liu, X.M., Yeung, K.W.K. et al. (2014). Biomimetic porous scaffolds for bone tissue engineering. *Mater. Sci. Eng., R* 80: 1–36. https://doi.org/10.1016/j.mser.2014.04.001.

85 Simonet, M., Schneider, O.D., Neuenschwander, P., and Stark, W.J. (2007). Ultraporous 3D polymer meshes by low-temperature electrospinning: use of ice crystals as a removable void template. *Polym. Eng. Sci.* 47 (12): 2020–2026. https://doi.org/10.1002/pen.20914.

86 Wright, L.D., Andric, T., and Freeman, J.W. (2011). Utilizing NaCl to increase the porosity of electrospun materials. *Mater. Sci. Eng. C Mater. Biol. Appl.* 31 (1): 30–36. https://doi.org/10.1016/j.msec.2010.02.001.

87 Phipps, M.C., Clem, W.C., Grunda, J.M. et al. (2012). Increasing the pore sizes of bone-mimetic electrospun scaffolds comprised of polycaprolactone, collagen I and hydroxyapatite to enhance cell infiltration. *Biomaterials* 33 (2): 524–534. https://doi.org/10.1016/j.biomaterials.2011.09.080.

88 Nedjari, S., Schlatter, G., and Hebraud, A. (2015). Thick electrospun honeycomb scaffolds with controlled pore size. *Mater. Lett.* 142: 180–183. https://doi.org/10.1016/j.matlet.2014.11.118.

89 Nedjari, S., Hebraud, A., Eap, S. et al. (2015). Electrostatic template-assisted deposition of microparticles on electrospun nanofibers: towards microstructured functional biochips for screening applications. *RSC Adv.* 5 (102): 83600–83607. https://doi.org/10.1039/c5ra15931h.

90 Nedjari, S., Eap, S., Hebraud, A. et al. (2014). Electrospun honeycomb as nests for controlled osteoblast spatial organization. *Macromol. Biosci.* 14 (11): 1580–1589. https://doi.org/10.1002/mabi.201400226.

91 Gupta, D., Venugopal, J., Mitra, S. et al. (2009). Nanostructured biocomposite substrates by electrospinning and electrospraying for the mineralization of osteoblasts. *Biomaterials* 30 (11): 2085–2094. https://doi.org/10.1016/j.biomaterials.2008.12.079.

92 Pereira, I.H.L., Ayres, E., Averous, L. et al. (2014). Differentiation of human adipose-derived stem cells seeded on mineralized electrospun co-axial poly(ε-caprolactone) (PCL)/gelatin nanofibers. *J. Mater. Sci. Mater. Med.* 25 (4): 1137–1148. https://doi.org/10.1007/s10856-013-5133-9.

93 Shepherd, L.M., Frey, M.W., and Joo, Y.L. (2017). Immersion electrospinning as a new method to direct fiber deposition. *Macromol. Mater. Eng.* 302 (10): 1700148. https://doi.org/10.1002/mame.201700148.

94 Duan, G., Jiang, S., Jérôme, V. et al. (2015). Ultralight, soft polymer sponges by self-assembly of short electrospun fibers in colloidal dispersions. *Adv. Funct. Mater.* 25 (19): 2850–2856. https://doi.org/10.1002/adfm.201500001.

95 Ye, K.Q., Liu, D.H., Kuang, H.Z. et al. (2019). Three-dimensional electrospun nanofibrous scaffolds displaying bone morphogenetic protein-2-derived peptides for the promotion of osteogenic differentiation of stem cells and bone

regeneration. *J. Colloid Interface Sci.* 534: 625–636. https://doi.org/10.1016/j.jcis.2018.09.071.

96 Wojak-Cwik, I.M., Rumian, L., Krok-Borkowicz, M. et al. (2019). Synergistic effect of bimodal pore distribution and artificial extracellular matrices in polymeric scaffolds on osteogenic differentiation of human mesenchymal stem cells. *Mater. Sci. Eng. C Mater. Biol. Appl.* 97: 12–22. https://doi.org/10.1016/j.msec.2018.12.012.

97 Cho, D., Lee, S., and Frey, M.W. (2012). Characterizing zeta potential of functional nanofibers in a microfluidic device. *J. Colloid Interface Sci.* 372 (1): 252–260. https://doi.org/10.1016/j.jcis.2012.01.007.

98 Novák, P. and Havlíček, V. (2016). Protein extraction and precipitation. In: *Proteomic Profiling and Analytical Chemistry* (Chapter 4), 2e (ed. P. Ciborowski and J. Silberring), 51–62. Boston, MA: Elsevier.

99 Cai, K., Frant, M., Bossert, J. et al. (2006). Surface functionalized titanium thin films: zeta-potential, protein adsorption and cell proliferation. *Colloids Surf. B Biointerfaces* 50 (1): 1–8. https://doi.org/10.1016/j.colsurfb.2006.03.016.

100 Marcotte, L. and Tabrizian, M. (2008). Sensing surfaces: challenges in studying the cell adhesion process and the cell adhesion forces on biomaterials. *IRBM* 29 (2): 77–88. https://doi.org/10.1016/j.rbmret.2007.11.019.

101 Nudelman, F., Lausch, A.J., Sommerdijk, N.A.J.M., and Sone, E.D. (2013). In vitro models of collagen biomineralization. *J. Struct. Biol.* 183 (2): 258–269. https://doi.org/10.1016/j.jsb.2013.04.003.

102 Tan, F., Liu, J., Song, K. et al. (2018). Effect of surface charge on osteoblastic proliferation and differentiation on a poly(ethylene glycol)-diacrylate hydrogel. *J. Mater. Sci.* 53 (2): 908–920. https://doi.org/10.1007/s10853-017-1558-8.

103 Yoshimoto, H., Shin, Y.M., Terai, H., and Vacanti, J.P. (2003). A biodegradable nanofiber scaffold by electrospinning and its potential for bone tissue engineering. *Biomaterials* 24 (12): 2077–2082. https://doi.org/10.1016/s0142-9612(02)00635-x.

104 Szewczyk, P.K., Metwally, S., Karbowniczek, J.E. et al. (2019). Surface-potential-controlled cell proliferation and collagen mineralization on electrospun polyvinylidene fluoride (PVDF) fiber scaffolds for bone regeneration. *ACS Biomater. Sci. Eng.* 5 (2): 582–593. https://doi.org/10.1021/acsbiomaterials.8b01108.

105 Metwally, S., Ferraris, S., Spriano, S. et al. (2020). Surface potential and roughness controlled cell adhesion and collagen formation in electrospun PCL fibers for bone regeneration. *Mater. Des.* 194: 108915. https://doi.org/10.1016/j.matdes.2020.108915.

16

Biopolymer Beads for Biomedical Applications

Poonam Trivedi[1], Subhash Tripathi[2], and Pedro Fardim[1,3]

[1]Åbo Akademi University, Laboratory of Fibre and Cellulose Technology, 20500 Turku, Finland
[2]Centre for Immunity and Immunotherapy, Seattle Children's Research Institute, 1900-9th Ave, 98101, Seattle, WA, USA
[3]KU Leuven, Department of Chemical Engineering, Celestijnenlaan 200F bus 2424, B-3001 Leuven, Belgium

16.1 Introduction

Nature has evolved over millions of years and produced extremely precise architectures in the form of biopolymers with functional features. Biopolymers are defined as the polymers synthesized by living organisms or chemically synthesized using a biological material [1]. Polysaccharides are the enzymatically synthesized biopolymers, in which monosaccharide units are the building blocks. They can be further differentiated into homopolysaccharide (only one type of monosaccharide) or heteropolysaccharide (different types of monosaccharides). Based upon the origin or source, the polysaccharides can be isolated from plants (e.g. cellulose, hemicellulose, lignin, starch, pectin, and guar gum), seaweeds (agar, alginate, carrageenan), animals (chitin, hyaluronan, and chondroitin sulfate), and bacteria and fungi (dextran, pullulan, cellulose) [2]. Depending upon the presence of functional moieties, they can be further classified as neutral (cellulose, dextran), acidic (hyaluronic acid, alginic acid), basic (chitin, chitosan), or sulfated (heparin sulfate, chondroitin sulfate) [3]. The polysaccharides are involved in various pivotal functions in the living organisms, for instance from providing structural support and cellular communication to energy storage. These biopolymers have found numerous applications from construction to the biomedicine, and still the scientific community is involved in exploring top-down and bottom-up approaches to design advanced materials for value-added applications. Owing to the properties such as biocompatibility, processability, and possibility of chemical functionalization, the biopolymers have been transformed into various forms such as fibers, films, beads, and composites. The beads designed from any biopolymer can be defined as a spherical particle prepared via dissolution, shaping, and regeneration of the biopolymer. The size may vary from μm to mm depending upon the source of biopolymer droplet ejection. The potential of designing pristine as well as functional beads from the biopolymers such as agarose, cellulose, dextran, and many more has provided a platform to utilize the

Functional Biomaterials: Design and Development for Biotechnology, Pharmacology, and Biomedicine, First Edition. Edited by Tamilselvan Mohan and Karin Stana Kleinschek.

entities in the various biomedical applications such as protein purification, drug delivery, and immunodiagnostics. The beads are now also explored in the area of cell encapsulation for therapeutics and diagnostics. This chapter focuses on the most utilized biopolymers, their chemical functionalization, the technological evolution in beads design, and the potential biomedical applications.

16.2 Agarose

Agarose is a biopolymer isolated from seaweed agar and is a linear polysaccharide consisting of 1,3-linked β-D-galactopyranose and 1,4-linked 3,6-anhydro-α-L-galactopyranose. It has a double helical structure with 0.95 nm axial periodicity, as revealed by X-ray diffraction measurements [4]. The presence of four free hydroxyl groups in each agarobiose unit provides opportunity for introducing functional moieties that can have effect on cross-linking capacity and hydrophilicity. The dissolution, melting, and gelation behavior of agarose are highly temperature dependent. It dissolves in water at 90–100 °C, melts at around 80–95 °C, and forms a gel at 32–45 °C. During gelation the random coiled structure of agarose transforms into double helix initially followed by clusters of helices in the final gel [5]. The agarose has been designed in the form of beads and has found applications in separation of biomolecules, vehicles for drug delivery, scaffolds for tissue engineering, actuators for optics and fluidics, and model extracellular matrices for biological studies.

16.2.1 Agarose Beads Preparation and Applications

Over the past two decades, the research in the area of agarose beads design and functionalization has provided solutions to the scientific community especially in the area of biochromatography to purify complex biological fluids. Agarose beads can be defined as hydrogel microspheres of varying particle diameter prepared from different concentrations of agarose. There have been various techniques patented to design agarose beads. The most studied techniques are (i) emulsification in a stirred vessel or high shear mixer [6], (ii) membrane emulsification [7], and (iii) spray gelation [8, 9].

In general, the agarose is dissolved in water and mixed with a hydrophobic solvent of choice. The emulsion formed is agitated to design droplets, which are stabilized by surfactant. Finally, the droplets are solidified by gelation and washed to remove any traces of solvents and surfactants. A more detailed explanation of previously mentioned emulsification techniques to design agarose beads is explained in the next paragraph.

(i) Emulsification in a stirred vessel or high shear mixer: The emulsification in a stirred vessel technique can be utilized to design composite beads. For example, researchers have prepared porous agarose-coated zirconia–silica particles by a three-phase emulsification process in which solid zirconia–silica particles

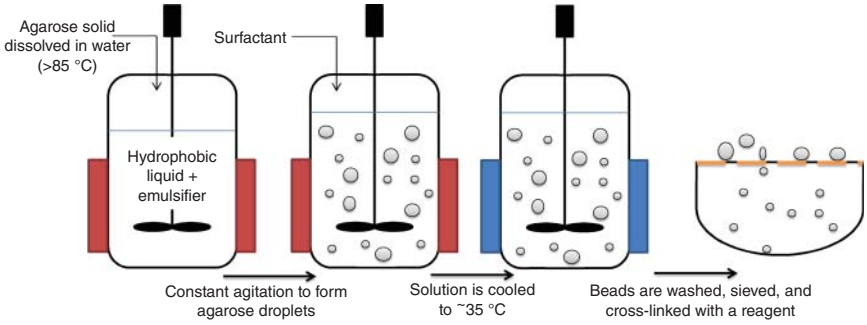

Figure 16.1 General method of making porous agarose beads via emulsification in a stirred vessel. Source: Nweke et al. [10]/Elsevier/CC BY 4.0.

(120 μm average diameter) were suspended in an aqueous solution of agarose that was emulsified in an oil–surfactant mixture in a stirred vessel to yield composite droplets, which upon cooling resulted in spherical particles. The agitation speed, surfactant concentration, oil viscosity, and slurry composition regulate the beads properties such as size, shape, and surface smoothness [6] (Figure 16.1).

(ii) Membrane emulsification: The membrane emulsification also utilizes the basic principle of emulsification where the aqueous solution of agarose at temperature above 50 °C is permeated through uniform pores of microporous membrane into the oil phase by the pressure of nitrogen gas to form uniform W/O emulsion, followed by cooling to form stable beads, as shown in Figure 16.2a. The mechanism of fine beads preparation from a coarse agarose emulsion is shown in Figure 16.2b. Different sized beads can be prepared by using membranes with different pore sizes [7, 11].

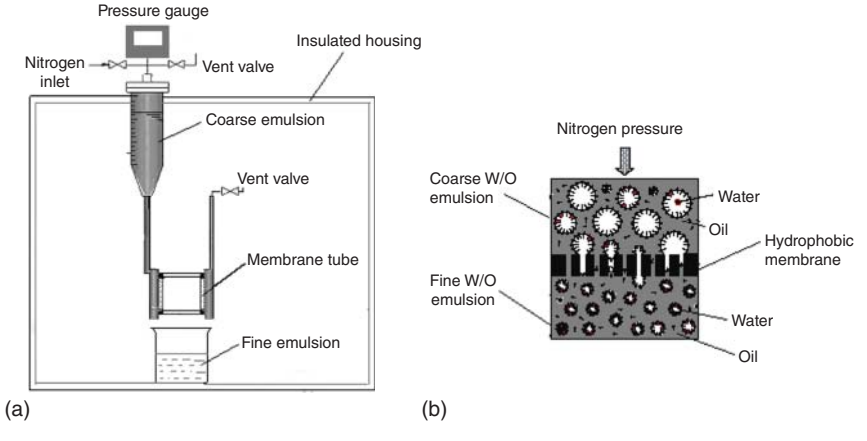

Figure 16.2 (a) Pictorial presentation of equipment for premix membrane emulsification and (b) principle of premix membrane emulsification for preparing W/O emulsion. Source: Zhou et al. [11]/with permission of Elsevier.

(iii) Spray gelation: The spray-gelation method utilizes a nozzle to spray the hot aqueous agarose solution that results in the formation of droplets. The droplets turn spherical mostly due to surface tension and after coming in contact with the nonsolvent transforms into stable beads, as shown in Figure 16.3 [8, 9].

The initial concentration of agarose in the solution also affects the matrix pore size of the designed beads. The agarose concentration in the commercially available beads varies from 4% to 9%. Higher the agarose concentration, smaller are the pore sizes in the beads. The beads can be further cross-linked with cross-linking agents such as epichlorohydrin [12], 2,3-dibromopropanol [13], and divinyl sulfone [14] to enhance the mechanical properties and pressure stability as shown in Figure 16.1. The highly cross-linked beads can be used for fast protein liquid chromatography (FPLC).

The presence of hydroxyl groups provides the opportunity for chemical functionalization of the agarose beads. The agarose beads can be functionalized to introduce various types of functional moieties such as amine, carboxylic, thiol, and hydrazide [15]. Various types of activated agarose beads can also be designed by introducing functional groups such as aldehyde, cyanogen bromide (CNBr), *N*-hydrosuccinamide (NHS), and carbonyldiimidazole (CDI) for specific coupling chemistries with various biological components [15, 16]. Surface functionalization of beads is comparatively easier than core due to poor reactivity and unavailability of the inner hydroxyl groups, which are already involved in the bead network formation. The core functionalization of beads could destroy the internal network structure causing beads shape deformation, reduction in mechanical strength, or final biopolymer dissolution. Therefore, the derivatization needs to be performed in such a way that it enhances the beads properties for any applications without disturbing the strength or mechanical properties of the beads.

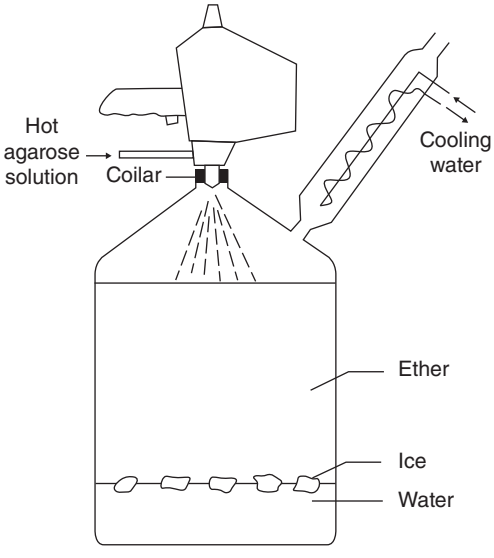

Figure 16.3 Pictorial representation of spray-gelation technique to design agarose beads. Source: Prescan et al. [9]/with permission of Elsevier.

16.2.1.1 Agarose Beads in Protein Purification

There are numerous commercial suppliers of agarose beads worldwide. For example, Sepharose is the GE trademark for cross-linked agarose beads. In protein chromatography, agarose beads are used to purify components based on various principles, e.g. size exclusion, affinity chromatography, and hydrophobic interaction chromatography. In size exclusion, the proteins are purified based on their molecular weight and the size exclusion limit of the beads is governed by the initial concentration of the agarose employed in the solution. For example, 4% initial agarose concentration beads have the size exclusion limit for globular proteins c. 30 000 kDa, whereas 9% have c. 150 kDa. In immobilized metal affinity chromatography (IMAC), transition metal ions such as nickel (Ni^{2+}) and cobalt (Co^{2+}) are immobilized to the agarose beads matrix through a chelating ligand, e.g. nitrilotriacetic acid (NTA) or iminodiacetic acid (IDA). They are especially used for the purification of his-tagged proteins [17, 18]. Agarose beads decorated with hydrophobic groups such as phenyl, octyl, or butyl are also another well-established mode to purify proteins. The mode is known as hydrophobic interaction chromatography, and the purification mechanism relies on the surface charge and hydrophobicity of the protein.

Agarose beads are also used for immunoprecipitation and antibody purification. They have been used as a support to attach a specific antibody, which is responsible for the purification of an antigen from the complex biological fluid [19]. The Protein A–bound agarose beads have been used to purify classes, subclasses, and fragments of immunoglobulins as well as isolation of immune complexes, while Protein G–bound agarose beads have been used for antibody immunoprecipitation and immunoglobulins or IgG fractions purification [20, 21]. The SA beads are also highly suitable as a solid support for microfluidic immunoassays as investigated [22]. Therefore, the protein purification niche of the agarose beads is already an established area, but still a lot of new investigations are ongoing to develop new functional beads for future applications.

16.2.1.2 Agarose Beads in Drug Delivery

Agarose beads have also been investigated for the drug loading and delivery. In a study, to achieve sustained release of ibuprofen or indomethacin from agarose beads, placebo beads were designed by dropwise addition of a hot aqueous agarose solution into a beaker of chilled mineral oil and water. The ethanolic solutions of drugs were used to load the drugs into the beads. The beads were further dried at room temperature. The drug release was followed at various temperatures and pH conditions. The results showed that the drug release was primarily diffusion controlled, and the release mechanism for indomethacin and ibuprofen is governed by swelling of the beads, dissolution of crystallized drug, and diffusion of dissolved drug from the beads [23]. Another study showed the potential of cyanogen-bromide-activated agarose beads to conjugate mitomycin C (MMC) for the timed release of the derivative of MMC for cancer chemotherapy. The MMC released successively for longer period from MMC–agarose beads *in vitro* and *in vivo* after intraperitoneal injection to mice. The MMC–agarose beads also exhibited almost identical inhibitory effect against the growth of Ehrlich ascites carcinoma (EAC) cells to free MMC [24].

Still none of the systems are commercial for any drug delivery to the clinical patients. Therefore, more investigation and research need to be performed in the future.

16.2.1.3 Agarose Beads in Cell Encapsulation and Tissue Engineering

The biopolymer-based hydrogel beads for biomedical applications have gained attention due to the potential of cells encapsulation in the biohydrogel matrix. Agarose provides an attractive platform for cell encapsulation due to its tendency to form hydrogels upon mild gelation with extensive intermolecular hydrogen bonding [25]. In a study, compressive bioreactors were used to design tissue-engineered cartilage using an agarose hydrogel. The designed hydrogel has almost matched the mechanical properties and sulfated glycosaminoglycan content of native articular cartilage [26]. The major drawback of agarose is the lack of receptors in the mammalian cells, which could bind to the agarose matrix thus overruling the potential use of agarose for any biomedical applications.

16.3 Cellulose

Cellulose is the most abundant biopolymer on earth and it consists of linearly arranged D-anhydroglucopyranose units (AGU) linked via β-(1,4) glucosidic covalent bonds at the molecular level. Each repeating AGU possesses three hydroxyl groups, one primary and two secondary. The primary hydroxyl group is present at C-6, and the secondary is at C-2 and C-3 positions. The shaping of cellulose in the form of beads, fibers, and scaffolds requires dissolution in a suitable solvent followed by regeneration. An extensive review on cellulose solvents can be found in the literature [27]. Broadly, the cellulose solvents can be classified as derivatizing and nonderivatizing solvents. Derivatizing solvents are the class of solvents that chemically react with the cellulose, and the intermediate formed is soluble in various solvents, e.g. carbon disulfide (CS_2) and formic acid. On the other hand, nonderivatizing solvents can dissolve cellulose directly without any stable intermediate formation, e.g. ionic liquid (IL) 1,5-diaza bicyclo[4.3.0]non-5-enium acetate ([DBNHH][OAc]), organic liquid salt solution *N*-methylmorpholineoxide-water ($NMMO/H_2O$), and aqueous or protic solvent 7–10% sodium hydroxide (NaOH) in water. The dissolution process is based on the fundamental mechanism of disruption of extensive inter- and intramolecular hydrogen bonding, van der Waals forces while regeneration is based upon reformation of the same network. The structure of cellulose at the macromolecular level is fascinating and decides various properties of cellulose such as solubilization and functionalization.

16.3.1 Cellulose Beads Preparation and Applications

Spherical cellulose beads were first prepared by Jr. John J. O'Neill in 1947. The viscose solution was used to prepare the beads in an aqueous coagulation medium and termed as cellulose pellets. A patent application was filed in the same year, which

was granted in 1951 [28]. Until now various procedures for designing cellulose beads have been developed with diameters ranging from about 10 μm to 1–3 mm using different solvents and techniques to obtain spherical particles.

The basic principle to design beads involves four steps: (i) cellulose or cellulose derivative dissolution in the solvent, (ii) spherical shaping of the biopolymer solution, (iii) solidification or sol–gel transition of the beads, and (iv) water washing and hygienic storage. The cellulose beads design technique has evolved from hand dropping the viscose solution into the coagulation bath as patented by J. O'Neill to the automated systems such as spinning drop atomization and spinning disc atomization. A detailed review on cellulose beads design and application is written by Martin Gericke [29]. In brief, cellulose beads can be designed by dropping or dispersion techniques, as shown in Figure 16.4c–g. The dropping technique involves the formation of spherical droplets of the cellulose or cellulose derivative solution followed by solidification of the droplets in a coagulation bath of a nonsolvent. For large-scale production, automated systems are employed, and the techniques such as spinning drop atomization and spinning disc atomization are useful. The beads properties such as shape and size are governed by solution viscosity, ejection speed, rotational speed, falling height, nozzle, or pore size [30]. Another automated technique to design beads is jet cutting, in which at high velocity constant stream of biopolymer solution comes out and a rotating knife apparatus cuts the stream into spherical particles.

In dispersion technique, the cellulose or cellulose derivative solution is mixed with an immiscible solvent under high rotational speed, thus resulting in the formation of an emulsion that is stabilized with the aid of surfactants [31]. The emulsion contains droplets of biopolymer, which can be solidified in coagulation medium. The size of the beads is governed by mixing speed, viscosity of the dispersion medium and cellulose solution, ratio of hydrophobic to hydrophilic solvent, and the amount of surfactant. The cellulose beads prepared by dispersion technique are generally 10 times smaller as compared to the beads prepared by dropping techniques.

The functionalization of cellulose beads is a prerequisite for any applications such as protein purification and water treatment. Thus, the three hydroxyl groups in an AGU provide the opportunity for introduction of the desired functional moiety. Heterogeneous mode of functionalization is the best approach to design functional beads. The cellulose beads are functionalized based upon the application. For example, anionic beads decorated with carboxymethyl or sulfoalkyl groups are used as ion exchangers [30, 32]. Hydrophobic cellulose beads can be designed by reaction with trimethylsilyl chloride or hexamethyldisilazane [33, 34]. The selective oxidative cleavage of C2–C3 with $NaIO_4$ results in the generation of carbonyl groups, which have been utilized for the enzyme immobilization [35]. Carboxylic cellulose beads can be designed by 2,2,6,6-tetramethylpiperidine 1-oxyl radical (TEMPO) catalyst-mediated oxidation, which results in the oxidation of C6 hydroxyl group [36]. The same system can also be explored to design zwitterionic beads by exploiting the carbonyl groups generated as intermediate during the reaction along with carboxylic groups. The carbonyl groups can be further coupled with hydrazide reagents to introduce cationic moieties in the beads [37]. Functional cellulose

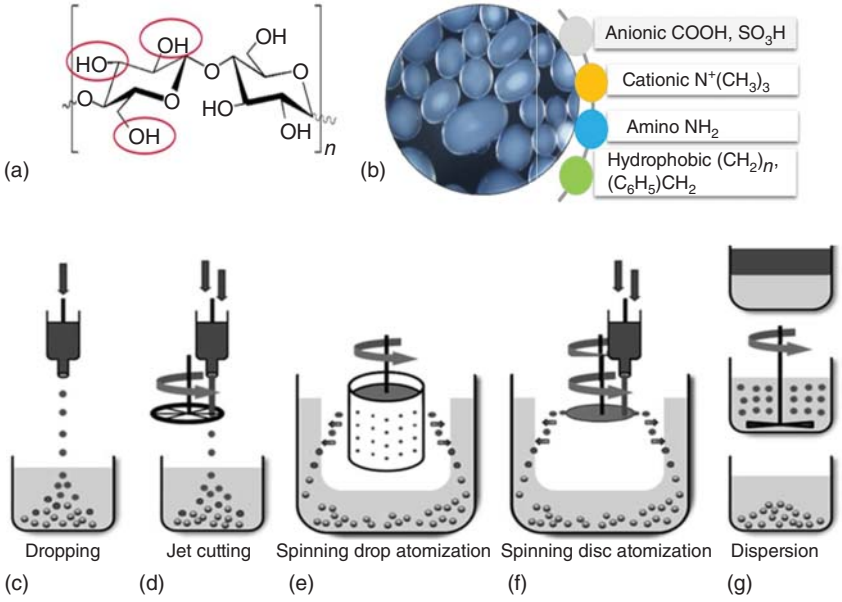

Figure 16.4 (a) Molecular structure of cellulose showing hydroxyl groups available for functionalization in an anhydroglucose unit, (b) possible functionalization of the cellulose beads, schematic drawings of the procedures to prepare cellulose beads by different techniques: dropping (c), jet cutting (d), spinning drop atomization (e), spinning disc atomization (f), and dispersion (g). Source: Gericke et al. [29]/with permission of American Chemical Society.

beads can be designed by blending with other compatible polymers [38]. There are various cellulose beads manufacturers and suppliers worldwide. Cellufine from JNC corporation and Viscopearl from Rengo company are the well-known suppliers of varieties of cellulose beads.

16.3.1.1 Cellulose Beads in Biochromatography

The cellulose beads have been extensively applied as a stationary phase in biochromatography due to spherical shape, lesser flow resistance, and high mechanical strength [39]. The porous cellulose beads have been utilized in size exclusion chromatography, where the separation is based upon the size of the hydrodynamic radii of the macromolecules and independent of any charge or ionic interaction [40]. Cellulose beads are also promising entities for immobilizing enzymes due to their biocompatibility, sustainability, and can be chemically modified. Generally, the immobilization of proteins is performed by coupling of their functional amino acid residues with reactive groups on the cellulose beads. Cellulose beads have also been used as bioaffinity matrix to purify antibody or its target by coupling the corresponding counterpart to cellulose beads [41, 42]. The cellulose beads modified with lysine, poly(lysine), or poly(ethyleneimine) have been applied for the removal of endotoxin and DNA from different biological samples, including blood [43, 44]. Dextran-sulfate-coated cellulose beads packed in a column are commercially used

for blood purification [45]. Cellulose acetate beads column known as Adacolumn (JIMRO, Takasaki, Japan) is used to purify the blood by selectively removing granulocyte and monocyte without disturbing either lymphocyte or platelet content [46]. Cellulose sulfate beads have shown the potential in binding different types of virus and virus-like particles [47, 48]. Now the latest inventions are more focused on utilizing cellulose or cellulose-based nanobeads for immunochromatography. A fast and easy immunochromatography assay was developed using dye-labeled cellulose nanobeads (CNBs) to detect proteins with hexahistidine tag (His-tag) and to characterize recombinant proteins during purification. The same assay can be used to detect other His-tagged proteins without protein-specific antibodies [49]. The commercial production of CNBs has been done by Asahi Kasei Fibers and named as NanoAct™ CNBs. These beads can be used for lateral flow immunoassay and other assay applications [50]. Cellulose-based nanobeads modified with α-tubulin were also used for the detection probe of competitive immunochromatographic (IC) assay for preliminary diagnosis of kidney injury [51]. In future, cellulose beads can still be explored to find potential application in the immunochromatography area.

16.3.1.2 Cellulose Beads in Drug Delivery and *In Vitro* Disease Models

Cellulose powder and granules have been used as a filler in the food and pharmaceutical industry due to their nontoxic nature. In case of drug delivery, sustained release of drugs is a prerequisite for any disease treatment. Cellulose beads are advantageous over conventional granular materials due to their higher surface area and can be loaded uniformly with high amounts of drugs [7]. Cellulose beads decorated with carboxymethyl or phosphate have shown the potential of being utilized as tablet matrix for the gradual release of poorly water-soluble drug prazosin hydrochloride [52]. Apart from drug-delivery carrier, pristine or other biopolymer mixed cellulose beads have the potential to be explored as *in vitro* disease models for drug testing by encapsulating the disease model cells. In a study, TEMPO-oxidized nano-fibrillar cellulose (ToNFC) macromolecules were transformed into beads via ionotropic gelation in calcium chloride ($CaCl_2$). OSTEO-1 rat bone cells were loaded into the beads and shown to maintain the viability of the cells for two weeks. These beads can have considerable potential application in cell therapy and regenerative medicine [53].

16.4 Alginate

Alginate is the most abundant marine biopolymer with polyanionic character and is extracted from various species of brown seaweeds and bacteria, *Pseudomonas* and *Azotobacter* [54]. It occurs in the form of calcium, sodium, and magnesium salts of alginic acid in the seaweeds. It is composed of (1,4)-linked β-D-mannuronic (M block) and α-L-guluronic (G block) acids [55]. The ratio between the G and M blocks depends on the seaweed source from which it is extracted and the culture or growth conditions. High content of guluronic blocks (G block) has been reported in alginates derived from seaweed stems, whereas alginates derived from seaweed leaves have shown higher content of mannuronic blocks (M block). Alginates with

higher content of GG blocks are shown to form stronger gels than those with a high content of MM blocks due to their greater ability to bind calcium [56]. The G blocks are known to provide rigidity to the polymeric structure, and higher concentration of G blocks in alginates results in the formation of stronger gels [57, 58]. Due to the polyanionic nature, alginate forms complexes with positively charged species such as metal cations. It is believed that cations prefer to bind the G blocks of the chains, but recent studies also suggest that the M block also plays a crucial role in cross-linking the polymer chains [59]. The main difference at the molecular level between algal and bacterial alginates is the presence of O-acetyl groups at positions C2 and/or C3 in the bacterial alginates [60].

16.4.1 Alginate Beads Preparation and Applications

The unique properties of alginates such as nontoxicity, biocompatibility, biodegradability, stability at high temperature, and hydrophilicity make them one of the most suitable biopolymers of choice for designing beads for biomedical applications. The alginate bead generation can be performed by external or internal mode of gelation. The external gelation method involves the diffusion of cations for alginate cross-linking exogenously. The simplest technique to design alginate beads externally involves the dissolution of sodium alginate in water followed by dropping beads manually or through automated system in the gelation solution mostly in calcium chloride of known concentration (Figure 16.5) [62].

A study was performed to design scalable alginate beads by dropwise method, which yielded up to 3500 gelled beads per minute of 2.8 ± 0.15 mm diameter and very narrow size distribution, as shown in Figure 16.4. The standard extrusion head

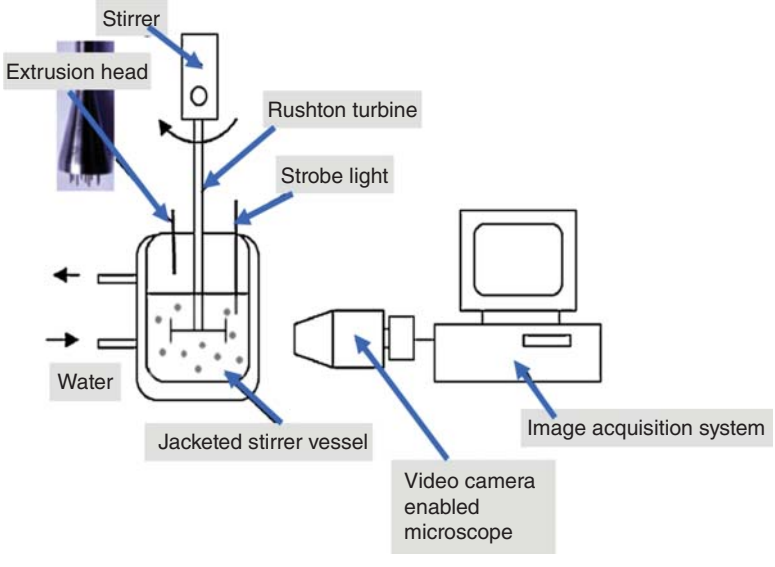

Figure 16.5 Schematic presentation of scalable alginate beads design system. Source: Swioklo et al. [61]/Elsevier/CC BY 4.0.

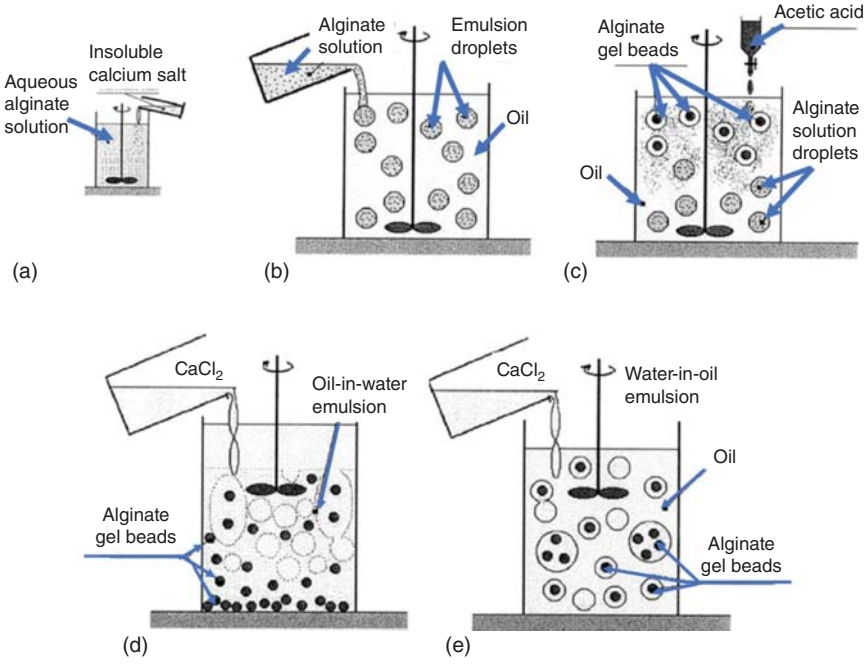

Figure 16.6 Different stages of the preparation of alginate beads by emulsification:internal gelation method. Source: Poncelet et al. [63]/with permission from Elsevier.

was customized to increase the number of droplets formation by including multiple needles. The increasing concentration of alginate in the solution resulted in the formation of beads with enhanced mechanical strength that could be clearly related to the increased gel network formation due to higher alginate concentration.

In internal gelation method, an insoluble source of cross-linking ions is required within the alginate solution. In a study, the internal gelation of the alginate solution was achieved rapidly through the release of calcium ions from an insoluble dispersed calcium complex in the aqueous phase. The authors described the beads formation in five steps, as shown in Figure 16.6 [63].

(a) Sodium alginate solution is mixed with calcium carbonate to prepare insoluble dispersed calcium complex in aqueous phase.
(b) The alginate–calcium–salt mixture was dispersed in canola oil by stirring, which resulted in the formation of beads.
(c) The calcium ion release from the beads was initiated by lowering the pH of the solution via gentle acidification using canola oil containing glacial acetic acid, which is an oil-soluble acid.
(d) The oilbead suspension was added to the calcium chloride solution. This resulted in external gelation of the beads due to coalescence between the aqueous droplets containing pregelled alginate beads and those containing the calcium chloride solution.

(e) After adding into a water in oil (w:o) emulsion of some critical volume of calcium chloride solution, the phase inversion in the emulsion occurs. After complete partitioning of beads to the aqueous phase, the oil was discarded, the beads were washed with 1% Tween 80 and filtered on a 30 mm sieve.

Alginate has also been tested in various biomedical applications, such as treatment of brain tumors [64], protective barrier to enhance cell therapies [65], and drug delivery. Alginate or alginate–copolymer beads have also been explored in biomedical applications such as drug delivery and cell encapsulation [61, 66].

16.4.1.1 Alginate Beads in Drug Delivery

The Food and Drug Administration (FDA) has approved several alginate salts as well as propylene glycol alginate derivative as GRAS (generally regarded as safe) ingredients for oral administration [67]. Pure or derivatized alginate or alginate–copolymer beads have been explored in drug-delivery applications. A study utilized periodate-oxidized sodium alginate to design beads with calcium ions to entrap flurbiprofen drug. The beads were covalently cross-linked with adipic dihydrazide (ADH). The oxidized alginate beads having degree of oxidation 1 mol%, entrapped 89% flurbiprofen and released almost all of its content within 1.5 hours in pH 7.2 phosphate buffer solution. The results showed stable nature of flurbiprofen in the beads; therefore, the authors propose the potential of oxidized beads as sustained oral delivery system for the drug [66].

In a study, pH-sensitive starch-*g*-poly(acrylic acid)/sodium alginate (St-*g*-PAA/SA) hydrogel beads were prepared for the controlled release of diclofenac sodium (DS) by cross-linking sodium alginate using calcium ions in the presence of the St-*g*-PAA superabsorbent. The pristine SA-DS hydrogel beads showed disintegration within three hours in phosphate buffer solution (pH 7.4), whereas the SA-DS beads disintegration was delayed by introducing a relevant amount of the St-*g*-PAA superabsorbent [68]. A research work showed the design of buoyant alginate beads design by mixing sodium alginate with vegetable oil and chitosan to study the release of incorporated metronidazole drug in the artificial gastric juice and guinea pigs gastric environment, respectively. The authors claim that the release properties of alginate gels are applicable not only for sustained release of drugs but also for targeting the gastric mucosa [69].

Carrageenan-sodium alginate (Caralgi) interpenetrating polymer network (IPN) hydrogel beads were prepared under mild conditions to study the release of water-soluble drug betamethasone acetate. The system exhibited a loading efficiency that is dependent on the pH and temperature. Maximum loading efficiency (71%) was achieved at pH 4.8 and 55 °C [70].

Alginate–guar gum hydrogel beads cross-linked with glutaraldehyde were designed to study the controlled delivery of protein drugs. The beads having an alginate to guar gum percentage combination of 3 : 1 showed better encapsulation efficiency of protein model drug (BSA) and bead-forming properties in the preliminary studies. Freeze-dried beads showed swelling ratios most suitable for drug release in simulated intestinal media and protein release was minimal at pH 1.2

(approximately 20%) and significantly higher (approximately 90%) at pH 7.4. The researchers propose that the presence of guar gum and glutaraldehyde cross-linking increases entrapment efficiency and prevents the rapid dissolution of alginate in higher pH of the intestine, ensuring a controlled release of the entrapped drug [71].

In a recent study, pH-responsive calcium alginate–chitosan (CHT) microbeads are designed to study the programmed release of encapsulated risedronate (RIS-antiosteoporotic drug) through a microfluidic device. The microbeads are resistant to the acidic environment of the stomach and may improve the therapeutic effectiveness and could reduce the gastric adverse effects associated with RIS by preventing its decomposition in the acidic condition of stomach [72]. Therefore, copolymers also play a crucial role in designing efficient biopolymer beads for the drug-delivery applications.

16.4.1.2 Alginate Beads as Cell Encapsulation Systems

Since alginate is biodegradable, nontoxic, and has controllable porosity, which is well suited for any cell encapsulation system, alginate beads have been extensively studied for microencapsulation of therapeutic agents and cells [73–75]. The first use of hydrogels for cell encapsulation was pioneered by Lim and Sun. They created calcium alginate microspheres for the encapsulation of islet cells as an approach to treat diabetes and were able to correct the diabetic state of rats for several weeks [76]. The work truly paved a way to the potential for cell encapsulation within hydrogel biomaterials to develop advanced hydrogels for the transplantation of therapeutic cells. A study was performed to design scalable alginate-encapsulation beads system to heighten the preservation of human adipose-derived stem cells (hASCs) during hypothermic storage. The encapsulated hASCs in the beads displayed no loss in cell viability and had a uniform distribution after high-volume production. After storage the released cells were able to attach and recover a normal morphology in culture conditions [61].

Another study showed the potential of utilizing alginate beads designed by internal method of emulsification for mouse insulinoma 6 (MIN6) cell immobilization and survival, similar to the beads designed by extrusion process, i.e. external gelation method. The authors claim that the emulsion process yielded $90 \pm 2\%$ MIN6 cell survival, and the cells expanded at the same rate in both bead types to form pseudo-islets with increased glucose stimulation index compared to cells in suspension. Thus, the emulsification process could also be a mode of choice for the production of immobilized or encapsulated cellular therapeutics on a clinical scale [77].

Alginates can also be mixed with other biopolymers to design beads with enhanced material properties. For example, RGD peptides conjugated to alginate improved human umbilical vein endothelial cell (HUVEC) proliferation and adhesion when compared to a nonmodified alginate group [78]. A study showed the potential of alginate hybrid beads design by mixing the calcium alginate with poly(ethylene glycol) (Alg-PEG-M) followed by extrusion process under physiological condition. A solution mixture of sodium alginate (Naalg) and multiarm vinyl sulfone-terminated PEG (PEG-VS) was extruded into a bath containing calcium

ions and a thiol cross-linker resulting in the formation of gelled spherical calcium alginate (Caalg) matrix [79].

16.5 Chitin and Chitosan

Chitin is the second most abundant biopolymer on earth, found in crustaceans, mushrooms, molluscs, cephalopods, and fungal mycellae, and is chemically composed of poly-*N*-acetylglucosamine. Chitosan is a derivative of chitin obtained after deacetylation, and chemically the major component is β-1,4-linked polymer of glucosamine (2-amino-2-deoxy-β-D-glucose) with minor amounts of *N*-acetylglucosamine. The dissolution of chitosan is pH dependent owing to the presence of amino groups that gets protonated. Chitosan is soluble under acidic conditions and solubility diminishes with increasing pH [80]. The chitosan can form complexes with polyanions such as alginate, pectin, and inorganic salts, and the ability to form complexes with polyanions is dependent upon the degree of deacetylation [81]. The degree of deacetylation, i.e. the availability of the free amino groups, influences the physical, mechanical, and biological properties of chitosan [82, 83]. Chitin and chitosan have been processed in the form of films, sponges, hydrogels, and beads for various biomedical applications, as shown in Figure 16.7 [84–86].

16.5.1 Chitin and Chitosan Beads Preparation and Applications

The chitin/chitosan beads design also follows the same principle as discussed in previous biopolymers agarose and cellulose. The biopolymers need to be dissolved in

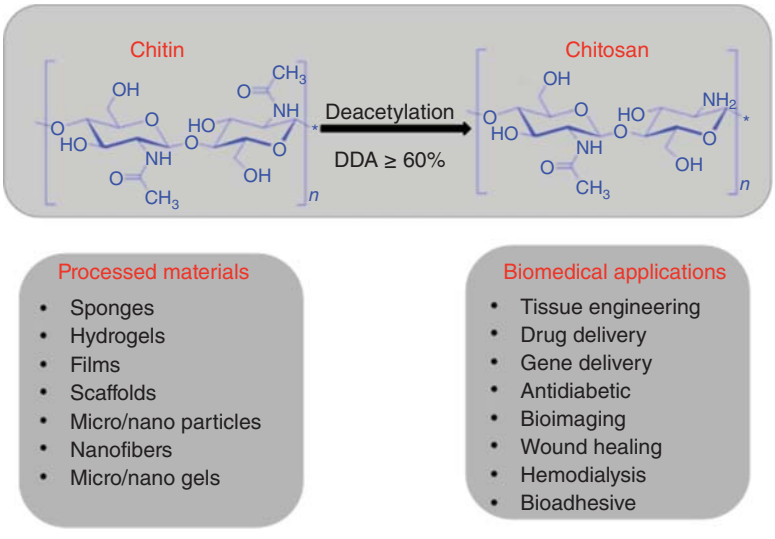

Figure 16.7 A pictorial representation of chitin and chitosan chemical structure, processed materials, and biomedical applications.

the best solvent composition followed by gelation in an antisolvent. To introduce certain specific characteristics such as anionic content, inorganic particles, and magnetic properties, the chitin/chitosan can also be blended with compatible polymers of choice.

Organic solvent salt mixture *N*,*N*-dimethylacetamide (DMA) and *N*-methyl-2-pyrrolidone (NMP) with LiCl at temperature above 100 °C has shown the potential of dissolving chitin. The LiCl forms a coordination complex with chitin that is dissolved in DMA and NMP. Inorganic bases such as NaOH, LiOH, and KOH as aqueous solutions are also the solvent systems of choice to dissolve chitin [87]. The addition of urea in the aqueous-based systems reduces the deacetylation reaction in chitin [88]. Ionic liquids (ILs), such as 1-butyl-3-methylimidazolium chloride (BminCl) and 1-butyl-3-methylimidazolium acetate (BminAc), are considered as green solvents due to nonvolatility, excellent solvation power, strong polarity and stability of end products, and wide temperature ranges in the liquid phase [89]. Chitosan is readily soluble in organic acidic solvents such as 1% acetic acid, L-glutamic acid, lactic acid, succinic acid, and formic acid [90]. The ability of acidic media to protonate the free amino group of the chitosan mainly controls the solubility. In case of inorganic acids, such as sulfuric acid, chitosan forms insoluble ionic complexes [91].

In a study, chitin beads were designed by dissolution in dimethylacetamide (DMAc)/lithium chloride (LiCl) or *N*-methyl-pyrrolidone (NMP)/LiCl solvents and coagulation in antisolvents water, ethanol, and acetone. The study showed that DMAc-based chitin solutions provided better quality beads as compared to NMP-based chitin solutions, and ethanol served as the best antisolvent for coagulation [92]. In a similar study, chitin beads were designed in the same solvent system, i.e. DMA/LiCl described before followed by surface carboxymethylation of the chitin beads. The carboxymethylation was performed with activation of beads in 50% (w/v) NaOH solution followed by reaction with 1.9 M monochloroacetic acid/2-propanol [93]. Another functionalization approach to introduce poly(4-vinyl pyridine) (P4VP) moiety was performed by grafting the chitin with (P4VP) using potassium persulfate ($K_2S_2O_8$) (KPS) as a redox initiator under homogeneous conditions. The potential of the grafted chitin to design physical beads was explored in ethanol as antisolvent. Similarly, organic titanium was used as cross-linking agent to design chitosan beads. The modified chitosan-titanium gel beads showed increased adsorption capacity, good mechanical behavior, strong acidic and alkali resistance as compared to the pristine chitosan beads [94]. There have been various cross-linking agents explored such as glutaraldehyde, epichlorohydrin, and genipin to design chitosan beads with enhanced mechanical properties [95]. Another study showed the design of physical chitosan-ZnO nanocomposite hydrogel beads that have higher swelling ratio in different aqueous solutions in comparison with neat hydrogel for drug-delivery applications [96].

16.5.1.1 Chitin/Chitosan in Drug Delivery

The chitin and chitosan beads have been explored in the area of drug delivery. The (P4VP)-grafted gel beads showed higher cholesterol and Fe^{3+} adsorption capacities

due to microporous bead surface and chemical modification than chitin beads [97]. Sometimes, the beads have also been termed as microspheres or hydrogel beads. Chitin dissolved in ionic liquid followed by sol–gel methodology to design microspheres was also evaluated for drug-delivery system. Dexamethasone was used to perform the experiments and showed sustainable release of the drug from the microspheres [98]. A study showed the potential of utilizing carboxymethyl chitosan to design hydrogel beads in 30% alcohol-aqueous binary solvent for entrapment and release of hydrophobic nutrients or drugs. The hydrogel beads were loaded with vitamin D3, and 96.9% encapsulation efficiency was obtained [99].

16.5.1.2 Chitin/Chitosan in Cell Encapsulation and Tissue Engineering

Chitosan and chitosan-based hydrogel beads have also been tested for cell culture for various applications. In an invention, the design of macroporous chitosan beads having 5–200 μm in size has been claimed with relatively large and uniform pores that are distributed from surface to core region. The macroporous chitosan beads were proposed to be utilized for cell culturing [100]. In another invention, alginate–chitosan hydrogel beads were prepared by combining the biopolymers together with the cartilage-forming cells [101]. A study shows the design of chitosan–cellulose-based hydrogel beads design in aq. NaOH–urea–water solvent system and different acidic mediums (2 M acetic acid, 2 M hydrochloric acid, and 2 M sulfuric acid) as antisolvent. The use of different acids as antisolvent has a clear impact on the retention of the chitosan in the hydrogel beads. The hydrogel beads have shown the potential for future testing in the area of breast cancer and bone cells culturing [81]. A study was performed to evaluate the blood compatibility of the pristine chitosan and polyelectrolyte complex having anticoagulant activity coated chitosan beads. The polyelectrolyte-coated beads showed improved compatibility with blood in comparison with the uncoated chitosan beads [102].

16.6 Conclusion and Outlook

The biopolymer beads design and their applications involved continuous progressive research efforts from different scientific communities such as chemistry, biotechnology, chemical engineering, biology, and many more. The pristine or functionalized biopolymer beads prepared from agarose, cellulose, alginate, chitin, or chitosan have found applications in various biomedical areas. There are various parameters that affect the final properties of the designed beads for any application. The choice of the solvent system for biopolymer dissolution, presence of a copolymer, the methodology to design beads and the gelation system, and the functionalization chemistry govern the beads shape, porosity, and mechanical strength. Also the postprocessing conditions such as solvent exchange, air drying, and lyophilization also affect the beads final properties. The availability of commercial biopolymer beads for various applications, especially biochromatography, provides a substantial motive for pursuing more research to find applications of the beads in tissue engineering, cell therapies, and *in vitro* drug testing. The future needs more strategic researches to design and develop precise application-based biopolymer beads.

References

1 Smith, A.M., Moxon, S., and Morris, G.A. (2016). Biopolymers as wound healing materials. In: *Wound Healing Biomaterials*, vol. 2, 261–287. Elsevier Inc. https://doi.org/10.1016/B978-1-78242-456-7.00013-1.

2 IAEA (2017). *The Radiation Chemistry of Polysaccharides*. IAEA.

3 Kennedy, J.F., Knill, C.J., and Thorley, M. (2001). Natural polymers for healing wounds. In: *Recent Advances in Environmentally Compatible Polymers*, 97–104. Elsevier. https://doi.org/10.1533/9781845693749.2.97.

4 Amsterdam, A., Er-El, Z., and Shaltiel, S. (1975). Ultrastructure of beaded agarose. *Arch. Biochem. Biophys.* 171 (2): 673–677. https://doi.org/10.1016/0003-9861(75)90079-X.

5 Umesh Adiga, P.S., Bhomra, A., Turri, M.G. et al. (2001). Automatic analysis of agarose gel images. *Bioinformatics (Oxford, England)* 17 (11): 1084–1090. https://doi.org/10.1093/BIOINFORMATICS/17.11.1084.

6 Jahanshahi, M., Pacek, A.W., Nienow, A.W., and Lyddiatt, A. (2003). Fabrication by three-phase emulsification of pellicular adsorbents customised for liquid fluidised bed adsorption of bioproducts. *J. Chem. Technol. Biotechnol.* 78 (11): 1111–1120. https://doi.org/10.1002/jctb.907.

7 Zhou, Q.Z., Wang, L.Y., Ma, G.H., and Su, Z.G. (2007). Preparation of uniform-sized agarose beads by microporous membrane emulsification technique. *J. Colloid Interface Sci.* 311 (1): 118–127. https://doi.org/10.1016/j.jcis.2007.02.040.

8 Egorov, A.M., Vakhabov, A.K., and Chernyak, V.Y. (1970). Isolation of agarose and granulation of agar and agarose gel. *J. Chromatogr. A* 46 (C): 143–148. https://doi.org/10.1016/S0021-9673(00)83981-3.

9 Prescan, E., Porumb, H., and Lascu, I. (1989). Simple method for the preparation of spherical agarose and composite gel particles. *J. Chromatogr. A* 469 (C): 396–398. https://doi.org/10.1016/S0021-9673(01)96475-1.

10 Nweke, M.C., McCartney, R.G., and Bracewell, D.G. (2017). Mechanical characterisation of agarose-based chromatography resins for biopharmaceutical manufacture. *J. Chromatogr. A* 1530: 129–137. https://doi.org/10.1016/j.chroma.2017.11.038.

11 Zhou, Q.Z., Wang, L.Y., Ma, G.H., and Su, Z.G. (2008). Multi-stage premix membrane emulsification for preparation of agarose microbeads with uniform size. *J. Membr. Sci.* 322 (1): 98–104. https://doi.org/10.1016/j.memsci.2008.05.025.

12 Porath, J. and Axén, R. (1976). Immobilization of enzymes to agar, agarose, and Sephadex support. *Methods Enzymol.* 44 (C): 19–45. https://doi.org/10.1016/S0076-6879(76)44005-3.

13 Porath, J., Ls, T., and Janson, J.C. (1975). Agar derivatives for chromatography, electrophoresis and gel-bound enzymes. III. Rigid agarose gels cross-linked with divinyl sulphone (DVS). *J. Chromatogr. A* 103 (1): 49–62. https://doi.org/10.1016/S0021-9673(00)83800-5.

14 Ls, T. (1975). Agar derivatives for chromatography, electrophoresis and gel-bound enzymes. IV. Benzylated dibromopropanol cross-linked sepharose as an amphophilic gel for hydrophobic salting-out chromatography of enzymes with special emphasis on denaturing risks. *J. Chromatogr. A* 111 (2): 373–387. https://doi.org/10.1016/S0021-9673(00)99287-2.

15 Cuatrecasas, P. (1970 Jun). Protein purification by affinity chromatography derivatizations of agarose and polyacrylamide beads. *J. Biol. Chem.* 245 (12): 3059–3065.

16 Punna, S., Kaltgrad, E., and Finn, M.G. (2005). "Clickable" agarose for affinity chromatography. *Bioconjugate Chem.* 16 (6): 1536–1541. https://doi.org/10.1021/bc0501496.

17 Block, H., Maertens, B., Spriestersbach, A. et al. (2009). Immobilized-metal affinity chromatography (IMAC). A review. In: *Methods in Enzymology* (Chapter 27), vol. 463, 439–473. Academic Press Inc. https://doi.org/10.1016/S0076-6879(09)63027-5.

18 Porath, J., Carlsson, J., Olsson, I., and Belfrage, G. (1975). Metal chelate affinity chromatography, a new approach to protein fractionation. *Nature* 258 (5536): 598–599. https://doi.org/10.1038/258598a0.

19 Mejía-Manzano, L.A., González-Valdez, J., Mayolo-Deloisa, K. et al. (2016). Covalent immobilization of antibodies for the preparation of immunoaffinity chromatographic supports. *Sep. Sci. Technol.* 51 (10): 1736–1743. https://doi.org/10.1080/01496395.2016.1174264.

20 Moser, A.C. and Hage, D.S. (2010). Immunoaffinity chromatography: an introduction to applications and recent developments. *Bioanalysis*. https://doi.org/10.4155/bio.10.31.

21 Sisson, T.H. and Castor, C.W. (1990). An improved method for immobilizing IgG antibodies on protein A-agarose. *J. Immunol. Methods* 127 (2): 215–220. https://doi.org/10.1016/0022-1759(90)90071-3.

22 Yang, Y., Nam, S.W., Lee, N.Y. et al. (2008). Superporous agarose beads as a solid support for microfluidic immunoassay. *Ultramicroscopy* 108 (10): 1384–1389. https://doi.org/10.1016/j.ultramic.2008.04.044.

23 Häglund, B.O., Upadrashta, S.M., Neau, S.H., and Cutrera, M.A. (1994). Dissolution controlled drug release from agarose beads. *Drug Dev. Ind. Pharm.* 20 (6): 947–959. https://doi.org/10.3109/03639049409038343.

24 Kojima, T., Hashida, M., Muranishi, S., and Sezaki, H. (1978). Antitumor activity of timed-release derivative of mitomycin C, agarose bead conjugate. *Chem. Pharm. Bull.* 26 (6): 1818–1824. https://doi.org/10.1248/cpb.26.1818.

25 Xiong, J.Y., Narayanan, J., Liu, X.Y. et al. (2005). Topology evolution and gelation mechanism of agarose gel. *J. Phys. Chem. B* 109 (12): 5638–5643. https://doi.org/10.1021/jp044473u.

26 Lima, E.G., Bian, L., Ng, K.W. et al. (2007). The beneficial effect of delayed compressive loading on tissue-engineered cartilage constructs cultured with TGF-β3. *Osteoarthr. Cartil.* 15 (9): 1025–1033. https://doi.org/10.1016/j.joca.2007.03.008.

27 Liebert, T. (2010). Cellulose solvents – remarkable history, bright future. In: *ACS Symposium Series*, vol. 1033, 3–54. American Chemical Society. https://doi.org/10.1021/bk-2010-1033.ch001.

28 O'Neil, Jr., J.J. (1951). Methods of producing cellulose pellets. US Patent 2,543,928, filed 19 June 1947 and issued 6 March 1951.

29 Gericke, M., Trygg, J., and Fardim, P. (2013). Functional cellulose beads: preparation, characterization, and applications. *Chem. Rev.* 113 (7): 4812–4836. https://doi.org/10.1021/cr300242j.

30 Ishimura, D., Morimoto, Y., and Saito, H. (1998). Influences of chemical modifications on the mechanical strength of cellulose beads. *Cellulose* 5 (2): 135–151. https://doi.org/10.1023/A:1009277216057.

31 Karbstein, H. and Schubert, H. (1995). Developments in the continuous mechanical production of oil-in-water macro-emulsions. *Chem. Eng. Process. Process Intensif.* 34 (3): 205–211. https://doi.org/10.1016/0255-2701(94)04005-2.

32 Peška, J., Štamberg, J., and Hradil, J. (1976). Chemical transformations of polymers. XIX. Ion exchange derivatives of bead cellulose. *Angew. Makromol. Chem.* 53 (1): 73–80. https://doi.org/10.1002/apmc.1976.050530106.

33 Schuyten, H.A., Weaver, J.W., David Reid, J., and Jurgens, J.F. (1948). Trimethylsilylcellulose. *J. Am. Chem. Soc.* 70 (5): 1919–1920. https://doi.org/10.1021/ja01185a079.

34 Mormann, W. and Demeter, J. (1999). Silylation of cellulose with hexamethyldisilazane in liquid ammonia-first examples of completely trimethylsilylated cellulose. *Macromolecules* 32 (5): 1706–1710. https://doi.org/10.1021/ma9814393.

35 Boeden, H.F., Pommerening, K., Becker, M. et al. (1991). Bead cellulose derivatives as supports for immobilization and chromatographic purification of proteins. *J. Chromatogr. A* 552 (C): 389–414. https://doi.org/10.1016/S0021-9673(01)95956-4.

36 Hirota, M., Tamura, N., Saito, T., and Isogai, A. (2009). Oxidation of regenerated cellulose with $NaClO_2$ catalyzed by TEMPO and NaClO under acid-neutral conditions. *Carbohydr. Polym.* 78 (2): 330–335. https://doi.org/10.1016/j.carbpol.2009.04.012.

37 Trivedi, P., Trygg, J., Saloranta, T., and Fardim, P. (2016). Synthesis of novel zwitterionic cellulose beads by oxidation and coupling chemistry in water. *Cellulose* 23 (3): 1751–1761. https://doi.org/10.1007/s10570-016-0939-5.

38 Trivedi, P., Schaller, J., Gustafsson, J., and Fardim, P. (2017). Supramolecular design of cellulose hydrogel beads. *J. Renewable Mater.* 5 (5): 400–409. https://doi.org/10.7569/JRM.2017.634143.

39 Kaster, J.A., de Oliveira, W., Glasser, W.G., and Velander, W.H. (1993). Optimization of pressure-flow limits, strength, intraparticle transport and dynamic capacity by hydrogel solids content and bead size in cellulose immunosorbents. *J. Chromatogr. A* 648 (1): 79–90. https://doi.org/10.1016/0021-9673(93)83289-5.

40 Vincent, P., Compoint, J.P., Fitton, V., and Santarelli, X. (2003). Evaluation of Matrex cellufine GH 25. *J. Biochem. Bioph. Methods* 56 (1–3): 69–78. https://doi.org/10.1016/S0165-022X(03)00073-3.

41 Weber, V., Linsberger, I., Ettenauer, M. et al. (2005). Development of specific adsorbents for human tumor necrosis factor-α: influence of antibody immobilization on performance and biocompatibility. *Biomacromolecules* 6 (4): 1864–1870. https://doi.org/10.1021/bm040074t.

42 Peng, L., Calton, G.J., and Burnett, J.W. (1987). Evaluation of activation methods with cellulose beads for immunosorbent purification of immunoglobulins. *J. Biotechnol.* 5 (4): 255–265. https://doi.org/10.1016/0168-1656(87)90023-X.

43 Fang, H., Wei, J., and Yu, Y.T. (2004). In vivo studies of endotoxin removal by lysine-cellulose adsorbents. *Biomaterials* 25 (23): 5433–5440. https://doi.org/10.1016/j.biomaterials.2003.12.035.

44 Sakata, M., Nakayama, M., Yanagi, K. et al. (2006). Selective removal of DNA from bioproducts by polycation-immobilized cellulose beads. *J. Liq. Chromatogr. Related Technol.* 29 (17): 2499–2512. https://doi.org/10.1080/10826070600914828.

45 Kobayashi, A., Nakatani, M., Furuyoshi, S., and Tani, N. (2002). In vitro evaluation of dextran sulfate cellulose beads for whole blood infusion low-density lipoprotein-hemoperfusion. *Ther. Apheresis*. https://doi.org/10.1046/j.1526-0968.2002.00421.x.

46 Hibi, T., Sameshima, Y., Sekiguchi, Y. et al. (2009). Treating ulcerative colitis by Adacolumn therapeutic leucocytapheresis: clinical efficacy and safety based on surveillance of 656 patients in 53 centres in Japan. *Dig. Liver Dis.* 41 (8): 570–577. https://doi.org/10.1016/j.dld.2008.11.020.

47 Pereira Aguilar, P., Schneider, T.A., Wetter, V. et al. (2019). Polymer-grafted chromatography media for the purification of enveloped virus-like particles, exemplified with HIV-1 gag VLP. *Vaccine* 37 (47): 7070–7080. https://doi.org/10.1016/j.vaccine.2019.07.001.

48 Yamamoto, S. and Miyagawa, E. (1999). Retention behavior of very large biomolecules in ion-exchange chromatography. *J. Chromatogr. A* 852: 25–30. Elsevier. https://doi.org/10.1016/S0021-9673(99)00594-4.

49 Choi, E.S., Lee, S.G., Lee, S.J., and Kim, E. (2015). Rapid detection of 6×-histidine-labeled recombinant proteins by immunochromatography using dye-labeled cellulose nanobeads. *Biotechnol. Lett.* 37 (3): 627–632. https://doi.org/10.1007/s10529-014-1731-y.

50 Asahi Kasei (n.d.). Commercialization of NanoAct™ cellulose nanobeads as labels for lateral flow immunoassay. Press Releases. https://www.asahi-kasei.co.jp/asahi/en/news/2014/e141216.html (accessed 31 March 2021).

51 Choi, E., Al Faruque, H., Kim, J. et al. (2020). Immunochromatographic assay to detect α-tubulin in urine for the diagnosis of kidney injury. *J. Clin. Lab. Anal.* 34 (1). https://doi.org/10.1002/jcla.23015.

52 Volkert, B., Wolf, B., Fischer, S. et al. (2009). Application of modified bead cellulose as a carrier of active ingredients. *Macromol. Symp.* 280 (1): 130–135. https://doi.org/10.1002/masy.200950615.

53 de Carvalho, R.A., Veronese, G., Carvalho, A.J.F. et al. (2016). The potential of TEMPO-oxidized nanofibrillar cellulose beads for cell delivery applications. *Cellulose* 23 (6): 3399–3405. https://doi.org/10.1007/s10570-016-1063-2.

54 Remminghorst, U. and Rehm, B.H.A. (2006). Bacterial alginates: from biosynthesis to applications. *Biotechnol. Lett.* https://doi.org/10.1007/s10529-006-9156-x.

55 Rowley, J.A., Madlambayan, G., and Mooney, D.J. (1999). Alginate hydrogels as synthetic extracellular matrix materials. *Biomaterials* 20 (1): 45–53. https://doi.org/10.1016/S0142-9612(98)00107-0.

56 Qin, Y. (2008). Alginate fibres: an overview of the production processes and applications in wound management. *Polym. Int.* 57 (2): 171–180. https://doi.org/10.1002/pi.2296.

57 Mancini, M., Moresi, M., and Rancini, R. (1999). Mechanical properties of alginate gels: empirical characterisation. *J. Food Eng.* 39 (4): 369–378. https://doi.org/10.1016/S0260-8774(99)00022-9.

58 Drury, J.L., Dennis, R.G., and Mooney, D.J. (2004). The tensile properties of alginate hydrogels. *Biomaterials* 25 (16): 3187–3199. https://doi.org/10.1016/j.biomaterials.2003.10.002.

59 Donati, I., Holtan, S., Mørch, Y.A. et al. (2005). New hypothesis on the role of alternating sequences in calcium-alginate gels. *Biomacromolecules* 6 (2): 1031–1040. https://doi.org/10.1021/bm049306e.

60 Draget, K.I., Smidsrød, O., and Skjåk-Bræk, G. (2002). Alginates from algae. In: *Biopolymers Online* (ed. E.J. Vandamme, S. De Baets and A. Steinbüchel). Wiley. https://doi.org/10.1002/3527600035.bpol6008.

61 Swioklo, S., Ding, P., Pacek, A.W., and Connon, C.J. (2017). Process parameters for the high-scale production of alginate-encapsulated stem cells for storage and distribution throughout the cell therapy supply chain. *Process Biochem.* 59: 289–296. https://doi.org/10.1016/j.procbio.2016.06.005.

62 Torre, M.L., Giunchedi, P., Maggi, L. et al. (1998). Formulation and characterization of calcium alginate beads containing ampicillin. *Pharm. Dev. Technol.* 3 (2): 193–198. https://doi.org/10.3109/10837459809028495.

63 Poncelet, D., Babak, V., Dulieu, C., and Picot, A. (1999). A physico-chemical approach to production of alginate beads by emulsification-internal ionotropic gelation. *Colloids Surf., A* 155 (2–3): 171–176. https://doi.org/10.1016/S0927-7757(98)00709-2.

64 Bhujbal, S.V., de Vos, P., and Niclou, S.P. (2014). Drug and cell encapsulation: alternative delivery options for the treatment of malignant brain tumors. *Adv. Drug Delivery Rev.* Elsevier. https://doi.org/10.1016/j.addr.2014.01.010.

65 de Vos, P., Faas, M.M., Strand, B., and Calafiore, R. (2006). Alginate-based microcapsules for immunoisolation of pancreatic islets. *Biomaterials*. https://doi.org/10.1016/j.biomaterials.2006.07.010.

66 Maiti, S., Singha, K., Ray, S. et al. (2009). Adipic acid dihydrazide treated partially oxidized alginate beads for sustained oral delivery of flurbiprofen. *Pharm. Dev. Technol.* 14 (5): 461–470. https://doi.org/10.1080/10837450802712658.

67 FDA (2018). Microorganisms & microbial-derived ingredients used in food (partial list). https://www.fda.gov/food/generally-recognized-safe-gras/microorganisms-microbial-derived-ingredients-used-food-partial-list (accessed 31 March 2022).

68 Chang, A. (2015). pH-sensitive starch-*g*-poly(acrylic acid)/sodium alginate hydrogels for controlled release of diclofenac sodium. *Iran. Polym. J.* 24 (2): 161–169. https://doi.org/10.1007/s13726-015-0311-x.

69 Murata, Y., Sasaki, N., Miyamoto, E., and Kawashima, S. (2000). Use of floating alginate gel beads for stomach-specific drug delivery. *Eur. J. Pharm. Biopharm.* 50 (2): 221–226. https://doi.org/10.1016/S0939-6411(00)00110-7.

70 Mohamadnia, Z., Zohuriaan-Mehr, M.J., Kabiri, K. et al. (2007). pH-sensitive IPN hydrogel beads of carrageenan-alginate for controlled drug delivery. *J. Bioact. Compat. Polym.* 22 (3): 342–356. https://doi.org/10.1177/0883911507078519.

71 George, M. and Abraham, T.E. (2007). pH sensitive alginate–guar gum hydrogel for the controlled delivery of protein drugs. *Int. J. Pharm.* 335 (1–2): 123–129. https://doi.org/10.1016/j.ijpharm.2006.11.009.

72 Khajuria, D.K., Vasireddi, R., Priydarshi, M.K., and Mahapatra, D.R. (2020). Ionic diffusion and drug release behavior of core-shell-functionalized alginate-chitosan-based hydrogel. *ACS Omega* 5 (1): 758–765. https://doi.org/10.1021/acsomega.9b03464.

73 Goh, C.H., Heng, P.W.S., and Chan, L.W. (2012). Alginates as a useful natural polymer for microencapsulation and therapeutic applications. *Carbohydr. Polym.* https://doi.org/10.1016/j.carbpol.2011.11.012.

74 Fernández-Hervás, M., Holgado, M., Fini, A., and Fell, J. (1998). In vitro evaluation of alginate beads of a diclofenac salt. *Int. J. Pharm.* 163 (1–2): 23–34. https://doi.org/10.1016/S0378-5173(97)00333-5.

75 Murua, A., Portero, A., Orive, G. et al. (2008). Cell microencapsulation technology: towards clinical application. *J. Controlled Release*. https://doi.org/10.1016/j.jconrel.2008.08.010.

76 Lim, F. and Sun, A.M. (1980). Microencapsulated islets as bioartificial endocrine pancreas. *Science* 210 (4472): 908–910. https://doi.org/10.1126/science.6776628.

77 Hoesli, C.A., Raghuram, K., Kiang, R.L.J. et al. (2011). Pancreatic cell immobilization in alginate beads produced by emulsion and internal gelation. *Biotechnol. Bioeng.* 108 (2): 424–434. https://doi.org/10.1002/bit.22959.

78 Yu, J., Gu, Y., Du, K.T. et al. (2009). The effect of injected RGD modified alginate on angiogenesis and left ventricular function in a chronic rat infarct model. *Biomaterials* 30 (5): 751–756. https://doi.org/10.1016/j.biomaterials.2008.09.059.

79 Mahou, R. and Wandrey, C. (2010). Alginate-poly(ethylene glycol) hybrid microspheres with adjustable physical properties. *Macromolecules* 43 (3): 1371–1378. https://doi.org/10.1021/ma902469f.

80 Rinaudo, M., Pavlov, G., and Desbrières, J. (1999). Influence of acetic acid concentration on the solubilization of chitosan. *Polymer* 40 (25): 7029–7032. https://doi.org/10.1016/S0032-3861(99)00056-7.

81 Trivedi, P., Saloranta-Simell, T., Maver, U. et al. (2018). Chitosan–cellulose multifunctional hydrogel beads: design, characterization and evaluation of cytocompatibility with breast adenocarcinoma and osteoblast cells. *Bioengineering* 5 (1): 3.

82 Lee, K.Y., Park, W.H., and Ha, W.S. (1997). Polyelectrolyte complexes of sodium alginate with chitosan or its derivatives for microcapsules. *J. Appl. Polym. Sci.* 63 (4): 425–432. https://doi.org/10.1002/(SICI)1097-4628(19970124)63:4<425::AID-APP3>3.0.CO;2-T.

83 Martins, G.V., Merino, E.G., Mano, J.F., and Alves, N.M. (2010). Crosslink effect and albumin adsorption onto chitosan/alginate multilayered systems: an in situ QCM-D study. *Macromol. Biosci.* 10 (12): 1444–1455. https://doi.org/10.1002/mabi.201000193.

84 Jayakumar, R., Prabaharan, M., Sudheesh Kumar, P.T. et al. (2011). Biomaterials based on chitin and chitosan in wound dressing applications. *Biotechnol. Adv.* https://doi.org/10.1016/j.biotechadv.2011.01.005.

85 Costa-Pinto, A.R., Reis, R.L., and Neves, N.M. (2011). Scaffolds based bone tissue engineering: the role of chitosan. *Tissue Eng. Part B* 17 (5): 331–347. https://doi.org/10.1089/ten.teb.2010.0704.

86 VandeVord, P.J., Matthew, H.W.T., DeSilva, S.P. et al. (2002). Evaluation of the biocompatibility of a chitosan scaffold in mice. *J. Biomed. Mater. Res.* 59 (3): 585–590. https://doi.org/10.1002/jbm.1270.

87 Einbu, A., Naess, S.N., Elgsaeter, A., and Vårum, K.M. (2004). Solution properties of chitin in alkali. *Biomacromolecules* 5 (5): 2048–2054. https://doi.org/10.1021/bm049710d.

88 Bi, S., Wang, M., Huang, L. et al. (2020). Evaluation of structure transformation and biocompatibility of chitosan in alkali/urea dissolution system for its large-scale application. *Int. J. Biol. Macromol.* 154: 758–764. https://doi.org/10.1016/j.ijbiomac.2020.03.075.

89 Wang, W.T., Zhu, J., Wang, X.L. et al. (2010). Dissolution behavior of chitin in ionic liquids. *J. Macromol. Sci. Part B Phys.* 49 (3): 528–541. https://doi.org/10.1080/00222341003595634.

90 Romanazzi, G., Gabler, F.M., Margosan, D. et al. (2009). Effect of chitosan dissolved in different acids on its ability to control postharvest gray mold of table grape. *Phytopathology* 99 (9): 1028–1036. https://doi.org/10.1094/PHYTO-99-9-1028.

91 Cui, Z., Xiang, Y., Si, J. et al. (2008). Ionic interactions between sulfuric acid and chitosan membranes. *Carbohydr. Polym.* 73 (1): 111–116. https://doi.org/10.1016/j.carbpol.2007.11.009.

92 Yilmaz, E. and Bengisu, M. (2003). Preparation and characterization of physical gels and beads from chitin solutions. *Carbohydr. Polym.* 54 (4): 479–488. https://doi.org/10.1016/S0144-8617(03)00211-X.

93 Yusof, N.L.B.M., Lim, L.Y., and Khor, E. (2001). Preparation and characterization of chitin beads as a wound dressing precursor. *J. Biomed. Mater. Res.* 54 (1): 59–68. https://doi.org/10.1002/1097-4636(200101)54:1<59::AID-JBM7>3.0.CO;2-U.

94 Xu, Y., Shen, C., and Gao, S. (2015). Preparation and characterization of chitosan gel beads crosslinked by organic titanium. *J. Polym. Res.* 22 (4): 1–10. https://doi.org/10.1007/s10965-015-0693-7.

95 Anupama, T., Wanchoo, R.K., Hardeep, and Soni, S.K. (2014). Chitosan hydrogel beads: a comparative study with glutaraldehyde, epichlorohydrin and genipin as crosslinkers. *J. Polym. Mater.* 31 (2): 211–223. https://web.s.ebscohost.com/abstract?direct=true&profile=ehost&scope=site&authtype=crawler&jrnl=09738622&AN=98178836&h=Ph0oDvos5brN6f5Qmvg5E26ZrQK31eELH3XwHoZF1WGVXGRB1lS3VqPhKoDQH6jPU8eL6hbpf0FBhpHpt2TBHA%3d%3d&crl=c&resultNs=AdminWebAuth&resultLocal=Err.

96 Yadollahi, M., Farhoudian, S., Barkhordari, S. et al. (2016). Facile synthesis of chitosan/ZnO bio-nanocomposite hydrogel beads as drug delivery systems. *Int. J. Biol. Macromol.* 82: 273–278. https://doi.org/10.1016/j.ijbiomac.2015.09.064.

97 Oylum, H., Yilmaz, E., and Yilmaz, O. (2013). Preparation of chitin-*g*-poly(4-vinylpyridine) beads. *J. Macromol. Sci. Part A Pure Appl. Chem.* 50 (2): 221–229. https://doi.org/10.1080/10601325.2013.742815.

98 Silva, S.S., Duarte, A.R.C., Mano, J.F., and Reis, R.L. (2013). Design and functionalization of chitin-based microsphere scaffolds. *Green Chem.* 15 (11): 3252–3258. https://doi.org/10.1039/c3gc41060a.

99 Luo, Y., Teng, Z., Wang, X., and Wang, Q. (2013). Development of carboxymethyl chitosan hydrogel beads in alcohol-aqueous binary solvent for nutrient delivery applications. *Food Hydrocolloids* 31 (2): 332–339. https://doi.org/10.1016/j.foodhyd.2012.11.011.

100 Jeong, S.Y., Bae, E., Kwon, I.C., and Choi, K. (2007). Macroporous chitosan beads and preparation method thereof. US20070148770A1, filed 30 November 2006.

101 Henrotin, Y., Sanchez, C., and Kesteloot, F. (2016). Cell cultivation in chitosan alginate hydrogel beads. US9480648B2. https://patents.google.com/patent/US9480648B2/en.

102 Paneva, D., Manolova, N., Rashkov, I., and Danchev, D. (2005). Gel beads composed of chitosan and polyacids and their blood compatibility. *J. Bioact. Compat. Polym.* 20 (2): 133–151. https://doi.org/10.1177/0883911505051855.

17

Recent Advances in 3D Printing in the Design and Application of Biopolymer-Based Scaffolds

Marko Milojević[1,2], Uroš Maver[1,2], and Boštjan Vihar[1,3]

[1] *University of Maribor, Institute of Biomedical Sciences, Faculty of Medicine, Taborska ulica 8, 2000 Maribor, Slovenia*
[2] *University of Maribor, Department of Pharmacology, Faculty of Medicine, Taborska ulica 8, 2000 Maribor, Slovenia*
[3] *IRNAS – Institute for Development of Advanced Applied Systems, Ltd., Limbuška cesta 76b, 2000 Maribor, Slovenia*

17.1 Introduction

The loss or failure of tissues or organs due to natural aging and disease is a critical medical challenge and a difficult and expensive problem in the healthcare system. Transplantation from living or deceased donors is currently the main treatment for organ or tissue failure, but the problem of organ shortage has escalated over the past 30 years. Many patients waiting for an organ transplant have died due to the shortage of suitable donors. At the same time, recipients with successful transplantation are subjected to continuous immunosuppression to prevent acute and chronic graft rejection [1]. Patient-specific artificial 3D replacement tissue/organs made from the patient's own (autologous) cells offer the possibility of overcoming current obstacles [2] and also minimize the risk of tissue/organ rejection and the need for lifelong use of immunosuppressants. The main goal of regenerative medicine (RM), which is to restore or replace diseased or damaged tissues/organs with healthy, functional alternatives, combined with the limited supply of organs worldwide [3], has motivated TE research to develop 3D support structures (scaffolds) that promote the regeneration of various tissues and organs, such as skin, bones, muscles, tendons, cartilage, and cardiac tissue [4]. The use of suitable scaffolds that support cell attachment, proliferation, differentiation, and tissue formation is currently the most promising TE approach for the successful fabrication of artificial tissues and organs. Scaffolds provide transplanted cells with the necessary mechanical support and physical structure to attach, grow, and maintain their physiological functions [5]. A suitable scaffold material must have favorable biocompatibility or cytocompatibility to provide a surface for attachment, proliferation, and differentiation of cells as well as subsequent

Functional Biomaterials: Design and Development for Biotechnology, Pharmacology, and Biomedicine, First Edition. Edited by Tamilselvan Mohan and Karin Stana Kleinschek.

secretion of the extracellular matrix (ECM), which contains structural proteins and bioactive molecules, including glycosaminoglycans (GAGs), collagen, fibronectin, various growth factors, and cytokines. The overall porosity of the material, pore size, and interconnectivity of the scaffold also play an important role in cell adhesion and migration, vascularization, and ingrowth of new tissue [6]. In addition, an "ideal" scaffold suitable for RM must simultaneously support the growth of different cell types and tissues, each with specific mechanical properties, chemical gradients, cell populations, and geometric structures. The scaffold-based approach to construct artificial tissues and organs is also advantageous for achieving the required mechanical properties and degradation kinetics and allows the targeted delivery of biomolecules and growth factors embedded in the scaffold [7].

However, the use of scaffolds still presents some challenges, such as the poor homogeneity within large porous 3D constructs and low initial cell-seeding density. Conventional TE scaffold production methods such as chemical/gas foaming, fiber bonding, particle/porogen salt leaching, solvent casting, freeze-drying, thermally induced phase separation, membrane lamination, foam gel, and electrospinning have severe limitations. They can only control the bulk properties but are often insufficient to fabricate precise pore size, shape, network, internal architecture, topology, and high mechanical strength constructs. In addition, pore size, porosity, and pore interconnectivity are random and heterogeneous, resulting in reduced reproducibility between scaffolds. The specific requirements for porosity and interconnectivity cannot be easily achieved even with traditional TE approaches. Other limitations are also the suboptimal distribution of cells due to the inaccuracies associated with the process of manual seeding the cells. This becomes problematic because the cells may need to be precisely arranged according to the needs and functions of the tissue [8]. The inability of classical TE methods to fabricate complex biomimetic structures leads to oversimplified tissue constructs, making the engineered tissues inaccurate with unrealistic cell microenvironments [9].

The field of TE is ready to address unmet clinical needs by developing new fabrication approaches and complementary strategies. Additive manufacturing (AM) and, in particular 3D printing, an important type of AM technology, is increasingly recognized as a possible solution for the construction of complex scaffolds, which are capable of promoting the regeneration of functional tissue. 3D bioprinting has several advantages over traditional TE methods and is a particularly promising approach to produce patient-specific autologous tissues and organs. Assisted with computer-aided design (CAD) technologies, bioprinting can produce complex 3D structures from the nano- to the micro-range efficiently and cost effectively [10]. However, the difference between "3D printing" and "3D bioprinting" must first be clarified, as these two terms are used interchangeably in the scientific community [11]. 3D printing is a rapid prototyping and AM technique used to fabricate complex 3D architectures with high precision through a layer-by-layer building process [12]. This automated, additive process facilitates the production of 3D products with precisely controlled architecture (external shape, internal pore geometry, and interconnectivity) with high reproducibility and repeatability [13].

And while both methods build a 3D object layer-by-layer from a 3D model, 3D printing technologies do not use cells or biological materials but can create porous polymer scaffolds for subsequent cell seeding. In 3D bioprinting, on the other hand, cell-laden bioinks and other biologicals are used directly to fabricate living tissue. The concept of 3D bioprinting is essentially an extension of AM techniques. Through the layered deposition of substrates such as living cells, nucleic acids, drug particles, proteins, components of the ECM, growth factors, and other biological factors, 3D bioprinting has the potential to produce complex, sophisticated biomimetic tissue constructs. Some of the many advantages of this technology are automation, high precision, high reproducibility and repeatability, geometric freedom and control (macro-morphology, pore size, porosity, interconnectivity), customizability, printability of a wide range of materials, the ability to incorporate and place proteins, growth factors, drugs, DNA, other biochemical cues, and cells with high spatiotemporal precision. The technology also enables the utilization of a wide range of cell densities and possibility of creating biochemical, mechanical, and cell density gradients that are present in native tissues [14, 15].

In 3D bioprinting, a comprehensive understanding of the composition and organization of its components is essential for the reproduction of the complex, heterogeneous architecture of functional tissues or organs [16]. This makes medical imaging technology an indispensable tool to provide information about the 3D structure and function at the cellular, tissue, and organ levels, thus supporting the design of patient-specific constructs. Medical imaging usually includes noninvasive imaging modalities such as computed tomography (CT) and magnetic resonance imaging (MRI). CAD, computer-aided manufacturing (CAM) tools, and mathematical modeling are also used to capture and digitize the complex topographic and architectural information of tissues [17]. The imaged tissue or organ model is divided into horizontal two-dimensional (2D) slices that are imported into a 3D bioprinter system for layer-wise deposition. Considering the available 3D bioprinting techniques, the cell types (differentiated or undifferentiated), biomaterials (synthetic or natural), and supporting biochemical factors are then selected. The configuration of these printing components drives the construction of the 3D tissues and organs. This integrated approach (imaging–design–fabrication) can reproduce more complex structures and incorporate mechanical and biochemical cues that are critical for the overall tissue/organ architecture and functionality [18]. Furthermore, by mimicking the natural, highly dynamic yet variable 3D structures, mechanical properties, and biochemical microenvironments, researchers can create tissue- or organ-specific 3D microenvironments, including vessels and neural networks, for the development of the specific functions of 3D bioprinted tissue/organ analogs [19].

To fully appreciate the speed at which the field of 3D bioprinting is evolving, we need to look back to its beginnings. The revolution in 3D models began a few decades ago when printing technology moved from 2D printing to an additive process in which successive layers of material are distributed to create 3D shapes [20]. 3D printing, as one of the 3D manufacturing technologies, was introduced only

34 years ago, when Charles Hull invented it in 1986. He received a patent for the liquid, photopolymer-based manufacturing technology of stereolithography (SLA) [21]. Later that year, a PhD student Carl Deckard developed selective laser sintering (SLS) [22]. Together, these two pioneering efforts are considered to be the birth of 3D printing, which has since been adopted as a biotechnological technique with widespread application in TE and RM [23]. In the early 1990s, a powder-based free-form manufacturing method was developed, which represents a significant development for 3D printing. In the initial phase, 3D printing technology was mainly used for rapid tooling with metals and ceramics [24]. However, in 2003, Tom Boland and coworker were the first to propose a cellular bioprinting technique based on traditional 2D inkjet technology [25]. The next big step for the industry came in 2009 when Organovo and Invetech created one of the first commercial 3D bioprinters [26]. Finally, in 2016, the Food and Drug Administration (FDA) issued draft guidance titled "Technical Considerations for Additive Manufactured Devices" that provided guidance on 3D printing techniques and products [27].

Currently, as mentioned earlier, organ shortage is still one of the biggest problems in the health sector [28]. And although the demand for organ transplants has increased significantly, supply cannot keep up with the growing demand. TE has great potential for solving this ever-growing crisis of organ shortage. Over the past two decades, bioprinting has been developed primarily to directly or indirectly fabricate scaffolds for the field of RM. By accurately positioning multiple cell types and biofactors in complex, multiscale architectures that better reflect the structural and biochemical complexity of native tissues, the technology offers an excellent alternative to produce biomimetic scaffolds that can be used for tissue regeneration. Due to its potential to produce functional 3D tissue constructs, it is also widely used in healthcare and pharmaceutical research, including disease modeling, drug discovery and testing, and high-throughput screening [29]. Given the ethical concerns and high costs associated with animal testing, bioprinted tissues could also be used as advanced *in vitro* model systems to reduce the need for animal testing [14]. Consequently, research in the field of bioprinting has increased considerably over the past decade. The number of publications related to 3D bioprinting has increased by more than 3000% in the last five years, indicating the rapid growth of this field [30]. In addition, with a compound annual growth rate of 26.5%, the global market potential for 3D bioprinting is expected to grow from US$ 411.4 million in 2016 to US$ 1.82 billion in 2022 [26, 31]. Recent advances and growing global awareness and need have led to the increased commercialization of 3D printing devices. The expanding bioprinting market has seen more and more companies enter the market, and the expiration of key patents for 3D printing is making 3D printers more accessible and affordable. For example, a fused deposition modeling (FDM) printer costs less than US$ 1000, compared to US$ 10 000 before the FDM patent expired in 2009. Several key patents for 3D printing (including SLS and SLA) have also expired between 2013 and 2015. This will lead to a new wave of open-source 3D printers that will drive research and product development while reducing production costs. The current focus is on bioprinting functional, living human 3D constructs with biological and mechanical properties closer to those of

native tissue/organs. Due to the high printing speed and the wide range of printable bioinks, the extrusion-based bioprinting approach is the most promising and widespread method to achieve this goal [32]. More than 30 000 extrusion-based 3D printers are sold worldwide each year, and academic institutions are increasingly buying and using micro-extrusion technology, particularly for research into tissue and organ engineering [33]. Considerable progress has been made to achieve this ultimate goal of TE, organ printing, but the fabrication of fully functional organs still has a long way to go [34]. The main challenges remain the reproduction of the complex microarchitecture of ECM components and the recapitulation of critical cell–cell and cell–ECM interactions within the bioprinted 3D constructs. Although tissue and organ printing is still in its infancy, 3D bioprinting represents a promising approach for the scalable and reproducible production of patient-specific constructs and for the further development of TE toward organ fabrication to ultimately address organ shortages and save lives [35].

In this book chapter, we give an overview of the latest advances in 3D bioprinting to produce polymer-based scaffolds for tissue and organ regeneration. First, the basic principles of the 3D bioprinting process are briefly explained. The preprocessing steps, which are important for the design of tissue-relevant constructs and include imaging and 3D modeling, are discussed in more detail. Next, the most used bioprinting technologies, namely stereolithography, light-based, droplet-based, and extrusion-based bioprinting, are discussed. We review the current state of the art for each printing modality and the advantages and limitations of each process. We will also present a novel 3D printing approach called four-dimensional (4D) bioprinting, which will be crucial for the development of dynamically responsive tissue constructs. We will then give an overview of the commonly used polymer-based materials that can be used as bioinks to create biomimetic scaffolds. We discuss the limitations of bioinks and describe common solutions to the problem. Due to the specific structural and biochemical requirements of tissues, a universal bioink cannot exist. However, very similar characteristics need to be considered in the optimization process for respective applications. Throughout the overview, we will also focus on solving the main limitations that hinder the development of thick tissue, namely the problem of vascularization.

17.2 Fundamental Principles of the 3D Bioprinting Process

A typical bioprinting process can generally be divided into three phases, namely preprocessing, processing, and postprocessing, as shown in Figure 17.1. Preprocessing includes imaging of the tissue or organ using CT, MRI, and ultrasound imaging techniques as well as the reconstruction of 3D models from the image. The generated 3D models are then converted into an instructions file, containing a sequence of coordinates and other process parameters, which can be accepted by the printer. The processing step begins with harvesting primary cells from patients, which are cultivated and expanded *ex vivo* for the bioprinting process. Although cancer cell lines and

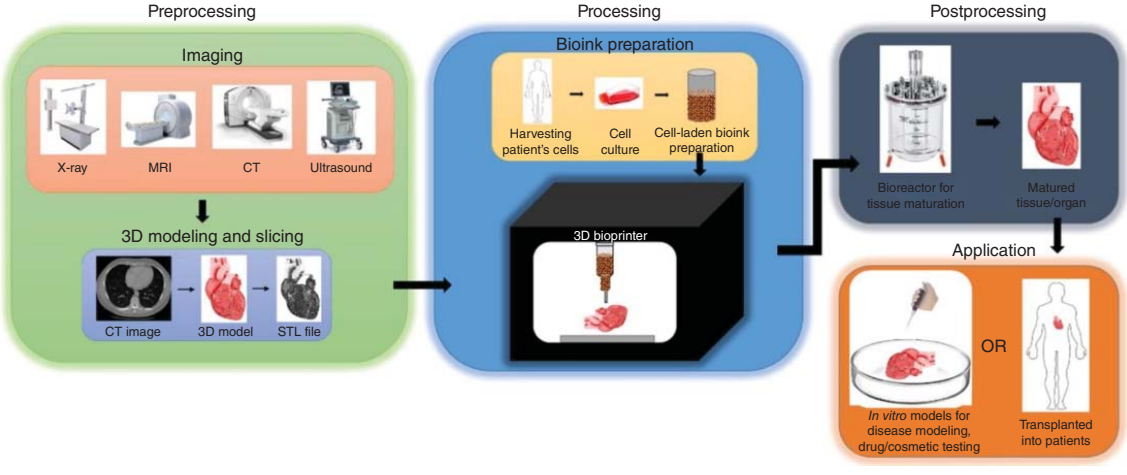

Figure 17.1 A typical bioprinting process consisting of three steps: (i) preprocessing (medical imaging with computed tomography [CT], X-ray imaging, magnetic resonance imaging [MRI], or ultrasound; 3D modeling and slicing; preparation of cell-laden bioink), (ii) processing (actual 3D bioprinting process), and (iii) postprocessing (tissue maturation in a bioreactor). Source: Vijayavenkataraman et al. [36]/with permission of Elsevier.

other nonhuman cells are used, the ideal prerequisite for fabricating transplantable living tissues would be the use of patients' cells. Suitable bioinks with properties that mimic the tissue to be printed are selected and the cells are suspended in these bioinks. The cell-laden bioinks are then, according to the 3D model, fabricated using a bioprinter into the desired tissue/organ. During postprocessing, the bioprinted tissue/organ is incubated in a bioreactor for tissue maturation before it is transplanted into patients or used as *in vitro* models for disease modeling or drug testing.

17.2.1 Preprocessing: The Design of Scaffolds with Tissue- and Organ-Level Complexity

An essential prerequisite for reproducing the complex, heterogeneous architecture of functional tissues and organs is a comprehensive understanding of the composition and organization of their components. Preprocessing includes the selection and preparation of bioinks and their structuring parameters as well as preparation of instructions for the bioprinter itself [33]. For more information on the selection of bioinks and the basic properties they must have, see Section 17.4 in this chapter. Preparing instructions for the bioprinter depends on the required geometrical features of the final scaffold. It can be achieved through several approaches with varying complexity: in the simplest form, the printing instructions (e.g. g-code) can be created directly, which is suitable for simple geometries (cubes, cylinders) with smaller sizes design (up to a few cm). When more complex structures are required, the process typically involves the construction of a 3D model, which is then translated into printable data, often by "slicing" the model into individual sequential layers. Furthermore, a 3D model can be obtained either by direct modeling using CAD [37] or by reconstructing data from medical imaging data. This provides information about the anatomy, histological structure, composition, and human organ topology and is of crucial importance when scaffolds have to precisely mimic the shape of a target or damaged tissue [38]. These technologies include most noninvasive imaging modalities, with CT and MRI being the most common, and ultrasound imaging and optical microscopy being less common.

The most common technique for obtaining medical images, CT imaging is used for both diagnostic and interventional procedures. It is based on the variable absorption of X-rays by different tissues. The X-ray source rotates around the object, and as the X-ray beam passes through the body, sensors measure the intensity and angle of the transmitted beam and record the data as a collection of pixels representing a small volume (voxel) of tissue [39]. This imaging method produces closely spaced axial sections of tissue architecture that, after surface rendering and stereolithographic processing, fully describe the tissue volume. Recently, an advanced CT technique (micro-CT) with high resolution from 1 to 200 μm has been developed and used to characterize the mechanical properties of scaffolds and microstructures [40], to visualize changes in bone density, and to assess tissue regeneration [41]. A second common approach, MRI, can also provide high spatial resolution in soft tissues, with the advantage of increased contrast resolution, which is useful for imaging soft tissues close to each other without exposure to ionizing radiation. MRI uses nuclear

magnetic resonance: a strong magnetic field causes a small fraction of the nuclei in the tissue to align with the magnetic field [42]. By detecting the excited radiofrequency signal of the hydrogen atoms in the samples via a magnetic resonance coil, images can be generated after processing by computer software. Two less frequently used imaging techniques are ultrasound imaging and optical microscopy. In the latter, images of 3D tissue models can be obtained by stacking many 2D images taken with an optical microscope. To do this, the modeling software must reassemble the prepared histological sections and align them precisely in the correct position [1]. Using optical microscopy methods, individual cells and tissues can be distinguished by staining. Ultrasound technology, on the other hand, uses the sound energy to scan the sample by emitting sound waves. The reflected waves are detected by a receiver and processed to generate computer images. Compared to MRI or CT, it has a limited resolution (1 mm × 1.5 mm × 0.2 mm); however, ultrasound imaging is a safe and simple method for differentiating the structure of the target tissue/organs, as there is no radiation exposure [43].

Since imaging methods mentioned earlier generate 2D data, these data usually have to be further processed and stacked to create a 3D model that can be further modified, e.g. by adding or removing details and surface smoothing. Finally, the 3D model is digitally sectioned in the desired planes, which can either be used directly (e.g. in certain stereolithographic applications) or converted into suitable fabrication instructions that can be used directly by the bioprinter. The types of instructions are highly dependent on the fabrication technique. However, perhaps the most common type is the g-code, which contains the sequence of spatial coordinates, movement speeds, and other printing parameters.

17.2.2 Processing

In 2010, Guillemot et al. defined 3D bioprinting as "*The use of computer-aided transfer processes for patterning and assembling living and non-living materials with a prescribed 2D or 3D organization in order to produce bioengineered structures serving in regenerative medicine, pharmacokinetic and basic cell biology studies*" [44]. As such, bioprinting is an umbrella that covers several different processes and can be divided into different categories in many different ways. Arguably the most straightforward way to divide 3D bioprinting for TE applications is into two forms, with living cells (cellular printing) and without incorporated living cells (acellular printing). With cellular 3D bioprinting, living cells are used directly in the manufacturing process of the constructs, along with the inherent advantages of rapid prototyping based on 3D printing. Different techniques have been developed to create 3D analogs of living tissues/organs, and each has different characteristics (strengths and limitations) in relation to the available conditions such as biological materials, resolution, printing speed, and cell viability. Depending on the printing modality (bioink deposition mechanism), the most representative techniques of cellular bioprinting are droplet based, extrusion based, and SLA. These techniques can also use acellular inks to create scaffolds. Still, after printing, an additional cell-seeding technique can be used to create artificial 3D scaffolds loaded with

cells for tissue/organ regeneration [45]. Variations in bioprinting technologies can influence the properties of living tissue/organ constructs. In comparison, acellular bioprinting technologies (e.g. laser-assisted bioprinting [LAB]) offer a wider range of applications for tissue regeneration, such as a wider choice of materials and manufacturing methods [12]. More importantly, without considering cell viability or bioactive components, 3D printing techniques involving higher temperatures, chemicals, and other harsh environments can be used to produce scaffolds [45]. Taking into account the specific requirements for the properties of the tissue/organs to be printed, the design of the process must take into account the capabilities and characteristics of the bioprinting systems (both bioinks and bioprinters). A more detailed description of some of the most important printing technologies can be found in this chapter under Section 17.3.

17.2.3 Postprocessing

Postprocessing includes the development of biomimetic structures, mechanical supports, and biological functionality. Still, the main purpose of this phase is the maturation (cross-linking, removing excess and toxic substances, etc.) of bioprinted tissue constructs for living applications [46]. Several additional manufacturing techniques, including substrate carriers and sacrificial templates, are potentially required to create higher mechanical elasticity/strength, more precise and complex structures, or multiple biological functions, as current printing techniques are limited [47]. More importantly, *in vivo* implantation, *in vitro* culture techniques (preferably in a bioreactor), or even *in situ* bioprinting can be used to induce and enhance construct maturation, thereby transforming constructs into functional tissues/organs [18].

17.3 Recent Advances in 3D Bioprinting Approaches and Their Application

Murphy and Atala [33] divided the bioprinting approaches based on the working principles into three main categories, namely droplet-based (e.g. inkjet bioprinting) [48], extrusion-based [49, 50], and laser-assisted bioprinting [51]. Several other papers [26, 36, 52, 53], which classify bioprinting in more detail, add several other categories. For example, Vijayavenkataraman et al. [36] add SLA to the classification, while Ng et al. [52] include microvalve-based printing as a fifth main category. Each of these techniques has different ranges of the resolution, manufacturing times, and limitations. In short, droplet-based bioprinting processes include methods for depositing bioinks in the form of droplets, which can be generated in various manners, e.g. by inkjet-based techniques, using micro-valves or laser-assisted forward transfer. Extrusion-based bioprinting is typically a continuous deposition process, where bioinks are forced through a nozzle by a driving mechanism, typically pneumatic, piston, or screw based. In addition to laser-assisted

forward transfer, light-based techniques are also used for photopolymerization, e.g. stereolithography, SLS, or related techniques. Here we briefly describe the core principles and discuss the advantages, limitations, and applications of four of the most frequently used 3D bioprinting methods (SLA, droplet based, extrusion based, and laser assisted) for the fabrication of scaffolds for the construction of tissues and organs. While this is not the subject of this review, we will also briefly discuss the topic of 4D bioprinting, which promises to overcome some of the limitations of traditional 3D printing approaches by providing the ability to fabricate constructs that can change over time.

17.3.1 Stereolithography

Stereolithography (SLA), classified as a photolithographic technique, is the original AM process after the technology was first developed in the mid-1980s by Charles Hull. It is based on the spatial solidification of liquid resin by photopolymerization and offers a high degree of spatial resolution and accuracy but is limited by the need for a photocrosslinkable material. The SLA process (vat photopolymerization) uses spatially controlled irradiation with light (UV) or laser to solidify a 2D geometric pattern that is layered by selective photopolymerization of the bioink in the reservoir. Based on the building process, SLA is commonly divided into two different types. In the bottom-up printing process, the photocurable resin is cured from below through a window at the bottom of the container using a beam spot via a light source. The building platform is lifted out of the resin vat, and a "peel" step is required between the individual layers. Alternatively, in the top-down approach, the building platform is lowered further into the solution after completion of the 2D cross-section so that the laser can cross-link and/or polymerize the next layer over the previous one. A CAD file usually controls the movement of the light, and the final 3D construct is built successively on 2D-patterned layers in a layer-by-layer method. At the same time, the building platform is moved vertically [54]. Once the structure is fabricated, the uncured resin can be easily removed. The top-down SLA approach is gaining traction over the traditional bottom-up SLA approach because it achieves higher printing speeds, requires less resin, reduces oxygen inhibition, and results in a smoother surface finish [55]. The overall mechanical properties of the bioprinted structure are mainly determined by the type and concentration of the bioinks, the scanning speed, and the laser power. When multiple layers are printed, the first layers can be repeatedly exposed to the laser, resulting in uneven mechanical strength or unwanted 3D structures/patterns. Still, the scaffold can be post-cured in a lightbox to strengthen the structure or convert any remaining monomer residues. Stereolithography printing offers the highest resolution (~6 μm) of all 3D print methods. The resolution depends on the exposure conditions (size of the laser spot, wavelength, power, exposure time/velocity, and the occurrence of absorption or scattering of the laser beam) as well as on the selection of the photoinitiator or possible UV absorbers [15]. With the development of micro-stereolithography (μSLA) a resolution of about 5 μm in the x/y-plane and 10 μm in the z-axis could be achieved [56]. Stereolithography, based on two-photon polymerization (2-PP), in which the polymerization process only takes place when

an atom absorbs two photons simultaneously, goes one step further and achieves a very high resolution in the nanometer range (~200 nm) [57]. The first study showing the possibility of producing cell-loaded hydrogel constructs with 2-PP was recently conducted by Ovsianikov et al. [58], where the biodegradable 3D tissue scaffolds (Figure 17.2) were prepared by photopolymerization of gelatin modified with methacrylamide moieties, which then supported the adhesion, proliferation,

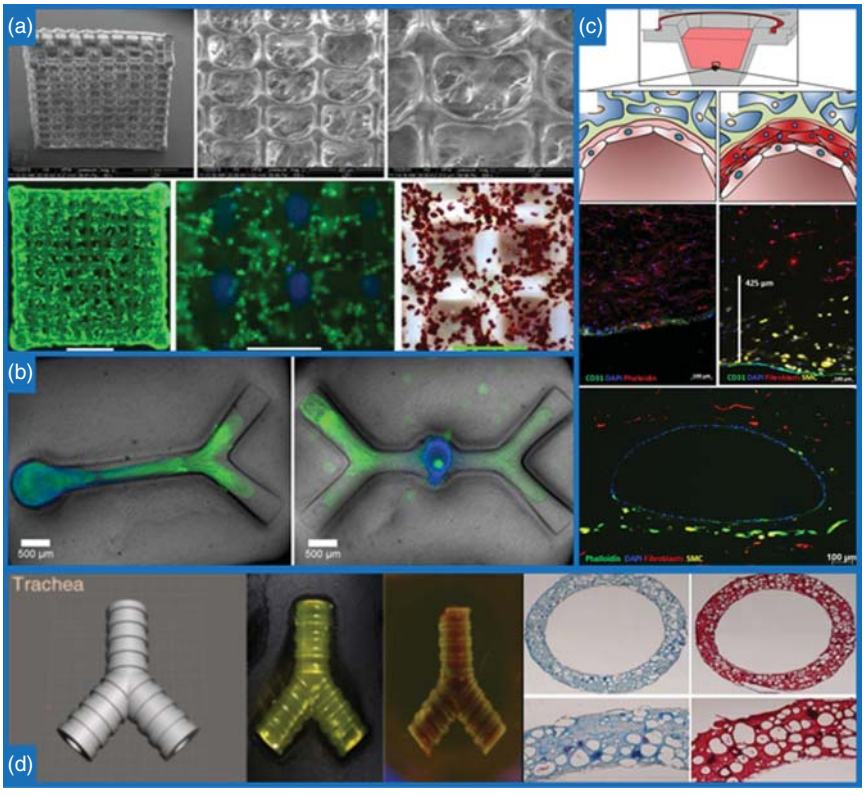

Figure 17.2 Examples of cell-laden scaffolds produced with various bioprinting techniques. (a) Images of the 2-PP-produced high-resolution gelatin scaffolds laden with human adipose-derived stem cells show intracellular lipid accumulation by Oil Red O staining. Source: Ovsianikov et al. [58]/MDPI/CC BY 3.0. (b) Micropatterned hydrogel constructs with incorporated dorsal root ganglia were fabricated by SLA. The images show polymerized PEG constructs (gray) with neurites labeled with Beta III tubulin (green). Source: Curley et al. [59]/with permission of MyJoVE Corporation. (c) Schematic cross-section and fluorescence micrographs of vascular-like channels created by DOD inkjet printing. A representative cross-sectional fluorescence microscopy image highlights the overall architecture of a multilayered vessel model after four days of dynamic cultivation; ECs are homogeneously distributed in the inner part of the lumen, surrounded by fibroblasts and SMCs. (Phalloidin in green, prelabeled fibroblasts in red, prelabeled smooth muscle cells [SMCs] in yellow, DAPI in blue.) Source: Schöneberg et al. [60]/Springer Nature/CC BY 4.0. (d) Complex silk fibroin-based scaffolds fabricated with LAB and incorporated with human chondrocytes exhibited superior histological cartilage-like properties (cell organization and ECM distribution), including collagen (blue-Masson's Trichrome staining) and proteoglycan (red-Safranin-O staining) *in vitro*. Source: Kim et al. [61]/Springer Nature/CC BY 4.0.

and differentiation of primary stem cells derived from adipose tissue into the expected lineage.

A recent development in the SLA printing field involves the continuous liquid interface production (CLIP) facilitated by a well-controlled oxygen-inhibited dead zone (persistent liquid interface), which prevents the resin from attaching to the UV window. CLIP uses an oxygen-permeable curing window (a thin, amorphous Teflon film) below the UV image projection plane to create an oxygen-containing zone between the solid part and the liquid precursor where solidification cannot occur. The rate of resin replenishment in this dead zone, the initiation efficiency, and the resin reactivity together determine the speed at which the construct can be formed continuously rather than layer by layer [62]. By using CLIP, Tumbleston et al. [63] could utilize SLA in a way that surpasses any 3D printing process. The novel implementation also surpasses conventional SLA techniques in terms of fabrication time and is only limited in terms of production time, which is based on the curing rates and viscosity of the resin, and not on the gradual layering seen in typical SLA. Their approach allowed the production of scaffolds in minutes (speeds of more than 1000 mm/h) instead of the hours required by traditional SLA techniques (typical speed of only a few mm/h) and the production of structures of a few tens of centimeters in size, which can contain features with resolutions below 100 μm. The range of photocurable resins is quite wide with CLIP. Still, the viscosity and reactivity of the monomers are more critical as they affect oxygen diffusion within the resin and the permeable curing window. There is also a compromise in this system where increasing the production speed leads to 3D objects with lower resolution.

As mentioned earlier, the main advantages of SLA techniques are their ability to produce complex designs with high resolution easily and to print constructs rapidly without the need for a substrate. Since it is a nozzle-free process, the problem of nozzle clogging is eliminated, and bioinks with high cell concentrations ($>10^6$ cells/ml) can be used. Despite several advantages that this process offers, it suffers from serious limitations that hinder its use in the bioprinting of cells and tissues. Firstly, although there are many materials to work with SLA, there are few biocompatible biomaterials that can be used [54]. Only photopolymerizable bioinks or bioinks containing a UV-activated photoinitiator can be used. Commonly photocurable materials include derivatives of polyethylene glycol (PEG) acrylate, polyethylene glycol methacrylate (PEGMA), poly(vinyl alcohol) (PVA), acrylated hyaluronic acid (HA), dextran methacrylate, acrylated, capped poly-1-caprolactone co-trimethylene carbonate, and polypropylene fumarate (PPF) [64]. Although there has been some work on the development of biodegradable photopolymerizable bioinks [65, 66], most photoinitiators are cytotoxic, and the viability of the cells after printing is rather low, so it is essential to use a cytocompatible photoinitiator. Recently, Grigoryan et al. [67] exploited the use of food dyes, which are widely used in the food industry, and showed that they could be used as potent photoabsorbers for the biocompatible photopolymerization of photocrosslinkable hydrogels. They showed that the use of such food dyes leads to increased resolution and reduced light diffusion in the constructs. This enabled them to create complicated alveolar-like vascular structures and perfuse them with red blood cells. However, it is important to note that

the hydrogel itself was not directly loaded with cells during fabrication. This hints to the second limitation of SLA, namely that the cells are exposed to UV radiation and are susceptible to cell lysis and DNA damage. Since photopolymerization is a radically induced chemical reaction, the free radicals can also damage the cell membrane, proteins, and nucleic acids. This limits the application of the technique and is the reason why studies in which the SLA bioprinting was performed directly with cells are sparse. These include the bioprinting of human dermal fibroblasts [65] and embryonic dorsal root ganglia (Figure 17.2) [59] as well as murine mesenchymal progenitor cells and embryonic fibroblasts [68]. Finally, SLA cannot form horizontal gradients in the constructs, and sometimes it is difficult to remove the supporting structure/remaining resin completely [54].

17.3.2 Droplet-Based Bioprinting

The main feature of droplet-based bioprinting is that the droplets of the cell-laden bioink are generated and deposited at predefined locations on the substrate. As a noncontact bioprint process, it offers a high-throughput method for the deposition of multiple cells and cell types or biologics in small droplets at a specific spatial position. Droplet-based techniques are usually divided into microvalve-based and inkjet bioprinting. However, some also include electrohydrodynamic jetting and acoustic-based bioprinting in this category. Inkjet bioprinting is further subdivided into continuous inkjet printing (CIJ) and generally preferred drop-on-demand (DOD). The latter DOD approach includes thermal, piezoelectric, electrostatic, or acoustic printing and is described later [69].

Inkjet bioprinting, which is granted with the earliest cell printing patent, has its origins in commercial 2D inkjet printing. In this noncontact technique, the bioink (consisting of biomaterials, bioactive factors, and cells) is stored in a cartridge or reservoir and then transferred to the ink chamber to eject picoliter-sized droplets [25]. By adjusting the properties of the bioink and the print patterns, inkjet bioprinting can easily create gradients within a 3D structure. All these properties of inkjet bioprinting allow its use for *in situ* production of heterocellular tissue [70]. As mentioned earlier, based on the droplet actuation mechanism, there are four existing approaches to inkjet droplet extrusion, namely thermal, piezoelectric, acoustic, and electrostatic inkjet printing. Among these, thermal and piezoelectric printing are the most commonly used methods for producing scaffolds [71]. The thermal actuation is based on a heating element that can superheat the bioink to generate steam bubbles to eject the droplets. Although the temperature reaches 200–300 °C, the process lasts only a few microseconds (~2 μs), resulting in an overall temperature increase of ~10 °C in the print head. Many results have shown that this temperature increase has minimal impact on the viability of both the printed cells and other integrated biologics [72]. The thermal inkjet printer can be easily modified for bioprinting and has the advantages of high throughput, low cost, and wide availability. It has, therefore, been used in numerous applications in biofabrication and biomedicine [70]. However, the risk of exposing cells and materials to thermal and mechanical stress, the low droplet directionality, the

uneven drop size, the frequent clogging of the nozzle, as well as the potentially unreliable cell encapsulation, are major disadvantages for the use of these printers in 3D bioprinting [33]. In piezoelectric technology, voltage causes a rapid change in the shape of the piezoelectric material, creating a pressure pulse in the liquid that forces an ink droplet out of the nozzle. Unlike thermal technology, the piezoelectric method does not use heat, so there is no coagulation or clogging of the nozzle [73]. In addition, the shape and size of the droplets can be adjusted by tuning the applied voltage to the piezoelectric material. It is also possible to use a greater variety of inks than with thermal inkjet printers because no volatile components are required. However, the voltage applied in piezoelectric bioprinting is about 15–25 kHz, which can cause lysis of the living cells similar to (ultra)sonication [74]. Other inkjet printers use an acoustic radiation force associated with an ultrasonic field to eject liquid droplets from an air–liquid interface. However, the acoustic frequencies used in these printers have the potential to cause damage to the cell membrane and cell lysis [75].

Overall, the advantages of inkjet bioprinting are the high resolution (~50 μm), the relatively high viability of the cells after printing (>80%), the ease of processing, the affordability, as well as the fact that it allows rapid fabrication with highly repeatable patterns (up to 10 000 droplets per second) [76]. Another advantage is the possibility to introduce concentration gradients of cells, materials, or growth factors in the entire 3D structure by changing the droplet density or size. Recent developments in this technique have reported control of droplet sizes and deposition rates from 1 to 300 pl in volume at up to 10 000 droplets/s [77, 78]. Droplet bioprinting also shows great potential for "scaffold-free" bioprinting by depositing cell layers in a sacrificial mold [15]. However, inkjet bioprinters still have limitations in terms of material viscosity, cell density, and mechanical strength. A general disadvantage of inkjet bioprinting is that the biological material must be in liquid form to allow droplet formation. Only low-viscosity bioinks (~3–12 mPa s) can be printed to avoid clogging of the nozzles and high shear stresses, which also limit the cell concentration in the bioink to $<10^6$ cells/ml [76]. The process, therefore, often requires an additional cross-linking step. In most cases, chemical, pH, or photocrosslinking gelation mechanisms are involved to ensure the stability of the bioprinted constructs [79]. Chemical modifications of naturally occurring materials and various cross-linking mechanisms alter both the chemical and material properties of the bioinks. They may even require products or conditions that are toxic to the cells. This, in turn, slows down the bioprinting process and leads to reduced viability and functionality [80]. One of the most recent successful applications of droplet-based bioprinting was performed by Schöneberg et al. [60] where they were able to successfully reproduce the three layers of a blood vessel (*tunica intima* – endothelium, *tunica media* – elastic, smooth muscle cells [SMCs], and the *tunica adventitia* – matrix of fibroblasts) using a natural cross-linking mechanism (Figure 17.2). In the study, they separately deposited droplets of gelatin with endothelial cells (ECs) to form the core of the structure, followed by a fibrinogen layer with SMCs and an outer thrombin layer. Once the process was complete, the collagen–fibrinogen-based bioink containing fibroblasts was rapidly cross-linked

with thrombin. Other remarkable examples of the inkjet bioprinting approach are the printing of cells and tissue constructs from bone [81], cartilage [82], skin [83], cardiac [84], and nerve tissue [85], as well as the *in situ* regeneration of functional skin [86] and cartilage [87].

17.3.3 Laser-Assisted Bioprinting

The LAB approach encompasses SLS and the more widespread laser-induced forward transfer (LIFT), which is discussed in more detail [88]. A typical LAB/LIFT system consists of a laser source (pulsed or continuous) with a focusing device, a laser-transparent printing ribbon (with or without a laser energy absorbing layer, e.g. gold or titanium) coated with a layer of biological material (e.g. hydrogel and/or cells), and a substrate or collector slide placed on a motorized table. The lasers irradiate the ribbon, causing the liquid biological materials to evaporate and reach the receiving substrate in droplet form, which is why it is often classified as a droplet-based technique. The receiving substrate contains a biopolymer or cell-culture medium to maintain cell adhesion and continued growth after the cells are transferred from the ribbon [89]. LIFT uses nanosecond lasers with UV or near-UV wavelengths as an energy source for printing hydrogels, cells, proteins, and ceramic materials [90]. The method has many unique advantages. It is a noncontact process and therefore leads to high cell viability after printing (>95%) [91]. Since it is a nozzle-free approach, the problem of clogging is also eliminated. The resolution of LIFT features in the pico- to micro-range. It is influenced by many factors, including laser fluence (energy emitted per unit area), surface tension, substrate wettability, the air gap between the ribbon and substrate, and the thickness and viscosity of the biological layer [92]. In addition to high resolution, the ability to print a single cell per droplet, the ability to print high cell densities (up to 10^8 cells per ml) compared to those observed in living tissues, and compatibility with a range of viscosities (1–300 mPa s) are some of its other advantages [51, 76].

There are several reports on the successful use of LIFT to print cells, peptides [93], and DNA [94] in a 3D spatial arrangement. Some of the experiments with the patterning of living human cells include HaCaT keratinocytes and NIH3T3 fibroblasts [95], dermal fibroblasts [96], human umbilical vein endothelial cells (HUVECs), and human umbilical vein smooth muscle cells (HUVSMCs) [97] as well as rat Schwann and astroglial cells [91]. Although less common than inkjet or microextrusion bioprinting, its high resolution and reproducibility make it a viable option for tissue- and organ-engineering applications [33]. In addition to simple cell patterning, the production of multilayered tissue constructs, such as skin tissue [98, 99] and corneal structures [100], has also been demonstrated using LIFT. In the latter study, Sorkio et al. [100] were the first to demonstrate the feasibility of using LIFT for corneal applications. They produced three types of human corneal structures, using recombinant human laminin and human collagen I as the basis for the functional bioinks. The bioprinted cornea-like tissues showed that they promote cell proliferation and viability, have morphological features similar to those of the human ocular epithelium, express key markers

of differentiated corneal epithelium, and form organized corneal stroma-like structures. In addition, the fabricated stromal structures attached to the host tissue and the migration of adipose tissue-derived stem cells into the host corneal stroma after transplantation in porcine organ cultures were observed. LIFT was also used by Kérourédan et al. [101] for vascularization and bone regeneration, where they deposited high cell density of endothelial progenitor cells using LIFT onto a collagen hydrogel previously cultured with stem cells from the apical papilla. They observed the formation of a capillary-like network [101] and, in a follow-up study after implantation, found significantly higher rates of vascularization and bone regeneration when ECs were cultured in specific patterns and densities than when they were randomly seeded [102]. On the other hand, Kim et al. have shown that naturally occurring polymers can be used as bioinks and have equivalent strength and stability properties to their synthetic alternatives. They created a silk fibroin-based bioink by a methacrylation process. These hydrogels showed excellent mechanical, rheological, and biocompatible properties, which makes them useful for possible application in various TE structures. When incorporated with human chondrocytes and bioprinted into a trachea-like form (Figure 17.2), these architectures showed cartilage-like properties, including cell organization and a matrix rich in proteoglycans and collagen [61].

Despite the numerous advantages of LAB over other bioprinting methods, there are also many challenges. The high resolution of LIFT requires rapid gelation kinetics to achieve high shape fidelity, resulting in a relatively low total flow rate [103]. In addition, there is always a risk of photonic cell damage, and the effect of laser radiation on the cells cannot be eliminated [104]. The high cost of these systems is also a concern for basic TE research, although, as with most 3D printing technologies, these costs are decreasing rapidly. The scalability of the process and the low throughput, as well as the time-consuming production of the laser printing ribbon and the complexity of controlling the laser pulses, add to the list of disadvantages of this method. The nature of the method makes it unsuitable for the production of full-scale tissue constructs suitable for RM, which limits its applications. However, as already mentioned, the method can be used for high-resolution structuring of multicellular microenvironments at the cellular level [105].

17.3.4 Extrusion-Based Bioprinting

Extrusion-based bioprinting is the most widespread and affordable of all bioprinting modalities. The bioprinter is usually driven by a pneumatic or mechanical system (piston or screw) to extrude bioinks discretely or continuously (in the form of cylindrical filaments) through the nozzle orifice. The printing process is repeated layer by layer to finally produce complex 3D constructs. The relatively high resolution of the process enables the bioprinter to accurately fabricate complex structures designed with CAD software and to facilitate the patterning of multiple cell types. Compared to droplet-based bioprinting, extrusion-based bioprinting enables fast printing, ease of use, and a wide selection of bioinks, including cell aggregates, cell-laden hydrogels, microcarriers (MCs), decellularized matrices, and synthetic

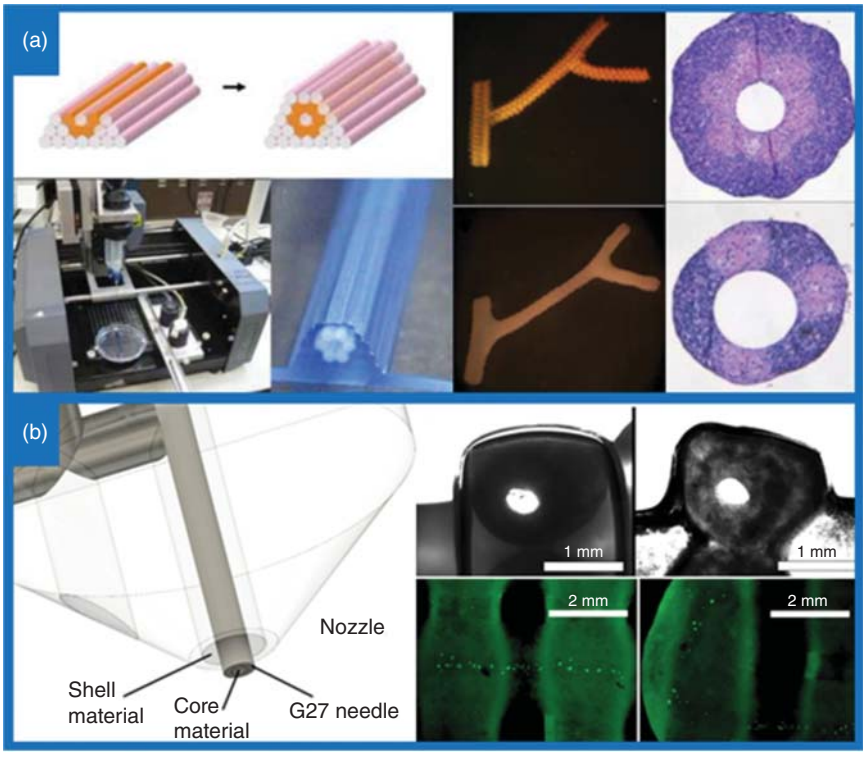

Figure 17.3 Extrusion-based 3D bioprinting of tubular structures. (a) Extrusion-based bioprinting was used for layer-by-layer deposition of agarose cylinders and multicellular smooth muscle cells cylinders (left) for the fabrication of hollow branched structures (right). Histological images show a concentric double-layered vascular wall made of HUVSMCs and human skin fibroblasts. Source: Norotte et al. [114]/with permission of Elsevier. (b) An easy-to-manufacture core–shell nozzle prototype (left) was used to bioprint perfusable alginate-based scaffolds (right) in a single processing step by cross-linking the hydrogel with $CaCl_2$ at the interface. The cross-sectional images of the scaffolds clearly show hollow strands that support the attachment and growth of HUVECs and can serve as artificial blood vessels. Source: Milojević et al. [115]/with permission of MyJoVE Corporation.

polymer fibers. This approach has been used in the bioprinting of cells, tissues, organ modules, and organ-on-a-chip devices for TE, cancer research, drug testing, and transplantation [36]. Several tissue types, including skin [14], skeletal muscle [106], bone [107], cardiac tissue [108], liver [109], cartilage [110], nervous tissue [111], *in vitro* pharmacokinetic [112], and tumor models [113] as well as branched vascular trees (Figure 17.3) [114], were fabricated using this technique.

Based on the dispensing drive, extrusion bioprinting can be classified into three types: more complex solenoid-based and simpler pneumatic and mechanical (piston or screw)-based extrusion [11]. Solenoid (electromagnetically driven) systems use electrical pulses to open a valve by canceling the magnetic pull force generated between a floating ferromagnetic plunger and a ferromagnetic ring magnet [116]. Pneumatic-based systems use compressed air to extrude filaments. They provide a

simpler method of controlling bioink extrusion and are force limited only by the air pressure capability of the system [117]. On the contrary, mechanically driven mechanisms have smaller and more complex components. Due to the delay of the compressed gas volume in pneumatic systems and the high complexity of electromagnetically driven systems, they also offer more direct control of the material flow and allow greater spatial resolution, albeit with reduced maximum force capability. While piston systems, which usually consist of syringes and needles, are generally better suited for bioinks with lower viscosity, the screw system can generate higher pressures for dispensing bioinks with higher viscosity. In the latter system, however, a large shear force along the nozzle can potentially damage the laden cells [11]. Microextrusion methods have a very wide range of fluid properties compatible with the process, with a wide range of biocompatible materials. Materials with viscosities from 30 to $>6 \times 107$ mPa/s [118] are compatible with microextrusion bioprinters, with higher viscosity materials often providing structural support for the printed construct and lower viscosity materials providing a suitable environment for maintaining cell viability and function [15]. Researchers often use materials that have shear-thinning properties and/or can be thermally cross-linked. Shear thinning is a non-Newtonian material behavior that causes a decrease in viscosity in response to an increase in shear rate [119]. The high shear rates present at the nozzle during biofabrication allow these materials to flow through the nozzle. During the deposition, the shear rate decreases, which leads to a strong increase in viscosity. Materials that flow at physiologically suitable temperatures (35–40 °C) but cross-link at room temperature are particularly useful for bioprinting applications [120]. Alternatively, some biocompatible materials flow at room temperature, which allows them to be extruded together with other biological components, but cross-link at body temperature to form a stable material [121]. The demand for bioinks with shear-thinning properties for successful printing limits the versatility of the bioinks that can be used.

Extrusion-based bioprinting has many advantages. The most important are the ability to continuously deposit highly viscous bioinks (~600 kPa s) at high printing speed and tolerance for heterogeneous formulations, which allows physiologically relevant cell densities [122]. This ultimately facilitates scalability, i.e. the ability to print tissue on a human scale, which is not possible with any of the other bioprinting methods. Although scalability is the biggest advantage of this technology, it comes at the expense of resolution. Extrusion-based bioprinting has the lowest resolution of all bioprinting systems [123]. The minimum feature size of the technology is generally over 100 μm. The best nonbiological microextrusion printers can achieve a resolution of 5 μm at a linear speed of 10–50 μm/s [33]. System resolution could be improved by reducing the nozzle diameter, but the increased shear force could damage the cells. Cell viability after microextrusion bioprinting is lower than with inkjet bioprinting and is typically 40–95% [76]. It depends on the viscosity of the bioink, cell concentration, and nozzle size, and the rate generally decreases as extrusion pressure increases and nozzle diameter decreases [52]. Although overall cell viability, which is essential for achieving tissue functionality, can be maintained with low pressures and large nozzle sizes, the drawback can be a significant loss of resolution and printing speed. Nozzle clogging is another inherent problem in

extrusion-based bioprinting. Another limitation of the process is the need for bioinks with shear-thinning properties for successful printing, which limits the versatility of the bioinks that can be used [15].

17.3.4.1 Solving the Problem of Vascularization Using Extrusion-Based Bioprinting

Probably the greatest disadvantage of extrusion bioprinting for the production of tissue-relevant scaffolds is the inability to produce hollow tubular structures of interconnected 3D networks that would allow blood perfusion and promote oxygen and nutrient diffusion [124]. Such channels can be additionally seeded with ECs and serve as artificial blood vessels [125]. Progress has been made toward larger tissue constructs, but the bottleneck remains the availability of bioinks as the necessary structural integrity, resolution, and biocompatibility have yet to be achieved. Recently, 3D extrusion of two different materials in a core–shell approach using coaxial needles for extrusion has gained attention [126–129], as it allows the production of tubes with hollow channels. Similar to conventional 3D microextrusion, core–shell printing is performed with a coaxial nozzle where two needles of different diameters are aligned on the same axis so that the wider needle encloses the narrower one. In this way, two materials can be extruded simultaneously, with one serving as the central filament or "inner" core and the other as the "outer" shell [129]. Up to now, coaxial bioprinting has been used to produce structures with solid material [130], core/shell [131], and hollow strands [128, 132]. The technique offers the possibility to combine materials with different mechanical properties, with the stiffer material supporting the softer one. More importantly, if the scaffold material (e.g. carboxymethyl cellulose, alginate) is extruded as a shell, while the core, which consists of the cross-linking agent (e.g. calcium chloride), is dosed from the inner capillary and rinsed out after printing, a continuous hollow tube can be produced [133]. Recently, a group of researchers introduced an easy-to-manufacture, simple-to-use, customizable core–shell nozzle with luer compatibility that can be used with a wide range of materials to directly fabricate hollow structures shown in Figure 17.3. They demonstrated its use by 3D printing alginate-based scaffolds in which the filament was cross-linked with a liquid core of $CaCl_2$. The latter was removed after printing, resulting in scaffolds with hollow filaments that supported the adhesion and growth of ECs [115]. Attalla et al. [134] have further developed the idea and presented a new nozzle design suitable for multiaxial extrusion to 3D print and pattern two- and three-layer hollow channel structures. Their nozzle design allows fast, easy, and cost-effective embedding of the structures in layers of gels and ECM. They demonstrated the ability to print distinct concentric layers of different cell types, namely ECs and fibroblasts. By embedding various layers of different cell-friendly materials (collagen and fibrin) next to materials with high mechanical strength (alginate), they were able to increase the long-term viability and growth of the cells without compromising structural integrity. These highly complex heterogeneous and hierarchical architectures show a great potential for the application of artificially produced tubular or fiber-like structures, including applications in vascular and nervous tissues. Kang et al. [135] presented a complex extrusion-based

3D printing technology called integrated tissue–organ printer (ITOP), which can produce stable, human-scale tissue constructs. They demonstrated the capabilities of ITOP by fabricating mandible and calvarial bone, cartilage, and skeletal muscles. The ITOP can produce complex, mechanically stable tissue scaffolds by printing cell-laden hydrogels together with biodegradable polymers in integrated patterns and anchoring them on sacrificial hydrogels. The system is also capable of incorporating microchannels into the hydrogel structure, which, through the supply of nutrients, led to a viability of up to 97%.

17.3.5 Combining Multiple 3D Bioprinting Approaches

Finally, it is important to stress that each of the bioprinting methods highlighted in this section has its advantages and disadvantages. No approach can achieve the goal of fabricating fully functional tissues or organs on its own. This makes it clear that for the successful bioprinting of physiologically relevant functional tissues, it will be crucial to develop hybrid bioprinting systems that combine the advantages of several bioprinting methods. Kim et al. [136] were among the first to report on a hybrid bioprinting system that can print simultaneously with extrusion- and inkjet-based dispensing methods. They demonstrated one-step bioprinting of a 3D model of human skin using this hybrid system, which consists of three printing methods – melt extrusion was used to print a poly(ε-caprolactone) (PCL) mesh that serves as a scaffold or support structure, extrusion-based bioprinting for the dermal layer, and inkjet-based bioprinting to pattern the keratinocytes over the dermal layer that forms the epidermal layer. Next, Lee et al. [137] used an already-developed hybrid system [138] of inkjet printing (for hydrogels) and FDM (thermoplastics) to improve the mechanical stability of scaffolds. They printed PCL and cell-laden hydrogels while using PEG as a sacrificial layer to construct complex-shaped scaffolds for ear regeneration. Using these complex ear-shaped scaffolds, positive *in vitro* results of chondrogenesis and adipogenesis were obtained from the coprinted chondrocytes and adipocytes. We recognize that the future of bioprinting lies in the development of such hybrid bioprinting systems that are capable of using different bioprinting modalities simultaneously, taking advantage of different methods and exploiting their limitations to bioprint fully functional, physiologically relevant tissues and organs with complex multilayered, multicellular architecture.

17.3.6 4D Bioprinting

In principle, 3D bioprinting only considers the initial state of the printed object and assumes that it is static and inanimate. However, engineered tissue constructs can undergo transformation (swelling, degradation, etc.) after the printing has finished, and controlling this transformation would be of enormous benefit to both RM and biomedical research. As a result, the concept of 4D bioprinting, which integrates time with 3D bioprinting as the fourth dimension, has recently entered the research discourse in TE. Here, time refers to the fact that smart biomaterials and bioprinted constructs can evolve their shapes and functionalities over time through externally

applied stimuli. The unique additional dimension of time provided by 4D bioprinting promises dynamic temporal control in addition to the spatial hierarchy in the fabricated tissues. It offers the possibility to create an immense variety of structures with the highest complexity and resolution [139]. Gao et al. define two types of 4D bioprinting. The first involves the printing of materials with inherent properties or functionalities that can reshape or transform in response to external stimuli. The second refers to the maturation of manufactured constructs in a time-dependent process [19]. Although the latter is proving to be a promising strategy for better reconstruction of native tissue and for overcoming the limitations of 3D bioprinting, it is a general principle of any TE process. Therefore, 4D bioprinting is better addressed when there is an active time-dependent change in biological constructs that leads to improved functionality beyond conventional tissue maturation [140]. Ramos and Moroni [140] categorize the shape transformation in 4D bioprinting into three main approaches. The first is comparable to the traditional scaffold-based approach and involves the shape transformation of cell-free constructs and the subsequent seeding of cells. This method is less attractive because living cells limit the choice of materials to be used and the fabrication method. The second approach involves first depositing cells on the 3D-printed scaffolds and then shape transforming the already cell-laden construct. This is a promising strategy to provide structural and topographical, time-dependent cues to the seeded cells. The third technique is the direct fabrication of a construct with a cell-laden material, followed by its shape transformation. Due to the limitations in controlling cell deposition during the 3D bioprinting process, this method proves to be the most challenging. However, since the shape transformation takes place while the cells are already incorporated into the construct, the second and third approaches have many advantages [140]. Broadly speaking, there are four categories of triggering stimuli: (i) manual transformation, (ii) spontaneous shape transformation, (iii) stimulus-responsive, and (iv) cell contraction [141]. Of all mentioned, the stimulus-responsive approach offers the most advantages since it allows precise temporal control of the shape transformation. It also allows the folding of multiple objects made of different materials at different scales. The process can be triggered by temperature, pH, moisture, electromagnetic fields, and light [139].

For applications in bone TE, Parameswaran-Thankam et al. [142] have synthesized an injectable thermoresponsive hydroxypropyl guar-graft-poly(*N*-vinylcaprolactam) copolymer and modified it with nano-hydroxyapatite. In addition to the excellent injectable and thermo-gelling properties suitable for osteoblastic cell growth, the guar-based hydrogel also enabled controlled drug delivery and formed apatite-like structures. Zhao et al. [143] also used thermoresponsive materials. They modified them with HA and chitosan to create novel injectable scaffolds with osteoinductive and osteoconductive activities to support the formation of new vascularized bone. To support the survival and proliferation of mesenchymal stem cells (MSCs) and to induce the early bone-forming marker alkaline phosphatase (ALP) as well as osteogenic regulators and the expression of bone markers, the authors combined the thermoresponsive hydrogel with graphene oxide. In addition, the *in vivo* transplantation of scaffolds resulted in well-mineralized and highly vascularized

trabecular bone formation. For applications in cartilage TE, Betsch et al. [144] have incorporated iron nanoparticles into a bioink based on agarose. During printing, they applied a magnetic-based mechanism to create constructs with alternating layers of random and aligned fibers (Figure 17.4). The chondrocyte-laden constructs with alternating layers of aligned and random fibers expressed significantly more collagen II compared to the exclusively randomly aligned fiber constructs. Furthermore, hydrogel mixtures with unidirectionally oriented collagen fibers showed significantly higher compression moduli compared to hydrogel mixtures with random fibers. The authors confirmed the importance of the structural and architectural properties of bioinks. Zhang et al. [146] also incorporated iron (Fe_3O_4) nanoparticles into a tetra-PEG/agar hydrogel and produced magnetically responsive dressings suitable for use in soft-tissue injuries.

In addition to the excellent biocompatibility, *in vivo* drug release studies showed that these hydrogels performed better than commercially available ointment systems in terms of restoring the injured soft tissue. A proof-of-concept patch with great potential for cardiac regeneration was recently demonstrated by Miao et al. [147]. Using a unique photolithographic–stereolithographic tandem strategy with smart soybean oil epoxidized acrylate inks, they created novel hierarchical 4D micro-patterns. The cardiomyogenic behavior of human mesenchymal stem cells (hMSCs) was regulated by the distinct topographic properties of the scaffolds, and the external stimulus exerted immediately after printing. The MSCs grew actively and were highly aligned along the micropatterns, forming an uninterrupted cell sheet. When external stimuli were applied, a 4D shape change was observed that transformed a 2D design into flower-like structures. In addition, the scaffolds possessed a shape-memory effect beyond the 4D features. Using SLA-based 4D printing, the same group also developed novel, multiresponsive architectures based on the same smart soybean oil epoxidized acrylate inks that use a universal concept of stress-induced shape transformation to achieve 4D reprogramming. The mechanism of the internal-stress-induced shape-changing process is shown in Figure 17.4. In addition, different pattern designs led to different 4D transformations, and the printed designs showed reversible dynamic shape changes and a shape-memory effect (Figure 17.4). The biomaterials have an enormous potential for applications in the regeneration of nerve tissue. They demonstrate this with a smart nerve guidance conduit on a graphene hybrid 4D construct, which offers excellent properties for nerve regeneration, including physical guidance, chemical cues, dynamic self-entubulation, and seamless integration (Figure 17.4) [145]. Using a "staircase effect" strategy to produce 4D anisotropic skeletal muscle tissue, the same group also studied the effects of topographic cues on skeletal muscle differentiation. Using a layered coating together with a shape-memory polymer, smart constructs with shape fix and recovery processes were produced. The topographic cues of such constructs significantly increased the expression of myogenic genes, suggesting their potential for use in TE constructs with highly organized and anisotropic ECM components [148].

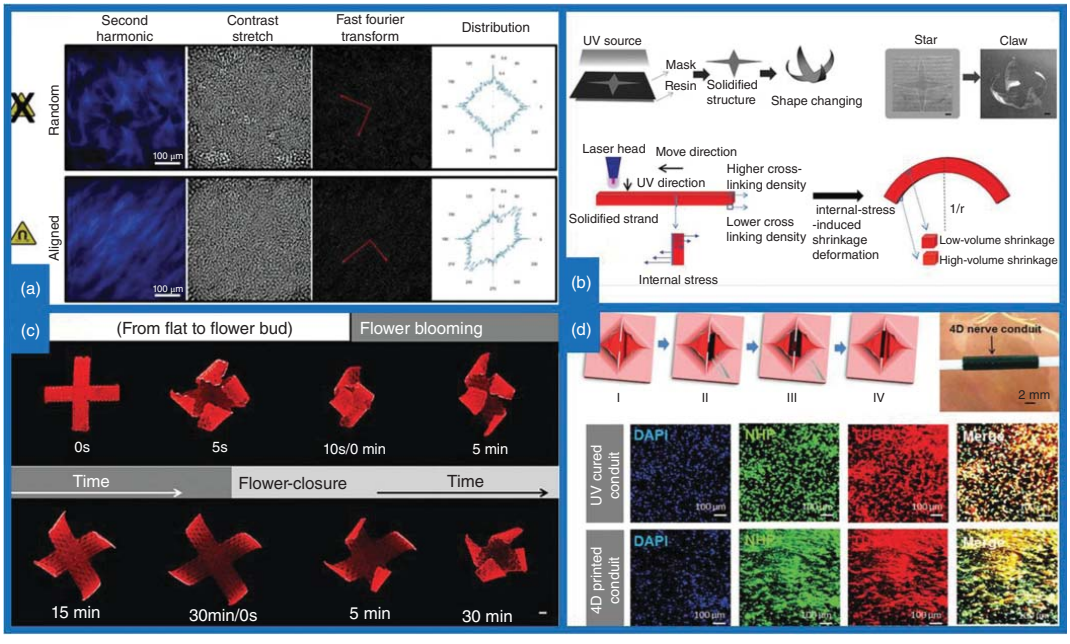

Figure 17.4 4D bioprinting. (a) Alignment of collagen fibers in printable bioinks in the presence or absence of a magnetic field. Images of pure type I collagen hydrogels show randomly oriented fibers in the absence of a magnetic field. In contrast, unidirectionally oriented fibers are visible when using a magnet that forces iron nanoparticles to move in one direction through the gel. Source: Betsch et al. [144]/with permission of John Wiley & Sons. (b) Images showing deformation of UV-cured soybean oil epoxidized acrylate by stress relaxation after immersion in ethanol. The illustration below shows the mechanism of the shape-changing process induced by internal stress. The uneven crosslinking density creates the modulus difference between the top and bottom sides due to laser energy attenuation, resulting in different volume shrinkage after stress relaxation. Source: Miao et al. [145]/with permission of John Wiley & Sons. (c) Beyond 4D bioprinting – a reversible dynamic process of opening the 4D bioprinted flower structure in ethanol and closing in water. Source: Reprinted (adapted) with permission from Miao et al. [145]/with permission of John Wiley & Sons. (d) Graphene nanohybrid for improving 4D curvature and 4D reprogrammable nerve guidance conduit. Illustrations of the full entubulation of the 4D nerve conduction channel via "thermomechanical programming" shape transformation. Immunofluorescence images below show enhanced neurogenic differentiation of hMSCs on 4D-printed nanohybrid conduits. Source: Miao et al. [145]/with permission of John Wiley & Son Inc.

17.4 Materials Used in 3D Bioprinting

In addition to the bioprinting techniques selected based on the targeted tissue requirements, appropriate bioink selection, including biomaterials, cells, and biochemical signals, is necessary for the successful fabrication of the construct. A bioink is defined as an "*A formulation of cells suitable for processing by an automated biofabrication technology that may also contain biologically active components and biomaterials* [149]." Different types of bioinks can be used depending on the specific bioprinting technique. They differ in composition and include, for example, cell-encapsulated gels, cell suspensions, or even tissue spheroids. It is important to note that the cells are the obligatory component of a material to be classified as bioink [149].

However, due to their beginnings in industrial prototyping, most 3D printing processes lack sufficiently developed biocompatible input materials [10]. Therefore, one of the major challenges in this area has been to find materials that are not only compatible with bioprinting and biological materials (e.g. cells, growth factors, surface ligands) but that can also provide the desired mechanical and functional properties for tissue constructs. Materials commonly used in the field of RM or as biomaterial inks for 3D printing are predominantly based either on naturally derived polymers, often isolated from animal or plant tissue, or on synthetic molecules [56]. Compared to metallic and inorganic materials, polymers are suitable candidates for TE applications due to their high biocompatibility, favorable physical properties such as lower density, easy modifiability, controlled degradability, low cost, and reduced environmental impact [150]. Among the different types of bioinks, polymer-based hydrogels have attracted attention due to their specific properties, such as a hydrophilic 3D structure capable of absorbing and retaining large amounts of water, adjustable physical and biochemical properties, biomimetic characteristics, biocompatibility, biodegradability, effective mass transfer, and the ability to form different shapes [151]. Hydrogels offer perfect "soft-material" systems for imitating the native ECM [152]. Except for the stiffest tissue types such as bones and teeth, hydrogels can mimic a range of elastic modulus values of most soft tissues in the body by manipulating the chemistry, cross-linking density, and polymer concentration. Therefore, they have been extensively used in a variety of biomedical applications, including the fabrication of tissue and organ scaffolds [153]. The most suitable methods for hydrogel printing are inkjet, light-assisted, and especially extrusion-based 3D printing systems [154]. The physicochemical properties and gelation method of hydrogels can be adjusted by chemical, physical, and enzymatic mechanisms or modulated by thermal/pH sensitivity [155]. However, there are only a limited number of suitable hydrogels that can act as bioinks, and modifying their properties remains a challenge [122]. In general, common hydrogels for 3D bioprinting are made from natural polymers such as alginate, agar, gelatin, cellulose, collagen, fibrinogen, fibrin, and HA [156]. Various key properties such as concentration, molecular weight, viscosity, gelation kinetics, and stiffness are important determinants when selecting a hydrogel for 3D bioprinting. Comprehensive overviews of the properties of hydrogels for 3D bioprinting can be found under references [122, 156, 157].

The biggest limitation of hydrogels remains their mechanical strength, which is essentially poor. Moreover, their composition can vary from one hydrogel to another, making it impossible to use the same hydrogel composition for many different specific applications. On the other hand, hydrogels made of synthetic polymers such as PEG, poly(acrylamide) (PAAM), poly(ethylene glycol)diacrylate (PEGDA), natural gelatin methacrylate (GelMA), and PVA have controllable chemical and mechanical properties [56]. In addition, the use of synthetic polymers such as PCL and poly(D,L-lactic-*co*-glycolic acid) (PLGA) and their combination with naturally derived hydrogels for scaffolding has led to higher mechanical strength, better processability, and controllable degradation rates [158]. However, these synthetic polymer scaffolds have a relatively low biological activity and are hydrophobic by nature. They must therefore be modified in such a way that they become bioactive by the incorporation of adhesive molecules during polymerization. In addition, the restriction of polylactone-type polymers is the release of acidic by-products during degradation, which causes inflammation of the surrounding tissue [159]. The recent progress of natural and synthetic biomaterials and bioinks for 3D printing of tissues and organs has been extensively investigated by Ng et al. [52].

Given the above considerations, it is not surprising that the four most common bioinks so far are made of hydrogels. According to the number of publications, these are the following: alginate, collagen, gelatin, and GelMA [52]. Due to its fast cross-linking properties, good printability, and low cost, alginate is still by far the most popular material for the production of bioinks and an excellent candidate for the bioprinting of large tissues [160]. The gelling properties of this versatile polysaccharide can be induced either by adding divalent cations as gelling agents [160] or by chemical modification of alginate-dialdehyde (ADA) with gelatin [161]. The viscosity of the alginate solution can be adjusted by changing the average molecular weight, molecular weight distribution, and average chain segment ratio [162]. Alginate is biodegradable, and although its degradation rate is slow, it can be increased by oxidation. However, it is bioinert due to the lack of cell adhesive moieties. This can be modified by adding cell adhesion signals, such as RGD (arginine–glycine–aspartic acid), to the polymers [163]. Cellulose, a plant-derived polysaccharide, is another widely used polymer for TE and RM purposes. As it is the most abundant organic compound on earth [164], it is a sustainable natural resource for the production of functional tissue scaffolds. In addition, cellulose can be made thermoresponsive by conversion into cellulose ethers, namely methyl cellulose, hydroxypropyl cellulose, and hydroxymethyl propyl cellulose [164]. However, processing into structures with complex architecture and high cellulose content remains a challenge. This limitation has prevented cellulose-based bioinks from reaching the level of structural control and mechanical properties. To solve this problem, Hausmann et al. [165] developed a simple approach to produce complex cellulose-based scaffolds that combines the shaping capabilities of 3D printing with a wet densification process. After the printing process, the structure density was increased by exchanging water with a poor solvent for the cellulose particles, which induces attractive interactions between the cellulose nanoparticles. This increased the concentration of cellulose in the 3D-printed structure to a

previously inaccessible value of 27.35 wt%. The cellulose-rich scaffolds (Figure 17.5) obtained by this process exhibited highly aligned microstructures and mechanical strength that was significantly higher than the one obtained by earlier additively manufactured cellulose-based materials.

Another popular polysaccharide is HA, which exhibits excellent biocompatibility and biodegradability. By modification with the methacrylate group, HA hydrogels can be formed when exposed to ultraviolet light [169]. Due to its strong mechanical strength, it could be a good candidate for printing hard tissues such as bones and cartilage [170]. In second place behind polysaccharides in terms of usability are the structural proteins, which can form highly complex, hierarchical, porous structures and provide essential cues for the regulation of cellular behavior and functions [33]. The main structural protein of the ECM is collagen, which is why bioinks based on collagen (collagen, gelatin, and GelMA) are widely used due to their excellent biocompatibility and broad availability. Collagen, a biocompatible and biodegradable polymer to which cells adhere and proliferate in, has been widely used to regenerate skin, bone, cartilage, and pancreatic islets [98, 122, 171], and has been widely used for 3D bioprinting [4]. A recent study has shown that highly complex hierarchical porous structures can be created by using a DOD inkjet bioprinting approach and collage-based macromolecular bioinks that manipulate the porosity within the bioprinted 3D collagen matrix [172]. In contrast, gelatin, a denatured form of collagen that is water soluble, biodegradable, noncytotoxic, and nonimmunogenic, is highly unstable at physiological temperature due to its thermoreversible cross-linking mechanism. However, using a cross-linking process, as demonstrated by Laronda et al. [166], who were able to produce functional ovaries (Figure 17.5) and restore fertility in mice, or by Irvine et al. [167], who have applied a novel enzymatic cross-linking approach of gelatin-based bioinks (Figure 17.5) by microbial transglutaminase to facilitate the printing of cell-laden hydrogels with high accuracy and structural fidelity. Gelation of gelatin can also be modified by adding methacrylate groups to the amine side groups of the gel. The modified gelatin gel is photocrosslinkable in the presence of a photoinitiator. The rheological property of GelMA can be chemically modified. For example, acetylation of free amino groups could change the viscosity of GelMA [173]. GelMA hydrogels with high cell viability have been printed and used to produce cartilage and cardiovascular structures [109]. Another popular protein-based material is fibrin because it can bind to many growth factors [174]. Fibrin gels have been printed to release vascular endothelial growth factor (VEGF) and promote vascularization [175]. It has been used to print tubular tissue structures such as proximal renal tubules [176] and thick vascular networks [177].

17.4.1 Combining Materials

Initially, 3D printing focused on processing pure polymers only, but as the technology grew, the development of composite inks evolved. The main objective of using composite inks is to improve the properties of the ink, such as processability, printability, mechanics (stiffness, strength, anisotropy, etc.), and bioactivity (improvement of cell function and tissue integration). Inzana et al. demonstrated

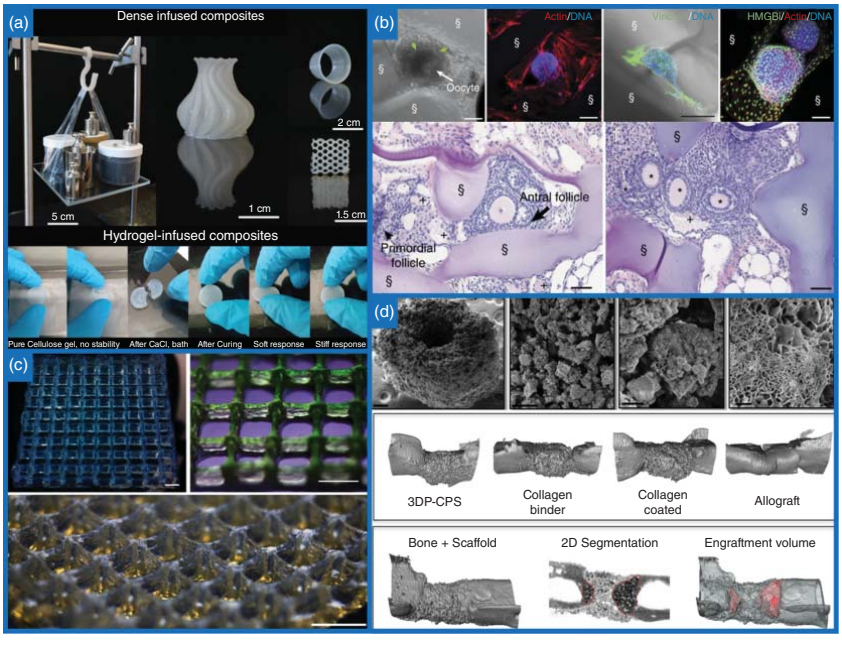

Figure 17.5 Materials used in 3D bioprinting. (a) 3D-printed functional parts with a high volume fraction of cellulose (27.35 vol%). Composites obtained after the infiltration of hydrogel with monomer and UV curing show stiff response when compressed along the strut direction and elastic deformation when tested at an angle of 45° relative to the strut axis. Source: Hausmann et al. [165]/with permission of John Wiley & Sons. (b) Light microscopy and confocal fluorescence images of follicle cultured within scaffold for eight days show that they maintained the basement membrane (green arrows) and a centralized oocyte (white arrow). Immunostaining confirmed that the follicle adheres to the gelatin struts of the 3D printed scaffold and is surrounded and anchored by stromal cells. Hematoxylin and eosin-stained cross-sections of ovarian bioprostheses removed three weeks after surgery, contained vessels and primordial, primary, secondary, and antral follicles within the gelatin scaffold struts. Source: Laronda et al. [166]/Springer Nature/CC BY 4.0. (c) 3D printed gelatin gel woodpile structure is viewed at increasing magnification and various perspectives. Source: Irvine et al. [167]/Springer Nature/CC BY. (d) Micrographs of 3D-printed calcium phosphate scaffolds with micro-porosity that are osteoconductive and enable bone ingrowth in a critically sized murine femoral defect. Source: Inzana et al. [168]/with permission of Elsevier.

the feasibility of the process. They used a ZPrinter® 450 to fabricate scaffolds for bone regeneration (Figure 17.5), made from a composite of calcium phosphate and type I collagen. The scaffold showed improved mechanical properties and cellular benefits *in vitro* [168]. Composites also play an important role in increasing the mechanical properties of hydrogels. For example, composite hydrogel scaffolds, such as those made with ceramic or glass particles, can retain their hydrophilic polymer network to mimic those of the innate tissue while increasing their mechanical strength to resist the compressive forces caused by cell proliferation and differentiation [5]. Composites can be the most important biomaterials for 3D printing of ECM-like scaffolds. For example, hydroxyapatite composites are widely used in bone TE. Hydroxyapatite is the most important inorganic composition of bone and has excellent biodegradability, osteoconductivity, and osteoinductivity. Hydroxyapatite–polymer composite hydrogels for 3D printing were prepared by mixing hydroxyapatite particles with polymers such as silk, collagen, and alginate [168, 178].

An alternative approach to increase the mechanical strength of hydrogels and increase the overall tissue stiffness is to deposit them next to thermoplastic polymers (e.g. PCL), resulting in so-called hybrid scaffolds. PCL is often chosen as a reinforcement thermoplastic polymer because of its good biocompatibility, relatively long degradation time (~2 years), and low melting temperature of 60 °C [179]. Due to its relatively low specific heat capacity and high thermal conductivity, it has a rapid cooling capability. This allows simultaneous printing with cell-laden hydrogels immediately after extrusion without significantly damaging the surrounding cells. A multinozzle deposition system has been developed that can deposit both biopolymers and thermoplastic polymers to create heterogeneous tissues with sufficient mechanical strength. In addition, different types of PCL scaffolds could be implemented to adjust the mechanical properties of the printed constructs without affecting the viability of the encapsulated cells within the hydrogel network [116]. For example, PCL/alginate-based hydrogels with increased mechanical strength for osteochondral tissue were bioprinted using a multihead tissue/organ building system. The desired stiffness was achieved by fabricating the PCL framework and filling the pores between the stacking lines with alginate. Osteoblast and chondrocyte cell types were successfully encapsulated in the pores of the PCL network [180]. More recently, Boere et al. [181] reinforced GelMA with a thermoplastic polymer mixture of poly(hydroxymethylglycolide-*co*-ε-caprolactone)/poly(ε-caprolactone) (pHMGCL/PCL) functionalized with a methacrylate group. The thermoplastic polymer mixture covalently bonded to the GelMA by photopolymerization led to a significant increase in the interfacial bond strength between the materials. Therefore, the reinforced hydrogels showed improved resistance to axial and rotational forces.

17.5 Designing the Ideal Bioink

The search for the optimal material or composition to fabricate 3D printed scaffolds is a constant challenge. As the variety of biological materials for TE applications

increases, the list of required material properties has become more specific and complex. First, the materials must have appropriate cross-linking mechanisms to facilitate deposition, and they should meet several physicochemical properties, such as the right viscosity and sufficient mechanical strength after cross-linking, to retain their 3D shapes after printing [156]. Such biocompatible materials are used to fabricate polymeric frameworks (scaffolds) or sacrificial parts to create complex 3D structures while maintaining high pattern fidelity [182]. In addition, the material, while protecting the cells from external forces by encapsulation [114], must have suitable swelling behavior and the short-term stability required to maintain the original mechanical properties, so that tissue structures such as pores and channels do not collapse. More importantly, the material should not only exhibit high biocompatibility but also provide the spectrum of biochemical (i.e. chemokines, growth factors, adhesion factors, or signaling proteins) and physical cues (i.e. interstitial flow, mechanical and structural properties of the ECM). This supports cellular attachment and promotes a favorable environment for cell survival, proliferation, motility, differentiation, and function [183]. The most important material properties that should be considered when designing a bioink are (i) biocompatibility, (ii) printability, (iii) material mimicry, and (iv) physicochemical properties, which include structural and mechanical properties, degradation kinetics, and swelling characteristics.

17.5.1 Biocompatibility

Biocompatibility and biological activity of the material are the first parameters to be considered when selecting a material for a bioink as they are necessary for tissue development and remodeling during (especially long-term) *in vivo* implantation. Since the materials must accommodate the encapsulated cells or facilitate engraftment with the endogenous tissue without generating an immune response, this crucial requirement considerably limits the number of suitable materials. Recent developments in TE have upgraded the goal of biocompatibility from the simple need for a material to play a passive role in tissue without causing unwanted local or systemic effects to the expectation that implanted materials passively enable or actively generate desired effects in the host [184]. While being cytocompatible, the material must provide a spectrum of biochemical signals (i.e. chemokines, growth factors, adhesion factors, or signaling proteins) that promote an environment for cell survival, motility, and differentiation. This also enables interaction with the body's own tissues and/or immune system, supports the corresponding cell activity, and facilitates molecular or mechanical signaling systems, all of which are essential for successful transplantation and function [33]. Naturally derived hydrogels are particularly attractive materials for bioprinting tissue/organ transplants, as they generally meet these requirements and provide an equally suitable environment for cells.

17.5.2 Printability

An important property of a suitable material is that it can be deposited with the desired spatial and temporal control, precisely and accurately. Printability refers

to the ability of the material to support manufacturing and rapid solidification. Properties that facilitate handling and deposition by the bioprinter include viscosity, gelation methods (cross-linking mechanisms), and rheological properties. Another key dilemma of the bioprinting process includes the selection of an optimal bioink concentration without compromising the print fidelity (requires high bioink concentration) or long-term cell viability (requires low bio-ink concentration). Some types of bioprinting technology, such as microextrusion, may require specific cross-linking mechanisms or shear-thinning properties of the material in order for the material to flow steadily and then rapidly stabilize upon deposition to form a 3D structure [79]. As mentioned earlier, microextrusion can also use highly viscous materials to maintain a 3D shape after deposition, with the final cross-linking occurring after fabrication. For other printing modalities, the deposition of highly viscous materials can be facilitated by adjustments to the curing process during bioprinting. Viscous inks that have kinetics that prevents deposition in the solution phase can be extruded as microparticles (e.g. poly(dimethylsiloxane), PDMS) that are cured before deposition [185]. On the other hand, inkjet printing is limited by material viscosity and requires materials with a fast cross-linking time to facilitate layering of a complex 3D structure. For low-viscosity solutions, the low degree of covalent cross-linking before extrusion can facilitate precise control of the rheological properties of bioinks to ensure printability. The printing process can also be designed to allow photocrosslinking through a transparent nozzle, allowing low-viscosity materials to be printed as stable filaments. Exposure after deposition leads to material flow, and exposure before extrusion leads to material fracture [186]. Further modifications to the printer hardware, such as photopermeable nozzles and switchable print heads fed from multiple reservoirs, will expand the possibilities for materials and complexity in biofabrication [157]. However, the printability and interrelation of bioinks in different bioprinters and on related substrates must always be first carefully evaluated to produce accurate, high-resolution patterns.

17.5.3 Biomimicry

17.5.3.1 Incorporation of Bioactive Molecules

The main objective of TE is to develop a biomimetic microenvironment that provides a complex site-specific combination of biochemical and mechanical cues that actively influence the attachment, migration, proliferation, differentiation, and function of both endogenous and exogenous cells [187]. The inclusion of bioactive factors, enzymatic recognition sites, gradients, and adhesion factors are among the conventional approaches used to modify biomaterials and improve their biomimicry [188]. For example, the encapsulation of bioactive molecules (e.g. growth factors or cytokines) in bioinks and their subsequent diffused release after bioprinting is a simple way to regulate cell behavior [189]. Techniques such as microspheres and hydrogels can be combined into 3D bioprinted scaffolds to achieve an efficient, sustained release of various bioactive factors [190]. Poldevaart et al. [191], for example, investigated the controlled release of VEGF from gelatin microparticles (GMPs) as a means to prolong VEGF activity at the preferred site

within 3D bioprinted scaffolds and the effects on subsequent vascularization. They used an extrusion bioprinter with a pneumatic dispensing system to produce Matrigel-alginate scaffolds with built-in VEGF-loaded GMPs. They showed that GMPs are suitable for the fabrication of scaffolds with sustained-release profiles of bioactive VEGF and that they can be used to create defined differentiation regions in 3D bioprinted heterogeneous constructs. In murine models, the use of GMPs to control the release of VEGF in a continuous, sustained manner (up to three weeks) resulted in significantly higher vascularization compared to scaffolds without growth factors and scaffolds with rapid release of VEGF. Biomimetic materials also control cell attachment and proliferation. Adding surface ligands to a material is a frequently used method to further improve both processes [192]. Additional approaches such as surface modification by physical adsorption or chemical bonding are typically used to increase cell attachment and proliferation and to regulate cell differentiation by interaction with cellular surface ligands and/or modulation of signaling pathways. However, the bulk modification of the material may affect its physicochemical properties and those of the resulting scaffolds. Conversely, postprocessing surface modification of printed scaffolds only changes the interactions between cell/tissue and material surface [193, 194].

To perfectly emulate native tissue, it is not only important to incorporate cells and bioactive components into a material, but also to mimic their native 3D spatial distribution in a construct (scaffold), which ensures the correct spatial distribution of cells and biochemical signals to control tissue formation and remodeling [195]. The creation of precise patterns of bioactive molecules can be achieved by various methods such as prepolymer mixing, modular assembly, and, more importantly, various 3D bioprinting techniques [196]. In the latter case, the development of aqueous bioinks has opened up the possibility of incorporating bioactive molecules and cells into 3D-printed scaffolds. It has been shown that scaffolds with multiple bioactive molecules and precise architecture can be created by SLA. Although SLA has the advantage of excellent resolution, it is difficult to print with multiple materials, which could limit the range of biochemical gradients that can be achieved. To achieve spatial control of more than one bioactive molecule, multiple resins loaded with different bioactive molecules must be used. In addition, the incorporation of different resins requires multiple washes and successive photopolymerization steps to remove uncrosslinked monomer. Using SLA, Gbureck et al. were able to produce calcium-phosphate-based scaffolds with VEGF and copper ions. They placed these factors precisely at the end of the closed pores within the implants and showed that both VEGF and copper improved vascularization compared to the unloaded controls [197]. One of the first studies to underline the significant influence of bioprinting bioactive molecules on the performance of scaffolds was conducted by Ilkhanizadeh et al. [198]. They used inkjet bioprinting to fabricate hydrogel scaffolds containing gradients of fibroblast growth factor 2 (FGF2) and ciliary neurotrophic factor (CNTF). The authors investigated the effect of these bioactive factors on the differentiation of neural stem cells. They showed that the concentration of cells increased in a way that correlated with the concentration gradient of CNTF. In a recent proof of concept, Liu et al. [199] used

extrusion bioprinting and described a novel design that can be used to create a hydrogel scaffold with simultaneous spatial control of up to seven different bioinks as seen in Figure 17.6. The design combines seven separate capillaries in a single point in the print head. Independently controlled pressure can be applied to each capillary, allowing the bioinks to be printed independently or simultaneously in any desired combination. The authors constructed a cylindrical scaffold with inwardly decreasing concentrations of hydroxyapatite through seven concentric circular GelMA and alginate rings. They also demonstrated a technique that allows different hydrogel concentrations, cell populations, or any other type of bioink to be contained in a controlled portion at different positions in a continuously printed fiber.

17.5.3.2 Mimicking the Native Physicochemical Properties

Furthermore, both the choice of material and the characteristics of the 3D bioprinted construct on all size scales (macro-, micro-, and nanoscale) influence the size and shape of the cells, which inevitably affects the differentiation process [202, 203]. Being the primary interface for cell interaction, the material surface plays a key role in guiding cell behavior and fate. The presence of micro- and nanotopological features such as ridges, steps, and grooves also influences cell attachment and, through cytoskeletal reassembly, proliferation, and differentiation [204]. It is known that especially micro- and nanoscale properties of materials influence cell adhesion, cell orientation and spatial positioning, expression of surface antigens, and thus cell motility. The resulting changes also lead to cytoskeletal re-arrangement, which modulates intracellular signaling pathways and ultimately influences transcriptional activity and gene expression [205, 206]. Ideally, the surface characteristics should be closely tailored to the critical aspects of the native or pathologically altered tissue. Recently, Milojević et al. [207] presented a simple approach for adjusting the surface properties of scaffolds. They created hybrid hydrogel formulations from commonly used materials (alginate, carboxymethyl cellulose, nanofibrillated cellulose [NFC]) and incorporated variable concentrations of nickel-copper nanoparticles into the hydrogels. They showed that the nanoparticles could be an effective tool not only for controlling the surface properties of scaffolds but also for manipulating the hydrogel viscosity and swelling as well as the degradation kinetics. 3D printed scaffolds also promoted cell adhesion, cell aggregation, and migration and supported the long-term growth of pancreatic cells, which also had a more physiologically relevant morphology.

17.5.3.3 Decellularized Extracellular Matrices

The application of these principles is useful in controlling the differentiation of cells in a scaffold to a specific phenotype. Still, the strategy to develop biomimetic materials for specific physiological functions requires a comprehensive understanding of the native tissue-specific composition and the localization of the bioactive components of the ECM in the tissue in question. Although bioinks provide critical biochemical cues that regulate cell behavior, most existing bioinks are not

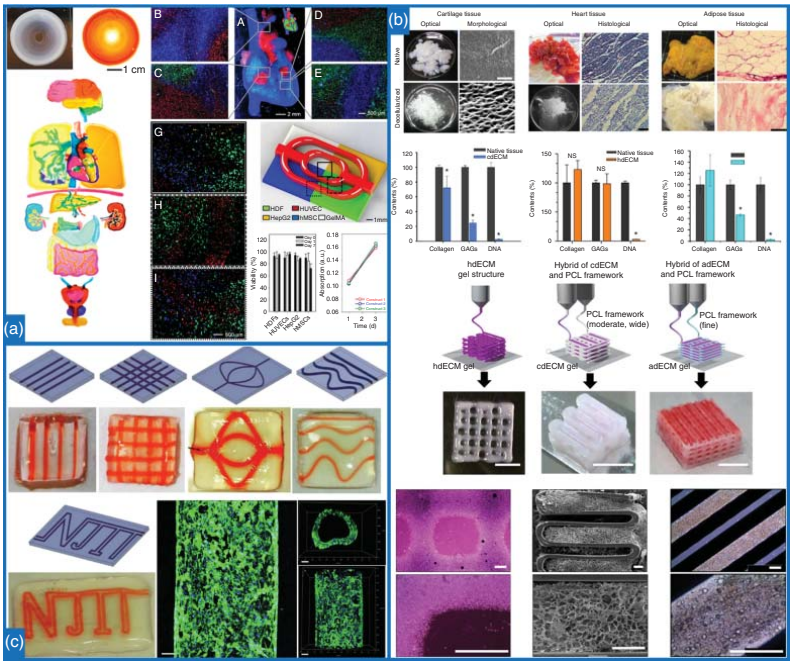

Figure 17.6 3D bioprinting of biomimetic scaffolds. (a) A continuous multimaterial extrusion bioprinter was able to print multimaterial constructs with continuous segments and concentric structures containing inward-out gradients. The authors demonstrated its applicability by bioprinting a multicomponent cell-laden hearth-like structure, as shown in the fluorescence images. Source: Liu et al. [199]/with permission of JohnWiley & Sons. (b) Optical and microscopic images of native and dECM cartilage (cdECM), heart (hdECM), and adipose (adECM) tissue with accompanying ECM components (collagen and GAGs) and DNA contents of native and dECM tissues. The bottom images show cdECM, hdECM, and adECM 3D bioprinted scaffolds consisting of dECM bioinks. Source: Pati et al. [200]/with permission of Springer Nature. (c) Digital designs and corresponding 3D scaffolds with incorporated channels. Cross-sectional and top view fluorescent images show hUVECs cultured within the perfusable channels. Source: Ji et al. [201]/with permission of Elsevier.

able to fully emulate the complexity of the native ECM. The ability to reproduce materials and scaffolds identical to the ECM using a bioprinting approach would be a breakthrough in TE and RM. Tissue decellularization methods [208] could provide intact ECM scaffolds (decellularized extracellular matrices, dECM) for a detailed analysis of ECM composition, localization, and biological functions [33]. dECM refers to the natural extracellular matrices obtained from different parts of native tissues and/or organs through a decellularization process. Such matrices closely mimic the complexity of the ECM, which plays a crucial role in regulating cell–cell and cell–biomaterial interactions [209]. The dECM for each tissue type can be obtained by different decellularization protocols. The protocol usually involves lysis and removal of the cellular components of the tissue by perfusion with deionized water or detergents. This leaves behind a tissue-specific ECM. While the composition and material properties of the dECM may vary depending on tissue source and processing method, the composition usually consists of common proteins/macromolecules such as collagen, laminin, fibronectin, elastin, and their tissue-specific GAGs, cytokines, and growth factors [210]. Over the years, various bioinks from dECM of different tissues and/or organs have been used for 3D printing. Some examples include adipose [211], cardiac [212], vascular [213], corneal [214], liver [215], muscle [216], and pancreatic [217] tissues as well as skin [218], dentin [219], and tendon [220]. In a recent study, Pati et al. [200] demonstrated, for the first time, the ability of dECM bioinks to be incorporated into 3D-printed cell-laden scaffolds capable of harboring cells and creating functional tissue. They developed a multihead tissue printing process to create cell-laden scaffolds using novel dECM bioinks made of decellularized fat, cartilage, or cardiac ECM (Figure 17.6). Human adipose-derived stem cells (hASCs) were cultivated in scaffolds from decellularized adipose tissue, human inferior turbinate-tissue derived mesenchymal stromal cells (hTMSCs) in decellularized cartilage and myoblasts in decellularized cardiac tissue. This approach allowed them to generate *in vitro* tissue analogs with either adipogenic or chondrogenic potential. They showed that hASCs or hTMSCs could be printed by encapsulation in a dECM gel and that *in vitro* culture did not modify cell survival and proliferation, but increased the commitment of stem cells toward either adipogenic lineage within the dECM from adipose tissue or chondrogenic lineage within the cartilage dECM. In addition, increased structural maturation of myoblasts was observed in constructs prepared with dECM from cardiac tissue. A major advantage of this method is the application of the tissue-specific ECM, which provides crucial cues for cells engraftment, survival, and long-term cell function.

However, even the best dECM bioinks are not able to perfectly replicate the complex ECM, since the highly specific spatial positioning of each structural protein within the native tissue is disrupted during preparation [52]. One of the challenges in tissue decellularization is to find a balance between the complete removal of cellular components and the preservation of fine vessels and other tissue structures. In addition, some toxicity has been observed when cells are grown on decellularized tissue scaffolds, possibly due to retention of the decellularization detergent within the ECM [221].

Since the cells produce and deposit the tissue ECM, bioprinted, self-organizing cell spheroids can create an environment that is best suited for their function. This provides a more native-like environment for cells and promotes better cell–cell interaction. By exploiting this process, scaffold-free TE has emerged in recent years, in which spheroids with high cell densities are cultivated without the use of a carrier material. Although the resulting structures are small, they can be assembled into larger structures. This approach might be of particular interest for induced pluripotent stem cells (iPSCs) until new hydrogels are discovered that can better maintain the viability and differentiation state of iPSCs [140].

17.5.4 Physicochemical Properties

17.5.4.1 Designing the Required Mechanical Properties

In addition to the decisive physicochemical parameters such as viscosity, wetting/swelling behavior, degradation kinetics, by-products, and gelling time [33], a suitable bioink should have appropriate mechanical properties that support the 3D structure after bioprinting [151]. Native tissues and/or organs also have unique anatomical structures that should be reproduced in a 3D construct because they perform highly complex and specific functions [222]. A suitable material is essential not only for maintaining the required 3D structure but also for producing specific mechanical cues. Therefore, the maintenance of these properties is essential for the function of the printed construct [79]. Hydrogels meet most of the required criteria and typically have good printability and have therefore been widely used for bioink design. On the other hand, hydrogels are usually soft and do not have self-supporting properties for printing complex 3D structures. They are susceptible to a variety of external conditions that, under their own weight, lead to melting, dissolution, or material deformation. This can be mitigated by postprocessing fixation methods, which usually involve physical or chemical cross-linking and can improve the mechanical stability of the structures. The most commonly used method is the covalent cross-linking of hydrogels, but this is not a favorable solution as the chemical cross-linking is irreversible and can lead to the formation of toxic by-products [223]. To adjust the mechanical properties of hydrogels and to obtain suitable hydrogels with desired biophysical properties, several parameters need to be controlled simultaneously, including temperature, reaction conditions, chain and functionality, chemical structure, methods, and degree of cross-linking, pH, and ionic strength [151, 224]. However, deviating from physiological conditions during scaffold preparation usually has a negative impact on most of the biologically active components of the bioink and reduce cell viability [225]. In addition, additives that are normally incorporated into bioinks to improve their mechanical stability can lead to inhomogeneity in the polymer network [226].

One approach to overcoming these limitations is the use of sacrificial materials (so-called fugitive inks), which improve the quality and fidelity of the printing process and only temporarily provide the required structural and mechanical properties [227]. Fugitive inks are used in two ways: either (i) during printing around the structure (in the form of a carrier bath) to support their formation in

open space and allow sufficient cross-linking in the structure [228, 229], or (ii) they can be incorporated within the structure and allow internal channels to form or function until the endogenously produced materials can adequately perform their function [33, 177]. The potential application for the development of vascular tissues using sacrificial materials was recently demonstrated by Ji et al. [201]. First, they constructed methacrylate alginate or methacrylate HA hydrogels with incorporated sacrificial ink (Pluronic). Using a sequential printing process, the photocurable hydrogel was printed layer by layer, each layer being exposed to light for a short time to create partially cross-linked, self-supporting layers. At the desired thickness, immediately after the deposition of the layer (before the partial cross-linking step), the sacrificial hydrogel was printed directly inside this viscous, uncrosslinked layer. The layer was then exposed to light to enclose and support the sacrificial hydrogel. Once the system was fully cross-linked, the sacrificial hydrogel was washed away, forming a channel, as can be seen in Figure 17.6. The authors also incorporated MSCs into the bioprinted matrix hydrogel and seeded ECs into the hollow channels, which were later perfused. After attachment within the channels, the ECs formed circumferentially confluent layers. The novelty of their method results from the fact that the matrix hydrogel and the sacrificial ink were not mixed during the deposition process, which enabled a high resolution of the final channel after perfusion. Recently, a new strategy called "Freeform Reversible Embedding Suspended Hydrogels" (FRESH) [230] has been developed. It uses a support bath made of a material that exhibits Bingham plastic behavior, which flows like a viscous liquid at high shear stresses but behaves like a rigid body at lower shear stresses. This property of the bath allows the syringe nozzle to move through the substrate with negligible resistance while supporting the extruded material and maintaining the geometry of the printed structure. In FRESH, the carrier material usually consists of a slurry of GMPs that is melted and removed after the structure is completed by simply raising the temperature to 37 °C. In addition to core–shell printing, FRESH presents another viable bioprinting strategy for the creation of 3D-printed perfusable microchannels. In a recent study, xanthan gum was deposited into $CaCl_2$-infused gelatin to form sacrificial earlobe-shaped channels. Using this method, the authors created complex 3D structures that were stable enough to support themselves and complex channel geometries that were uniformly perfusable [230]. Along with gelatin, another frequently used "fugitive" material is Pluronic F-127 (PF127), a synthetic polymer based or poloxamer. Due to its higher printability, the use of PF127 bioink results in significantly smaller microchannels (≥100 μm diameter) compared to gelatin channels (≥700 μm diameter) [177].

Another interesting approach for improving materials mechanical properties is the addition of laponite nanoclay to a bioink, which causes a rapid increase in viscosity when shear stress is reduced and gives the bioprinted structure good structural stability. The incorporation of laponite nanoclay does not influence the cross-linking mechanisms, so that hydrogel composites, which can retain their complex 3D structures with self-supporting properties, can be produced even before complete cross-linking [231].

17.5.4.2 Physicochemical Gradients

Secondly, materials must be carefully selected based on the required mechanical properties of the final construct, and different requirements are needed for different types of tissues [232]. To fully mimic the properties of native tissues, the mechanical properties of a 3D-printed construct should mimic those of the *in vivo* tissue, which also encompasses physical gradients that are not only present at boundaries between different tissue types but are also present within a single tissue [233]. Physical gradients are defined as changes in physical properties such as material porosity, morphology, or stiffness throughout the ECM. Such gradients of mechanical properties at both the macroscopic and microscopic levels play a crucial role in regulating cell behavior and allow the formation of complex anisotropic tissues [151]. The biomechanical cues and interactions between cells and substrate also control the cell phenotype and genotype [234]. In particular, substrate stiffness influences cell proliferation, adhesion, contractility, growth, and migration and is the key regulator of phenotypic and genotypic responses of a wide range of cell types [235]. For example, it has been shown that substrate stiffness controls the differentiation and migration of MSCs into different cell types such as myoblasts, osteoblasts, and neurons [236]. Furthermore, cells exposed to stiffer substrates experience a higher modulus of elasticity in their plasma membrane with a better-organized actin cytoskeleton. Cells cultivated on stiffer substrates proliferate faster and migrate more slowly than cells cultivated on soft substrates [237]. In fact, Hadjipanayi et al. showed that the cells migrate to stiffer surfaces, a phenomenon that has since been referred to as durotaxis [238]. The development of tissue scaffolds with heterogeneous mechanical properties would thus serve better to imitate the native cellular environment and further support the function of specific cell populations. There are a limited number of studies that use extrusion-based 3D printing to create gradient scaffolds and investigate the influence of mechanical gradients on tissue formation. Recently, Di Luca et al. [239] investigated the influence of scaffolds with stiffness gradients on osteochondral regeneration. They created stiffness-gradient scaffolds by bioprinting PLA, PCL, and poly(ethylene oxide terephthalate)/poly(butylene terephthalate) (PEOT/PBT) copolymers in different ratios. They showed that cells on homogeneous scaffolds showed higher activity of ALP compared to cells on gradient scaffolds. Within the gradient scaffolds, however, microenvironments were created that showed regions of high ALP activity. The authors concluded that these high activity regions are due to the surface energy gradients generated by the different materials within the constructs. Other approaches to modify mechanical properties could use changes in cross-link density using SLA or other light-based approaches or changes in extrusion parameters to change the fiber or layer thickness. In addition, most tissues exhibit anisotropy, which further complicates the physical requirements of scaffolds [240]. The effects of anisotropic materials on tissue regeneration have only been researched to a limited extent since the production of anisotropic materials using classical manufacturing methods has been an extremely difficult task until now. However, AM allows precise control over the scaffold design, so that anisotropic materials can be reliably designed

and fabricated. Recently, Cox et al. [241] have fabricated a hydroxyapatite-based scaffold using powder-fusion pressure. They showed that the anisotropic behavior of the scaffolds could be easily controlled by changing the architectural design.

Another important physical gradient to be considered when designing a scaffold for tissue regeneration are pore gradients. The success of tissue ingrowth into a scaffold is strongly dependent on the pore size and overall porosity [242]. Highly porous biomaterials support *de novo* tissue regeneration by (i) providing a large surface area for cell attachment and growth, (ii) promoting the transport of nutrients and waste products, (iii) facilitating mechanical interlocking with adjacent tissue, and (iv) allowing vascularization of the construct [243]. Although native tissue is inherently porous, it is not homogeneously distributed. Instead, it is distributed in a way that maximizes the overall performance of the tissue [244]. Therefore, a scaffold with only one uniform pore size would have functional limitations. Scaffolds with pore gradients have been shown to prolong static culturing by increasing accessibility to nutrients and oxygen [245]. An ideal scaffold should have a tissue-specific graded porosity that maximizes the regenerative potential of the scaffold [246]. 3D bioprinting opened the possibility of precisely controlling the pore geometry, interconnectivity, and pore size and, in particular, creating regions with variable pore size within a single scaffold. Although there are not many examples that focus on gradient generation, SLA, and other light- or laser-based printing methods have the potential to create constructs with gradient pore sizes and concentrations. The high resolution of these techniques could allow very specific and targeted placement of pores within a scaffold [247]. Several other methods have also been developed to create functional gradient architectures [248–250]. For example, Sobral et al. [251] have applied 3D extrusion bioprinting and investigated the influence of pore size gradients on cell-seeding efficiency. Scaffolds with alternating pore sizes of 100 and 750 μm were produced by the deposition of PCL. It was shown that a graded pore structure increases seeding efficiency compared to an ungraded architecture. The authors hypothesized that this effect is due to more tortuous channels within the heterogeneous scaffolds, which increases the residence time of the cells and increases the probability of contact between the scaffold and the cell.

17.5.4.3 Swelling and Degradation Behavior

Other important physicochemical parameters for the fidelity of the bioprinted construct are its swelling behavior, contractile characteristics, and degradation kinetics. The first parameter is mainly determined by the degree of cross-linking and charge densities [225] and influences the final shape and size of the printed 3D construct [121]. In general, the use of high degrees of cross-linking in hydrogels results in lower swelling ratios, which leads to smaller pore sizes [252], reduces the diffusion of oxygen and nutrients required for cell survival, and limits the removal of waste products from the encapsulated cells [253]. Although highly cross-linked hydrogels offer good shape retention after bioprinting, they are not always optimal from a biological point of view due to the impairment of cell migration and

proliferation and thus inhibit the remodeling and functional integration of the construct [122]. A possible solution to this problem is the use of already-mentioned hybrid scaffolds that combine tissue-specific optimized hydrogels with materials that offer mechanical stability and facilitate shape retention [182]. On the contrary, over-swelling materials can potentially lead to the absorption of fluid from the surrounding tissue. In contrast, high contraction leads to the closure of pores or vessels, which are essential for cell migration and nutrient delivery. The understating of these responses is important when using multiple materials with different swelling or contraction behavior, as this could potentially lead to loss of layer integrity or deformation of the final construct.

Ultimately, if a 3D bioprinted construct is to differentiate into functional tissue, the cells must eventually proliferate and replace the printed material with new ECM. Nondegradable hydrogels may have the disadvantage of being elastic when interacting with cells. At the same time, the ECM of various human tissues such as the brain, liver, and adipose tissue is viscoelastic and has a certain degree of stress relaxation [254]. Besides, *in vitro* cellular studies have shown that cell morphology, proliferation, and migration in hydrogels are inhibited if the hydrogels are not degraded over time [255]. As the material degrades, the embedded cells drive the remodeling process by secreting proteases that initiate the degradation of the biomaterial or, in the case of hydrolytic polymers, by remodeling the matrices during the loss of the biomaterial [26]. The cells then produce ECM proteins that define the new tissue [256]. Several aspects of degradation should be carefully considered. The first is the ability to control the rate of degradation, which should ideally match the cells' ability to produce their own ECM to replace the material. This is a challenge because materials with appropriate functional and mechanical properties for a given tissue may not match the cells' ability to replace the material during degradation [33]. In addition, as scaffolds degrade, they can further influence the remodeling process, depending on whether toxic by-products are produced during degradation. The second important factor to consider is therefore degradation by-products, which usually define the biocompatibility of degradable materials. Ideally, the degradation products should be nontoxic, easily metabolized, and quickly eliminated from the body. Toxic products may include small proteins and molecules that affect cell physiology either directly or by creating an unfavorable environment, e.g. by influencing pH, temperature, or other factors that may affect cell viability and function. For example, some high-molecular-weight polymers that are initially inert may be broken down into oligomers or monomers, which are recognized by the cells and may cause inflammation and other adverse effects [56].

17.6 Application of 3D Bioprinting for the Fabrication of Tissues and Organs

There has been significant progress in the field of bioprinting in the past decade. Different types of functional tissue are printed and tested. This section is, therefore,

focused on the current state of the art in the use of 3D bioprinting to produce skin, cardiac, bone, and cartilage tissue, which have attracted the most interest in recent years.

17.6.1 Skin

The skin is a three-layer structure (outer epidermis, a middle dermis, and inner hypodermis) that is made from several types of cells, including keratinocytes, fibroblasts, and melanocytes. It performs several vital functions, such as regulatory (thermal, hydration, and excretory), perceptive (touch, temperature, and pain), and protective (barrier, UV light absorption, immune monitoring, and mechanical) functions. Due to the enormous market demand, bioprinting of skin has recently attracted a lot of attention. It is expected that skin will be one of the first bioprinted tissues to be used clinically or for drug/cosmetic testing [257]. Although the production of tissue-engineered skin constructs may seem like a simple process, native skin has a highly complex 3D structure that requires precise structuring of cells and biomaterials to facilitate important cell–cell and cell–biomaterial interactions. Considerable progress has been made in this area, and many bioprinting processes for printing skin tissue constructs that structurally and biologically mimic native human skin have been explored. Using LIFT, Koch et al. [99] were among the first to report on the bioprinting of skin cells (NIH3T3 fibroblasts and HaCaT human immortalized keratinocytes). Cells suspended in collagen hydrogel were printed to form a 3D skin tissue construct consisting of 20 layers of fibroblasts and 20 layers of keratinocytes. After 10 days, the constructs showed good viability and exhibited tissue morphogenesis. Lee et al. [98] used the microvalve bioprinting method to print HFF-1 fibroblasts and HaCaT keratinocytes suspended in collagen hydrogel to form a multilayer skin construct consisting of dermal and epidermal layers. Histological examination and immunofluorescence characterization after 14 days revealed morphological similarities of the printed construct to native *in vivo* human skin tissue. Using the same technique, Rimann et al. [258] were the first to show that bioprinting can be used on a production scale, with the fabrication of a multilayer skin construct taking only several minutes (not including the cultivation time). Human primary dermal fibroblasts and epidermal keratinocytes were suspended in a PEG-based photopolymerizable bioink for bioprinting. The epidermal layer was printed after different periods of time (up to six weeks) after the cultivation of the printed dermal construct. The importance of the quality of the dermal layer to produce biomimetic skin tissue was shown, as the formation of *stratum corneum* was observed only in the constructs cultured for six weeks before printing the epidermal layer. Fibroblasts in the dermal layer proliferated up to 42 days and produced their own ECM. With the help of microvalve printing, an attempt was also made to integrate other cell types present in the skin, such as melanocytes. Min et al. [259] reported on the bioprinting of a pigmented full-thickness skin model shown in Figure 17.7.

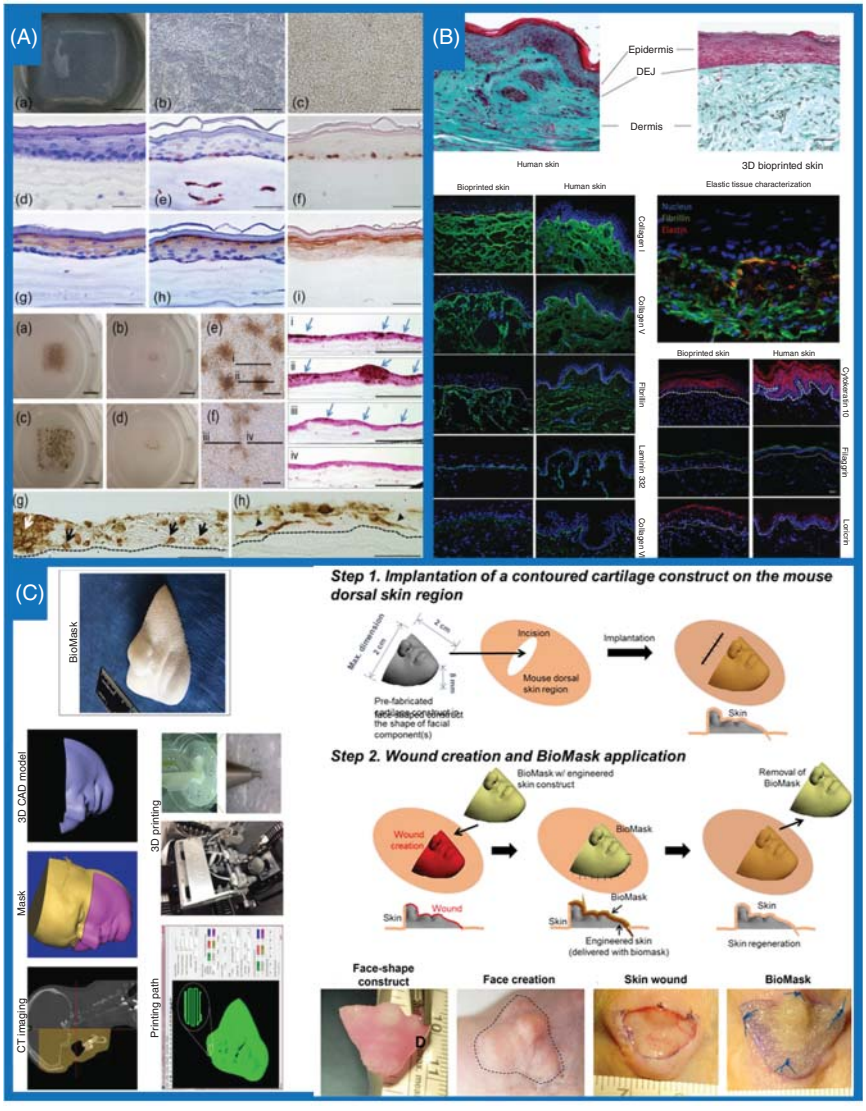

Figure 17.7 3D bioprinting of skin tissue constructs. (A) Microscopic cross-sectional images for structural and histological examination of 3D bioprinted biomimetic skin without (top) and with (bottom) included melanocytes. The blue arrows indicate the areas of pigmentation, while the black arrows show the dermal–epidermal junction. Source: Min et al. [259]/with permission of John Wiley & Sons. (B) Optical microscopy images (top) of normal human skin and bioprinted skin after 26 days of culture, with tissues stained with Masson's Trichrome. Fluorescent microscopy observations (bottom) of epidermal differentiation and dermal marker profiles of bioprinted skin compared to normal human skin from a healthy donor. Source: Pourchet et al. [260]/with permission of John Wiley & Sons. (C) Bioprinting workflow (left) from medical imaging data to BioMask fabrication and illustrations of facial skin wound animal model creation and surgical procedure of BioMask application (right). Source: Seol et al. [261]/with permission of Elsevier.

To fabricate a pigmented skin construct, epidermal melanocytes and keratinocytes suspended in a collagen hydrogel were printed on the dermal layer (fibroblasts) cultivated the day before on an air–liquid interface culture. Histological examination and immunocytochemical characterization after 10 days showed evidence of pigmentation and melanin granules within the epidermal layer. More recently, Ng et al. [262] have been using a two-step DOD strategy to produce 3D biomimetic hierarchical porous structures found in native skin tissue. Their strategy facilitates the deposition of cell droplets to mimic the epidermal melanin units (predefined patterning of keratinocytes and melanocytes at the desired positions) and the manipulation of the microenvironment. The characterization of bioprinted pigmented skin constructs has shown that they exhibit high similarity to native skin tissue in terms of the presence of well-developed, stratified epidermal layers and the presence of a continuous layer of basement membrane proteins. Two research teams used extrusion-based bioprinting to fabricate biomimetic skin tissue constructs. Using primary human fibroblasts and keratinocytes suspended in a gelatin/alginate/fibrinogen hydrogel, Pourchet et al. [260] produced a human skin construct. The histological and morphological characterization (Figure 17.7) of the bioprinted skin 26 days after printing showed the characteristics of human skin, both at the molecular and macromolecular levels, as evidenced by biomarkers of the dermal layer and epidermal differentiation. Cubo et al. [263] used a multinozzle extrusion bioprinting system to produce human bilayered skin. Three syringes were used, whereby cell-containing media was extruded through the first nozzle, the second contained a human plasma with fibrinogen and tranexamic acid, and the third contained a cross-linking solution. Human epidermal keratinocytes suspended in cell media were printed onto the dermal layer prepared from human dermal fibroblasts after a 30-minute incubation. *In vitro* and *in vivo* studies showed that the printed skin showed structural and biological similarities to native human skin. Recently, Derr et al. [264] have produced a fully 3D bioprinted skin equivalent using a similar configuration with three syringes. The dermis-mimicking layer was prepared with a hydrogel-containing gelatin, fibrinogen, type I collagen, and elastin incorporated with fibroblasts. The epidermis consisted exclusively of keratinocytes in the culture medium, and the basal layer was a solution of laminin/entactin. This bioprinted skin equivalent showed high cell viability, good barrier function, and was morphologically similar to native tissue. Huang et al. [265] also used an extrusion-based system to print epithelial progenitor cells and dermal homogenates suspended in a gelatin/alginate hydrogel. *In vitro* and *in vivo* studies confirmed the differentiation of epithelial progenitor cells into functional sweat glands. A similar study was recently conducted by Cheng et al. [266]. To induce differentiation, they used bioinks based on alginate/gelatin and showed that epidermal progenitor cells injected on the bioink differentiate into sweat gland-like cells. After seven days, the cells expressed keratin-associated markers.

Furthermore, it was shown that the stiffness of bioink was similar to that of mouse dermal tissue. Liu et al. [267] also developed bioprinted skin structures

with a similar hydrogel composed of alginate/gelatin. Human epithelial cells and MSCs were bioprinted to form two-layer skin-like constructs of the epidermis and stromal layers *in vitro*. These constructs showed rheological properties corresponding to their potential applications, including shear-thinning behavior and temperature-dependent viscosity, and support high cell viability. Closer to a possible application in clinical situations is a novel approach developed by Seol et al. called "BioMask" [261]. This is a customized engineered skin substitute (Figure 17.7) combined with a wound-dressing layer. More precisely, it consists of three layers: (i) a porous polyurethane layer, (ii) a hydrogel layer loaded with keratinocytes (HA, glycerol, gelatin, and fibrinogen), and (iii) a hydrogel layer loaded with fibroblasts (HA, glycerol, gelatin, and fibrinogen). Using CT images of skin wounds, the authors precisely deposited dressing material and cell-laden hydrogels into the wound. The *in vivo* results demonstrated skin contraction, and the histological examination showed the regeneration of skin tissue consisting of epidermal and dermal layers.

17.6.2 Heart

The cardiovascular system consists of the heart and blood vessels, which include arteries, veins, and capillaries. The fabrication of hollow-perfusable scaffolds using various bioprinting approaches, vascular networks, and novel manufacturing strategies that support the creation of channel structures was a major focus of this chapter and is discussed in great detail throughout the review. Hence, the focus of this section will be mainly on the production of functional cardiac tissue.

The number of valve replacement surgeries is increasing, and conventional TE methods cannot reconstruct the valve's native anatomy and replicate the heterogeneous cell populations. However, bioprinting has proven to be a viable alternative for the construction of biomimetic heart valves [268]. The advantages of bioprinting over other TE methods include the exact replication of complex biomimetic architecture (e.g. tricuspid valve), the ability to create mechanically heterogeneous structures, and the spatial control of valve cells (e.g. valve interstitial cells [VIC] and SMCs) [108]. Duan et al. [123] were among the first to successfully bioprint an aortic valve conduit from porcine aortic VICs and human aortic root SMCs suspended in an alginate/gelatin hydrogel. Using a similar approach, the same group [269] bioprinted a tricuspid valve using human aortic valve interstitial cells (HAVICs) suspended in a methacrylated HA/methacrylated gelatin hydrogel. After seven days, the constructs maintained post-printing cell viability of over 90%. Histological and immunohistochemical analysis showed cell proliferation, ECM production, and significant gene expression of αSMA, vimentin, periostin, and collagen 1A1. However, the printed construct did not meet the mechanical requirements of native valve tissue.

The main reason why cardiovascular diseases are the most common cause of death worldwide is the fact that the myocardium has a severely limited ability

to regenerate. Therefore, the greatest motivation for cardiac TE is to fabricate human-engineered cardiac tissues that are very similar to native myocardium tissue. Using LIFT, Gaebel et al. [270] patterned HUVECs and hMSCs on a cardiac patch made of polyester urethane urea (PEUU). A patch with randomly seeded cells was used as a control. *In vivo* studies demonstrated that the bioprinted patch with spatially arranged cells showed more blood vessel formation and increased capillary density as well as led to a significant improvement in the functionality of infarcted hearts eight weeks after transplantation in rats. The Gaetani team published two studies in which they used extrusion-based bioprinting to fabricate cardiac tissue. In the first [271], human fetal cardiomyocyte progenitor cells (hCMPCs) suspended in alginate hydrogel were printed into a tissue construct with cardiogenic potential. The viability of the cells postprinting was 89% after seven days, and the cells retained their cardiac lineage with upregulated gene expression of early cardiac transcription factors and the sarcomeric protein troponin T. In the second study [272], they fabricated functional cardiac tissue constructs from hCMPCs suspended in gelatin/HA matrix and implanted them into mice that exhibited improved cardiac performance. In contrast, Wang et al. [273] have recently used sacrificial 3D bioprinting to produce functional and contractile tissue (Figure 17.8). The constructs were made from a fibrin-based cardiomyocyte-laden hydrogel, a sacrificial gelatin-based hydrogel, and PCL. The constructs were characterized concerning cardiac cell synchronization, beat behavior, electrophysiological properties, and measurement of the contractile force. These constructs had a highly organized structure with the unique physiological and biomechanical properties of native cardiac tissue. They showed physiological responses to known cardiac drugs in terms of beating frequency and contractile forces.

Skylar-Scott et al. [275] also used sacrificial 3D bioprinting and reported on a novel approach called sacrificial writing into functional tissue (SWIFT). The authors used the technique to fabricate organ-specific tissues with high cell density ($\sim 10^8$ cells/ml) and to create perfusable vascular channels. To achieve this, they used patient-specific iPSC-derived organoids as "organ building blocks" suspended in a collagen-based ECM solution. These structures were then compacted and printed into a gelatin-based sacrificial ink to create vascularized structures. As an example, they created a perfusable cardiac tissue composed of organ building blocks of iPSC-derived cells mixed with dermal fibroblasts and the collagen-based ECM. When the construct was fused into a disc-shaped form, it began beating synchronously over seven days with calcium waves propagating rhythmically and rapidly throughout the tissue. This architecture was then perfused and, in the course of eight days, developed a pervasive sarcomeric configuration with increased contractility and beat synchrony. In addition, the authors printed an arterial vascular network geometry within the cardiac matrix using patient-specific structural data to accurately reproduce the geometry of the left anterior descending coronary artery. Lee et al. [276] report on an improved method of 3D bioprinting collagen using

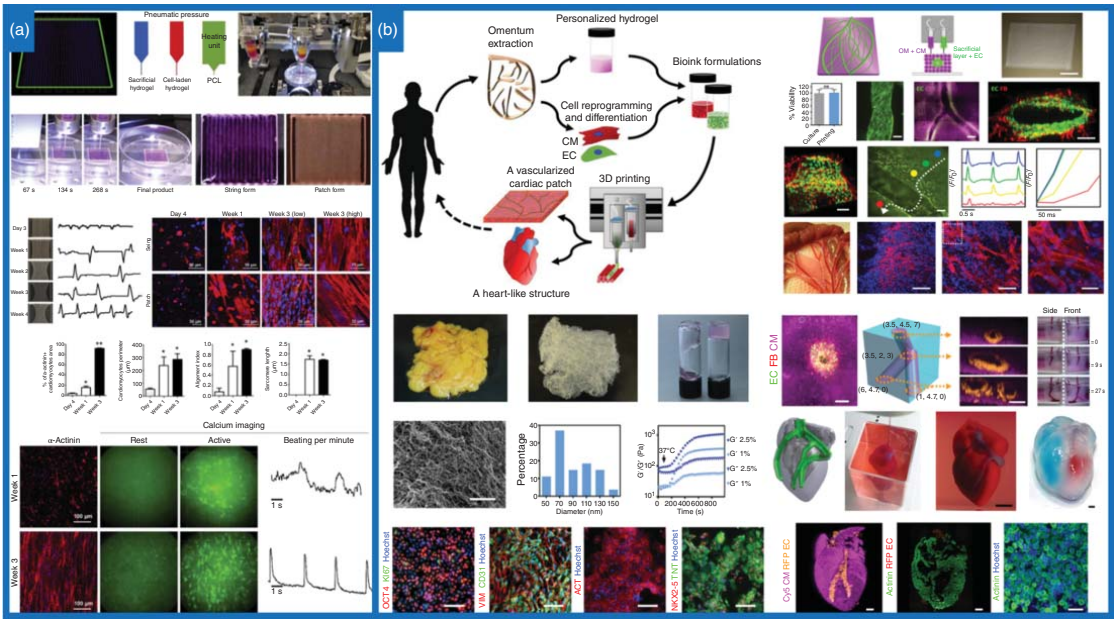

Figure 17.8 3D bioprinting of cardiac tissue. (a) Bioprinting of cardiac tissue constructs in string or patch form using the customized ITOP system (top). Gross appearance and cardiac beating measurement with time as well as immunofluorescent images of bioprinted cardiac tissues (middle). Bioprinted cardiomyocytes expressed α-actinin (red), connexin (green), and cell nuclei (blue). Immunofluorescence for α-actinin of bioprinted cardiac tissues in culture, representing different levels of cellular organization and tissue development: α-actinin (red) and cell nuclei (blue) as well as calcium imaging analysis for synchronization of bioprinted cardiac tissues (bottom). After three weeks, bioprinted cardiac tissue showed regular synchronous contractile behavior. Source: Wang et al. [273]/with permission of Elsevier. (b) An omentum tissue was extracted from the patient, and while the cells were separated from the matrix, the latter was processed into a thermoresponsive hydrogel. The cells were reprogrammed to become pluripotent and then differentiated into cardiomyocytes and ECs, followed by encapsulation within the hydrogel to produce the bioinks used for printing. The bioinks were then printed to create vascularized patches and complex cellularized structures (top left). Bioink characterization: human omentum before/after decellularization and morphological, rheological, and immunocytochemical analysis of the dECM bioinks (bottom left). 3D bioprinting of personalized vascularized cardiac patches (top right) and bioprinting of thick vascularized tissues (bottom right). Source: Noor et al. [274]/John Wiley & Sons/CC BY 4.0.

FRESH for the production of components of the human heart at various scales, from the capillaries to the whole organ. The control of the pH-driven gelation allows a resolution of the filaments of 20 μm. The authors developed a porous microstructure that allows rapid cellular infiltration and microvascularization as well as mechanical strength for the fabrication and perfusion of multiscale vasculature and tricuspid valves. When printed with human cardiomyocytes and cardiac fibroblasts, the ventricles showed synchronized contractions, the propagation of the directional action potential, and wall thickening of up to 14% during peak systole. In addition, the FRESH-bioprinted entire neonatal human heart accurately reproduced the anatomical patient-specific features, including the atrial and ventricular chambers, trabeculae, and the pulmonary and aortic valves as determined by μCT. In addition, the selection of an optimal bioink material is also crucial for improved functional maturation of cardiomyocytes. The successful differentiation of iPSCs on GelMA scaffolds for the production of cardiac tissue was recently demonstrated by Kerscher et al. [277]. In addition, Noor et al. [274] have 3D printed thick, vascularized and perfusable cardiac patches using an omental tissue biopsy to develop decellularized matrices that fully match the immunological, cellular, biochemical, and anatomical characteristics of the patient (Figure 17.8). The extracted omental cells were reprogrammed into iPSC and subsequently differentiated into either cardiomyocytes or ECs. Using supporting medium consisting of sodium alginate, xanthan gum, and calcium carbonate, they were able to fabricate functional vascularized patches that mimicked the patient's anatomy, with elongated cardiomyocytes with actininic striation.

17.6.3 Bone

The human bone has a highly complex hierarchical structure that performs various biological, mechanical, and chemical functions. It consists of two different regions: the outer compact bone (cortical bone) and the inner trabecular bone (cancellous bone), which contain several cell types. The bone has a complex hierarchical structure containing both inorganic crystalline minerals (hydroxyapatite) and organic components (type I, III, IV collagen, and fibrillin) in a highly ordered network [278]. Since it is a dynamic vascularized tissue, it is capable of self-healing and remodeling without scarring. However, its self-regenerative capacity is not sufficient if there is a large bone defect, and there is a need for bone implants (autografts, allografts, or artificial replacements) [279]. Successful bone TE requires mechanically stable, biocompatible bone scaffolds with a controlled pore size (200–350 μm), degradation rate, and sustained release of biomolecules (for osteogenesis and angiogenesis) that serve as temporary bone implants [244, 280]. Traditional approaches have focused primarily on shape and mechanical stability and include the use of porous metal, ceramic, or polymer scaffolds that can support bone regeneration and growth. With the progress of bioprinting technologies, more complex bone structures could be printed. Several types of cells suspended in a hydrogel could be spatially arranged to form a biomimetic bone construct for testing and clinical transplantation.

Some studies [138] used extrusion-based printing to produce alginate-based scaffolds that promoted osteogenic differentiation. In another study, Neufurth et al. [281] used pneumatic extrusion printing (Figure 17.9) to fabricate alginate/gelatin scaffolds with integrated osteogenic sarcoma cells (SaOS-2). When an overlay of agarose and the calcium salt of polyphosphate [polyP·Ca^{2+} complex] was added to the scaffolds, an increase in cell proliferation and mineralization was observed. In order to improve the structural and osteogenic properties of mechanically unfavorable alginate-based bioinks, Choe et al. [285] have incorporated graphene oxide in inks. The composites were used to print scaffolds, which improved the osteogenic differentiation of MSCs. Duarte-Campos et al. [282] investigated how material stiffness influences osteogenic differentiation. For this purpose, they bioprinted agarose/collagen scaffolds (Figure 17.9) with different stiffness values. They were able to fine-tune the hydrogel stiffness by adjusting the concentration of collagen in the final polymer mixture. Recently, Wei et al. [283] further improved the osteogenic differentiation of adult stem cells. The authors developed a silk/fibroin-based composite (together with gelatin, HA, and tricalcium phosphate) and coated it with human platelet-rich plasma (PRP). Human adipose-derived MSC cultured on the 3D printed composite structures (Figure 17.9) showed significantly increased gene expression levels of late osteogenic markers and improved growth and proliferation profiles.

Similarly, Lai et al. [286] have also developed novel porous composite scaffolds made of magnesium, poly(lactide-*co*-glycolide), and β-tricalcium phosphate. The scaffolds were fabricated with low-temperature AM and transplanted into rabbit models with defects in femoral condyle defects. After 12 weeks postoperatively, newly formed vessels and significant bone formation with complex architecture were observed. The constructs exhibited well-designed biomimetic structures and improved mechanical properties, making them a promising composite biomaterial for the repair of challenging bone defects. Levato et al. [287] used a novel approach to bioprint osteochondral graft models by incorporating PLA MCs into hydrogels. The micron-sized particles with the high specific surface area were functionalized with human recombinant collagen type I and designed to promote cell attachment and proliferation. MSCs and MCs were suspended in a GelMA/gellan gum hydrogel supplemented with D-mannose and Irgacure 2959 and bioprinted by extrusion bioprinting. The constructs were evaluated for ALP activity and secretion of osteocalcin (OCN) and stained with alizarin red. The analysis showed that the cells differentiated and deposited a mineralized matrix. Gao et al. [288] used inkjet bioprinting to print hMSCs suspended in PEG-GelMA hydrogel supplemented with Irgacure 2959. PEG-hydrogel supplemented with Irgacure 2959 served as a control. As demonstrated by gene and protein expression analysis (RUNX2, SP7, DLX5, ALPL, Col1A1, IBSP, BGLAP, SPP1, Col10A1, MMP13, SOX9, Col2A1, ACAN) performed 21 days after printing, the addition of GelMA compared to the control promoted early differentiation of hMSCs to the osteogenic lineage. A recent study by Keriquel et al. [284] demonstrated the use of LAB in bone tissue regeneration by examining the effects of different cellular patterns on bone regeneration potential. Using LIFT, they *in situ* printed mesenchymal stromal cells suspended

in a nano-hydroxyapatite/collagen hydrogel on a calvaria defect model in mice, as illustrated in Figure 17.9. Two different patterns were printed, a ring and a disc, and the printed constructs were monitored for 42 days. μCT images were taken, and histological staining was performed to evaluate the bone regeneration rate. The results showed that bone regeneration was only marginal in a ring geometry observed at the periphery of the defect. In contrast, a substantial new bone formation well distributed over the defect was observed in the disc geometry. Cui et al. [195] present a proof-of-concept study for the production of a vascularized, hierarchical, biomimetic construct with multiphase properties. The authors used a hybrid bioprinting system consisting of SLA bioprinting and an FDM printer to produce vascularized biphasic bone constructs (Figure 17.9). SLA bioprinting was used for printing cell-laden GelMA hydrogel and FDM for printing PLA fibers. PLA scaffolds were coated with polydopamine on which BMP2 peptides were immobilized, representing the bone region in the biphasic construct. VEGF peptide-conjugated GelMA represented the vascular region. A co-encapsulation of hMSCs and HUVECs in the GelMA hydrogel was bioprinted by SLA bioprinting onto the PLA scaffold,

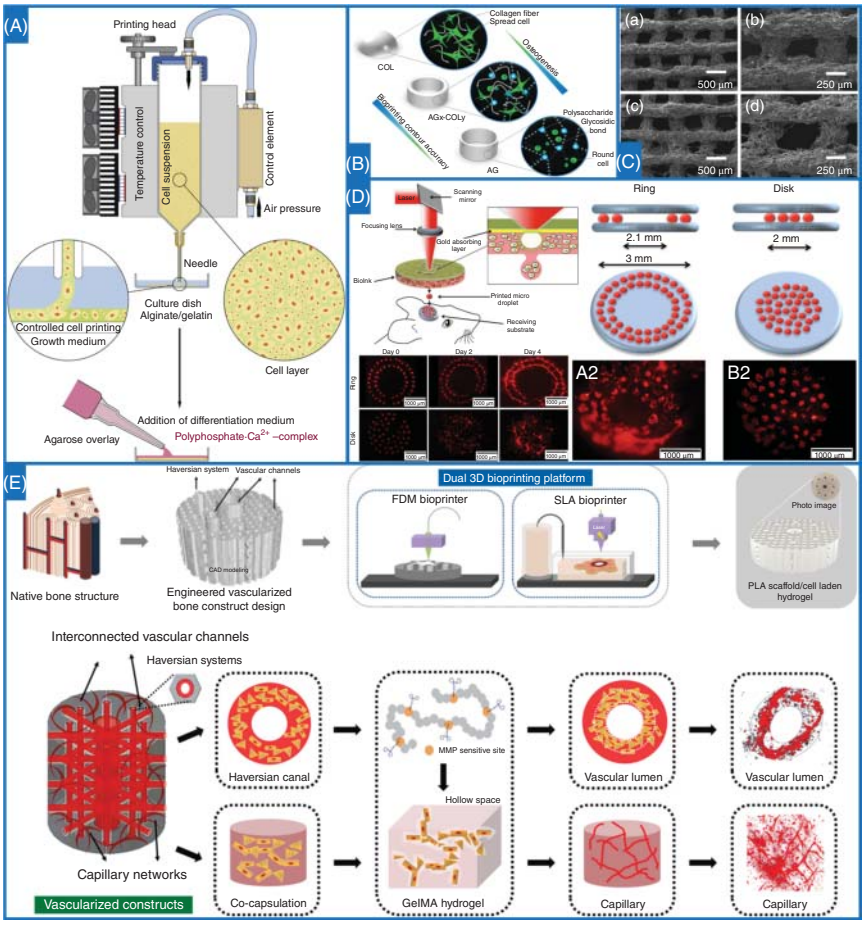

Figure 17.9 3D bioprinting of bone tissue. (A) Sketch of the process for 3D cell printing of scaffolds, which are then coated with an agarose overlay using the 3D-Bioplotter from Envisiontec. The SaOS-2 cells are encapsulated into alginate/gelatin. This cell suspension is filled into a cartridge. Using a control element connected to the computer-guided printing apparatus, the alginate/gelatin/SaOS-2 cells are fed through a needle into a $CaCl_2$ bath. This scaffold is immersed into McCoy's medium/FCS and overlayed with an agarose layer containing polyP·Ca^{2+} complex as a differentiation medium. Source: Neufurth et al. [281]/with permission of Elsevier. (B) Two-component combination for improved printability and cell response. Pure collagen hydrogels allow the cells to expand, but pure agarose hydrogels limit cell elongation. The combination of both components can potentially lead to an increased number of spread cells, which may ultimately contribute to improved osteogenesis *in vitro*. Source: Duarte Campos et al. [282]/with permission of John Wiley & Sons. (C) Scanning electron microscope images of composite silk/fibroin-based scaffolds without (top) or with (bottom) PRP treatment. Source: Wei et al. [283]/with permission of Elsevier. Reprinted (adapted), Dick Holland Regenerative Medicine Program. (D) Schematic representation of the laser-assisted bioprinting (LAB) approach (top left). Schematic representation of the tested *in vivo* LAB geometries, namely a ring and a disk with representative fluorescence images of ring-shaped and disk-shaped printed tomato-positive D1 cells on days 0, 2, and 4. Source: Keriquel et al. [284]/Springer Nature/CC BY 4.0. (E) Schematic representation of the biomimetic architectural design and hierarchical manufacturing process of a constructed vascularized biphasic bone construct using a dual 3D bioprinting platform. Schematic representation of the native bone structure, CAD modeling of the vascularized bone design, schematic of the FDM/SLA 3D biphasic bioprinting platform, and photo representation of the vascularized 3D bone construct (top). Schematic representation of the microstructural design of a vascularized construct based on a matrix metalloprotease-sensitive GelMA hydrogel. The development of vascular lumen and capillary network formation can be achieved in different regions during the culture period (bottom). Source: Cui et al. [195]/with permission of John Wiley & Sons.

which was preseeded with hMSCs. The osteogenic and angiogenic differentiation of the printed biphasic construct was evaluated four weeks after printing by ALP activity, collagen type I expression, determination of VEGF secretion, quantification of calcium deposition, and the differentiation markers osteopontin for osteogenic differentiation, von Willebrand factor as angiogenic-specific marker and CD31 for ECs representing capillary network formation.

17.6.4 Cartilage

Osteoarthritis, a degenerative joint disease characterized by progressive loss of hyaline cartilage in the synovial joints, affects millions of people worldwide [289]. Artificial TE cartilage is considered a potential alternative therapy because it promises to address many of the limitations of joint arthroplasty, which is currently the gold standard therapy for this disease. Cartilage is an avascular tissue with a small number of cells (10–15%), which explains its limited regenerative capacity. Due to its relative compositional simplicity, it was listed as one of the first tissues to be successfully artificially produced. However, current TE approaches do not allow the production of specific native cartilage tissues with different layers, structures, and components. With the advent of bioprinting, the inherent disadvantages of native cartilage tissue could soon be used as an advantage, as nonvascularized tissue with low cell density is comparatively easier to produce than vascularized highly

complex tissue [52]. Current bioprinting techniques allow the high-resolution fabrication of complex tissues, and together with an in-depth knowledge of the histological and anatomical structure of cartilage, it is possible to produce biomimetic cartilage tissue constructs that are very similar to native tissues.

The most commonly used hydrogels for cartilage bioprinting are alginate and collagen. However, it is difficult to maintain shape fidelity with these hydrogels. To improve shape fidelity, Rhee et al. [290] used a highly concentrated collagen hydrogel for bioprinting of meniscal fibro-chondrocytes. The higher the collagen concentration used, the higher was the shape fidelity. Recently, Nguyen et al. [291] reported on the use of NFC to improve the shape retention of hydrogels and to provide structural and mechanical support. The authors mixed NFC with sodium alginate to improve the shape fidelity of the alginate hydrogel. Although higher cell viability was observed at lower concentrations (60 wt%) of NFC, a higher concentration of NFC (80 wt%) resulted in a structurally more stable alginate-based scaffold. In addition, when the group incorporated iPSCs into two different hydrogels (alginate/NFC and HA/NFC hydrogel), the cells showed different pluripotency after printing. While pluripotency was maintained in the alginate/NFC hydrogel and hyaline-like cartilage tissue formed after five weeks, the cells in the HA/NFC gel underwent phenotypic changes away from pluripotency. It was also found that the incorporation of HA into bioinks upregulates the production of type II collagen and GAGs [292]. This shows that the choice of material for bioink plays an important role in the bioprinting of cells, as it influences the differentiation after printing. For example, Daly et al. [293] compared four different materials commonly used for bioprinting of cartilage, namely PEGMA, GelMA, alginate, and agarose. The results showed that PEGMA and GelMA scaffolds promote the development of fibrocartilage-like tissue, while alginate and agarose hydrogels promote the development of hyaline-like cartilage. Although both natural and synthetic biomaterials are used in 3D printing to fabricate cartilage tissue constructs, the use of natural and synthetic bioinks has its respective advantages and limitations [294]. Therefore, it would be fruitful to combine the positive effects of different natural and synthetic materials to create synergy with the hybrid cartilage scaffold. The synthetic polymers serve as a structural framework for improved mechanical properties, while the natural hydrogel serves as a carrier for cell encapsulation. Synthetic polymers such as PCL, polyglycolic acid (PGA), hydroxyapatite, and methacrylate have been successfully coupled with hydrogels to improve the mechanical properties [295]. Furthermore, studies have shown that cell viability and metabolism are significantly increased when hybrid scaffolds are used. Compared to pure PLGA scaffolds, hybrid PLGA constructs with cell-laden alginate have significantly higher GAG levels [296]. Similar studies with hybrid PLGA constructs with cell-laden gelatin showed that the cells retained their natural morphology after implantation [297].

Pore size also plays an important role in the regulation of cell activity and ECM secretion; cells grown in scaffolds with large pore sizes of up to 400 μm showed higher GAG secretion compared to scaffolds with smaller pore sizes (100–200 μm).

An optimal pore size of 200–500 μm increases chondrocyte activity and ECM production [298]. More recently, Castilho et al. [299] have developed microfiber-reinforced hydrogels that simultaneously support cartilage formation and capture the zonal depth-dependent mechanical properties of native cartilage. By combining PCL with a GelMA hydrogel, the authors developed a two-layer microfiber architecture (Figure 17.10). The first layer consisted of a densely distributed, crossed fiber mat, which improved the load-bearing properties of the construct, and the deep layer had a uniform box structure. The acellular composite structure showed a

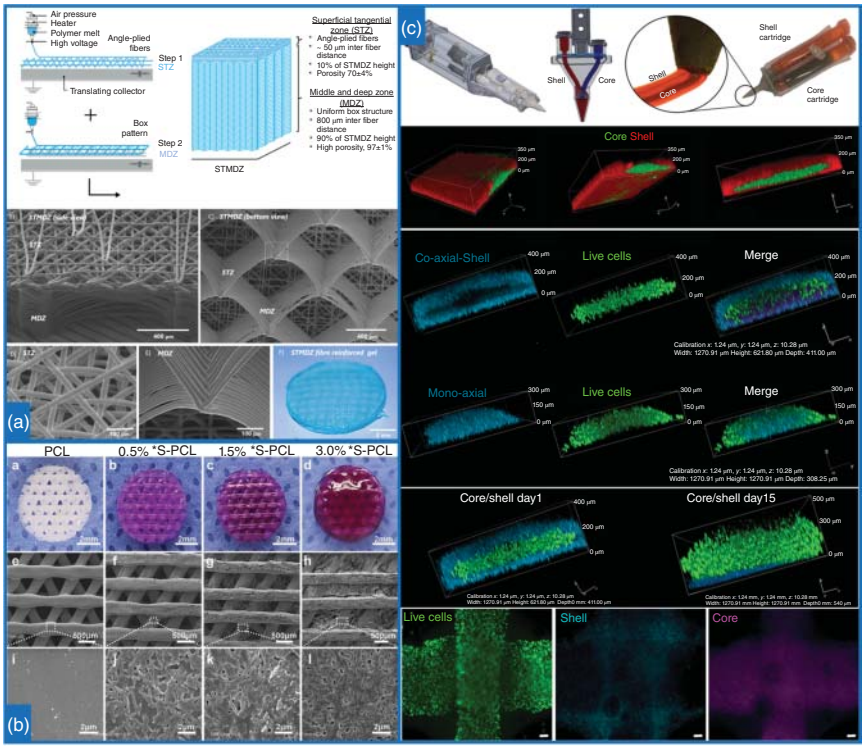

Figure 17.10 3D bioprinting of cartilage tissue. (a) Design and melt electrowriting of bilayered fiber-reinforced scaffolds with a superficial tangential zone (top). Images of bioprinted constructs (bottom). Source: Castilho et al. [299]/with permission of Elsevier. (b) The digital photographs and corresponding SEM images of 3D bioprinted PCL scaffolds and self-assembled peptide-hydrogel-coated PCL scaffolds. Source: Li et al. [300]/with permission of John Wiley & Sons. (c) Schematic view of the 3D coaxial handheld printer and the coaxial nozzle as well as representative 3D rendered confocal images of the core/shell printed sample labeled with fluorescent beads. The shell is shown in the red channel, while the core is shown in green (top). Representative 3D rendered confocal images show that coaxial printing produces 3D printed samples with high cell viability and that the design allows cell proliferation (middle). Representative epifluorescent images of Calcein-AM (green channel) stained cells after seven days after printing indicate that the core/shell print allows layered deposition of cell-laden hydrogels with structural integrity (bottom). Source: Duchi et al. [301]/John Wiley & Sons/CC BY 4.0.

stress relaxation response comparable to the tested native cartilage, and significant production of sulfated GAGs and collagen type II was observed when cultured with chondrocytes under mechanical conditioning. Since cartilage damage is often associated with subchondral bone injuries, it is important to design novel scaffolds that support both cartilage and subchondral bone regeneration. Li et al. [300] address this requirement by coating PCL scaffolds with a self-assembling peptide hydrogel to promote proliferation and osteogenic differentiation of MSCs and to preserve the chondrocyte phenotype. When implanted *in vivo*, these structures (Figure 17.10) induce the simultaneous regeneration of cartilage and subchondral bone. Extrusion bioprinting systems and their upgraded versions are most used for the production of cartilage tissue.

For example, Shim et al. [182] have successfully produced multilayer hybrid tissue constructs using two individual extrusion print heads (one for PCL/PLGA deposition and the second for hydrogel deposition). In contrast, Duchi et al. [301] presented a proof-of-concept study showing the potential of bioprinting for *in situ* cartilage repair. The authors reported on hand-held, coaxial, extrusion-based bioprinting (Figure 17.10) for *in situ* cartilage bioprinting, whereas a core–shell structure with an acellular, photocrosslinkable shell, and a cellular core was printed. The core consisted of adipose-derived stromal stem cells suspended in GelMA/hyaluronic acid methacryloyl (HAMa) hydrogel, and the shell consisted of GelMA/HAMa hydrogel with lithium-acylphosphinate as photoinitiator. The shell structure was later cross-linked with high-intensity UV light. The cell viability after printing was very high (>90%) after seven days. However, the study lacks a detailed biological characterization to assess the long-term effects of printing and UV irradiation. There are also other bioprinting approaches for cartilage bioprinting. For example, Cui et al. [302] used thermal inkjet bioprinting to create a 3D cartilage construct by suspending human chondrocytes in PEGDA hydrogel supplemented with Irgacure. The cells were viable and maintained the chondrogenic phenotype for up to six weeks after printing.

17.7 Concluding Remarks

The field of 3D bioprinting has developed rapidly over the last thirty years. This technology has demonstrated its remarkable potential, and researchers have already succeeded in producing tissue scaffolds that can mature into vascularized and functional tissues. Despite the progress in bioprinting systems, a central dilemma of bioprinting is the need to find a balance between the speed of production for human-scale tissue/organs and the resolution required to construct intricate capillary networks and accurately mimic the native ECM. In addition, the choice of bioinks, based mainly on their rheological properties and cross-linking mechanisms, is severely limited, mainly due to the required printing conditions. Another great challenge is also the production of sufficiently stable and mechanically rigid constructions suitable for transplantation. The recent development of dECM bioinks represents an important step toward the fabrication

of functional tissue scaffolds. Still, even the best dECM bioinks are not able to fully replicate the complex, highly specific spatial position of each individual cell, bioactive molecule, or ECM protein. Decellularized tissue scaffolds must serve as templates for analyzing the localization and composition of different ECM proteins/cells and improve our understanding of the native ECM. The comprehensive understanding of the spatial arrangement of cells and ECM building blocks within tissue constructs needs to be coupled with the development of advanced bioprinting strategies and polymers. A new generation of smart polymers that change their shape or other properties in response to external stimuli such as temperature, pH, or magnetic field must be used to create programmable tissue scaffolds. To achieve complete biomimicry within anatomically relevant tissue constructs, advanced hybrid multimaterial bioprinting approaches will also be required. New complementary strategies (e.g. the coupling of a bioprinter, a bioreactor, and a perfusion system into a single system) that ensure the maturation and assembly of the bioprinted tissue constructs into vascularized, functional tissues/organs that can potentially be used for transplantation need to be developed. In addition, advances in tissue culture techniques will be necessary to overcome the limitations of maturation of 3D bioprinted multicellular constructs into functional tissues. Only concurrent developments in 3D bioprinting technology, advances in polymer sciences, and tissue culture methods will make 3D bioprinting of tissues and organs suitable for transplantation an imminent reality.

Acknowledgments

This research was funded by Slovenian Research Agency for Research (grant numbers: P3-0036, J3-1762, and L4-1843, as well as the Young Researcher programme) and Ministry for Education, Science and Sport (grant number: Raziskovalci-2.1-UM-MF-952028).

References

1 Chua, C.K. and Yeong, W.Y. (2014). *Bioprinting: Principles and Applications*. World Scientific Publishing Co Inc.
2 Ventola, C.L. (2014). Medical applications for 3D printing: current and projected uses. *P & T* 39 (10): 704–711.
3 Abouna, G.M. (2008). Organ shortage crisis: problems and possible solutions. *Transplant. Proc.* 40 (1): 34–38.
4 Xia, Z., Jin, S., and Ye, K. (2018). Tissue and organ 3D bioprinting. *SLAS Technol.: Transl. Life Sci. Innovat.* 23 (4): 301–314.
5 Do, A.-V., Khorsand, B., Geary, S.M., and Salem, A.K. (2015). 3D Printing of scaffolds for tissue regeneration applications. *Adv. Healthc. Mater.* 4 (12): 1742–1762.

6 Liu, X., Meng, H., Guo, Q. et al. (2018). Tissue-derived scaffolds and cells for articular cartilage tissue engineering: characteristics, applications and progress. *Cell Tissue Res.* 372 (1): 13–22.

7 Chua, C.K. and Leong, K.F. (2014). *3D Printing and Additive Manufacturing: Principles and Applications (with Companion Media Pack) of Rapid Prototyping*, 4e. World Scientific Publishing Company.

8 Wüst, S., Müller, R., and Hofmann, S. (2011). Controlled positioning of cells in biomaterials-approaches towards 3D tissue printing. *J. Funct. Biomater.* 2 (3): 119–154.

9 Zhang, Y.S., Duchamp, M., Oklu, R. et al. (2016). Bioprinting the cancer microenvironment. *ACS Biomater. Sci. Eng.* 2 (10): 1710–1721.

10 Jang, J., Yi, H.-G., and Cho, D.-W. (2016). 3D Printed tissue models: present and future. *ACS Biomater. Sci. Eng.* 2 (10): 1722–1731.

11 Ozbolat, I.T. and Hospodiuk, M. (2016). Current advances and future perspectives in extrusion-based bioprinting. *Biomaterials* 76: 321–343.

12 O'Brien, C.M., Holmes, B., Faucett, S., and Zhang, L.G. (2015). Three-dimensional printing of nanomaterial scaffolds for complex tissue regeneration. *Tissue Eng. Part B Rev.* 21 (1): 103–114.

13 Derby, B. (2012). Printing and prototyping of tissues and scaffolds. *Science* 338 (6109): 921–926.

14 Vijayavenkataraman, S., Lu, W., and Fuh, J. (2016). 3D Bioprinting of skin: a state-of-the-art review on modelling, materials, and processes. *Biofabrication* 8 (3): 032001.

15 Cui, H., Nowicki, M., Fisher, J.P., and Zhang, L.G. (2017). 3D Bioprinting for organ regeneration. *Adv. Healthc. Mater.* 6 (1): https://doi.org/10.1002/adhm.201601118.

16 Dvir, T., Timko, B.P., Kohane, D.S., and Langer, R. (2011). Nanotechnological strategies for engineering complex tissues. *Nat. Nanotechnol.* 6 (1): 13–22.

17 Rengier, F., Mehndiratta, A., von Tengg-Kobligk, H. et al. (2010). 3D Printing based on imaging data: review of medical applications. *Int. J. Comput. Assist. Radiol. Surg.* 5 (4): 335–341.

18 Ozbolat, I.T. (2015). Bioprinting scale-up tissue and organ constructs for transplantation. *Trends Biotechnol.* 33 (7): 395–400.

19 Gao, B., Yang, Q., Zhao, X. et al. (2016). 4D Bioprinting for biomedical applications. *Trends Biotechnol.* 34 (9): 746–756.

20 Kruth, J.P. (1991). Material incress manufacturing by rapid prototyping techniques. *CIRP Ann.* 40 (2): 603–614.

21 Shafiee, A. and Atala, A. (2016). Printing technologies for medical applications. *Trends Mol. Med.* 22 (3): 254–265.

22 Deckard, C.R., Beaman, J.J., and Darrah, J.F. (1992). Method for selective laser sintering with layerwise cross-scanning. Google Patents US5155324A.

23 Hull, C.W. (1984). Apparatus for production of three-dimensional objects by stereolithography. United States Patent US4575330A, Appl., No. 638905, Filed.

24 Bose, S., Vahabzadeh, S., and Bandyopadhyay, A. (2013). Bone tissue engineering using 3D printing. *Mater. Today* 16 (12): 496–504.

25 Wilson, W.C. Jr. and Boland, T. (2003). Cell and organ printing 1: protein and cell printers. *Anat. Rec. A Discov. Mol. Cell. Evol. Biol.* 272 (2): 491–496.

26 Jose, R.R., Rodriguez, M.J., Dixon, T.A. et al. (2016). Evolution of bioinks and additive manufacturing technologies for 3D bioprinting. *ACS Biomater. Sci. Eng.* 2 (10): 1662–1678.

27 Food and Drug Administration (2016). Technical considerations for additive manufactured devices-draft guidance for industry and Food and Drug Administration staff, Rockville, MD.

28 Wu, C., Wang, B., Zhang, C. et al. (2017). Bioprinting: an assessment based on manufacturing readiness levels. *Crit. Rev. Biotechnol.* 37 (3): 333–354.

29 Peng, W., Datta, P., Ayan, B. et al. (2017). 3D Bioprinting for drug discovery and development in pharmaceutics. *Acta Biomater.* 57: 26–46.

30 Rodríguez-Salvador, M., Rio-Belver, R.M., and Garechana-Anacabe, G. (2017). Scientometric and patentometric analyses to determine the knowledge landscape in innovative technologies: the case of 3D bioprinting. *PLoS One* 12 (6): e0180375, 22.

31 Liaw, C.-Y. and Guvendiren, M. (2017). Current and emerging applications of 3D printing in medicine. *Biofabrication* 9 (2): 024102.

32 Choudhury, D., Anand, S., and Naing, M.W. (2018). The arrival of commercial bioprinters–towards 3D bioprinting revolution. *Int. J. Bioprint.* 4 (2): 139.

33 Murphy, S.V. and Atala, A. (2014). 3D bioprinting of tissues and organs. *Nat. Biotechnol.* 32 (8): 773.

34 Vijayavenkataraman, S., Lu, W.F., and Fuh, J.Y.H. (2016). 3D Bioprinting – an ethical, legal and social aspects (ELSA) framework. *Bioprinting* 1–2: 11–21.

35 Lee, J.M., Ng, W.L., and Yeong, W.Y. (2019). Resolution and shape in bioprinting: strategizing towards complex tissue and organ printing. *Appl. Phys. Rev.* 6 (1): 011307.

36 Vijayavenkataraman, S., Yan, W.-C., Lu, W.F. et al. (2018). 3D Bioprinting of tissues and organs for regenerative medicine. *Adv. Drug Deliv. Rev.* 132: 296–332.

37 Horn, T.J. and Harrysson, O.L.A. (2012). Overview of current additive manufacturing technologies and selected applications. *Sci. Prog.* 95 (3): 255–282.

38 Rezende, R.A., Kasyanov, V., Mironov, V., and da Silva, J.V.L. (2015). Organ printing as an information technology. *Procedia Eng.* 110: 151–158.

39 Feldkamp, L.A., Davis, L.C., and Kress, J.W. (1984). Practical cone-beam algorithm. *J. Opt. Soc. Am. A* 1 (6): 612–619.

40 Kriete, A., Breithecker, A., and Rau, W. (2001). 3D Imaging of lung tissue by confocal microscopy and micro-CT. In: *Proceedings of SPIE - The International Society for Optical Engineering* (ed. D.D. Duncan, P.C. Johnson, D.D. Duncan, et al.), 469–476. Society of Photo-Optical Instrumentation Engineers (SPIE).

41 Tuan, H.S. and Hutmacher, D.W. (2005). Application of micro CT and computation modeling in bone tissue engineering. *Comput.-Aided Des.* 37 (11): 1151–1161.

42 Pykett, I.L., Newhouse, J.H., Buonanno, F.S. et al. (1982). Principles of nuclear magnetic resonance imaging. *Radiology* 143 (1): 157–168.

43 Elliott, M.R. and Thrush, A.J. (1996). Measurement of resolution in intravascular ultrasound images. *Physiol. Meas.* 17 (4): 259–265.

44 Guillemot, F., Mironov, V., and Nakamura, M. (2010). Bioprinting is coming of age: report from the International Conference on Bioprinting and Biofabrication in Bordeaux (3B'09). *Biofabrication* 2 (1): 010201.

45 Zhang, X. and Zhang, Y. (2015). Tissue engineering applications of three-dimensional bioprinting. *Cell Biochem. Biophys.* 72 (3): 777–782.

46 Mironov, V., Kasyanov, V., and Markwald, R.R. (2011). Organ printing: from bioprinter to organ biofabrication line. *Curr. Opin. Biotechnol.* 22 (5): 667–673.

47 Mandrycky, C., Wang, Z., Kim, K., and Kim, D.-H. (2016). 3D Bioprinting for engineering complex tissues. *Biotechnol. Adv.* 34 (4): 422–434.

48 Xu, T., Zhao, W., Zhu, J.-M. et al. (2013). Complex heterogeneous tissue constructs containing multiple cell types prepared by inkjet printing technology. *Biomaterials* 34 (1): 130–139.

49 Shor, L., Güçeri, S., Chang, R. et al. (2009). Precision extruding deposition (PED) fabrication of polycaprolactone (PCL) scaffolds for bone tissue engineering. *Biofabrication* 1 (1): 015003.

50 Cohen, D.L., Malone, E., Lipson, H., and Bonassar, L.J. (2006). Direct freeform fabrication of seeded hydrogels in arbitrary geometries. *Tissue Eng.* 12 (5): 1325–1335.

51 Guillotin, B., Souquet, A., Catros, S. et al. (2010). Laser assisted bioprinting of engineered tissue with high cell density and microscale organization. *Biomaterials* 31 (28): 7250–7256.

52 Ng, W.L., Chua, C.K., and Shen, Y.-F. (2019). Print me an organ! Why we are not there yet. *Progr. Polym. Sci.* 97: 101145.

53 Huang, Y., Zhang, X.F., Gao, G. et al. (2017). 3D bioprinting and the current applications in tissue engineering. *Biotechnol. J.* 12 (8): 1600734.

54 Melchels, F.P.W., Feijen, J., and Grijpma, D.W. (2010). A review on stereolithography and its applications in biomedical engineering. *Biomaterials* 31 (24): 6121–6130.

55 Chan, B.P. and Leong, K.W. (2008). Scaffolding in tissue engineering: general approaches and tissue-specific considerations. *Eur. Spine J.* 17 (4): 467–479.

56 Guvendiren, M., Molde, J., Soares, R.M., and Kohn, J. (2016). Designing biomaterials for 3D printing. *ACS Biomater. Sci. Eng.* 2 (10): 1679–1693.

57 Lee, K.-S., Kim, R.H., Yang, D.-Y., and Park, S.H. (2008). Advances in 3D nano/microfabrication using two-photon initiated polymerization. *Prog. Polym. Sci.* 33 (6): 631–681.

58 Ovsianikov, A., Deiwick, A., Van Vlierberghe, S. et al. (2011). Laser fabrication of 3D gelatin scaffolds for the generation of bioartificial tissues. *Materials (Basel, Switzerland)* 4 (1): 288–299.

59 Curley, J.L., Jennings, S.R., and Moore, M.J. (2011). Fabrication of micropatterned hydrogels for neural culture systems using dynamic mask projection photolithography. *JoVE (J. Visual. Exp.)* 48: e2636.

60 Schöneberg, J., De Lorenzi, F., Theek, B. et al. (2018). Engineering biofunctional in vitro vessel models using a multilayer bioprinting technique. *Sci. Rep.* 8 (1): 10430.

61 Kim, S.H., Yeon, Y.K., Lee, J.M. et al. (2018). Precisely printable and biocompatible silk fibroin bioink for digital light processing 3D printing. *Nat. Commun.* 9 (1): 1620.

62 Stansbury, J.W. and Idacavage, M.J. (2016). 3D Printing with polymers: challenges among expanding options and opportunities. *Dent. Mater.* 32 (1): 54–64.

63 Tumbleston, J.R., Shirvanyants, D., Ermoshkin, N. et al. (2015). Continuous liquid interface production of 3D objects. *Science* 347 (6228): 1349–1352.

64 Chia, H.N. and Wu, B.M. (2015). Recent advances in 3D printing of biomaterials. *J. Biol. Eng.* 9: 4–4.

65 Arcaute, K., Mann, B.K., and Wicker, R.B. (2006). Stereolithography of three-dimensional bioactive poly(ethylene glycol) constructs with encapsulated cells. *Ann. Biomed. Eng.* 34 (9): 1429–1441.

66 Dhariwala, B., Hunt, E., and Boland, T. (2004). Rapid prototyping of tissue-engineering constructs, using photopolymerizable hydrogels and stereolithography. *Tissue Eng.* 10 (9–10): 1316–1322.

67 Grigoryan, B., Paulsen, S.J., Corbett, D.C. et al. (2019). Multivascular networks and functional intravascular topologies within biocompatible hydrogels. *Science* 364 (6439): 458–464.

68 Soman, P., Chung, P.H., Zhang, A.P., and Chen, S. (2013). Digital microfabrication of user-defined 3D microstructures in cell-laden hydrogels. *Biotechnol. Bioeng.* 110 (11): 3038–3047.

69 Tse, C.C.W. and Smith, P.J. (2018). Inkjet printing for biomedical applications. In: *Cell-Based Microarrays* (ed. J.M. Walker), 107–117. Clifton, N.J.: Humana Press.

70 Cui, X., Boland, T., D'Lima, D.D., and Lotz, M.K. (2012). Thermal inkjet printing in tissue engineering and regenerative medicine. *Recent Pat. Drug Deliv. Formul.* 6 (2): 149–155.

71 Ihalainen, P., Määttänen, A., and Sandler, N. (2015). Printing technologies for biomolecule and cell-based applications. *Int. J. Pharm.* 494 (2): 585–592.

72 Cui, X., Dean, D., Ruggeri, Z.M., and Boland, T. (2010). Cell damage evaluation of thermal inkjet printed Chinese hamster ovary cells. *Biotechnol. Bioeng.* 106 (6): 963–969.

73 Nakamura, M., Kobayashi, A., Takagi, F. et al. (2005). Biocompatible inkjet printing technique for designed seeding of individual living cells. *Tissue Eng.* 11 (11–12): 1658–1666.

74 Saunders, R.E., Gough, J.E., and Derby, B. (2008). Delivery of human fibroblast cells by piezoelectric drop-on-demand inkjet printing. *Biomaterials* 29 (2): 193–203.

75 Fang, Y., Frampton, J.P., Raghavan, S. et al. (2012). Rapid generation of multiplexed cell cocultures using acoustic droplet ejection followed by aqueous two-phase exclusion patterning. *Tissue Eng. Part C Methods* 18 (9): 647–657.

76 Pedde, R.D., Mirani, B., Navaei, A. et al. (2017). Emerging biofabrication strategies for engineering complex tissue constructs. *Adv. Mater.* 29 (19): 1606061.

77 Demirci, U. and Montesano, G. (2007). Single cell epitaxy by acoustic picolitre droplets. *Lab Chip* 7 (9): 1139–1145.

78 Sekitani, T., Noguchi, Y., Zschieschang, U. et al. (2008). Organic transistors manufactured using inkjet technology with subfemtoliter accuracy. *Proc. Natl. Acad. Sci. U.S.A.* 105 (13): 4976–4980.

79 Murphy, S.V., Skardal, A., and Atala, A. (2013). Evaluation of hydrogels for bio-printing applications. *J. Biomed. Mater. Res. A* 101 (1): 272–284.

80 Hennink, W.E. and van Nostrum, C.F. (2002). Novel crosslinking methods to design hydrogels. *Adv. Drug Deliv. Rev.* 54 (1): 13–36.

81 Saijo, H., Igawa, K., Kanno, Y. et al. (2009). Maxillofacial reconstruction using custom-made artificial bones fabricated by inkjet printing technology. *J. Artif. Organs* 12 (3): 200–205.

82 Xu, T., Binder, K.W., Albanna, M.Z. et al. (2012). Hybrid printing of mechanically and biologically improved constructs for cartilage tissue engineering applications. *Biofabrication* 5 (1): 015001.

83 Binder, K.W., Zhao, W., Aboushwareb, T. et al. (2010). In situ bioprinting of the skin for burns. *J. Am. Coll. Surg.* 211 (3): S76.

84 Xu, T., Baicu, C., Aho, M. et al. (2009). Fabrication and characterization of bio-engineered cardiac pseudo tissues. *Biofabrication* 1 (3): 035001.

85 Tse, C., Whiteley, R., Yu, T. et al. (2016). Inkjet printing Schwann cells and neuronal analogue NG108-15 cells. *Biofabrication* 8 (1): 015017.

86 Skardal, A., Mack, D., Kapetanovic, E. et al. (2012). Bioprinted amniotic fluid-derived stem cells accelerate healing of large skin wounds. *Stem Cells Transl. Med.* 1 (11): 792–802.

87 Cui, X., Breitenkamp, K., Finn, M.G. et al. (2012). Direct human cartilage repair using three-dimensional bioprinting technology. *Tissue Eng. Part A* 18 (11–12): 1304–1312.

88 Chrisey, D.B., Pique, A., Fitz-Gerald, J. et al. (2000). New approach to laser direct writing active and passive mesoscopic circuit elements. *Appl. Surf. Sci.* 154–155: 593–600.

89 Barron, J.A., Ringeisen, B.R., Kim, H. et al. (2004). Application of laser printing to mammalian cells. *Thin Solid Films* 453: 383–387.

90 Trombetta, R., Inzana, J.A., Schwarz, E.M. et al. (2017). 3D Printing of calcium phosphate ceramics for bone tissue engineering and drug delivery. *Ann. Biomed. Eng.* 45 (1): 23–44.

91 Hopp, B., Smausz, T., Kresz, N. et al. (2005). Survival and proliferative ability of various living cell types after laser-induced forward transfer. *Tissue Eng.* 11 (11–12): 1817–1823.

92 Guillemot, F., Souquet, A., Catros, S., and Guillotin, B. (2010). Laser-assisted cell printing: principle, physical parameters versus cell fate and perspectives in tissue engineering. *Nanomedicine* 5 (3): 507–515.

93 Dinca, V., Kasotakis, E., Catherine, J. et al. (2008). Directed three-dimensional patterning of self-assembled peptide fibrils. *Nano Lett.* 8 (2): 538–543.

94 Colina, M., Serra, P., Fernández-Pradas, J.M. et al. (2005). DNA deposition through laser induced forward transfer. *Biosens. Bioelectron.* 20 (8): 1638–1642.

95 Koch, L., Kuhn, S., Sorg, H. et al. (2009). Laser printing of skin cells and human stem cells. *Tissue Eng. Part C Methods* 16 (5): 847–854.

96 Wu, P.K., Ringeisen, B.R., Callahan, J. et al. (2001). The deposition, structure, pattern deposition, and activity of biomaterial thin-films by matrix-assisted pulsed-laser evaporation (MAPLE) and MAPLE direct write. *Thin Solid Films* 398–399: 607–614.

97 Wu, P.K. and Ringeisen, B.R. (2010). Development of human umbilical vein endothelial cell (HUVEC) and human umbilical vein smooth muscle cell (HUVSMC) branch/stem structures on hydrogel layers via biological laser printing (BioLP). *Biofabrication* 2 (1): 014111.

98 Lee, V., Singh, G., Trasatti, J.P. et al. (2013). Design and fabrication of human skin by three-dimensional bioprinting. *Tissue Eng. Part C Methods* 20 (6): 473–484.

99 Koch, L., Deiwick, A., Schlie, S. et al. (2012). Skin tissue generation by laser cell printing. *Biotechnol. Bioeng.* 109 (7): 1855–1863.

100 Sorkio, A., Koch, L., Koivusalo, L. et al. (2018). Human stem cell based corneal tissue mimicking structures using laser-assisted 3D bioprinting and functional bioinks. *Biomaterials* 171: 57–71.

101 Kérourédan, O., Bourget, J.-M., Rémy, M. et al. (2019). Micropatterning of endothelial cells to create a capillary-like network with defined architecture by laser-assisted bioprinting. *J. Mater. Sci. Mater. Med.* 30 (2): 28.

102 Kérourédan, O., Hakobyan, D., Rémy, M. et al. (2019). In situ prevascularization designed by laser-assisted bioprinting: effect on bone regeneration. *Biofabrication* 11 (4): 045002.

103 Guillotin, B. and Guillemot, F. (2011). Cell patterning technologies for organotypic tissue fabrication. *Trends Biotechnol.* 29 (4): 183–190.

104 Schiele, N.R., Corr, D.T., Huang, Y. et al. (2010). Laser-based direct-write techniques for cell printing. *Biofabrication* 2 (3): 032001.

105 Burks, H.E., Phamduy, T.B., Azimi, M.S. et al. (2016). Laser direct-write onto live tissues: a novel model for studying cancer cell migration. *J. Cell. Physiol.* 231 (11): 2333–2338.

106 Kim, J.H., Seol, Y.-J., Ko, I.K. et al. (2018). 3D bioprinted human skeletal muscle constructs for muscle function restoration. *Sci Rep* 8: 12307. https://doi.org/10.1038/s41598-018-29968-5.

107 Byambaa, B., Annabi, N., Yue, K. et al. (2017). Bioprinted osteogenic and vasculogenic patterns for engineering 3D bone tissue. *Adv. Healthc. Mater.* 6 (16): 1700015.

108 Duan, B. (2017). State-of-the-art review of 3D bioprinting for cardiovascular tissue engineering. *Ann. Biomed. Eng.* 45 (1): 195–209.

109 Billiet, T., Gevaert, E., De Schryver, T. et al. (2014). The 3D printing of gelatin methacrylamide cell-laden tissue-engineered constructs with high cell viability. *Biomaterials* 35 (1): 49–62.

110 Mouser, V.H., Levato, R., Bonassar, L.J. et al. (2017). Three-dimensional bioprinting and its potential in the field of articular cartilage regeneration. *Cartilage* 8 (4): 327–340.

111 Hsieh, F.-Y. and Hsu, S.-h. (2015). 3D Bioprinting: a new insight into the therapeutic strategy of neural tissue regeneration. *Organogenesis* 11 (4): 153–158.

112 Chang, R., Nam, J., and Sun, W. (2008). Direct cell writing of 3D microorgan for in vitro pharmacokinetic model. *Tissue Eng. Part C Methods* 14 (2): 157–166.

113 Xu, F., Celli, J., Rizvi, I. et al. (2011). A three-dimensional in vitro ovarian cancer coculture model using a high-throughput cell patterning platform. *Biotechnol. J.* 6 (2): 204–212.

114 Norotte, C., Marga, F.S., Niklason, L.E., and Forgacs, G. (2009). Scaffold-free vascular tissue engineering using bioprinting. *Biomaterials* 30 (30): 5910–5917.

115 Milojević, M., Vihar, B., Banović, L. et al. (2019). Core/shell printing scaffolds for tissue engineering of tubular structures. *JoVE (J. Visual. Exp.)* 151: e59951.

116 Khalil, S., Nam, J., and Sun, W. (2005). Multi-nozzle deposition for construction of 3D biopolymer tissue scaffolds. *Rapid Prototyp. J.* 11 (1): 9–17.

117 Panwar, A. and Tan, L.P. (2016). Current status of bioinks for micro-extrusion-based 3D bioprinting. *Molecules (Basel, Switzerland)* 21 (6): 685.

118 Jones, N. (2012). Science in three dimensions: the print revolution. *Nature* 487: 22–23.

119 Guvendiren, M., Lu, H.D., and Burdick, J.A. (2012). Shear-thinning hydrogels for biomedical applications. *Soft Matter* 8 (2): 260–272.

120 Smith, C.M., Christian, J.J., Warren, W.L., and Williams, S.K. (2007). Characterizing environmental factors that impact the viability of tissue-engineered constructs fabricated by a direct-write bioassembly tool. *Tissue Eng.* 13 (2): 373–383.

121 Schuurman, W., Levett, P.A., Pot, M.W. et al. (2013). Gelatin-methacrylamide hydrogels as potential biomaterials for fabrication of tissue-engineered cartilage constructs. *Macromol. Biosci.* 13 (5): 551–561.

122 Malda, J., Visser, J., Melchels, F.P. et al. (2013). 25th Anniversary article: engineering hydrogels for biofabrication. *Adv. Mater.* 25 (36): 5011–5028.

123 Duan, B., Hockaday, L.A., Kang, K.H., and Butcher, J.T. (2013). 3D Bioprinting of heterogeneous aortic valve conduits with alginate/gelatin hydrogels. *J. Biomed. Mater. Res. A* 101A (5): 1255–1264.

124 Langer, R. and Vacanti, J. (2016). Advances in tissue engineering. *J. Pediatr. Surg.* 51 (1): 8–12.

125 Hoch, E., Tovar, G.E., and Borchers, K. (2014). Bioprinting of artificial blood vessels: current approaches towards a demanding goal. *Eur. J. Cardio-Thorac. Surg.* 46 (5): 767–778.

126 Yeo, M., Lee, J.S., Chun, W., and Kim, G.H. (2016). An innovative collagen-based cell-printing method for obtaining human adipose stem cell-laden structures consisting of core-sheath structures for tissue engineering. *Biomacromolecules* 17 (4): 1365–1375.

127 Liu, W., Zhong, Z., Hu, N. et al. (2018). Coaxial extrusion bioprinting of 3D microfibrous constructs with cell-favorable gelatin methacryloyl microenvironments. *Biofabrication* 10 (2): 024102.

128 Gao, Q., He, Y., Fu, J.Z. et al. (2015). Coaxial nozzle-assisted 3D bioprinting with built-in microchannels for nutrients delivery. *Biomaterials* 61: 203–215.

129 Akkineni, A.R., Ahlfeld, T., Lode, A., and Gelinsky, M. (2016). A versatile method for combining different biopolymers in a core/shell fashion by 3D plotting to achieve mechanically robust constructs. *Biofabrication* 8 (4): 045001.

130 Colosi, C., Shin, S.R., Manoharan, V. et al. (2016). Microfluidic bioprinting of heterogeneous 3D tissue constructs using low-viscosity bioink. *Adv. Mater. (Deerfield Beach, Fla.)* 28 (4): 677–684.

131 Kim, G., Ahn, S., Kim, Y. et al. (2011). Coaxial structured collagen–alginate scaffolds: fabrication, physical properties, and biomedical application for skin tissue regeneration. *J. Mater. Chem.* 21 (17): 6165–6172.

132 Luo, Y., Lode, A., and Gelinsky, M. (2013). Direct plotting of three-dimensional hollow fiber scaffolds based on concentrated alginate pastes for tissue engineering. *Adv. Healthc. Mater.* 2 (6): 777–783.

133 Mistry, P., Aied, A., Alexander, M. et al. (2017). Bioprinting using mechanically robust core-shell cell-laden hydrogel strands. *Macromol. Biosci.* 17 (6).

134 Attalla, R., Puersten, E., Jain, N., and Selvaganapathy, P.R. (2018). 3D Bioprinting of heterogeneous bi- and tri-layered hollow channels within gel scaffolds using scalable multi-axial microfluidic extrusion nozzle. *Biofabrication* 11 (1): 015012.

135 Kang, H.-W., Lee, S.J., Ko, I.K. et al. (2016). A 3D bioprinting system to produce human-scale tissue constructs with structural integrity. *Nat. Biotechnol.* 34 (3): 312–319.

136 Kim, B.S., Lee, J.-S., Gao, G., and Cho, D.-W. (2017). Direct 3D cell-printing of human skin with functional transwell system. *Biofabrication* 9 (2): 025034.

137 Lee, J.-S., Hong, J.M., Jung, J.W. et al. (2014). 3D Printing of composite tissue with complex shape applied to ear regeneration. *Biofabrication* 6 (2): 024103.

138 Fedorovich, N.E., De Wijn, J.R., Verbout, A.J. et al. (2008). Three-dimensional fiber deposition of cell-laden, viable, patterned constructs for bone tissue printing. *Tissue Eng. Part A* 14 (1): 127–133.

139 Sydney Gladman, A., Matsumoto, E.A., Nuzzo, R.G. et al. (2016). Biomimetic 4D printing. *Nat. Mater.* 15 (4): 413–418.

140 Ramos, T. and Moroni, L. (2019). Tissue engineering and regenerative medicine 2019: the role of biofabrication—a year in review. *Tissue Eng. Part C Methods* 26 (2): 91–106.

141 Ionov, L. (2018). 4D Biofabrication: materials, methods, and applications. *Adv. Healthc. Mater.* 7 (17): 1800412.

142 Parameswaran-Thankam, A., Parnell, C.M., Watanabe, F. et al. (2018). Guar-based injectable thermoresponsive hydrogel as a scaffold for bone cell growth and controlled drug delivery. *ACS Omega* 3 (11): 15158–15167.

143 Zhao, C., Zeng, Z., Qazvini, N.T. et al. (2018). Thermoresponsive citrate-based graphene oxide scaffold enhances bone regeneration from BMP9-stimulated

adipose-derived mesenchymal stem cells. *ACS Biomater. Sci. Eng.* 4 (8): 2943–2955.

144 Betsch, M., Cristian, C., Lin, Y.-Y. et al. (2018). Incorporating 4D into bioprinting: real-time magnetically directed collagen fiber alignment for generating complex multilayered tissues. *Adv. Healthc. Mater.* 7 (21): 1800894.

145 Miao, S., Cui, H., Nowicki, M. et al. (2018). Stereolithographic 4D bioprinting of multiresponsive architectures for neural engineering. *Adv. Biosyst.* 2 (9): 1800101.

146 Zhang, L., Zuo, X., Li, S. et al. (2019). Synergistic therapy of magnetism-responsive hydrogel for soft tissue injuries. *Bioact. Mater.* 4: 160–166.

147 Miao, S., Cui, H., Nowicki, M. et al. (2018). Photolithographic-stereolithographic-tandem fabrication of 4D smart scaffolds for improved stem cell cardiomyogenic differentiation. *Biofabrication* 10 (3): 035007.

148 Miao, S., Nowicki, M., Cui, H. et al. (2019). 4D Anisotropic skeletal muscle tissue constructs fabricated by staircase effect strategy. *Biofabrication* 11 (3): 035030.

149 Groll, J., Burdick, J., Cho, D. et al. (2018). A definition of bioinks and their distinction from biomaterial inks. *Biofabrication* 11 (1): 013001.

150 Boffito, M., Sartori, S., and Ciardelli, G. (2014). Polymeric scaffolds for cardiac tissue engineering: requirements and fabrication technologies. *Polym. Int.* 63 (1): 2–11.

151 Vedadghavami, A., Minooei, F., Mohammadi, M.H. et al. (2017). Manufacturing of hydrogel biomaterials with controlled mechanical properties for tissue engineering applications. *Acta Biomater.* 62: 42–63.

152 Seliktar, D. (2012). Designing cell-compatible hydrogels for biomedical applications. *Science* 336 (6085): 1124–1128.

153 Buwalda, S.J., Boere, K.W.M., Dijkstra, P.J. et al. (2014). Hydrogels in a historical perspective: from simple networks to smart materials. *J. Control. Release* 190: 254–273.

154 Billiet, T., Vandenhaute, M., Schelfhout, J. et al. (2012). A review of trends and limitations in hydrogel-rapid prototyping for tissue engineering. *Biomaterials* 33 (26): 6020–6041.

155 Karoyo, A.H. and Wilson, L.D. (2017). Physicochemical properties and the gelation process of supramolecular hydrogels: a review. *Gels* 3 (1): 1.

156 Melchels, F.P., Domingos, M.A., Klein, T.J. et al. (2012). Additive manufacturing of tissues and organs. *Prog. Polym. Sci.* 37 (8): 1079–1104.

157 Moroni, L., Burdick, J.A., Highley, C. et al. (2018). Biofabrication strategies for 3D in vitro models and regenerative medicine. *Nat. Rev. Mater.* 3 (5): 21–37.

158 Chen, M., Le, D.Q.S., Baatrup, A. et al. (2011). Self-assembled composite matrix in a hierarchical 3-D scaffold for bone tissue engineering. *Acta Biomater.* 7 (5): 2244–2255.

159 Verhulsel, M., Vignes, M., Descroix, S. et al. (2014). A review of microfabrication and hydrogel engineering for micro-organs on chips. *Biomaterials* 35 (6): 1816–1832.

160 Lee, K.Y. and Mooney, D.J. (2012). Alginate: properties and biomedical applications. *Prog. Polym. Sci.* 37 (1): 106–126.

161 Zehnder, T., Sarker, B., Boccaccini, A.R., and Detsch, R. (2015). Evaluation of an alginate–gelatine crosslinked hydrogel for bioplotting. *Biofabrication* 7 (2): 025001.

162 Chung, J.H., Naficy, S., Yue, Z. et al. (2013). Bio-ink properties and printability for extrusion printing living cells. *Biomater. Sci.* 1 (7): 763–773.

163 Jia, J., Richards, D.J., Pollard, S. et al. (2014). Engineering alginate as bioink for bioprinting. *Acta Biomater.* 10 (10): 4323–4331.

164 Diekjürgen, D. and Grainger, D.W. (2017). Polysaccharide matrices used in 3D in vitro cell culture systems. *Biomaterials* 141: 96–115.

165 Hausmann, M.K., Siqueira, G., Libanori, R. et al. (2020). Complex-shaped cellulose composites made by wet densification of 3D printed scaffolds. *Adv. Funct. Mater.* 30 (4): 1904127.

166 Laronda, M.M., Rutz, A.L., Xiao, S. et al. (2017). A bioprosthetic ovary created using 3D printed microporous scaffolds restores ovarian function in sterilized mice. *Nat. Commun.* 8 (1): 15261.

167 Irvine, S.A., Agrawal, A., Lee, B.H. et al. (2015). Printing cell-laden gelatin constructs by free-form fabrication and enzymatic protein crosslinking. *Biomed. Microdevices* 17 (1): 16–16.

168 Inzana, J.A., Olvera, D., Fuller, S.M. et al. (2014). 3D printing of composite calcium phosphate and collagen scaffolds for bone regeneration. *Biomaterials* 35 (13): 4026–4034.

169 Pescosolido, L., Schuurman, W., Malda, J. et al. (2011). Hyaluronic acid and dextran-based semi-IPN hydrogels as biomaterials for bioprinting. *Biomacromolecules* 12 (5): 1831–1838.

170 Poldervaart, M.T., Goversen, B., De Ruijter, M. et al. (2017). 3D Bioprinting of methacrylated hyaluronic acid (MeHA) hydrogel with intrinsic osteogenicity. *PLoS One* 12 (6): e0177628, 15.

171 Wang, W., Jin, S., and Ye, K. (2016). Development of islet organoids from H9 human embryonic stem cells in biomimetic 3D scaffolds. *Stem Cells Dev.* 26 (6): 394–404.

172 Ng, W.L., Goh, M.H., Yeong, W.Y., and Naing, M.W. (2018). Applying macromolecular crowding to 3D bioprinting: fabrication of 3D hierarchical porous collagen-based hydrogel constructs. *Biomater. Sci.* 6 (3): 562–574.

173 Hoch, E., Hirth, T., Tovar, G.E., and Borchers, K. (2013). Chemical tailoring of gelatin to adjust its chemical and physical properties for functional bioprinting. *J. Mater. Chem. B* 1 (41): 5675–5685.

174 Janmey, P.A., Winer, J.P., and Weisel, J.W. (2009). Fibrin gels and their clinical and bioengineering applications. *J. R. Soc. Interface* 6 (30): 1–10.

175 Lee, Y.-B., Polio, S., Lee, W. et al. (2010). Bio-printing of collagen and VEGF-releasing fibrin gel scaffolds for neural stem cell culture. *Exp. Neurol.* 223 (2): 645–652.

176 Homan, K.A., Kolesky, D.B., Skylar-Scott, M.A. et al. (2016). Bioprinting of 3D convoluted renal proximal tubules on perfusable chips. *Sci. Rep.* 6 (1): 34845.

177 Kolesky, D.B., Homan, K.A., Skylar-Scott, M.A., and Lewis, J.A. (2016). Three-dimensional bioprinting of thick vascularized tissues. *Proc. Natl. Acad. Sci. U.S.A.* 113 (12): 3179–3184.

178 Sun, L., Parker, S.T., Syoji, D. et al. (2012). Direct-write assembly of 3D silk/hydroxyapatite scaffolds for bone co-cultures. *Adv. Healthc. Mater.* 1 (6): 729–735.

179 Serrano, M.C., Pagani, R., Vallet-Regí, M. et al. (2004). In vitro biocompatibility assessment of poly(ε-caprolactone) films using L929 mouse fibroblasts. *Biomaterials* 25 (25): 5603–5611.

180 Shim, J.-H., Lee, J.-S., Kim, J.Y., and Cho, D.-W. (2012). Bioprinting of a mechanically enhanced three-dimensional dual cell-laden construct for osteochondral tissue engineering using a multi-head tissue/organ building system. *J. Micromech. Microeng.* 22 (8): 085014.

181 Boere, K.W.M., Visser, J., Seyednejad, H. et al. (2014). Covalent attachment of a three-dimensionally printed thermoplast to a gelatin hydrogel for mechanically enhanced cartilage constructs. *Acta Biomater.* 10 (6): 2602–2611.

182 Shim, J.-H., Kim, J.Y., Park, M. et al. (2011). Development of a hybrid scaffold with synthetic biomaterials and hydrogel using solid freeform fabrication technology. *Biofabrication* 3 (3): 034102.

183 Griffith, L.G. and Swartz, M.A. (2006). Capturing complex 3D tissue physiology in vitro. *Nat. Rev. Mol. Cell Biol.* 7 (3): 211–224.

184 Williams, D.F. (2008). On the mechanisms of biocompatibility. *Biomaterials* 29 (20): 2941–2953.

185 Roh, S., Parekh, D.P., Bharti, B. et al. (2017). 3D Printing by multiphase silicone/water capillary inks. *Adv. Mater.* 29 (30): 1701554.

186 Ouyang, L., Highley, C.B., Sun, W., and Burdick, J.A. (2017). A generalizable strategy for the 3D bioprinting of hydrogels from nonviscous photo-crosslinkable inks. *Adv. Mater.* 29 (8): 1604983.

187 Murphy, W.L., McDevitt, T.C., and Engler, A.J. (2014). Materials as stem cell regulators. *Nat. Mater.* 13 (6): 547–557.

188 Mitchell, A.C., Briquez, P.S., Hubbell, J.A., and Cochran, J.R. (2016). Engineering growth factors for regenerative medicine applications. *Acta Biomater.* 30: 1–12.

189 Park, J.Y., Shim, J.-H., Choi, S.-A. et al. (2015). 3D Printing technology to control BMP-2 and VEGF delivery spatially and temporally to promote large-volume bone regeneration. *J. Mater. Chem. B* 3 (27): 5415–5425.

190 Tarafder, S., Koch, A., Jun, Y. et al. (2016). Micro-precise spatiotemporal delivery system embedded in 3D printing for complex tissue regeneration. *Biofabrication* 8 (2): 025003.

191 Poldervaart, M.T., Gremmels, H., van Deventer, K. et al. (2014). Prolonged presence of VEGF promotes vascularization in 3D bioprinted scaffolds with defined architecture. *J. Control. Release* 184: 58–66.

192 Hersel, U., Dahmen, C., and Kessler, H. (2003). RGD modified polymers: biomaterials for stimulated cell adhesion and beyond. *Biomaterials* 24 (24): 4385–4415.

193 Lee, S.J., Lee, D., Yoon, T.R. et al. (2016). Surface modification of 3D-printed porous scaffolds via mussel-inspired polydopamine and effective immobilization of rhBMP-2 to promote osteogenic differentiation for bone tissue engineering. *Acta Biomater.* 40: 182–191.

194 Holmes, B., Zhu, W., Li, J. et al. (2015). Development of novel three-dimensional printed scaffolds for osteochondral regeneration. *Tissue Eng. Part A* 21 (1–2): 403–415.

195 Cui, H., Zhu, W., Nowicki, M. et al. (2016). Hierarchical fabrication of engineered vascularized bone biphasic constructs via dual 3D bioprinting: integrating regional bioactive factors into architectural design. *Adv. Healthc. Mater.* 5 (17): 2174–2181.

196 Samorezov, J.E. and Alsberg, E. (2015). Spatial regulation of controlled bioactive factor delivery for bone tissue engineering. *Adv. Drug Deliv. Rev.* 84: 45–67.

197 Gbureck, U., Hölzel, T., Doillon, C.J. et al. (2007). Direct printing of bioceramic implants with spatially localized angiogenic factors. *Adv. Mater.* 19 (6): 795–800.

198 Ilkhanizadeh, S., Teixeira, A.I., and Hermanson, O. (2007). Inkjet printing of macromolecules on hydrogels to steer neural stem cell differentiation. *Biomaterials* 28 (27): 3936–3943.

199 Liu, W., Zhang, Y.S., Heinrich, M.A. et al. (2017). Rapid continuous multimaterial extrusion bioprinting. *Adv. Mater. (Deerfield Beach, Fla.)* 29 (3): https://doi.org/10.1002/adma.201604630.

200 Pati, F., Jang, J., Ha, D.-H. et al. (2014). Printing three-dimensional tissue analogues with decellularized extracellular matrix bioink. *Nat. Commun.* 5: 3935–3935.

201 Ji, S., Almeida, E., and Guvendiren, M. (2019). 3D bioprinting of complex channels within cell-laden hydrogels. *Acta Biomater.* 95: 214–224.

202 Karp, J.M., Yeh, J., Eng, G. et al. (2007). Controlling size, shape and homogeneity of embryoid bodies using poly(ethylene glycol) microwells. *Lab Chip* 7 (6): 786–794.

203 Discher, D.E., Janmey, P., and Wang, Y.-l. (2005). Tissue cells feel and respond to the stiffness of their substrate. *Science* 310 (5751): 1139–1143.

204 Teixeira, A.I., Nealey, P.F., and Murphy, C.J. (2004). Responses of human keratocytes to micro- and nanostructured substrates. *J. Biomed. Mater. Res. A* 71A (3): 369–376.

205 Zhang, K., Fan, Y., Dunne, N., and Li, X. (2018). Effect of microporosity on scaffolds for bone tissue engineering. *Regenerat. Biomater.* 5 (2): 115–124.

206 Ghasemi-Mobarakeh, L., Prabhakaran, M.P., Tian, L. et al. (2015). Structural properties of scaffolds: crucial parameters towards stem cells differentiation. *World J. Stem Cells* 7 (4): 728.

207 Milojević, M., Gradišnik, L., Stergar, J. et al. (2019). Development of multifunctional 3D printed bioscaffolds from polysaccharides and NiCu nanoparticles and their application. *Appl. Surf. Sci.* 488: 836–852.

208 Baptista, P.M., Orlando, G., Mirmalek-Sani, S.-H. et al. (2009). Whole organ decellularization-a tool for bioscaffold fabrication and organ bioengineering.

2009 Annual International Conference of the IEEE Engineering in Medicine and Biology Society, IEEE, 2009, pp. 6526–6529.

209 Gilbert, T.W., Sellaro, T.L., and Badylak, S.F. (2006). Decellularization of tissues and organs. *Biomaterials* 27 (19): 3675–3683.

210 Badylak, S.F., Freytes, D.O., and Gilbert, T.W. (2009). Extracellular matrix as a biological scaffold material: structure and function. *Acta Biomater.* 5 (1): 1–13.

211 Pati, F., Ha, D.-H., Jang, J. et al. (2015). Biomimetic 3D tissue printing for soft tissue regeneration. *Biomaterials* 62: 164–175.

212 Jang, J., Park, H.-J., Kim, S.-W. et al. (2017). 3D Printed complex tissue construct using stem cell-laden decellularized extracellular matrix bioinks for cardiac repair. *Biomaterials* 112: 264–274.

213 Gao, G., Lee, J.H., Jang, J. et al. (2017). Tissue engineered bio-blood-vessels constructed using a tissue-specific bioink and 3D coaxial cell printing technique: a novel therapy for ischemic disease. *Adv. Funct. Mater.* 27 (33): 1700798.

214 Kim, H., Park, M.-N., Kim, J. et al. (2019). Characterization of cornea-specific bioink: high transparency, improved in vivo safety. *J. Tissue Eng.* 10: https://doi.org/10.1177/2041731418823382.

215 Lee, H., Han, W., Kim, H. et al. (2017). Development of liver decellularized extracellular matrix bioink for three-dimensional cell printing-based liver tissue engineering. *Biomacromolecules* 18 (4): 1229–1237.

216 Choi, Y.-J., Kim, T.G., Jeong, J. et al. (2016). 3D Cell printing of functional skeletal muscle constructs using skeletal muscle-derived bioink. *Adv. Healthc. Mater.* 5 (20): 2636–2645.

217 Kim, J., Shim, I.K., Hwang, D.G. et al. (2019). 3D Cell printing of islet-laden pancreatic tissue-derived extracellular matrix bioink constructs for enhancing pancreatic functions. *J. Mater. Chem. B* 7 (10): 1773–1781.

218 Kim, B.S., Kwon, Y.W., Kong, J.-S. et al. (2018). 3D Cell printing of in vitro stabilized skin model and in vivo pre-vascularized skin patch using tissue-specific extracellular matrix bioink: a step towards advanced skin tissue engineering. *Biomaterials* 168: 38–53.

219 Athirasala, A., Tahayeri, A., Thrivikraman, G. et al. (2018). A dentin-derived hydrogel bioink for 3D bioprinting of cell laden scaffolds for regenerative dentistry. *Biofabrication* 10 (2): 024101.

220 Toprakhisar, B., Nadernezhad, A., Bakirci, E. et al. (2018). Development of bioink from decellularized tendon extracellular matrix for 3D bioprinting. *Macromol. Biosci.* 18 (10): 1800024.

221 Sullivan, D.C., Mirmalek-Sani, S.-H., Deegan, D.B. et al. (2012). Decellularization methods of porcine kidneys for whole organ engineering using a high-throughput system. *Biomaterials* 33 (31): 7756–7764.

222 Rizzo, D.C. (2015). *Fundamentals of Anatomy and Physiology*. Cengage Learning.

223 Ghoorchian, A., Simon, J.R., Bharti, B. et al. (2015). Bioinspired reversibly cross-linked hydrogels comprising polypeptide micelles exhibit enhanced mechanical properties. *Adv. Funct. Mater.* 25 (21): 3122–3130.

224 Hennink, W.E. and van Nostrum, C.F. (2012). Novel crosslinking methods to design hydrogels. *Adv. Drug Deliv. Rev.* 64: 223–236.

225 Hölzl, K., Lin, S., Tytgat, L. et al. (2016). Bioink properties before, during and after 3D bioprinting. *Biofabrication* 8 (3): 032002.

226 Rodriguez, M.J., Brown, J., Giordano, J. et al. (2017). Silk based bioinks for soft tissue reconstruction using 3-dimensional (3D) printing with in vitro and in vivo assessments. *Biomaterials* 117: 105–115.

227 Suntornnond, R., An, J., and Chua, C.K. (2017). Suntornnond, R., An, J., & Chua, C. K. (2017). Roles of support materials in 3D bioprinting - Present and future. *Int. J. Bioprinting*, 3(1), 006. https://doi.org/10.18063/IJB.2017.01.006.

228 Miller, J.S., Stevens, K.R., Yang, M.T. et al. (2012). Rapid casting of patterned vascular networks for perfusable engineered three-dimensional tissues. *Nat. Mater.* 11 (9): 768–774.

229 Hinton, T.J., Jallerat, Q., Palchesko, R.N. et al. (2015). Three-dimensional printing of complex biological structures by freeform reversible embedding of suspended hydrogels. *Sci. Adv.* 1 (9): e1500758.

230 Štumberger, G. and Vihar, B. (2018). Freeform perfusable microfluidics embedded in hydrogel matrices. *Materials* 11 (12): 2529.

231 Jin, Y., Liu, C., Chai, W. et al. (2017). Self-supporting nanoclay as internal scaffold material for direct printing of soft hydrogel composite structures in air. *ACS Appl. Mater. Interfaces* 9 (20): 17456–17465.

232 Hutmacher, D.W. (2000). Scaffolds in tissue engineering bone and cartilage. *Biomaterials* 21 (24): 2529–2543.

233 Oyen, M.L. (2014). Mechanical characterisation of hydrogel materials. *Int. Mater. Rev.* 59 (1): 44–59.

234 Tibbitt, M.W. and Anseth, K.S. (2009). Hydrogels as extracellular matrix mimics for 3D cell culture. *Biotechnol. Bioeng.* 103 (4): 655–663.

235 Loessner, D., Stok, K.S., Lutolf, M.P. et al. (2010). Bioengineered 3D platform to explore cell-ECM interactions and drug resistance of epithelial ovarian cancer cells. *Biomaterials* 31 (32): 8494–8506.

236 Engler, A.J., Sen, S., Sweeney, H.L., and Discher, D.E. (2006). Matrix elasticity directs stem cell lineage specification. *Cell* 126 (4): 677–689.

237 Ghosh, K., Pan, Z., Guan, E. et al. (2007). Cell adaptation to a physiologically relevant ECM mimic with different viscoelastic properties. *Biomaterials* 28 (4): 671–679.

238 Hadjipanayi, E., Mudera, V., and Brown, R.A. (2009). Guiding cell migration in 3D: a collagen matrix with graded directional stiffness. *Cell Motil.* 66 (3): 121–128.

239 Di Luca, A., Longoni, A., Criscenti, G. et al. (2016). Surface energy and stiffness discrete gradients in additive manufactured scaffolds for osteochondral regeneration. *Biofabrication* 8 (1): 015014.

240 Place, E.S., Evans, N.D., and Stevens, M.M. (2009). Complexity in biomaterials for tissue engineering. *Nat. Mater.* 8 (6): 457–470.

241 Cox, S.C., Thornby, J.A., Gibbons, G.J. et al. (2015). 3D Printing of porous hydroxyapatite scaffolds intended for use in bone tissue engineering applications. *Mater. Sci. Eng. C* 47: 237–247.

242 Ameer, J.M., Pr, A.K., and Kasoju, N. (2019). Strategies to tune electrospun scaffold porosity for effective cell response in tissue engineering. *J. Funct. Biomater.* 10 (3): 30.

243 Loh, Q.L. and Choong, C. (2013). Three-dimensional scaffolds for tissue engineering applications: role of porosity and pore size. *Tissue Eng. Part B Rev.* 19 (6): 485–502.

244 Hutmacher, D.W., Sittinger, M., and Risbud, M.V. (2004). Scaffold-based tissue engineering: rationale for computer-aided design and solid free-form fabrication systems. *Trends Biotechnol.* 22 (7): 354–362.

245 Melchels, F.P.W., Barradas, A.M.C., van Blitterswijk, C.A. et al. (2010). Effects of the architecture of tissue engineering scaffolds on cell seeding and culturing. *Acta Biomater.* 6 (11): 4208–4217.

246 Singh, M., Berkland, C., and Detamore, M.S. (2008). Strategies and applications for incorporating physical and chemical signal gradients in tissue engineering. *Tissue Eng. Part B Rev.* 14 (4): 341–366.

247 Yang, S., Dennehy, C.E., and Tsourounis, C. (2002). Characterizing adverse events reported to the california poison control system on herbal remedies and dietary supplements. *J. Herb. Pharmacother.* 2 (3): 1–11.

248 Trachtenberg, J.E., Mountziaris, P.M., Miller, J.S. et al. (2014). Open-source three-dimensional printing of biodegradable polymer scaffolds for tissue engineering. *J. Biomed. Mater. Res. A* 102 (12): 4326–4335.

249 Trachtenberg, J.E., Placone, J.K., Smith, B.T. et al. (2016). Extrusion-based 3D printing of poly(propylene fumarate) in a full-factorial design. *ACS Biomater. Sci. Eng.* 2 (10): 1771–1780.

250 Moroni, L., de Wijn, J.R., and van Blitterswijk, C.A. (2006). 3D Fiber-deposited scaffolds for tissue engineering: influence of pores geometry and architecture on dynamic mechanical properties. *Biomaterials* 27 (7): 974–985.

251 Sobral, J.M., Caridade, S.G., Sousa, R.A. et al. (2011). Three-dimensional plotted scaffolds with controlled pore size gradients: effect of scaffold geometry on mechanical performance and cell seeding efficiency. *Acta Biomater.* 7 (3): 1009–1018.

252 Bencherif, S.A., Srinivasan, A., Horkay, F. et al. (2008). Influence of the degree of methacrylation on hyaluronic acid hydrogels properties. *Biomaterials* 29 (12): 1739–1749.

253 Van Hoorick, J., Declercq, H., De Muynck, A. et al. (2015). Indirect additive manufacturing as an elegant tool for the production of self-supporting low density gelatin scaffolds. *J. Mater. Sci. Mater. Med.* 26 (10): 247.

254 Chaudhuri, O., Gu, L., Klumpers, D. et al. (2016). Hydrogels with tunable stress relaxation regulate stem cell fate and activity. *Nat. Mater.* 15 (3): 326–334.

255 Alsberg, E., Kong, H., Hirano, Y. et al. (2003). Regulating bone formation via controlled scaffold degradation. *J. Dent. Res.* 82 (11): 903–908.

256 West, J.L. and Hubbell, J.A. (1999). Polymeric biomaterials with degradation sites for proteases involved in cell migration. *Macromolecules* 32 (1): 241–244.
257 Vijayavenkataraman, S. (2017). 3D bioprinted skin: the first 'to-be' successful printed organ? *Fut. Med.* 1 (3): 143–144.
258 Rimann, M., Bono, E., Annaheim, H. et al. (2016). Standardized 3D bioprinting of soft tissue models with human primary cells. *J. Lab. Autom.* 21 (4): 496–509.
259 Min, D., Lee, W., Bae, I.H. et al. (2018). Bioprinting of biomimetic skin containing melanocytes. *Exp. Dermatol.* 27 (5): 453–459.
260 Pourchet, L.J., Thepot, A., Albouy, M. et al. (2017). Human skin 3D bioprinting using scaffold-free approach. *Adv. Healthc. Mater.* 6 (4): 1601101.
261 Seol, Y.-J., Lee, H., Copus, J.S. et al. (2018). 3D Bioprinted BioMask for facial skin reconstruction. *Bioprinting (Amsterdam, Netherlands)* 10: e00028.
262 Ng, W.L., Qi, J.T.Z., Yeong, W.Y., and Naing, M.W. (2018). Proof-of-concept: 3D bioprinting of pigmented human skin constructs. *Biofabrication* 10 (2): 025005.
263 Cubo, N., Garcia, M., del Cañizo, J.F. et al. (2016). 3D bioprinting of functional human skin: production and in vivo analysis. *Biofabrication* 9 (1): 015006.
264 Derr, K., Zou, J., Luo, K. et al. (2019). Fully three-dimensional bioprinted skin equivalent constructs with validated morphology and barrier function. *Tissue Eng. Part C Methods* 25 (6): 334–343.
265 Huang, S., Yao, B., Xie, J., and Fu, X. (2016). 3D Bioprinted extracellular matrix mimics facilitate directed differentiation of epithelial progenitors for sweat gland regeneration. *Acta Biomater.* 32: 170–177.
266 Cheng, L., Yao, B., Hu, T. et al. (2019). Properties of an alginate-gelatin-based bioink and its potential impact on cell migration, proliferation, and differentiation. *Int. J. Biol. Macromol.* 135: 1107–1113.
267 Liu, P., Shen, H., Zhi, Y. et al. (2019). 3D Bioprinting and in vitro study of bilayered membranous construct with human cells-laden alginate/gelatin composite hydrogels. *Colloids Surf., B* 181: 1026–1034.
268 Cheung, D.Y., Duan, B., and Butcher, J.T. (2015). Current progress in tissue engineering of heart valves: multiscale problems, multiscale solutions. *Expert Opin. Biol. Ther.* 15 (8): 1155–1172.
269 Duan, B., Kapetanovic, E., Hockaday, L.A., and Butcher, J.T. (2014). Three-dimensional printed trileaflet valve conduits using biological hydrogels and human valve interstitial cells. *Acta Biomater.* 10 (5): 1836–1846.
270 Gaebel, R., Ma, N., Liu, J. et al. (2011). Patterning human stem cells and endothelial cells with laser printing for cardiac regeneration. *Biomaterials* 32 (35): 9218–9230.
271 Gaetani, R., Doevendans, P.A., Metz, C.H.G. et al. (2012). Cardiac tissue engineering using tissue printing technology and human cardiac progenitor cells. *Biomaterials* 33 (6): 1782–1790.
272 Gaetani, R., Feyen, D.A.M., Verhage, V. et al. (2015). Epicardial application of cardiac progenitor cells in a 3D-printed gelatin/hyaluronic acid patch preserves cardiac function after myocardial infarction. *Biomaterials* 61: 339–348.
273 Wang, Z., Lee, S.J., Cheng, H.-J. et al. (2018). 3D bioprinted functional and contractile cardiac tissue constructs. *Acta Biomater.* 70: 48–56.

274 Noor, N., Shapira, A., Edri, R. et al. (2019). 3D Printing of personalized thick and perfusable cardiac patches and hearts. *Adv. Sci.* 6 (11): 1900344.

275 Skylar-Scott, M.A., Uzel, S.G.M., Nam, L.L. et al. (2019). Biomanufacturing of organ-specific tissues with high cellular density and embedded vascular channels. *Sci. Adv.* 5 (9): eaaw2459.

276 Lee, A., Hudson, A., Shiwarski, D. et al. (2019). 3D bioprinting of collagen to rebuild components of the human heart. *Science* 365 (6452): 482–487.

277 Kerscher, P., Kaczmarek, J.A., Head, S.E. et al. (2017). Direct production of human cardiac tissues by pluripotent stem cell encapsulation in gelatin methacryloyl. *ACS Biomater. Sci. Eng.* 3 (8): 1499–1509.

278 Currey, J.D. (2006). *Bones: Structure and Mechanics*. Princeton University Press.

279 Tang, D., Tare, R.S., Yang, L.-Y. et al. (2016). Biofabrication of bone tissue: approaches, challenges and translation for bone regeneration. *Biomaterials* 83: 363–382.

280 Bose, S., Roy, M., and Bandyopadhyay, A. (2012). Recent advances in bone tissue engineering scaffolds. *Trends Biotechnol.* 30 (10): 546–554.

281 Neufurth, M., Wang, X., Schröder, H.C. et al. (2014). Engineering a morphogenetically active hydrogel for bioprinting of bioartificial tissue derived from human osteoblast-like SaOS-$_2$ cells. *Biomaterials* 35 (31): 8810–8819.

282 Duarte-Campos, D.F., Blaeser, A., Buellesbach, K. et al. (2016). Bioprinting organotypic hydrogels with improved mesenchymal stem cell remodeling and mineralization properties for bone tissue engineering. *Adv. Healthc. Mater.* 5 (11): 1336–1345.

283 Wei, L., Wu, S., Kuss, M. et al. (2019). 3D Printing of silk fibroin-based hybrid scaffold treated with platelet rich plasma for bone tissue engineering. *Bioact. Mater.* 4: 256–260.

284 Keriquel, V., Oliveira, H., Rémy, M. et al. (2017). In situ printing of mesenchymal stromal cells, by laser-assisted bioprinting, for in vivo bone regeneration applications. *Sci. Rep.* 7 (1): 1–10.

285 Choe, G., Oh, S., Seok, J.M. et al. (2019). Graphene oxide/alginate composites as novel bioinks for three-dimensional mesenchymal stem cell printing and bone regeneration applications. *Nanoscale* 11 (48): 23275–23285.

286 Lai, Y., Li, Y., Cao, H. et al. (2019). Osteogenic magnesium incorporated into PLGA/TCP porous scaffold by 3D printing for repairing challenging bone defect. *Biomaterials* 197: 207–219.

287 Levato, R., Visser, J., Planell, J.A. et al. (2014). Biofabrication of tissue constructs by 3D bioprinting of cell-laden microcarriers. *Biofabrication* 6 (3): 035020.

288 Gao, G., Schilling, A.F., Hubbell, K. et al. (2015). Improved properties of bone and cartilage tissue from 3D inkjet-bioprinted human mesenchymal stem cells by simultaneous deposition and photocrosslinking in PEG-GelMA. *Biotechnol. Lett.* 37 (11): 2349–2355.

289 Zhang, Y. and Jordan, J.M. (2010). Epidemiology of osteoarthritis. *Clin. Geriatr. Med.* 26 (3): 355–369.

290 Rhee, S., Puetzer, J.L., Mason, B.N. et al. (2016). 3D Bioprinting of spatially heterogeneous collagen constructs for cartilage tissue engineering. *ACS Biomater. Sci. Eng.* 2 (10): 1800–1805.

291 Nguyen, D., Hägg, D.A., Forsman, A. et al. (2017). Cartilage tissue engineering by the 3D bioprinting of iPS cells in a nanocellulose/alginate bioink. *Sci. Rep.* 7 (1): 658.

292 Erickson, I.E., Huang, A.H., Sengupta, S. et al. (2009). Macromer density influences mesenchymal stem cell chondrogenesis and maturation in photocrosslinked hyaluronic acid hydrogels. *Osteoarthr. Cartil.* 17 (12): 1639–1648.

293 Daly, A.C., Critchley, S.E., Rencsok, E.M., and Kelly, D.J. (2016). A comparison of different bioinks for 3D bioprinting of fibrocartilage and hyaline cartilage. *Biofabrication* 8 (4): 045002.

294 Izadifar, Z., Chen, X., and Kulyk, W. (2012). Strategic design and fabrication of engineered scaffolds for articular cartilage repair. *J. Funct. Biomater.* 3 (4): 799–838.

295 Di Bella, C., Fosang, A., Donati, D.M. et al. (2015). 3D Bioprinting of cartilage for orthopedic surgeons: reading between the lines. *Front. Surg.* 2: 39.

296 Marijnissen, W.J.C.M., van Osch, G.J.V.M., Aigner, J. et al. (2000). Tissue-engineered cartilage using serially passaged articular chondrocytes. Chondrocytes in alginate, combined in vivo with a synthetic (E210) or biologic biodegradable carrier (DBM). *Biomaterials* 21 (6): 571–580.

297 Dai, W., Kawazoe, N., Lin, X. et al. (2010). The influence of structural design of PLGA/collagen hybrid scaffolds in cartilage tissue engineering. *Biomaterials* 31 (8): 2141–2152.

298 Yamane, S., Iwasaki, N., Kasahara, Y. et al. (2007). Effect of pore size on in vitro cartilage formation using chitosan-based hyaluronic acid hybrid polymer fibers. *J. Biomed. Mater. Res. A* 81A (3): 586–593.

299 Castilho, M., Mouser, V., Chen, M. et al. (2019). Bi-layered micro-fibre reinforced hydrogels for articular cartilage regeneration. *Acta Biomater.* 95: 297–306.

300 Li, L., Li, J., Guo, J. et al. (2019). 3D Molecularly functionalized cell-free biomimetic scaffolds for osteochondral regeneration. *Adv. Funct. Mater.* 29 (6): 1807356.

301 Duchi, S., Onofrillo, C., O'Connell, C.D. et al. (2017). Handheld co-axial bioprinting: application to in situ surgical cartilage repair. *Sci. Rep.* 7 (1): 1–12.

302 Cui, X., Gao, G., Yonezawa, T., and Dai, G. (2014). Human cartilage tissue fabrication using three-dimensional inkjet printing technology. *JoVE (J. Visual. Exp.)* 88: e51294.

Index

Functional Biomaterials: Design and Development for Biotechnology, Pharmacology, and Biomedicine, First Edition. Edited by Tamilselvan Mohan and Karin Stana Kleinschek.

f

g

h

i

k

l

m

n

o

p

q

y

z